Annalen der Meteorologie

Nr. 25

10th International Cloud Physics Conference Preprints

Volume II

Bad Homburg v. d. H.

15. – 20. August 1988

Offenbach am Main 1988

Im Selbstverlag des Deutschen Wetterdienstes

Die für die Veröffentlichung als Vorabdruck zur 10. Internationalen Konferenz für Wolkenphysik 1988 eingesandten Manuskripte stellen erweiterte Zusammenfassungen der Vorträge dar. Für ihren Inhalt sind die Verfasser verantwortlich. Die Wiedergabe dieser Zusammenfassungen nimmt eine spätere ausführliche Veröffentlichung durch die Autoren an anderer Stelle nicht vorweg.

ISSN 0072-4122
ISBN 3-88148-240-7

Herausgeber und Verlag:
Deutscher Wetterdienst
Frankfurter Str. 135
D-6050 Offenbach am Main

Redaktionsschluß: 10. Mai 1988

International Sponsors

International Association of Meteorology and Atmospheric Physics (IAMAP)

International Commission on Cloud Physics (ICCP)

USAF European Office of Aerospace Research and Development, London

US Army Research Office, London

Sponsors in the Federal Republic of Germany

Ministry for Research and Technology (BMFT)

German Weather Service (DWD)

German Meteorological Society (DMG)

German Aerospace Research Establishment (DFVLR)

The City of Bad Homburg

International Program Committee

Prof. Dr. P. V. Hobbs	(USA), (Chairman)
Dr. A. A. Chernikov	(USSR)
Dr. A. J. Heymsfield	(USA)
Dr. P. Jonas	(UK)
Prof. Dr. Z. Levin	(Israel)
Prof. Dr. R. List	(Canada)
Prof. Dr. H. D. Orville	(USA)
Prof. Dr. H. R. Pruppacher	(FRG)
Prof. Dr. R. G. Soulage	(France)
Dr. T. Takeda	(Japan)
Prof. Dr. B. Zhao	(PRC)

National Organizing Committee

Prof. Dr. H. R. Pruppacher (Chairman)

Prof. Dr. H. W. Georgii

Prof. Dr. H. Grassl

Prof. Dr. F. Herbert

Prof. Dr. E. Raschke

Dr. H. Reiser

Prof. Dr. U. Schumann

TABLE OF CONTENTS

Page

Author Index XXIV

Preface 1

SESSION 1: CLOUD MICROPHYSICS I: LABORATORY STUDIES

THE EFFECT OF CHARGE ON THE COALESCENCE OF SMALL PRECIPITATION DROPS AT TERMINAL VELOCITY 4
H. T. Ochs III, R. R. Czys and J. Q. Feng, Illinois State Water Survey, Champaign, IL, USA

WAKE-EXITED RAINDROP OSCILLATIONS 7
K. V. Beard and H. T. Ochs, Illinois State Water Survey, Champaign, IL, USA

TEMPORAL VARIATIONS OF SNOW CRYSTAL GROWTH PARAMETERS. 9
T. Takahashi, N. Fukuta**, T. Endoh* and G. Wakahama*, *The Institute of Low Temperature Science, Hokkaido University, Sapporo, JAPAN, **University of Utah, Salt Lake City, UT, USA*

EMPIRICAL EQUATIONS OF ICE CRYSTAL GROWTH MICROPHYSICS FOR MODELLING AND ANALYSIS 12
C. R. Redder and N. Fukuta, University of Utah, Salt Lake City, UT, USA

THE CONTRAST STUDY OF NEW MODEL ON ICE CRYSTAL GROWTH. 15
A.-S. Wang, Institute of Atmospheric Physics, Academia Sinica, Beijing, PRC

A WIND TUNNEL STUDY ON THE MELTING OF SNOW FLAKES. 18
S. K. Mitra, O. Vohl, H. R. Pruppacher, Johannes Gutenberg-Universität, Mainz, FRG

EVAPORATION AND MELTING OF ICE CRYSTALS: A LABORATORY STUDY 22
R. G. Oraltay and J. Hallett, Desert Research Institute, Reno, NV, USA

A NEW MECHANISM FOR ICE INITIATION IN WARM-BASED MIDWESTERN CUMULI 25
R. R. Czys, Illinois State Water Survey, Champaign, IL, USA

SPREADING OF SUPERCOOLED WATER DROPLETS ON AN ICE SURFACE 28
Y. Dong and J. Hallett, Desert Research Institute, Reno, NV, USA

A MODEL OF THE ELECTROSTATIC-AERODYNAMIC SHAPE OF RAINDROPS 31
C. Chuang and K. V. Beard, University of Illinois, Urbana, IL, USA

SESSION 2: CLOUD MICROPHYSICS II: FIELD MEASUREMENTS AND THEORY

MEASUREMENTS OF THE PARTITIONING OF AEROSOL MASS AND NUMBER BETWEEN CLOUD DROPLETS AND INTERSTITIAL AIR 34
J. Ogren, J. Heintzenberg and K. Noone, University of Stockholm, Stockholm, SWEDEN

THE CALCULATION OF SUPERSATURATIONS AND GROWTH OF DROPLETS IN CONTINENTAL CUMULUS CLOUDS 37
K. N. Bower and T. W. Choularton, UMIST, Manchester, UK

ON THE OBSERVATIONS OF CLOUD TEMPERATURE AND LIQUID WATER CONTENT USING A LYMAN-α AND AN FSSP SENSOR. 40
J. B. Jensen and D. Baumgartner, NCAR, Boulder, CO, USA and G. B. Raga, University of Washington, Seattle, WA, USA

EVALUATION OF DROPLET GROWTH RATES IN HAWAIIAN OROGRAPHIC CLOUDS. 43
D. Baumgartner, NCAR, Boulder, CO, USA

STUDIES OF WARM-RAIN DEVELOPMENT..... 46
W. A. Cooper, NCAR, Boulder, CO, USA

RADAR OBSERVATIONS AND MODELLING OF WARM RAIN INITIATION..... 49
A. J. Illingworth and I. J. Caylor, UMIST, Manchester, UK

A TEST OF ICE CRYSTAL PRODUCTION BY AIRCRAFT..... 52
G. Vali, R. D. Kelly and F. Serrano, University of Wyoming, Laramie, WY, USA

AIRBORNE STUDIES OF THE ICE PHASE IN MARITIME CLOUDS AROUND THE BRITISH ISLES..... 55
P. R. A. Brown, Meteorological Office, Bracknell, Berkshire, UK and T. W. Choularton, UMIST, UK

PRECIPITATION INITIATION MECHANISMS IN CLOUDS OVER NORTH INDIA..... 58
R. N. Chatterjee, P. Prakash, G. Singh and R. K. Kapoor, Indian Institute of Tropical Meteorology, Pune, INDIA

EVIDENCE OF PREFERENTIAL ZONES OF ICE MULTIPLICATION BY SPLINTERING IN CONVECTIVE CELLS..... 62
J.-F. Gayet, C. Duroure and R. G. Soulage, LAMP, Aubière, FRANCE

MICROPHYSICAL CHARACTERISTICS OF WARM-BASED CUMULI: OBSERVATIONS AT −10° C..... 64
R. R. Cyzs, Illinois State Water Survey, Champaign, IL, USA

SESSION 3: CLOUD MICROPHYSICS III. ENTRAINMENT AND MIXING

A COMPARATIVE STUDY OF LABORATORY THERMALS AND ATMOSPHERIC CLOUDS..... 67
H. Johari, G. Taylor**, M. Baker** and R. Breidenthal*, *Dept. of Aeronautics and Astronautics, **Geophysics Program, University of Washington, Seattle, USA*

ENTRAINMENT AND FINE-SCALE (MOLECULAR) MIXING..... 70
I. R. Paluch and D. G. Baumgardner, NCAR, CO, USA

AIRBORNE STUDIES OF THE INFLUENCE OF ENTRAINMENT ON THE VERTICAL AND HORIZONTAL MICROPHYSICAL STRUCTURE OF SMALL CUMULUS CLOUDS..... 73
J. Latham, UMIST, Manchester, UK, and A. M. Blyth, New Mexico Institute of Mining & Technology, Socorro, NM, USA

ENTRAINMENT SITES, MIXING PROCESSES IN WARM CONVECTIVE CLOUDS. EFFECT ON DROPLET GROWTH..... 76
E. Hicks, A. Rigaud, J. Gagneux, C. Pontikis, Météorologie Nationale EERM/CRPA, Magny les Hameaux, FRANCE

STRUCTURE OF UPPER CLOUDS BOUNDARY USING THE LIDAR DATA..... 79
V. E. Zuev, V. S. Shamanaev, I. E. Penner and I. V. Samokhvalov, Institute of Atmospheric Optics, Siberian Branch USSR Academy of Sciences, Tomsk, USSR

TURBULENT TRANSPORT PROCESSES WITHIN AND BELOW SMALL CUMULUS CLOUDS..... 82
A. M. Jochum, Institut für Physik der Atmosphäre, DFVLR, Oberpfaffenhofen, FRG

INSTABILITY THEORY IN CLOUDS AND THE PARAMETRIZATION OF EDDY VISCOSITY COEFFICIENTS..... 85
Y. Takaya, Meteorological Research Institute, Tsukuba, JAPAN

THREE DIMENSIONAL CUMULUS ENTRAINMENT STUDIES..... 88
T. L. Clark, P. K. Smolarkiewicz and W. D. Hall, NCAR, Boulder, CO, USA

HETEROGENEOUS MIXING MEASUREMENTS IN SMALL NON PRECIPITATING CUMULI..... 91
J. L. Brenguier, Direction de la Météorologie National EERM/CNRM, Toulouse Cedex, FRANCE

SESSION 4: CLOUD MICROPHYSICS IV: NUMERICAL MODELING

THE CASE FOR SUBGRID-SCALE CONDENSATION IN NUMERICAL CLOUD MODELS..... 94
F. B. Lipps and R. S. Hemler, Princeton University, Princeton, NJ, USA

THE EFFECT OF TURBULENCE ON THE COLLECTION OF CLOUD DROPS: A STOCHASTIC MODEL..... 97
G. W. Reuter, McGill University, Montreal, CANADA

THE EFFECT OF ICE PHYSICAL PROCESSES ON THE NUMERICAL SIMULATION OF WEST AFRICAN SQUALL LINES..... 100
W. D. Hall, NCAR, Boulder, CO, USA, and J. P. Lafore, CNRM, Toulouse, FRANCE

NUMERICAL SIMULATION OF MICROPHYSICAL PROCESSES IN CUMULONIMBUS..... 103
Z. Hu and G. He, Academy of Meteorological Sciences, Beijing, PRC

A COMPARATIVE STUDY OF TWO MICROPHYSICAL SCHEMES IN A β MESOSCALE MODEL..... 106
E. Richard and N. Chaumerliac, LAMP, OPGC, Clermont-Ferrand, FRANCE

GENERALIZED MICROPHYSICS SCHEME FOR USE IN MESOSCALE/CLOUD MODELS..... 109
G. J. Tripoli, University of Wisconsin, Madison, WI, USA, and P. J. Flatau and W. R. Cotton, Colorado State University, Fort Collins, CO, USA

THE STUDY OF NUMERICAL SIMULATION ON THE FORMATION OF THE CLOUD DROPLET SPECTRA IN CUMULUS CLOUDS..... 112
H. Xiao, H. XU, and M. Huang, Institute of Atmospheric Physics, Academia Sinica, Beijing, PRC

SESSION 5: CLOUDS AND RADIATION

SOME OUTSTANDING PROBLEMS ON THE INFLUENCE OF CLOUDS ON RADIATION..... 115
G. L. Stephens, Colorado State University, Fort Collins, CO, USA

THEORY ON THE UNCERTAINTY IN CLOUD MICROPHYSICAL PROCESSES AND CLIMATE..... 118
K. N. Liou and S. C. Ou, University of Utah, Salt Lake City, UT, USA

IN SITU MEASUREMENTS OF "SHIP TRACKS"..... 121
L. F. Radke, J. H. Lyons and P. V. Hobbs, University of Washington, Seattle, USA, and J. E. Coakley, NCAR, Boulder, CO, USA

RADIATION INDUCES GROWTH AND EVAPORATION OF DROPLETS IN BOUNDARY LAYER CLOUDS..... 124
R. Davies, McGill University, Montreal, Quebec, CANADA

CLOUD AND AEROSOL OPTICAL DEPTHS: PRELIMINARY RESULTS FROM FIFE..... 125
R. F. Pueschel, P. B. Russell*, T. P. Ackerman**, D. S. Colburn*, R. C. Wrigley*, M. A. Spanner***, and J. M. Livingston****,*
**NASA, Ames Research Center, Moffett Field, CA, USA,*
***Pennsylvania State University, PA, USA,*
****TGS Technology, Moffett Field, CA, USA,*
*****SRI International, Menlo Park, CA, USA*

AN OBSERVATIONAL STUDY OF RADIATIVELY DRIVEN CONVECTION..... 127
S. Nicholls, Meteorological Office, Bracknell, Berkshire, UK

RADIATIVE INFLUENCES ON PRECIPITATING MESOSCALE SYSTEMS..... 130
W. R. Cotton and S. Chen, Colorado State University, Fort Collins, CO, USA, and G. Tripoli, University of Wisconsin, Madison, WI, USA

CIRRUS MICROPHYSICS AND INFRARED RADIATIVE TRANSFER: A CASE STUDY. 133
T. P. Ackerman, A. J. Heymsfield**, F. P. J. Valero*** and St. Kinne****
**Dept. of Meteorology, Pennsylvania State University, PA, USA*
***NCAR, Boulder, CO, USA,*
****NASA, Ames Research Center, Space Science Division Moffett, CA, USA*

POSTER SESSION A: CLOUD MICROPHYSICS AND CHEMISTRY

THE COLLECTION EFFICIENCY OF A MASSIVE FOG COLLECTOR. 135
R. S. Schemenauer and P. I. Joe, Atmospheric Environment Service, Downsview, Ontario, CANADA

THE USE OF AUTOMATIC PARTICLE RECOGNITION TO IMPROVE THE DETERMINATION OF BULK QUANTITIES FROM PMS 2-D PROBE DATA IN CIRRUS. 138
A. G. Darlison and P. R. A. Brown, Meteorological Office, Bracknell, Berkshire, UK

THE COMPARISON OF HOLOGRAPHIC AND 2-D PROBE MEASUREMENTS OF ICE CRYSTALS. 141
P. R. A. Brown and A. G. Darlison, Meteorological Office, Bracknell, Berkshire, UK

DEVELOPMENT OF HYDROMETEOR VIDEO SONDE. 144
M. Murakami and T. Matsuo, Meteorological Research Institute, Tsukuba, JAPAN

THE STUDY OF THE INTERSTITIAL AEROSOL PARTICLES AND CLOUD DROPLETS WITH DIGITAL IMAGE ANALYSIS OF DIFFRACTION IMAGES. 148
R. Jaenicke and R. Sörensen, University of Mainz, Mainz, FRG

ON THE DETERMINATION OF DROPLET SIZE DISTRIBUTIONS WITH THE CONTERFLOW VIRTUAL IMPACTOR. 151
B. Johansson and J. Heintzenberg, University of Stockholm, Stockholm, SWEDEN

MULTIPARAMETER CHARACTERIZATION OF RAINDROP SIZE DISTRIBUTION BY THE POLARIMETRIC DFVLR RADAR: FIRST RESULTS. 154
M. Chandra, A. Schroth and E. Lüneburg, DFVLR, Institut für HF-Technik, Weßling, FRG

AN INVESTIGATION OF THE EFFECT OF ELECTRICAL CHARGES ON THE COLLISION EFFICIENCY OF CLOUD DROPS. 158
V. M. Kim, Institute of Experimental Meteorology, Obninsk, USSR

MICROPHYSICAL AND ELECTRICAL PHENOMENA DURING FREEZING OF WATER DROPS. 161
A. Kh. Adzhiev and S. T. Tomazov, High Mountain Geophysical Institute, Nalchik, USSR

A DESCRIPTION OF CONDENSATION PROCESSES IN A TURBULENT THREE-PHASE CLOUD. 164
L. N. Novosyolov and A. S. Stepanov, Institute of Experimental Meteorology, Obninsk, USSR

EFFECT OF THE ELECTRIC FIELD ON THE RAINDROP SHAPE. 166
G. G. Magradze, Academy of Sciences of the Georgian SSR, Tbilisi, USSR

DAMPED OSCILLATION REPRESENTATION OF DROP-SPECTRUM EVOLUTION DUE TO COALESCENCE AND BREAKUP. 169
P. S. Brown, Trinity College, Hartford, CT, USA

KINETIC EQUATION FOR POLLUTED CLOUD DROPLET SPECTRUM. 172
I. M. Enukashvily, Israel Meteorological Service, Bet-Dagan, ISRAEL

LIQUID WATER CONTENT, MEDIAN VOLUME DIAMETER, AND TEMPERATURE IN DEPENDENCE ON THE HEIGHT ABOVE THE CLOUD BASE FOR DIFFERENT TYPES OF CLOUDS. 175
H.-E. Hoffmann and R. Roth, DFVLR-Oberpfaffenhofen, Institut Physik der Atmosphäre, Weßling, FRG

A DETAILED EXAMINATION OF DISCONTINUITIES IN NATURAL RAIN SPECTRA. 178
H. C. Vaughan, Iowa State University, Ames, IA, USA

CRYSTALLIZATION OF SUPERCOOLED SOLUTIONS. 180
K. Harrison and J. Hallett, Desert Research Institute, Reno, NV, USA

KINETICS OF ICE CRYSTAL FORMATION ON AEROSOL PARTICLES IN SUPERCOOLED FOG. 183
B. Z. Gorbunov, A. E. Paschenko and H. Kakutkina, Institute of Chem. Kinetics and Combustion, Novosibirsk, USSR

ABOUT SECONDARY ICE CRYSTAL PRODUCTION. 185
T. G. Gzirishvili and V. G. Khorguany, Academy of Sciences of the Georgian SSR, Tbilisi, USSR

EXPERIMENTAL STUDIES ON SECONDARY ICE PARTICLE PRODUCTION. .. 188
A. Yamashita, H. Konishi, W. Shimada, M. Miyatake and K. Tani, Osaka Kyoiku University, Osaka, JAPAN

PROPORTION OF RIMING GROWTH PROCESS IN SNOWFALL PHENOMENA. 190
T. Harimaya and M. Sato, Hokkaido University, Sapporo, JAPAN

THREE-DIMENSIONAL STRUCTURES OF SNOW CRYSTALS SHOWN BY STEREO-PHOTOMICROGRAPHS. 193
K. Iwai, Shinshu University, Nagano, JAPAN

ON THE VARIATION OF FALLING VELOCITY OF EARLY SNOWFLAKES. 196
M. Kajikawa, Akita University, Akita, JAPAN

A PARAMETERIZATION SCHEME FOR THE COALESCENCE OF WATER DROPS USING THE STOCHASTIC COLLECTION EQUATION. 199
C. Lüpkes, K. D. Beheng and G. Doms, Johann Wolfgang Goethe-Universität, Frankfurt am Main, FRG

ON THE DYNAMICS OF THE FALLING ICE CRYSTAL ZONE. 202
J. Podzimek, University of Missouri, Rolla, MO, USA

A NEW DATABASE OF ICE PARTICLE SIZE SPECTRA FOR ALTITUDES UP TO 10 KM, (30,000 FT). 205
R. K. Jeck, Naval Research Laboratory, Washington, DC, USA

A VERTICAL WIND TUNNEL FOR THE STUDY OF SNOWFLAKES AND EFFECTS OF ACCUMULATED SNOW ON MATERIALS. 208
K. Isono, Nagoya University, Tokyo, JAPAN; J. Kobayashi, Japan Weather Association, Tokyo; JAPAN; T. Gonda, Science University of Tokyo, Chiba, JAPAN; Y. Sasyo, and T. Mori, Suga Test Instruments Co. Ltd.; JAPAN

PROPERTIES OF THE PRECIPITATION EMBRYOS EVOLUTION IN CHARACTERISTIC HAWAIIAN BANDCLOUDS. 211
A. Rigaud, E. Hicks, J. Gagneux and C. Pontikis, Direction Météorologique Nationale EERM/CRPA, Magny les Hameaux, FRANCE

PATTERN OF AIR BUBBLE INCLUSIONS IN ATMOSPHERIC ICE FORMED DURING ACCRETION GROWTH. 214
P. Gribelin, P. Personne and H. Isaka, LAMP, Aubière, FRANCE

ANALYSIS OF HAILSTONES FROM A SEVERE STORM AND THEIR SIMULATED EVOLUTION. 217
L. Levi, Consejo Nacional de Investigaciones Cientificas y Tēcnicas, ARGENTINA, and L. Lubart, Servicio Meteorológico Nacional, Buenos Aires, ARGENTINA

THE COLLECTION EFFICIENCIES OF SOFT-HAILSTONES FOR SUPER-COOLED WATER DROPLETS AND ICE CRYSTALS. 220
W. D. Keith and C. P. R. Saunders, UMIST, Manchester, UK

SIMULATION OF CONICAL GRAUPEL BY USING A BALLISTIC MODEL. 223
P. Personne, Chr. Duroure and H. Isaka, LAMP, Aubière, FRANCE

COMPARISON OF MODEL RESULTS FOR MODELS OF DIFFERING MICROPHYSICAL DETAIL..... 226
R. D. Farley and H. D. Orville, South Dakota School of Mines and Technology, Rapid City, SD, USA

AIRBORNE "CLOUD SIEVING"..... 229
E. E. Hindman, Physics and Atmospheric Science Department, Drexel University, PA, USA

CLOUD CAPTURE BY A MOUNTAIN TOP FOREST: ACIDITY AND DOSAGE DURATION. 232
V. K. Saxena and N.-H. Lin, North Carolina State University, Raleigh, NC, USA

DETERMINATION OF CHEMICAL REACTION RATES IN FOG. 235
R. Dlugi and W. Seidl, Meteorologisches Institut der Universität München, Munich, FRG

INSOLUBLE PARTICLES IN HYDROMETEORS. 238
M. Krämer and L. Schütz, University of Mainz, FRG

BELOW CLOUD SCAVENGING BY RAIN AND DRIZZLE. 241
B. T. McGann and S. G. Jennings, University College, Galway, IRELAND

STUDIES OF CLOUD MICRO-CHEMICAL PHYSICS. 243
R. L. Pitter and W. G. Finnegan, Desert Research Institute, Reno, NV, USA

KINETICS AND MECHANISM OF THE Fe-CATALYZED AUTO-OXIDATION OF S(IV)-OXIDES IN AQUEOUS SOLUTION. 246
J. Kraft, M. Dellert, P. Braun and R. Van Eldik, University of Witten/Herdecke, FRG

THE EFFECT OF AEROSOLS ON THE pH OF SNOWFALLS..... 249
M. Kumai, U.S. Army Cold Regions Research and Engineering Laboratory, Hannover, NH, USA

IONIC CONCENTRATIONS OF RIME ICE AND SNOW AND BERGERON PROCESS..... 251
S. H. Huang, Nanjing University, Nanjing, PRC, R. A. Castillo, Western Connecticut State University, Danbury, CT, USA, and V. A. Monhen, ASCR, SUNY, NY, USA

CHEMICAL NATURE OF PRECIPITATION AT VISAKHAPATNAM. 254
S. Nizamuddin, Andhra University, Waltair, INDIA

A ONE-DIMENSIONAL NUMERICAL MODEL TO SIMULATE LIQUID PHASE CHEMICAL REACTIONS WITHIN RADIATION FOG. 255
R. Forkel and W. Seidl, Meteorologisches Institut der Universität München, Munich, FRG

SESSION 6: CLOUD CHEMISTRY AND ACIDIC PRECIPITATION I: MEASUREMENTS

THE EFFECT OF FREEZING ON THE COMPOSITION OF CLOUD DROPLETS. 258
J. V. Iribarne and T. Pyshnov, University of Toronto, Toronto, Ontario, CANADA

SOME EFFECTS OF CLOUD MICROPHYSICS ON CLOUD CHEMISTRY..... 261
D. A. Hegg and P. V. Hobbs, University of Washington, Seattle, WA, USA

PROCESSES DETERMINING CLOUDWATER COMPOSITION: FIELD EVIDENCE FOR INCLOUD REACTIVE SCAVENGING OF SO_2..... 264
P. H. Daum, Brookhaven National Laboratory, Upton, NY, USA

ACIDIFICATION OF STRATIFORM CLOUDS AND THEIR AEROSOL SCAVENGING PROPERTIES. 267
R. A. Castillo, Western Connecticut State University, Danbury, CT, USA, and J. Deluisi, NOAA, Boulder, CO, USA

MICROPHYSICAL, DYNAMICAL AND CHEMICAL ASPECTS OF SCAVENGING PROCESSES DURING WINTER PRECIPITATION. 270
A. Waldvogel, T. Schumann and B. Zinder, Atmospheric Physics ETH, Zürich, SWITZERLAND

VERTICAL PROFILES OF POLLUTANTS INSIDE AND OUTSIDE OF CLOUD. .. 273
G. A. Isaac and W. R. Leaitch, Atmospheric Environment Service, Downsview, Ontario, CANADA

RESULTS OF TIME AND HEIGHT RESOLVED SCAVENGING EXPERIMENTS. 276
L. Kins, Universität München, Munich, FRG, and F. X. Meixner, Fraunhofer Institut für Atmosph., Garmisch-Partenkirchen, FRG, and K. P. Müller, Kernforschungsanlage Jülich, Institut für Atmosph. Chemie, Jülich, FRG

OXIDATION REGIMES IN OROGRAPHIC CAPPING CLOUD. 279
P. A. Clark, G. P. Gervat, T. A. Hill, and A. R. W. Marsh, Central Electricity Research Laboratories, Leatherhead, Surrey, UK, and A. S. Chandler, T. W. Choularton, and M. J. Gay, UMIST, Manchester, UK

AN EXAMINATION OF THE CHEMICAL AND PHYSICAL VARIABILITY OF CLOUDS AT A MOUNTAIN-TOP SITE IN CENTRAL SWEDEN. 282
K. J. Noone, J. A. Ogren and J. Heintzenberg, Stockholm University, Stockholm, SWEDEN

INFLUENCES OF CLOUD MICROPHYSIC ON CONTINENTAL AND MARINE PRECIPITATION CHEMISTRY. 285
F. Parungo and C. Nagamoto, NOAA/ERL, Boulder, CO, USA

CONCENTRATIONS IN RAIN EVENTS COLLECTED SEQUENTIALLY: MEASUREMENTS VERSUS RESULTS OF A SIMPLE SCAVENGING MODEL. 288
J.-L. Jaffrezo and J.-L. Colin, Université Paris, Paris Cedex, FRANCE

EXPERIMENTS ON MICROPHYSICS AND CHEMISTRY OF RADIATION FOGS. 291
K. H. Enderle, H. Obenland, and W. Jaeschke, Johann Wolfgang-Goethe Universität, Frankfurt am Main, FRG

SESSION 7: CLOUD CHEMISTRY AND ACIDIC PRECIPITATION II: NUMERICAL MODELING

CHEMICAL EVOLUTION WITHIN A CLOUD MODEL FEATURING A POLYDISPERSE DROPLET SIZE SPECTRUM. 294
T. A. Hill, UMIST, Manchester, UK

MODELING STUDIES ON THE FORMATION, GROWTH, DISSIPATION, AND ACIDIFICATION OF CUMULUS CLOUDS. 297
S. K. Nair and L. K. Peters, University of Kentucky, Lexington, KY, USA

A NUMERICAL INVESTIGATION OF SULFATE PRODUCTION AND DEPOSITION IN MIDLATITUDE CONTINENTAL CUMULUS CLOUDS. 300
G. Taylor, University of Washington, Seattle, WA, USA

A NUMERICAL SIMULATION OF THE ACIDIFICATION PROCESS OF RAIN WATER BELOW THE CLOUD AND THE MECHANISM OF ACID RAIN FORMATION IN AREA OF CHONGQING. 303
M. Huang and S. Liu, Institute of Atmospheric Physics, Academia Sinica, Beijing, PRC

EFFECTS OF CLOUD MICROPHYSICAL PROCESSES ON TRACE CHEMICAL REMOVAL EFFICIENCIES. 306
D. Lamb and J. P. Chen, The Pennsylvania State University, University Park, PA, USA

DYNAMIC, RADIATIVE AND CHEMICAL EFFECTS OF CLOUDS ON TROPOSPHERIC TRACE GASES. 309
C. J. Walcek, SUNY, Albany, NY, USA

PARAMETERIZATIONS OF MICROPHYSICAL PROCESSES IN CLOUDS FOR APPLICATION IN MODELS OF REGIONAL ATMOSPHERIC DEPOSITION..... 312
I. Y. Lee, Argonne National Laboratory, Argonne, IL, USA

A MODEL OF WET DEPOSITION TO COMPLEX TERRAIN BY THE SEEDER-FEEDER PROCESS..... 316
A. Jones and T. W. Choularton, UMIST, Manchester, UK

METEOROLOGICAL AND CHEMICAL INFLUENCING FACTORS ON ACIDITY PRODUCTION IN A MESOSCALE MODEL WITH QUASI-SPECTRAL MICROPHYSICS..... 319
N. Chaumerliac and R. Rosset, LAMP, Aubière, FRANCE

SESSION 8: INSTRUMENTATION

A COMPARISON OF RADIOMETRIC AND IMMERSION TEMPERATURE MEASUREMENTS IN WATER CLOUDS..... 322
S. Nicholls, E. L. Simmons, N. C. Atkinson and S. D. Rudman, Meteorological Office, Bracknell, Berkshire, UK

CALIBRATION OF PMS FSSP AND 1D-C PROBES FOR CLOUD DROPLET MEASUREMENTS..... 325
J.-F. Gayet, LAMP, Aubière, FRANCE

RADAR OBSERVATIONS OF PRECIPITATION MICROSTRUCTURE: THE MORPHOLOGY OF LINEAR DEPOLARIZATION MEASUREMENTS IN CLOUD..... 328
P. H. Herzegh, NCAR, Boulder, CO, USA, and A. R. Jameson, Applied Research Corporation, Landover, MD, USA

MULTIPARAMETER DOPPLER RADAR OBSERVATIONS OF A SQUALL LINE WITH THE POLARIMETRIC DFVLR RADAR..... 330
P. Meischner, V. N. Bringi and T. Jank; DFVLR-Oberpfaffenhofen, Weßling, FRG

A POOR MANS OPTICAL FOG DETECTOR..... 333
R. K. A. M. Mallant, Netherlands Energy Research Foundation, ECN, Petten, THE NETHERLANDS

APPLICATIONS OF THE NCAR ELECTRA DOPPLER RADAR FOR THE STUDY OF PHYSICAL PARAMETERS OF CLOUDS..... 335
C. Walther, C. Frush and P. Hildebrand, NCAR, Boulder, CO, USA

INTERCOMPARISONS OF AIRCRAFT MEASUREMENTS WITH LIDAR RETURNS FROM AEROSOL, ICE CRYSTALS, AND WATER DROPLETS..... 338
W. R. Leaitch and R. M. Hoff, Atmospheric Environment Service, Downsview Ontario, CANADA, and A. I. Carswell, S. Pal and G. A. Cunningham, York University, Downsview, Ontario, CANADA

A NEW AIRBORNE DEVICE FOR MEASUREMENT OF CLOUD PARTICLES USING VIDEO-MICROSCOPE..... 341
T. Tanaka, T. Matsuo, K. Okada, and I. Ichimura, Meteorological Research Institute, Ibaraki, JAPAN, and S. Ichikawa and A. Tokuda, Sankei Co. Ltd., JAPAN

SESSION 9: OROGRAPHIC CLOUDS

ON THE SMALL SCALE TOPOGRAPHICAL INFLUENCES ON PRECIPITATION..... 344
W. W. Grabowski, Polish Academy of Science, Warsaw, POLAND

A NUMERICAL INVESTIGATION OF AN OROGRAPHIC PRECIPITATION EVENT..... 347
M. P. Meyers and W. R. Cotton, Colorado State University, Fort Collins, CO, USA

COMPLEX MICROPHYSICAL INTERACTIONS WITHIN A CENTRAL SIERRA NEVADA OROGRAPHIC CLOUD SYSTEM..... 350
R. M. Rauber, University of Illinois, Urbana, IL, USA

COMPARISON OF OROGRAPHIC CLOUD AND PRECIPITATION DEVELOPMENT OF THREE DIFFERENT GEOGRAPHIC LOCATIONS USING A 3-D NESTED GRID CLOUD MODEL. 353
R. M. Rasmussen, Bureau of Reclamation, Denver, CO, USA, and P. Smolarkiewicz, W. D. Hall and T. Clark, NCAR, Boulder, CO, USA

MICROPHYSICAL OBSERVATIONS OVER THE ATLAS MOUNTAINS IN MAROCCO. 356
O. Baddour, Météorologie Nationale, Casablanca, Royaume du Maroc, and R. M. Rasmussen, Bureau of Reclamation, Denver, CO, USA

MICROPHYSICAL AND DYNAMICAL INTERACTIONS IN COLORADO FRONT RANGE UPSLOPE STORMS. 359
D. A. Wesley, M. J. Weisbluth, R. A. Pielke and W. R. Cotton, Colorado State University, Fort Collins, CO, USA

CHARACTERISTICS OF RADAR ECHO OF A SNOWBAND FORMED IN THE LEE SIDE OF A MOUNTAIN. 362
Y. Fujiyoshi, T. Endoh and G. Wakahama, Institute of Low Temperature Science, Hokkaido University, Sapporo, JAPAN

POSTER SESSION B: CLOUD MACROPHYSICS

STUDY ON CLOUD AND RAIN PROCESS BY MICROWAVE RADIOMETER OBSERVATION. 364
B. Zhao, Peking University, Beijing, PRC

A NEW DROPSONDE FOR CLOUD PROBINGS. 366
D. E. Gaytandjiev, Hydrometeorological Service, Sofia, BULGARIA

HUMIDITY MEASUREMENTS DURING CLOUD FORMATION USING INFRARED HYGROMETRY. 369
P. J. DeMott and D. C. Rogers, Colorado State University, Fort Collins, CO, USA

IDENTIFICATION OF PRECIPITATION PARTICLES USING DUAL POLARIZATION RADAR. 372
A. J. Illingworth and I. J. Caylor, UMIST, Manchester, UK

Z-R RELATIONS FORM AIRBORNE 2D-P MEASUREMENTS IN HAWAIIAN SHOWERS. 375
R. J. Kubesh, K. V. Beard and D. B. Johnson, Illinois State Water Survey, Champaign, IL, USA

COMPARISON BETWEEN AIRCRAFT AND DOPPLER RADAR MEASUREMENTS DURING ENCC (VOVES 1983). 378
H. Sauvageot, Laboratoire Aérologie Campistrous, FRANCE, and A. Rigaud, E. Hicks and C. Pontikis, Météorologie Nationale EERM/CRPA, Magny les Hameaux, FRANCE

EHF ATTENUATION THROUGH THE MELTING LAYER 380
A. J. Barnes, Jr., Air Force Geophysics Laboratory, Hanscom AFB, MA, USA

SIZE DISTRIBUTION OF PRECIPITATION PARTICLES IN MIDLATITUDE MESOSCALE CONVECTIVE COMPLEXES. 383
J. D. Yeh, B. F. Fan and W. R. Cotton, Colorado State University, Fort Collins, CO, USA

A PRELIMINARY RESEARCH ON THE RADIATION FOG IN XISHUANG BANNA 386
Y. Huang, W. Xu, Meteorological Bureau of Yunnan Province, Yunnan, PRC, Z. Li, W. Huang, L. Fan, Nanjing Institute of Meteorology, Nanjing, PRC

THE BASIC CHARACTERISTICS OF THE WINTER NORTHERN XINJIANG STRATIFORM CLOUD SYSTEM 389
Z. Gao and J. Zhang, Weather Modification Office, Xinjiang, PRC

THE RAINFALL ENHANCEMENT BY TWO LAYER CLOUD STRUCTURE OBSERVED AT OROFURE MOUNTAIN RANGE, HOKKAIDO, JAPAN 393
K. Kikuchi, K. Iwanami and T. Taniguchi, Hokkaido University, Sapporo, Japan

NUMERICAL SIMULATION OF COASTAL CLOUDS WHEN SOLAR RADIATION IS BLOCKED BY SMOKE 396
C. R. Molenkamp, Lawrence Livermore National Laboratory, Livermore, CA, USA

LONG-LIVED HAWAIIAN RAIN BANDS 398
P. Smolarkiewicz, and T. L. Clark, NCAR, Boulder, CO, USA, and R. Rasmussen, Bureau of Reclamation, Denver, CO, USA

A LONG-LASTING RAINSTORM TRAVELLING ALONG A STATIONARY FRONT 401
H. Sakakibara and A. Tabata, Meteorological Research Institute, Ibaraki, JAPAN

THREE-DIMENSIONAL AIRFLOW AND VORTICITY BUDGET OF RAINBANDS IN A WARM OCCLUSION 404
O. Hertzman and P. V. Hobbs, University of Washington, Seattle, WA, USA

DOPPLER RADAR OBSERVATION OF CONVERGENCE BAND CLOUD FORMED ON THE WEST COAST OF HOKKAIDO ISLAND, JAPAN 407
Y. Fujiyoshi, K. Tsuboki and G. Wakahama, Institute of Low Temperature Science, Hokkaido University, Sapporo, JAPAN

THE USE OF OXYGEN ISOTOPES IN STUDIES OF ICE PHASE PRECIPITATION FROM WINTER STORMS 410
B. Demoz, J. A. Warburton and R. L. Stone, Desert Research Institute, Reno, NV, USA

NUMERICAL SENSITIVITY STUDY OF THE MORPHOLOGY OF LAKE-EFFECT SNOW STORMS OVER LAKE MICHIGAN 413
M. Hjelmfelt, NCAR, Boulder, CO, USA

DOPPLER RADAR OBSERVATIONS OF SNOW PARTICLES IN WINTER CONVECTIVE CLOUDS 416
H. Konishi, Osaka Kyoiku University, Osaka, Japan, and T. Endoh and G. Wakahama, Institute of Low Temperature Science, Hokkaido University, Sapporo, JAPAN

THE RELATIONSHIP BETWEEN ENTRAINMENT RATE AND SOME PRODUCTS OF 1-D Cb MODEL 419
M. Curic and D. Janc, University of Belgrad, Beograd, YUGOSLAVIA

ON THE ENTRAINMENT IN CUMULI – A CONTRIBUTION TO A CASE STUDY 422
I. Nemesova, Institute of the Physics of the Atmosphere, Prague, CZECHOSLOVAKIA

A FINE RESOLUTION TWO-DIMENSIONAL NUMERICAL STUDY OF A CLOUD-CAPPED BOUNDARY LAYER 425
M. K. MacVean and S. Nicholls, Meteorological Office, Bracknell, Berkshire, UK

A NUMERICAL METHOD FOR INTEGRATING THE THERMAL CONVECTION EQUATIONS IN THE ATMOSPHERE 428
I. M. Enukashvily, Israel Meteorological Service, Bet-Dagan, ISRAEL

A DIAGNOSTIC STUDY OF VERTICAL FLUXES IN CUMULUS CLOUDS USING MODEL OUTPUT DATA 431
M. J. Weissbluth and W. R. Cotton, Colorado State University, Fort Collins, CO, USA

EFFICIENCY OF DEEP CONVECTIVE CLOUDS RELATED WITH SOME PARAMETERS OF OCCURRENCE OVER THE ARGENTIN TERRITORY 434
M. E. Saluzzi, Universidad de Buenos Aires, Conicet, Buenos Aires, ARGENTINA

CHARACTERISTICS OF MESOSCALE CLOUD SYSTEMS DEVELOPED IN THE MARITIME SUBTROPICS 437
M. Ishihara, A. Tabata, K. Akaeda, T. Yokoyama and H. Sakakibara, Meteorological Research Institute, Ibaraki, JAPAN

ON THE MERGER OF TWO SMALL CONVECTIVE RADAR ECHOES 440
B. Ackerman and P. C. Kennedy, Illinois State Water Survey, Champaign, IL, USA

MULTIPLE DOPPLER RADAR OBSERVATIONS OF AIRFLOW FIELDS DURING CONVECTIVE ECHO MERGERS 443
P. C. Kennedy, Illinois State Water Survey, Champaign, IL, USA

RESULTS FROM WARM RAIN STUDIES IN PENANG, MALAYSIA 446
R. List, D. Hudak and R. Nissen, University of Toronto, Toronto, Ontario, CANADA, and N. P. Tung, S. K. Soo and T. S. Kang, Malaysian Meteorological Service, Petaling Jaya, MALAYSIA

THE KINEMATICS OF MESO-GAMMA SCALE PRECIPITATION SYSTEMS 449
P. I. Joe, C. L. Crozier and T. R. Nichols, Atmospheric Environment Service, Downsview, Ontario, CANADA

THE ORIGIN OF AIR MASSES LEADING TO SEVERE HAILSTORMS IN SOUTHWESTERN FRANCE 452
J. Dessens, Centre de Recherches Atmosphériques, Lannemezan, FRANCE, and Fournier d'Albe, Dormont, Saint-Pierre de Bailleul, FRANCE

RADAR REMOTE SENSING OF MELTING HAIL 455
V. N. Bringi and P. Meischner, DFVLR, Institut für Physik der Atmosphäre, Weßling, FRG

TEST OF PARAMETERIZATION SCHEMES FOR CLOUD MICROPHYSICAL PROCESSES IN A 3-D MESOSCALE MODEL 458
L. Levkov, D. Jacob, D. Eppel and H. Graßl, Forschungszentrum Geesthacht, Geesthacht, FRG

DEVELOPMENT OF ANALYTICAL METHODS FOR THE INVESTIGATION OF CLOUDS, FOG AND RAIN, TOGETHER WITH THE GASEOUS PHASE, AND RESULTS OF FIELD MEASUREMENTS 461
K. Bächmann, U. Sprenger, G. R. Fuchs-Pohl, W. Schmied, and P. Zeißler, Technische Hochschule Darmstadt, FRG

RAIN AEROSOL COUPLING IN MARITIME, URBAN AND RURAL AREA. SCAVENGING RATIOS MEASUREMENTS IN RELATION WITH TRANSPORT 463
J. L. Colin and J. L. Jaffrezo, Université Paris, Paris Cedex, FRANCE

THE RAINOUT REMOVAL OF SULFUR DIOXIDE AND ACIDIFICATION OF PRECIPITATION FROM STRATIFORM CLOUDS 466
Q. Yu, Peking University, Beijing, PRC

SESSION 10: CIRRUS CLOUDS

STRUCTURAL AND TEXTURAL CHARACTERISTICS OF CIRRUS CLOUDS 468
K. S. Kuo, R. M. Welch and S. K. Sengupta, South Dakota School of Mines and Technology, Rapid City, SD, USA

CIRRUS CLOUDS AND MESOSCALE ATMOSPHERIC PROCESSES 471
E. P. Borisenkov and T. A. Bazlova, Main Geophysical Observatory, Leningrad, USSR

MESOSCALE AND MICROSCALE STRUCTURE OF CIRRUS CLOUDS: THREE CASE STUDIES 473
K. Sassen and M. Griffin, University of Utah, Salt Lake City, UT, USA

VERTICAL VELOCITIES WITHIN A CIRRUS CLOUD FROM DOPPLER LIDAR AND AIRCRAFT MEASUREMENTS DURING "FIRE": IMPLICATIONS FOR PARTICLE GROWTH 476
I. Gultepe and A. Heymsfield, NCAR, Boulder, CO, USA

HYDROMETEOR DEVELOPMENT IN COLD CLOUDS IN "FIRE" 479
A. J. Heymsfield and N. C. Knight, NCAR, Boulder, CO, USA

THE EMPIRICAL MODEL OF THE STRUCTURE OF CIRRUS CLOUDS IN MIDDLE LATITUDES 482
A. L. Kosarev, I. P. Mazin and A. N. Nevzorov, Central Aerological Observatory, Moscow Region, USSR

MODELLING THE INITIAL ICE CRYSTAL SPECTRUM IN CIRRUS CLOUD 485
A. G. Darlison, Meteorological Office, Bracknell, Berkshire, UK

EFFECTS OF CIRRUS COMPOSITION ON ATMOSPHERIC RADIATION BUDGETS 488
St. Kinne, NASA Ames Research Center, Moffett Field, CA, USA, and K. N. Liou, University of Utah, Salt Lake City, UT, USA

SESSION 11: BOUNDARY-LAYER PROCESSES, FOGS AND LAYER CLOUDS

A RADIATION-FOG MODEL WITH DETAILED MICROPHYSICS 490
A. Bott, U. Sievers and W. Zdunkowski, Johannes Gutenberg-Universität, Mainz, FRG

SMALL SCALE STRUCTURE OF A RADIATIVE FOG: A NUMERICAL STUDY 493
P. K. Smolarkiewicz, NCAR, Boulder, CO, USA, and D. Fitzjarrald, State University of New York, Albany, NY, USA

NUMERICAL STUDIES ON THE EVOLUTION OF RADIATION FOG 496
W. Wobrock, Johann Wolfgang-Goethe Universität, Frankfurt am Main, FRG

A NUMERICAL STUDY OF MESOSCALE PERTURBATIONS IN STRATIFORM BOUNDARY LAYER CLOUD FIELDS 499
M. Tjernström, Uppsala University, Uppsala, SWEDEN

A NUMERICAL STUDY OF RADIATION FOG OVER THE YANGTZE RIVER 503
M.-W. Qian and X. Lei, Institute of Atmospheric Physics, Academia Sinica, Beijing, PRC

PRECIPITATION MECHANISM OF PRECIPITUS STRATIFORMIS OVER JILIN PROVINCE IN SPRING 507
X.-L. Wang, D.-Z. Jin, Y.-Z. Li and C. R. Zheng, Meteorological Institute of Jilin Province, Changchun, PRC

AIRCRAFT OBSERVATIONS AND SIMULATIONS OF ARCTIC STRATUS CLOUDS 509
J. E. Finger and P. Wendling, Institut für Physik der Atmosphäre, DFVLR, Weßling, FRG

DIURNAL VARIATION OF A STRATOCUMULUS-TOPPED ATMOSPHERIC BOUNDARY LAYER OVER SEA 511
P. G. Duynkerke, KNMI, AE De Bilt, THE NETHERLANDS

INTEGRATED FOG WATER SAMPLING SYSTEM 514
L. Schütz, M. Krämer, B. Friederich and F. Franken, Johannes Gutenberg-Universität, Mainz, FRG

USE OF LIDAR DATA IN SHORT-TERM FORECAST OF STRATIFORM CLOUDINESS BASE HEIGHT 515
S. I. Kolev, O. P. Parvanov**, L. A. Kostadinov***, and I. N. Kolev**,*
**Institute of Hydrology and Meteorology, Sofia, BULGARIA,*
***Institute of Electronics, Sofia, BULGARIA,*
****Hydrometeorological Service, Sofia, BULGARIA*

SESSION 12: CYCLONES, FRONTS AND RAINBANDS

WATER CONTENT OF WINTER CLOUDS OVER ETS 518
A. S. Azarov, N. A. Bezrukova, N. F. Buranbaev, A. V. Coldaev and A. A. Chernikov, Central Aerological Observatory, Dolgoprudny, Moscow Region, USSR

MICROPHYSICAL STRUCTURE OF JAPANESE WARM-FRONTAL CLOUDS OBSERVED WITH A NEW TYPE SONDE (HYVIS)..... 521
M. Murakami, T. Matsuo, H. Mizuno and Y. Yamada, Meteorological Research Institute, Ibaraki, JAPAN

COLD FRONTAL PASSAGE OVER THE SIERRA BARRIER..... 525
J. D. Marwitz, University of Wyoming, Laramie, WY, USA

A NUMERICAL MODELING STUDY OF COLD-FRONTAL RAINBANDS..... 527
D. J. Knight and P. V. Hobbs, University of Washington, Seattle, WA, USA

NUMERICAL SIMULATION OF RAINBANDS CAUSED BY MESO-ß SCALE POTENTIAL VORTICITY ANOMALIES..... 529
H. R. Cho and D. S. T. Chan, University of Toronto, Toronto, Ontario, CANADA

SIMULATION OF FRONTAL CLOUDS AND PRECIPITATION USING A MESOSCALE WEATHER PREDICTION MODEL..... 532
E. Müller and U. Wacker, Deutscher Wetterdienst, Offenbach/M., FRG

LONG LASTING TRADE WIND RAINBANDS..... 535
T. Takahashi, Kyushu University, Fukuoka, JAPAN

CHARACTERISTICS OF CUMULUS BANDCLOUDS OFF THE COAST OF HAWAI..... 538
G. B. Raga, J. B. Jensen**, J. Wettlaufer*, and M. B. Baker*, *University of Washington, Seattle, WA, USA, **NCAR Boulder, CO, USA*

STRUCTURE OF LAYER CLOUDS AS OBSERVED SIMULTANEOUSLY BY A MICROWAVE RADIOMETER AND AN 8.6 MM RADAR..... 541
G. Liu and T. Takeda, Water Research Institute, Nagoya University, Nagoya, JAPAN

ANALYSIS OF SINGLE DOPPLER RADAR DATA: WIND FIELD AND PRECIPITATION OBSERVATIONS DURING A FRONTAL PASSAGE..... 544
M. Hagen, Institut für Physik der Atmosphäre – DFVLR, Oberpfaffenhofen, FRG

THE OCCURRENCE OF ICE IN CLOUDS ASSOCIATED WITH EXTRATROPICAL CYCLONES..... 547
R. T. Bruintjes, South African Weather Bureau, Pretoria, REPUBLIC OF SOUTH AFRICA

SESSION 13: GRAUPEL AND HAIL

THE SUPERCOOLING OF SURFACE WATER SKINS OF SPHERICAL AND SPHEROIDAL HAILSTONES..... 551
R. List, F. Garcia-Garcia, R. Kuhn and B. Greenan, University of Toronto, Toronto, Ontario, CANADA

MICROPHYSICAL CONCEPT OF HAIL FORMATION..... 554
M. I. Tlisov and V. G. Khorguani, High-Mountain Geophysical Institute, Nalchik, USSR

STUDIES OF ARTIFICIAL HAILSTONES UNDER DIFFERENT EXPERIMENTAL CONDITIONS..... 557
F. Prodi, Istituto FISBAT-CNR, Bologna, ITALY, and A.-S. Wang, Institute of Atmospheric Physics, Academia Sinica, Beijing, PRC

WIND TUNNEL HAILSTONE GROWTH USING DOPPLER RADAR DERIVED TRAJECTORIES..... 560
G. B. Lesins, University of Oklahoma, Norman, OK, USA

THE EFFECT OF SUPERCOOLED DROPLET ELECTRICAL CHARGES ON THE HAIL GROWTH COAGULATIVE PROCESS..... 563
T. G. Bliadze, A. I. Kartsivadze, A. M. Okudjava and T. N. Saliashvili, Institute of Geophysics, Georgian Academy of Sciences, Tbilisi, USSR

GROWTH OF HAILSTONES IN CONVECTIVE CLOUDS. RESULTS OF MEASUREMENTS AND NUMERICAL EXPERIMENTS 566
S. Stoyanov, Hydrometeorological Service, Sofia, BULGARIA, M. Tlisov, High Mountain Geophysical Institute, Nalchik, USSR, and I. Geresdi, Cs. Zoltán, Cs. Székely, K. Molńar, Meteorological Service, Szalánta, HUNGARY

HAIL IMPACTS, HAIL NETS AND DAMAGE..... 569
D. Roos, Council for Scientific and Industrial Research, Pretoria, SOUTH AFRICA, and S. F. Durrant, University of Surrey, Guildford, UK

COMPARISON OF THE SHAPE AND SIZE DISTRIBUTIONS OF RAINDROPS AND HAILSTONES..... 572
P. K. Wang, University of Wisconsin, Madison, Wisconsin, USA

TWO STAGE HAILSTONE GROWTH IN THE AUGUST 1, 1981 CCOPE STORM 574
J. C. Pflaum, University of Oklahoma, Norman, OK, USA, and R. M. Rasmussen, Bureau of Reclamation, Denver, CO, USA

ON SOME CHARACTERISTICS DETERMINING THE DEVELOPMENT OF HAIL PROCESSES IN BULGARIA 576
P. Simeonov, Hydrometeorological Service, Sofia, BULGARIA, and D. Sirakov, Sofia University, Sofia, BULGARIA

SESSION 14: CONVECTIVE CLOUDS I: MEASUREMENTS

MEASUREMENTS OF CLOUD DROPS; THEIR AEROSOL CONTENT AND CLOUD INTERSTITIAL NUCLEI NEAR THE BASES OF CONVECTIVE CLOUDS IN ISRAEL..... 579
Z. Levin, E. Ganor, C. Price and D. Pardess, Tel Aviv University, Ramat Aviv, ISRAEL

MICROPHYSICAL CHARACTERISTICS OF CONVECTIVE CLOUDS OVER THE SOUTH-CENTRAL UNITED STATES..... 582
M. R. Poellot, University of North Dakota, Grand Forks, ND, USA, and J. C. Pflaum, University of Oklahoma, Norman, OK, USA

INVESTIGATION BY TRACER METHOD OF THE CONVECTIVE CELLS OF CUMULONIMBUS CLOUDS..... 585
L. A. Dinevich, State Hydrometeorological Committee, USSR, and S. S. Salavejus, Institute of Physics of the Academy of Sciences, Lithuanian SSR

INVESTIGATING MIXING AND THE ACTIVATION OF ICE WITH GASEOUS TRACER TECHNIQUES..... 588
J. L. Stith, University of North Dakota, Grand Forks, ND, USA, M. K. Politovich and R. F. Reinking, NOAA/ERL, Boulder, CO, USA, and A. Detwiler and P. L. Smith, South Dakota School of Mines and Technology, Rapid City, SD, USA

FIRST FORMATION OF PRECIPITATION IN AN ISOLATED CONCECTIVE CLOUD..... 591
C. A. Knight, NCAR, Boulder, CO, USA

RETRIEVAL OF DYNAMIC VARIABLES IN DOPPLER-OBSERVED CONVECTIVE CLOUD SYSTEMS 594
C. E. Hane, National Severe Storms Laboratory NOAA, Norman, OK, USA

THE EFFECTS OF THE EXISTENCE OF STRATIFORM CLOUD ON THE DEVELOPMENT OF CUMULUS CLOUD AND ITS PRECIPITATION..... 597
M. Huang, Y. Hong, H. Xu and H. Zhou, Institute of Atmospheric Physics, Academia Sinica, Beijing, PRC

A CASE STUDY OF A SLOW-MOVING CONVECTIVE BAND OBSERVED BY A DOPPLER RADAR..... 600
K. Akaeda, M. Ishihara, A. Tabata, T. Yokoyama and H. Sakakibara, Meteorological Research Institute, Ibaraki, JAPAN

SESSION 15: CONVECTIVE CLOUDS II: THEORY AND NUMERICAL MODELING

ANALYSIS OF DIFFERENT APROACHES TO MATHEMATICAL DESCRIPTION OF CONVECTION 603
M. V. Buikov, Ukrainian Regional Research Institute, Kiev, USSR

ORGANIZATION OF CLOUD CONVECTION BY GRAVITY WAVES IN THE LOWER TROPOSHERE 606
J. M. Radziwill, University of Warsaw, POLAND

DRAG EFFECT IN CONVECTIVE DRAFTS 609
K. E. Haman and S. P. Malinowski, University of Warsaw, Warsaw, POLAND

MOISTURE CONVERGENCE AS A SOURCE OF EXPLOSIVE GROWTH IN MODELED CUMULUS CLOUDS 612
J. H. Helsdon, Jr., H. D. Orville, R. D. Farley and F. J. Kopp, South Dakota School of Mines and Technology, Rapid City, SD, USA

THE EFFECTS OF COLD WATER SURFACE ON WARM CUMULUS CLOUDS-NUMERICAL EXPERIMENT 615
F. Kong, M. Huang and H. Xu, Institute of Atmospheric Physics, Academia Sinica, Beijing, PRC

COMPREHENSIVE RESEARCH OF CONVECTIVE CLOUD DYNAMICS FROM THE DATA OF AIRCRAFT AND NUMERICAL EXPERIMENTS 618
J. A. Dovgaljuk, V. P. Drachova, A. D. Egorov, A. A. Sinkevich, E. N. Stankova, V. D. Stepanenko, Main Geophysical Observatory, Leningrad, USSR

A STUDY ON NUMERICAL SIMULATION OF CLOUD MERGERS AND INTERACTIONS 621
M. Huang, H. Xu and W. Ji, Institute of Atmospheric Physics, Academia Sinica, Beijing, PRC

SMOOTH PARTICLE HYDRODYNAMICS AS APPLIED TO 2-D CUMMULUS TYPE CONVECTION 624
A. Gadian, UMIST, Manchester, UK

CONVECTION WAVES AND THEIR STRUCTURAL IMPACT ON CLOUD FIELDS 626
T. Hauf and T. L. Clark, NCAR, Boulder, CO, USA

COMPARISON BETWEEN NUMERICAL CLOUD RESULTS AND OBSERVATIONS 629
B. Mitzeva and V. Andreev, University of Sofia, Sofia, BULGARIA

SESSION 16: THUNDERSTORMS

LOCAL ENVIRONMENTAL CONDITIONS INFLUENCING THE GROWTH AND INTERNAL STRUCTURE OF NON SEVERE THUNDERSTORMS 632
N. E. Westcott, Illinois State Water Survey, Champaign, IL, USA

DOPPLER RADAR STUDY OF A WEAKLY SHEARED THUNDERSTORM 635
D. J. Raymond and A. M. Blyth, New Mexico Institute of Mining & Technology, Socorro, NM, USA

INTERIOR CHARACTERISTICS AT MID LEVELS OF THUNDERSTORMS IN THE SOUTHEASTERN UNITED STATES 638
D. F. Musil and P. L. Smith, South Dakota School of Mines and Technology, Rapid City, SD, USA

ELECTRIFICATION OF THE 31 JULY 1984 NEW MEXICO MOUNTAIN THUNDERSTORM 641
C. L. Ziegler, National Severe Storms Laboratory, Norman, OK, USA, and P. S. Ray and S. L. Lang, Florida State University, Tallahassee, FL, USA

RETRIEVAL OF MICROPHYSICAL VARIABLES IN NEW MEXICAN MONTAIN THUNDERSTORMS FROM DOPPLER RADAR DATA..... 644
P. S. Ray, C. L. Ziegler**, and S. L. Lang*, *Florida State University, Tallahassee, FL, USA, **National Severe Storms Laboratory, Norman, OK, USA*

ON THE ROLE OF PRECIPITATION IN MAINTENANCE OF DOWNDRAFTS IN CUMULONIMBUS CLOUDS..... 647
H. Pawloska-Mankiewicz, University of Warsaw, POLAND

INFLUENCE OF THUNDERSTORM-GENERATED ACOUSTIC WAVE ON COAGULATION..... 650
M. Curic, University of Belgrad, Beograd, YUGOSLAVIA, and Z. Vukovic, Hydrometeorological Institute of Serbia, Beograd, YUGOSLAVIA

SESSION 17: SATELLITE STUDIES

SATELLITE-SURFACE LINKAGE TO ESTIMATE MID-LATITUDINAL PRECIPITATION FEATURES..... 653
M. Scholl, Freie Universität Berlin, Berlin, FRG

RESULTS FROM THE RAINFALL ESTIMATION STUDIES BASED ON METEOSAT DATA..... 656
O. M. Turpeinen, European Space Operations Centre, Darmstadt, FRG

COMPARISON OF SATELLITE DATA WITH SURFACE-BASED REMOTE SENSING MEASUREMENTS IN UTAH WINTER OROGRAPHIC STORMS..... 659
D. C. Rogers, Colorado State University, Fort Collins, CO, USA, and K. Sassen and G. C. Dodd, University of Utah, Salt Lake City, UT, USA

PASSIVE MICROWAVE OBSERVATIONS OF THUNDERSTORMS FROM HIGH-ALTITUDE AIRCRAFT..... 662
G. M. Heymsfield, NASA Goddard Space Flight Center, Greenbelt, MD, USA, and R. Fulton, General Sciences Corporation, Laurel, MD, USA

NUMERICAL FRONTAL ANALYSIS SCHEME FOR OPERATIONAL INTERPRETATIONS OF SATELLITE PICTURES AND PRECIPITATION ESTIMATIONS..... 665
L. Lesch, Institut für Meteorologie, Freie Universität Berlin, Berlin, FRG

SESSION 18: SEVERE STORMS AND HURRICANES

A MIDDLE LATITUDE SQUALL LINE IN FRANCE..... 666
G. Jaubert, M. Chong and J. M. Giudicelli, Direction de la Météorologie Nationale (EERM/CNRM), Toulouse Cedex, FRANCE

A STUDY OF THE DYNAMICS OF SQUALL LINES USING A NON-HYDROSTATIC CLOUD MODEL..... 669
D. B. Parsons, R. Rotunno, J. B. Klemp and M. L. Weisman, NCAR, Boulder, CO, USA

PHYSICAL PROCESSES AND OBSERVED FEATURES IN MICROBURST-PRODUCING STORMS..... 672
M. Hjelmfelt and C. Kessinger, NCAR, Boulder, CO, USA

ON THE MICROPHYSICS OF MICROBURSTS..... 675
H. D. Orville, F. J. Kopp, R. D. Farley and Y. C. Chi, South Dakota School of Mines and Technology, Rapid City, SD, USA

OBSERVATION OF MICROBURSTS FROM SNOW CLOUDS IN WINTER MONSOON SEASON..... 678
H. Uyeda, R. Shirooka and K. Kikuchi, Hokkaido University, Sapporo, JAPAN

EVOLUTION OF CONVECTIVE STORM ALONG BOUNDARY LAYER CONVERGENCE LINES..... 681
J. Wilson and C. Müller, NCAR, Boulder, CO, USA

THE STRUCTURE OF THE CONVECTIVE CELLS AND THE DYNAMICS OF HAILSTORM DEVELOPMENT IN ALAZANI VALLEY 684
A. I. Kartsivadze, T. G. Salukvadze, R. I. Doreuli, E. I. Khelaya, and A. Sh. Balavadze, Institute of Geophysics, Georgian Academy of Sciences, Tbilisi, USSR

EVOLUTION OF MESOCYCLONIC CIRCULATION IN SEVERE STORMS 687
P. I. Joe and C. L. Crozier, Atmospheric Environment Service, Toronto, Ontario, CANADA

A NUMERICAL STUDY OF MULTICELLULAR SEVERE CONVECTIVE STORMS FOLLOWED BY LONG-LASTING HEAVY RAINFALL 690
J. Shiino, Meteorological Research Institute, Ibaraki, JAPAN

3-D NUMERICAL MODELING AND RADAR OBSERVATIONS OF DEEP CONVECTIVE CLOUDS 693
H. Höller, Institut für Physik der Atmosphäre, DFVLR-Oberpfaffenhofen, Weßling, FRG

OBSERVED STRUCTURE AND EVOLUTION OF A MESOVORTEX IN THE TRAILING STRATIFORM REGION OF A MCC 696
J. Verlinde and W. R. Cotton, Colorado State University, Fort Collins, CO, USA

MELTING LAYER STRUCTURE IN MCC STRATIFORM PRECIPITATION 699
P. T. Willis, Atlantic Oceanographic and Meteorological Laboratories, Miami, FL, USA, and A. J. Heymsfield, NCAR, Boulder, CO, USA

DUAL-DOPPLER AND AIRBORNE MICROPHYSICAL OBSERVATIONS IN THE STRATIFORM REGION OF THE 10-11 JUNE MCS OVER KANSAS DURING PRESTORM 702
S. A. Rutledge, R. A. Houze Jr.**, A. J. Heymsfield***, and M. I. Biggerstaff** *Oregon State University, Corvallis, OR, USA, **University of Washington, Seattle, WA, USA, ***NCAR, Boulder, CO, USA*

VERTICAL DRAFTS IN THE CONVECTIVE REGIONS OF MESOSCALE CONVECTIVE SYSTEMS IN KANSAS 705
M. I. Biggerstaff and R. A. Houze, Jr., University of Washington, Seatlle, WA, USA, and S. A. Rutledge, Oregon State University, Corvallis, OR, USA

MESOSCALE PATTERNS OF ICE PARTICLE CHARACTERISTICS IN HURRICANE NORBERT 708
R. A. Houze, Jr., University of Washington, Seattle, WA, USA, and F. D. Marks, Jr., and R. A. Black, Hurricane Research Division NOAA/AOML, Miami, FL, USA

THE BULK WATER BUDGET OF HURRICANE NORBERT (1984) AS DETERMINED FROM THERMODYNAMIC AND MICROPHYSICAL ANALYSES RETRIEVED FROM AIRBORNE DOPPLER RADAR 711
J. F. Gamache, F. D. Marks, Jr. and R. A. Black, Hurricane Research Division, NOAA/AOML, Miami, FL, USA, and R. A. Houze, Jr., University of Washington, Seattle, WA, USA

MICROPHYSICS IN A CONVECTIVE CLOUD SYSTEM ASSOCIATED WITH A MESOSCALE CONVECTIVE COMPLEX – AND NUMERICAL SIMULATION 714
B. F. Fan, J. D. Yeh and W. R. Cotton, Colorado State University, Fort Collins, CO, USA, annd G. J. Tripoli, University of Wisconsin, Madison, WI, USA

OBSERVATIONAL ANALYSIS OF MESOSCALE CONVECTIVE SYSTEM GROWTH AND STRUCTURE 717
K. R. Knupp, University of Alabama, Huntsville, AL, USA

INVESTIGATION OF THUNDER AND HAIL CLOUDS USING REMOTE METHODS 719
M. R. Vatyan, M. G. Bakhsoliani, N. E. Lomidze, G. B. Brylev, B. E. Peskov, USSR

STUDIES OF CONVECTIVE CLOUDS DEVELOPMENT IN CENTRAL ASIA 723
A. D. Dzhuraev, H. A. Imamdzhanov, B. Sh. Kadyrov and V. P. Kurbatkin, The Bugaev Central Asian Regional Research Institute, Tashkent, USSR

Ackerman, B. 440
Ackerman, T.P. 125, 133,
Adzhiev, A.Kh. 161
Akaeda, K, 437, 600
Andreev, V. 629
Atkinson, N.C. 322
Azarov, A.S. 518

Baddour, O. 356
Baechmann, K. 461
Baker, M. B. 67, 538
Bakhsoliani, M.G. 719
Balavadze, A.Sh. 684
Barnes jr., A.J. 380
Baumgardner, D.G. 40, 43, 70
Bazlova, T.A. 471
Beard, K.V. 7, 31, 375
Beheng, K.D. 199
Bezrukova, N.A. 518
Biggerstaff, M.I. 702, 705
Black, R.A. 708, 711
Bliadze, T.G. 563
Blyth, A.M. 73, 635
Borisenkov, E.P. 471
Bott, A. 490
Bower, K. 37
Braun, P. 246
Breidenthal, R. 67
Brenguier, J.L. 91
Bringi, V.N. 330, 455
Brown jr., Ph. S. 169
Brown, P.R.A. 55, 138, 141
Bruintjes, R.T. 547
Brylev, G.B. 719
Biukov, M.V. 6o3
Buranbaev, N.F. 518

Carswell, A.I. 338
Castillo, R.A. 251, 267
Caylor, I.J. 49, 372
Chan, D.S.T. 529
Chandler, A.S. 279
Chandra, M. 154
Chatterjee, R.N. 58
Chaumerliac, N. 106, 319
Chen, J.P. 306
Chen, S. 130
Chernikov, A.A. 518
Chi, Y.C. 675
Cho, H.R. 529
Chong, M. 666
Choularton, T.W. 37, 55, 279, 316
Chuang, C. 31
Clark, P.A. 279
Clark, T.L. 88, 353, 398, 626
Coakley, J.E. 121
Colburn, D.C. 125
Coldaev, A.V. 518
Colin, J.-L. 288, 463
Cooper, W.A. 46
Cotton, W.R. 109, 130, 347, 359, 383, 431, 699, 714
Crozier, C.L. 449, 687, 696
Cunningham, G.A. 338
Curic, M. 419, 650
Czys, R.R. 4, 25, 64

Darlison, A.G. 138, 141, 485
Daum, P.H. 264
Davies, R. 124
Dellert, M. 246
Deluisi, J. 267
DeMott, P.J. 369
Demoz, B. 410
Dessens, J. 452
Detwiler, A. 588
Dinevich, L.A. 585
Dlugi, R. 235
Dodd, G.C. 659
Doms, G. 199
Dong, Y. 28
Doreuli, R.I. 684
Dovgaljuk, J.A. 618
Drachova, V.P. 618
Duroure, Chr. 62, 223
Durrant, S.F. 569
Duynkerke, P.G. 511
Dzhuraev, A.D. 723

Egorov, A.D. 618
Eldik, R. v. 246
Enderle, K.H. 291
Endoh, T. 9, 362, 416
Enukashvily, I.M. 172, 428
Eppel, D. 458

Fan, B.F. 383, 714
Fan, L. 386
Farley, R.D. 226, 612, 675
Feng, J.Q. 4
Finger, J.E. 509
Finnegan, W.G. 243
Fitzjarrald, D. 493
Flatau, P.J. 109
Forkel, R. 255
Fournier d'Albe, E.M. 452
Franken, F. 514
Friederich, B. 514
Frush, C. 335
Fuchs-Pohl, G.R. 461

Fujiyoshi, Y. 362, 407
Fukuta, N. 9, 12
Fulton, R. 662

Gadian, A. 624
Gagneux, J. 76, 211
Gamache, J.F. 711
Ganor, E. 579
Gao, Z. 389
Garcia-Garcia, F. 551
Gay, M.J. 279
Gayet, J.-F. 62, 325
Gaytandjiev, D.E. 366
Geresdi, I. 566
Gervat, G.P. 279
Giudicelli., J.M. 666
Gonda, T. 208
Gorbunov, B. 183
Grabowski, W.W. 344
Grassl, H. 458
Greenan, B. 551
Gribelin, P. 214
Griffin, M. 473
Gutelpe, I. 476
Gzirishvili, T. 185

Hagen, M. 544
Hall, W.D. 88, 100, 353
Hallett, J. 22, 28, 180
Haman, K.E. 609
Hane, C.E. 594
Harimaya, T. 190
Harrison, K. 180
Hauf, T. 626
He, G. 103
Hegg, D.A. 261
Heintzenberg, J. 34, 151, 282
Helsdon jr., J.H. 612
Hemler, R.S. 94
Hertzman, O. 404
Herzegh, P.H. 328
Heymsfield, A.J. 133, 476, 479, 699, 702
Heymsfield, G.M. 662
Hicks, E. 76, 211, 378
Hildebrand, P. 335
Hill, T.A. 279, 294
Hindman, E.E. 229
Hjelmfelt, M. 413, 672
Hobbs, P.V. 1, 121, 261, 404, 527
Hoeller, H. 693
Hoff, R.M. 338
Hoffmann, H.-E. 175
Hong, Y. 597
Houze jr., R.A. 702, 705, 708, 711
Hu, Z. 103
Huang, M. 112, 303, 597, 615, 621
Huang, S.H. 251
Huang, W. 386
Huang, Y. 386
Hudak, D. 446

Ichikawa, S. 341
Ichimura, I. 341
Illingworth, A.J. 49, 372
Imamdzhanov, H.A. 723
Iribarne, J.V. 258
Isaac, G.A. 273
Isaka, H. 214, 223
Ishihara, M. 437, 600
Isono, K. 208
Iwai, K. 193
Iwanami, K. 393

Jacob, D. 458
Jaenicke, R. 148
Jaeschke, W. 291
Jaffrezo, J.-L. 288, 463
Jameson, A.R. 328
Janc, D. 419
Jank, T. 330
Jaubert, G. 666
Jeck, R. 205
Jennings, S.G. 241
Jensen, J.B. 40, 538
Ji, W. 621
Jin, D.-Z. 507
Jochum, A.M. 82
Joe, P.I. 135, 449, 687
Johansson, B. 151
Johari, H. 67
Johnson, D.B. 375
Jones, A. 316

Kadyrov, B.Sh. 723
Kajikawa, M. 196
Kakutkina, H. 183
Kang, T.S. 446
Kapoor, R.K. 58
Kartsivadze, A.I. 563, 684
Keith, W.D. 220
Kelly, R.D. 52
Kennedy, P.C. 440, 443
Kessinger, C. 672
Khelaya, E.I. 684
Khorguani, V. 185
Kikuchi, K. 393, 678
Kim, V.M. 158
Kinne, St. 133, 488
Kins, L. 276
Klemp, J.B. 669
Knight, C.A. 591
Knight, D.J. 527
Knight, N.C. 479
Knupp, K.R. 717
Kobayashi, J. 208

Kolev, I.N. 515
Kolev, S.I. 515
Kong, F. 615
Konishi, H. 188, 416
Kopp, F.J. 612, 675
Kosarev, A.L. 482
Kostadinov, L.A. 515
Kraemer, M. 238, 514
Kraft, J. 246
Kubesh, R.J. 375
Kuhn, R. 551
Kumai, M. 249
Kuo, K.S. 468
Kurbatkin, V.P. 723

Lafore, J.P. 100
Lamb, D. 306
Lang, S.L. 641, 644
Latham, J. 73
Leaitch, W.R. 273, 338
Lee, I.Y. 312
Lei, X. 503
Lesch, L. 665
Lesins, G.B. 560
Levi, L. 217
Levin, Z. 579
Levkov, L. 458
Li, Y.-Z. 507
Li, Z. 386
Lin, N.-H. 232
Liou, K.-N. 118, 488
Lipps, F.B. 94
List, R. 446, 551
Liu, G. 541
Liu, S. 303
Livingston, J.M. 125
Lomidze, N.E. 719
Lubart, L. 217
Lueneburg, E. 154
Luepkes, C. 199
Lyons, J.H. 121

MacVean, M.K. 425
Magradze, G. 166
Malinowski, S.P. 609
Mallant, R.K.A.M. 333
Marks jr., F.D. 708, 711
Marsh, A.R.W. 279
Marwitz, J.D. 525
Matsuo, T. 144, 341, 521
Mazin, I.P. 482
McGann, B.T. 241
Meischner, P. 330, 455
Meixner, F.X. 276
Meyers, M.P. 347
Mitra, S.K. 18
Mitzeva, B. 629
Mitzuno, H. 521
Miyatake, M. 188
Molenkamp, C.R. 396
Molnar, K. 566
Monhen, V.A. 251
Mori, T. 208
Mueller, C. 681
Mueller, E. 532
Mueller, K.P. 276
Murakami, M. 144, 521
Musil, D.F. 638

Nagamoto, C. 285
Nair, S.K. 297
Nemesova, I. 422
Nevzorov, A.N. 482
Nicholls, S. 127, 322, 425
Nichols, T.R. 449
Nissen, R. 446
Nizamuddin, S. 254
Noone, K. 34, 282
Novosyolov, L.N. 164

Obenland, H. 291
Ochs, H.T. 4, 7
Ogren, J. 34, 282
Okada, K. 341
Okudjava, A.M. 563
Oraltay, R.G. 22
Orville, H.D. 226, 612, 675
Ou, S.C. 118

Pal, S. 338
Paluch, I.R. 70
Pardess, D. 579
Parsons, D.B. 669
Parungo, F. 285
Parvanov, O.P. 515
Paschenko, A. 183
Pawloska-Mankiewicz, H. 647
Penner, I.E. 79
Personne. P. 214, 223
Peskov, B.E. 719
Peters, L.K. 297
Pflaum, J.C. 574, 582
Pielke, R.A. 359
Pitter, R.L. 243
Podzimek, J. 202
Poellot, M.R. 582
Politovich, M.K. 588
Pontikis, C. 76, 211, 378
Prakash, P. 58
Price, C. 579
Prodi, F. 557
Pruppacher, H.R. 18
Pueschel, R.F. 125
Pyshnov, T. 258

Qian, M.-W. 503

Radke, L.F. 121
Radziwill, J.M. 606
Raga, G. 40, 538
Rasmussen, R.M. 353, 356, 398, 574
Rauber, R.M. 350
Ray, P.S. 641, 644
Raymond, D.J. 635
Redder, C.R. 12
Reinking, R.F. 588
Reuter, G. 97
Richard, E. 106
Rigaud, A. 76, 211, 378
Rogers, D.C. 369, 659
Roos, D. 569
Rosset, R. 319
Roth, R. 175
Rotunno, R. 669
Rudman, S.D. 322
Russel, P.B. 125
Rutledge, S.A. 702, 705

Sakakibara, H. 401, 437, 600
Salavejus, S.S. 585
Saliashvili, T.N. 563
Salukvadze, T.G. 684
Saluzzi, M.E. 434
Samokhvalov, I.V. 79
Sassen, K. 473, 659
Sasyo, Y. 208
Sato, M. 190
Saunders, C.P.R. 220
Sauvageot, H. 378
Saxena, V.K. 232
Schemenauer R.S. 135
Schmied, W. 461
Scholl, M. 653
Schroth, A. 154
Schuetz, L. 238, 514
Schumann, T. 270
Seidl, W. 235, 255
Sengupta, S.K. 468
Serrano, F. 52
Shamanaev, V.S. 79
Shiino, J. 690
Shimada, W. 188
Shirooka, R. 678
Sievers, U. 490
Simeonov, P. 576
Simmons, E.L. 322
Singh, G. 58
Sinkevich, A.A. 618
Sirakov, D. 576
Smith, P.L. 588, 638
Smolarkiewicz, P.K. 88, 353, 398, 493
Soerensen, R. 148
Soo, S.K. 446
Soulage, R.G. 62
Spanner, M.A. 125
Sprenger, U. 461
Stankova, E.N. 618
Stepanenko, V.D. 618
Stepanov, A.S. 164
Stephens, G.L. 115
Stith, J.L. 588
Stone, R.L. 410
Stoyanov, S. 566
Szekely, Cs. 566

Tabata, A. 401, 437, 600
Takahashi, T. 9, 535
Takaya, Y. 85
Takeda, T. 341, 541
Tanaka, T. 341
Tani, K. 188
Taniguchi, T. 393
Taylor, G. 67, 300
Tjernstroem, M. 499
Tlisov, M.I. 554, 566
Tokuda, A. 341
Tomazov, S.T. 161
Tripoli, G.J. 109, 130, 714
Tsuboki, K. 407
Tung, N.P. 446
Turpeinen, O.M. 656

Uyeda, H. 678

Valero, F.P.J. 133
Vali, G. 52
Vatyan, M.R. 719
Vaughan, H.C. 178
Verlinde, J. 696
Vohl, O. 18
Vukovic, Z. 650

Wacker, U. 532
Wakahama, G. 9, 362, 407, 416
Walcek, C.J. 309
Waldvogel, A. 270
Walther, C. 335
Wang, A.-S. 15, 557
Wang, P.K. 572
Wang, X.-L. 507
Warburton, J.A. 410
Weisman, M.L. 669
Weissbluth, M.J. 359, 431
Welch, R.M. 468
Wendling, P. 509
Wesley, D.A. 359
Westcott, N.E. 632
Wettlaufer, J. 538
Willis, P.T. 699
Wilson, J. 681
Wobrock, W. 496
Wrigley, R.C. 125

Xiao, H. 112
Xu, H. 112. 597, 615, 621
Xu, W. 386

Yamada, Y. 521
Yamashita, A. 188
Yeh, J.D. 383, 714
Yokoyama, T. 437, 603
Yu, Q. 466

Zdunkowski, W. 490
Zeissler, P. 461
Zhang, J. 389
Zhao, B. 364
Zheng, C.R. 507
Zhou, H. 597
Ziegler, C.L. 641, 644
Zinder, B. 270
Zoltan, Cs. 566
Zuev, V.E. 79

HUMIDITY MEASUREMENTS DURING CLOUD FORMATION USING INFRARED HYGROMETRY

Paul J. DeMott and David C. Rogers
Department of Atmospheric Science
Colorado State University, Fort Collins, CO, USA 80523

1. INTRODUCTION

In recent years, the technology has been developed to measure humidity by differential absorption of infrared radiation (e.g., Nelson, 1982 and Cerni et al., 1987). Potential applications to cloud physics are fast response humidity measurement by aircraft and the measurement of water supersaturation in cloudy air. A prototype infrared transmittance hygrometer designed by the OPHIR Corporation is currently installed in the dynamic (controlled expansion) cloud chamber (DCC) at Colorado State University. The cloud chamber permits the simulation of a variety of air parcel/cloud conditions and was used to help evaluate the basic performance of the hygrometer. In particular, the capability for the measuring supersaturation with cloud droplets present was critically examined.

2. THEORY OF HYGROMETER OPERATION

The infrared transmittance hygrometer at CSU employs the dual-wavelength infrared absorption technique. A background of the history and theory of development of this technique for water vapor has been given by Cerni et al. (1987). The technique utilizes a primary wavelength within an strongly absorbing portion of the gaseous absorption band and a reference wavelength just outside the band. The instrument at CSU uses two absorption bands at 2.67μm and 2.59μm and the non-absorbing band at 2.43μm. The Beer-Lambert Absorption Law states that the absorption of collimated, monochromatic radiation is proportional to the amount of absorbing gas present over the path length involved. For narrow band radiation that can be practically isolated by interference filters, Beer's Law is not strictly valid, but corrections to it are straightforward (see, for example, Bogolomova et al., 1974). The ratio of transmittance at the primary wavelength and that at the reference wavelength is then a direct measure of water vapor absorption. Because the measurement is a ratio and because the two wavelengths are closely spaced, interference by cloud particles should be filtered out. This assumption is evaluated.

The infrared hygrometer provides a secondary measurement of atmospheric humidity. Measured transmittance must be calibrated to absolute humidity determined by a standard procedure. Relative humidity is obtained by simulataneous measurement of temperature.

In the CSU instrument, a beam from a broadband source (heated filament) is passed through the inner volume of the DCC. The path is folded by a mirror for a 218 cm total length. The beam is then split into two equal intensity beams which are sent to separate photoconductive detectors. One of the detectors is preceded by a 2.43 μm interference filter. The other detector is preceded by a motorized wheel that holds 2.67μm, 2.59μm, and 2.43μm filters. Fast response measurement is obtained by using both detectors at once. Measurement can also be obtained using only the one detector and rotating the filter wheel alternately between a vapor channel and the 2.43 μm channel . These measurements are ~2 s apart. Data reported here used this latter method.

3. EXPERIMENTAL

3.1 DYNAMIC CLOUD CHAMBER

The CSU dynamic cloud chamber was used to simulate adiabatic expansion in an air parcel in order to form clouds. The chamber has been described in its current configuration by DeMott (1988). Adiabatic expansion is simulated in the DCC by the evacuation of a 2 m^3 volume within which is a 1.2 m^3 volume enclosed by a perforated, force-cooled copper liner. The temperature of the liner is controlled to follow as closely as possible the simulated adiabatic cooling from evacuation. Temperature, pressure, humidity (dewpoint hygrometer), and cloud droplet sizes and concentrations (FSSP-100) nucleated are measured in time within the inner volume. The infrared hygrometer is physically mounted at the same height as the FSSP and the inlet for the optical condensation-type dewpoint hygrometer. Concentrations of CCN (ammonium sulfate aerosols) and initial temperature and dewpoint temperature are specified to form a cloud of known characterisitics at a desired temperature and pressure. Evacuation control, cooling control, and data acquisition are done by microcomputer. Simulated ascents are programmed based on equations for dry adiabatic expansion to cloud point and moist adiabatic expansion in cloud.

3.2 CALIBRATION TESTS

The calibration procedures included determining detector response, calibrating transmission against humidity measured by dewpoint hygrometry, and assessing the effects

of pressure. The detector conductance versus radiant intensity was determined by placing perforated disks with differing areas of blockage in front of the return beam. Transmittance is calculated from intensity values normalized by intensities at absolute vacuum (no humidity) for each filter position. Normalized transmittance (using the 2.59μm vapor channel) is therefore given by,

$$T = \frac{(I_{2.59}/I_{2.59,vac})}{(I_{2.43}/I_{2.43,vac})} \qquad (1)$$

where,

$I_{2.59}$ = real time radiant intensity 2.59 μm
$I_{2.59,vac}$ = radiant intensity 2.59 μm at vacuum
$I_{2.43}$ = real time radiant intensity 2.43 μm
$I_{2.43,vac}$ = radiant intensity 2.43 μm at vacuum

When the 2.67 μm vapor channel is used, appropriate terms replace the 2.59 μm terms in (1). The ratio bracketed in the numerator is simply the water vapor measurement term, and the denominator measures the adjustment in transmittance due to any blocking of the beam by cloud particles or dirty optics.

The calibration of normalized transmittance versus absolute humidity (ρ) is embodied in the functional form for transmittance that is assumed. Following Bogolomova et al. (1974),

$$T = \exp(-\kappa(\rho)^{\beta}) \qquad (2)$$

where β and κ coefficients are primarily functions of pressure. This expression analytically accounts for the pressure broadening phenomenon of radiative transfer. It can be assumed with negligible error that β is independent of pressure for air over the atmospheric range of pressures. Thus, β was obtained from a calibration of T versus ρ at room pressure (830 mb), as shown in Figure 1. Absolute humidity was determined using a General Eastern model 1200 EPS optical condensation-type dewpoint hygrometer and ambient temperature measurement plus standard thermodynamic equations. The functional dependence of κ on pressure was determined by measuring T during isothermal expansions with varying initial absolute humidities and using (2) with the independently determined β.

3.3 PERFORMANCE EXPERIMENTS

The experiments for testing the response of the infrared hygrometer were standardized to the extent that simulated updraft was always 2.5 m s^{-1} and thermodynamic cloud point was ~0°C. Expansion continued through cloud formation at a rate of about 1°C min^{-1} to near -15°C. The results reported here are for a cloud with continental-type cloud droplet concentrations and sizes. Both water vapor channels were monitored (at ~20 s intervals)

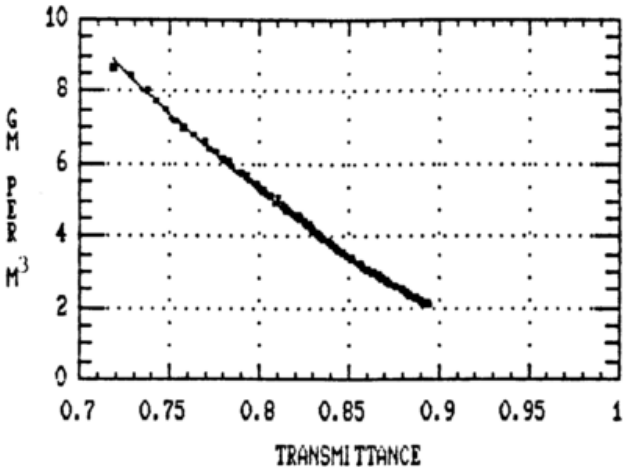


Fig. 1. Calibration data of absolute humidity versus T at constant pressure. Data were fitted to (2) to obtain β.

during experiments and comparisons of calculated relative humidity by the infrared versus dewpoint hygrometry techniques were made. Calculations were made with the cloud droplet measurements (15 size channels)to assess the potential influence of Mie-scattering on cloud extinction at the absorbing and non-absorbing infrared wavelengths. The Mie theory algorithms of Wiscombe (1980) were used.

4. RESULTS

The results from a particular continuous expansion experiment are presented in Figures 2 to 5. Figures 2 and 3 show time histories of relative humidity from the 2.59μm and 2.67μm vapor channels and from the dewpoint hygrometer. Cloud point was very near 790 s. Cloud droplet concentration and mean diameter are shown in Figure 4. Numbers decayed in time due to sedimentation.

Below water saturation, the agreement between the two methods of humidity measurement is excellent. Above water saturation (in-cloud) the cooled mirror instrument overestimates relative humidity since cloud particles are evaporated into the air sample. Also, the infrared technique appears sensitive to the effect of scatterers, contrary to a basic assumption behind the ratiometric technique. Initial measurements of water supersaturation at cloud point between 1 and 2% agree with parcel model calculations (not shown here). However, both infrared channels produce erroneous relative humidity values as the expansion continues and the cloud particles grow to larger sizes. The error is greater for the 2.67μm channel.

Mie scattering and extinction calculations were done to evaluate these effects on the infrared measurements. The ratios of vapor channel transmittance through cloud to transmittance at 2.43μm, as predicted

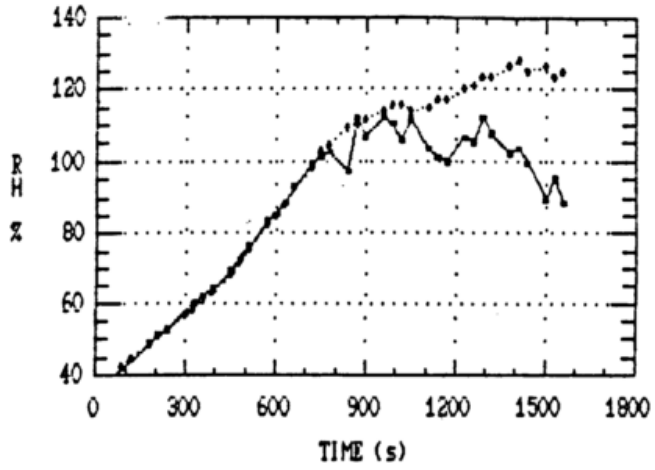


Fig. 2. Relative humidities measured 2.59μm infrared (⊕) and cooled mirror (⊙) techniques. Cloud formed at 790 s.

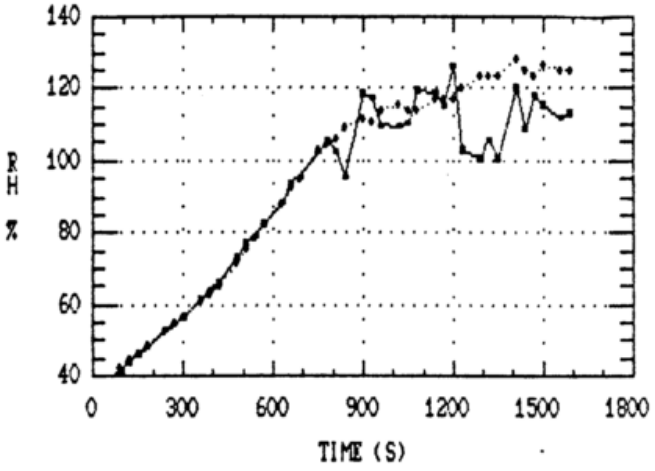


Fig. 3. Same experiment as Figure 2, but 2.67μm

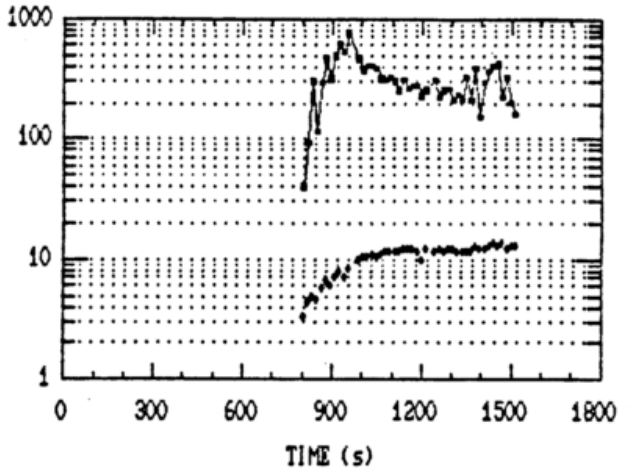


Fig. 4. Concentrations (⊕ cm^{-3}) and average diameter (⊙ μm) of FSSP cloud droplet measurements for the experiment in Figures 2 and 3.

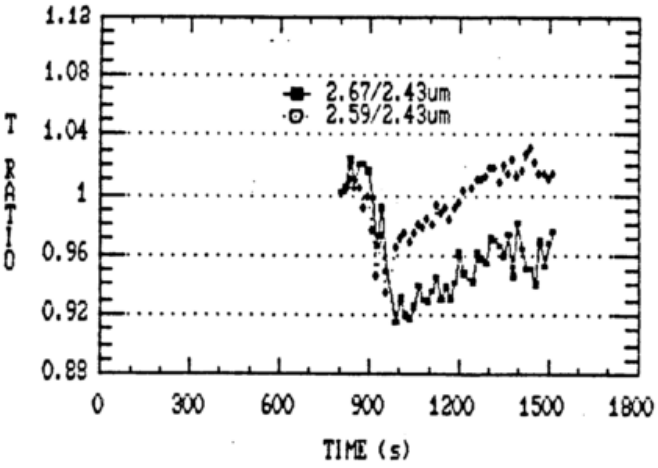


Fig. 5. Change in the ratio of Transmittance due to Mie scattering and extinction effects as calculated from droplet measurements in Figure 4.

by the Mie-scattering model, are shown in Figure 5. The qualitative sense of the calculations agrees fairly well with the observed effect on measurement of relative humidity by the infrared hygrometer. For example, the underestimate of relative humidity near 800 s is consistent with the predicted overestimate of transmittance due to different scattering at the vapor and reference wavelengths. Also, the overestimate of relative humidity peaking between 900 and 1200 s agrees with the predicted underestimate of T. The effects observed for the 2.67μm channel are greater than for the 2.59μm channel, also as predicted. When these errors are corrected and relative humidity is recomputed, the relative humidity errors are too large, as much as 4 times those actually observed. Possible reasons for this descrepancy are the artificial broadening of droplet spectra by the FSSP, unresolved temperature fluctuations in cloud, and the need to account for the 1% bandwidth of the filters in the Mie calculations. Our evaluations of the infrared technique are continuing for other environmental conditions and for clouds with different droplet spectra and with ice crystals present or absent.

5. ACKNOWLEDGEMENTS

This research was sponsored by the National Science Foundation Grant No. ATM-851937 and USAF contract F33657-86-C-3002.

6. REFERENCES

Bogolomova, L.V., VI. Dianov-Klokov and S.L. Zubkovskiy, 1974: Double-Beam infrared spectrometer for measuring humidity fluctuations in the atmosphere. Isvestia, Atmospheric and Ocean Physics, 10, no. 9, 933-942.

Cerni, T.A. , D. Hauschultz, L.P. Nelson and D. Rottner, 1987: An atmospheric infrared hygrometer. Preprints, 6th Symp. on Meteor. Obs. and Instr., 12-16 Jan., New Orleans, LA, AMS.

DeMott, P.J., 1988: Comparisons of the behavior of AgI-type ice nucleating aerosols in laboratory-simulated clouds. To be published in J. Wea. Mod., 20.

Nelson, L.D., 1982: Non-contact sensing of atmospheric temperature, humidity and supersaturation. Preprints, AMS Conf. Cloud Physics, 1982, Chicago, Ill., 293-296.

Wiscombe, 1980: Improved Mie-scattering algorithms. Appl. Optics, 19, 1505-1509.

IDENTIFICATION OF PRECIPITATION PARTICLES USING DUAL POLARIZATION RADAR

Anthony J Illingworth and I Jeff Caylor

Visiting Scientist,
NCAR*, Boulder
Colorado 80307

Dept of Physics
UMIST
Manchester M60 1QD, UK

1. INTRODUCTION

The S band Chilbolton radar in the UK has a quarter degree beamwidth and can transmit pulses (separation 1.6msec) which are alternately polarised in the horizontal and vertical direction. For co-polar reception we can obtain the radar reflectivity factors for the two polarizations, ZH and ZV, and then derive ZDR, the differential reflectivity (10 log (ZH/ZV)). ZDR is a measure of mean shape, which for raindrops gives drop size. We shall also discuss results of the time series data obtained by recording the power received from each transmitted pulse. The cross-polar return, ZHV, and the linear depolarization (LDR=10log(ZHV,ZV)) can also be obtained, which provides information on particle fall mode. The Chilbolton antenna can detect values of LDR as low as -32dB. Results (reported elsewhere) show how the canting angle of raindrops and the mean axial ratio of tumbling graupel may be derived from LDR.

2. DIFFERENTIAL REFLECTIVITY, ZDR

The application of Z and ZDR to estimate both the size and concentration of raindrops is well known (e.g. ILLINGWORTH et al, 1987). Until recently PRUPPACHER and PITTER (1972) provided the best estimate of drop shapes. Small adjustmnets to these shapes now appear appropriate. From ZDR radar data GODDARD et al (1983) argued that millimetre drops are slightly more spherical; this suggestion has been confirmed by CHANDRASEKAR et al (1988). To explain ZDR values measured in heavy rain, CAYLOR and ILLINGWORTH (1987) postulated that drops larger than 4mm must be more oblate than the Pruppacher and Pitter shapes; BEARD and CHUANG (1987) have recently confirmed that larger drops are more oblate. Direct measurements of equilibrium drop shapes are now in agreement with radar inferences, and any naturally occurring drop oscillations do not appear to bias the radar measurements.

Interpretation of the ZDR of ice is more difficult (HALL et al, 1984, ILLINGWORTH et al 1987), but measurements in mature convective clouds with the Chilbolton radar consistently show ZDR values within 0.1dB of zero where the temperature is below freezing, apparently in contradiction with the common observations that graupel is conical indicating a non-random fall mode.

3. TIME SERIES CORRELATION OF ZH AND ZV

Figure 1 shows time series data obtained at a single 75m gate in 210 milliseconds from 64 pulse pairs transmitted with alternate horizontal and vertical polarisations. Successive estimates fluctuate as the particles reshuffle in space. ZDR is normally derived by comparing the linear averages of these 64 estimates, as shown by the straight lines in the Figures. Figure 1 shows a zero ZDR for small spherical raindrops. Additional information is available from p(H,V), the correlation of ZH and ZV, which here is equal to 0.99; for spheres the theoretical value is unity. Some statistical properties of p(H,V) are discussed by BRINGI et al (1983).

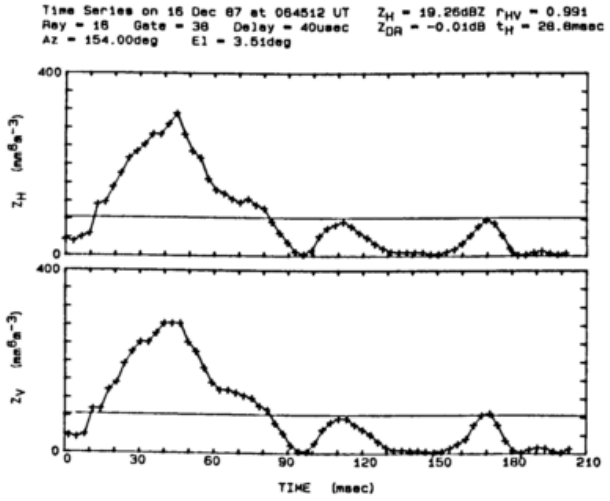


Figure 1. Time series pair showing the high correlation of ZH and ZV expected in light rain.

*The National Center for Atmospheric Research is sponsored by the National Science Foundation.

p(H,V) will be less than one if the scattering amplitudes for the two polarizations from each particle arrive at the antenna with a non constant amplitude ratio or with a phase difference. A distribution of differently sized particles will be the most important effect in reducing p(H,V). A p(H,V) of 0.432 in the melting layer (Figure 2) confirms this. The bright band in Z is quite pronounced in the vertical profiles plotted in Figure 3; the maximum value of Z is 15dBZ higher than in the rain below, indicating that the particles must be of low density ice and are probably snowflakes. The ZDR profile shows a bright band in ZDR 200m below that in Z. This depression of the ZDR bright band is a common occurrence in stratiform clouds, and increases as Z becomes larger; the melting snowflake apparently reaching its maximum degree of oblateness after it has started to collapse. The low value of p(H,V) in the bright band is probably caused by the coexistence of half-melted snowflakes and smaller raindrops.

A spectral analysis (Figure 4) of the time series in the melting layer (Figure 2) shows an interesting component from 40-60Hz which is greater in ZH than ZV, and is not observed in the time series for the snow above or the rain below the bright band.

We are currently developing Monte Carlo models to predict the reduction in p(H,V) for the following hydrometeors:

a) Monodispersed oblates - small phase differences between the amplitude pair from each particle due to losses or particle asymmetry.

b) Monodispersed tumbling oblates (e.g. graupel).

c) Polydispersed tumbling oblates (e.g.graupel).

d) Precessing and nutating polydispered oblates (e.g.snow and melting snow).

e) Differently shaped aligned oblates (e.g.rain).

In rain with a ZDR of 0.5dB we have found a significant fall of p(H,V) to about 0.95; but have not yet estalished if p(H,V) can be used as an independent estimate of the breadth of the size distribution.

The lowest values of p(H,V) in the ice in convective clouds, should occur when the difference in the horizontal and vertical scattering amplitudes of the particle is largest; this may well occur when slightly aspherical particles enter the Mie region, and could be a way of detecting large hail in clouds. If particles are tumbling then those with axes rotated at 45deg will dominate the cross-polar return, and therefore the cross-polar time series may contain information on tumbling rates.

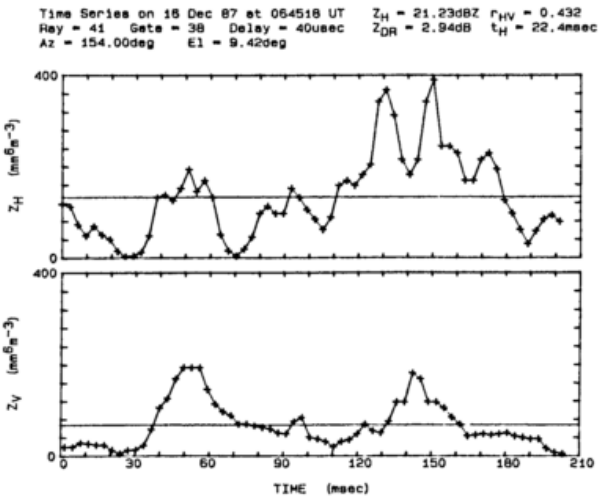


Figure 2. Time series pair observed in the melting layer of a stratiform cloud showing a lower correlation.

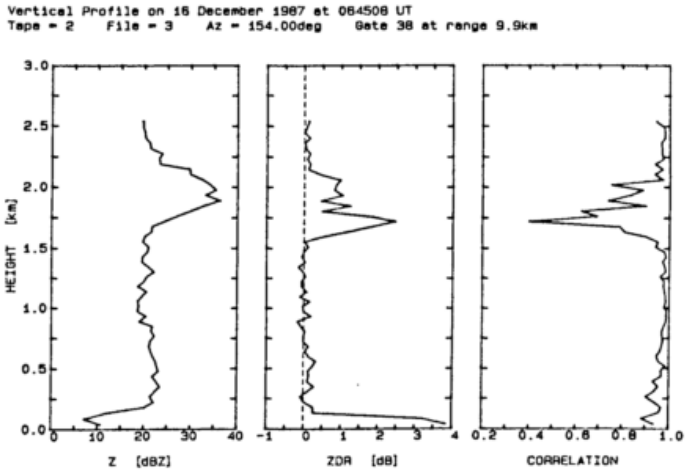


Figure 3. Profile of the vertical structure of a stratiform rain cloud from which the time series in Figures 1 and 2 are taken.

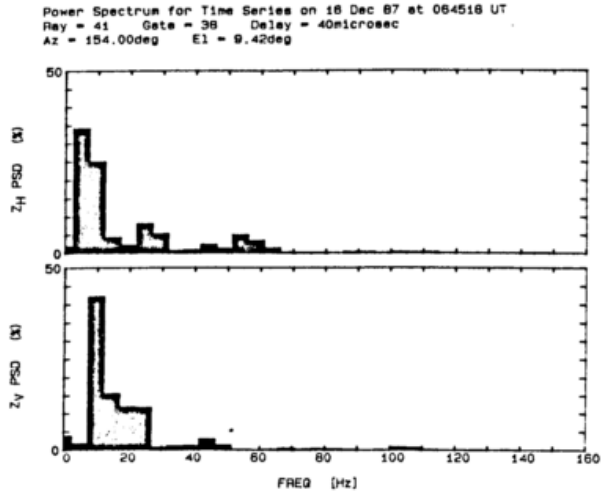


Figure 4. Normalised power spectrum for the time series of Figure 2.

4. ZDR FLARE ARTEFACTS AND IMPLICATIONS FOR DOPPLER ANALYSIS

WILSON and REUM (1988) analyse the Doppler properties of a radar artefact called a "flare echo", which extends downrange of some intense radar storm echoes. It is caused by triple scattering from a high Z region at height h, down to the ground, then back to the radar via the precipitation, thus forming a spurious echo a distance h behind the intense core. This flare has a Doppler velocity of equal magnitude to that of the core but with a reversed sign.

Figure 5, from the Chilbolton radar, has a flare echo where ZDR reaches +9dB. At a range of 87km Z reaches 70dBZ, and the flare may be identified by the column of positive ZDR inclined at 45deg to the vertical, extending from the ground at 88km range to an altitude of 4km at a range of 91km. We believe that this high value of ZDR arises because the triple scattering of the flare echo is confined to the ZH channel; for the vertical polarization the induced dipoles within the cloud should not radiate along their axes down to the ground.

Clearly such values of +9dB cannot be identified in terms of hydrometeors, but in less obvious cases positive values of ZDR towards the back of high Z regions could be erroneously interpreted as hydrometeors. ZDR artefacts caused by flare echoes should be much more widespread and intense at C and X band than at S band.

Doppler measurements are usually made using the ZH channel, but these arguments suggest that Doppler problems associated with flare echoes would be reduced if the ZV channel was used. An analysis of the MAYPOLE data, obtained by the NCAR CP2 S-band radar, reveals that the Doppler derived velocities from ZH and ZV are normally identical apart from flare regions. Further studies are underway to see if such arguments are valid at C and X band.

ACKNOWLEDGEMENTS

This research was supported by the Meteorological Office, by NERC Grant GR3/5896 and by AFOSR-87-0046. Our co-workers S M Cherry and J W F Goddard pioneered the implementation and interpretation of the ZDR data at Chilbolton. We thank R E Carbone, P H Herzegh, V N Bringi and T A Seliga for supplying us with data from the MAYPOLE '84 programme. IJC acknowledges the assistance of an ORS scholarship and AJI thanks members of the FOF at NCAR for many useful discussions.

REFERENCES

BEARD, K.V.; CHUANG, D.: J. Atmos. Sci. 44 (1987) 1509-1524.

BRINGI, V.N.; SELIGA, T.A.; CHERRY, S.M.: IEEE Trans Geo & Remote Sensing GE-21 (1983) 215-220.

CAYLOR, I.J.; ILLINGWORTH, A.J.: 22nd Conf. Radar Meteorology, Amer. Metereol. Soc. (1980) 88-91.

CHANDRASEKAR, V.; COOPER, W.A.; BRINGI, V.N.: submitted to J. Atmos. Sci. (1988).

GODDARD, J.W.F.; CHERRY, S.M.; BRINGI, V.N.: J. Appl. Met. 21 (1983) 252-256.

HALL, M.P.H.; GODDARD, J.W.F.; CHERRY, S.M.: Radio Sci. 19 (1984) 132-140.

ILLINGWORTH, A.J.; GODDARD, J.W.F.; CHERRY, S.M.: Q. J. Roy. Meteorol. Soc. 113 (1987) 469-489.

PRUPPACHER, H.R.; PITTER, R.L.: J. Atmos. Sci. 28 (1971) 86-94.

WILSON, J.W.; REUM, D.: J. Ocean & Atmos. Tech. (to be published 1988).

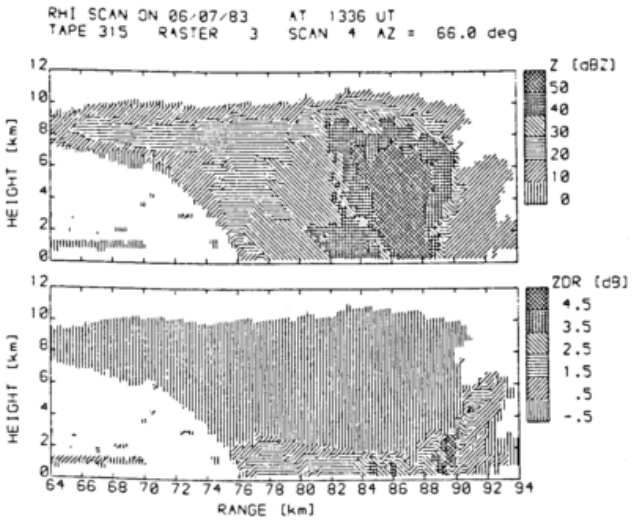


Figure 5. A vertical scan of a mature convective cloud showing a flare echo in ZDR near 88km range.

Z-R RELATIONS FROM AIRBORNE 2D-P MEASUREMENTS IN HAWAIIAN SHOWERS

Rodney J. Kubesh and Kenneth V. Beard

Climate and Meteorology Section, Illinois State Water Survey
2204 Griffith Drive, Champaign, Illinois 61820

David B. Johnson, U.S. Bureau of Reclamation

1. INTRODUCTION

Many investigators have computed empirical relationships between the radar reflectivity factor Z and the rainfall rate R, expressed in power law form as $Z = AR^b$. Relations vary widely depending on location, rain type and synoptic conditions (see Battan, 1973). Obtaining appropriate relationships is complicated by the spatial and temporal variability of precipitation, especially when using disdrometer data to compute Z and R.

Here we present Z-R relations for trade-wind showers off the coast of Hawaii near Hilo from measurements obtained during the 1985 Joint Hawaiian Warm Rain Project. The data were taken with an airborne disdrometer (PMS 2D-P) and were collected in the early morning band clouds (typically 20°C bases, 10°C tops) that form offshore of Hilo. Aircraft penetrations of rain shafts, both within and beneath clouds, were made with the University of Wyoming King Air (operated by NCAR).

2. MEASUREMENT AND ANALYSIS

Both Z and R were computed from 2D-P drop size distributions. We used only Z-R values obtained from drop images that satisfied a spherical particle test. Concentrations were corrected for drops with centers outside of the diode array. In addition, all data obtained during orographic cloud flights or associated with ice particles (a rare occurrence) were excluded.

The basic Z-R data suffers from the small sample volumes characteristic of the 2D-P probe (typically 20-70 L per buffer). According to Mueller and Sims (1966) sample volumes for raindrop size distributions should be at least 1 m^3 to reduce the sample size variance to a small fraction of the total variance. To increase the sample volume, we combined data from contiguous seconds. The largest practical time was 15 seconds (corresponding to 1.3 km of aircraft travel and comparable to a radar volume dimension at medium range).

To obtain the correct spatial averaging we used the equivalent of the ensemble drop concentration by averaging values of Z and R weighted by the sample volumes. The data were considered contiguous if the stop times of the successive PMS buffer showed drops present every second. Averaging over 15 seconds increased the sample volume to 0.7 m^3.

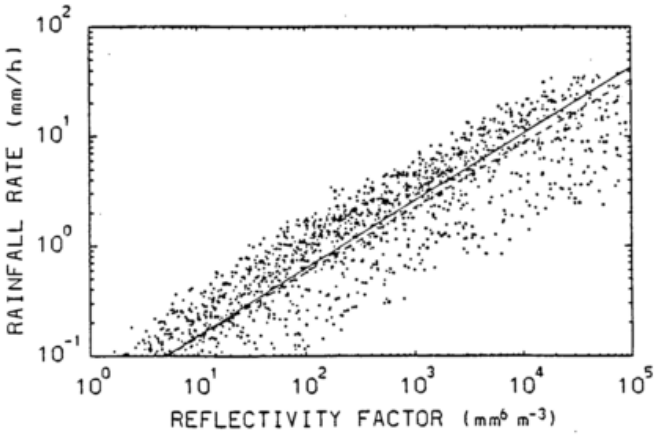


Fig. 1. Z-R scatter diagram. The solid line is the regression for the 15-second data and the dashed line is the regression for bin averaging (Section 4).

A scatter diagram for the 15-second averages is shown in Fig. 1. To estimate rainfall rate from the radar measurement, R was treated as the dependent variable using logarithmic values of Z and R to yield the regression $R = 0.0375Z^{0.612}$ (solid line). [The regression for Z as the dependent variable is $Z=203.6R^{1.50}$.]

Table 1. Z-R relation from Hawaiian shower data. R is the dependent variable, as depicted in Fig. 1, with coefficients for the Z-R formula in the form $Z = AR^b$. The upper row is for 15-second data, and the lower row for bin averaging (Section 4).

A	b	ρ	σ	ε
214	1.63	.959	1.06	.299
257	1.70	.991	.71	.097

The regression with R as the dependent variable is given in Table 1—but inverted to the conventional form, $Z = AR^b$. Also shown in Table 1 are the correlation coefficient (ρ), standard deviation (σ) and the standard error of estimate [$\varepsilon = \sigma\,(1-\rho^2)^{1/2}$]. The correlation

coefficient, which is the fraction of variation explained by the regression, is high (ρ= 0.979), in part because Z and R are computed from the same data. For log-normal data the standard error predicts a rainfall rate uncertainty in the range $10^{-\epsilon}R$ to $10^{+\epsilon}R$ or $0.5R$ to $2.0R$. However, because of skewness (evident in Fig. 1), the standard error provides only a rough estimate of the uncertainty in predicting rainfall rate from measurements of Z.

3. DROP CONCENTRATIONS

Our set of 1786 Z-R estimates contains a total sample volume of 1265 m^3 with 2.54 million drops. This is an impressively large data set for disdrometer measurements in one type of precipitation. However, the adequacy of the Z-R relation in Fig. 1 depends on the whether *individual* samples are representative. Although each sample contains about 1400 drops, Z and R are strongly weighted by drop size, and so it is important that most samples contain representative numbers of large drops. It is clear that a 15-second sample with its 0.7 m^3 volume cannot be used to estimate drop concentrations of less about than 10 m^{-3} (*e.g.*, according to Cornford (1967) a factor of 2 uncertainty in concentration at the 95% confidence level requires about 10 drops.)

Drop size distributions from the 15-second averages are shown in Fig. 2 in four rainfall rate categories: R < 0.1, 0.1-1, 1-10, >10 mm/h with sizes reduced by the effect of equilibrium axis ratios. The dashed lines give an exponential distribution for convective showers (Sekhon and Srivastava (1971)) using the average rainfall rates. Fig. 2 shows the surprisingly large drops that exist in these warm clouds, occurring at concentrations in excess of an exponential distribution (Beard *et al.*, 1986). In light to heavy rains (R > 1 mm/h) another noticeable change from exponential is the depletion of drizzle drops. For R < 1 mm/h the concentrations of drizzle is higher than the corresponding exponential, and there are no drops larger than d = 4 mm. These latter distributions appear similar to Blanchard's (1953) for the orographic clouds downstream from our study area.

In light to heavy rains the larger drops (d = 3-5 mm) have concentrations of about 10^{-5} per liter (per 0.1 mm interval), or 0.2 m^{-3} for the 2 mm interval. Thus, the concentration of larger drops in these showers is much too low even for a rough estimate from the 0.7 m^{-3} volume of a 15-second sample.

The large scatter in Fig. 1 is apparently due to the

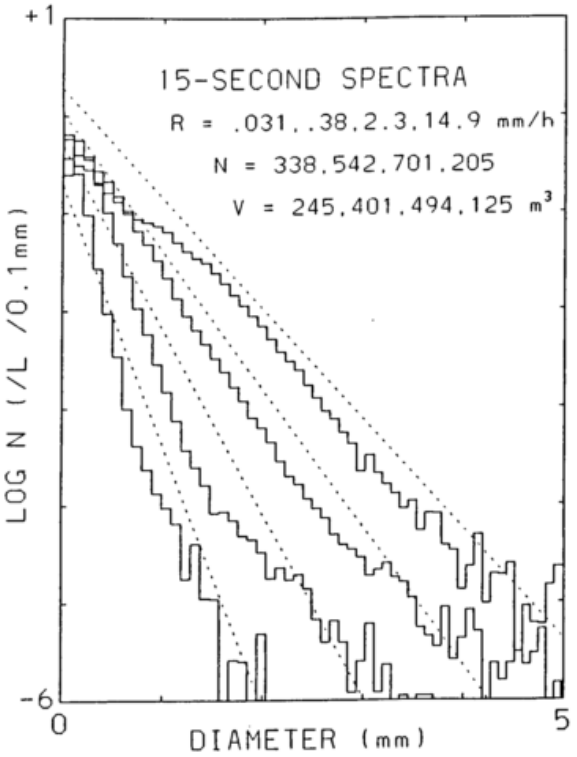


Fig. 2. Drop size distributions for 15-second averages in 4 rainfall rate categories: R < 0.1, 0.1-1,1-10, >10 mm/h. Listed are the respective average rates (R), the numbers of samples (N) and sample volumes (V).

inadequacy in sampling large raindrops. The effect of adding a single large drop to a sample is to increases Z considerably more than R leading to a skewness toward larger Z and lower R. A simulation of PMS 2D-P sampling using idealized exponential distributions and a random arrival scheme showed a similar skewness from hit or miss sampling of large raindrops. Skewed Z-R data were a regular feature of these Hawaiian showers.

We found that the contiguous averaging process helps the sampling problem somewhat. For instance, the variance is reduced from 1.22 for the single buffer data to 1.06 for the 15-second averages. But contiguous averaging cannot be extended further because of the limited size of the rainshowers.

4. BIN AVERAGING OF Z-R DATA

Another averaging process has been used by Mueller (1966) in which R from raindrop camera data was averaged in Z categories of 0.1 decade intervals (1 dB bins). The procedure was used to test whether a fitted regression was sensitive to the least squares method; it yielded a similar result to the regression. We adopted this method to provide additional averaging of the 15-second PMS data. Fig. 3 shows our regression (solid line) and a regression through the number-weighted average values

of Z and R in 1 dB Z-bins (lower dotted line). Since there were typically 30 to 40 15-second averages per bin, the sample volume was increased to about 25 m^3 (or to about 5 large raindrops per sample). [Averaging in 3 dB bins tripled the number of large drops per sample with no appreciable affect on the regression.]

Bin averaging is only partially physical; it averages R properly, but uses artificial groups of Z. We also used the conjugate method of averaging the 15-second data in 0.1 decade intervals of R (upper dotted line). Since we have no strong physical reason for preferring one method over the other, we chose a mean 1 dB bin result given in Table 1 ($Z=257R^{1.70}$) and shown as dashed lines in Figs. 1 and 3. [The mean result for 3 dB bins is essentially the same: $Z=266R^{1.69}$.] The scatter for the 1 dB bin data is much smaller than in Fig. 1, *e.g.*, the standard error is 0.097 (Table 1) which predicts a rainfall rate uncertainty of 0.80R to 1.25R.

5. DISCUSSION

The mean bin method agrees with the 15-second regression only at a very low rainfall rate (0.1 mm/h) where large raindrops are absent. For appreciable R the bin method predicts a lower rainfall rate for a given reflectivity. The trend of increasing intercept and slope was noting for all averaging, *i.e.*, A = 80, 142, 214, 257, 266 and b = 1.51, 1.60, 1.61, 1.70, 1.69 for the single buffer, 6-second, 15-second, 1 dB bin and 3 dB bin methods, respectively. These trends are the expected effect of including better estimates of large drop concentrations in Z-R data. [The increase in A (rightward drift in the regression) is an effect of averaging with high Z scatter at all rainfall rates (see Fig. 1), whereas the increase in b (decrease in slope) results from averaging with relatively more scatter in Z at higher rainfall rates.]

The best Z-R relation for these Hawaiian showers appears to be $Z = (260 \pm 5)R^{1.70 \pm 0.01}$ based on the convergence of both A and b as averaging provides more adequate estimates of large drop concentrations. In comparison Blanchard found $Z = (17\text{-}31)R^{1.55\text{-}1.71}$ for the orographic clouds near Hilo, and Mueller found $Z = 125R^{1.47}$ for trade-wind showers in the Marshall Islands. Our relation predicts reflectivity factors that are 3-12 dB higher in light to heavy rainfalls—apparently as a result of higher concentrations of large raindrops.

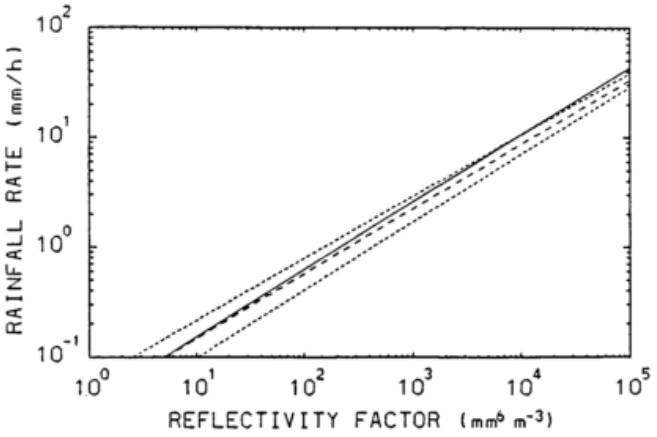


Fig. 3. Bin averaging of 15-second data. Regressions are shown for the Z-bin method (lower dotted line), the R-bin method (upper dotted line), the mean bin result (dashed line), and the 15-second data (solid line).

6. ACKNOWLEDGMENTS

The authors appreciate the assistance of Darrel Baumgardner in obtaining and interpreting archive data. This material is based upon work supported by the National Science Foundation under Grant ATM83-18669. Any opinions, findings, and conclusions or recommendations expressed in this material are those of the authors and do not necessarily reflect the views of the National Science Foundation.

7. REFERENCES

Battan, L. J., 1973: *Radar Observations of the Atmosphere*. Univ. Chicago Press, Chicago, 324 pp.

Beard, K. V., D. B. Johnson and D. Baumgardner, 1986: Aircraft observations of large raindrops in warm, shallow, convective clouds. *Geophys. Res. Lett., 19*, 991-994.

Blanchard, D. C., 1953: Raindrop size distributions in Hawaiian rains. *J. Meteor., 10*, 457–473.

Cornford, S. G., 1967: Sampling errors in measurements of raindrop and cloud droplet concentrations. *Meteor. Mag., 96*, 271-282

Mueller E. A., 1966: Radar cross sections from drop size spectra. Ph.D. thesis, Univ. of Illinois.

Mueller E. A., and A. L. Sims, 1966: The influence of sampling volume on raindrop size spectra. *12th Conf. on Radar Meteor.*, Amer. Meteor. Soc, 135–141.

Sekhon, R. S., and R. C. Srivastava, 1971: Doppler radar observations of drop-size distributions in a thunderstorm. *J. Atmos. Sci., 28*, 983-984.

COMPARISON BETWEEN AIRCRAFT AND DOPPLER RADAR MEASUREMENTS DURING ENCC (VOVES 1983)

Henri SAUVAGEOT*, Arlette RIGAUD**, Elizabeth HICKS**, Constantin PONTIKIS**
* Laboratoire d'Aérologie, Campistrous
** Météorologie Nationale, EERM/CRPA, Magny les Hameaux

1- INTRODUCTION

The interpretation of radar reflectivity data in terms of pertinent cloud parameters such as liquid water contents Q_L or mean droplet diameter D is an important goal of radar meteorology.

An empirical formula relating radar reflectivities to liquid water contents has been presented by Atlas (1954). Later Sauvageot and Omar (1987) proposed a similar formula obtained by using data collected during the "COCAGNE 3" experiment. This formula :

$$Z = 0.068\ Q^{1.94} \qquad (1)$$

can be used to calculate radar reflectivities in cloudy air regions containing droplets with a maximum diameter smaller than 200µm.

The goal of this paper was to check this $Z\text{-}Q_L$ formula by using data sets obtained during the "ENCC 1983" experiment in Voves (Pontikis et al.,1987). The data sets concern non precipitating clouds simultaneously observed by a 8mm Doppler radar and sampled by using an instrumented aircraft.

2- DATA SETS

The "ENCC 1983" experiment in Voves took place from 1 to 20 September 1983. All clouds observed during this period were convective. Some developped after the passage of a cold front resulting in a cool region with numerous cumuli having flat bases at nearly 1100 meters. The whole cloud layer within a radius of 100 Kms was explored by the 8mm Doppler radar RABELAIS of the Laboratoire d'Aérologie de Toulouse. The dynamic, thermodynamic and microphysical measurements were obtained by using the instrumented EERM Pipper Aztec aircraft. The mean aircraft velocity inside clouds was about 70m.s^{-1} and the data collection frequency was 1HZ. Liquid water contents were both measured by using the Johnson-Williams device or calculated by using the FSSP data. For exemple figure 1 presents the evolution of the liquid water contents as function of time for the 805mb level sampled the 9 of september 1983.

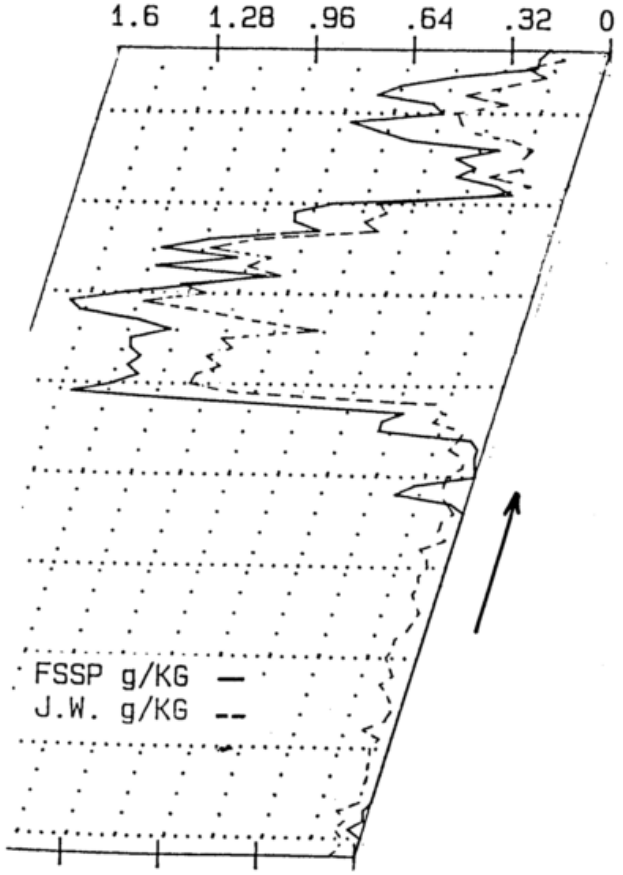


FIGURE 1 : FSSP and JW liquid water contents (g/Kg) on the 805mb level sampled on 9 September 1983

3- RESULTS AND CONCLUSION

For this analysis three cloud groups have been considered. They concern clouds sampled respectively on the 9, 12 and 15 september 1983. Most of the clouds were non precipitating with reflectivities lower than -15 dBZ. The vertical variation of reflectivity was week, while the horizontal one

showed a 1Km scale variation corresponding to a cloud band structure. The reflectivity Z according to time has been calculated by using the liquid water content measurements and formula (1). Figures 2 and 3 present the calculated reflectivities according to time for different levels of the concerned cloud groups. The upper and lower limits of the values obtained by the 8mm radar are also plotted. The agreement between calculated and observed reflectivities is satisfactory for the levels near cloud base.

In figure 4 the calculated reflectivities in a 700m zone are larger than the observed ones. This fact is probably due to the different sampling volumes for aircraft and radar measurements. Probably drops with diameters larger than 200µm were present at this level near cloud top in a volume smaller than the radar impulsion one.

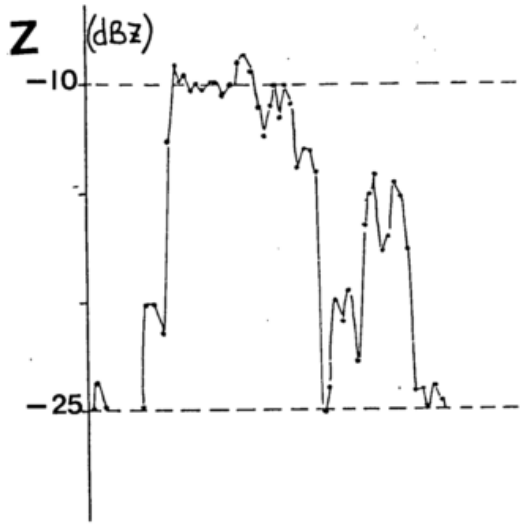


FIGURE 2 : Calculated reflectivities on the 805mb level sampled on 9 September 1983

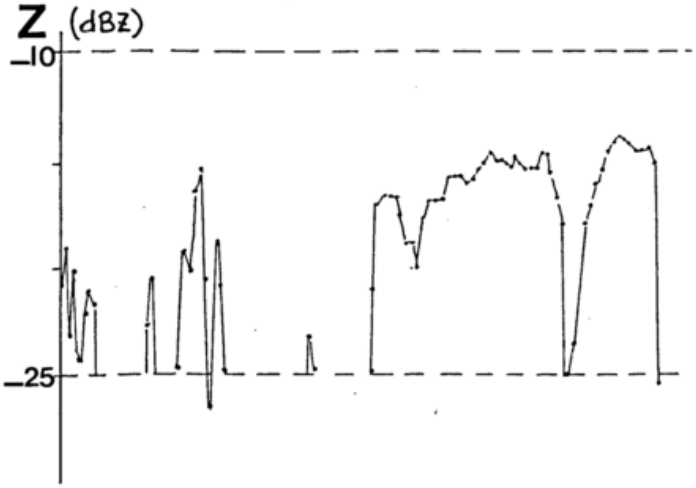


FIGURE 3 : Calculated reflectivities on the 810mb level sampled on 15 September 1983

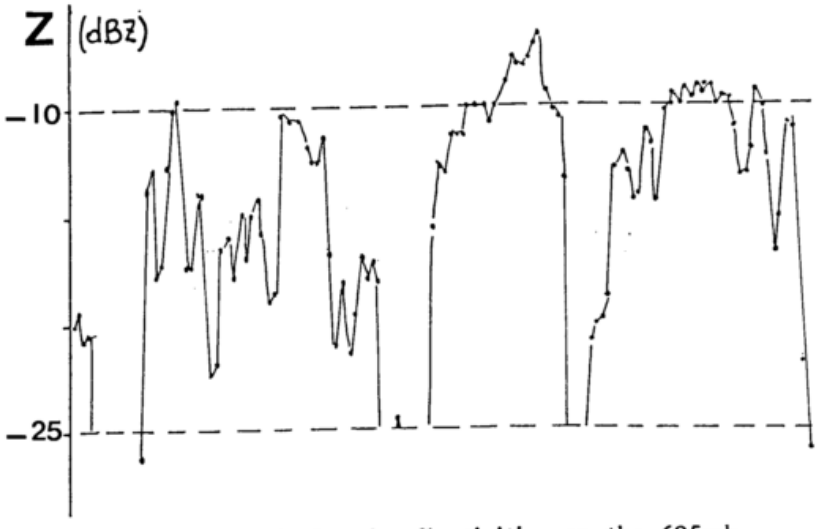


FIGURE 4 : Calculated reflectivities on the 695mb level sampled on 15 September 1983

BIBLIOGRAPHY

ATLAS D. (1954) The estimation of cloud parameters by radar. J. Met. 11, 309-317

SAUVAGEOT H., OMAR J. (1987) Radar reflectivity of cumulus clouds. J.A.O.T. 4, 264-272

PONTIKIS C., RIGAUD A., HICKS E. (1987) Entrainment and mixing as related to the microphysical properties of shallow warm cumulus clouds. J.A.S. 44(15), 2150-2165

EHF ATTENUATION THROUGH THE MELTING LAYER

Arnold A. Barnes, Jr.

Air Force Geophysics Laboratory: AFGL/LYA
Hanscom AFB, MA 01731-5000 U.S.A.

1 INTRODUCTION

Recently there has been a move to higher frequencies as the lower EHF communication bands have become more crowded. Above 20 GHz the signals are attenuated by intervening precipitation. For those satellite communication systems which operate at low signal-to-noise ratios, the attenuation due to precipitation can cause systems outages which for some operations cannot easily be circumvented by alternate routes or equipment.

A 35 GHz signal from a satellite experiences very little attenuation while passing through the ice and snow regions in the upper parts of the storm. However, as soon as it encounters wet snow in the melting layer, the attenuation increases markedly because of the change in the index of refraction of the precipitation particles. As the snow particles melt they collapse into raindrops which fall faster than the snow. Below the melting layer the spherical rain drops attenuate the signals. Rain attenuation has and is being studied by other groups, and relationships have been established between attenuation, rain rates and drop size distributions. Studies have reported that attenuation in the melting layer is two to ten times that in rain (Nishitsugi, et al, 1971;Oguchi, 1983). Since the large wet snow flakes in the melting layer are about the same size as the wavelengths (~ 8mm), this should not be unexpected. In designing our Weather Attenuation Program emphasis was given to studies in the melting layer, and we drew heavily on our previous cloud microphysical studies of the melting layer, (Schaller, et al, 1982; Fukuta, et al, 1983; Cohen and Sweeney, 1983) and our studies of large scale storm systems (Barnes, et al, 1982).

2 PROGRAM OVERVIEW

Signal strengths from the 38 GHz transmitter aboard satellite LES-8 were recorded and they clearly demonstrated the attenuation due to the precipitation between the satellite and the ground receiving site at Lincoln Laboratory which is located on Hanscom AFB. Airborne meteorological data were collected by the instrumented aircraft. End products included ice/water content, particle size distributions, temperature, humidity and aircraft position. A new instrument designed to measure the mass of ice and/or water was also tested for collection of precipitation mass information within the melting layer where both snow and rain coexist (Plank, 1987). The program was conducted in the greater Boston area from 15 March through 22 May 1986 and ten cases were obtained even though rainfall during this period was much below normal. Figure 1. depicts the program.

3 LES-8 ATTENUATION

Satellite LES-8 was in a quasi-geostationary orbit which moved north and south during a siderial day. It was always above the horizon as seen from Lincoln Laboratory, and varied in elevation angle from 8 to 49 degrees above the horizon. Its 38.04 GHz transmitter fed into a steerable dish which operated in an autotrack mode to point its 1° beam at the Lincoln Laboratory dish receiving antenna. The received signals were recorded and compared with signals recorded during periods of clear weather. We observed attenuation in excess of 15 dB during periods of moderate to heavy showers and 6db in steady rain. Figure 2. is an example of observed precipitation attenuation.

It was discovered that there was a 1 to 2 dB loss of signal when the radome covering the receiving antenna was wet. This was measured by spraying the radome with water on a clear, dry day. There is also increased attenuation as the radome gets dirty. Cleaning of the radome every four years or so reduces the attenuation by approximately 1dB (H. Hoover, 1986, personal communication).

4 GROUND BASED EQUIPMENT

At the Sudbury site a Joss distrometer was used to measure drop size distributions, and the total rainfall was measured with a tipping bucket raingauge. At Hanscom AFB a second Joss distrometer was used during the latter half of the program. A fast response rain-rate meter, a fall velocity meter and standard meteorological equipment which provided temperature, dewpoint and wind velocity were used. The non-standard equipment was developed by the Cloud Physics Branch and has been patented by the Air Force (Gibbons, et al, 1983; Plank and Berthel, 1983). Loransondes (rawinsondes using LORAN to obtain winds) which were developed for AFGL under contract, provided detail soundings.

5 THE M-METER

Past work suggests that EHF attenuation is a function of the relative mass of ice, snow and rain in the volume through which the signals pass (Ebersole, et al, 1984). Airborne measurement of the precipitation mass has been difficult. The PMS instruments which measure

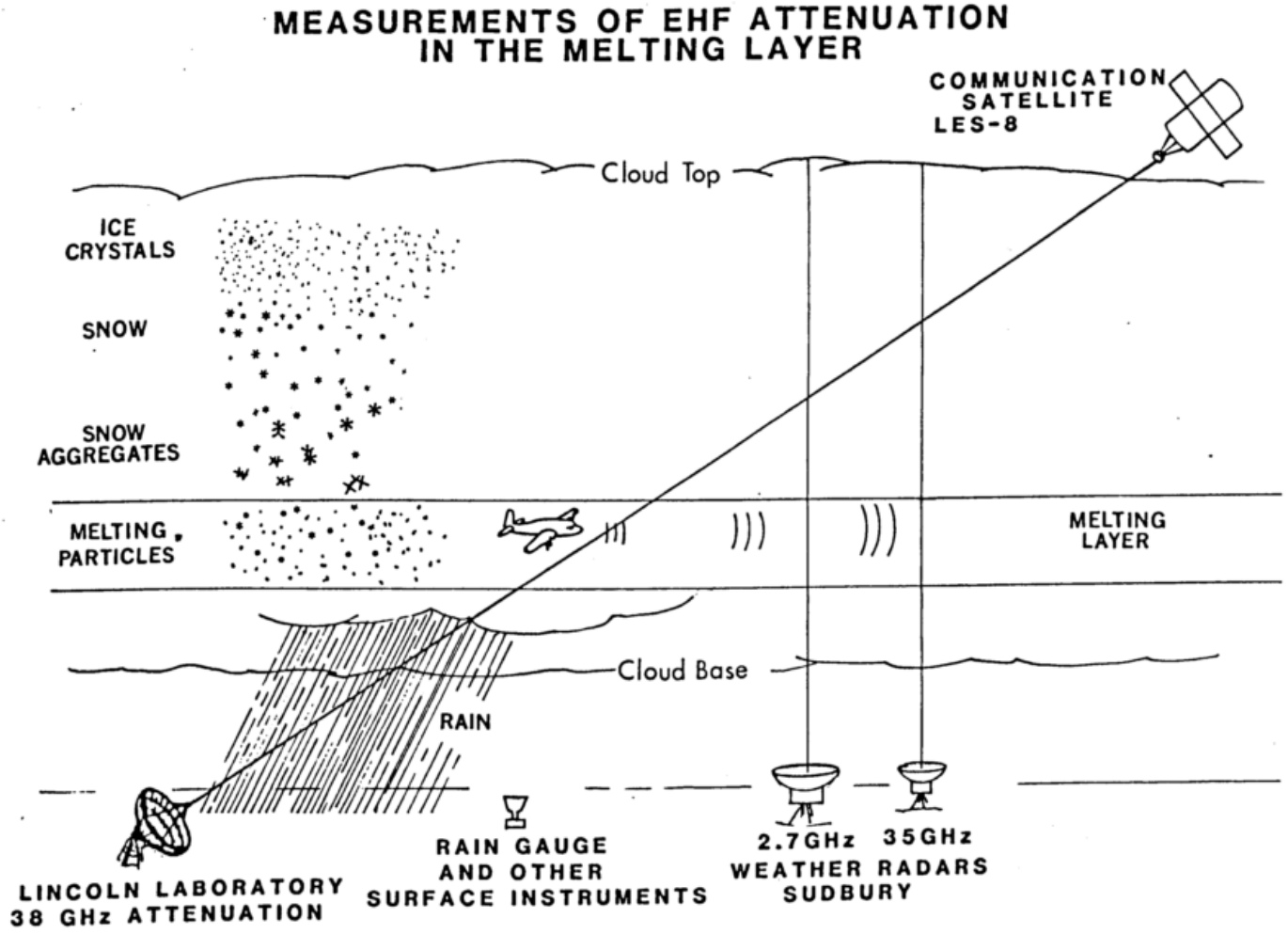


Figure 1. Depiction of the AFGL 1986 Weather Attenuation Program

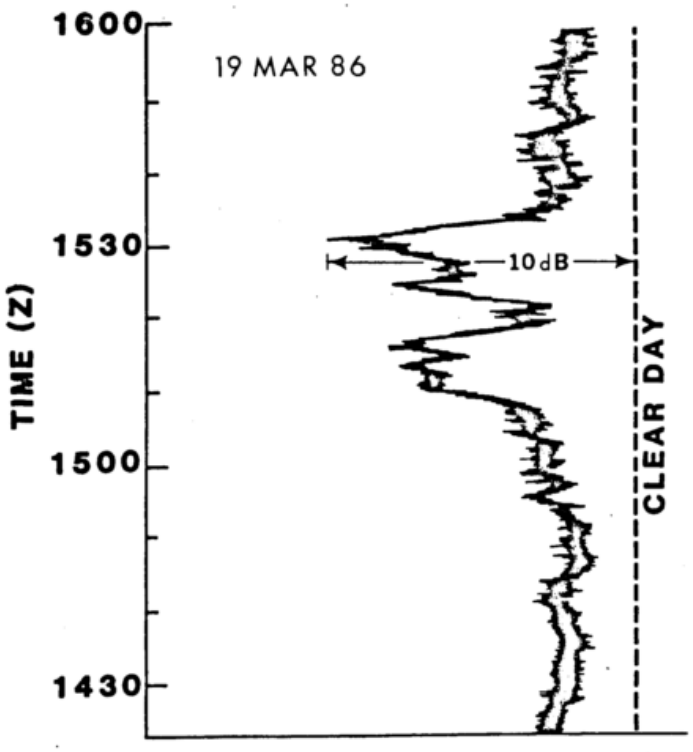


Figure 2. Attenuation of the LES-8 36 GHz signal due to precipitation

particle size and shape give very good measurements of mass when operating in rain where the particles are spherical and the density is essentially constant at 1.0 gm/cm^3. In ice and snow the particles are irregular, the densities vary widely, and so called "L-to-D" relationships are used depending on the crystal habit and size (Cunningham, 1978; Heymsfield, 1972; Heymsfield and Knollenberg, 1972; Knollenberg, 1975; Plank, 1977). As mentioned above, we are particularly interested in the melting layer, and it is in this layer where "L-to-D" relationships are practically useless.

The M-Meter (Plank, 1987) makes use of the mass of the precipitation directly to obtain measurements (see Figure 3.). The housing is attached to the aircraft and contains the detector which measures the rotation speed of the spinner, which is located at the base of the cone shaped deflector. The spinner has slanted fins which causes it to spin as it passes through the air. When precipitation particles get into the fins they slow the rate of rotation (reduce the angular momentum) because they are more dense than air. To keep the particles from bouncing off of the cone shaped deflector and not passing through the fins, there is an outside deflector supported from the housing by four outriggers.

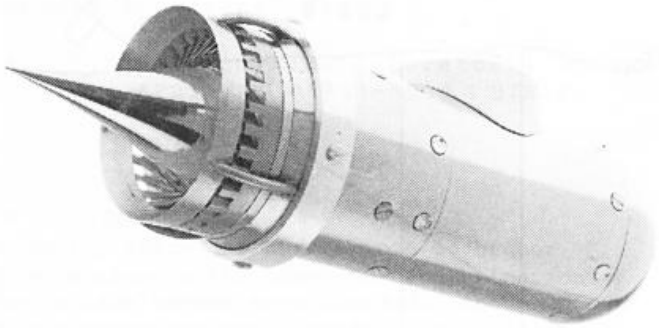


Figure 3. The M-Meter

This instrument was first flight tested on the Weather Attenuation Program and was found to be more sensitive than anticipated. In fact, the accuracy was limited on these test flights due to the inaccuracy of the calculated true air speed. We believe that accuracies of .01 gm/m^3 are achievable. The present design works well from 100 to 180 knots (50 to 93 m/s) and can be extended to 200 knots (103 m/s). In order to operate at higher true air speeds, the spinner must be redesigned.

6 RESULTS

Ten different precipitation events were investigated even though the amount of rainfall was much below normal for this 69 day period.

The 38 GHz signals from satellite LES-8 showed attenuations in excess of 15dB during some of the showers while light continuous precipitation gave attenuations of about 6dB. We were concerned about the attenuation due to the radome covering the receiving dish at Lincoln Laboratory being wetted by the rain, so we sprayed the radome on a clear, dry day and found a loss of one to two dB.

The other ground based and airborne equipment operated normally on almost all occasions, but one Joss distrometer did not operate properly prior to the first of May.

Tests with the M-meter went better than expected. Speed and altitude corrections were close to predicted, but the sensitivity was greater than expected and was found to be limited by the accuracy of the calculated true air speed.

7 REFERENCES

Barnes, A.A., I.D. Cohen and D.W. McLeod, 1982: Investigations of Large Scale Storm Systems. AFGL-TR-82-0169. AD A1198962.

Cohen, I.D., and H.F. Sweeney, 1983: Melting Layer Survey - Final Report, AFGL-TR-83-0200. AD A137911.

Cunningham, R.M., 1978: Analysis of particle spectral data from optical array (PMS) 1D and 2D sensors. Preprints, Fourth Symposium on Meteorological Observation and Instrumentation, AMS, Denver, 345-350. AFGL-TR-78-0102. AD A053541.

Ebersole, J.F., W.K. Chang, J. Hallett and R.G. Hohlfeld, 1984: Effects of hydrometeors on electromagnetic wave propagation. AFGL-TR-84-0318. AD A155379.

Fukuta, N., R.C. Savage, G.I. Donovan and C-M. Liu, 1983: The Microphysics of Snow Crystal and Snowflake Melting. AFGL-TR-83-0066. AD A129030.

Gibbons, L.C., A.J. Matthews, R.O. Berthel and V.G. Plank, 1983: Snow Characterization Instruments. AFGL-TR-83-0063. AD A131984.

Heymsfield, A.J.,1972: Ice crystal terminal velocities, J. Atmos. Sci., 29, 1348-1357.

Heymsfield, A.J. and R.G. Knollenberg, 1972: Properties of cirrus-generating cells, J. Atmos. Sci., 29(7), 1358-1366.

Knollenberg, R.G., 1975: The response of optical array spectrometer to ice and snow; A study of probe size to crystal mass relationships. Final report. AFCRL-TR-75-0494. AD A020276.

Nishitsuji, A., A. Matsumoto, K. Hatori, K. Ono, Y. Kawase, N. Nagai, S. Yajimi, and T. Ushizaka, 1971: On the Millimeter Wave Propagation Test at Snowfall, in SHF and EHF Propagation in Snowy Districts, A. Matsumoto and A. Nishitsuji, Eds. (monograph Ser. of the Res. Inst. of Appl. Electricity, Hokkaido Univ., Sapporo, Japan), No. 19, 1-20.

Oguchi, T., 1983: Electromagnetic Wave Propagation and Scattering in Rain and Other Hydrometeors. Proceedings of the IEEE, 71, No.9, September 1983, 1029-1078.

Plank, V.G., 1977: Hydrometeor data and analytical-theoretical investigation pertaining to the SAMS rain erosion program of the 1972-73 season at Wallops Island, Virginia. AFGL/SAMS Report No. 5. AFGL-TR-77-0149. AD A051192.

Plank, V.G., 1987: The M-Meter. Preprints, Second Airborne Science Workshop, Miami, Florida, 3-6 February 1987, 171-173.

Plank, V.G., and R.O. Berthel, 1983: High Resolution Rain and Snow Rate Measurements. AFGL-TR-83-0107. AD A128296.

Schaller, R.C., I.D. Cohen, A.A. Barnes and L.C. Gibbons, 1982: A Survey of Melting Layer Research. AFGL-TR-82-0007. AD A115224.

SIZE DISTRIBUTION OF PRECIPITATION PARTICLES IN MIDLATITUDE MESOSCALE CONVECTIVE COMPLEXES

Jia-Dong Yeh, Bei-Fen Fan and William R. Cotton

Department of Atmospheric Science, Colorado State University,
Fort Collins, CO 80523

1 Introduction

Measurements of precipitation particle size distributions above and beneath the melting layer in the transition region and stratiform region of two mid-latitude mesoscale convective complexes during the 1984 Airborne Investigations of Mesoscale Convective Systems (AIMCS) and the 1985 PRE-STORM experiments were analyzed to understand how well the observed particle size distributions can be approximated by various types of distribution functions, such as exponential and log-normal distributions. The parameterization problem of microphysics in cloud modeling is also discussed.

2 Data

There are 78 samples of the hydrometeor size spectra obtained from the stratiform region of an AIMCS case (15 July 1984) and 149 samples taken from the PRE-STORM case of 4 June 1985. Among them 62 samples were taken from the transition region during the horizontal flight at the 5150 m level ($-6.7°$ - $-8.5°C$), 41 samples were taken from the stratiform region at the same level, and 46 samples were taken during the vertical sounding flight from the 6100 m ($-13.0°C$) to 3000 m ($+1.2°C$) levels in the stratiform region.

3 The exponential fit to hydrometeor size spectra

The Marshall-Palmer distribution

$$N(D) = N_0 e^{-\lambda D} \tag{1}$$

is applied extensively in the parameterization of microphysics in numerical cloud models. It is determined completely by the slope parameter λ and intercept parameter N_0. Generally, the intercept parameter N_0 is assumed constant, while in some cloud models the slope parameter λ is assumed constant. Observational evidence, however, suggest that both the slope λ and intercept N_0 depend on meteorological conditions, cloud conditions, and time and location of the sample taken in the cloud system (Waldvogel, 1974). The measurements in the midlatitude mesoscale convective complexes in this study show that the exponential distribution fits the observational precipitation particle size spectra well in the entire measured region. The average linear crrelation coefficients for $\ln N(D)$ and D is -0.96 for water drops and -0.92 for ice particles in the stratiform region of the AIMCS case, and -0.96 and -0.98 for the ice particles in the transition region and stratiform region of the PRE-STORM case, respectively. Fig. 1 shows the scatter plots of intercept N_0 as a function of slope λ. It can be seen from Fig. 1 that the slope λ does not vary much for water drops in the AIMCS case, its mean value is about $17(\pm 3.6)$ cm. So λ may be considered approximately a constant as suggested by Cotton *et al.* (1986). The sample size of water drop size spectra from the PRE-STORM case is too small to be meaningful. For ice particles, however, both N_0 and λ are variable. The values of intercept parameter N_0 vary up to 3 orders of magnitude, from 4×10^{-3} to $3 \times 10^{0} cm^{-4}$, and slope parameter λ vary about 7 times on magnitude, from 6 to 45 cm^{-1}. Therefore, assuming the slope parameter or the intercept parameter as constant in modeling the stratiform region of MCSs is not appropriate. As a consequense, one cannot diagnose the particle concentrations from the prognostic values of mixing ratio. Therefore it is necessary to develop a set of prognostic equations of particle number concentration in a parameterized cloud microphysics model. Here we propose an approximate empirical approach to diagnose the particle concentration from the prognostic value of mixing ratio.

There is some correlation between the intercept N_0 and slope λ as shown in Fig. 1, which is reflected by the fact that decreasing values of λ usually correspond to decreasing values of N_0. That is particularly reasonable for the mature cloud system in which the main processes affecting the size spectrum are self-collection, aggregation and collisional breakup. The best fit line has a form

$$N_0 = a\lambda^b \tag{2}$$

with a correlation coefficient of 0.94 between $\ln N_0$ and $\ln \lambda$ (AIMCS case when $a = 1.1 \times 10^{-4}$ and $b = 2.8$), and 0.89 (PRE-STORM case when $a = 3.4 \times 10^{-6}$ and $b = 3.8$).

There does not seems to be an obvious relation between the distribution parameters (N_0 and λ) and the water content (WC). However, assuming an exponential distribution and the definition of water content, we fit an empirical relation of the form

$$\lambda = c + d\left(\frac{N_0}{WC}\right)^{\frac{1}{4}} \tag{3}$$

where c, d are different for water and ice particles and depending on the cloud system condition. For AIMCS case, the correlation coefficient is 0.73 for water drops when $c = 0.96$ and $d = 1.28$, and 0.98 for ice particles when $c = -7.1$ and $d = 1.33$. For the PRE-STORM case, the correlation is also pretty good for ice particles, being 0.98 when $c = -2.0$ and $d = 0.86$. Fig. 2 shows the degree of linear correlation. Based on Eq. 2 and Eq. 3, the size spectrum parameters can be inferred from the prognostic value of water content WC and, thus, the size distribution and number concentration from the integration of Eq. 1.

4 The lognormal fit to hydrometeor size spectra

Although the results of observational and theoretical studies of the evolution of hydrometeor size distributions generally support that the exponential distribution is a good approximation to the size distribution of precipitation particles, important deviation from it have been noted. Feingold and Levin (1986) argued that an exponential distribution cannot adequately describe the observed raindrop size distributions. They, as well as others in the past, suggested that a lognormal distribution

$$N(D) = \frac{N_T}{\sqrt{2\pi}\ln\sigma_g D} exp[-\frac{\ln^2(\frac{D}{D_g})}{2\ln^2\sigma_g}] \tag{4}$$

better fits the observational raindrop size distributions. The parameter of the lognormal distribution N_T is total number concentration of particle, D_g is the geometric mean of the particle diameter, and σ_g represents the standard deviation. We are interested in whether the lognormal distribution better fits observed particle spectra than the exponential distribution aloft for the ice particles in the midlatitude mesoscale convective complexes.

For measuring the goodness of fit of a distribution function to an observational particle size distribution, we use a relative standard error (coefficient of variability) defined as

$$CV = \frac{1}{N_T}\{\frac{1}{n}\sum_{i=1}^{n}[N_i(observ) - N_i(fit)]^2\}^{\frac{1}{2}} \quad (5)$$

where i represents the ith size category of particles. We use CV to compare the goodness of fit of the lognormal and exponential distribution for the ice particle data taken from horizontal flight in the transition region and stratiform region of the PRE-STORM case. Table 1 presents a comparison of the average relative standard error (CV) for these two distribution functions, the mean values of distribution parameters are also presented in Table 1. The results of the tests indicate that the lognormal distribution is a better fit for ice particles in both the transition region and stratiform region. Fig. 3 illustrates the result of applying these two formula to the mean size distributions in the transition and stratiform regions. It can be seen from Fig. 3 that the lognormal distribution better approximates the small particle size range, while the exponential model is better in the larger size range.

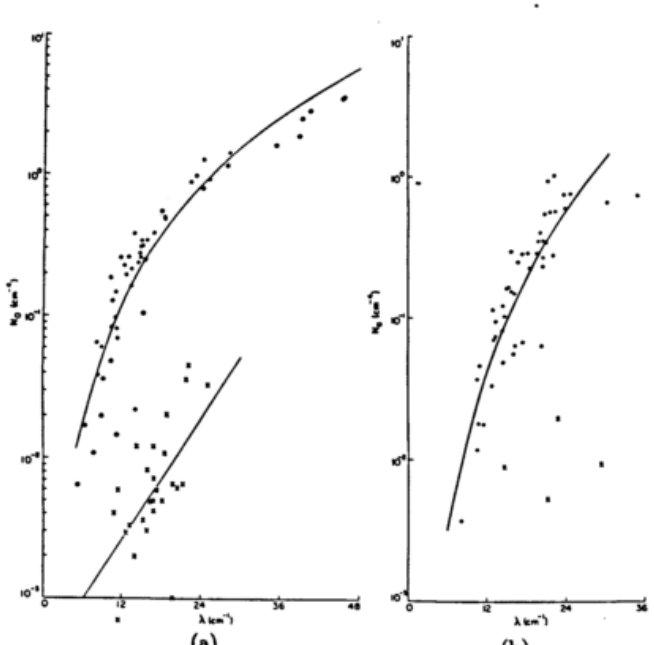
Under the assumption of lognormal distribution, the water content $WC(gm^{-3})$ and radar reflectivity $Z(mm^6m^{-3})$ can be represented (Feingold and Levin, 1986) as

$$WC = \frac{\pi}{6} \times 10^{-3} N_T D_g exp(\frac{9}{2}\ln^2\sigma_g) \quad (6)$$

$$Z = N_T D_g^6 exp(18\ln^2\sigma_g) \quad (7)$$

If we can get a certain relation between D_g and σ_g, then the number concentration N_T and, thus, the size spectrum of precipitation particle at any time can be inferred from the water content WC and radar reflectivity Z. Fig. 4 exhibit a good correlation between the $\ln\sigma_g$ and $\ln D_g$ (with linear correlation coefficient of 0.91). The best fit line has a form as

$$\sigma_g = 12.65 D_g^{0.56} \quad (8)$$



(a) (b)

Fig. 1 Scatter diagrams of intercept parameter N_0 plotted as a function of slope parameter λ of exponential distribution fitting the observed particle size spectra. (a) is for AIMCS case and (b) for PRE-STORM case.

Then the particle number concentration can be diagnosed from the water content WC and radar reflectivity Z using the equations mentioned above, which should be useful in parameterized cloud microphysics models.

5 Empirical aggregation efficiency

One of the main problems in modeling snowflake aggregation is that of determining the collection efficiency among crystals, which is complicated by the nonuniform vertical and horizontal motions of ice particles, and also affected by a variety of factors, such as the crystal habits, air humidity and temperature, and the presense of supercooled cloud droplets. A few laboratory studies made in restrictive conditions obtained conflicting results. We therefore apply Passarelli's (1978) scheme to estimate the collection efficiency in the stratiform region of the PRE-STORM MCC case during its mature stage. Passarelli used the moment conservation equations for total mass and reflectivity factor fluxes for aggregating snowflakes to diagnose the mean collection efficiency. For the case of steady, constant mass flux of snow, the resulting explicit expression of the mean collection efficiency $\overline{E}$ in a layer is

$$\overline{E} = (\lambda^{-1-b_1} - \lambda_0^{-1-b_1})\frac{12\Gamma(7+b_1)\lambda^{4+b_1}}{(1+b_1)\pi N_0 h I(b_1)} \quad (9)$$

where h is the height below a reference level($z = 0$), N_0 and λ the exponential distribution parameters at $z = h$, λ_0 is the value of λ at $z = 0$, b_1 is a parameter in the particle fall speed equation ($v(D) = a_1 D^{b_1}$), and $I(b_1)$ is a function of b_1. In the case of $b_1 = 0.25$, we obtained $I(b_1) = 566$. We calculated the exponential distribution parameters N_0 and λ at various levels during the vertical sounding flight. Using the best fit lines of $N_0(z)$ and $\lambda(z)$ as shown in Fig. 5, the mean collection efficiencies at various layers can be calculated. We obtained an empirical formula as

$$\overline{E(T_s)} = 10^{0.235+0.0633T_s}. \quad (10)$$

This equation has been used in the simulation of ice-phase microphysics in another paper of this conference (Fan *et al.*, 1988).

Acknowledgements

This research was supported by the National Science Foundation under Grant #ATM-8512480 and by the Army Research Office under contract #DAAL03-86-K-0175.

REFERENCES

Cotton. W. R., G. J. Tripoli, R.M. Rauber, and E. A. Mulvihill, 1986: Numerical simulation of the effects of varying ice crystal nucleatioin rates and aggregation processes on orographic snowfall. J. Clim. Appl. Meteor., **25** , 1658-1680.

Fan, Bei-Fen, Jia-Dong Yeh, W. R. Cotton and G. J. Tripoli, 1988: Micropgysics in deep convective cloud system associated with a mesoscale convective complex-numerical simulation. 10*th* Internatioal Cloud Physics Conference, 15-20 August 1988, Bad Homburg, FRG.

Feingold, G., and Z. Levin, 1986: The lognormal fit to raindrop spectra from frontal convective clouds in Israel. J. Clim. Appl. Meteor., **25** , 1346-1363.

Passarelli, R.E., 1978: Theoretical and observational study of snow-size spectra and snowflake aggregation efficiencies. *J. Atmos. Sci.*, **35**, 882-889.

Waldvogel, A., 1974: The N_0 jump of raindrop spectra, J. Atmos. Sci., **31** , 1067-1078.

Table 1. Average values of CV and mean distribution parameters for lognormal and exponential distribution fit in the transition and stratiform regions of PRE-STORM MCC case

	Sample Number	Lognormal Distribution			Exponential Distribution			
		$D_g(10^{-2}cm)$	σ_g	$CV1(10^{-2})$	$N_0(cm^{-4})$	$\lambda(cm^{-1})$	R	$CV2(10^{-2})$
Transition Region	62	3.28	1.90	4.09	0.30	22.5	-0.96	8.63
Stratiform Region	41	5.15	2.33	2.56	0.06	13.0	-0.98	3.50

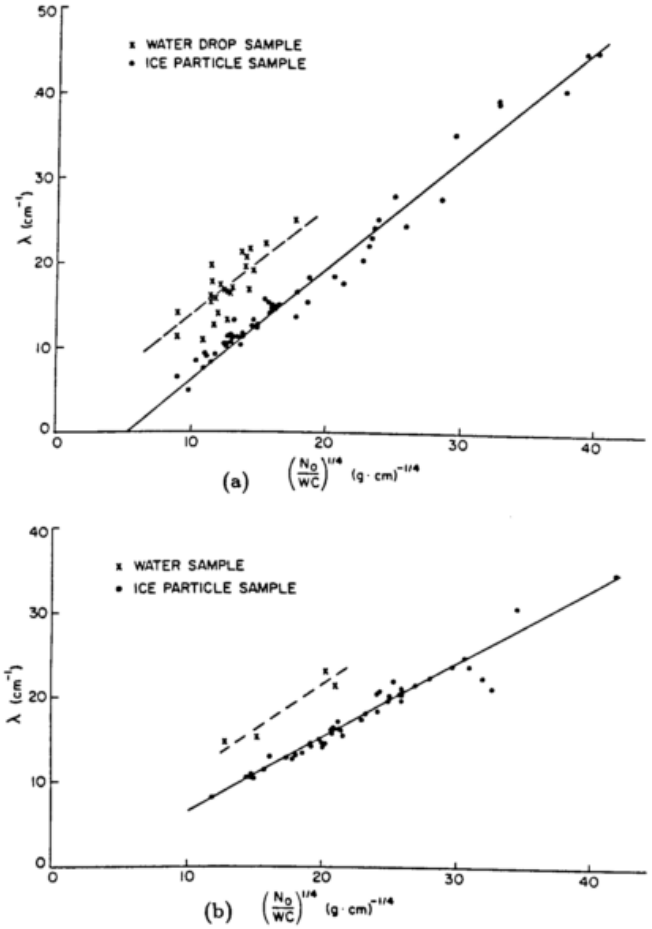


Fig. 2 Scatter diagrams of slope parameter λ plotted as a function of combined variable $(N_0/WC)^{1/4}$ for AIMCS case (a) and PRE-STORM case (b). Solid line is the best fit for ice particle samples; dashed line is for water drops.

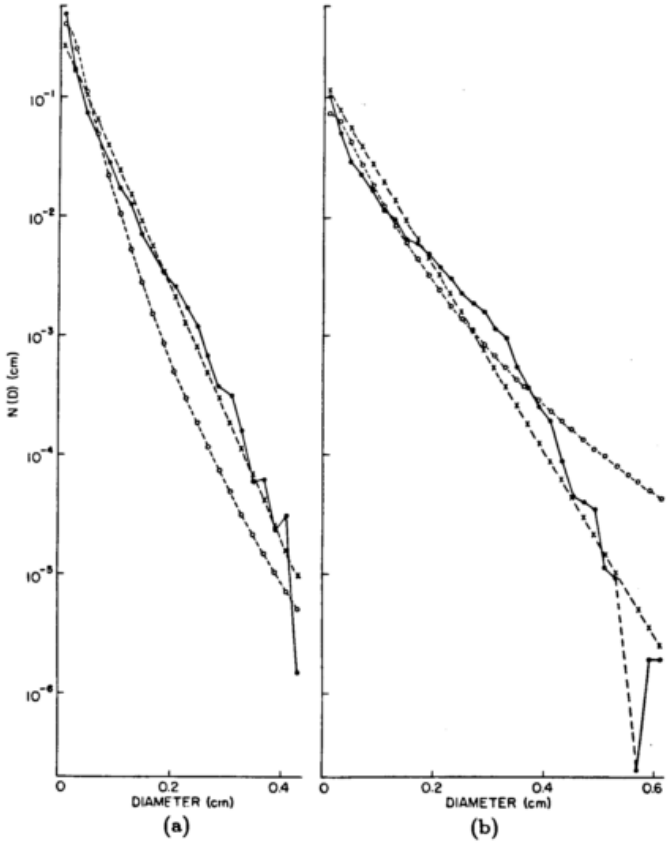


Fig. 3 Mean size distribution in the transition region and stratiform region of PRE-STORM MCC case (solid line), and the corresponding fitting lines of exponential distribution (dashed lines) and lognormal distribution (dotted lines).

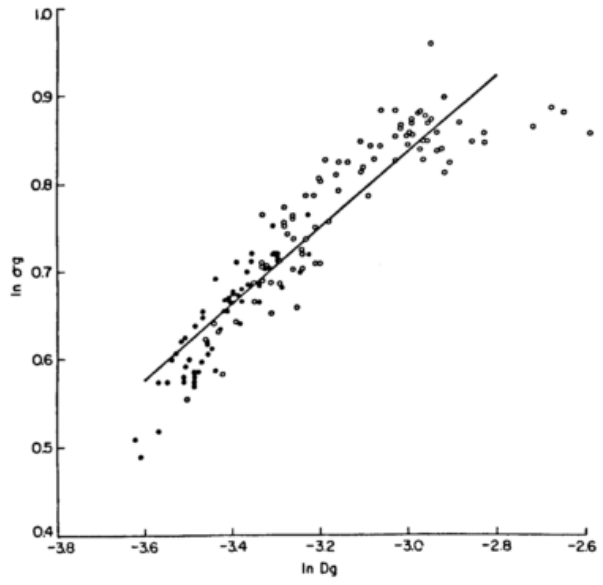


Fig. 4 Scatter diagram of lognormal distribution parameters $\ln \sigma_g$ and $\ln D_g$ for PRE-STORM case.

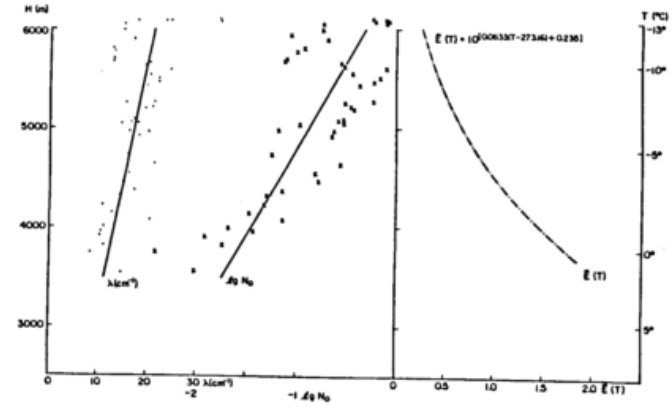


Fig. 5 Scatter diagrams of exponential distribution parameters λ and N_0 at various levels in the stratiform region and corresponding regression lines. Right side is the empirical aggregation efficiency calculated from $\lambda(z)$ and $N_0(z)$ as a function of temperature.

A PRELIMINARY RESEARCH ON THE RADIATION FOG IN XISHUANGBANNA

Huang Yusheng , Xu Wenrong
Meteorological Bureau of Yunnan Province, Yunnan, P.R.C.
Li Zihua , Huang Wanjuan , Fan Ling
Nanjing Institute of Meteorology , Nanjing , P.R.C.

1. INTRODUCTION

Located in the south of Yunnan Province of China , Xishuangbanna is the largest,tropical forest area in China's mainland, famous for its frequent foggy days.

Fog caused by radiation in this area was sampled for 28 days from Dec. 26, 1986 to Feb.18, 1987. A tri-combination dropsize spectrometer was used for sampling fog spectra. GZW-1 type lower-layer radiosounds were used for the vertical temperature profile in the boundary layer. In order to know the distribution of fog and temperature in the mountain region, an observing car was used 77 times along the twisty road from Jinghong to Mengyang to get data at intervals of 1 km.

2. TEMPORAL AND SPATIAL DISTRIBUTION OF RADIATION FOG IN WINTER

Table 1 gives the number of foggy days at 4 meteorological stations, located in 4 basins of Xishuangbanna.It is seen that the annual average number of foggy days in this area is more than 130 .

Fig.1 shows part of the car observations on Jan.6, 1987.Conclusions can be drawn as follows:

1). During the first stage of fog formation, the fog layer is very shallow and the visibility is 200-300m (Fig.1a). Then the layer is getting thicker and thicker until 30 minutes before the fog dissipates.

2). Fog dissipation begins from the bottom . It takes about 3 hours for the whole fog layer to disappear (Fig.1c). As a result, fog in the basin of Xishuangbanna often doesn't touch the ground.

3). Fog is found thicker and has poorer visibility on the north side than on the south side of the hill.

Table 1. The number of foggy days registered at 4 stations in Xishuangbanna

	Jinghong	Mengla	Dameng-long	Menghai
Average(day)	132	152	135	138
Maximum(day)	184	208	168	167
Minimum(day)	87	94	103	110
Temporal period of data	1954-1980	1957-1980	1958-1980	1958-1980

3. MICROSTRUCTURE OF FOG

The smallest water particle which can be captured by the dropsize spectrometer is 3.5 μm in diameter. So, the fog drops used in this study are 3.5 μm or more in diameter.

3.1 Some of the microphysical parameters

Table 2 gives the microphysical parameters observed at Jinghong, Mengyang and Menghai.It shows that the water content

of the fog in Xishuangbanna is comparatively low in general. But of the three observational points, the fog in the Jinghong basin was the weakest in strength, the lowest in the number density and water content, and the smallest in dropsize scale. In contrast with Jinghong fog is Mengyang fog.

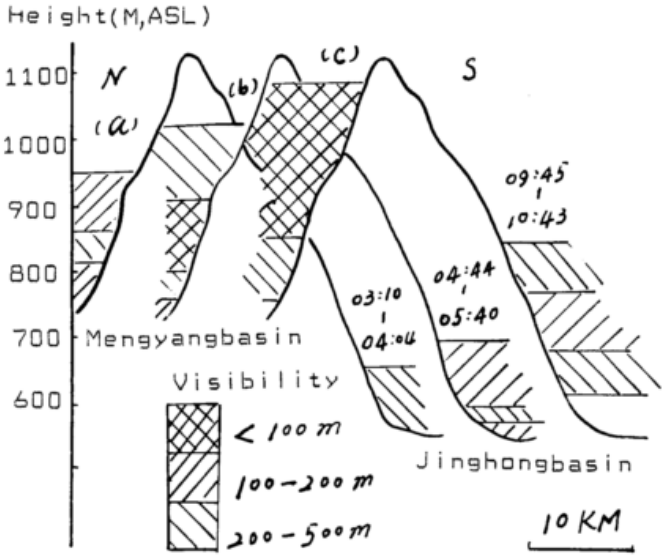


Fig.1. The temporal and spatial distributions of fog observed by the moving car

Table 2. The microphysical parameters of fog

Observational point	Range of Dia. (um)	Mean (μm)	Number density (cm^{-3})	Water content (gm^{-3})
Jinghong	3.5-51.6	12.0	21.7	0.07
Menghong	4.3-58.3	21.1	31.6	0.26
Menghai	4.6-53.0	19.6	27.3	0.13

3.2. Dropsize spectrum of fog

As is shown in Fig.2 , the Jinghong spectrum has only one peak with a mode of 3.5 μm in diameter, while the Menghai spectrum is multipeaked with a mode of 21μm in diameter and its second and third peaks are at 28 and 35 μm , respectively. The Menghai spectrum is not only wider but also has larger drops than the Jinghong spectrum.

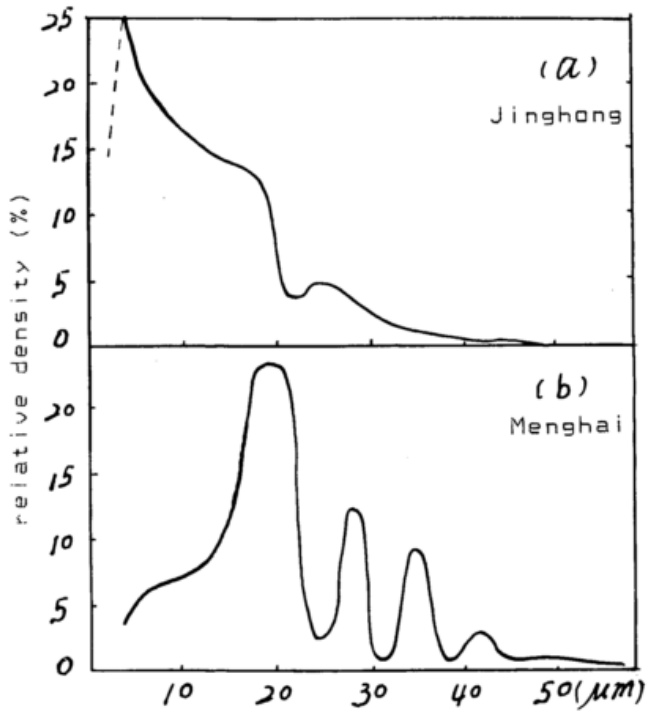


Fig.2.Dropsize spectra of fog

The change in fog spectrum can be taken as a parameter which represents different stages during the residence of fog. On Jan. 9 , 1987, fog developed at 02:00 (Beijing Time) and disappeared at 11:30 . Some of the observations of the spectra from 06:00 to 10:00 are shown in Fig.3 . It can be clearly seen that the spectra at 06:00 were of single-peak type and had a mode of 10.5 μm in diameter and more than 80% of the fog drops ranged from 10.5 to 17.5 μm in diameter. In the developing stage, the fog spectrum evolved into a multipeak type. The original peak moved rightward continuously and, meanwhile, the second and third peaks appeared on its right. But from 10 o'clock on, larger drops decreased considerably, and the peaks in the larger drop area disappeared, while the smaller drops increased and the peaks returned to its original position and projected again. These are the

typical characteristics in the dissipating stage of the fog.

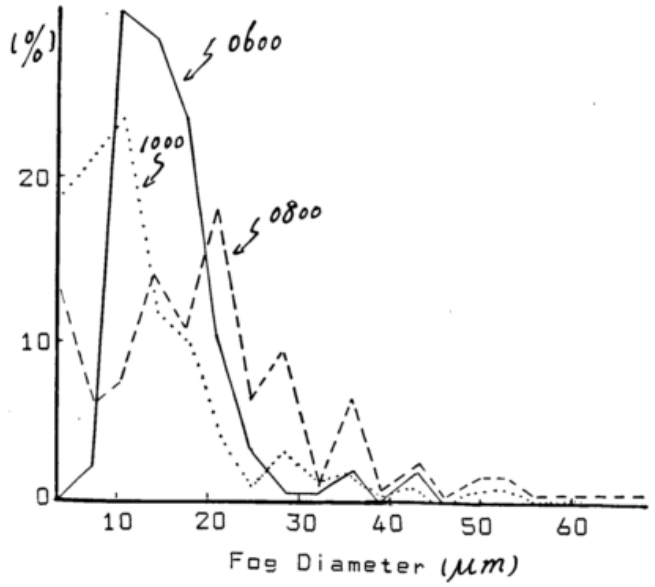


Fig.3. Evolution of the fog spectrum at Mengyang on Jan.9

4. FEATURES OF VERTICAL TEMPERATURE PROFILES IN FOG

Fig.4 shows the time-height section of the air temperature in the lower layer during the evolution of the fog. The evolution of the fog can be generally divided into 4 stages, i.e., formation, development, persistence and dissipation. The forming stage lasted for a comparatively short time. As shown in Fig.4, fog formed before 04:00 , developed from 04:00 to 07:00 and lasted until it began to dissipate at 10:00. We can conclude that before fog starts to form an inversion exists from the ground to the height of a few tens of meters and, from this layer up to the height of 250m, the gradiant temperature is very small. As time goes on, the air temperature near the ground decrease sharply, which results in the formation of the fog in the layer below 100m. In the developing stage, a cold center exists in the layer between 100 and 200 meters.Because the air temperature above 250m height decreases repidly, the cold center moves upward and meanwhile, the height of the fog top increases. But a warm ridge appears in a layer under the cold center and makes the lower part of the fog start to dissipate. The primary features in the third stage is that the cold center goes up to the height of 300m, with the fog top between 280 and 300m, and meanwhile the fog near the ground disappears, and the fog exists only in the layer between 180 and 280m. The dissipating stage begins when the air temperature near the ground increases. And then the temperature in the upper layer increases quickly . So the rise of the air temperature in the whole layer accelerates the fog dissipation. It is noted that the dissipation starts from the bottom, i.e. the fog bottom keeps going higher until the fog disappears completely.

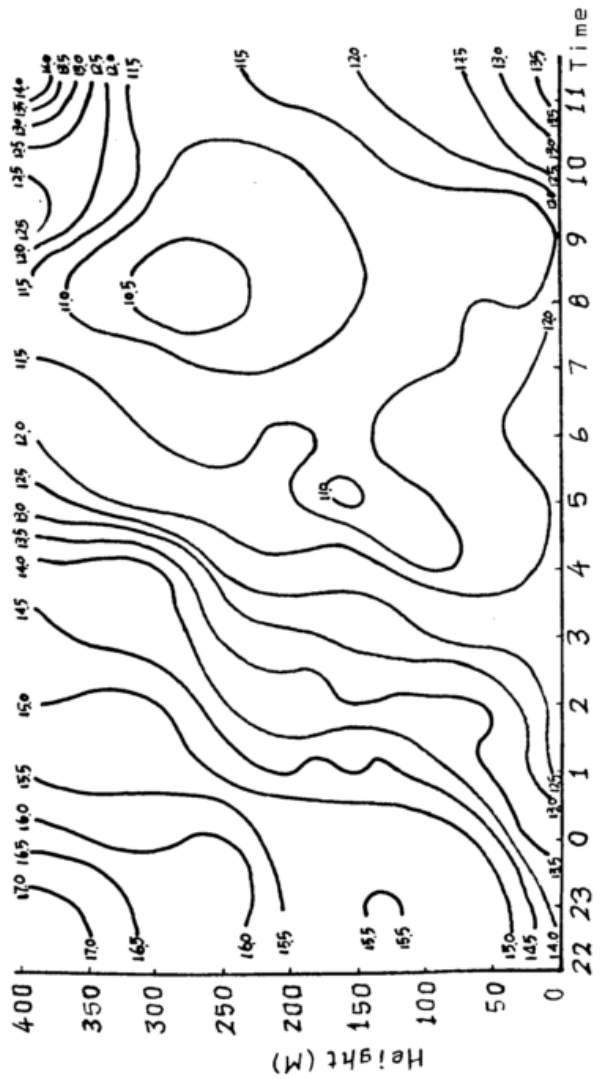


Fig.4. Time-height section of lower air temperature on Jan.6 , 1987 at Jinghong

THE BASIC CHARACTERISTICS

OF THE WINTER NORTHERN XINJIANG STRATIFORM CLOUD SYSTEM

Gao Ziyi Zhang Jianxin

Weather Modification Office,Xinjiang,China

1. INTRODUCTION

Since 1978,an operational winter stratiform cloud seeding program using majorly airborne to augment surface snow cover and to protect winter wheat has been conducted at the northern foot of central Tian Shan Mountains of the Xinjiang,China.The extensive measurements of the cloud and the precipitation,which include aircraft,radar,radiosondeand radiowind,tehered balloon and ground-based precipitation physics observations,have been done simultaneously. The basic purpose of these observations was to understand the physical processes associated with the formation of winter precipitation in this region and to evaluate precipitation augmentation potential.

This article will attempt to give a summary of basic characteristics for the winter stratiform cloud systems ranging from synoptic properties of the cloud system to the microphysical characteristics of the cloud elements formed these systems.

2. GENERAL CHARACTERISTICS

Based upon preliminary analysis for data collected during last several years,the general characteristics of the Xinjiang winter stratiform cloud systems can be described briefly as follow:

1) The organized winter cloud systems responsible for most of the precipitation in the northern Xinjiang during the winter almost always form under the synoptic situations of the upper-level low pressure control and the surface cold front passage. They have quite often a multi-level structure consisted of 2-3 cloud levels.One important water vapour source for precipitation production and particularly for lower cloud formation is the local water storage under the intensive inversion layers that occurred often during the winter. The intense precipitation produce in company with cold air invasion. There is a clear relationship between process precipitation and maximum of drop in temperature. The precipitation elements in the cloud system grow mainly within the boundary layer below 1500m, precipitation from the regions of the cloud above 3000m account for approximately 5-30% of the total precipitation.An estimation based on precipitation intensity variation with height suggest that boundary layers exist rather intense updraft speed reaching a few tencms^{-1}. That predominantly northwesterly flow occured behind cold front is elevated by spicific topograph of Tian San Mountains oriented west-east is probably one important factor which may cause precipitation production primarily postfrontal lower-levels.

2) The cloud top temperatures are mostly not colder than -30°C, among them about 50% are warmer than -24°C.Their warmer cloud tops lead up to insufficiency of the natural glaciazation of the cloud systems. The average concentrations of the ice crystal and the snow crystal are an of magnitude at $10^{0}L^{-1}$ and $10^{-1}L^{-1}$ respectively. They are less than the some areas of China and foreign countries lain in the about same latitude.. The surface ice nuclei concentrations correspond with cloud ice crystal concentrations. Average and maximum of ice nuclei measured at -20°C are $4.5L^{-1}$ and

$7.5L^{-1}$ respectively.It seems that secondary ice crystal production mechanisms are not active.As opposed to lower ice particle concentrations,the regions of the cloud that contain supercooled liquid water are deeper ranging generally from a few hundred meters to more than thousand meters in which liquid water contents approach $0.1-0.3gm^{-3}$.The supercooled droplet size spectra are fairly narrow and are typically contineutal in nature with a rather high degree of colloidal stability.In the general,precipitation formation in the Xinjiang winter stratiform cloud systems is a typical Bergeron-Findeisen mechanism of rain formation,ice crystal formation and its subsequent growth seems to be the major snowforming process.

3) The "seeder-feeder" mechanism play an important role for precipitation formation and evolution.The relative dispositions between "seeder" clouds and "feeder" clouds in time and space have significant difference for various cases.The intense "seeder"clouds have band-form or stripe-form distribution features in the middle troposphere.Upper level intense "snowfall bands", in which snow crystal flux densities reach $10^3-10^4 m^{-2}s^{-1}$,have a width of a few ten meters.During the early stage of the precipitation,"feeder" clouds have often much more supercooled liquid water contents.However,when "seeder" clouds move over them,supercooled liquid water within the "feeder" clouds are exhausted quite rapidly.By the time,radar reflectivity factors are significantly on the low side.During the early stage of the precipitation,approximately 40% of the winter stratiform cloud systems contain liquid water or have suitable conditions to the growth of the snow crystals.But,precipitation efficiences are lower for lack of upper level "seeder" clouds.Therefore,these clouds will be utilized as seeding target clouds.

3. A CASE PRESENTMENT

This case presents a weak cold front precipitation process that occurred at 15 December 1980.The aircraft measurements have been conducted from 0935 to 1247 and from 1514 to 1640 respectively(all times are Peking time).The ground-based precipitation observations which included snow crystal samling and snowfall intensity measurement have been done.The main-body cloud of the cloud system had a depth of 4-5 Km,and consisted of upper-level cloud(As) and lower-level cloud(Sc).The front part of the cloud system that located approximately 120Km east of the main-body cloud was majorly As;the rear part of the cloud system was majorly Sc.

Between 0935 and 0956,a vertical sounding in deep main-body cloud indicated that average concentrations of ice crystal and snow crystal were $21.9L^{-1}$ and $1.47L^{-1}$ respectively.There was not liquid water below 3200m(all heights are above mean sea level).From 3200m-level to 4300m level,lower liquid water whose average and maximum were only $0.0017gm^{-3}$ and $0.0037gm^{-3}$ respectively were measured.Sequently,a few of horizontal panetrating flights in the main-body cloud obtained same results as given above.

Fig.1-3 show separately vertical distributions of ice crystal concentration,snow crystal concentration and liquid water content in the main-body cloud.

However,aircraft measuremets at front part of the cloud system obtained different results,average liquid water content reached $0.020gm^{-3}$ that was about ten times as high as main-body cloud.But average ice crystal concentration at cloud top was only $0.05L^{-1}$.In adition,average drop size spec-

trum at cloud top was fairly narrow, the majority of the drops were smaller than 12μm(see Fig. 4).

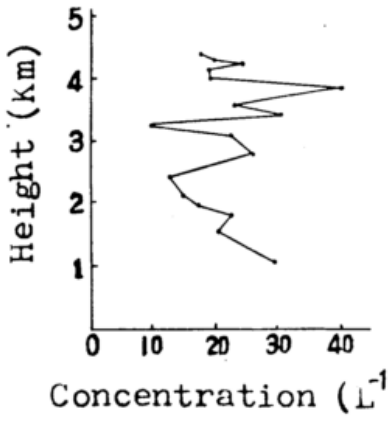


Fig.1 : Ice crystal concentration(L^{-1}) as a function of height

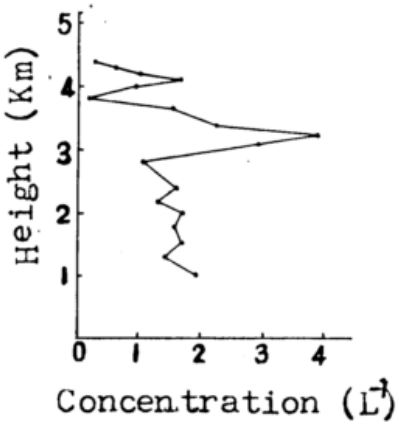


Fig.2 : Snow crystal concentration(L^{-1}) as a function of height

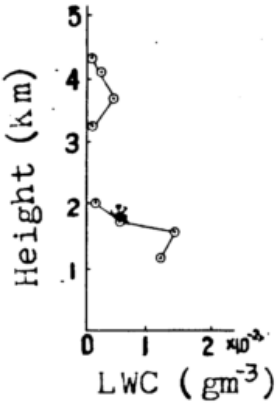


Fig.3 : Liquid water content(gm^{-3}) as a function of height

During second flight between 1514 and 1640,shallow low cloud that located near part of the cloud system were found to have highest liquid water contents,average and maximum approached 0.05gm^{-3} and 0.16gm^{-3} respectively,but average and maximum of ice crystal concentrations were only 0.36L^{-1} and 4.3L^{-1}.Widest droplet size spectrum arised at the mid-lower part of the cloud,largest drops were 49μm(see Fig.5).

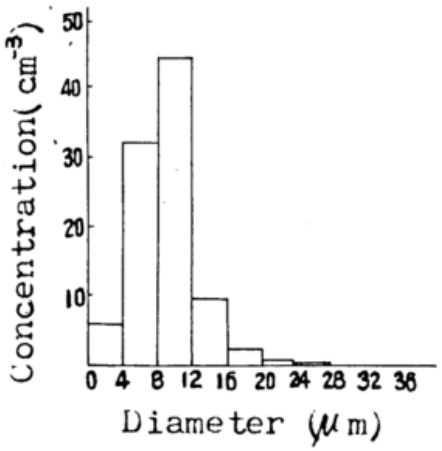


Fig.4 : Droplet size spectrum at cloud top

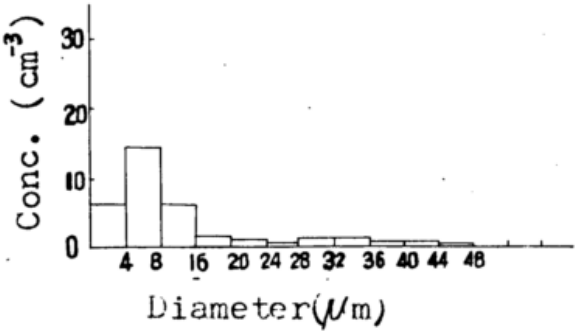


Fig.5 : Droplet size spectrum at 1380m elevation

Evidence suggested that the microphysical characteritics of the cloud system had significant difference for various regions of the cloud system. The front part of the cloud system contained much more liquid water,but natural glaciazation of the cloud was insufficient.

Based on ground precipitation observations,Fig.6 show the variations of snow crystal flux for various habits.Fig.7 show simultaneusly the evolutions of both snow crystal flux(for all

habits) and precipitation rate.

From Fig.6 and fig.7,we can find that characteristics of precipitation of the cloud system are relate to the frontal zone position.Prior to frontal passage(before 0600),precipitation consisted primarily of spatial dendritic and sheath crystals, and precipitation rates were less than 0.2mm.h^{-1}.During passage(between 0600 and 1200),aircraft and surface observations found that the dominant crystal habits were column and irregular,and snow crystal flux reached maximum of 5500$m^{-2}s^{-1}$ at 0700.After 1 hour, precipitation rate also increased to peak of 1.0mm.h^{-1}.

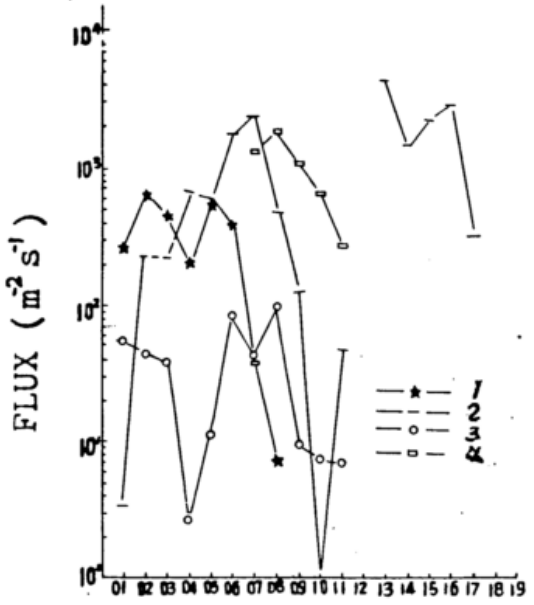


Fig.6 : Time evolution of the flux of snow crystal for various shapes
1: dendritic;2 : needle or sheath;3; plate;4:column

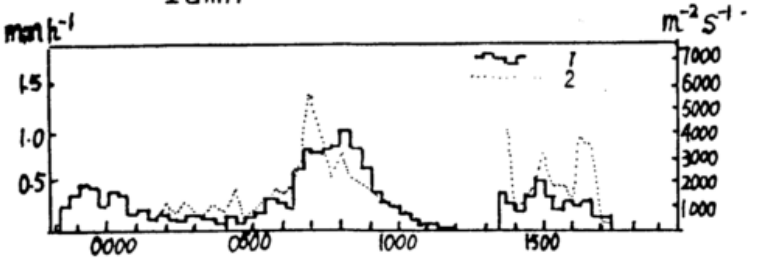


Fig.7 : Time evolution of snow crystal flux for all shapes and time evolution of precipitation rate
1;precipitation rate
2:snow crystal flux

After passage(after 1200), aircraft observation found that surface precipitation fell primarily from postfrontal low cloud. The major snow crystals were needle,flux and rate arised again higher values of about 4000$m^{-2}s^{-1}$ and 0.52mmh^{-1} respectively.However postfrontal precipitation contributed little to total precipitation because of its short duration.The main-body cloud precipitation accounted for approximately 56% of the total process precipitation.

4. ACKNOWLEDGMENTS

The Academy of Meteorological Science as a director and a cooperator participated in the research program of the Xinjiang winter stratiform cloud system. Now this program also is being supported by the Meteorological Science Foundation Committee, State Meteorological Administration,China.We take this opportunity to thank them heartily.

REFERENCE

Q,Wang.;L,You.;Z,Hu.:The study onthe winter stratocumulus cloud over Ürumqi,Xinjiang, China-structure and evolution.Acta Met.Sinica.45(1987) No.1,P.2-12.

THE RAINFALL ENHANCEMENT BY TWO LAYER CLOUD STRUCTURE OBSERVED AT OROFURE MOUNTAIN RANGE, HOKKAIDO, JAPAN

Katsuhiro Kikuchi, Koyuru Iwanami and Takashi Taniguchi

Department of Geophysics, Faculty of Science,
Hokkaido University, Sapporo 060, Japan

1. INTRODUCTION

It is well known that the southeastern slope of the Orofure mountain range in Hokkaido has abundant rainfalls. Heavy orographic rainfalls in this range arise from a combination of the lower layer clouds caused by uplifting of the warm wet air from the Pacific Ocean and the precipitation from the upper level clouds of the synoptic scale disturbance. The numerical experiments by Kikuchi et al. (1988) support this conclusion. A two layer cloud structure model, that is, a seeder and feeder mechanism, of orographic rainfalls was first proposed by Bergeron (1965). And the importance of this mechanism has been emphasized by many investigators (Takeda et al., 1976; Hill et al., 1981). There seem to be no reports, however, of the interaction between the upper seeder cloud and lower feeder cloud by radar observation directly. Radar observations, therefore, were carried out at this mountain range from August to September in 1985 and 1986.

2. OBSERVATION AREA

Fig. 1 shows the horizontal distribution of total rainfall amount on Sept. 7, 1985. The observation network includes two valleys, that is, S-line along the Shiraoi River and T-line along the Shikiu River. The H-line was located on the ridge between the former two lines. Our weather radar was set up on the hill to the southeast of Muroran City in order to watch the southeastern slope of the range.

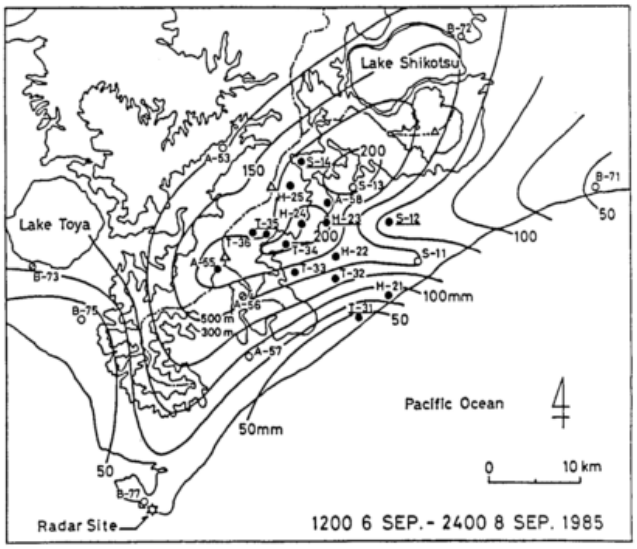


Fig. 1 Horizontal distribution of total rainfall amount.

3. RESULT

At 09 JST on September 7, 1985, a depression which was located to the northeast offshore of the Korean Peninsula one day prior to moved to the northeast. The warm front associated with this depression passed near Muroran, and the observation area was located in front of this warm front. The maximum peak of the rainfall amount more than 200 mm was located on the southeastern slope and S-13 raingauge site recorded 218 mm. Fig. 2 shows the time series of rainfall intensities per 20 min on the day of the sites on S-line. At the S-13 and 14 in the mountainous region, it was raining continuously from midnight and reached maximum from 05 to 06 JST at the S-13. This feature was similar to H-line and T-line, likewise. At 0420 JST, a shallow precipitating cloud existed on 2.0 km

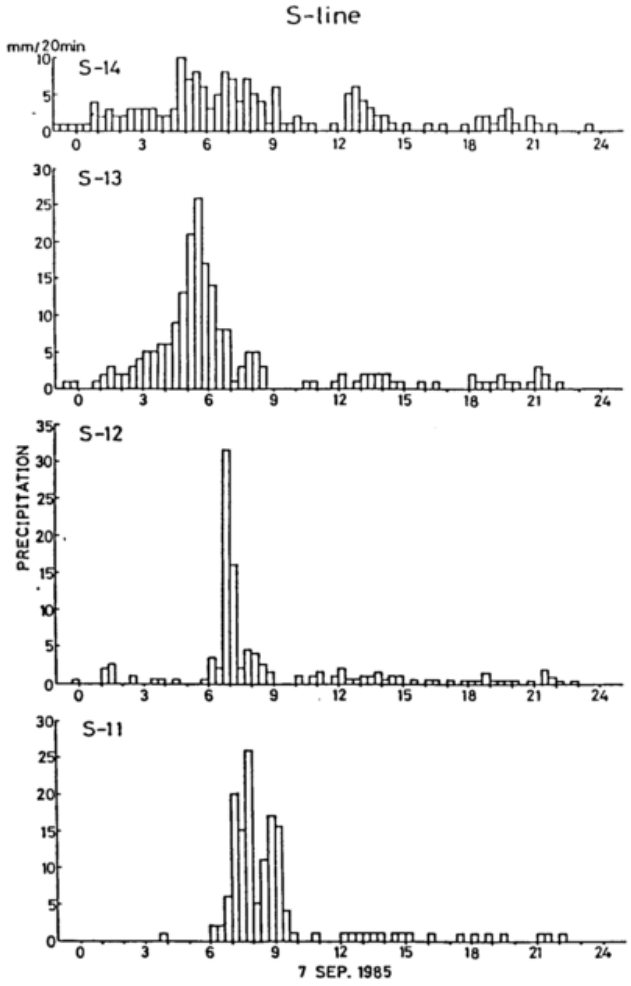


Fig. 2 Time series of rainfall intensity per 20 min. along the S-line.

CAPPI which produced a weak continuous rain on the southeastern slope. This precipitating cloud is an orographic one. The deep precipitating cloud associated with the front existed at the northwestern side of the range on both 2.0 and 4.0 km CAPPIs. At 0520 JST, this precipitating cloud moved over the crest and spread out on the southeastern slope. Fig.3 shows the RHI time series along the T-line and rainfall intensities for 10 min at T-32 and T-34. The shallow orographic precipitating cloud whose echo top was lower than 4 km provided continuous rainfall at T-34. The deep precipitating cloud associated with the front whose echo top was close to 10 km approached this area from the northwest, and moved beyond the crest over the southeastern slope. Associated with this intrusion, the echo in the lower layer became suddenly stronger than 35 dBZ.

4. DISCUSSION AND CONCLUSION

Based on these radar echo and rainfall

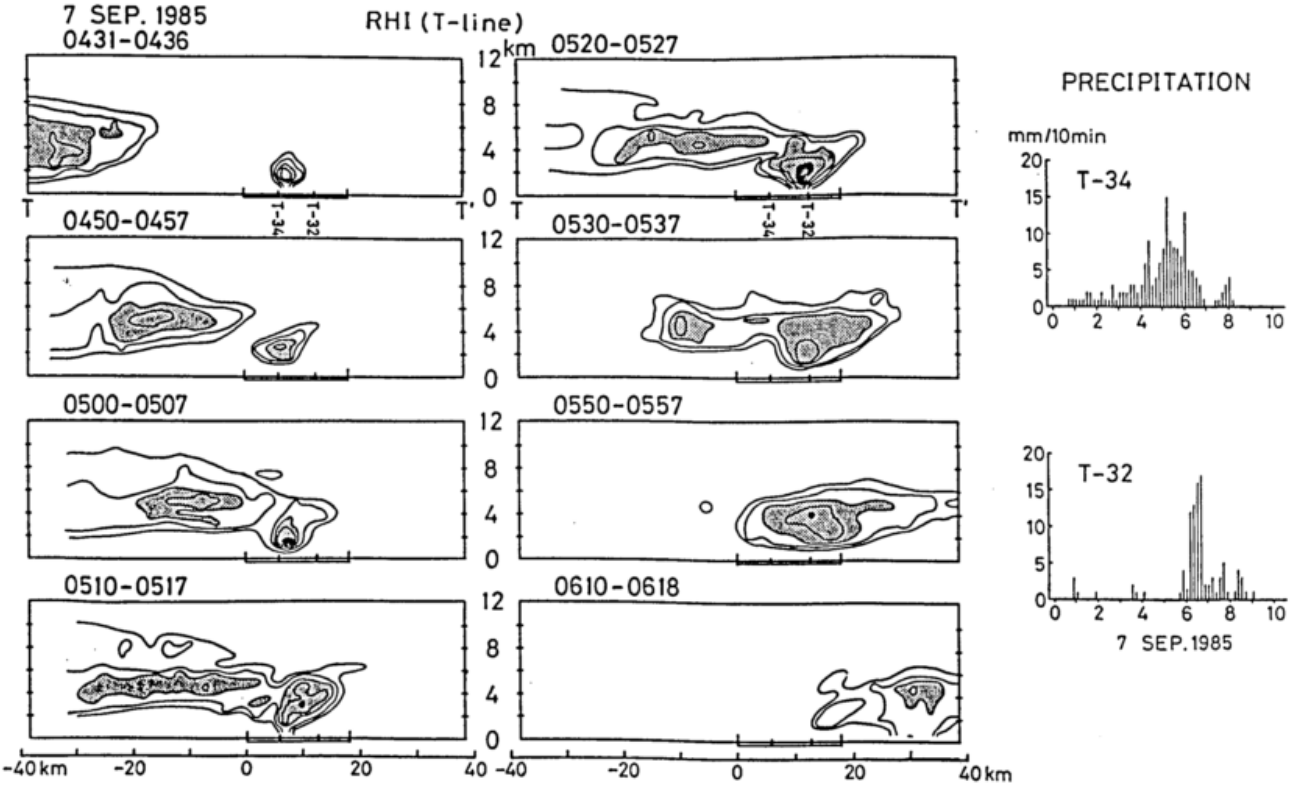


Fig. 3 Time series of the vertical crosssections (RHI) along the T-line and rainfall intensity at T-32 and T-34.

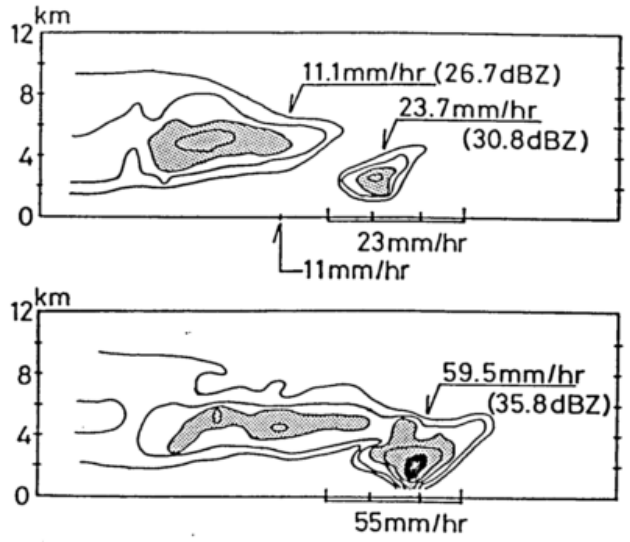


Fig. 4 Estimated rainfall intensity. The upper part shows the result before intrusion of upper cloud to the southeastern slope and the bottom part after that.

data an attempt was made to estimate the rainfall intensities of both precipitating clouds. The rainfall intensity of the combined precipitating cloud was estimated by the surface rainfall intensity at T-34 from 05 to 06 JST. The result is shown in the lower part of each RHI picture in Fig. 4. The rainfall intensities on the ground of the deep precipitating cloud and the orographic cloud are 11 and 23 mm/hr, respectively, and a simple summation of them is 34 mm/hr. On the other hand, when they were combined, the rainfall intensity was 55 mm/hr and this value was larger about 60 % than the simple summation. Next, we used the Z-R relation in this observation area, $Z=23R^{1.25}$, which we calculated from the 50 sets of PPI radar and raingauge data at the most suitable site (A-57). By this method, the rainfall intensities of the precipitating cloud and the orographic cloud are 11.1 and 23.7 mm/hr. On the other hand, the intensity of the precipitating cloud when both of them were combined is 59.5 mm/hr, and about 70 % larger than the simple summation of 34.8 mm/hr. This result is shown in the upper part of each RHI in Fig. 4. We can conclude, therefore, that the interaction which increases effectively the rainfall intensity worked between the upper precipitating cloud and the lower orographic cloud when the upper cloud passed over the orographic cloud.

5. REFERENCES

Bergeron, T.: On the low-level redistribution of atmospheric water caused by orography. Suppl. Proc. Int. Conf. Cloud Physics, Tokyo (1965) p. 96-100.

Hill, F. F., K. A. Browning and M. Badar: Radar and raingauge observations of orographic rain over South Wales. Quart. J. R. Meteor. Soc., 107 (1981) p. 643-670.

Kikuchi, K., N. Horie, T. Harimaya and T. Konno: Orographic rainfalls of Orofure mountain range in Hokkaido, Japan. J. Meteor. Soc. Japan, 66 (1988)

Takeda, T., M. Moriyama and Y. Iwasaka: A case study of heavy rain in Owase area. J. Meteor. Soc. Japan, 54 (1976) p. 32-41.

NUMERICAL SIMULATION OF COASTAL CLOUDS WHEN SOLAR RADIATION IS BLOCKED BY SMOKE

Charles R. Molenkamp
Lawrence Livermore National Laboratory, University of California
Livermore, California 94550

1. INTRODUCTION

In the event of a major nuclear exchange, a large quantity of smoke would be injected into the atmosphere by the many fires ignited by the explosions (CRUTZEN and BIRKS, 1982). This smoke would greatly reduce the amount of incident solar radiation reaching the ground so that continental regions would begin to cool rapidly (TURCO, et al., 1983). Maritime regions, on the other hand, would cool slowly, because of the much greater heat capacity of the ocean, leading to the development of a temperature gradient across the continental coastlines. It has been suggested that this temperature gradient would induce convergence in the flow field and produce a region of precipitation that could rapidly scavenge much of the smoke (TELLER, 1984; SINGER, 1984; NATIONAL RESEARCH COUNCIL, 1985). This hypothesis of enhanced coastal precipitation is being investigated using an extended version of the Colorado State University Mesoscale Model (MAHRER and PIELKE, 1977) to simulate air flow, clouds and precipitation near continental coastlines.

2. PREVIOUS STUDIES

The model was previously modified to include the formation of fog and clouds and the transport and diffusion of smoke (MOLENKAMP, 1988ab). The longwave radiation parameterization was also changed to take into account the effects of clouds.

Cloud formation was incorporated into the model by adding a new liquid water field while retaining the original specific humidity field but letting it represent the sum of vapor and cloud water. The specific humidity conservation equation was retained for the sum of vapor and cloud water, a procedure that is valid as long as the cloud droplets have negligible terminal velocities. At each time step the liquid water content is determined by assuming the atmosphere is either subsaturated, if the actual vapor pressure is less than the saturation vapor pressure, or exactly saturated. If there is either condensation or evaporation, the temperature and liquid water content are adjusted iteratively. This iteration is made computationally efficient by taking into account the relationship between changes in saturation vapor pressure and temperature given by the Clausius-Clapeyron equation.

Because of the importance of longwave radiative cooling of the atmosphere and the surface in the current problem, a more detailed and accurate parameterization was developed. The upward and downward fluxes at each level are calculated by vertically integrating the appropriate transfer equations through the atmosphere. Emissivities are evaluated using the broadband method of LIOU and OU (1983) considering three water vapor bands and the carbon dioxide band as well as an overlap correction. The optical depths in each layer, including pressure and temperture broadening, are estimated using the technique of LIOU and OU (1981). When a layer of cloud is present in the model, it is treated as a boundary for the clear air flux calculation; the boundary flux is calculated assuming the cloud is radiatively gray. The optical thickness of the cloud is evaluated following STEPHENS (1978). Because relatively small amounts of liquid water produce emissivities very close to 1, most clouds act as black bodies.

In previous simulations of both east and west coasts with a moderate westerly synoptic wind and with solar radiation completely blocked by smoke, continental cooling leads to the formation of fog or low clouds over land. When fog forms, the layer of most rapid cooling moves to the top of the cloud while the potential temperature inside the cloud becomes nearly constant. As higher layers become saturated, the cloud expands vertically, and the liquid water content increases. Over the ocean, the atmosphere cools radiatively while the sea surface remains at constant temperature; this leads to a reduction of the thermal stability and enhancement of the vertical mixing of moisture that is injected into the atmosphere from the sea. Eventually a cloud layer forms over the ocean that is very similar to that over land. Once similar cloud layers have formed over land and sea, the cooling rates become nearly identical, and there is no mechanism to force the vertical growth of clouds into the upper atmosphere where they can scavenge the smoke. These simulations also demonstrated the important role condensation of moisture plays in moderating the rate of atmospheric cooling over land during the time when solar radiation is blocked by smoke.

3. PRECIPITATION FALLOUT

In the previous simulations, the amount of cloud water increased to amounts of over 1 g/kg, which is more liquid water than would normally be found in the atmosphere in these conditions. Consequently, a precipitation mechanism has been added to the model to allow the liquid water to fall out. Rather than add just a new rain water field and a representation of the appropriate interactions, the entire cloud microphysics parameterization was replaced with a modified Orville parameterization (LIN, FARLEY and ORVILLE, 1983). The new parameterization allows for the inclusion of cloud ice and snow in addition to cloud water and rain; however, graupel and hail are not allowed to form in the mesoscale simulations.

The advection of rain and snow is evaluated using the technique of SMOLARKIEWICZ (1983, 1984), which is much better suited to these variables than the cubic spline technique used for the other prognostic variables. Another modification used in the calculation for the vertical advection of rain and snow is to divide the time step into several smaller steps. This procedure is necessary because the terminal velocities of rain and snow, which are much larger than the vertical velocities for all the other variables that move with the air, produce values for the Courant condition that are greater than 1 in the relatively thin model layers near the surface.

Simulations with the new model, including deposition of liquid water by rain, are currently in progress and will be presented at the conference. Since the temperature in the lower part of the atmosphere, where all the condensation occurs, is above freezing no cloud ice or snow is formed in these simulations.

4. ACKNOWLEDGEMENTS

I am very grateful to Dr. Roger Pielke for giving me a copy of the Colorado State University mesoscale model and for the help that he, Dick McNider, Bob Kessler and Ray Arritt have given me in understanding various parts of the model.

This work was performed under the auspices of the U. S. Department of Energy by the Lawrence Livermore National Laboratory under Contract W-7405-Eng-48.

5. REFERENCES

CRUTZEN, P.J.; BIRKS, J.W.: The Atmosphere after a Nuclear War: Twilight at Noon. Ambio 11 (1982) 115-125.

LIN. Y.L.; FARLEY, R.D.; ORVILLE, H.D.: Bulk Parameterization of the Snow Field in a Cloud Model. J. Climate Appl. Meteor. 22 (1983) 1065-1092.

LIOU, K.N.; OU, S.S.: Parameterization of Infrared Transfer in Cloudy Atmospheres. J. Atmos. Sci. 38 (1981) 2707-2716.

LIOU, K.N.; OU, S.S.: Theory of Equilibrium Temperatures in Radiative-Turbulent Atmospheres. J. Atmos. Sci. 40 (1983) 214-229.

MAHRER, Y.; PIELKE, R.A.: A Numerical Study of the Airflow over Irregular Terrain. Beitr. Phys. Atmos. 50 (1977) 98-113.

MOLENKAMP, C.R.: The Development of Low Level Coastal Flow Fields when Solar Radiation is Blocked by Smoke. Accepted by Aerosols and Climate (1988a).

MOLENKAMP, C.R.: Numerical Simulation of Coastal Flows when Solar Radiation is Blocked by Smoke. Submitted to J. Appl. Meteor. (1988b)

NATIONAL RESEARCH COUNCIL: The Effects on the Atmosphere of a Major Nuclear Exchange. Washington: National Academy Press 1985.

SINGER, S.F.: Is the "Nuclear Winter" Real? Nature 310 (1984) 625.

SMOLARKIEWICZ, P.K.: A Simple Positive Definite Advection Scheme with Small Implicit Diffusion. Mon. Wea. Rev. 111 (1983) 479-486.

SMOLARKIEWICZ, P.K.: A Fully Multidimensional Positive Definite Advection Transport Algorithm with Small Implicit Diffusion. J. Comp. Phys. 54 (1984) 325-362.

STEPHENS, G.L.: Radiation Profiles in Extended Water Clouds. II: Parameterization Schemes. J. Atmos. Sci. 35 (1978) 2123-2132.

TELLER, E.: Widespread After-effects of Nuclear War. Nature 310 (1984) 621-624.

TURCO, R.P.; TOON, O.B.; ACKERMAN, T.; POLLACK, J.B.; SAGAN, C.: Nuclear Winter: Global Consequences of Multiple Nuclear Explosions. Science 222 (1983) 1283-1292.

LONG-LIVED HAWAIIAN RAIN BANDS

Piotr K. Smolarkiewicz
National Center for Atmospheric Research[1]
Boulder, Colorado 80307

and

Roy Rasmussen
Bureau of Reclamation
Denver, Colorado

Terry L. Clark
National Center for Atmospheric Research[1]
Boulder, Colorado 80307

1. INTRODUCTION

The big island of Hawaii has one of the highest annual precipitation rates in the world, reaching 300 inches/year at some locations. A significant fraction of this rainfall is thought to fall from long-lived rain bands, which initiate just upwind of the island, and propagate onshore under certain conditions. In our previous work (SMOLARKIEWICZ et al., 1988), SRC, we showed using Clark's 3-dimensional anelastic model that these band clouds are initially forced by an arc shaped quasi-stationary low-level convergence zone located just upwind of the island. This convergence zone results from interaction of a strongly stratified fluid flow with an island obstacle (low Froude number effect). Nocturnal cooling along the volcano slopes was shown to enhance the dynamically induced low-level convergence and associated updrafts. Most of the clouds initiated at the convergence zone dissipated soon after moving away from the low-level forcing region. In the current study we show that under certain situations, part of the low-level convergence line moves on shore together with the cloud, resulting in a long-lived rain producing system (nearly 1 hour of continuous rain). A series of numerical sensitivity experiments suggest that the event is related to a surging of the downslope flow which leads to enhanced off-shore convergence, and a stronger band cloud and precipitation.

2. DISCUSSION OF THE RESULTS

The numerical setup of the experiments discussed and the model have been described in SRC. Figure 1 displays the third nested domain solution (grid resolution $\Delta X = \Delta Y \approx 1$ km, $\Delta Z \approx 62$ m) at 1 am, seven hours following model initiation at the approximate time of sunset, for the case of 1 August 1985. The well-defined updraft band with indications of multiple band structure is apparent in plate b. The updraft and the associated band cloud (plate d) form along the separation line of the surface flow clearly seen in plate a. Convergence of the low-level flow along the separation line is apparent in plate b displaying the u component of velocity (far upstream low-level wind is -10 m/s). Clouds originate just upwind of the separation line and propagate following the flow at the approximate cloud base level within the region downwind of the separation line. This flow has a strong component along the line. Once clouds leave the vicinity of the separation line they loose support from the low-level forcing and dissipate. At the same time new clouds form along the low-level convergence zone. In SRC we have shown that this overall quasi-steady solution (including downslope flow clearly seen in plates a and b) is primarily related to the effect of a low-level blocking exerted by the island on the mean trade wind flow. The nocturnal cooling along the volcano slopes amplifies the dynamic response. Following considerations on the properties of strongly stratified flows past three-dimensional obstacles we have offered simple predictability criterion for the band cloud occurence in terms of Froude number, height of the mountain and the lifted condensation and free convection level.

A more detailed analysis of the model results indicates that the flow on the lower upwind side of the island is subject to weak, semi-periodic oscillations with $\sim$ 3 h period. With respect to processes occurring on the scale of the island (global response), these oscillations are of minor importance. For instance, they result in $\sim \pm 2\%$ variability of the wave drag. These oscillations, however, embody surging of the upwind downslope flow with subsequent, local enhancement of the convergence zone and the associated band updrafts and clouds. A cause for the flow oscillation and the surging is not yet understood. Without additional evidence this feature of the solutions might be attributed to numerical artifacts

[1]The National Center for Atmospheric Research is sponsored by the National Science Foundation

and neglected. However, National Weather Service observations of wind speed at Hilo for the month of July 1985 also show the presence of 2–3 hourly surges of downslope flow on the evening of July 31, as well as on a number of other days. Moreover, laboratory experiments of HUNT and SNYDER (1980) provide evidence on intermitent behavior of the upwind downslope flow. Finally, recent calculations with dry, constant, uniformly stratified, nonrotating flow past a cone (Froude number $\approx .3$) also exhibit pulsations of the lower upwind side flow. Since the lee-vorticies in the cone experiment do not shed, the vortex shedding in Hawaii (SRC) may be eliminated as a possible explanation for the surging.

In the experiment discussed the two surges were observed at $\sim$ 4 and $\sim$ 7 hours following model initiation. The results shown in Fig. 1 correspond to the beginning of the second surge. The onset of the surge in $\sim NE$ direction may be seen in plates a and b, in the middle part of the western boundary of the domain. Figure 2 shows the model solution one hour later. The well-developed downslope flow pulse is apparent in plates a and b. In response to the surge the low-level flow separation line undulates and approaches shore line near Cape Kumakahi (the eastern most point of the shore line). In this region, the low-level flow upwind to the separation line increases resulting in the reversed low-level wind shear. This locally enhances the band cloud which follows deformation of the convergence zone while precipitating continuously for nearly one hour. This result is in good agreement with observations made by TAKAHASHI (1981) on the behavior and location

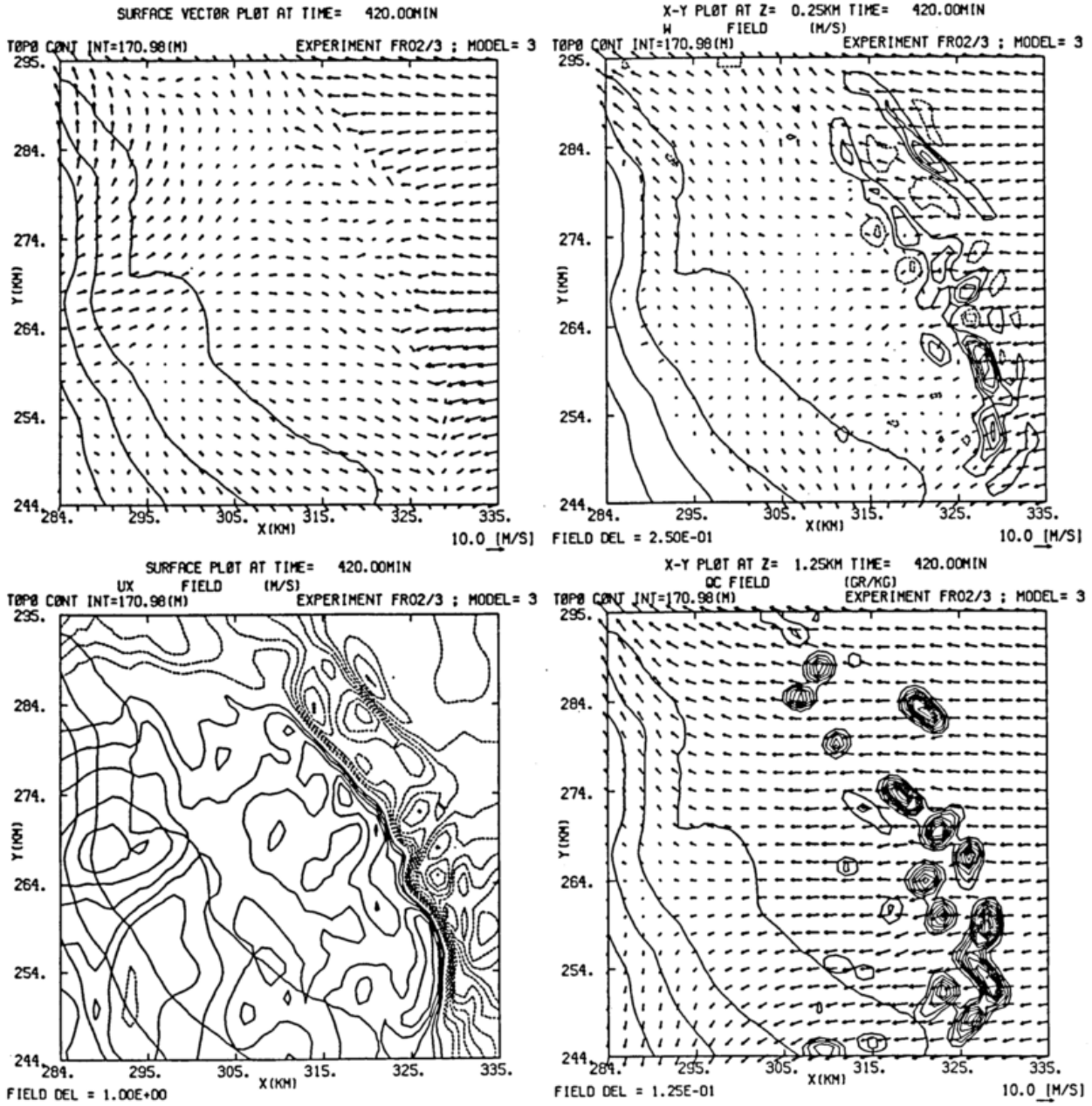


Figure 1. See description in text

of the long-lived Hawaiian rain bands. He suggested that evaporative cooling and precipitation loading forced the downslope flow back and allowed the band to propagate. This was investigated by turning off the model rainwater, which resulted in no significant changes in the solution. The effect of condensational heating on the propagation characteristics of the band was examined in a control experiment with latent heat release arbitrarily suppressed. This simulation also produced a propagating band cloud, but with much weaker intensity and at slightly different location and time. The depth of the band cloud was only 1 km, which is half of this in the regular experiment, and the cloud became more continuous and had a greater horizontal extent than in the normal run. These results suggest that the propagation characteristics of the long-lived band is not significantly affected by the latent heat release or precipitation but that it is mostly related to the larger scale forcing.

4. REFERENCES

HUNT, C. R.; SNYDER, W. H.; Experiments on stably and neutrally stratified flow over a model three-dimensional hill, *J. Fluid Mech.*, **96**, 671-704.

SMOLARKIEWICZ, P. K.; CLARK, T. L.; The multi-dimensional positive definite advection transport algorithm: Further development and applications, *J. Comput. Phys.* **67** (1986) 396-438.

SMOLARKIEWICZ, P. K.; RASMUSSEN, R.; CLARK, T. L.; On the dynamics of Hawaiian cloud bands: Island forcing, *J. Atmos. Sci.* (1988), in press.

TAKAHASHI, T.; Warm rain study in Hawaii-Rain initation, *J. Atmos. Sci.* **38** (1981) 347-369.

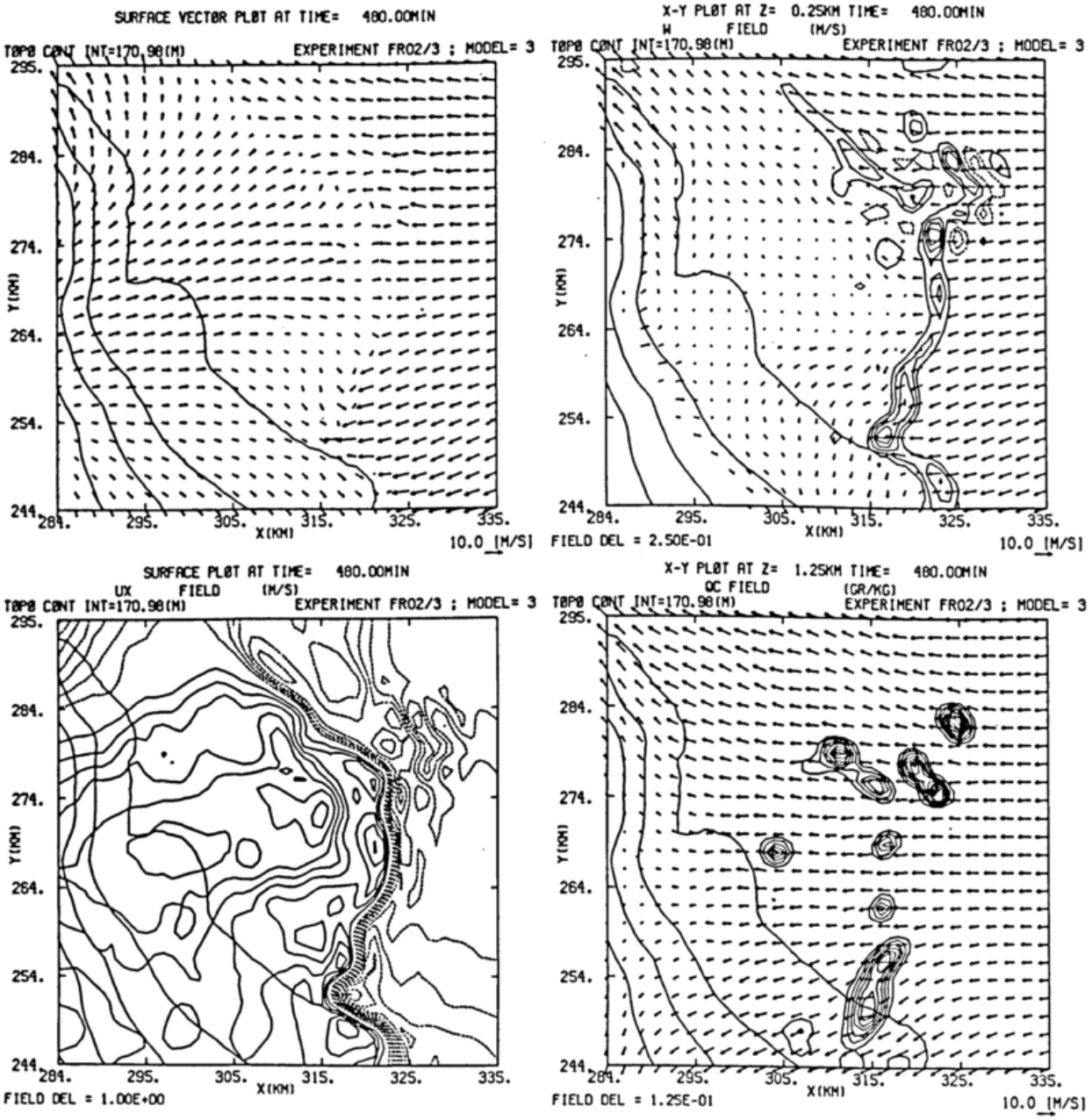


Figure 2. See description in text

A LONG-LASTING RAINSTORM TRAVELING ALONG A STATIONARY FRONT

Hitoshi Sakakibara and Akira Tabata

Meteorological Research Institute
Tsukuba, Ibaraki 305, Japan

1. INTRODUCTION

A long-lasting rainstorm on a stationary front was observed by the C-band Doppler radar of Meteorological Research Institute on 25-26 September 1981. The storm produced heavy rain of 40-50 mm in one hour, it lasted for more than 10 hours and it traveled more than 350 km. Although precipitation systems in cyclones have been extensively studied (Houze and Hobbs, 1982), long-lasting rainstorms on fronts have not been documented well. The objective of the present paper is to describe the mesoscale features and three-dimensional structure of the rainstorm.

2. DATA

The Doppler data were used to describe the three-dimensional structure of the rainstorm. Six volume scans were made with 128 km range of observation from 2254 JST on 25 September to 0243 JST on 26 September. Eight PPI scans with elevation angles of 1° to 14° formed each volume scan. We also used the operational data to describe the mesoscale features of the rainstorm.

3. ENVIRONMENTAL CONDITIONS

The surface chart for 21 JST (Japan Standard Time) on 25 September 1981 is shown in Fig.1. There was a slowly moving and slowly developing extratropical cyclone in the southern part of the Sea of Japan. A stationary front was located along the Pacific coast of central Japan. The rainstorm traveled along this stationary front. At 850 hPa, a mesoscale trough (L~600km) was found west of the rainstorm on the stationary front and strong winds were observed on the east side of the trough. Upper-air soundings around the rainstorm (not shown) indicate small potential instability.

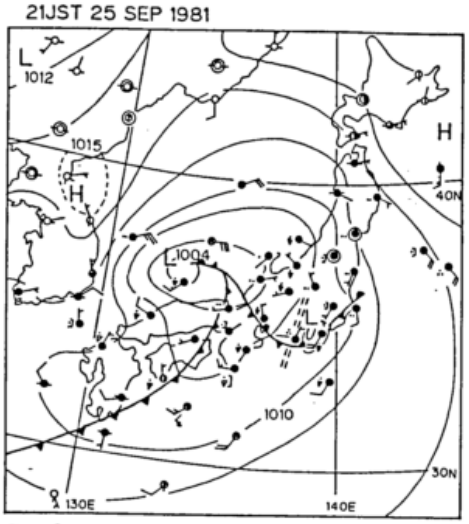


Fig.1 Surface chart for 21 JST on 25 September 1981. Double dashed lines indicate the position of a mesoscale trough at 850 hPa.

4. EVOLUTION OF THE RAINSTORM

The evolution of the rainstorm was shown by the hourly rainfall amounts observed by a dense surface network (Fig.2). Scattered areas with rainfall were organized into the rainstorm by 16 JST. The rainstorm traveled along the stationary front with a speed of 35 km/hr for more than 10 hours. The horizontal scale of the area with heavy rain was about 30 km and the duration of the heavy rain at the surface stations was about 1 hour. The maximum of hourly rainfall amount was 40-50 mm.

The rainstorm was associated with a mesoscale low which developed south of stationary front. Figure 3 is a local surface chart at 00 JST on 26 September. The stationary front to the south of the heavy rain area extended toward the north and strong southerly wind was observed on the southern side. The mesoscale low was located south of the stationary front

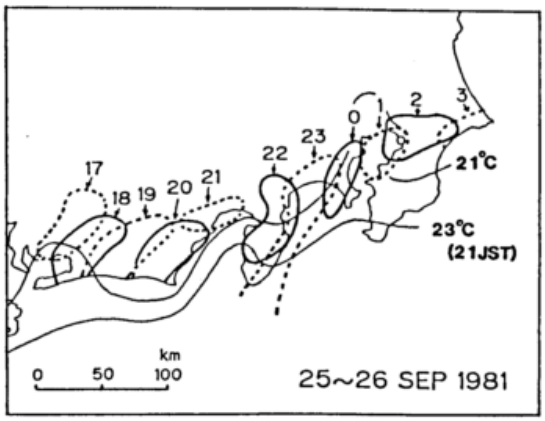


Fig.2 Isopleths of hourly rainfall amount of 16 mm. Numbers indicate the time of observation (JST). Frontal zone is indicated by isotherms of 21 and 23°C.

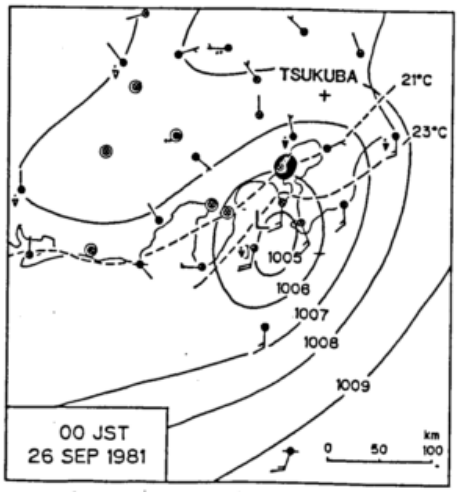


Fig.3 Local surface chart for 00 JST on 26 September 1981. Solid shading indicates the heavy rain area (≧10mm/20min).

in the strong southerly flow. These facts suggest that the heavy rain fell from fast ascending warm air over the stationary front and the mesoscale low was formed by deep, warm air near the front.

5. HORIZONTAL STRUCTURE OF THE RAINSTORM

The distribution of reflectivity and Doppler velocity did not change essentially during the period from 2254 JST to 0134 JST on 26 September. Figure 4a shows that at 2345 JST the echoes of the rainstorm were forming a band of high reflectivity about 30 km wide and about 80 km long. On the northeast side of the band there was a low-reflectivity area of rather stratiform cloud.

The Doppler-velocity field in Fig.4b shows two

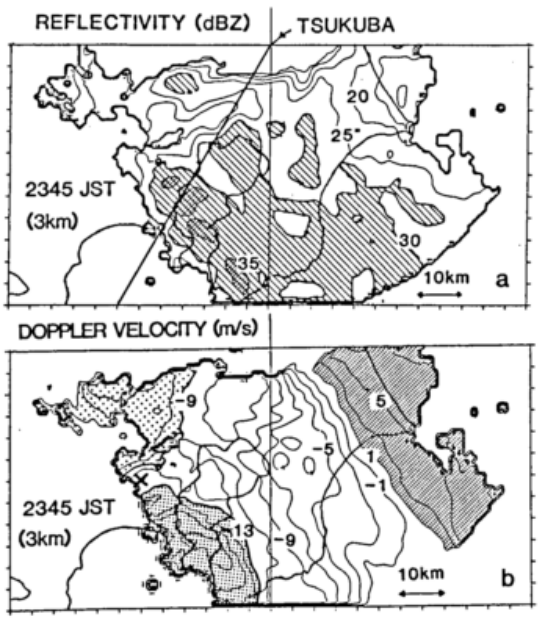


Fig.4 Reflectivity (a) and Doppler velocity (b) at the 3-km level for 2345 JST on 25 September 1981. Solid straight line in (a) indicates the position of vertical cross sections in Fig.5. Light and heavy dotted shadings in (b) indicate lower (>-9m/s) and higher (< -13m/s) Doppler velocity, respectively. Cross symbol indicates the center of the circulation.

remarkable features. One of them is a cyclonic circulation embedded in the mean flow (225°, 11 ms^{-1}) at the 3 km level. A pair of high (-19 ms^{-1}) and low (-5 ms^{-1}) Doppler velocity areas is observed to the southwest of the radar. The center of the circulation was located over the stationary front. The rainstorm was located in the eastern part of the circulation. The other remarkable feature is the sharp gradient of Doppler velocity ($5x10^{-4}s^{-1}$) in the band. This gradient means that the slowly moving air in front of the rainstorm was overtaken by the fast moving air from the rear (southwest) of the storm.

6. VERTICAL STRUCTURE OF THE RAINSTORM

Reflectivity and Doppler velocity in a vertical plane which crossed the rainstorm are shown in Fig.5. The main feature of the reflectivity field in the rainstorm (Fig.5a) was a high reflectivity area near the rear edge.

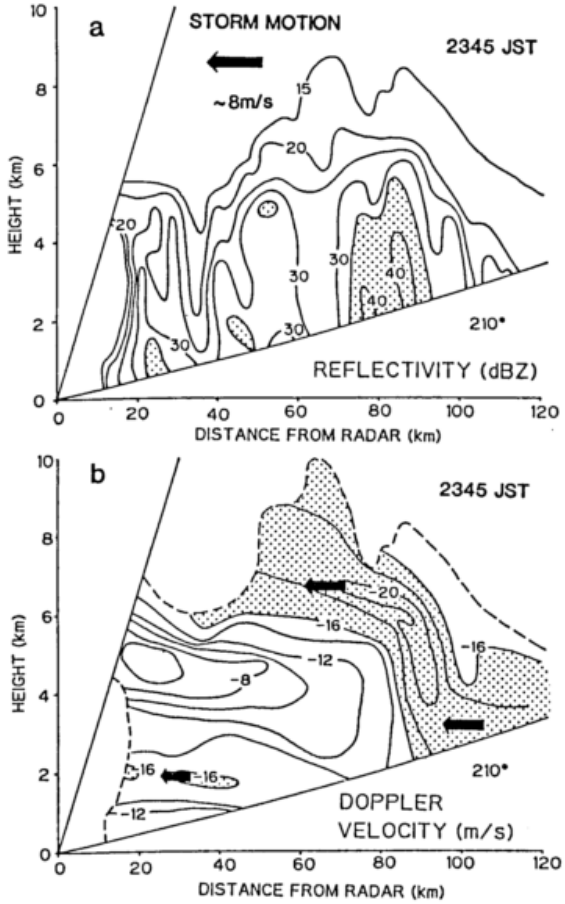


Fig.5 Reflectivity (a) and Doppler velocity (b) along 210° azimuth for 2345 JST on 25 September 1981.

The main feature of the Doppler velocity field (Fig.5b) is a slant area of high Doppler velocity near the rear edge. The air below 4 km on the southwest of the rainstorm ascended over the stationary front with a slope of about 3/10 and reached about 6 km. This ascending motion occurred at the rear edge of the intense echo. High reflectivity cores exceeding 40 dBZ were observed below the slantwise updraft. The depth of the air south of the stationary front which subsequently ascended over the front was about 4 km which suggests accumulation of warm air resulting in decrease of surface pressure.

There was an area with distinctly low Doppler velocity on the northeast side of the storm at height of 4-5 km. Since the rainstorm moved about 8 ms^{-1} in this cross section, there was an inflow from the front side. The upper-air soundings indicate that the air in the inflow was relatively cold compared to the ascending air. Since the environment was moist throughout the whole layer (not shown), evaporation of precipitation particles in the inflow air was not high as shown in Fig.5a. The vertical cross section of Doppler velocity suggests that between 50 and 70 km there were convergence at the 4.5 km level and divergence at the 2 km level. This means downdraft just before the deep updraft. The zone of high Doppler velocity on the front side of the storm at the 2 km level is an outflow from the downdraft.

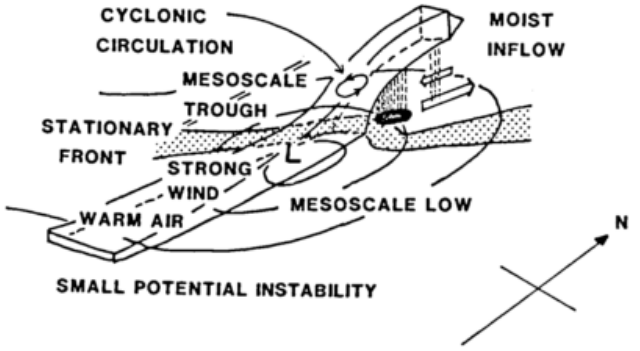


Fig.6 A Schematic model of the rainstorm.

7. CONCLUSIONS

The results are summarized in a schematic model (Fig.6), in which the rainstorm is looked from the southeast. Warm air near the surface was rapidly moving from the south toward the stationary front on the eastern side of the mesoscale trough at 850 hPa. The stationary front extended northward, where warm, strong, southerly wind was observed. The depth of the layer of the warm air increased near the stationary front. Consequently a mesoscale low formed south of the front at the surface. The warm air ascended over the stationary front and caused heavy rain below the front. The ascending motion showed slightly convective nature. There was an inflow relative to the rainstorm on the front (northeast) side at middle levels. Since this inflow air was moist, the inflow did not reduce the rainfall through evaporation.

REFERENCE

Houze,R.A.Jr. and Hobbs,P.V. 1982: Organization and structure of precipitating cloud systems, Advances in Geophys.,24,225-315.

THREE-DIMENSIONAL AIRFLOW AND VORTICITY BUDGET OF RAINBANDS IN A WARM OCCLUSION

Owen Hertzman and Peter V. Hobbs
Atmospheric Sciences Department, University of Washington,
Seattle, Washington 98195 USA

1. INTRODUCTION

The importance of rainbands in the organization of precipitation in midlatitude cyclones has been documented in earlier studies (e.g., Hobbs et al., 1980; Herzegh and Hobbs, 1980, 1981). In the present study, two rainbands in a young, warm occlusion are examined using dual-Doppler radar data and supporting mesoscale measurements. The rainbands are examined in three dimensions and down to smaller scales than in previous studies.

The data used in this study were collected on 30 January 1982 during the CYCLES (Cyclonic Extratropical Storms) Project on the Washington Coast. The radars were NCAR's CP-3 and CP-4, 5.5 cm wavelength, Doppler radars, which were operated as a dual-Doppler scanning pair. The high density of data from these radars permits the resolution of horizontal and vertical motions within the rainbands down to a horizontal scale of ~ 3.5 km. These measurements are used to derive 3-D airflows, convergence-divergence, and vorticity distributions. A Lagrangian vorticity budget for one of the rainbands is computed from averages of these data. Kinematic fields are described with respect to the motions of small-scale precipitation cores within the rainbands. The 3-D motions in this core-relative frame provide insights into the relationship between kinematic and precipitation fields.

2. VORTICITY DISTRIBUTION

The rainbands were situated near the centers of regions of cyclonic vorticity (ζ) and upward motion in the occlusion. The rainbands were 45 - 90 km wide, > 250 km long, and oriented perpendicular to the wind shear vector in the vertical and parallel to the orientation of the cold front. The speed of the rainbands normal to their major axes was ~ 15 m s^{-1}. Relative to the motions of the rainbands, the small-mesoscale precipitation cores moved primarily along the length of the rainbands at 11 - 17 m s^{-1}.

The vertical profiles of ζ, averaged over ~ 40 km in the horizontal for each rainband, show peak values of about 2×10^{-4} s^{-1}. Maximum values of ζ at the minimum resolvable scale (~ 3.5 km) were greater than this by about a factor of 5. Within each rainband, and located at the height of the maximum value of ζ, there was a non-divergent, cyclonic circulation with a horizontal scale of ~ 40 km. The divergence and vertical shears of the horizontal wind components at these levels were weak; thus, the vorticity to maintain the cyclonic circulations must have come from air parcels advected to these levels.

3. VORTICITY BUDGET

A Lagrangian budget of ζ for the rainband that contained the main updraft in the warm occlusion shows that the primary source term for ζ was the tilting of the horizontal vorticity associated with the shear in the vertical of the wind *across* the width of the rainband. Vertical profiles of the stretching and tilting terms of the vertical vorticity budget averaged over the width and 35 km of the length of the rainband are shown in Fig. 1. The profiles indicate that vortex stretching was a strong source of vorticity in the boundary layer, but near zero or a sink for ζ aloft. Although the overall effect of stretching was positive, it was much less so than would be inferred from the product of the absolute vorticity and the convergence computed from averages at the ~ 40 km scale. The vertical profile of the dominant tilting term (solid squares in Fig. 1) showed modest positive contributions in the lowest 3 km, where substantial vertical shears of the wind across the rainband and gradients of vertical motion along the rainband were present. The tilting of the horizontal vorticity associated with the vertical shear of the wind along the rainband

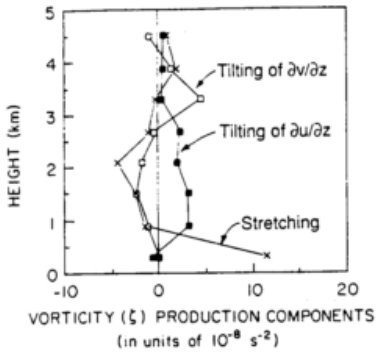


Fig. 1: Vertical profiles of the components of vorticity (ζ) production in a rainband: stretching (crosses), tilting of the vertical shear of the across-band wind component (solid squares), and tilting of the vertical shear of the along-band wind-component (open squares). Data for 1715 PST on 30 January 1982.

was unimportant in this case, probably because of a lack of a jet along the front.

4. AIRFLOW

The dual-Doppler airflow measurements with respect to the precipitation cores in the two rainbands are shown schematically in Fig. 2. As indicated in this figure, the moist airflow at low levels was strongly from the front to the rear of the rainband (AD), near the rear of the system it was upward in the main updraft (DF), and at mid- and upper-levels it was weakly forward and upward (FG and FHK). Thus, moist air was primarily supplied to the leading rainband 1 from the rear at mid-levels. The main updraft was from low-level convergence beneath rainband 2, just ahead of the surface occluded front. A secondary updraft feeding rainband 1 was forced by the nose of the cold air aloft. The magnitudes of the updrafts were ~ 1.5 m s^{-1} on the small scale (~ 5 km) and ~ 0.3 m s^{-1} on the band-scale (the broad arrows in Fig. 2).

The horizontal circulations in each rainband, mentioned in Section 2 and shown by the circled M's in Fig. 2, were located near the primary and secondary updrafts above the freezing level. Between, and at the edges of, the rainbands the vorticity was less cyclonic and the updrafts were weaker.

5. DISCUSSION

Recent numerical (Knight and Hobbs, 1988) and

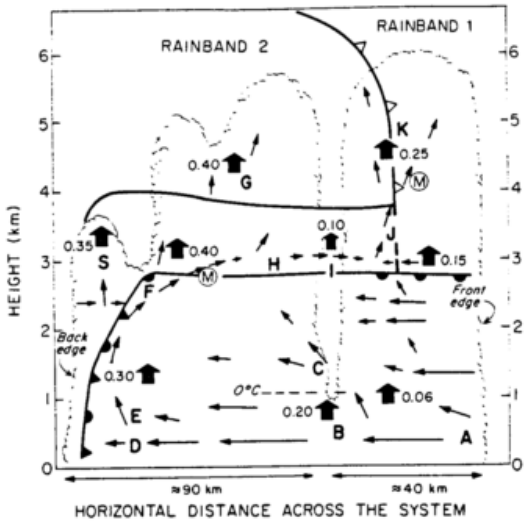


Fig. 2: Schematic of the two rainbands in the warm occlusion in a vertical plane across the width of the rainbands. The cloud-like scalloped outline indicates the boundary of the radar echo. The broad arrows show the vertical airflow, with the numbers beside each arrow being the vertical airspeed (in m s^{-1}) averaged over horizontal areas of 35 km x 35 km. The thin arrows show the airflow relative to the precipitation cores. The airflow below 3 km in rainband 1, and below 1.5 km in rainband 2, was strongly into the plane of the figure.

observational (Wolfsberg et al., 1986) studies of rainbands in extratropical cyclones suggest that some bands are the result of the release of conditional symmetric instability by lifting in the frontal zone. However, the two rainbands described in this paper do not appear to have been produced by symmetric instability, since their orientation was perpendicular to the direction predicted by that mechanism. Although we do not have a dynamic explanation for the rainbands, we can explain some of their features.

Both of the rainbands appeared to be maintained through the interaction of small-scale updrafts and band-scale, non-divergent, cyclonic circulations. The updrafts enhanced the growth of precipitation particles at and above the level of the band-scale, non-divergent, cyclonic circulations. The magnitudes of the updrafts ($\geq$ 0.75 m s^{-1}) were sufficient to suspend precipitation-sized snow particles for periods of about 1 h and to condense significant amounts of cloud water (near FG and JK in Fig. 2). The precipitation cores within the

rainbands were small-mesoscale regions of enhanced precipitation, which were produced by the small-mesoscale updrafts. The organized horizontal circulations determined, in part, the horizontal scale of the falling hydrometeors across the widths of the rainbands. The motion of the cores along the length of the rainbands, and the orientation of the low-level moist flow (which provided the condensate for the precipitation growth) organized the precipitation into bands. If the small-scale updrafts had been close to the band average values of ~ 0.3 m s^{-1}, the banded nature of the precipitation would have been much less, since the time that the hydrometeors would have spent in the region of the band-scale circulation would have been greatly reduced.

For further details on this study the reader is referred to Hertzman and Hobbs (1988).

Acknowledgments. Research supported by NSF Grant ATM-8311147.

6. REFERENCES

HERTZMAN, O.; HOBBS, P. V.: The mesoscale and microscale structure and organization of clouds and precipitation in midlatitude cyclones. XIV: Three-dimensional airflow and vorticity budget of rainbands in a warm occlusion. *J. Atmos. Sci.*, 45 (1988) (in press).

HERZEGH, P. H.; HOBBS, P. V.: The mesoscale and microscale structure and organization of clouds and precipitation in midlatitude cyclones. II: Warm-frontal clouds. *J. Atmos. Sci.*, 35 (1980), 597-611.

HERZEGH, P. H.; HOBBS, P. V.: The mesoscale and microscale structure and organization of clouds and precipitation in midlatitude cyclones. IV: Vertical air Motions and microphysical structures of prefrontal cold surge clouds and cold-frontal clouds. *J. Atmos. Sci.*, 38 (1981), 1771-1784.

HOBBS, P. V.; MATEJKA, T. J.; HERZEGH, P. H.; LOCATELLI, J. D.; HOUZE, R. A., JR.: The mesoscale and microscale structure and organization of clouds and precipitation in midlatitude cyclones. I: A case study of a cold front. *J. Atmos. Sci.*, 37 (1980), 568-596.

KNIGHT, D. J.; HOBBS, P. V.: The mesoscale and microscale structure and organization of clouds and precipitation in midlatitude cyclones. XV: A numerical modeling study of frontogenesis and cold frontal rainbands. *J. Atmos. Sci.*, 45 (1988) (in press).

WOLFSBERG, D. G.; EMANUEL, K. E.; PASARELLI, R. E.: Band formation in a New England winter storm. *Mon. Wea. Rev.*, 114 (1986), 1552-1569.

DOPPLER RADAR OBSERVATION OF CONVERGENCE BAND CLOUD FORMED ON THE WEST COAST OF HOKKAIDO ISLAND, JAPAN

Yasushi Fujiyoshi, Kazuhisa Tsuboki and Gorow Wakahama
Institute of Low Temperature Science, Hokkaido Univ., Sapporo

1. INTRODUCTION

Small scale cyclone is occasionally formed off the west coast of Hokkaido Island in mid-winter. It brings heavy snowfall locally in the western coastal regions. Possible mechanisms of its occurrence have been discussed by many Japanese researchers. When such a small scale cyclone is analyzed on a surface weather map, meteorological satellite catches broad (several tens kilometers) and long (several hundreds kilometers) band cloud along the west coast (Fig.1).



Fig.1: Satellite imagery of convergence band cloud (indicated by a thick arrow).

The cloud is considered to be formed along a convergence line between two air masses with relatively warm and wet (north-western side) and with cold and dry (north-eastern side). Thus, it is called as convergence band cloud (Okabayashi and Satomi 1971; Muramatsu et al. 1975). Heavy snowfall caused by the convergence band cloud is, therefore, a drastic precipitation phenomenon which appears along convergence line of air masses with different density and wind direction. In this paper we will report the radar echo and dynamical structure of convergence band cloud observed by using a Doppler radar with 3.2 cm in wavelength on Jan.26, 1985 at Sapporo.

2.VERTICAL PROFILE OF HORIZONTAL WIND VELOCITY

Figure 2 shows an example of vertical profile of Doppler velocity, in which the azimuth is 315° parallel to the direction of echo movement. Each value in Fig.2 can be regarded as a horizontal component of wind velocity within the vertical cross section, since only Doppler velocities less than 20° in elevation angle are involved in the figure.

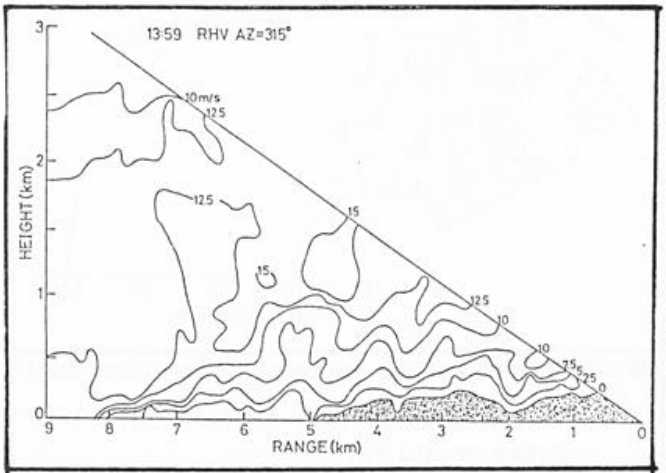


Fig.2:Vertical cross section of Doppler velocities. Unit is m/s.

Vertical structure of the wind is different between two regions far from and within 8 km in horizontal distance. In the region far from 8 km, Doppler velocity is almost the same from the ground to the upper atmosphere, and vertical shear of the wind velocity is small. In contrast, profiles of Doppler velocity are divided into three layers in the latter region; i) land breeze layer (0-250 m in altitude, shaded in the figure)where wind blows from the land to the sea, ii) shear layer (250-1000 m in altitude) where vertical wind

shear is large, iii) high-speed wind layer (above 1000 m in altitude) with small wind shear and high speed.

As shown in the figure, the front of the shear layer (named shear front) exists in the point about 3 km farther than that of land breeze layer. The pattern of shear layer near the front indicates wedge-shaped with 14° in elevation angle. The upper boundary of shear layer show wave-like pattern with 1 km in wavelength, which is considered to be caused by the Kelvin-Helmholtz instability.

3. DISCONTINUOUS LINE AND SNOWFALL AREA

Figure 3 shows an example of horizontal section of radar echo, in which a discontinuous line of the wind represented by thick dashed line was detected by means of a Doppler radar.

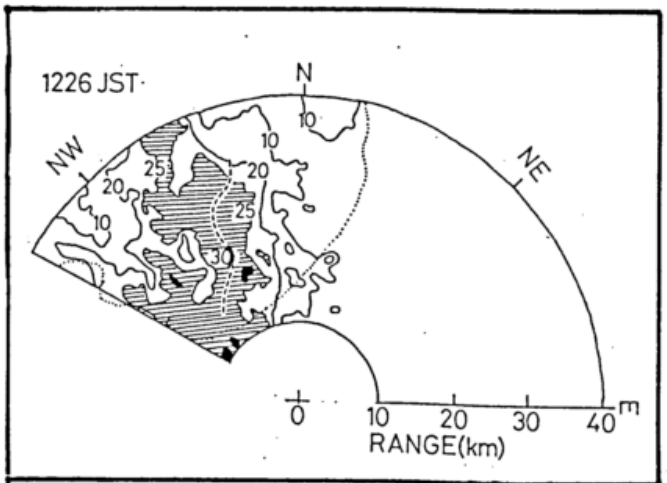


Fig.3:PPI radar-echo pattern. Elevation angle is 1°. Unit is dBZ. Dotted line indicates coastline.

As shown in the figure, strong echo regions exist in and along the west side of discontinuous line. Echo intensity is rapidly weakened in the east side of the line. Two strong echo regions exist parallel with each other from the north to the south. The echo regions alternate in intensity; when the east one is weakened, the west one then becomes strong in intensity. As a result, such a strong region seems to move west to east as a phase. The moving velocity is fairly comparable with retreating rate of the discontinuous line. Although the strong echo regions moves almost west to east at a speed of 4 m/s, all echo cells move northwest to southeast at about three times higher speed.

Figure 4 shows an example of vertical cross section of radar echo, in which an arrow on the ground denotes the position of shear front detected by a Doppler radar.

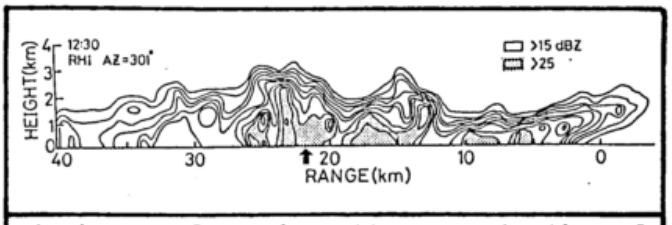


Fig.4:RHI radar-echo pattern. Azimuth angle is 301°.

Convective cloud just above the shear front is about 1 km taller and stronger in intensity compared with that being distant from the front. The level of echo top becomes lower as the cloud goes to the inland. Gradient of the echo stands straight in the range further than the shear front. It begins to decline rapidly within the range of the shear front. The convective clouds are aligned with separation, distance about 10 km. Each convective cloud is composed of small convective cells which are in different developing stages.

4. TWO-DIMENSIONAL VERTICAL PROFILE OF THE WIND

A Doppler radar makes it possible to provide information on vertical profiles of wind above the observational point. On the basis of three components of wind at each level, we can draw a picture of time-height cross section of two dimensional wind field within east-west cross section perpendicular to the moving direction of discontinuous line. Time axis is exchangeable to horizontal distance by postulating steady state of the wind field. Figure 5 shows the wind field relative to the movement of discontinuous line. Air-stream goes upward along the upper-most of the shear layer. Distinctive circulations appear between the shear layer and the land breeze layer. Their sizes become large with increasing the thickness of the shear layer.

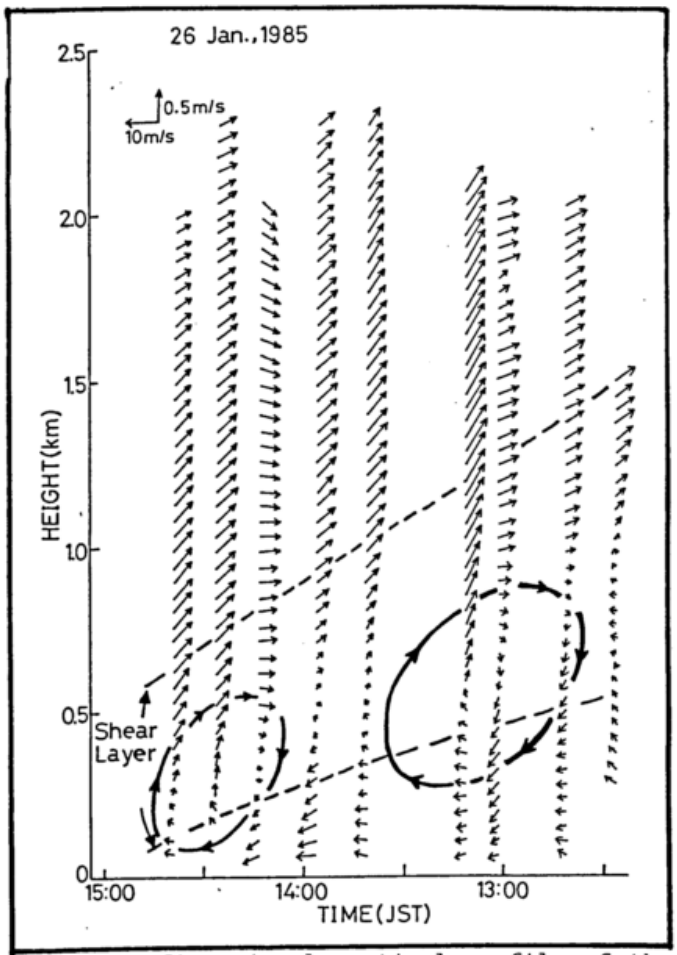


Fig.5:Two-dimensional vertical profile of the wind field relative to the movement of discontinuous line.

5. CONCLUDING REMARKS

Radar echo and dynamical structures of convergence band cloud (warm frontal type) have been elucidated at the first time by means of a Doppler radar. The case studied seems to be the simplest example of convergence band cloud in structure. Similar analyses are to be performed for convergence band cloud (cold frontal type) with more complex structure.

REFERENCES

Muramatsu,T.,; Ogura,S.; Kobayashi,N: The Heavy Snowfall arisen from Small Scale Cyclone on the West Coast of Hokkaido Island. Tenki. 22(1975), 369-379(in Japanese).

Okabayashi,T.; Satomi,M.: A Study on the Snowfall and its Original Clouds by the Meteorological Radar and Satellite (Part I). Tenki.18(1971),573-581(in Japanese).

Thorpe,S.A.: Experiments on Instability and Turbulence in s Stratified Shear Flow. J.Fluid Mech. 61(1973),731-751.

THE USE OF OXYGEN ISOTOPES IN STUDIES OF ICE PHASE PRECIPITATION FROM WINTER STORMS

Belay Demoz, J.A. Warburton and R.L. Stone

Desert Research Institute, University of Nevada System

1. INTRODUCTION

Stable isotopes of water have long been used as tracers in studies of the atmospheric water cycle. In particular the earlier work of Epstein (1951), Dansgaard (1964), Friedman (1953) and others are notable. More recently the isotopic record in snow and ice in polar regions has been used to obtain information on paleoclimate and shorter-term variations in climatic events. Significant contributions by Epstein et al (1965), Barkov et al (1977), Hammer et al (1978), Lorius et al (1969) and Jouzel and Merlivat (1984) are noted amongst many others. A study of the stable isotopic composition of ice-phase precipitation in Antarctica by Picciotto et al (1960), traced the origin of this precipitation in relation to cloud base and cloud top elevations. This work yielded a substantially linear relationship between the stable isotopic composition of the Antarctic precipitation and the mean temperature altitude of the clouds from which the precipitation fell. The relationship determined for that geographic location in the Antarctic summer, was $\delta = -(0.9T + 6.4)$, where T is the precipitation formation temperature in degrees Celsius and δ represents the stable $^{18}O/^{16}O$ isotopic ratio for the precipitation in parts per mil °/oo with respect to SMOW (Standard Mean Ocean Water). This gradient (almost 1 °/oo per °C) for the range of temperatures observed, is similar to the gradient determined by the modeling work of Jouzel and Merlivat (1984) over the same temperature range.

A somewhat similar approach has been used in the present investigation for estimating the weighted mean altitudes in storm systems at which supercooled water vapor and liquid water were captured by ice-phase precipitation in the Central Sierra Nevada of the western United States.

2. PROCEDURES FOLLOWED

As reported by Warburton and DeFelice (1986) from earlier studies in the Sierra Nevada, a tentative relationship between the $\delta^{18}O$ values and the weighted mean temperature of formation of the precipitation in this geographic region was determined as: $\delta = -(0.9T + 3.4)$. Additionally, this work showed that when accretional ice growth was significant in the precipitation collected at the ground, that the predominant ice crystal habit formation temperature as determined by the Magono-Lee classification system did not match the isotopically derived ice formation temperature. In these cases the evidence showed that most of the ice-phase water had been captured from the lower, warmer layers of the clouds passing over the area. In other cases there was good agreement between the two derived temperatures, but these were always when there was little, if any accretional growth on the precipitating ice particles. A second important observation from these previous observations, was that there was no apparent relationship between the oxygen isotopic composition of the freshly falling snow and the ambient temperature at the ground where the snow was being collected.

These same procedures have been followed during the 1984-85 and 1985-86 winter seasons, collecting freshly falling snow at the surface near the 2000 meters elevations in the Central Sierra Nevada. Ice crystal replication was

conducted at the same time and observations of crystals were also made with a 2DC aspirated particle probe. The stable isotopic composition of the snow samples was done by mass spectrometry in the DRI laboratories to determine the oxygen isotope ratios. Snow samples were collected at one half to one hour intervals.

3. RESULTS

Sequential snow sampling was conducted at Kingvale, California, near the crest of the Sierra Nevada, during 10 sampling periods which occurred during eight (8) winter storms between 28 January and 27 March 1985. This yielded 190 individual samples for isotopic and ice crystal analysis.

During the 1985-86 season, eleven (11) storm events were sampled, yielding 210 samples for analysis. The results from the two seasons were quite similar. Figure 1 shows a histogram of the 1985-86 results. It is a frequency distribution of the isotopic ratios measured.

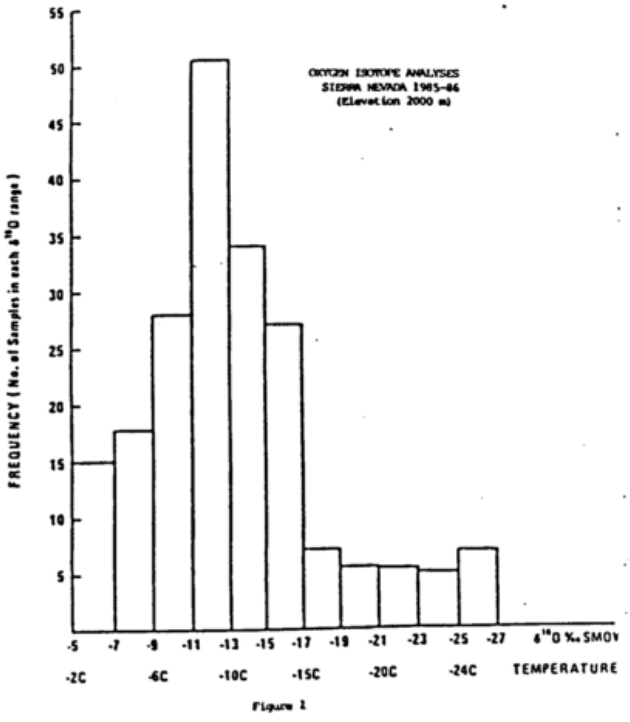


Figure 1

The abscissa also gives an isotopically derived mean "temperature" of formation based upon the relationship previously derived for this geographic region in winter.

We see that 80% of the precipitation probably develops at temperatures warmer than -15°C with a peak in the distribution around -10°C. When combined with the 190 samples from the 1984-85 season, we have found that 50% of the samples correspond to ice-phase formation temperatures warmer than -10°C.

The Poster Session at the conference will present several of the detailed case studies from the 1984-85 winter season. This presentation will provide information on ice crystal habits, degrees of riming, precipitation rates and stable isotopic compositions. It will also include mesoscale atmospheric data showing air mass trajectories and upper air soundings which provide independent measurements and estimates of cloud temperatures.

4. REFERENCES

Barkov, N.I., Korotkovich, E.S., Gordienko, F.G. and Kotlyakov, V.M. (1977): The isotope analysis of ice cores from Vostok Station (Antarctica) to the depth of 950 m. Isotopes and impurities in Snow and Ice, IAHS, AISH Publ. 118, 382-387.

Dansgaard, W. (1964):Stable isotopes in Precipitation. Tellus, 16, 437-467.

Epstein S. (1961): The variation of the $^{18}O/^{16}O$ ratio in nature and some geological implications. In P.H. Abelson (Editor), Researches in Geochemistry. Wiley. N.Y. 217-240.

Epstein, S., Sharp, R.P., and Gow, A.J. (1965): Six years' record of Oxygen and Hydrogen isotope variations in South Pole firn. J. Geophys. Res. 70, 1809-1814.

Friedman, I. (1953): Deuterium content of natural water and other substances. Geochim. Cosmochim. Acta., 4, 39.

Hammer, C.V., Clausen, H.B., et al., (1978): Dating of Greenland ice cores by flow models, isotopes, volcanic debris, and continental dust. J. Glaciol. 20. 3-26.

Jouzel, J. and Merlivat, L. (1984): Deuterium and Oxygen 18 in precipitation. Modeling the isotopic effects during snow formation. J. Geophys. Res.89 (11), 749-757.

Lorius, C., Merlivat, L. and Hageman, R., (1969): Variation in the mean deuterium content of precipitation in Antarctica. J. Geophys. Res., 74, 7027-7031.

Picciotto, E., DeMaere, X. and Friedman I. (1960): Isotopic composition and temperature of formations of Antarctic snows. Nature, 1897; 857-859.

Warburton, J.A., and T.P. DeFelice. (1986): Oxygen Isotopic Composition of Central Sierra Nevada Precipitation. 1. Identification of Ice-Phase water Capture Regions in Winter Storms. Atmos.Research, 20. 11-22.

Numerical Sensitivity Study of the Morphology of Lake-Effect Snow Storms over Lake Michigan

Mark Hjelmfelt

National Center for Atmospheric Research†
P. O. Box 3000, Boulder, Colorado 80307

1. INTRODUCTION

The Great Lakes of North America exert significant effects on the weather in their vicinity. In fall and winter months, when cold arctic air masses cross the lakes, "lake-effect" snow storms may occur. Under suitable conditions of lake-air temperature differences, wind speed, fetch, and stability, strong organized convection may develop in the boundary layer. The resulting lines or bands of cumulus or strato-cumulus clouds may produce considerable amounts of snow. While the classic lake-effect storms occur in the cold air behind the synoptic-scale disturbances in conditions of stability that tend to suppress convection, lake-effect enhancements of larger-scale storms may also be significant. Braham and Dungey (1984) estimated that one-fourth to one-half of the yearly snowfall on the shores of Lake Michigan could be attributed to lake-effects.

Braham and Kelly (1982) and Forbes and Merritt (1984) have identified four general morphological types of lake-effect snow storms. These are shown schematically in Fig. 1: a) broad area coverage, which may become organized into wind parallel bands (Kelly, 1982) or open-cells (Braham, 1986) is the most common type (Kelly, 1986); b) shoreline bands with a line of convection roughly parallel to the lee shore and a well-developed land breeze on the lee shore (Braham, 1983) can produce very heavy snowfalls near the lake shore; c) mid-lake bands with low-level convergence centered over the lake (Passarelli and Braham, 1981) may produce heavy snows where the band crosses the shoreline at the southern end of the lake; d) mesoscale vortices with a well-developed cyclonic flow pattern in the boundary layer (Forbes and Merritt, 1984; Pease et al., 1988) can also occur.

In this study, numerical simulations are used to examine the influence of environmental parameters on the morphology of lake-effect snow storms over Lake Michigan. A series of model sensitivity studies are performed to examine the effects of lake-land temperature difference, atmospheric boundary layer stability, humidity, and wind speed and direction on the morphology of simulated storms. The intention is to generate a numerical climatology for comparison with theory and observations.

2. MODEL

These studies are performed using the Colorado State Mesoscale Model (Pielke, 1974, 1984; McNider and Pielke, 1981; Hjelmfelt and Braham, 1983). This model has previously been shown to produce good simulations of lake-effect snow storms in simulations of the 10 December 1977 shoreline band storm (Hjelmfelt and Braham, 1983) and the mesoscale spiral vortex that occurred on 19 October 1972 (Pease et al., 1988).

The model is a three-dimensional, Eulerian, hydrostatic, primitive equation model with a detailed boundary layer parameterization (Pielke, 1984). The present study employs the model with an 8 km horizontal grid spacing and a variable vertical grid with levels at 10, 100, 500, and continuing at 500 m intervals to 5 km. Precipitation is included via a simple condensation scheme (Hjelmfelt and Braham, 1983) and includes evaporation below cloud base exponentially inversely proportional to the relative humidity.

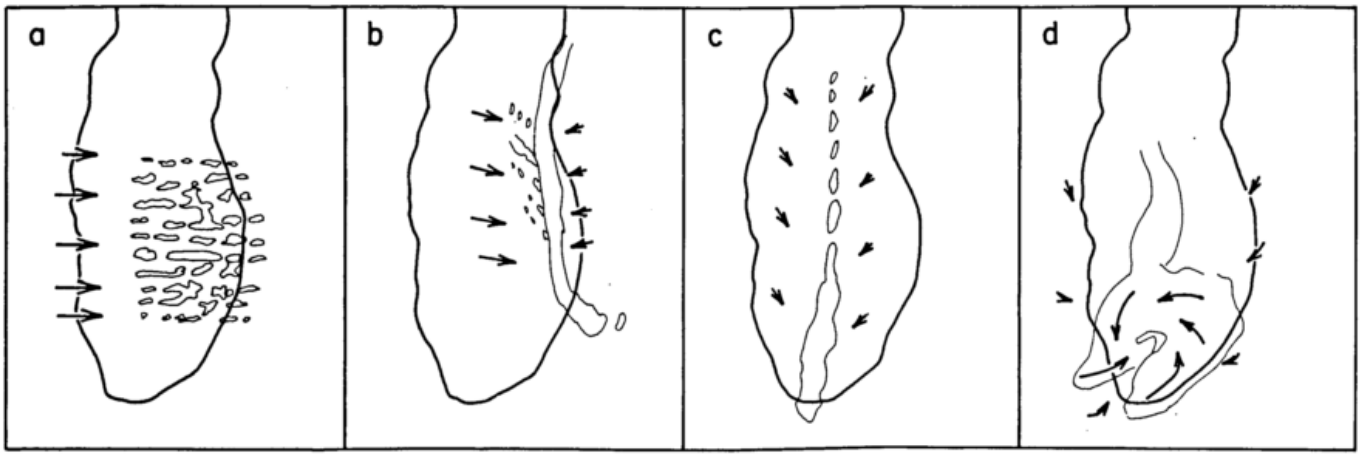


Figure 1. Schematic of four morphological types of lake-effect snow storms over Lake Michigan as defined from observations: a) broad area coverage, b) shoreline band, c) mid-lake band, and d) mesoscale vortex.

† NCAR is sponsored by the National Science Foundation.

In the present study, the simulated area is assumed to be in a constant, uniform synoptic environment. The environmental parameters are varied independently to examine their impact on the expression of the above morphological types. Simulations are carried out until the model approaches a steady state.

3. SIMULATED MORPHOLOGY

Simulations are performed for a variety of conditions and various model fields plotted. Figure 2 shows examples of simulations exhibiting features of the four morphological types seen in observations. These results were obtained in the course of completing a matrix of sensitivity runs and are not the result of fine tuning the simulations to obtain the best examples of each type.

Figure 2a shows the results of a model simulation with strong lake-land temperature difference (ΔT=18), strong westerly winds (10 m s^{-1}), and a moderately strong stability ($\Delta\theta$=5° km^{-1}). In this case, the winds show no reversal of direction on the lee shore, there is not a strong, well-defined band of convection, and cloud covers a broad area downwind of the lake. In fine scale, this case might exhibit wind parallel bands of clouds (Kelly, 1984). However, this can not be determined with an 8 km grid.

Figure 2b shows a shoreline band. The land breeze is hard to see in this figure but can be quite strong (Hjelmfelt and Braham, 1983). Convection is confined to a narrow band near the lake shore with precipitation rates exceeding 1 mm/hr. This simulation was made with a strong lake-land temperature difference (ΔT=18), weak westerly winds (2 m s^{-1}), and a moderately strong stability ($\Delta\theta$=5° km^{-1}).

A mid-lake band appears in the results shown in Fig. 2c. This simulation was made with a weaker lake-land temperature difference (ΔT=12), moderate northerly winds (6 m s^{-1}), and strong stability ($\Delta\theta$=8° km^{-1}). Both convection and cloud cover are restricted to a band over the middle of the lake. Strong local enhancement occurs where the band crosses the lake's southern shore.

Figure 2d gives an example of a vortex. In this case, the simulation was made with a strong lake-land temperature difference (ΔT=18), weak northerly winds (2 m s^{-1}), and low stability ($\Delta\theta$=2° km^{-1}). The vectors are harder to see with weak winds, but the cloud band indicates the vortex at the southern end of the lake.

4. SENSITIVITY STUDIES

Sensitivity studies have been made for lake-land temperature differences of 5–18°, where the lake was kept at a constant 0°C. The upwind atmospheric sounding was given surface (1000 mb) to 3 km (about 700 mb) stabilities of 2, 5, and 8 $\Delta\theta$ km^{-1}. Winds were permitted to take on values of 2, 6 and 10 m s^{-1} for westerly and northerly directions. Relative humidities in the boundary layer were varied between 25–75%.

As the temperature of the air flowing off the upwind shore onto the lake decreases, the strength of the lake-induced circulations increases. Combined with winds, this is the most important factor in determining the strength and morphology of convection. Precipitation did not occur for the conditions studied at ΔT=10°, but always did for ΔT=18°. As ΔT increases, the potential for developing land breezes and shoreline bands increases; at ΔT=12, a 6 m s^{-1} wind was too strong to permit a shoreline band or land breeze to develop, while at ΔT=18 a shoreline band could be obtained. These results are consistent with a forecaster's rule of thumb that a lake-air ΔT of 13° is needed to get appreciable snow on the eastern shore of Lake Michigan (Rothrock, 1969).

Decreasing stability gives rise to a more convective, deeper response. Actually, perturbations in the low-level flow may be stronger in the more stable case because all the activity is confined to a shallower layer. Thus, land breezes may be somewhat easier to develop in conditions of high stability. The deeper response of the less stable cases, however, can produce more precipitation, even in

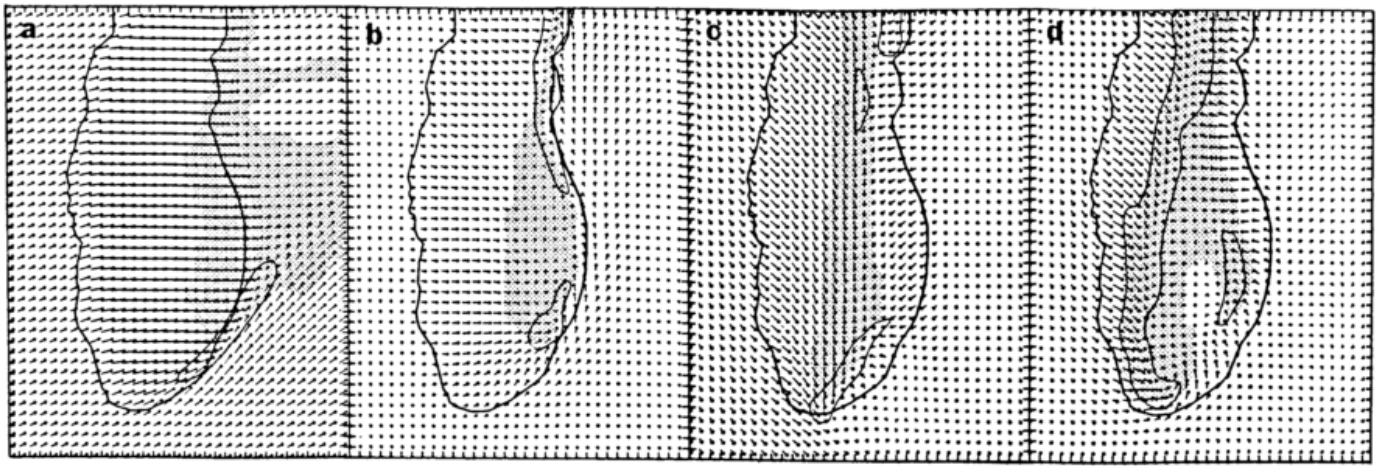


Figure 2. Examples of numerical simulations of the four observed morphological types of lake-effect snow storms over Lake Michigan, as in Fig. 1. Grid marks are at 8 km intervals and vectors are scaled to 8 km per grid interval. Areas of cloud cover are shaded. Contours are for vertical velocities at 1 km above the surface, contours at 10, 40, 80 cm s^{-1}.

this model. In nature, as the mesoscale response breaks into convective elements, much more vigorous convection and precipitation formation may occur. This increased convective nature may eventually cause a breakdown of the larger-scale patterns shown in Figs. 1 and 2. For a case with a large lake-land temperature difference (ΔT=18), strong westerly winds (10 m s^{-1}), but only low stability ($\Delta\theta$ km^{-1}=2), the area pattern in Fig. 2a broke down into three small areas of stronger vertical velocities spaced along the eastern shore. This result is similar to that discussed by Hsu (1987).

Winds exert a strong controlling influence on lake snow morphology. Weak to moderate westerly winds are conducive to the development of a land breeze and shoreline band, while stronger winds are more conducive to development of wind parallel bands. Very weak winds, especially from the north, may be conducive to the development of a vortex; otherwise the development of land breezes from both shores may create a mid-lake band. Stronger northerly winds enhance support for the development of mid-lake bands.

For a lake-land ΔT=15° km^{-1} and a strong stability of $\Delta\theta$ km^{-1}= 8, even strong west winds (10 m s^{-1}) gave a land breeze on the eastern shore. For low stability ($\Delta\theta$ km^{-1}= 2), only a 2 m s^{-1}westerly wind gave a land breeze. Moderate stability ($\Delta\theta$ km^{-1}= 5) yielded just a hint of a land breeze component for a 6 m s^{-1} west wind.

The humidity of the upstream sounding helps to regulate the cloud base height and cloud depth and the potential for precipitation formation. In some cases, its effect can be notable.

5. DISCUSSION

Space does not permit a full discussion of the matrix of simulations. Comparisons with observations and theory also must be held for a more complete forum.

Actual lake-effect storms occur in a dynamic, changing environment and so may not actually achieve the organization that conditions are driving it toward. Thus, the present study indicates steady state tendencies that must be interpreted in the real world in the context of changing dynamic conditions. Horizontal gradients of surface temperatures and winds across the domain and more complicated atmospheric structure (e.g., a low boundary layer stability with a strong, low-level capping inversion) also complicate real world situations. The present work, however, provides a context and background for forecasting experiments that include the effects of regional weather patterns and also for fine-scale studies of cloud structure and microphysical processes.

6. ACKNOWLEDGEMENTS

Special thanks to Ms. D. Davis for editing and typing the manuscript. The interest and encouragement of Dr. R. Braham, Jr. for this work is also acknowledged. This work is funded partially by NCAR, the National Science Foundation, and the Federal Aviation Administration through Interagency Agreement DTFA01-82-Y-10513.

7. REFERENCES

Braham, R.R., Jr., 1986: Cloud and motion fields in open-cell convection over Lake Michigan. *Preprints: 23rd Conference on Radar Meteorology*, Snowmass, Colo., Amer. Meteor. Soc., Boston, **3**, JP202-JP205.

Braham, R.R., Jr., 1983: The midwest snow storm of 8-11 December 1977. *Mon. Wea. Rev.*, **111**, 253-272.

Braham, R.R., Jr., and M.J. Dungey, 1984: Quantitative estimates of the effect of Lake Michigan on snowfall. *J. Climate Appl. Meteor.*, **23**, 939-949.

Braham, R.R., Jr., and R.D. Kelly, 1982: Lake-effect snow storms on Lake Michigan, U.S.A. *Cloud Dynamics*, E. Agee and T. Asai, eds., D. Reidel, 87-101.

Forbes, G.S., and J.M. Merritt, 1984: Mesoscale vortices over the Great Lakes in wintertime. *Mon. Wea. Rev.*, **112**, 377-381.

Hjelmfelt, M.R., and R.R. Braham, Jr., 1983: Numerical simulation of the airflow over Lake Michigan for a major lake-effect snow event. *Mon. Wea. Rev.*, **111**, 205-219.

Hsu, H., 1987: Mesoscale lake-effect snowstorms in the vicinity of Lake Michigan: Linear theory and numerical simulations. *J. Atmos. Sci.*, **44**, 1019-1040.

Kelly, R.D., 1986: Mesoscale frequencies and seasonal snow falls for different types of Lake Michigan snow storms. *J. Climate Appl. Meteor.*, **25**, 308-321.

Kelly, R.D., 1984: Horizontal roll and boundary layer interrelationships observed over Lake Michigan. *J. Atmos. Sci.*, **41**, 1816-1826.

Kelly, R.D., 1982: A single Doppler radar study of horizontal-roll convection in a lake-effect storm. *J. Atmos. Sci.*, **39**, 1521-1531.

McNider, R.T., and R.A. Pielke, 1981: Diurnal boundary-layer development over sloping terrain. *J. Atmos. Sci.*, **38**, 2198-2212.

Passarelli, R.E., and R.R. Braham, Jr., 1981: The role of the winter land breeze in the formation of Great Lakes snowstorms. *Bull. Amer. Meteor. Soc.*, **62**, 482-491.

Pease, S.R., W.A. Lyons, C.S. Keen, and M.R. Hjelmfelt, 1988: Mesoscale spiral vortex embedded within a Lake Michigan snow squall band: High resolution satellite observations and numerical model simulations. *Mon. Wea. Rev.*, **116**, (in press).

Pielke, R.A., 1974: A three-dimensional model of the sea breeze over South Florida. *Mon. Wea. Rev.*, **102**, 115-139.

Pielke, R.A., 1984: *Mesoscale Meteorological Modeling*, Academic Press, New York, 599 pp.

Rothrock, H.J., 1969: An aid in forecasting significant lake snows. Tech Memo, WBTM CR-30, National Weather Service, Central Region, Kansas City, Mo., 12 pp.

DOPPLER RADAR OBSERVATIONS OF SNOW PARTICLES IN WINTER CONVECTIVE CLOUDS

Hiroyuki Konishi*, Tatsuo Endoh** and Gorow Wakahama**

* Osaka Kyoiku University

** Institute of Low Temperature Science, Hokkaido University

1. INTRODUCTION

On the coast of the Japan Sea heavy snowfalls from convective clouds are frequently brought by prevailing north-west wind in winter. In Sapporo, located on the north east coast of the Japan sea, the type of snow particles falling on these days is almost always graupels or snowflake aggregates and it often changes from graupels to aggregates and sometimes from aggregates to graupels at the interval of about 10 minutes in a series of snowfall. The present paper describes the movements of these particles observed by a Doppler radar comparing with the change of precipitating particles observed at the radar site.

2. OBSERVATION

Observations of snow particles of winter convective clouds were carried out at ILTS in Sapporo in 1986. A 3-dimensional Doppler radar and an observation tower to measure the diameter and fall velocity of snow particles continuously were set on the roof of the main building(Fig.1). The size of the tower was 3 m (in height) x 0.9 m x 0.6 m and trajectories of snow particles fallen into the tower were photographed three times per a minute illuminating by a stroboscopic light. The diameter, the fall velocity and the number concentration of observed particles were obtained by analyzing photographs.

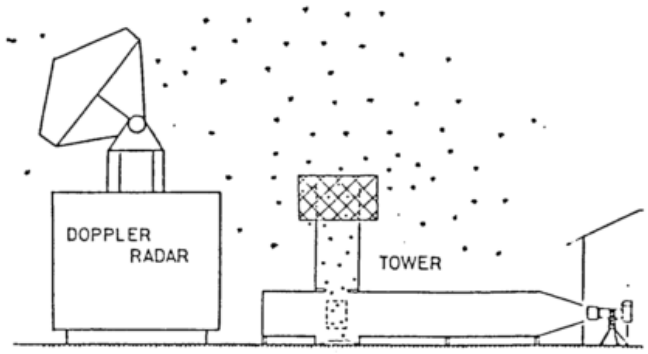


Fig.1 Section of observation tower and Doppler radar

3. RESULT

The relationship between the average diameter and the fall velocity of particles during a series of snowfall is shown in Fig.2. An open circle in this figure shows a relation between the averaged diameter and the averaged fall velocity of particles fallen in a minute. In this series of snowfall forty open circles are shown because it lasted for about forty minutes. In this figure, the region of graupels is clearly separated from that of aggregates, the fall velocity of graupels became larger in proportion to the size and, on the other hand, the fall velocity of aggregates was almost constant for the size range between 1 mm and 3 mm in averaged

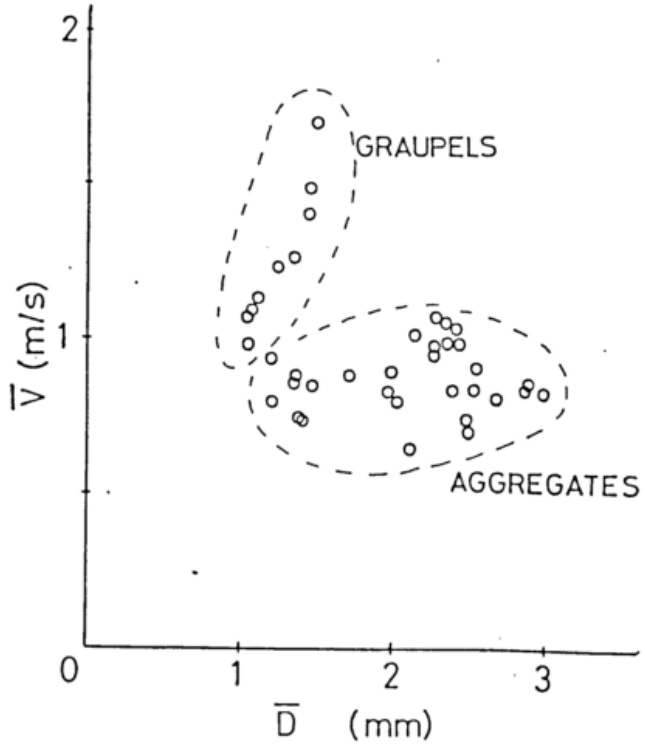


Fig.2 The relationship between averaged diameter and fall velocity

diameter. Two types of particle, graupels and aggregates, were rarely observed to fall at the same time on the ground. In a series of snowfall the fall velocity of graupels was high at first and gradually decreased. However the fall velocity and the diameter of aggregates were almost constant throughout the snowfall. The time-height cross section of radar reflectivity and and the changes of snowfall rate at the ground on this day is shown in Fig.3. The snowfall rate was high at first when graupels fell, and it gradually decreased with the decrease of the height of echo top and graupels were replaced by aggregates at 03:25. Comparing the upper cross section with the lower snowfall rate, the larger hatched region(right) the smaller hatched region(left) were inferred to be those of graupels and aggregates respectively. The variation of vertical Doppler velocity with height at high reflectivity region(>25 dBz) for graupels and aggregates is shown in Fig.4. For graupels, the fall velocity was small (about 1 m/s) inside the clouds and large (>2.5 m/s) at the level just below the cloud base as compared with the fall velocity at the ground. On the other hand for aggregates, the averaged vertical velocity was about 1 m/s and almost constant between the cloud top and the ground in spite of the region of high reflectivity increased below the cloud base.

Fig.5 shows four cases of the variation of reflectivities and vertical Doppler velocities in the echo core region from the echo top to the ground. Corresponding size spectra of snow particles at the ground are also shown in this figure. For graupels(case a) the vertical Doppler velocity became gradually large from the cloud base to the ground, although the reflectivity showed no clear difference between the echo top and the ground. Inside the cloud convective activity was inferred to be large because the ranges of Doppler velocity shown by bars were large and high reflectivity regions extended close to the echo top.

For aggregates(case b,c and d) the vertical Doppler velocity changed little between the echo top and the ground, and the radar reflectivity of the lower levels became gradually large in the case of large snowfall intensity on the ground(case b). In the case of small snowfall intensity(case d), however, it varied sharply near the ground.

Passarelli(1978), Kenneth and Passarelli(1982) observed the height evolution of snow size

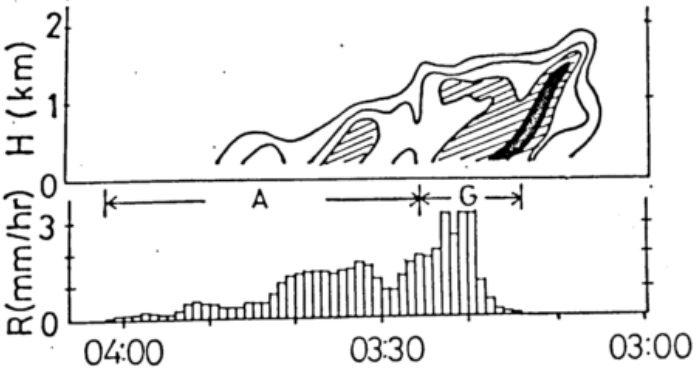


Fig.3 Time-height cross section and snowfall rate in a series of snowfall.
Contour lines of radar echo indicate 15,20,25 and 30 dBZ. (14 Feb. 1986) A:aggregates; G:graupels

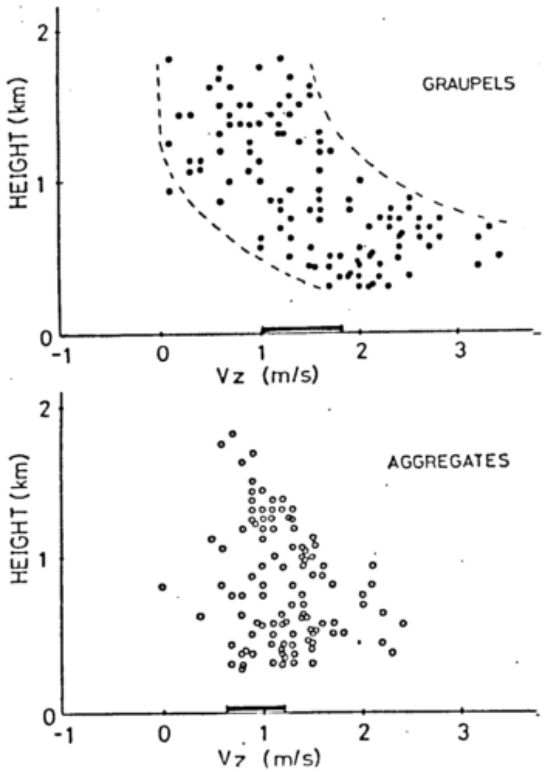


Fig.4 Height distributions of vertical Doppler velocities for highly reflectivite(>25 dBZ) graupels(upper figure) and aggregates (lower figure). Solid lines at 0 km indicate the range of the fall velocity of these particles observed at the ground.

spectra by aircraft in natural clouds. They have shown aggregates advanced descending altitude and the slope of spectra is smaller because of increasing of large aggregates. In our cases(Fig.5), the size spectra on the ground shows increasing concentration of large particles with increasing altitude of echo top

4. SUMMARY

Graupels were formed near the cloud top where updraft was inferred to be prevailing; they fell below the cloud base, where downdraft probably produced by these falling particles exist. On the other hand, aggregates grew slowly in comparatively weak upcurrents between the cloud top and the ground. When the cloud top was high and the number concentration of the particles was large, the occurrence of large aggregates increased because particles were inferred to aggregate themselves for falling long distance.

5. REFERENCES

KENNETH, K.L. and R.E.PASSARELLI,Jr.:The Growth of Snow in Winter Storms:An Airborne Observational Study.
J.Atmos.Sci.,39(1982),697-706.

PASSARELLI,R.E.,Jr.:Theoretical and Observational Study of Snow-Size Spectra and Snowflake Aggregation Efficiencies.
J.Atmos.Sci.,35(1978),882-889.

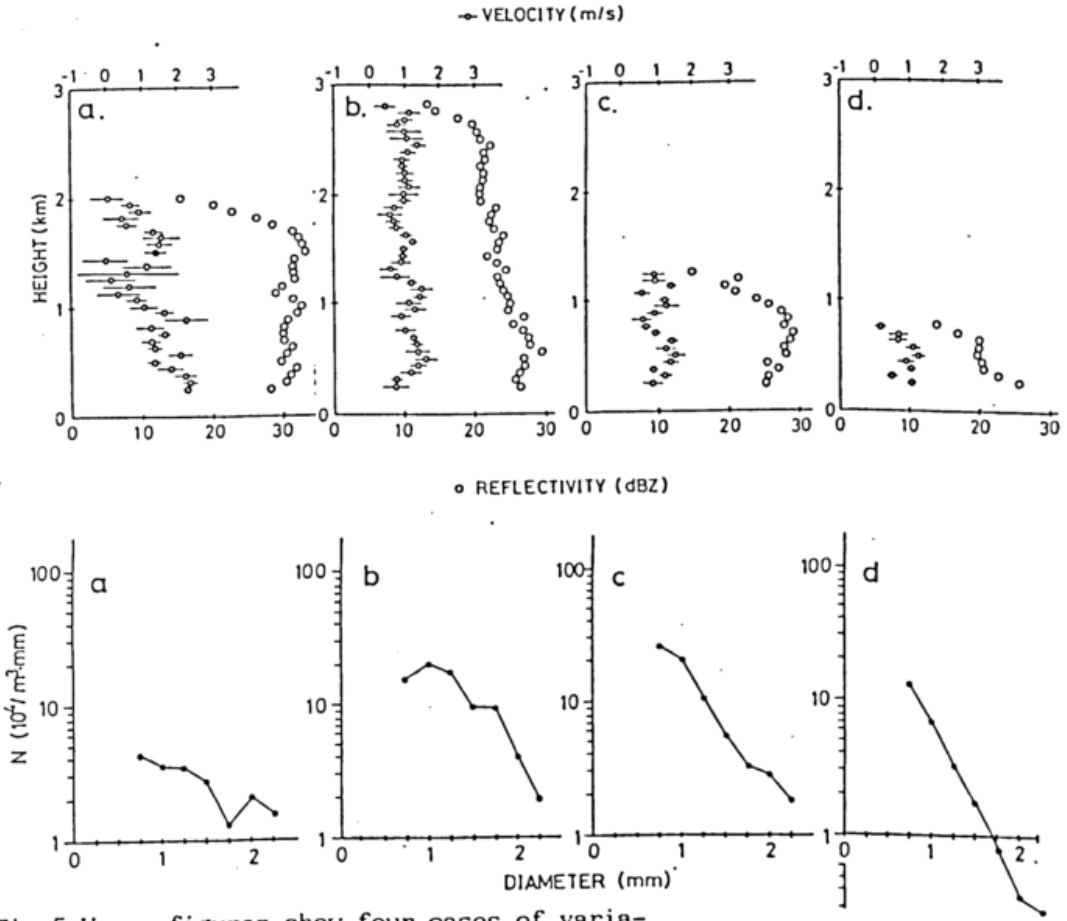


Fig.5 Upper figures show four cases of variations of vertical Doppler velocities and reflectivities in core regions with altitude. Lower figures are four cases of size spectra of snow particles observed at the ground.(a,b,c and d correspond to upper a,b,c and d respectively)

THE RELATIONSHIP BETWEEN ENTRAINMENT RATE AND SOME PRODUCTS OF 1-D Cb MODEL

Mladjen Ćurić and Dejan Janc
Institute of Meteorology, University of Belgrade
Yugoslavia

1. INTRODUCTION

The treatment of entrainment processes is one of the principal problem of 1-D cloud models. In order to improve some cloud model outputs with regard to operative use, we introduced the new entrainment parameterization in the 1-D time-dependent hydrostatic Cb cloud model. Despite the facts that real distinction of dynamic and turbulent mixing processes is practically very difficult (Randall and Huffman, 1982), the entrainment rate is treated as the sum of the three terms: the constant term; the term which is proportionate to the absolute value of vertical velocity similarly to Wisner et al. (1972) and describes turbulent mixing processes and the term which depends on the vertical velocity avection term and describes organized entrainment (detrainment) processes.

2. THE ENTRAINMENT PARAMETERIZATION

The entrainment processes is investigated in 1-D hydrostatic time-dependent model given by Wisner et al. (1972) with improvements of microphysical scheme parameterization (Orville et al., 1975; Lin et al., 1983). The given model assumed that the cloud consists of the vertical core and the environment. The initial profile of the vertical core is taken to be in the form of a cone in accordance with e.g. Battan (1982):

$$r = r_o + Az \qquad (1)$$

where r_o=5 km and A=0.2.

If we analyze the entrainment at some level we need know the differential segment area of the vertical core. So,

$$dS = \pi(2r+dr)\left[(dz)^2+(dr)^2\right]^{1/2} \qquad (2)$$

where dr and dz are differential changes of the core radius and the height respectively.

We suppose that the entrainment rate may be written in the general form:

$$\mu = \begin{cases} F_o+F_1(|w|,dS)+F_2(w\frac{\partial w}{\partial z},dS) & \text{for } w\frac{\partial w}{\partial z}\geq 0 \\ F_o+F_1(|w|,dS)-F_2(w\frac{\partial w}{\partial z},dS) & \text{for } w\frac{\partial w}{\partial z}<0 \end{cases} \qquad (3)$$

By use of dimensional analysis and Pi-theorem we derive finally the entrainment rate in the form:

$$\mu = \begin{cases} a+b|w|dS^{-1/2}+c(|w\partial w/\partial z|/dS)^{1/2} & \text{for } w\partial w/\partial z \geq 0 \\ a+b|w|dS^{-1/2}-c(|w\partial w/\partial z|/dS)^{1/2} & \text{for } w\partial w/\partial z < 0. \end{cases} \qquad (4)$$

where a, b and c are constants defined in the calibration procedure. The whole time, we choose that a=0. The second term is always positive due to the fact that the turbulent mixing processes are independent of vertical velocity sign. The third term may be positive or negative in some regions of the cloud. When the updraft is dominant the mechanism of compensating entrainment will be occurred when the vertical velocity gradient is positive and the

detrainment when it is negative (e.g. in the upper part of the cloud). Further, in the downward motion zone the vertical velocity advection term may be also negative and causes the air detrainment.

3. THE SENSITIVITY EXPERIMENTS

The rawin-sonde data of 30th of June, 1980 (Ćurić, 1982) is used for sensitivity experiments. The other initial and boundary conditions, time and grid steps and numerical techniques are the same as in the work of Ćurić and Janc (1987). For time interval Δt=60 min the observed cloud top heights very in the interval 56-67 dBZ. In Tables 1-5 are time variations of the model maxima values of radar reflectivity, vertical velocity, liquid and ice water mixing ratios and temperature excess. The model top height vary in the interval 11.8-12.2 km and approximatively coincide with time-averaged value of the measured heights.

t(min) / μ(s^{-1})	0	5	10	20	30	40	50	60
μ_1	6.0	11.1	9.2	9.8	9.5	8.5	8.0	7.3
μ_2	6.0	13.8	9.5	9.5	9.2	9.0	8.9	8.8
μ_3	6.0	17,5	19.3	20.6	14.6	12.7	11.4	13.9
μ_4	6.0	15.1	10.9	8.3	8.2	8.7	9.1	9.3
μ_5	6.0	15.0	12.8	8.4	7.9	9.1	9.1	9.4
μ_6	6.0	13.4	7.9	6.4	8.7	8.0	8.1	7.9
μ_7	6.0	13.3	8.1	5.7	7.8	7.0	7.9	7.9

Table 1. The maxima values of vertical velocity (m/s) as function of time for entrainment rates: μ_1-coefficient used by Wisner et al. (1972); μ_2= 0.2/R; μ_3 from equ.(4), b=0.5, c=5; μ_4-μ_7 same as μ_3 but for values (0; 10), (0.5; 10), (0.5; 15), (0.5; 25) respectively

For Wisner's entrainment rate (μ_1) and μ_2 (μ_2=0.2/r) the vertical velocity maximum showstime change in the intervals 7.3-11.1 m/s and 8.8-13.8 m/s respectively (Tab.1). The maximum radar reflectivity also shows time changes and decreases but its value is underestimated with comparison to observed value, (Tab.2) The liquid water mixing ratio maxima values are relatively small (Tab.4). Temperature excesses vary in the interval 4.4-5.8 ^{o}C (Tab.5).

t(min) / μ(s^{-1})	0	5	10	20	30	40	50	60
μ_1	0	50.8	50.3	43.3	37.4	15.0	45.8	42.9
μ_2	0	51.6	52.1	43.3	15.5	36.2	40.0	24.3
μ_3	0	52.7	54.7	56.4	41.9	37.3	27.3	41.1
μ_4	0	52.6	55.5	57.2	57.9	54.9	30.7	53.3
μ_5	0	52.4	55.8	69.6	58.6	35.2	27.7	54.8
μ_6	0	52.7	55.1	32.5	32.5	60.2	61.4	62.2
μ_7	0	52.4	55.2	43.4	36.1	68.6	60.5	59.2

Table 2. Same as 1 but for reflectivity (dBZ)

For entrainment rate (4) the maximum vertical velocity is mainly greater than for previous ones except for cases μ_6(b=0, c=15) and μ_7(b=0.5, c=15). The maximum radar reflectivity factors are better coincided with observed values (Tab.2). The liquid and ice water

t(min) / μ(s^{-1})	0	5	10	20	30	40	50	60
μ_1	4.6	3.9	3.6	2.8	2.7	2.6	2.3	2.2
μ_2	4.6	4.4	3.8	3.1	3.0	3.0	2.9	2.8
μ_3	4.6	6.0	7.0	6.3	7.2	6.1	4.5	5.4
μ_4	4.6	5.2	6.9	6.4	5.6	4.6	6.0	5.0
μ_5	4.6	5.1	3.3	6.5	6.1	4.5	4.9	4.8
μ_6	4.6	4.8	4.0	5.1	5.0	5.0	5.0	5.1
μ_7	4.6	4.8	4.4	5.0	5.1	4.9	5.1	5.2

Table 3. Same as 1 but for liquid water mixing ratio (g/kg)

mixing ratios are mainly greater than for cases of μ_1 and μ_2, (Tables 3 and

4), but temperature excesses are somewhat lower except for case μ_3(b=0, c=5), (Tab.5).

t(min) μ(s-1)	0	5	10	20	30	40	50	60
μ_1	0	0.1	0.1	0.5	0.5	0.008	0.002	0.001
μ_2	0	0.1	0.1	0.4	0.1	0.05	0.04	0.03
μ_3	0	0.01	0.2	1.0	10.1	4.3	5.4	3.5
μ_4	0	0.1	0.2	1.2	2.0	1.9	2.0	2.1
μ_5	0	0.1	0.2	1.6	2.0	o.8	2.0	2.1
μ_6	0	0	0.1	0.2	0.8	1.5	1.5	1.6
μ_7	0	0.1	0.2	0.5	1.0	1.4	1.5	1.6

Table 4. The same as 1 but for ice mixing ratio (g/kg)

When the value of c decreases the vertical velocity advection term causes greater maxima values of vertical velocities, liquid and ice water mixing ratios and temperature excesses or quasi-adiabatic case. By increase of the value of the constant c, the entrainment becomes overrated for values c>15. As can be seen, the model outputs are very sensitive for variations of constant c.

t(min) μ(s-1)	0	5	10	20	30	40	50	60
μ_1	0	5.7	4.9	4.9	4.7	4.7	4.5	4.4
μ_2	0	5.8	4.8	4.8	4.7	4.6	4.5	4.4
μ_3	0	6.8	6.4	6.5	4.4	4.2	4.2	4.4
μ_4	0	5.9	4.6	3.6	3.8	3.7	3.8	3.9
μ_5	0	6.0	4.7	3.7	3.7	3.7	3.8	4.0
μ_6	0	5.2	3.9	3.3	3.4	3.6	3.6	3.6
μ_7	0	5.3	4.0	3.2	3.5	3.5	3.6	3.6

Table 5. The same as 1 but for temperature excess (°C).

For values of constant b (b<0.5) the maximum values are mainly less sensitive than for the variation of constant c except for the maximum radar reflectivity. For greater values of b and especially for b>1.0 the entrainment is overrated for all combinations of c.

REFERENCES:

Battan,L.J., 1982: The variable nature of thunderstorm updrafts and precipitation.In: E.M.Agee and T.Asai(Eds.), Cloud Dynamics, Reidel,Dordrecht,pp 233-242.

Ćurić.M., 1980: Dynamics of a cold air outflow from the base of the thunderstorm. A simple model.J.Rech.Atmos., 14, 493-498.

Ćurić,M., and D.Janc, 1987: On the influence of entrainment and forced lifting on some products of a 1-D model of a Cb cloud. Atmos.Rech.,21, 151-169.

Lin,Yl.,Farley,R.D. and H.D.Orville, 1983: Bulk parameterization of the snow field in a cloud model.J.Climate Appl.Meteorol., 22, 1065-1092.

Orville,H.D., Kopp,F.J., and C.G.Myers, 1975: The dynamics and thermodynamics of precipitation loading. Pure Appl. Geophys.,113, 983-1004.

Randal, D.A., and G.J.Huffman, 1982: Entrainment and detrainment in a simple cumulus cloud model. J.Atmos. Sci., 39, 2793-2806.

Wisner,C., Orville,H.D., and C.G.Myers, 1972: A numerical model of a hail-bearing cloud. J.Atmos.Sci., 29, 1160-1181.

ON THE ENTRAINMENT IN CUMULI - A CONTRIBUTION TO A CASE STUDY

Ivana Nemešová

Institute of the Physics of the Atmosphere, CAS, Prague

1. INTRODUCTION

The paper deals with a complementary analysis of mixing and entrainment to the case published by Drs C.Pontikis and A.Rigaud (PONTIKIS ET AL 1987,in press) who made available the data collected during the ENCC Experiment, France. Two types of analysis were used, the Paluch analysis (PALUCH 1979,p.2467) and the saturation point analysis (BETTS 1982,p.2182),both of them making use of conserved parameters and a mixing line structure.

2. A CASE STUDY

2.1 GENERAL FEATURES OF OBSERVATIONS

On 9.9.1983, a group of small cumuli with flat bases at the level of 1.1 km and of the depth of 1.2 km was sampled; during the afternoon a large nonprecipitating cumulus developed, the top of which kept remaining at the level of 3.2 km during the sampling time between 15.45-16.45 GMT.The measurement inside the clouds were made by an instrumented EERM Piper-Aztec aircraft.In-cloud temperature T_c was measured by the Rosemount probe, the LWC (liquid water content) was measured by both,the Johnson-Williams hot-wire device and the FSSP spectrometer. The Johnson-Williams values of the LWC were used in all our thermodynamic analyses.Fig.1 shows the clear air sounding for the day together with the scheme of the flight procedure in the sampled clouds. The main characteristics of the group of cumuli and the isolated cumulus are given in Table 1.

	cumuli	isolated cumulus
cloud base - CB /km/	1.1	1.0
cloud top - CT /km/	2.3	3.2
CB clear air temperature /°C/	10.6	11.2
CT clear air temperature /°C/	3.0	-0.5
mean horizontal dimension /km/	1.5	3.0
estimated updraft dimension /km/	0.5	0.9

Table 1

The mean CB conditions of the isolated cumulus were determined by the aircraft: p=890 hPa,T_c = 11.6°C, Q_T(total water mixing ratio)= 9.5 g/kg. The measurement in the CB of the cumuli were not available; an estimation was made:p= 890 hPa,T_c = T_E+ 0.4, where T_E is the environmental temperature, Q_T corresponds to the saturation at the temperature T_c.In Fig.2, the values of the ratio LWC/LWCA (LWCA is the adiabatic LWC) are shown together with Warner's data. Typical data

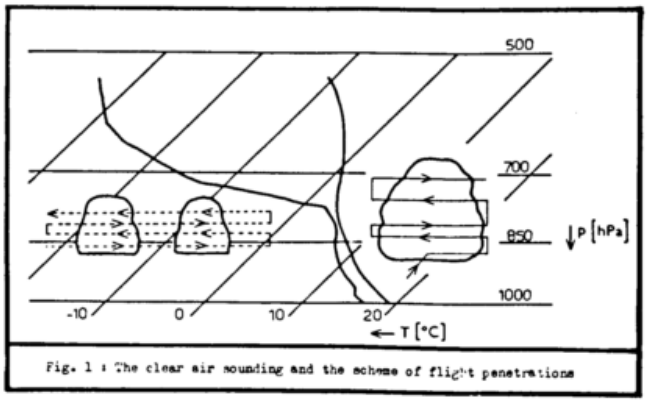


Fig. 1 : The clear air sounding and the scheme of flight penetrations

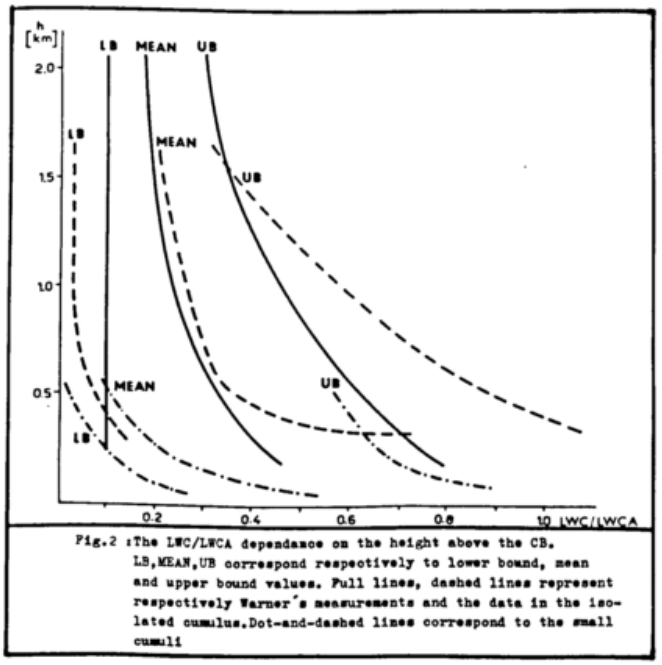


Fig.2 :The LWC/LWCA dependance on the height above the CB. LB,MEAN,UB correspond respectively to lower bound, mean and upper bound values. Full lines, dashed lines represent respectively Warner's measurements and the data in the isolated cumulus.Dot-and-dashed lines correspond to the small cumuli

collected in the isolated cumulus allow to discern three main regions: the updraft and downdraft regions and the transition region in between. The observed spectra in the transition region are mostly bimodal while in the small cumuli only monomodal spectra are found.

2.2 THERMODYNAMIC ANALYSES

Two types of thermodynamic analysis were used to make conclusions about the mechanism of entrainment in the case under study. Both of them make use of conserved parameters under the assumption that there are only two "source" regions of air with distinct properties taking part in the mixing.

a) Paluch analysis

Paluch diagrams, the plot of wet equivalent temperature Θ_q and Q_T, for the isolated cumulus clearly support the cloud top entrainment hypothesis; in the top regions mixing between cloud tower air and clear air environment leads to evaporative cooling and penetrative downdrafts. The entrained air levels were determined in the layer 3.2-3.6 km. We tried to make use of Paluch analysis to determine the entrained air levels for the small cumuli. The diagrams seemed to support the lateral entrainment hypothesis. We used our modified method (NEMESOVA 1985, p.300) for the estimation of entrained air levels. The method is applied under the condition that a density equilibrium temperature is attained in mixed cloud regions. The results are shown in Fig.3. The height levels are normalized so that hn >1 for levels above a CT and hn < 0 for levels below a CB. hn_c means a level inside a vertical extent of a cloud. In this system the lateral entrainment is represented by the straight line hn= hn_c. We can see some interesting features in Fig.3. Up to the level of the last penetration hn_c=0.6 (1.8 km) the curves lie very near the lateral entrainment line, for both the mean values of LWC and the lower bound of the LWC. The curve (UB) for the observed maxima of LWCs and of T_cs lies nearly horizontally: the entrained air origin can be placed below the CB. From Fig.3 we may conclude that up to the highest penetration level the lateral entrainment prevails.

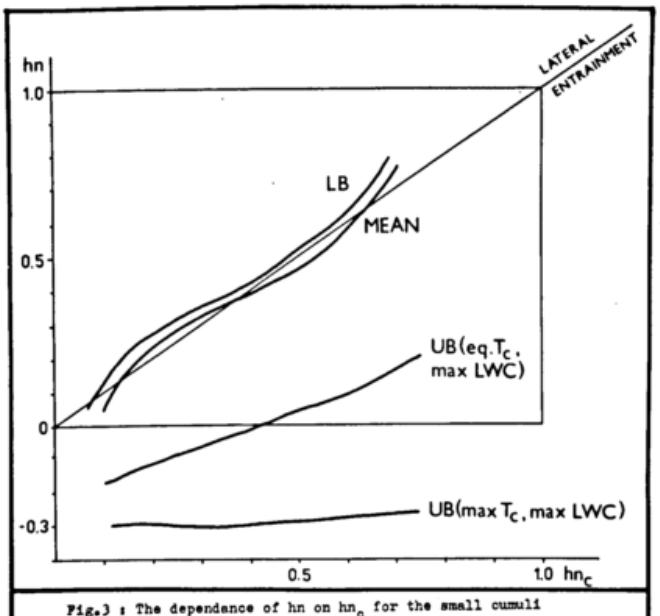


Fig.3 : The dependance of hn on hn_c for the small cumuli

b) Saturation point analysis

The saturation point (SP) coordinate system was introduced to represent the properties of clear and cloudy air in terms of conserved variables. On a thermodynamic diagram all the possible mixtures lie on the mixing line connecting the SPs of both the regions involved in mixing. Since the CTs and CBs are known for our sounding, we make the analysis of the mixing possibilities for both the studied cases. For the time being, we ignore the sampled in-cloud data. The diagram analysis was transferred into a numerical one, which is used for a classification of the thermodynamic structure of different convective regimes. The output of the procedures concerning the CT mixing are the following:

i) Parameter σ_D, expressing the mutual positions of the lines involved in mixing, the value of which move in the range 0 - 1; σ_D = 0 corresponds to the descent to the CB, σ_D = 1 corresponds to a no descent case.

ii) The possible lowest downdraft equilibrium level h_D.

iii) The minimum temperature resulting from cloud -clear air evaporative mixing at the CT.

	σ_D	h_D /m/	T_{cmin} /°C/	F
cumuli	0.69	1800	2.8	0.9
isolated cumulus	0.01	970	-3.0	0.7

Table 2

iv)Fraction F of the cloudy air in the mixture with the CT clear air.

The results are summarized in Table 2.

The computed values show that evaporative downdrafts are highly probable in the isolated cumulus; in an extreme case, they can even reach the CB level. This fact agrees well with the existence of a downdraft region in the lowest penetration level.On the contrary, conditions for a downdraft in the small cumuli are not very favourable. The lowest possible downdraft can theoretically reach only the level of 1.8km which is well above the highest penetration level in the sampled clouds. This fact also seems to evidence the lateral entrainment as a dominant mixing mechanism in these cumuli.

When we used the mixing line analysis for the in-cloud data we found that there were in principle two mixing lines, one representing the mixing in the small cumuli and the other for the CT mixing in the isolated cumulus.The situation is illustrated by the plot in Fig.4. The plot resembles a vertical θ_E sounding. The sounding is close to the mixing line structure for the small cumuli up to θ_S minimum.In-cloud values of θ_{ES} and Q_T for the small cumuli mostly lie to the left of the θ_E profile, but very close. On the contrary, the in-cloud data for the isolated cumulus are found on the right side of the θ_E profile and represent not only the actual mixing line for the cumulus but also a possible new mixing line; generally, both the clouds and the environment are adjusting toward a similar mixing line as is the case which was established for the small cumuli.

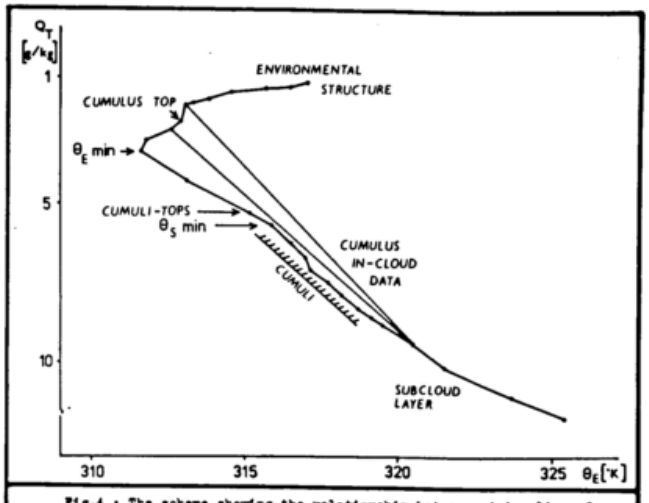


Fig.4 : The scheme showing the relationship between mixing lines for cloud environment and in-cloud data

3. CONCLUSIONS

Our thermodynamic analyses suggest that both, the lateral and cloud top entrainment are important processes, however, in principle they represent extremes.On the basis of the discussion of the mixing lines in the case under study one may speculate that both the types of entrainment probably act simultaneously: for the small cumuli the CT entrainment is likely to exist in the top part of clouds where the penetration data are not available, and a lateral entrainment may have some influence in the lower half of the isolated cumulus. Contributions by which both types of entrainment influence a general dilution of different clouds probably vary according to environmental characteristics which control main cloud features.

REFERENCES

BETTS A.K.: Cloud Thermodynamic Models in Saturation Point Coordinates. J.Atm.Sci.39 (1982), p.2182

BETTS A.K.: Mixing Line Analysis of Clouds and Cloudy Boundary Layers. J.Atm.Sci. 42 (1985), p.2751

NEMESOVA I.:On the Entrainment in Nonprecipitating Cumuli. Studia Geoph.et Geod. 29 (1985), p.300

PALUCH I.:The Entrainment Mechanism in Colorado Cumuli. J.Atm.Sci. 36 (1979), p.2467

PONTIKIS C., RIGAUD A., HICKS E.: Entrainment and Mixing as Related to the Microphysical Properties of a Shallow Warm Cumulus Clouds. Submitted to J.Atm.Sci. 44 (1987)

A FINE RESOLUTION, TWO-DIMENSIONAL NUMERICAL STUDY OF A CLOUD-CAPPED BOUNDARY LAYER

M.K. MacVean and S. Nicholls

Meteorological Office, Bracknell, England

1. INTRODUCTION AND BACKGROUND

Extensive sheets of stratocumulus cloud at the top of the boundary layer are frequently observed in numerous areas of the world, particularly over the sea. Because of the cloud's effect on the energy balance, it exerts a significant influence on climate, as well as on local weather. However, both forecast and climate models have, in general, been unsatisfactory in their handling of such features. In the last few years there have been a number of numerical studies of the cloud-capped boundary layer, using a variety of different models, ranging from one-dimensional, ensemble-averaged models (Duynkerke and Driedonks, 1987) to three-dimensional large-eddy simulations (Moeng, 1986) At the same time, there has been a significant increase in the size of the observational database, with notable contributions from Brost et al (1982a,b) and Nicholls and Leighton (1986), culminating in the recent FIRE experiment off the coast of California.

Most large-eddy simulations that have been carried out to date have had relatively coarse vertical resolution ($25m$ or more). This is too coarse to model accurately the processes occurring in the region of the capping inversion and such models are then subject to serious finite-difference errors. Because of the computational resources required, the use of finer resolution limits consideration to a two-dimensional domain, if a significant region of parameter space is to be explored. Although, in reality, the motions would be three-dimensional, previous work has shown that study of the two-dimensional problem provides useful information, provided that the turbulence is basically buoyancy- rather than shear-driven. In this paper we present preliminary results from a simulation carried out using a two-dimensional model with fine resolution. The turbulent energy budget is compared with the results of an observational study using aircraft, carried out over the North Sea in 1982-3.

2. MODEL DETAILS AND DEVELOPMENT

The current model was developed from that described by Mason (1985) and includes a reasonably accurate calculation of condensation, together with an idealized representation of long-wave cooling due to liquid water. Short-wave radiative effects are neglected. A domain $10km$ long and $4km$ high is used, with periodic lateral boundary conditions. The horizontal grid spacing is uniform ($\sim 80m$), while a smoothly varying vertical mesh spacing is employed, with $9m$ resolution over a range of heights spanning the expected inversion height. Suitable "balanced" initial conditions for the two-dimensional model, containing a cloud layer, were obtained by first integrating a 1-D version of the model from an initial state in which the relative humidity was 90% up to $1100m$. The surface was maintained at saturation, while the relative humidity above $1150m$ was 20%. The initial potential temperature varied piecewise linearly between $280.15K$ at the surface, $281.2K$ at $1100m$, $291.4K$ at $1150m$, $297.3K$ at $1550m$ and $311.6K$ at $4000m$. A surface heat flux of $12.6Wm^{-2}$ was imposed, together with a net long-wave cooling from cloud (when present) of $64.4Wm^{-2}$. The basic geostrophic wind was $9ms^{-1}$. The model parameters and initial data were chosen to be relevant to the situation in which the observational data were obtained. The profiles obtained from the 1-D model were smoothed, to remove discontinuities in gradient, before use in the 2-D model. A white-noise velocity perturbation was used to initiate the eddies.

The region of large static stability at the inversion acts as an almost-rigid lid. Energetic updraughts impinging on it thus lead to intense local sharpening of the curvature of the temperature and humidity profiles, to the point where these profiles exhibit discontinuous vertical gradients at the inversion. This tendency appears to be present, however smooth the initial mean profiles and whatever vertical resolution is used. It is well documented how badly centred differences in advection terms cope with such discontinuities. The errors take the form of oscillations about the "correct" local profile, the amplitude of which can be sufficient to reduce the Richardson Number (Ri) in otherwise stable regions to below the critical value locally and thus induce spurious mixing. This renders the changes irreversible and the errors accumulate, with the profiles

above the inversion becoming more and more unrealistic. The corresponding errors immediately below the inversion are not immediately obvious in the profiles, as they occur in a region which, in the mean, is well-mixed anyway; there must, however, be a spurious contribution to the mixing in the boundary layer as well. Examination of other workers' results (e.g. Moeng, 1986, Fig.6; Mason, 1985, Figs.2 and 5) shows such errors to be ubiquitous.

In an attempt to overcome these difficulties, the 3rd-order upwind scheme proposed by Leonard (1979) was implemented, for the advection of scalars in the model. While this scheme reduced the magnitude of the problem, serious errors still occurred. The only way found of avoiding these errors, was to ensure sufficient mixing to counteract the tendency for discontinuities in gradient to form. In stable conditions, the mixing length in our sub-grid parametrization originally decreased to zero at a critical Ri; this was modified to reduce to a minimum value δ. Values of order $1m$ appear necessary to give acceptable mean profiles (Fig.1) - finite difference errors, as described above, are just apparent but are so scattered in space and time that they are of no significance. Although with $\delta = 1m$, typical values of the implied background viscosity are very small compared to the peak viscosity, they occur in conjunction with very large values of the vertical gradients at the inversion. This results in large subgrid-scale contributions to the vertical fluxes in the capping layer. Taking as a crude measure of entrainment, the rate of change of h, the inversion height, it may be seen that the value of δ is of significance for the overall energy budget. The rate of change is about $3.9 \times 10^{-3} ms^{-1}$ with $\delta = 0$ but rises to $4.6 \times 10^{-3} ms^{-1}$, with $\delta = 1m$. On the one hand, the background mixing in the capping layer might be regarded as a physically unrealistic effect, which would be expected to enhance entrainment. On the other hand, however, the effect of the finite-difference errors with $\delta = 0$ is such as to increase the contrast across the capping layer and thus artificially render entrainment more difficult. It is plausible that the optimum choice of δ is a function of grid spacing, becoming smaller as the resolution becomes finer.Thus, it might be possible to retain realistic mean profiles, while decreasing the importance of the background mixing, by going to yet finer vertical resolution (of order $1m$).

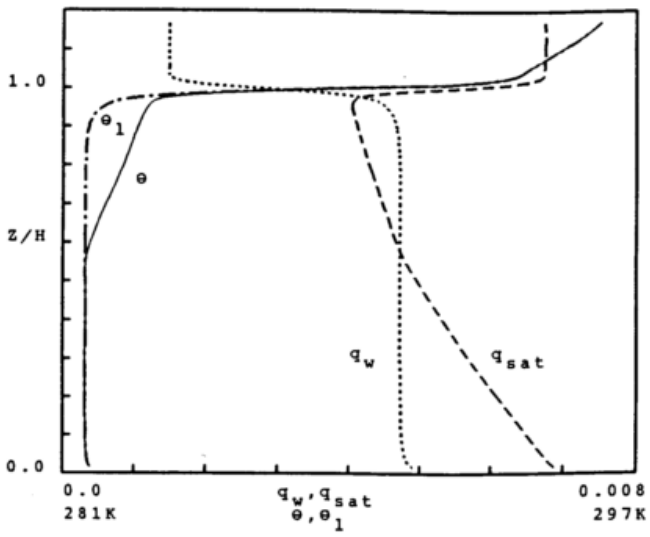


FIG. 1. Mean profiles of potential temperature (θ), liquid water potential temperature (θ_l), total water mixing ratio (q_w) and saturation mixing ratio (q_{sat}).

3. RESULTS

Figure 2 shows the instantaneous fields of vertical velocity and liquid water mixing ratio at the end of the 1 hour period over which the mean profiles shown in Figs. 1 and 3 were averaged. It shows vigorous updraughts with widths of between 1 and $1.5km$, separated by downdraughts of similar scale. All the eddies extend throughout the depth of the boundary layer, with the downdraughts having a more complicated structure, particularly within the cloud. A clear correlation between updraughts and high liquid water content is apparent.

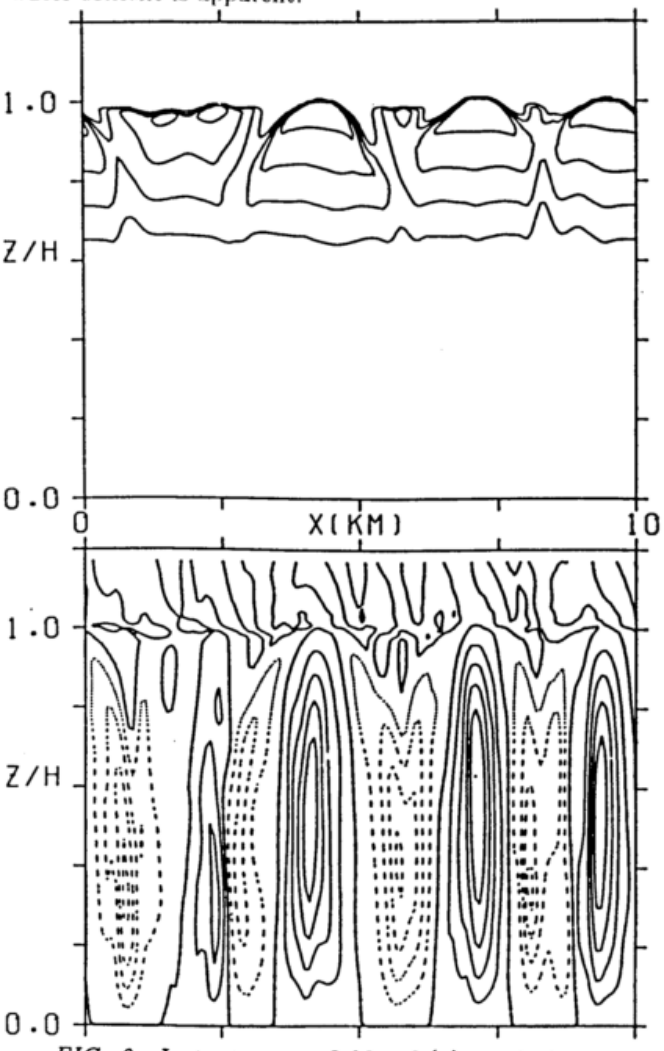


FIG. 2. Instantaneous fields of (a) vertical velocity (contour interval $0.53 ms^{-1}$) and (b) liquid water mixing ratio (contour interval 1.7×10^{-4}).

FIG. 3. Terms in the turbulent kinetic energy budget of the model. The off-scale maximum of *PTR* is 2.97.

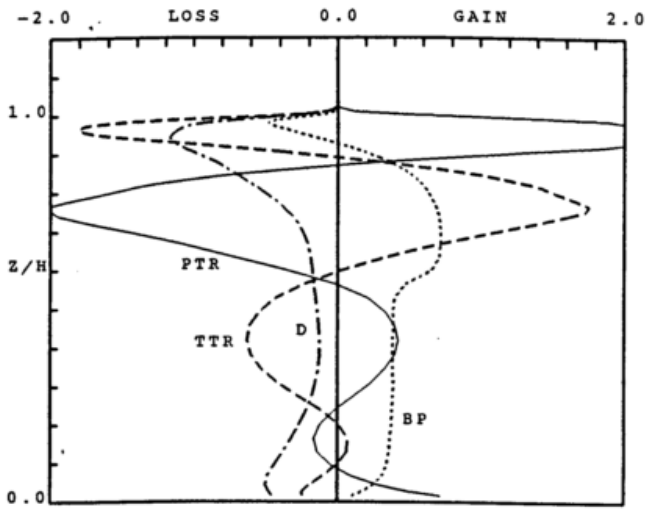


FIG. 4. Terms in the turbulent kinetic energy budget derived from observations.

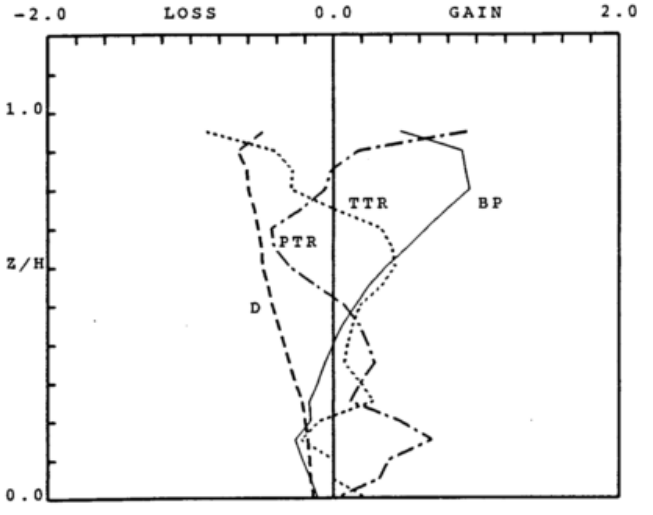


Figure 3 shows various components of the budget for the turbulent kinetic energy (E') in the simulation. All terms have been normalized with 2.5 times the average buoyancy flux over the mixed layer. The statistics calculated from our $10km$ domain over a period of 1 hour are not quantitatively very stable; it is clear that averaging should be performed over a larger number of eddies. Nevertheless, the results presented here should be qualitatively representative. The profile labelled *BP* is the buoyancy production $< w'B' >$; *D* is the dissipation implied by the sub-grid stress terms; *TTR* is the turbulent transport term $-\partial/\partial z < w'E' >$, while *PTR* is the pressure transport term $-\partial/\partial z < w'p' >$. Here the primes indicate deviations from the instantaneous horizontal means and <> indicates a time and space average. The time rate of change and shear production terms (not shown) are negligible away from the surface.

Figure 4 shows corresponding quantities derived from the observations described in Nicholls and Leighton (1986). The definitions of *BP* and *TTR* are as above, while the dissipation was deduced from the energy spectrum on the basis of inertial sub-range theory. No observations were available from which to calculate *PTR*; instead, it was calculated as the residual in the energy budget. The time rate of change and shear production terms were generally found to be negligible.

Comparison of Figs.3 and 4 shows qualitative agreement in the top half of the mixed layer, although the magnitude of the individual terms differs significantly. In both cases there is substantial cancellation between *TTR* and *PTR* - this was not the case in the simulations reported by Moeng (1986). It is also significant that in our simulation, all the terms in the energy budget become negligible immediately above the inversion. In Moeng's work, however, the terms remain large for a significant distance above the inversion, which seems to be indicative of serious finite-difference errors. Finally, it should be noted that although the current simulation reproduces the observed, large, negative values of *TTR* just below the inversion, this is associated, in the model, with the divergence of the vertical transport of the horizontal rather than the vertical component of kinetic energy. In our simulation (and indeed in most others), $< w'^3 >$ is positive in the upper half of the boundary layer, while the observations show negative values. This indicates a serious shortcoming of the model: as can be seen in Fig.2, it fails to produce the intense, narrow downdraughts associated with cloud-top cooling, which are observed in reality. Subsequent work will seek to remedy this defect and investigate the dependence of the entrainment processes at the inversion on the model parameters.

4. REFERENCES

Brost,R.A., D.H.Lenschow and J.C.Wyngaard, 1982: Marine stratocumulus layers. Part I: Mean conditions. *J.Atmos.Sci.*, **39**, 800-817.

Duynkerke,P.G. and A.G.M.Driedonks, 1987: A model for the turbulent structure of the stratocumulus-topped atmospheric boundary layer. *J.Atmos.Sci.*, **44**, 43-64.

Leonard,B.P., 1979: A stable and accurate convective modelling procedure based on quadratic upstream interpolation. *Computer Methods in Applied Mechanics and Engineering*, **19**.

Mason,P.J., 1985: A numerical study of cloud streets in the planetary boundary layer. *Bound.-Layer Meteor.*, **32**, 281-304.

Moeng,C-H., 1986: Large-eddy simulations of a stratus-topped boundary layer. Part 1: Structure and budgets. *J.Atmos.Sci.*, **43**, 2886-2900.

Nicholls,S. and J.Leighton, 1986: An observational study of the structure of stratiform cloud sheets: Part 1. Structure. *Quart.J.Roy.Meteor.Soc.*, **112**, 431-460.

A NUMERICAL METHOD FOR INTEGRATING THE THERMAL CONVECTION EQUATIONS IN THE ATMOSPHERE

Isaac M. Enukashvily

Depart. for Research and Development. Israel Meteorological Service.
P.O. Box 25, Bet - Dagan, Israel.

1. INTRODUCTION

Direct numerical simulation of turbulent flows based on numerical integration of Navier-Stokes equations as well as investigation of the thermal convection equations (TCE) which involve no empirical parameters to describe the highly anisotropic convective eddies and their transport characteristics have received increasing attention in recent years (ORSZAG,1977; HERRING,1963; RAYMOND,1979).
In this study spectral method is developed for direct numerical simulation of thermal convection and convective turbulence.
To obtain a set of orthogonal expansion functions and to satisfy boundary conditions as well as to provide reasonable convergence of the spectral method the analytic solution of the heat diffusion equation is used as a weighting function. The spectral method is tested for a model three dimensional problem of thermal convection with a single perturbation source for temperature. Linearized equations of convective instability (LECI) (CHANDRASEKHAR, 1961) are solved as a Cauchy problem by spectral method with Hermite orthogonal functions as well as by the Fourier integrals method. Preliminary numerical computations by spectral method are performed for TCE including nonlinear terms.

2. SPECTRAL METHOD

TCE in the Boussinsq approximation can be written as (CHANDRASEKHAR, 1961; GUTMAN, 1969)

$$\partial u_\alpha/\partial t=-\partial P/\partial x_\alpha+\nu\Delta u_\alpha+\varepsilon_{\alpha 3}\Lambda\theta-N(u_\alpha) \qquad ,(1)$$

$$\partial\theta/\partial t+Sw=\chi\Delta\theta-N(\theta) \qquad ,(2)$$

$$\Delta P=\Lambda\partial\theta/\partial z+\nu\sigma\Delta w-\sigma\partial w/\partial t-\sum_{\alpha=1}^{3}\partial N(u_\alpha)/\partial x_\alpha \qquad ,(3)$$

where $u_\alpha(u,v,w)$ are the three dimensional velocity components; θ and P are deviations respectively from some constant potential temperature θ_o and from the hydrostatic pressure normalized by density. $N(u_\alpha),N(\theta)$ are nonlinear inertial terms; ν-the kinematic viscosity; χ-the thermal diffusivity; $\Lambda=g/\theta_o$, g-gravity; $\varepsilon_{\alpha 3}$ is the Kronecker delta; $x_\alpha(x,y,z)$-the spatial coordinates; t-time. Δ is the Laplace operator.

$S=\gamma_a-\gamma_o$; γ_a is the dry adiabatic lapse rate; $\gamma_o=-dT_o/dz$; $\sigma=-(1/\rho_o)*(d\rho_o/dz)$; $T_o(z)$ and $\rho_o(z)$ are initial reference values of temperature and of hydrostatic density respectively. At t=0 and z>0 the following initial conditions are adopted:

$$u_\alpha(x,y,z,0)=0;\ \theta(x,y,z,0)=\theta_{oo}\exp(-\beta^2r^2) \qquad ,(4)$$

where $r^2=x^2+y^2+z^2$, and β,θ_{oo} are initial temperature perturbation parameters. The rigid (no slip) boundary conditions at z=0 are imposed on TCE (1) - (3)

$$u_\alpha(x,y,0,t)=0;\ \theta(x,y,0,t)=0 \qquad ,(5)$$

The spectral method for numerical integrating TCE is to seek a solution of the form (COURANT, HILBERT,1951;ORSZAG,1977)

$$\xi=W^{1/2}\sum_{i=0}^{\infty}\sum_{j=0}^{\infty}\sum_{K=0}^{\infty}\phi_{ijk}(t)H_i(x)*H_j(y)H_k(z) \qquad ,(6)$$

where $\xi=u_\alpha,\theta,P$; $\phi_{ijk}(t)$ are Fourier components; $H_i(x),H_j(y),H_k(z)$ are orthogonal polynomials with wieghting function $W(x_\alpha,t)$. When the expansions (6) are used to (1)-(3) we obtain an infinite set of coupled differential equations

for $\emptyset_{ijk}(t)$. Our truncation procedure is to set all $\emptyset_{ijk}(t)$ of indexes greater then a certain integers I,J,K equal to Zero (RITCHTMYER,MORTON,1972; HERRING,1963;ENUKASHVILY,1980). The proper choice of W(x,y,z,t) is very important to the success of spectral method. To obtain $W(x_\alpha,t)$ the heat diffusion equation (eq.(2) with S=0,N(θ)=0,$\chi=\nu$) is solved as an initial value problem with (4)-(5) for θ(SOMMERFELD,1950); so we have:

$$\theta=(\theta_{oo}A^3/\beta^3)\exp(-A^2r^2)*$$

$$*\mathrm{erf}(\xi(z,t)) \qquad ,(7)$$

$$A=\beta/(1+4\beta^2\nu t)^{1/2} ;$$

$$\xi(z,t)=z/(A(4\nu t)^{1/2})$$

Orthogonal polynomials with weighting functions

$W_\alpha=\exp(-A^2x_\alpha^2)$ in the range

$(-\infty\le x_\alpha\le\infty)$ are Hermite polynomials (COURANT,HILBERT,1951). To obtain orthogonal polynomials with weighting function

$$W_3=\exp(-A^2z^2)\mathrm{erf}(\xi(z,t)) \qquad ,(8)$$

in $(0\le z\le\infty)$ the Shmidt's method (MORSE,FESHBACH,1953) may be used. For example setting approximately

$\mathrm{erf}(\xi)\sim(2/\pi^{1/2})\xi$, we obtain

$$W_3(z,t)=Z^{1/2}\exp(-Z) \qquad ,(9)$$

where $Z=A^2z^2$;Orthogonal polynomials with weighting function (9) in $(0\le z\le\infty)$ are the known Laguerre polynomials.
The weighting function (9) and the corresponding orthonogal expansion functions satisfy the boundary conditions (5). Usually to investigate convective instability and transition to turbulent convection (CHANDRASEKHAR ,1961) TCE (1)-(3) are splitted up into LECI (eq. (1)-(3) with σ=0, $N(u_\alpha)=0$,N(θ)=0) and nonlinear terms. The Fourier integrals method may be used to obtain analytic solution of LECI considered as a Cauchy problem with (4). From the other hand for erf(ξ) close to one the analytic solution (7) transforms to solution of the same heat diffusion equation with (4) for θ and (8) transforms to the weighting function for Hermite polynomials. These two factors promted us to test the spectral method developed in this study for numerical integrating LECI considered as a Cauchy problem with (4) and for the range $(-\infty\le x_\alpha\le\infty)$.

3. TEST PROBLEM SOLUTION

Application of the Fourier integrals method (COURANT,HILBERT, 1951) to LECI gives

$$\Phi_i=\eta\int_0^\infty\Omega_i k^2\exp(-\xi k^2)dk \qquad ,(10)$$

$$P=\eta\lambda\int_0^\infty\Omega_5 k\exp(-\xi k^2)dk \qquad ,(11)$$

where $\Phi_i(u,v,w,\theta)$ is four - dimensional vector;

$$\Omega_1=(\lambda/\gamma)(x/R)\int_0^\pi \mathrm{Sh}\mu\,\mathrm{Sin}\psi\,J_1(\epsilon)*$$

$$*\mathrm{Sin}\omega\,\mathrm{Cos}\omega\,d\omega\ ;\ \Omega_2=(y/x)\Omega_1;$$

$$\Omega_3=(\lambda/\gamma)\int_0^\pi \mathrm{Sh}\mu\,\mathrm{Cos}\psi\,J_0(\epsilon)*$$

$$*\mathrm{Sin}^2\omega\,d\omega\ ;$$

$$\Omega_4=\int_0^\pi \mathrm{Ch}\mu\,\mathrm{Cos}\psi\,J_0(\epsilon)\,\mathrm{Sin}\omega\,d\omega\ ;$$

$$\Omega_5=\int_0^\pi \mathrm{Ch}\mu\,\mathrm{Sin}\psi\,J_0(\epsilon)\,\mathrm{Sin}\omega\,\mathrm{Cos}\omega\,d\omega;$$

$\eta=\theta_{oo}/(4\beta^3\pi^{1/2})$; $\xi=\nu t+(1/4\beta^2)$;

$R^2=x^2+y^2$; $\gamma^2=-\lambda S$; $\mu=\gamma t\mathrm{Sin}\omega$;

$\psi=kz\mathrm{Cos}\omega$; $\epsilon=kR\mathrm{Sin}\omega$;

J_0 and J_1 are the Bessel functions of the first kind. Using the spectral method for integrating LECI with the same (4),we take

$$W(x_\alpha,t)=\exp(-A^2r^2) \qquad ,(12)$$

Substituting the expansions (6) with (12) in LECI and using known recurrence formulas for Hermite polynomials we obtain

$$\partial(\emptyset_i)_{lmn}/\partial t=\gamma A^2\{-0.25*$$

$$*[(\emptyset_i)_{l-2,m,n}+(\emptyset_i)_{l,m-2,n}+$$

$$+(\emptyset_i)_{l,m,n-2}]-(l+m+n+4.5)(\emptyset_i)_{lmn}+$$

$$+3(l+1)(l+2)(\emptyset_i)_{l+2,m,n}+3(m+1)*$$

$$*(m+2)(\emptyset_i)_{l,m+2,n}+3(n+1)(n+2)*$$

$$*(\emptyset_i)_{l,m,n+2}\}+G_i+\xi_{i3}\theta_{lmn} \quad ,(13)$$

where again $\emptyset_i(u,v,w,\theta)$ is four dimensional vector;

$$G_1=A[0.5P_{l-1,m,n}-$$

$$-(l+1)P_{l+1,m,n}] \quad ,(14)$$

$$G_2=A[0.5P_{l,m-1,n}-$$

$$-(m+1)P_{l,m+1,n}] \quad ,(15)$$

$$G_3=A[0.5P_{l,m,n-1}-$$

$$-(n+1)p_{l,m,n+1}] \quad ,(16)$$

$$G_4=-Sw_{lmn}(t) \quad ,(17)$$

In (14)-(16) the Fourier components $P_{lmn}(t)$ are expressed by $\theta_{lmn}(t)$ using the Poisson equation (3) with $\sigma=0$ and $N(u_\alpha)=0$. An infinite set of coupled differential equations for $\emptyset_{ijk}(t)$ are derived as well for TCE (1)-(3) including nonlinear terms. Our numerical procedure for integrating the truncated set of equations (13)-(17) is to assign an initial set of Fourier components to $(\emptyset_i)_{lmn}$ corresponding to initial conditions (4) and to allow the system to evolve with time.

4. CONCLUDING REMARKS

4.1 The spectral method is developed for numerical integrating TCE and for direct numerical simulation of thermal convection and convective turbulence.

4.2 A comparison between numerical computations for LECI obtained by the spectral method and by the Fourier integrals method as well shows even for I,J,K=3 a good agreement for θ and U_α.

4.3 Preliminary numerical computations by spectral method are performed for LECI to investigate convective instability of the atmosphere and transition to turbulent convection in terms of thermal convection parameters.

4.4 Preliminary numerical computations by spectral method are performed as well for TCE (1)-(3) including nonlinear inertial terms.

Acknowledgments. The author thanks A.Ianetz,H.Rosenthal and T.Benamram for discussions.

5. REFERENCES

5.1 CHANDRASEKHAR,R.:Hydrodynamic and hydromagnetic stability. Clarendon Press,Oxford,1961.

5.2 COURANT,R.;HILBERT,D.:Methods of mathematical physics.Gosizdat, Moscow,1951.

5.3 ENUKASHVILY,I.M.:A numerical method for integrating the kinetic equation of coalescence and breakup of cloud droplets. J,Atmos.Sci. 37 (1980), 2521-2534.

5.4 GUTMAN,L.N.:Introduction to nonlinear theory of mesometeorological processes. Gidrometizdat, Leningrad,1969.

5.5 HERRING,J,R.:Investigation of problems in thermal convection. J.Atmos.Sci.20(1963) 325-338.

5.6 MORSE,Ph.; FESHBACH,H.:Methods of theoretical physics,part 1,2; Mc.Graw-Hill,1953.

5.7 ORSZAG,S.A.:Numerical simulation of turbulent flows. Handbook of turbulence,vol.1; Edited by W.Frost and T.MOULDEN Plenum press,1977.

5.8 RAYMOND,D.J.:A two-scale model of moist nonprecipitating convection. J.Atmos.Sci. 36 (1979), 816-831.

5.9 RICHTMYER,R.D.; MORTON,K.W.: Difference methods for initial value problems.Mir,Moscow,1972.

5.10 SOMMERFELD,A.:Partial differential equations of physics.Mir,Moscow,1950.

A DIAGNOSTIC STUDY OF VERTICAL FLUXES IN CUMULUS CLOUDS USING MODEL OUTPUT DATA

M.J. Weissbluth and W.R. Cotton

Dept. of Atmospheric Science, Colorado State University, Fort Collins, CO 80523

1 Introduction

Given that a numerical simulation of an event is 'correct', the model data provides an extensive data base from which analysis may be done. This data base is essentially perfect in that there is complete spatial and temporal coverage over the domain. If the simulation is performed within the framework of a cloud model, that is the grid size is small enough to explicitly resolve the convection, then one of the possible uses of these data is to study the nature of convection and its interaction with the environment.

A natural extension of the above study is its application to the cumulus parameterization problem. By averaging over approrpriate portions of the domain and separating variables into mean and peturbation parts, the averaged correlations would precisely represent the quantity which should be parameterized using a courser grid. Since the spatial extent of the averaging operator can be conveniently altered, the correlations could be calculated to represent the sub-grid scale effects on various grid sizes. Furthermore, various mean quantities could be related to the correlations to understand the scale relationships and feedbacks between convection and its forcing.

2 Data base

The numerically simulated data base includes a mid-lattitude supercell, Florida sea-breeze convection and a tropicall squall line. All simulations were performed using the Colorado State University Regional Atmospheric Modeling System (CSU RAMS) which employed the non-hydrostatic, fully compressible, equations with parameterized microphysics (Tripoli and Cotton, 1982). The supercell was observed on 2 August 1982 during the CCOPE experiments (Miller *et. al.*, 1988) and was simulated using a 40 km x 40 km x 21 km domain with a grid resolution of 750 m in all directions. The Florida sea-breeze convection was simulated by using a composite sounding (Tripoli and Cotton, 1980 over the Florida penninsula. The domain was 120 km x 20 km x 20 km, with a grid resolution of 750 m in all directions and used cyclic boundary conditions in the meridional direction. The simulation was therefore three-dimensional concerning the cloud-scale and quasi-three-dimensional concerning the mesoscale. In order to simulate convection and its interaction with the environment as accurately as possible, a dynamic initialization with a moist bubble was not used. Rather, the simulation began at 10:00 EST and allowed the sea-breeze to develop realistically through radiational forcing over the peninsula. Convection first developed along both the east and west sea-breeze fronts as they propagated on-shore as shown in Fig. 2b. Figs. 2c and 2d show the subsequent deep convection as the sea-breeze fronts converge. The tropical squall line (Nicholls and Weissbluth, 1988) was simulated over the ocean.

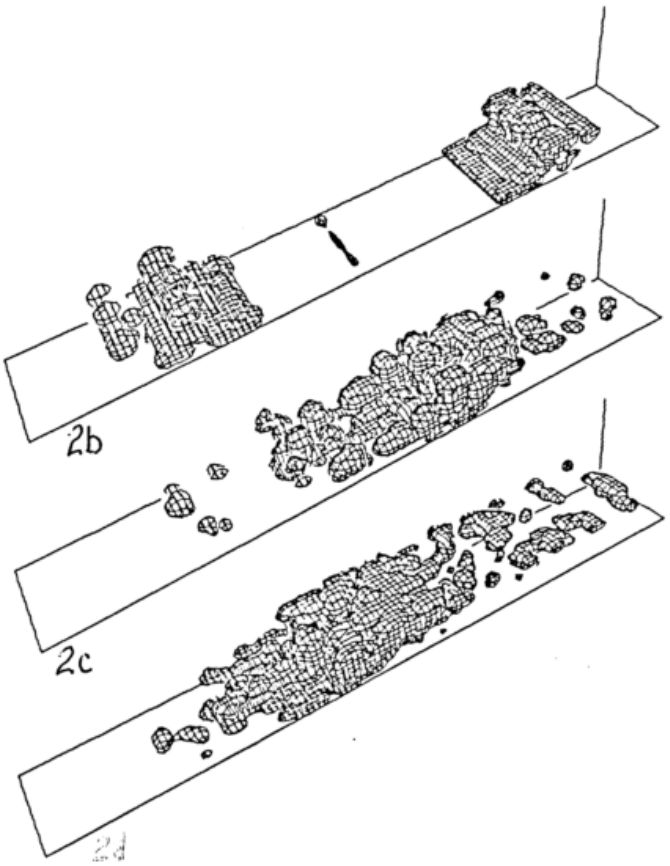


Figure 2b. Representation of the cloud field for the Florida sea-breeze convection at 7800 sec. Contours of liquid water greater than 0.01 g/kg are shown.

Figure 2c. As in Fig. 2b except at 11400 sec.

Figure 2d. As in Fig. 2b except at 14400 sec.

3 Results and discussion

The time evolution of the vertical velocity variance ($\overline{w'w'}$) is especially interesting since it is a measure of the strength of convection. Furthermore, this variance exhibits striking similarities when analyzed for the aforementioned cases which may indicate that all convection is fundamentally similar. Figs. 1a, 2a and 3a show the $\overline{w'w'}$averaged over the model grids for the CCOPE supercell, the Florida sea breeze convection and the tropical squall line, respectively. Fig. 1a exhibits the steadiest system since $\overline{w'w'}$is nearly constant after an hour. The $\overline{w'w'}$field pulses in the upper troposphere with a period of about 20 min. This pulsing is also apparent in the other $\overline{w'w'}$fields, but as of yet it is difficult to say whether or not it is important.

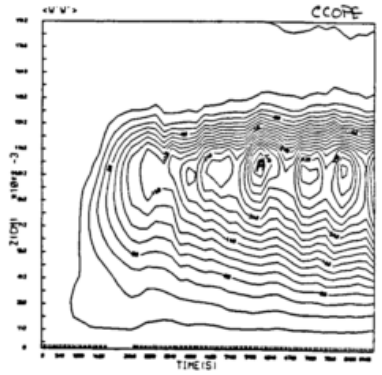


Figure 1a. Time series of $\overline{w'w'}$ for the CCOPE supercell to 9000. sec. Contours range from 0. to 360000 with an interval of 20000. cm^2/s^2.

Fig. 2a displays a relatively complicated field of $\overline{w'w'}$ for sea breeze convection. This reflects the transient nature of the many individual clouds which comprise the overall convection. The $\overline{w'w'}$ centers near 4 and 5 km represent the shallower convection while the centers near 11 km represent deeper convection. The different types of convection are more clearly illustrated in Figs. 2b-2d which show areas of the domain with cloud water greater than 0.1 g/kg. Fig. 2b portrays the convergence along the eastward and westward propagating sea breeze fronts. This is relatively shallow convection and would be represented by the $\overline{w'w'}$ centers in the lower troposphere. Figs. 2c and 2d show the clouds after the sea breeze fronts have converged; deep convection is evident and is represented by $\overline{w'w'}$ centers high in the troposphere.

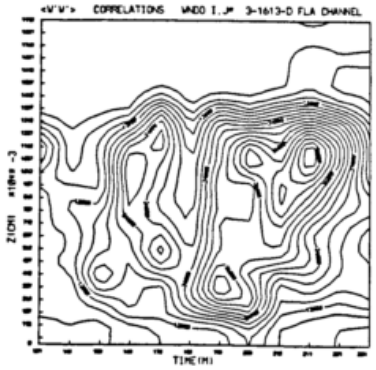


Figure 2a. Time series of $\overline{w'w'}$ for the Florida sea-breeze convection from 130 min to 240 min. Contours range from 0. to 51000 with an interval of 3000. cm^2/s^2.

Fig 3a shows the time evolution of $\overline{w'w'}$ for a tropical squall line. The convection here is centered near 11 km. The system is not long lived and its decay is possibly foreshadowed by the lowering and eventual disappearance of the $\overline{w'w'}$ centers. Also of interest are some of the other covariances. Figs. 3b and 3c show the $\overline{w'r'_t}$ and $\overline{w'\theta'_{il}}$ covariances. The variable θ_{il} is an ice-liquid potential temperature that remains unchanged in the presence of all phase changes (Tripoli and Cotton, 1981). Note the similarity to the $\overline{w'w'}$ curve. The similarity is present in the CCOPE supercell and the Florida sea-breeze simulations as well, and may be taken advantage of in the cumulus parametrization scheme discussed later.

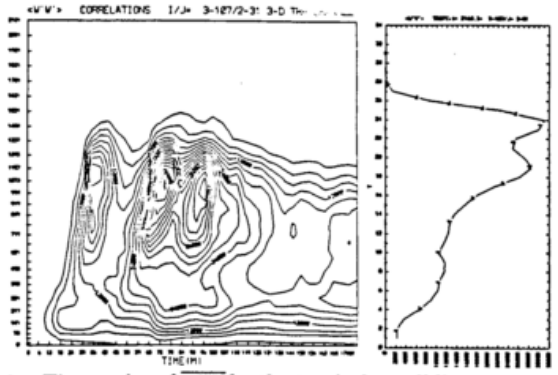


Figure 3a. Time series of $\overline{w'w'}$ for the tropical squall line. to 180 min. Contours range from 0. to 5400. with an interval of 3000 cm^2/s^2. A vertical profile at 36 min is shown to the right.

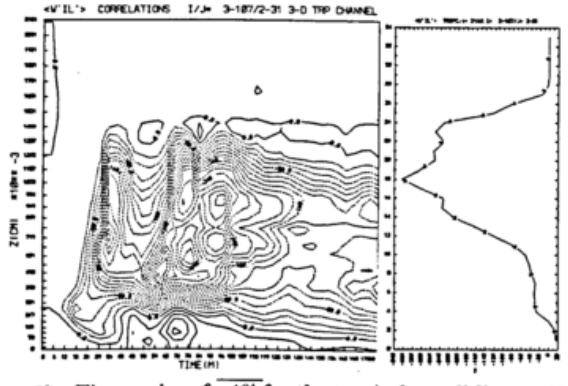


Figure 3b. Time series of $\overline{w'\theta'_{il}}$ for the tropical squall line to 180min. Contours range from -340. to 90. with an interval of 20 K. A vertical profile at 36 min is shown to the right.

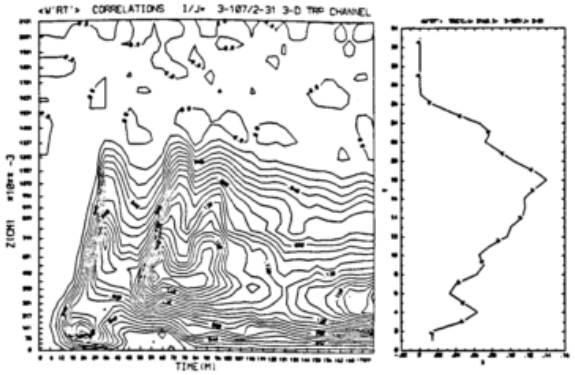


Figure 3c. Time series of $\overline{w'r'_t}$ for the tropical squall line to 180 min. Contours range from 0.00 to 0.21 with an interval of 0.01 cm/s. A vertical profile at 36 min is shown to the right.

A term analysis program has also been formulated to determine the individual terms that force $\overline{w'w'}$. An example is shown in Figs 1b and 1c which show a term analysis of $d\overline{w'w'}/dt$ for the CCOPE supercell on either side of the pulse labelled A in Fig 1a. The total tendency is the solid line labelled MOD or TRM. The three main forcing terms are bouyancy (BOY), pressure gradient (PGF) and advection (ADV). All these terms are an order of magnitude greater than their sum, indicating that a delicate balance exists. At a cursory glance, it appears that the pressure gradient and bouyancy forces might play a role in forcing the observed pulses. When $\overline{w'w'}$ is increasing with time, BOY<PGF and when PGF<BOY, $\overline{w'w'}$ is decreasing with time.

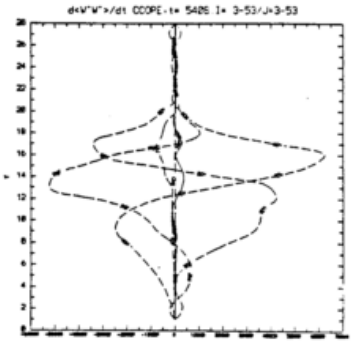


Figure 1b. Term analysis for the CCOPE supercell at 5408 sec. The solid lines indicate the model generated tendency while the dashed lines show conributions of pressure gradient forces (PGF), advection (ADV), bouyancy forces (BOY) and diffusion (DIF) to the tendency.

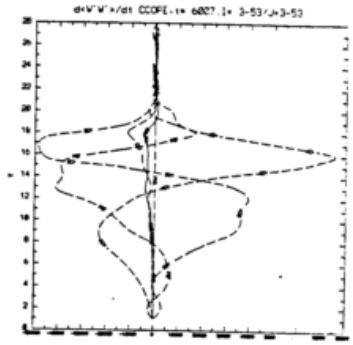


Figure 1c. As in Fig. 1b except at 6007 sec.

4 The cumulus parameterization problem

An immediate application of this approach would be in the cumulus parameterization. Basically formulated, the problem arises when the model variables are separated into mean and perturbation parts. This leads to second order terms in the mean equations which can be interpreted as sub-grid scale effects and must be parameterized. The assumptions used to derive the sub-grid scale effects are termed the closure assumptions. Traditional approaches in mesoscale models have used idealized 1-D cloud models to determine mass (and sometimes momentum) fluxes and distribute them in the vertical. However, this is very scale dependent; as the grid size of the numerical model changes, the relationships between the large-scale variables and the sub-grid scale fluxes also change. This forces limited applicability for many of the presently used schemes. Moreover, for mesoscale systems smaller than the Rossby radius of deformation (as defined in Frank, 1983), convection is not in balance with the larger-scale flow and simple equilibrium approximations (e.g. Arakawa and Schubert, 1977) are not appropriate. Thus the cumulus parameterization problem is not well-posed for such systems.

Use of higher-order closure theory involves forming prognostic equations on the sub-grid scale correlations in order to determine their effects on the large-scale fields. The advantage is the terms are explicitly calculated; the drawbacks are that third-order correlations appear which must be calculated and the number of equations that must be solved increase geometrically. Due to the relative computational inefficiency of higher-order closure theory, its use has been confined to small-scale models or to shallow cumuli.

A hybrid of the two above-mentioned approaches would seem to capture the advantages of each. Prognostic equations consisting of the important forcing terms would be formulated and these terms would then be parameterized. The diagnostic analysis suggests that similarities between the profiles of $\overline{w'w'}$ and vertical eddy fluxes may allow simplifying assumptions that will greatly reduce the number of prognostic variables. The advantages of this approach are maintaining relative simplicity while calculating pseudo-explicitly the sub-grid scale effects of convection.

5 Conclusions

Three different types of convective system were compared and similarities between their analyzed fields were highlighted. The vertical velocity variance seems to be a rather universal measure of convection regardless of the forcing of convection or its environment. Furthermore, vertical mass and moisture covariances appear strongly linked to $\overline{w'w'}$. For these reasons, $\overline{w'w'}$ might be the appropriate variable on which to base a hybrid cumulus parameterization scheme.

Acknowledgements

We would like to thank Brenda Thompson for her help in processing this manuscript. This research was funded by the National Science Foundation under grant ATM-8512480 and NASA under grant NAG5-359. All computations were performed on the National Center for Atmospheric Research (NCAR) Cray X-MP48 computer. NCAR is supported by the National Science Foundation.

References

Arakawa, A. and W.H. Schubert, 1974: Interaction of a cumulus cloud ensemble with the large-scale environment. Part I. *J. Atmos. Sci.*, **31**, 674-701.

Frank, W.M., 1983: The cumulus parameterization problem. *Mon. Wea. Rev.* **111**, 1859-1871.

Miller, M.J., J.D. Tuttle and C.K. Knight, 1988: Airflow and hail growth in a severe northern High Plains suoercell. Accepted for publication in *J. Atmos. Sci.*

Nicholls, M.E. and M.J. Weissbluth, 1988: A Comparison of two-dimensional and Quasi-three-dimensional simulations of a tropical sqaull line. Conditionally accepted for publication in *J. Atmos. Sci.*

Tripoli, G.J., and W.R. Cotton, 1980: A numerical investigation of several factors leading to the observed variable intensity of deep convection over South Florida. *J. Appl. Meteor.*, **19**, 1037-1063.

Tripoli, G.J., and W.R. Cotton, 1981: The use of ice-liquid water potential temperature as a thermodynamic variable in deep atmospheric models. *Mon. Wea. Rev.*, **109**, 1094-1102.

Tripoli, G.J., and W.R. Cotton, 1982: The Colorado State University three-dimensional cloud/mesoscale model - 1982. Part I: General theoretical framework and sensitivity experiments. *J. de Rech. Atmos.*, **16**, 185-220.

EFFICIENCY OF DEEP CONVECTIVE CLOUDS RELATED WITH SOME PARAMETERS OF OCCURENCE OVER THE ARGENTINE TERRITORY

María Elena Saluzzi

Meteorological Department
U.B.A. - C.O.N.I.C.E.T. - Bs. As.
Argentina

1. INTRODUCTION

On account of the diverse geographic situations and the latitudinal extension, the comparative study of the high convective clouds is possible in Argentina.

However, this studies result a function of available resources and means, that could be applied for make them.

A relatively significative number of thunderstorms that ocurred in diverse zones, had been collected and well studied.

The occurrence region of convective storms in the country, is between the northen extreme (Tropic of Capricorn latitud) to the bounding zone of 40°S and from lee of the Andes to the humid Pampa next to Atlantic Ocean and the biggest rivers in the litoral.

The studies thunderstorms comprise diverses stages inner this big region (more or less 2.000.000 km²) some located in orographic zones (lee of the Andes and the Córdoba's sierrs) but not to the north of 28°N paralel. For this reason the convective actitity in the extreme north zone is not illustrated, (there are not adecuated observation means).

2. THE CONSIDERED THUNDERSTORMS AND THEIR OCCURRENCE REGIONS.

Ten thunderstorms ocurred in the Mendoza's north region, direct to lee of the Andes, with good knowledge of solid and liquid precipitation, plus one Córdoba's thunderstorm with hail that corresponds to thunderstorms with orographic influence, are studied. Also in this category can be considered the Neuquén's hailstorm, although this zone is more distance of Andes which in this latitude are not so much high.

This gathering put on relevance the importance that the geographies characteristics of occurrence region have for the thunderstorms. In fact, all the mentioned storms are hailstorms that occur lee of mountains.

The other studied storms are storms of flatness; they occur over the semiarid pampa (La Pampa province) or over the humid pampa (Buenos Aires province and city).

These thunderstorms are of predominant liquid precipitation. Although the Buenos Aires thunderstorms give hail when they cross the sieras in the middle of the provincee, this thunderstorm was of liquid precipitation over all the province.

In general, the convective clouds are of short life and tracks. The common track is of the order of 50km since its detection, until the thunderstorm reaches its maturity, precipitates and decays.

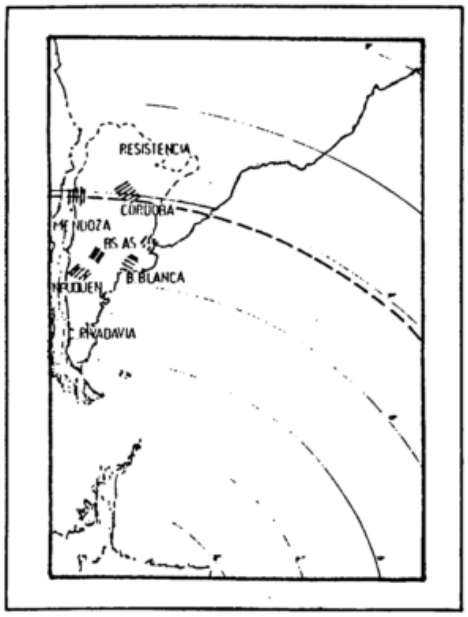


Fig. 1: Occurrence regions of the thunderstorms

The thunderstorms, if persist, can generate new active clouds. This is notable and persistent in the thunderstorms of Bahía Blanca-Ezeiza that go over plus 500 km, in the Bs. As. province. The clouds are in continous renovation and go to the sea as the same time as they grow.

The total group of thunderstorms comprise many years (1985 to1986) and, with one exception they are all summer thunderstorms. The exception is the May's thunderstorms that gave liquid precipitation until Bs. As. city.

3. THE HAILSTORMS

3.1 The Mendoza's thunderstorms

This are a group of ten thunderstorms between the years 76 to 78, all hailstorms with different intensity of precipitation.

The behaviour of the analized convective cloud and different parameters, procuring characterize each big storm, is abriged in Table Number I.

This analysis is carried out comparing the data obtained from surface observation and the soundings corresponding with the thunderstorms hour and the data of solid and liquid precipitation.

The solid precipitation data proceed from hail-pad network installed over the region and the liquid precipitation data from pluvio-

Date	T_{BC} (°C)	TABLE I			
		$\frac{\Delta T}{\Delta H}$ (500-300)mb °C/mgb	Energy J/kg	Precipitation . (mm)	D max (cm)
11-30-76	14.9	-0.72	2257	23.7	0.35 E01
12-14-77	13.6	-0.71	2598	34.8	0.32 E01
02-25-78	12.7	-0.70	2714	33.4	0.29 E01
01-18-77	11.5	-0.68	630	14.1	0.27 E01
02-10-78	12.0	-0.81	2146	0.0	0.20 E01
12-06-76	11.3	-0.69	1795	35.5	0.20 E01
12-22-76	11.5	-0.74	1535	32.7	0.16 E01
01-23=78	7.9	-0.60	485	0.0	0.16 E01
01-21-78	6.9	-0.58	1424	3.4	0.14 E01
12-30-77	6.8	-0.67	----	----	--------

metric stations of S.M.N.(National Meteorological Service).
The order is function of maximum diameter of hail and the results are in good correlation with the temperature of cloud base.

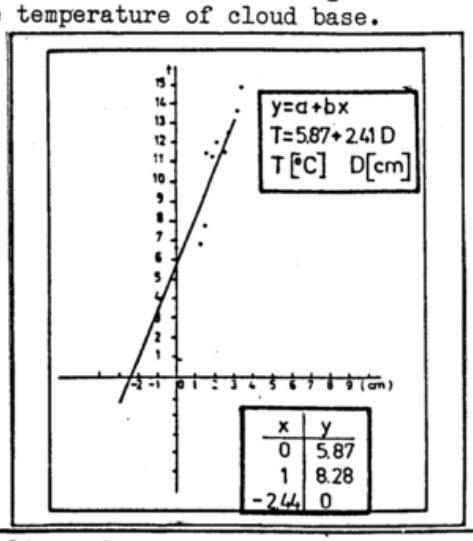


Fig. 2: Line of regretion for Mendoza's hailstorm

The correlation coefficient between these two parameters, $r^2=0.78$ says that, in spite of the little sample, there is a good correspondence. The relation is the biggest diameter tense, highest temperature of cloud base. This must have a climatological limit, for the maximum and the minimum of the parameters. The others showed parameters and also another investigated have no significative correlation and suggested that are grouped from thresholds values that all exceed, in the sample (Fig.2).

3.2 CORDOBA AND NEUQUEN'S HAILSTORMS
The other hailstorms were in Neuquén and Córdoba provinces. Their parameters are shown in Table II.
If we apply the line of regretion that resulted for the Mendoza's hailstorms, we can say "a priori", the hail diameter. This can be done when we know the cloud base temperature (calculated by the cloud model). If for this thunderstorms the correlation would be valid also.
Result for Córdoba D=3.46 = 3.5 cm
and for Neuquén D=1.9 =2 cm
In the recolected sample the diameters were 4.2 and 3.8 cm in each one. A discrete discrepancy in both thunderstorms that don't invalide the supposition made is observed.

4. THE THUNDERSTORMS OF LIQUID PRECIPITATION
The liquid precipitation thunderstorms were produced over La Pampa province (semiarid pampa) and over Bs. As. province (in this thunderstorm was also registered some hail).

4.1 LA Pampa's thunderstorms
The La Pampa's thunderstorms are grouped in Table III. Here the order is provided for the intensity of the liquid precipitation and is noted that the base cloud temperature (calculated for the model) is also decreasing. This anticipates very strong correlation. In fact it was $r^2=0.99$ even though the considered thunderstorms are only four. The line of regretion allows to anticipate that the threshold of base cloud temperature for rain is 5.1°C for the region under consideration.

TABLE III. HAILSTORM OF CORDOBA AND NEUQUEN

Date and Place	T surf °C	T BC °C	Level of BC (mgp)	$\bar{H}$ and $\bar{T}$ sub-cloud % °C	T/ H °C mgp 500-300mb	Precipitation . (mm)	D max (cm)
Córdoba 11-07-81	21.6	14.2	2300	80 18.3	-0.73	6115	4.2
Neuquén 02-15-87	19.6	10.4	3490	42 18.0	-0.81	15.2	2.8

TABLE III. LA PAMPA'S THUNDERSTORM

Date and Place	T (°C) CR	$\Delta\underline{T}$ 500 to 300 mb ΔH °C/mgp	Level CB (mgp)	$\bar{H}$ and $\bar{T}$ (%°C) sub-cloud 'layer		Precipitation . mm
02-26-76	13.6	-0.67	1370	72	19.6	78.3
02-23-75	13.3	-0.69	1650	100	13.8	75.0
02-01-76	9.1	-0.74	2430	52	18.1	42.0
11-27-75	7.1	-0.70	1750	70	15.3	15.2
BUENOS AIRES' THUNDERSTORM						
Ezeiza	7.7	-0.77	2220	62	21.7	16.3
11-26-86	0.5	-0.70	2670	32	10.7	0.3

4.2 THE BIGGEST THUNDERSTORMS OF PROVINCE OF BUENOS AIRES

Some differents features distinguish this thunderstorms from other thunderstorms analyzed . In first attention its macro-behaviour: it is a complex thunderstorm that thranslates from SO to NE, running over the Bs. As. province, from B.Blanca, plus 500 km. It doesn't show any convective cloud only some that mature, go to the adjacent ocean and simultaneously generate new clouds in the left side of the old cloud, in direction of advance.

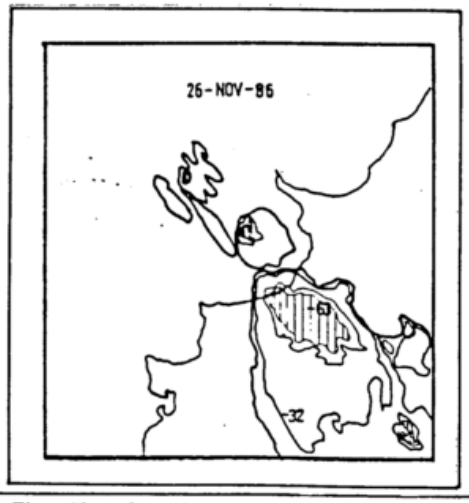


Fig.3: The thunderstorms over Bs.As. province

One of these big clouds gave hail when it crossed over La Ventana and Tandilia's sierras. The satellite photo anticipates the solid precipitation possibility. However it was a liquid precipitation thunderstorm, over all the way, and reached the city of Bs.As. and surrounds from the south of the province.One unusual characteristics is the calid and dry winds, in the surounding air that persevere, with strong north component, in B.Blanca and Ezeiza, from 940mb until 700mb, from two previous days. This stream only is destroyed the 3/26 in the 24 U.T.C. Bs.As. sounding, when the thunderstorms have declined.This destruction is a result of the strong convection in the zone, since the mentioned conditions persevere in the B.Blanca's sounding until the day 11/27. The characteristics of this thunderstorm in the analysis of B.Blanca and Bs.As' sounds, can be seen in Table III. The correlation anticipates a precipitation of 24mm for thunderstorms of liquid precipitation if the Tcb is 7,7°C, in the flatness. Values from 37.7mm (Dolores maximum) to 16.3mm (Ezeiza) are registered along the travel of the thunderstorm, as it was anticipated.

5. DISCUSSION AND COUNCLUSIONS

Seventeen convective thunderstorms that occur in diverse zones in the country have been investigated and some particularities of them entailed with its efficuiency to produce liquid or solid precipitation.

Without exception, it is possible to detect (in the samples) that: 1)All the thunderstorms examined have evolutioned until they gave solid precipitation when they were in situation of lee of the mountain. 2) The base cloud temperature calculated applying the undimentional cloud model with detailed microphysics is in highest correlation with the maximum diameter of hail and with the amount of liquid precipitation measured in the pluviometrics network. 3)This correlation makes evident that the water quantity that ingresses in the cloud from its base, according to the updraft, is in direct entail with the intensity of precipita tionthat the convective cloud gets. So that there is a physic reason for the correlations found.

AKNOWLEDGMENTS

The National Meteorological Service and the Computadora Ciéntifica, Graciela del Franco and the synoptic-meteorology technicyan Marcelo Sánchez have coopareted for this work. We are thankfull to all of them for their support.

REFERENCES

Cheng, L. and others;1985; Hailstone Size Distributions and Their Relationship to Storm Thermodynamics; Journal of Climate and Applied Meterorology, Vol.24,N°10. Canada

Ghidella de Hurtis, M.; Saluzzi, M.E.;1979; Estudio de un modelo nmérico de nube convectiva; Geoacta, Vol.10,N°1,pag 111-112.Argentina

Saluzzi, M.E.;1983; Aspectos físicos de la convección severa en Mendoza; Dto. de Meteorología, Tesis. Argentina

CHARACTERISTICS OF MESOSCALE CLOUD SYSYTEMS DEVELOPED IN THE MARITIME SUBTROPICS

Masahito Ishihara, Akira Tabata, Kenji Akaeda,
Tatsuo Yokoyama, and Hitoshi Sakakibara

Meteorological Research Institute
1-1 Nagamine, Tsukuba, Ibaraki 305, Japan

1. Introduction

An unique frontal zone is formed in East Asia including Japan, China and Taiwan in the season from late spring to early summer accompanying active convection. It is called the Baiu front. The frontal zone is located at the periphery of the subtropical anticyclone over the Pacific and many mesoscale cloud systems develop (Ninomiya and Akiyama, 1972).

A field experiment was made from 20 May to 15 July 1987 in the region around Okinawa Islands, which are located in the southwestern portion of Japan. Objectives of the experiment are, (1) to know how convections are organized on mesoscale in the maritime subtropical region correlated or not correlated to the Baiu front, (2) to study kinematical and dynamical structure of these mesoscale cloud systems, and (3) to compare the structure with that of midlatitude and tropical mesoscale systems which haye been well documented (Ogura and Liou, 1980 ; Houze and Bette, 1981).

The experimental area is shown in Fig.1. The MRI 3cm Doppler radar was sited near Naha City at the southern end of Okinawa Island. The experimental area comprises four conventional 5cm radars sites and four routine upper sounding stations. Hourly observations of the GMS-III satellite were made through the experimental period.

This paper describes the classification of mesoscale cloud systems developed in the experimental area, and shows kinematical structure of a squall cluster-type cloud system using mainly Doppler radar data. Akaeda et al. (1988) presents the evolution of another mesoscale cloud system observed in the experiment.

2. Synoptic situations

The experimental area was located at the southwestern periphery of the subtropical anticyclone at middle and lower troposphere in this season as shown in Fig.1. This southeasterly was merged with the southwesterly flow emanating from the south of Tibetan Plateau and a large-scale confluence was formed at the the Baiu frontal zone (Murakami, 1959). The satellite data shows an active convective zone corresponding to the Baiu-front aligned from northeast to southwest in the experimental area and another high convective activity zone of ITCZ extending from the equator to near Philippine.

3. Classification of cloud systems

Cloud systems developed in the experimental area are classified into three categories on the basis of satellite and radar observations as follows:

Type 1: Frontal cloud systems. These occurred at the Baiu frontal zone, and had largest horizontal extent in the cloud systems observed in the experiment. The satellite data showed that a broad high level cloud zone oriented parallel to the surface front, and the radar data indicates that smaller scale precipitation bands were embedded in the zone aligned parallel to the 700-900 mb winds.

Type 2: Warm sector cloud systems. These cloud systems developed in warm sector just ahead of the Baiu front with relatively small horizontal scale (20 to 200 km).

Type 3: Cloud clusters. They occurred remote from the Baiu front under the situation of small baroclinicity in the subtropical anticyclone. These systems had horizontal dimension of 150 to 400 km and lifetimes of half day to two days. They were subdivided into two types as cloud clusters observed in the Atlantic tropics during GATE did (Leary and Houze, 1979). Type 3a systems were squall clusters in which convective radar echo cells were organized to an elongated line. Type 3b systems were nonsquall cluster. Intense convective echoes in nonsquall clusters were not so tightly organized as squall clusters. Both type 3a and type 3b clusters generally

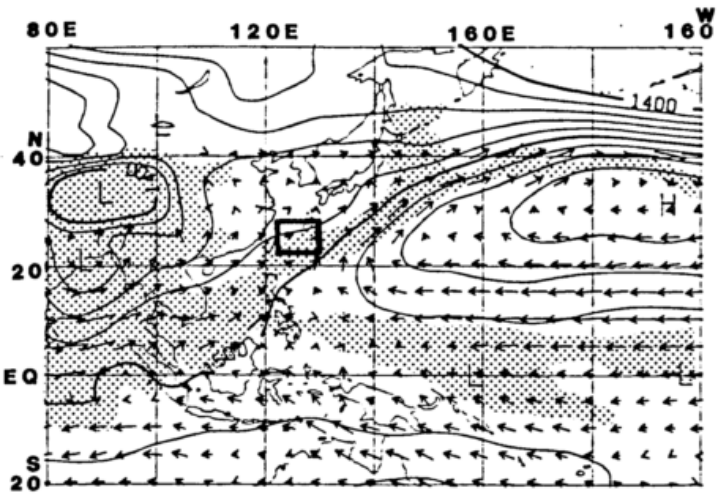


Fig.1 Monthly mean geopotential heights and wind vectors at 850 mb for June 1987. The areas with monthly mean equivalent black-body temperature less than -25°C are shaded (published from JMA, 1987). A solid rectangle indicates the experimental area.

advanced toward the upwind side of the surface wind.

4. Time change of stratification

Figure 2 shows time-height sections over Naha City for the experimental period. Passages of cloud systems are noted at the top of the figure.

The passage of type 1 systems were characterized by large decreases of equivalent potential temperature (θ_e) and abrupt changes of wind direction from southerly to northerly near the surface. Temperature changes were, however, relatively small (less than 3° C). These indicates that the Baiu front is identified by the zone with large horizontal moisture gradient at lower troposphere rather than temperature gradient as pointed out by Matsumoto et al. (1970). While type 3 systems passed, easterly wind prevailed below the 800 mb level. The easterly wind appeared corresponding to the subtropical anticyclone over the Pacific. Changes of θ_e at the lowest level were not so large as those of type 1 systems. It means that alternation of air masses did not occur at the passages of the cloud clusters.

After the passages of the cloud clusters on 21, 25 May and 4, 5 June, dry layers less than 60 % of relative humidity were seen at near the 800 mb level (not shown) accompanying warming of about 1° C. These dry layers probably resulted from the mesoscale downdrafts beneath the anvil clouds which were discussed by Zipser (1977) and Houze (1977) concerning tropical squall clusters.

A cold anomaly of 5° C and pronounced backing of winds were seen at the middle and upper troposphere on 5 and 6 June. This anomaly was formed by advection of cold air with positive vorticity from higher latitudes. The evolution of the cloud clusters occurred on these days might be effected by the cold vortex.

Temperature deviations of about -4° C near the tropopause are seen associated with the clusters on 25 May and 4, 5 June. These cold anomalies resemble those observed at the top of the tropical clusters developed near Borneo (Johnson and Kriete, 1982). They discussed the cause of the cooling and proposed three possibilities, overshooting of cumulonimbus, forced mesoscale ascent in anvil region, and radiative cooling.

5. Squall cluster of 20 May 1987

On this day there was no large-scale disturbance in the experimental area, and three cloud clusters of type 3 were developed. One of them was a squall cluster.

Figure 3 illustrates a composite map of the radars and the satellite data at 2100 GMT 21 May. A distinct convective band aligned from northeast to southwest with the length of 400 km. The total area of radar echoes reached 5 x 10^4 km^2. Cirrus shield higher than 11.5 km covered all the precipitating area and extended ahead of the cluster (southeastward). Individual echo cells consisting of the convective band moved northeastward parallel to the winds at 800 to 700 mb levels, but successive formation of new cells at the southeastern side of old cells made the cluster move southeastward at the speed of 6.0 m/s.

Figure 4 shows vertical cross sections along the propagating direction of the cluster (120°). Horizontal and vertical components of airflow were calculated from obtained Doppler velocity and the continuity equation assuming two dimensionality of the cluster.

From the reflectivity pattern (Fig.4 a), this cluster was divided into four regions as follows:

1. forward stratiform region: This was weak reflectivity area less than nearly 20 dBZ consisting of the front part of the cluster.

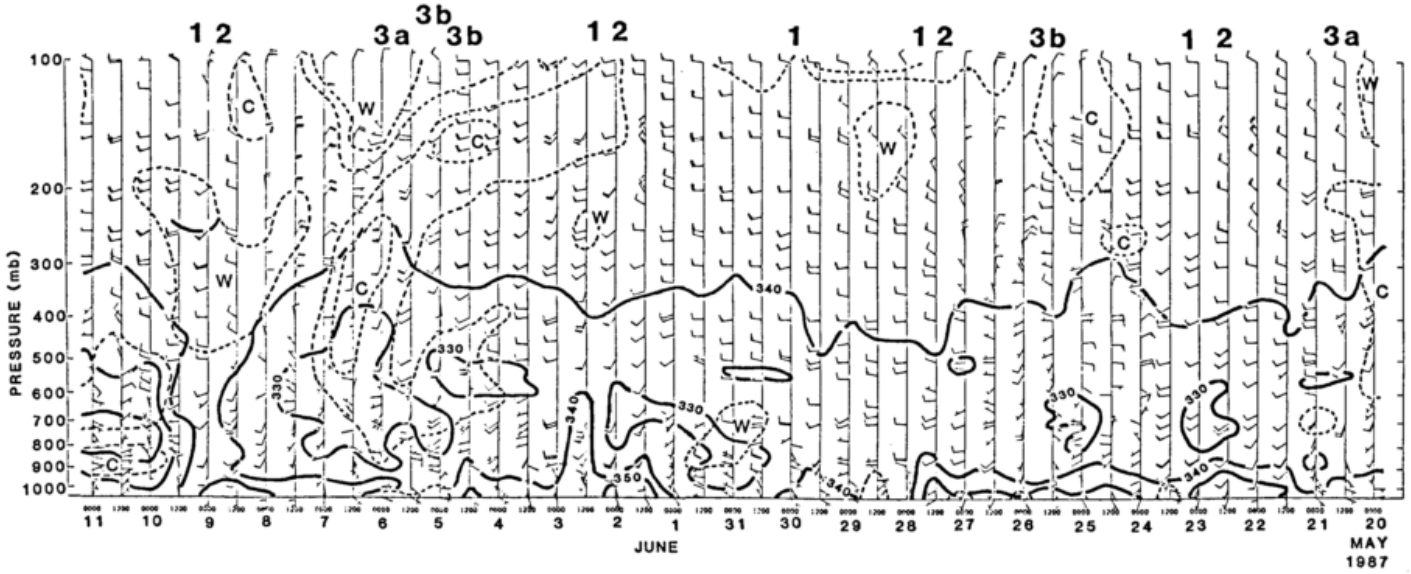


Fig.2 Time-height section of upper air sounding over Naha City from 20 May to 11 June 1987. Winds (full barb indcates 10 m/s), equivalent potential temperarture (solid lines), and temperature deviations from the mean during the experimental period (contours of -4°, -2°, +2° and +4° are shown by dashed lines). Notations, 1, 2, 3a and 3b, at the top indicate times of the passage of cloud systems of type 1, type 2, type 3a, and type 3b, respectively.

Vertical velocity in this region was less than 3 m/s except for the boundary between this region and the following convective region at X = -40km. At the boundary an intense convective-scale downdraft occurred.

2. Convective region: This region consisted of a deep convective cell at X = -32 km and a newly formed cell at X = -37 km, Z = 5 km. Three convective-scale updrafts formed a rearward- tilting updraft zone. The new cell had maximum intensity of updraft (15 m/s at 7 km). Behind the updraft zone, a convective-scale downdraft was seen. The lowest level at the maximum reflectivity region at X = -32 km was prevailed by a weak downdraft zone.
3. Transition zone: This name was given by Smull and Houze (1985) in their analysis of a midlatitude squall line. This was minimum reflectivity zone between the convective region and the following stratiform region. A convective-scale downdraft was seen at the center of the region. A weak downdraft zone less than 2 m/s was found below the 4 km level.
4. Stratiform region: This region was characterized by a bright band at the 4 km level and by a relatively high reflectivity zone above the bright band. A convective-scale updraft existed at the boundary between the transition zone and this stratiform region. A mesoscale downdraft less than 1 m/s was dominant below 8 km.

Air flow relative to the cluster is shown in Fig.4c. The convective updraft at the convective region and the mesoscale downdraft in the stratiform region are well depicted. This cluster had several unique features, and also had characteristics in common with squall clusters which have been observed in the tropics and the midlatitudes.

Acknowledgments. This field experiment was supported by many staff members of Naha Meteorological Observatory.

References

Akaeda, K. , M. Ishihara, A. Tabata, T. Yokoyama, and H. Sakakibara, 1988: A case study of slow-moving convective band observed by a Doppler radar. Preprints of 10th Int. Cloud Phsics Conf. at Bad Homburg.

Houze, R. A. Jr., 1977: Structure and dynamics of a tropical squall-line system. Mon. Wea. Rev., 105, 1540-1977.

--------, and A. K. Betts, 1981: Convection in GATE. Rev. Geophys. Space Phys., 129, 541-576.

Johnson, R. H. and D. C. Kriete, 1982: Thermodynamic and circulation characterisitcs of winter monsoon tropical mesoscale convection. Mon. Wea. Rev., 110, 1898-1991.

Matsumoto, S., S. Yoshizumi, and M. Takeuchi, 1970: On the steructure iiof the "Baiu Front" and associated intermediate scale disturbances in the lower atmosphere. J. Meteor. Soc. Japan, 48, 479-491.

Murakami, T., 1959: The general circulation and water vapor balance over the Far East during the rainy season. Geophys. Mag., 29, 131-171.

Ninomiya, K., and T. Akiyama, 1972: Medeum-scale echo clusters in the Baiu front as revealed by multi radar composite echo maps. Part I. J. Meteor. Soc. Japan, 50, 558-569.

Ogura, Y., and M. T. Liou, 1980: The structure of a mid-latitude squall line: a case study. J. Atmos. Sci., 37, 553-567.

Smull, B. F., and R. A. Houze, Jr., 1985: A midlatitude squall line with a trailing region of stratiform rain: radar and satellite observations., Mon. Wea. Rev., 113, 117-133.

Zipser, E. J., 1977: Mesoscale and convective-scale downdrafts as distinct components of squall-line structure. Mon. Wea. Rev., 105, 1568-1589.

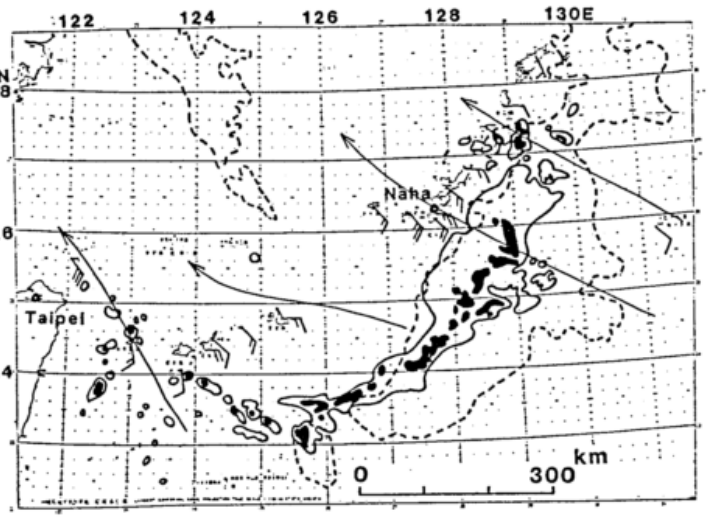


Fig.3 Composite map of radar echoes at 2100 GMT on 20 May 1987. Contours indicate the weakest detectable echoes and 33 dBZ. Dashed lines are contours for -51°C (11.5 km in height) of black-body temperature observed by GMS-III. Stream lines are deduced from surface station data.

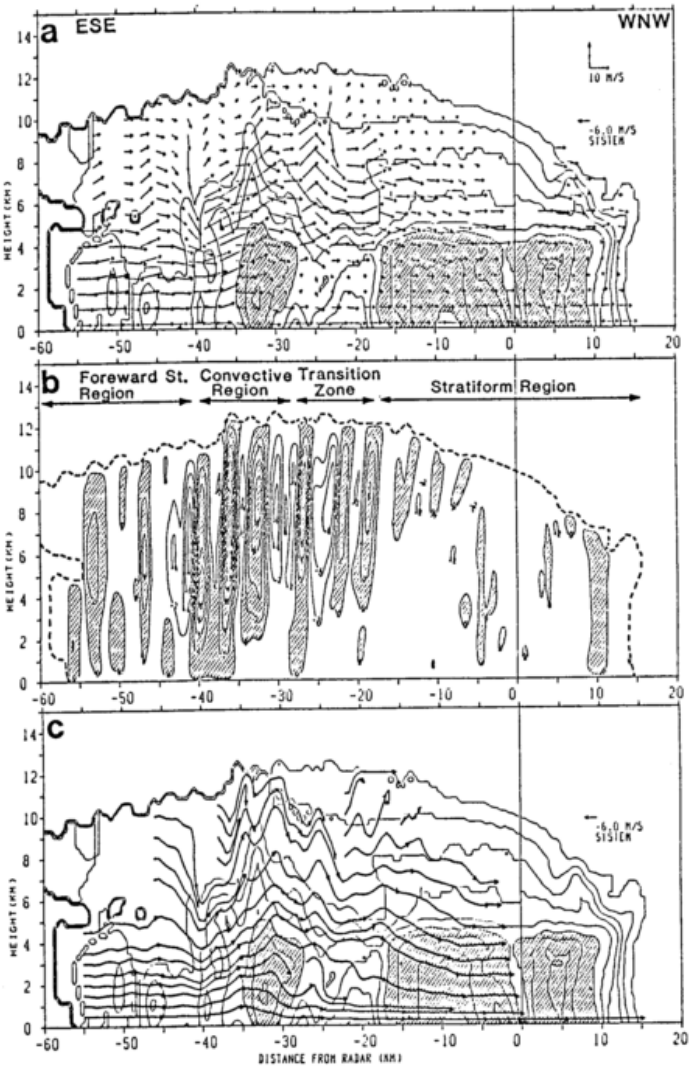


Fig.4 Vertical cross sections of the squall line along the direction of the propagation of the cluster (120°) at 1723 GMT 20 May. (a) Reflectivity and 2-dimensional wind vecotrs relative to the system. The contour intrerval is 5 dBZ. Areas greater than 30 dBZ are shaded. (b) Vertical velocity. The contour interval is 2 m/s. Updraft areas are shaded. (c) System-relative stream lines derived from horizontal and vertical wind components. The system moved from right to left at 6 m/s.

ON THE MERGER OF TWO SMALL CONVECTIVE RADAR ECHOES

Bernice Ackerman and Patrick C. Kennedy

Climate and Meteorology Section
Illinois State Water Survey
Champaign, IL 61820

1. INTRODUCTION

The union of two small convective clouds of nearly the same size and age is described, with focus on the Doppler velocity fields in the vicinity of the echo bridge between the two. In another paper in these proceedings, Kennedy (1988) discusses the merging of a small cloud with a pre-existing rainstorm. The data base, analysis techniques and environmental conditions are basically the same for the two events and the reader is referred to the Kennedy paper for information concerning these aspects of the study discussed here.

The two clouds (identified hereafter as K and L) were first detected as small echoes in the layer from 3 to 4 km. The echoes expanded rapidly and within a few minutes of first appearance were about 6 km in diameter and extended upward to 8-9 km, although reflectivities remained modest (maxima less than 30 dbz). The two clouds evolved similarly, first with a single reflectivity core, then expanding with the development of a second core on the upwind (west) side. This resulted in elongation of the echoes along the wind and the system took on the appearance of a WSW-ENE line. The distance between the clouds (edge to edge as defined by the 15 dbz contour) was initially about 6 km but decreased as the clouds expanded horizontally. The gap was first bridged by a narrow echo at 4 km at 1539 CDT, roughly 12 minutes after the clouds first attained threshold reflectivities.

2. VELOCITY FIELDS AND CLOUD EVOLUTION

The cloud wind fields as the echo bridge was forming are shown for 3 or 4 levels in Figs. 1 and 2. They are based on Doppler measurements from the CP3 and CHILL radars (see Figure 1 in Kennedy's paper). The point wind vectors are perturbation winds, i.e., deviations from the average of all point winds in the two clouds at the specified level. The CHILL scan did not cover the entirety of Cloud L; consequently velocities could not be calculated for the western portion.

At 1539, the easterly wind components were stronger on the downwind sides of the clouds than on the upwind edges at both 3 and 4 km (Fig. 1). Thus movement of cloud particles from cloud L into the gap between the pair,

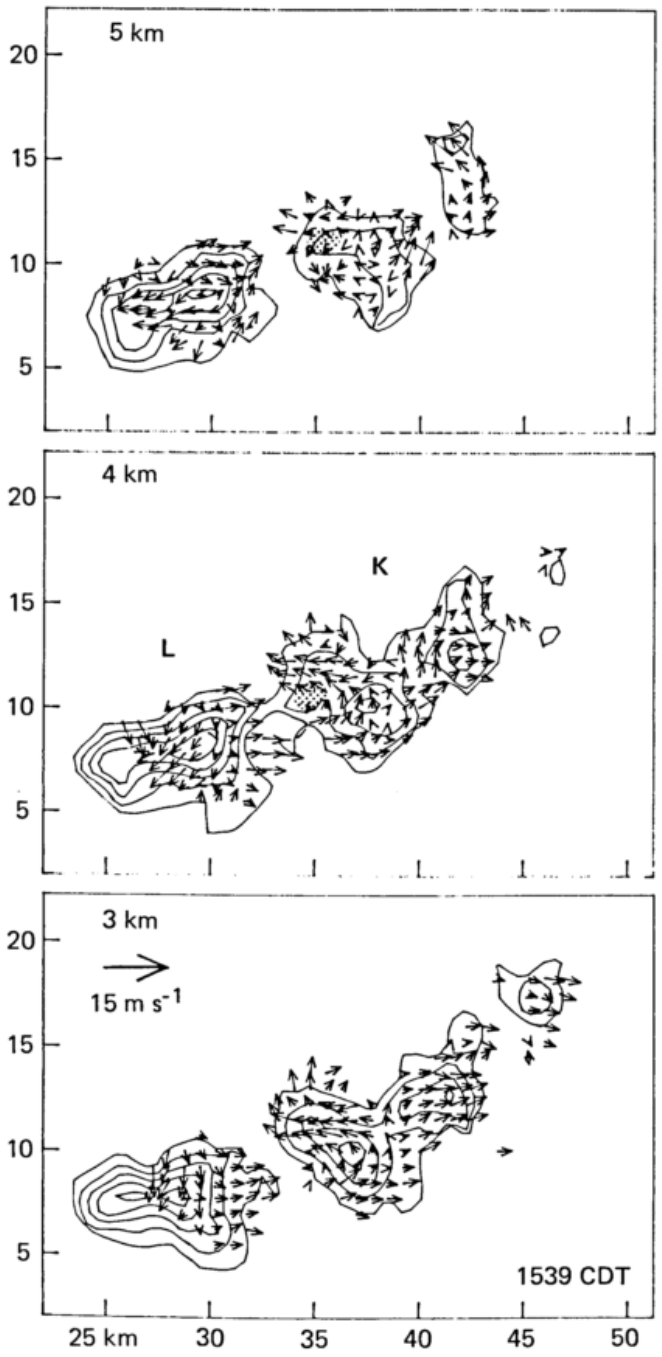


Figure 1. Perturbation winds and reflectivities at 1539 CDT. Reflectivity contours are at 5 dbz intervals, starting at 15 dbz. The scales along the x and y axes give distances east and north, resp., from the CP3 radar. Shaded area in Cloud K indicate updrafts referred to in text.

without matching receding particle motion on the west side of K, served to close the distance between the two clouds and probably also to play a role in forming the initial echo bridge. Moreover the velocity patterns indicate outflow from the updraft in the northwestern portion of K at 4 and 5 km, which also could have brought developed cloud particles into the gap.

By 1542 (Fig. 2) the echo bridge had reached reflectivities of 15 to 20 dbz and extended from 2 km to 5 km. Also K had expanded in the northwest, in the relative location where northwest particle motion is seen in the velocity field 3 minutes earlier. Particle motion to the east was still larger along L's eastern edge than that along K's western border, but only slightly and this primarily in the southern half of the "gap" region. However in the north, there was westward particle motion from K into the bridge, particularly at 4 and 5 km. In addition, a small updraft developed at 3 km in the northwest end of K. This became an extension of the pre-existing updraft at higher altitudes and at 4 and 5 km extended into the northern part of the low reflectivity bridge.

The differential in particle motions in the eastern and western sections of Cloud L and the expansion of Cloud K to the northwest, which included the development of a new cell, are perceived as being important factors in the further strengthening of the echo bond between the two clouds. By 1545 the two clouds were joined by the 20 dbz contour at levels from 2 to 5 km. The differential motion in the two cells of Cloud L had caused an elongation of the echo in the east-west direction (Fig. 3). At the same time the development on the northwest (upshear) edge of Cloud K had generated a new reflectivity core at 4 km which extended back into the bridging region. Within the next 10 minutes the eastern portion of Cloud L was no longer definable in the reflectivity pattern and the merger between the two clouds became complete in the sense that they no longer were identifiable as separate entities. What remained was a narrow cloud line about 30 km long which was composed of several reflectivity cores.

3. DISCUSSION

The early stages in the union of these two small clouds appears to have been due to two factors. The initial bridge was probably a consequence of differential particle motions in the upwind and downwind sections of the two clouds. This amounts to transport of particles into the gap. The eastern edge of Cloud L was essentially inert, although the possibility of a very weak downdraft cannot be ruled out. We also speculate that it may have contained fairly large water particles.

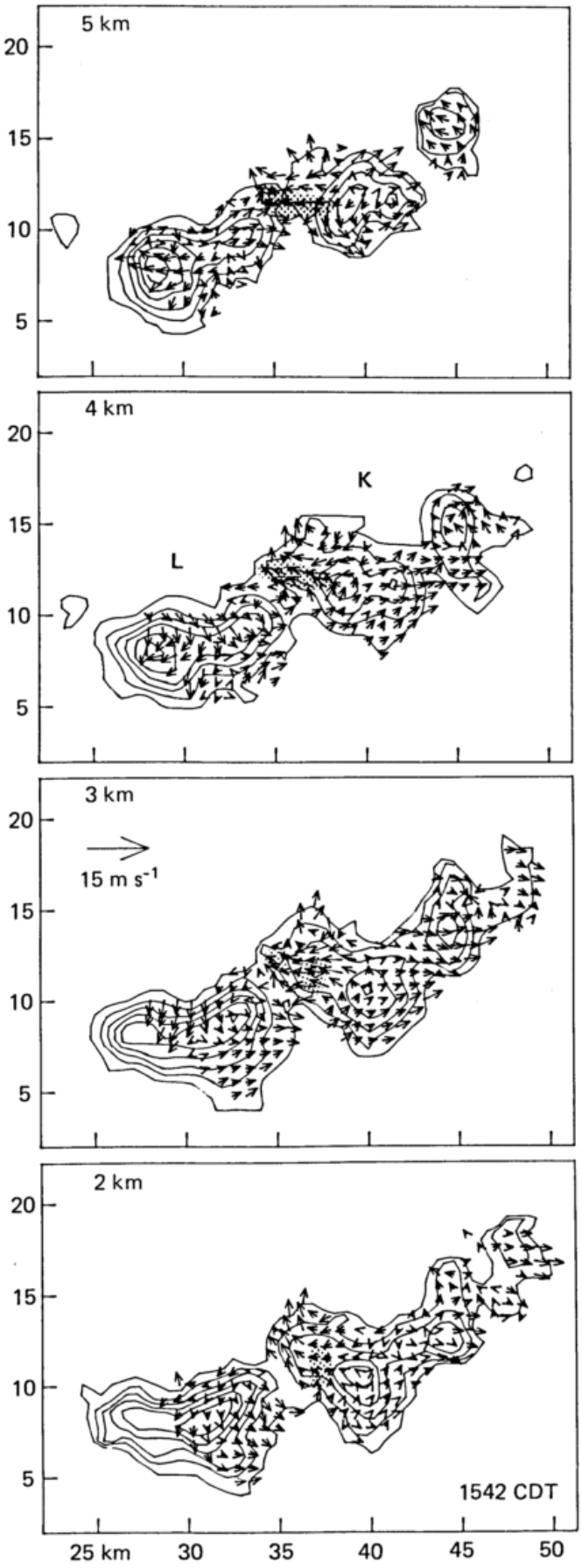


Figure 2. As in Figure 1 but for 1542 CDT. The closed contour in the bridge at 4 km indicates reflectivities between 12 and 15 dbz.

The development of an updraft and new cell at mid-levels in the western portion of Cloud K, extending into the area of the initial bridge appears to have been the vehicle for strengthening the bridge and ultimately for the more complete merger of the two cloud masses. A similar mechanism was proposed by Kennedy (1988) and Westcott and Kennedy (1988) for the merging of a small cloud with a large rainstorm. While in the latter event, low-level outflow and convergence also played a role in initiating and/or enhancing updrafts in the vicinity of the gap, this does not appear to have been a factor in the event discussed in this paper. The clouds were very small and no measurable rain was detected in the dense network in the area until 1555 CDT, when the process of consolidation of the two clouds was nearly complete.

4. ACKNOWLEDGEMENTS. This work was supported by the National Science Foundation under grants ATM 84-12039 and ATM 87-15893 and by the State of Illinois.

REFERENCES

KENNEDY, P. C.: Multiple Doppler Radar Observations of Airflow Fields During Convective Echo Mergers. These Proceedings. 1988.

WESTCOTT, N. E; KENNEDY, P.C.: Cell Development and Merger in an Illinois Thunderstorm Observed by Doppler Radar. J. of Atmos. Sci., Vol. 45 (1988); in press.

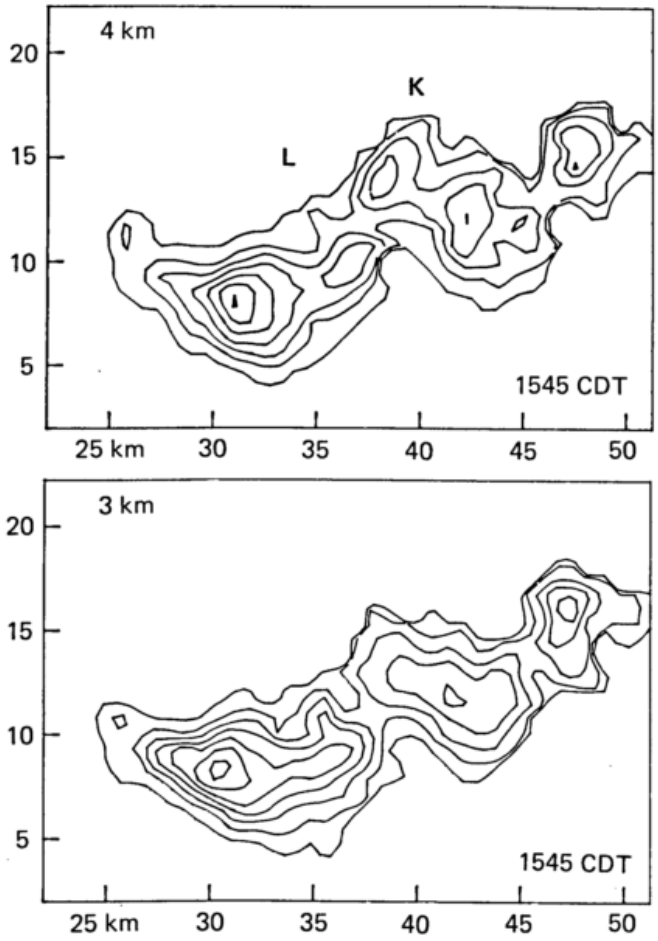


Figure 3. Reflectivity patterns at 1545 CDT. Contours are at 5 dbz intervals starting at 15 dbz. Axis labels as in Figure 1.

Multiple Doppler Radar Observations of Airflow Fields During Convective Echo Mergers

Patrick C. Kennedy

Illinois State Water Survey
Champaign, Illinois 61820 USA

1. Introduction

It has been recognized that mergers among convective radar echoes can result in significant increases in precipitation amounts and areal extent (Tao and Simpson 1984). In general, mergers may involve mechanisms that range from consolidation of updrafts to unions of inactive detrained cloud material (Westcott, 1984). Some specific merger processes involving perturbation pressure effects (Orville et al., 1980), and outflow interactions (Tao and Simpson, 1984) have been identified in numerical simulations. Radar observations of echo mergers have been made during investigations of the organization of multicell thunderstorms (Foote and Frank, 1983). The objective of this paper to expand the understanding of convective echo merger mechanisms by focusing on the three dimensional airflow fields that accompanied a particular merger case in a multicell storm.

2. Data and Analysis Procedures.

The data were collected during project NIMROD (Fujita, 1979). Coordinated volume scans were made every three minutes by the Doppler radars shown in Fig. 1. Special soundings were made from the Yorkville (YKV) radar site.

The data analysis was done at the Water Survey using the CAPRICORN software package developed at the University of Chicago (Peterson, 1984). Details of the data reduction process are contained in Westcott and Kennedy (1988). Due to inconsistencies in radar coverage near the storm top, vertical air velocities were based on upward integration of the anelastic mass continuity equation from a lower boundary condition of $w = 0$. Incomplete radar sampling of divergence maxima near the surface resulted in an underestimate of downdraft strength in these analyses. Furthermore, the upward integration in a column of grid points could not start until the base of the echo reached the 250 m level. This delayed the observation of the organized vertical velocity patterns that define convective cells. As these organized velocity patterns were eventually noted near the maxima in the reflectivity field, the detection of reflectivity cores has been used here to infer the existence convective cells.

3. Storm Environmental Conditions

The storm of interest was one of several that occurred between 1700 and 1830 CDT on 7 June 1978 some 50 km ahead of a cold front that passed northeastern Illinois at 10 m s^{-1}. The YKV 1745 sounding showed moderate conditional instability (Fig. 2). The wind shear vector was oriented towards the southeast in the lowest 5 km of this sounding with a magnitude of 1.7×10^{-3} s^{-1} between the surface and 7 km.

The evolution of the first two cells in this storm (A and B) was analyzed by Peterson (1984). In his analysis as well as the present one, the mean echo system motion was from 252 degrees at 12 m s^{-1}. New cell formation occurred periodically near the rear flank of the storm. The present velocity analyses center around the development of cell D which took place between pre-existing cells C and B.

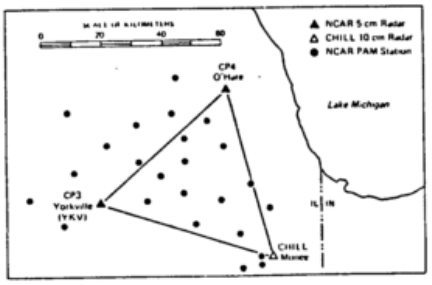


Fig. 1: Project NIMROD radar network.

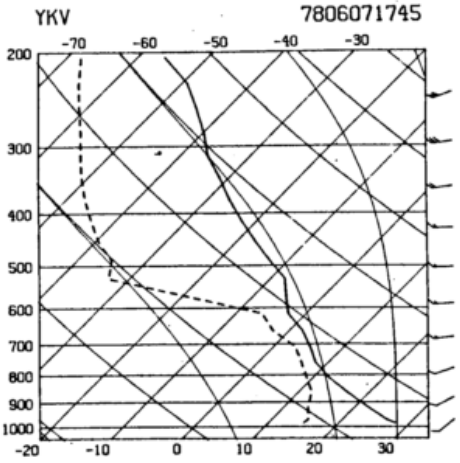


Fig. 2: Skew T - log P plot of YKV 1745 CDT sounding, wind barbs in m s^{-1}.

4. Storm Relative Velocity Patterns

The formation of cell D was preceded by the onset at 1754 (Fig. 3a) of a downdraft (1-2 m s^{-1}) at heights below the 55 dBZ contour of cell B (x=12.5). In response to outflow from this downdraft, 250 m convergence (not shown) was enhanced between cells B and C (x=8). A weak echo "bridge" developed at a height of 3 km above this convergence area.

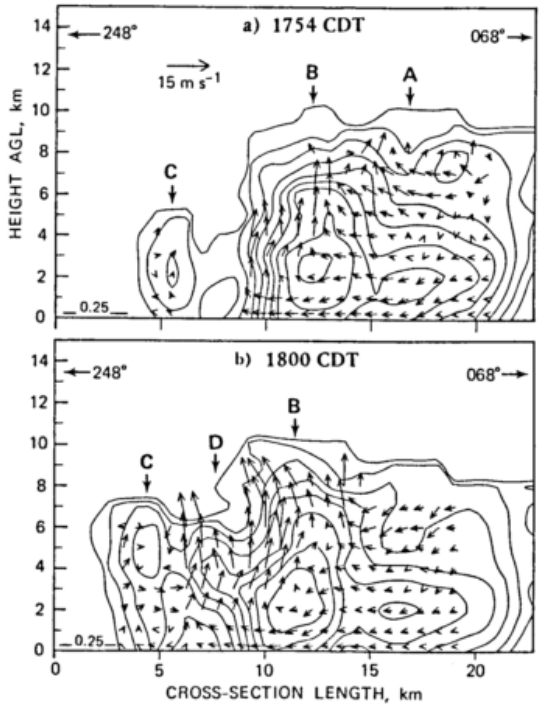


Fig. 3: Storm relative airflow in vertical planes, (a) 1754, (b) 1800. Starting contour 15 dBZ; interval of 5 dBZ.

At 1754 the 4 km horizontal airflow patterns (Fig. 4a) contained counter rotating vorticies that flanked the cell B updraft. The flow field in cell C at 4 km was independent of that in cell B and reflected the environmental flow overtaking the echo at this level. The most apparent feature at 6 km (Fig. 4b) was the diffluent flow associated with the cell B updraft (x=25,y=25).

At 1800 the merger between cell C and B had occurred through the rapid development of cell D (Fig. 3b). At this time cell D already contained a maximum updraft of some 10 m s^{-1}. By 1803 cell D had altered the horizontal flow patterns. At 4 km (Fig. 5a) flow from the united updraft areas of cells B and D towards cell C had developed (x=27,y=25). The reflectivity bridge joining cells C and D had strengthened appreciably between 1754 and 1803. At 6 km radially diffluent velocities were present centered on the upshear side of the reflectivity cores (Fig. 5b). Flow from cell D towards the southern part of cell C was observed at 6 km (x=27,y=25) as well as at 4 km.

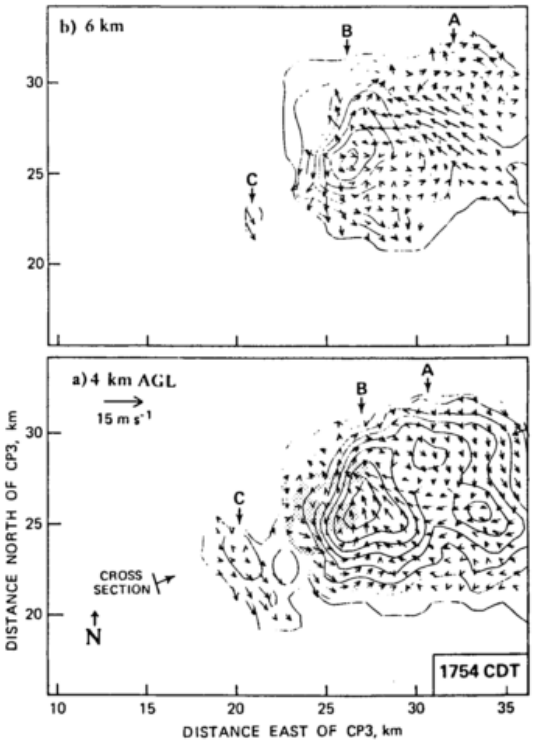


Fig. 4: Storm relative airflow, (a) 4 km, (b) 6km AGL. 4 km updrafts- stippled: > +5 m s^{-1} interior unstippled: > +7.5 m s^{-1}. Reflectivity contours as in Fig. 3.

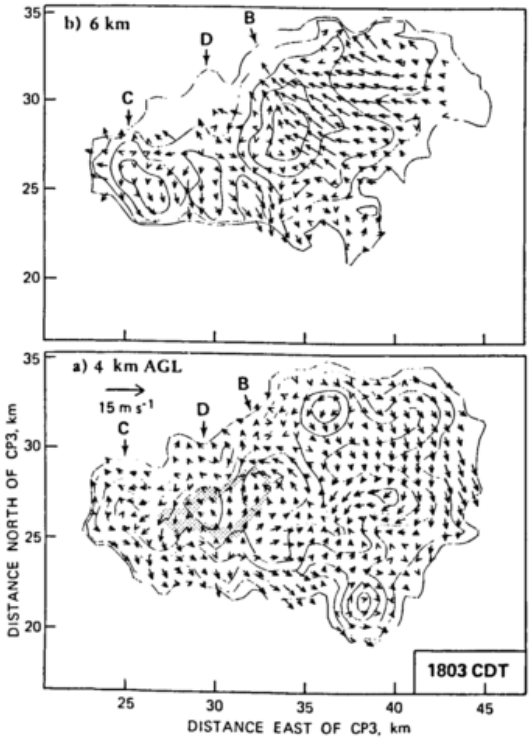


Fig. 5: As in Fig. 4 except for 1803 CDT.

5. Discussion and Conclusions.

Strengthening of the intercell flow and the reflectivity bond at 4 and 6 km between cells C and D was observed as the updraft of cell D became more vigorous.

An estimate of the relative vigor of the cells was made based on updraft mass flux through the 4 km level (Fig. 6). Only vertical velocity values that equaled or exceeded 7.5 m s^{-1} were used in the calculation.

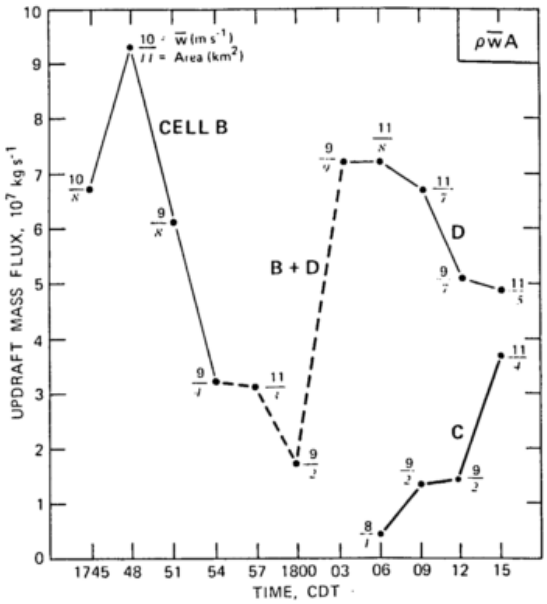


Fig. 6: Updraft mass flux curves (see text).

At 1803 the demise of cell B was evident; cell D's rapid intensification caused its updraft mass flux to exceed that of cell C at this time. It was during this peak that the intercell flow from cell D towards cell C was most pronounced at 4 and 6 km. Later horizontal velocity analyses (not shown) indicate that this intercell flow direction reversed by 1812 as cell C became more vigorous and its updraft mass flux began to approach that of cell D.

Based on mass conservation, radial outflow may be expected at heights above the maximum updraft level. An estimate of the magnitude of the outflow component (Vr) from the incompressible mass continuity equation in cylindrical coordinates is given by:

$$Vr = - (r^2/2R) (dw/dz) \qquad (1)$$

where r is the updraft radius, R is the radial distance from the updraft boundary at which the calculation is made, and dw/dz is the updraft speed change with height. Representative values for these quantities in this case are: r=1.5 km, R=1 km, and dw/dz = -2 m s^{-1} km^{-1}. Their substitution into (1) shows that a storm relative outflow component of 2.3 m s^{-1} could be expected above the maximum updraft level (4 to 5 km) adjacent to the updraft boundaries. The magnitude of the environmental flow (Fig. 2) past the moving storm was less than 2 - 3 m s^{-1} below 7 km. This wind shear profile permitted the existence of the several m s^{-1} outflow component aloft that was observed.

It is possible that this elevated radial outflow may have promoted the observed echo development between cells C and D. Strengthening of this echo bridge may have resulted from the transport of radar detectable particles from active updrafts by the outflow aloft. In addition, smaller particles transported by the outflow may have enhanced echo development by a "seeding" mechanism similar to that reported by Simpson (1980) where particles grown in an established cell were visually observed to fall into an adjacent developing cloud. The intercell environment may also have been made more conducive to echo development by moistening and cooling due to evaporation of radially transported particles. The relatively low wind shear magnitude present in this case permitted the extension of these radial outflow effects into the intercell area. The resultant environmental modifications aloft may have acted in concert with increased low level convergence to promote the observed echo merger via new cell growth.

Acknowledgments. The contributions of N. Westcott and Drs. B. Ackerman, R. Srivastava, and R. Peterson are recognized. This work was supported by NSF grant ATM84-12039.

References.

Foote, G. B. and H. W. Frank, 1983: Case study of a hail storm in Colorado. Part III: Airflow from triple Doppler measurements. J. Atmos. Sci., 40, 686-707.

Fujita, T. T., 1979: Objectives, operation, and results of project NIMROD. Preprints, 11th Conf. Severe Local Storms. Boston, Amer. Meteor. Soc., 259-266.

Orville, H. D., Kuo, Y-H., R. D. Farley and C. S. Hwang, 1980: Numerical Simulation of Cloud Interactions. J. Rech. Atmos., 14, 499-516.

Peterson, R. E., 1984: A triple-Doppler radar analysis of a discretely propagating multicell convective storm. J. Atmos. Sci., 41, 2973-2990.

Simpson, J., 1980: Downdrafts as Linkages in Dynamic Cumulus Seeding Effects. J. Appl. Meteor., 19, 477-487.

Tao, W-K. and J. Simpson, 1984: Cloud Interaction and Merging: Numerical Simulations. J. Atmos. Sci., 41, 2901-2917.

Westcott, N. E., 1984: A historical perspective on cloud mergers. Bull. Amer. Meteor. Soc., 65, 219-226.

Westcott, N. E. and P. C. Kennedy, 1988: Cell development and merger in an Illinois thunderstorm observed by Doppler radar. in review for publication in J. Atmos. Sci.

RESULTS FROM WARM RAIN STUDIES IN PENANG, MALAYSIA

Roland List, D. Hudak and R. Nissen
Department of Physics, University of Toronto, Toronto, M5S 1A7, Canada
and
N.P. Tung, S.K.Soo and T.S. Kang
Malaysian Meteorological Service, 46667 Petaling Jaya, Malaysia

1. INTRODUCTION

The main purpose of the warm rain studies, undertaken jointly by the Malaysian Meteorological Service and the University of Toronto in Penang, is to learn more about formation and evolution of precipitation in a tropical country where the 0oC level is at about 5 km and substantial rainfall is from warm clouds, i.e. clouds which do not contain ice particles. The first phase undertaken in October/November 1986 addressed the problem of raindrop spectra evolution, and the collection of a meteorological data set which would allow the development of improved warm rain models.

The evolution of warm rain has attracted more interest because, with the laboratory data sets on raindrop interactions by MCTAGGARTCOWAN and LIST (1975) and LOW and LIST (1982) [LL], and the parameterizations by GILLESPIE and LIST (1978) [GL] and LL, the base for modelling was created. Box models based on LL appeared by VALDEZ and YOUNG (1985) [VY], BROWN (1986) and LIST et al. (1987) [LDS], while shaft models were used by GL and LDS. These models had one result in common, they all showed that after sufficient fall or time of evolution the resulting distribution was at or close to equilibrium. GL stated that equilibrium was achieved numerically, while LDS provided the mathematical proof that the equilibrium distribution can be separated into a product of a shape function and the rainfall rate R. In other words, all equilibrium distributions are self-similar, they differ by a factor R. VY and LDS showed that the "equilibrium" distribution has three peaks, while BROWN (1986) could only find two peaks. Measurements by WILLIS (1984) above cloud base in hurricane clouds also gave three peaks at the locations predicted by theory and laboratory experiments.

Thus, a major purpose of the Joint Warm Rain Experiment is to find if such equilibrium distributions exist in nature. Such distributions represent possible solutions of the equations of rain evolution as they are now accepted. The existence and location of the peaks, however, is either a result of the LL parameterization or due to numerical errors (VY used an approach different from that of LDS, whereas BROWN (1986) uses the same as LDS).

Box and shaft models have only dimensions 0 and 1, respectively, which may not be representative for nature, except perhaps in steady, widespread rain. Nevertheless, it is worthwhile to investigate rain spectra in the tropics, because equilibrium should be achieved very closely in warm rain during all phases of evolution. This is not the case in mid-latitudes where rain normally starts out as ice and where the first rain spectra below the 0oC level after melting are closely linked to the ice particle spectra. Then equilibrium requires time to be established.

2. THE EXPERIMENT

The operation center and the ground equipment were located at the Meteorological Office at the airport in Penang (5o25'N, 100o10'E). The facilities were those of a standard weather forecast office with twice daily radiosonde ascents. Available was an S-band radar at Butterworth Airforce Base, 23.5 km away on the mainland. PPI and RHI pictures could be transmitted to a console in the operations room, up to four on one screen. RHI slices were normally provided through the airport location as well as 1o off. A Kingair was available for cloud physics studies, satellite pictures were available

after the fact. The raindrop spectrometers used were a Joss-Waldvogel Disdrometer with a range from 0.3 to 4.5 mm and a PMS 2-D Laser Grey Scale Probe with an effective diode width of 15 um and a sampling width of 0.96 mm. Both spectrometers were directly connected to an IBM AT computer for data collection and processing.

Eighteen rain events were recorded with at least the Disdrometer in operation. Ten cases represent warm rain, four came from stratiform and six from convective clouds, while eight events occurred when the rain came from clouds with ice particles, three from convective and five from stratiform clouds. The total rainfall amounted to 105.4mm.

3. RESULTS

a) Peaks were found with the Joss-Waldvogel Disdrometer at diameters of about 1 and 2 mm (predicted by numerical model at 0.8 and 1.8 mm), while a flat third peak was sometimes seen with the PMS Probe around 0.3 mm (predicted at 0.28 mm). These peaks were more pronounced in steady rain than in rain of varying intensity.

b) In non-steady rain the drops seemed to arrive in packets, first the large ones, then successively smaller ones. Often new packets arrived before the old ones had completely disappeared. Thus, at any given time two or more peaks could be observed, depending on which part of the packets were arriving at the ground. Even in these packets it was evident that there were higher concentrations of drops at diameters corresponding to the "equilibrium" peaks.

c) There was no difference between the rain spectra from clouds with or without ice particles.

d) It was found that, due to dead-time effects, the Disdrometer was unable to measure smaller (<1.5 mm) raindrops properly during heavy rain. Whether this explains the lack of shape conservation of spectra is not certain. Instruments which are better geared to microphysical studies of rain are necessary (the Disdrometer is fine for radar reflectivities).

e) LIST (1988) showed that the radar reflectivity of equilibrium distributions is proportional to the rainfall rate (and not a power function as in the standard Marshall-Palmer distribution). In other words, the radar reflectivity in steady warm rain is proportional to the rainfall rate. Since no differences were found in the spectra of warm and cold rain, this statement is valid for steady tropical rain in general. Since only four steady rain cases with about 120 one-minute rain spectra form the basis of this statement, further measurements will be necessary to expand the data set and to support this claim. For these four cases the three peak numerical model predicted the reflectivities calculated on the basis of the measured spectra very well. No general statement can be made about the other observed rain cases because no unbiased equipment was available for the spectra measurement.

In summary, the first phase of the Joint Warm Rain Experiment has produced a number of far reaching findings on warm rain and tropical rain in general. It seems that real raindrop distributions in the tropics may be close to the predicted equilibrium distributions. Their existence is important because radar data processing and interpretation may become very simple, thus easing hydrological measurements including interpretation of data taken during the forthcoming Tropical Rain Measurement Mission (TRMM), which applies radar and passive sounders from satellite to assess precipitation in the tropical region between latitudes 30oS to 30oN or 37oN.

There is another important conclusion. If equilibrium raindrop distributions exist and

we know their exact shape, then any measured distribution may indicate a point in the spectrum evolution, which we know is in the direction to equilibrium. It is only the non-equilibrium distribution which carries information from regions higher up. This will be of some importance in mid-latitude rain.

The real world is neither one-dimensional nor quasi steady-state and the question remains to be solved: can shear or time-shifted release of drop packets from pulsating or periodically regenerated clouds mix drop packages? These and other non-steady questions need to be understood. Numerical modelling will create a basis for in-depth data interpretation and for a more effective use of aircraft and radar in the next field phase.

The basic data set will be made available by the Malaysian Meteorological Service in the form of a report, and details have either been published (List et al., 1988) or will be forthcoming in the standard literature.

ACKNOWLEDGMENTS. The support by the Minister of Science and Technology of Malaysia, Datuk Stephen Yong, Professor George E. Connell, President of the University of Toronto, and Dr. Jingjay Hanchanlash from the Canadian International Development Research Center is very much appreciated.

REFERENCES

BROWN, P.S., 1986: Analysis of the Low-List drop-breakup formulation. J. Climate and Appl. Meteor., 25, 313-321.

GILLESPIE, J.R., and R. LIST, 1978: Effects of collision-induced breakup on drop size distributions in steady state updrafts. Pageoph., 117, 599-626.

LIST, R., 1988: A linear radar equation for steady tropical rain. J. Atmos. Sci.(subm.)

LIST, R., N.R. DONALDSON and R.E. STEWART, 1987: Temporal evolution of drop spectra to collisional equilibrium in steady state updrafts. J. Atmos. Sci., 44, 362-372

LIST, R., D. HUDAK, R. NISSEN, N.P. TUNG, S.K. SOO and T.S. KANG, 1988: Raindrop size distributions in warm rain at Penang. Tropical Precipitation Measurements. Deepak Publishing, Hampton VI.

LOW, T., and R. LIST, 1982: Collision, coalescence and breakup of raindrops. Parts I and II. J. Atmos. Sci., 39, 1591-1618.

MCTAGGART-COWAN, J.D., and R. LIST, 1975: Collision and breakup of water drops at terminal velocity. J. Atmos. Sci. , 32, 1401-1411.

VALDEZ, M.P., and K.C. YOUNG, 1985: Number luxes in equilibrium populations: A Markov chain analysis. J. Atmos. Sci., 41, 1024-1036.

WILLIS, P.T., 1984: Functional fits of observed drop size distributions and parameterizations of rain. J. Atmos. Sci., 41, 1648-1661.

THE KINEMATICS OF MESO-GAMMA SCALE PRECIPITATION SYSTEMS

P.I. Joe, C.L.Crozier and T.R. Nichols
Atmospheric Environment Service,
King Weather Research Station,
4905 Dufferin St., Toronto, Ont., M3H 5T4

1 Introduction

Mesoscale convective systems (MCS) remain a problem for the forecaster because of the lack of observations on an appropriate time and size scale. Doppler radar observations have revealed *two dimensional* kinematic structures which can explain the trailing stratiform region behind a leading squall line (SMULL AND HOUZE 1987, RUTLEDGE AND HOUZE 1987). Two MCS passed through the coverage area of the operational King City Doppler radar in southern Ontario, Canada. (See CROZIER ET AL 1988. In brief, the 5 cm Enterprise radar spends 5 minutes performing a 24 elevation conventional volume scan and 5 minutes performing a 3 elevation Doppler scan. This cycle is repeated every 10 minutes.) Both of these systems exhibited *three dimensional wind fields* similar to larger scale synoptic scale occlusion systems (BROWNING 1985). The systems were too small to be resolved by the standard synoptic observation network. They travelled quickly and had a lifecycle of 12 to 24 hours.

2 CASE 1: DUAL INFLOW JETS 17 JULY 1986

2.1 DESCRIPTION

An occluded MCS passed within range of the operational King City Doppler radar on 17 July 1986. Wind speeds of 36m/s at 3.5 km were 17 m/s greater than any of the upper air rawinsonde measurements around the MCS.

At 50 kPa a broad ridge was located along the Mississippi valley to northwestern Ontario. A wide shallow northwest-southeast warm front lay over southern Ontario with the surface position 200 km southwest of the radar site. The warm air was unstable with θ_w near 20C. Late on 16 July, a minor short wave induced a weak perturbation on the front which developed into a convective system. As the MCS moved into radar range, it was in its mature phase with a well developed leading convective rainband on its southern edge translating along the front at 24 m/s from 330°.

2.2 PRECIPITATION STRUCTURE

The MCS consisted of a large amorphous radar echo approximately $230km \times 300km$ in areal extent (Fig. 1). It appeared to be a combination of the occlusion/linear-trailing stratiform mesoscale convective modes as described by BLANCHARD AND WATSON (1986). The MCS exhibited reflectivity features of a leading narrow convective rain band ($\simeq 10km$ in width), followed by a low reflectivity transition region ($\simeq 20km$ in width), followed by a trailing stratiform region extending 140 KM to the rear found in MCS's with more linear characteristics (SMULL AND HOUZE 1985,1987). There was also a region of stratiform rain to the north of the convective rain band which was to the left of the direction of movement. The shape of the reflectivity pattern suggested rotation of the complex though this can not be proven conclusively.



Figure 1: Reflectivity 0.5° PPI at 1410Z illustrating the leading convective rain band and stratiform rain region. See Fig. 2 for reflectivity and spatial scale.

Fig. 2 shows a vertical cross section along the line A-AA in Fig. 1. The section shows that the echo in the leading convective band extended to a height of 14 km with maximum reflectivities in the 40-50 dBZ range. The transition zone is marked by low reflectivities with values no greater than 25 dBZ. The stratiform region shows a bright band at a height

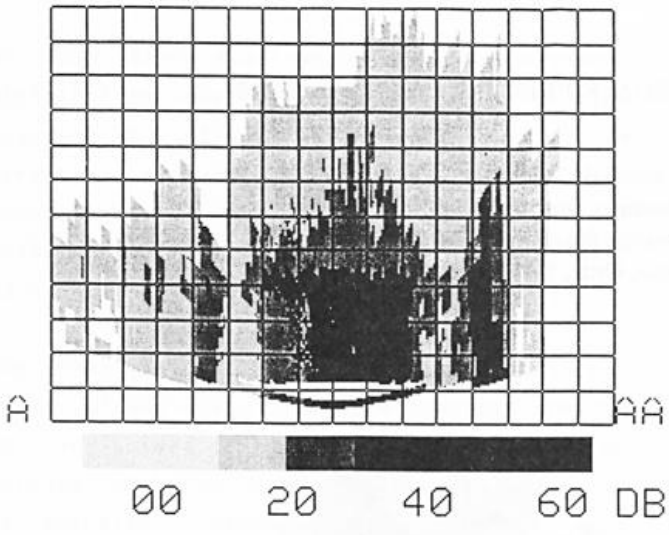


Figure 2: Vertical Cross-section through A-AA in Fig.1. Horizontal and vertical grid lines are 20km and 1km apart, respectively.

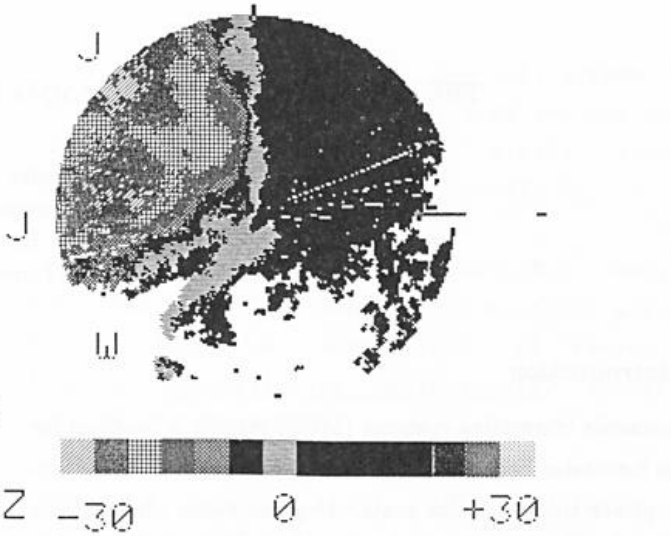


Figure 3: Radial velocity PPI at 1320Z illustrating the dual rear inflow jets (J) and the warm conveyor belt (W). Spatial scale is the same as in Fig. 2.

of 3.5 to 4 km (MSL) of 30 to 40 dBZ.

2.3 VELOCITY STRUCTURE

Fig. 3 shows the 1.4° radial velocity PPI, illustrating several features not observed in the linear MCS case of SMULL AND HOUZE (1985,1987); these include a low level flow parallel to and ahead of the convective band (W) flowing from the southwest to the northeast up the warm frontal surface and dual jets flowing from the rear to the front of the system (J). The dual jets converge and descend into the rear of the convective band, then diverge with one branch ascending and curving by the band on its left or northeastern extent and the other descending. The inflow-outflow of these jets behind the convective rain band are not symmetric about the radar location, indicating that the jets are turning as they move through the MCS.

3 CASE 2: COMMA SYSTEM 6 MAY 1986

3.1 DESCRIPTION

A mesoscale convective line moved eastward across Southern Ontario at 27 m/s. A few of the cells in the line produced severe weather - marble sized hail, "torrential rain" and strong winds. At 50kPa, a weak north-south ridge lay just east of the radar site and a strengthening southwesterly flow was becoming established. At 1200Z, a short-wave trough was located in the vicinity of Chicago and was approaching the radar at 27m/s. Associated with the short-wave was a pinched and weak, lower tropospheric frontal wave.

GOES infra-red satellite images indicated that an intense line of convection had formed on the cold front prior to 0000Z (not shown). By 1200Z, satellite imagery showed that this line had weakened substantially but that a small area of convection had developed on the warm front near the wave.

3.2 PRECIPITATION STRUCTURE

When the system was fully within radar range (maximum range of 226 km) around 1930Z, the radar images indicated a slight bow shape to the line. There was a relatively narrow (less than 15km wide and 200 km long) convective band followed by a larger region of primarily light stratiform precipitation. Most of this precipitation evaporated before reaching the ground. Several small (less than 5km diameter) but intense convective cells (maximum reflectivities greater than 60 dBZ) were located at northern end of the band.

3.3 VELOCITY STRUCTURE

Doppler radial velocities indicated a southwesterly warm conveyor belt wind maximum in the low levels reaching values greater than 30 m/s between 1 and 1.5 km above ground (CARLSON 1986, BROWNING 1985) flowing towards the warm frontal surface. The strong convection that existed on the front ahead of this flow peaked in intensity as the wind core maximum approached the convective band then weakened rapidly when overtaken by the jet maximum.

The winds between 2 and 3 km were 6 to 12 m/s less which provided a storm relative rearward flow aloft. This was also evident as radar indicated precipitation particles spreading

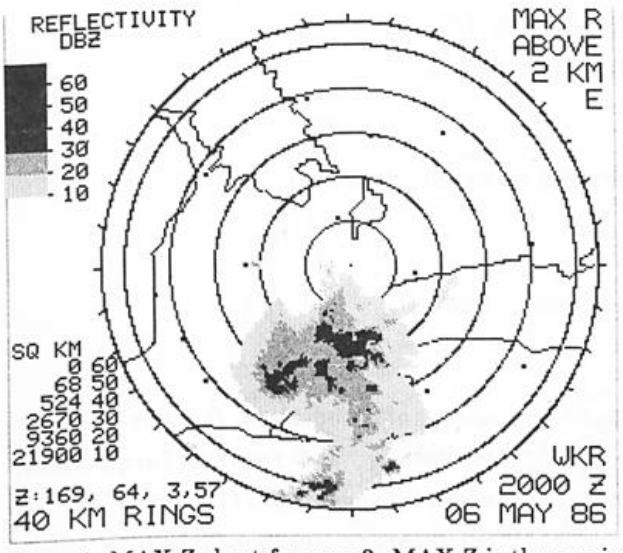


Figure 4: MAX Z chart for case 2. MAX Z is the maximum reflectivity in a column above 2 km.

out to the rear forming the MCS anvil; similar to the two dimensional vertical wind field structure observed in case 1 when viewed perpendicular to the convective rain band.

The existence of a large area of precipitation aloft and little on the ground implied a descending dry air flow. A Doppler radial velocity core near 26 m/s was observed to descend along the back edge of the system.

Fig. 4 shows that by 2000Z, the complex had assumed a classical comma-like shape of an occluding lower tropospheric frontal system. The warm conveyor belt was still visible in the Doppler data although the core was now both higher and weaker. The descending air flow in the rear of the system was still evident both from Doppler velocities and from the drynotch visible on low level CAPPIs. In addition, a line of enhanced precipitation had begun to develop on the leading edge of the kata-frontal flow.

5 DISCUSSION AND CONCLUSIONS

The two MCS can be described as mesoscale frontal systems. Both systems developed on a weak baroclinic zone. A warm conveyor belt-like flow could be observed ascending the warm front leading to the development of convective rain bands. Vertical cross-sections of the velocity field perpendicular to the rain bands showed a high level front to rear flow aloft and rear inflow at midlevels. Jets of cold drier air aloft were observed which eroded the precipitation in the rear stratiform region.

In the first case presented, two rear inflow jets could be observed which can be attributed to the airflow from two different air streams. One tongue of drier air descends and forms the rear inflow jet and the second tongue rises above Doppler viewing heights.

In the second case, the system evolved very quickly. The air in the rear jet was much drier than in the first system and dissipated the precipitation in the trailing stratiform region. This air then ascended the warm frontal surface to form an upper level front and a second rain band.

These three dimensional flows are consistent with the synoptic scale conveyor belt models of BROWNING (1985). However, the time and space scales of these systems are much smaller and are not resolved by the observations made by synoptic scale networks. These systems require observation by sensors like Doppler radars, radiometers and wind profilers in order to improve their prediction.

References

BLANCHARD, D.O. and A.I. WATSON, 1986: Modes of mesoscale convection observed during the pre-storm program, Preprints of the joint 23rd Conf. on Radar Met. and Cloud Phys., Snowmass, Colorado, J155-158.

BROWNING, K.A., 1985: Conceptual models of precipitation systems, ESA journal, 9, 157-180.

CARLSON, T.N., 1980: Airflow through midlatitude cyclones and the comma cloud pattern, Mon. Wea. Rev., 108, 1498-1509.

CROZIER, C.L., P.I. JOE, T.R. NICHOLS, J.W. SCOTT AND H.N. HERSCOVITCH, 1988: The Operational King City Doppler radar, In preparation.

MADDOX, R.A., 1980: Mesoscale convective complexes, Bull. Amer. Met. Soc., 61, 1374-1387.

RUTLEDGE, S.A. and R.A. HOUZE, JR., 1987: A diagnostic modeling study of the trailing stratiform region of a midlatitude squall line, J. Atmos. Sci., 44, 2640-2656.

SMULL, B.F. and R.A. HOUZE, JR., 1985: A midlatitude squall line with a trailing region of stratiform rain: radar and satellite observation., Mon. Wea. Rev., 113, 117-133.

SMULL, B.F. and R.A. HOUZE, JR., 1987: Dual-Doppler radar analysis of a midlatitude squall line with a trailing region of stratiform rain, J. Atmos. Sci., 44, 2128-2148.

THE ORIGIN OF AIR MASSES LEADING TO SEVERE HAILSTORMS IN SOUTHWESTERN FRANCE

Jean Dessens
Centre de Recherches Atmosphériques, Lannemezan, France
and
E.M. Fournier d'Albe
Dormont, Saint-Pierre de Bailleul, France

The knowledge of the origin of air masses in which hailstorms develop is useful both for the weather forecaster, who needs an evaluation of the potential energy available in the atmosphere, and for the cloud physicist, who has to explain the hailstone growth processes in relation with the atmospheric nuclei content. The computerization of back trajectories is now a convenient method for discussing the origin of air masses. This paper gives a preliminary analysis of back trajectories for a selection of extremely damaging hail days in Aquitaine.

Table 1 gives the data on the most severe hail days during the last eight years in Aquitaine. These days were selected both for the economic impact of the damage, and for the large dimensions of the hailstones. Detailed data on these hail occurrences are published in annual reports (ANELFA, 1981-1988). Since the beginning of the eighties, Saharan dust intrusions have been frequent in the atmosphere of southwestern France, and it is noteworthy that for 6 hail days of Table 1, hailfalls were associated with spectacular dust events consisting of a visible amount of dust in the atmosphere, like the "brume sèche" of Sahelian regions, followed by dry or wet falls of red dust.

The computation of back trajectories is made

Table 1. Major hail days in Aquitaine, with the main characteristics of the back trajectories arriving near the place and time of hailfalls.

	N°	Day	Largest hailstone diameter (mm)	Trajectories	
				Terminal point(1)	Travel time (hr) from nearest coast at the 900 mb level
Hail	1	14 Jun 1980	40	Lannemezan	50
	2	8 May 1981	30	Bordeaux	24
	3	20 Jul 1982	50	Toulouse	14
	4	1 Jun 1983	30	-	18
	5	27 May 1985	30	Lannemezan	46
	6	11 Jun 1987	25	Mt de Marsan	46
	7	14 Jul 1987	50	Limoux	13
Hail and Saharan dust	8	18 Jul 1983	80	Bordeaux	26
	9	26 Jul 1983	80	Bayonne	24
	10	20 Jun 1984	20	Lannemezan	13
	11	2 Jun 1985	40	-	18
	12	30 Jul 1986	25	-	72
	13	16 Sep 1986	40	-	41

(1) Arrival time is 1800 UT in all the cases.

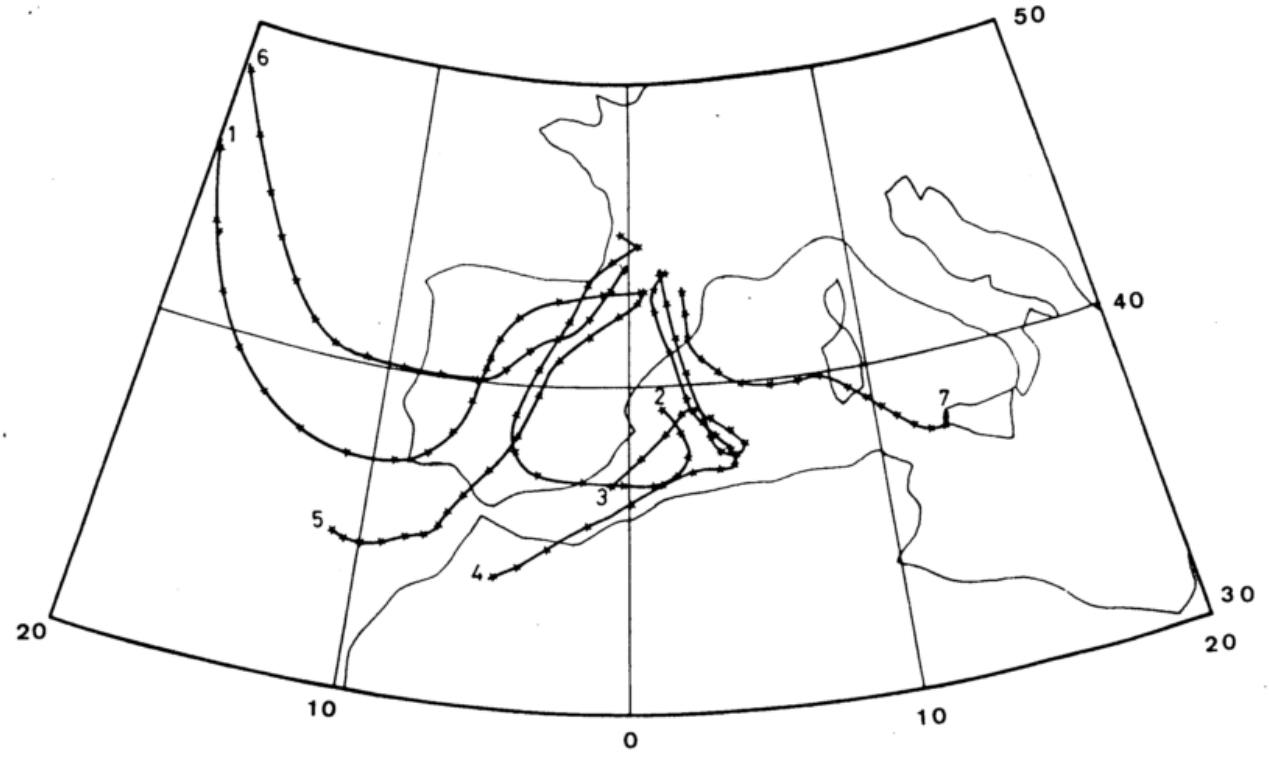


Fig. 1. Back trajectories at 900 mb arriving in southwestern France at the place and time of severe hailfalls. Each trajectory segment corresponds to a 6 hr period.

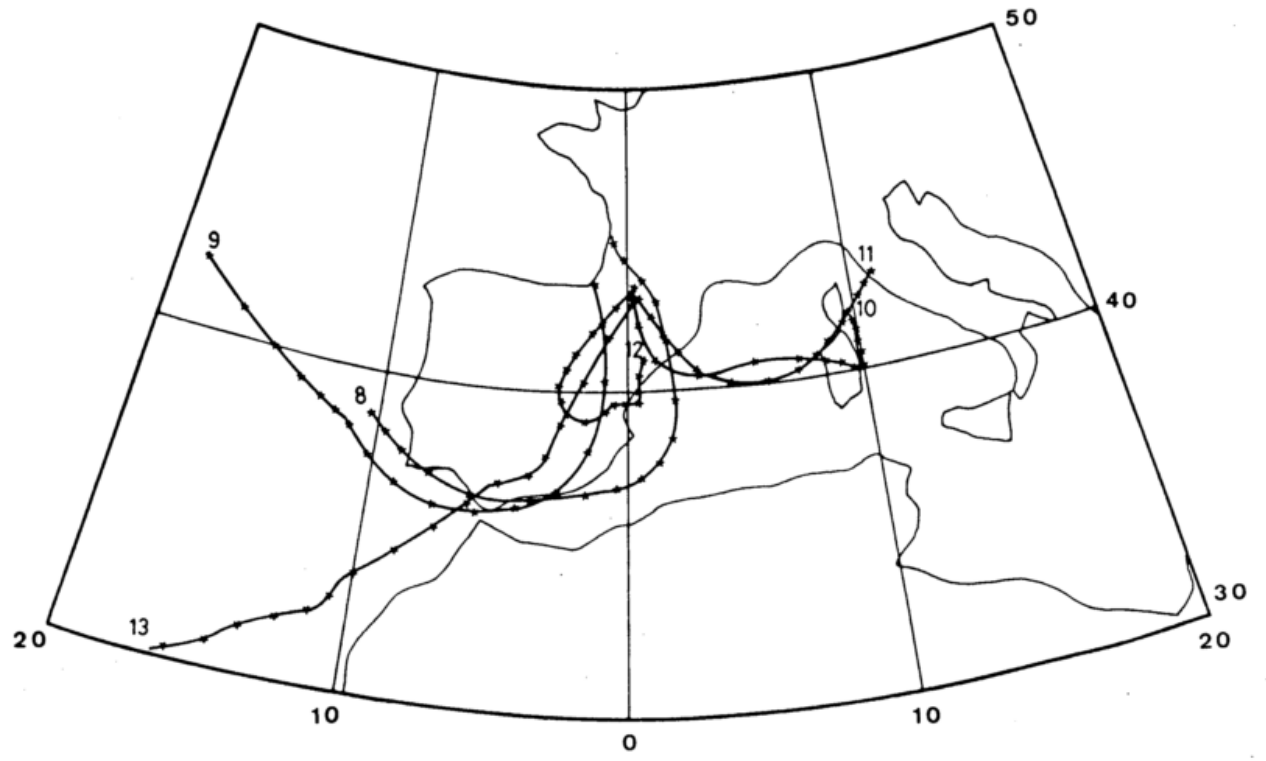


Fig. 2. Same as Fig. 1 for hailfalls concomitant with a Saharan dust intrusion.

by the French Meteorological Service, using the data of the European Centre for Medium Range Weather Forecast (Martin et al., 1984). For each hail day, the trajectories arriving at the 900 and 200 mb levels near the time and place of the main hailfalls were computed.

The trajectories at 900 mb for the 4 days preceding their arrival are shown in Fig. 1 (hail) and Fig. 2 (hail and Saharan dust). These trajectories show that the low level inflow on these occasions did not come from the Atlantic, and that when it came from the Mediterranean, the air masses were not of recent oceanic origin (Table 1). The trajectories related to the dust events are not very different from the others.

The trajectories at 200 mb (not reproduced here) indicate a fast inflow of air coming in about ten hours from the Southwestern Coast of the Iberian Peninsula. For some of the 13 days, the back trajectories at 500 mb were also computed ; they are very similar to the 200 mb trajectories, though sometimes passing nearer to or over the African continent, specially in cases n° 10 and 11.

Two preliminary conclusions may be suggested :

1. Although southwestern France faces the Atlantic Ocean, the air masses in which severe hail situations develop are not of direct Atlantic origin. The chemical composition of the lower atmosphere is of a semi-continental type, the concentration of hygroscopic nuclei being presumably low.

2. A fast upper inflow of air from the northwest coast of Africa may explain why, on several occasions, hailfalls have coincided with spectacular Saharan dust incursions. The presence of dust aerosol in other similar cases, has been noted, for instance by Stevenson (1969) after the dust fall and severe storms of 1 July 1968 in England.

There are several reasons to suppose that the presence of desert dust in clouds changes their microphysics : (a) altocumulus castellanus which develop in Saharan air masses often produce unexpected large drops which are dust-loaded ; (b) a proof of the role of dust storm aerosol in hailstone chemistry is given by Gitlin (1978), who examined the inorganic composition of hailstones ; and (c) large hailstones falling in France during Saharan dust incursions are observed as "unusual", often described as lumps or plates of ice, or with remarkable protuberances.

The cause of the observed tendency, for hail to develop over southwestern France preferentially in air which is not of recent oceanic origin, may be sought either in the dynamic characteristics of the air masses or in their aerosol content (for example, high concentrations of dust particles and/or low concentrations of hygroscopic nuclei). Further studies will be needed to explain this observed tendency.

REFERENCES

ANELFA, 1981-1988 : Annual Reports, n° 29 to 36 (Available on request : ANELFA, 52 rue A. Duméril, 31400 Toulouse, France).

GITLIN, S.N., 1978 : Microprobe analysis of project DUSTORM hailstone samples. J. Appl. Meteor., 17, 64-72.

MARTIN, D., J.P. GRANIER, M. IMBARD and B. STRAUSS, 1984 : Application d'un modèle de transport à longue distance au panache de l'Etna. Electricité de France, Rapport EDF-DER-HE/32.84.17.

STEVENSON, C.M., 1969 : The dust fall and severe storms of 1 July 1968. Weather, 24, 126-132.

RADAR REMOTE SENSING OF MELTING HAIL

V.N. Bringi and P. Meischner

Institut für Physik der Atmosphäre, DFVLR, 8031 Oberpfaffenhofen, F.R.G.

1 Introduction

The remote sensing of hydrometeors has been greatly advanced with the development of polarimetric radar techniques. In this paper we present model calculations for melting hail for explaining very high differential reflectivity, Z_{DR} values, observed in summer 1987 (see the accompanying paper MEISCHNER et al.) using the advanced, polarimetric Doppler radar of DFVLR (SCHROTH et al., 1988). Using a coupled microphysical-electromagnetic model, we show that the Z_{DR} observations can be used to detect small melting hail within the main precipitation shaft of convective clouds.

It is known that the vertical profile of Z_{DR} is an indicator of the onset and progression of melting ice into raindrops (HALL et al., 1984). BRINGI et al. (1986a) modelled the melting behaviour of low density conical graupel and have successfully compared the model results to Z_{DR} data using the NCAR CP-2 radar. It is also established that by combining reflectivity and Z_{DR} it is possible to detect hailshafts (BRINGI et al., 1984, 1986b; AYDIN et al., 1986; ILLINGWORTH et al., 1987). Recent wind-tunnel studies of hail melting by RASMUSSEN et al., 1984, have provided impetus for coupling microphysically-detailed hail melting models with polarimetric backscatter models. This is based on the variables particle size, particle shape and composition, particle orientation relative to the incident radar beam, and particle dielectric constant and their distributions within the radar resolution volume. In particular, the mean and standard deviations of particle sizes, shapes and orientations are relevant parameters. It is convenient to assume a particle size spectrum of the gamma form. For particle shapes we consider spheroidal and conical shapes. Melting particles are assumed to be composed of 2 layers, e.g., an inner ice core covered by a shell of melt water. Particle orientation distribution or canting angle distributions can be modelled as Gaussian with a mean canting angle $\overline{\Theta} \approx 0°$ and variable standard deviations σ.

2 Microphysical / Electromagnetic Model of Melting Hail

We use the detailed microphysical melting hail model of RASMUSSEN et al., 1984 with maximum initial hail diameters of 12 mm. Wind-tunnel studies by RASMUSSEN et al. show that for hail sizes $\leq 12mm$, shedding of the melt water does not occur. Input to the one-dimensional melting model consists of a typical environmental sounding which we have taken from the Oberpfaffenhofen area. For each hail size, the model computes various microphysical parameters such as density, water fraction, particle temperature, etc., as a function of height.

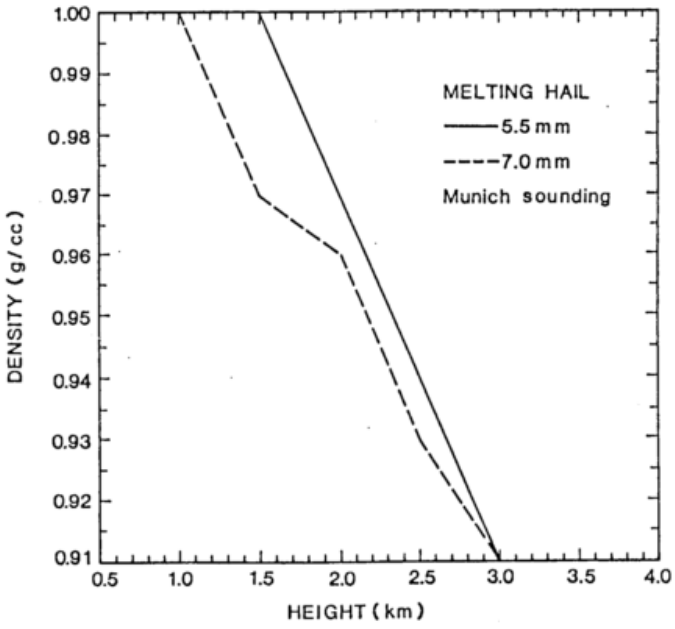


Figure 1. Particle density versus height

Normally, particles are initialized at the 0° C level and allowed to fall independently in still air. Fig. 1 shows an example of the vertical profile of particle density for an initial hail size of 5.5 and 7 mm. The initial hail density is assumed to be 0.9 gcm^{-3} while the initial water-fraction is zero. The initial shape is assumed to be spherical. As the particle melts the water is distributed as a uniform concentric water coat with thicknesses between 0.1 and 0.2 mm. As the water-fraction increases further it is distributed as an oblate shell surrounding the spherical ice core. Upon complete melting the particle assumes the equilibrium oblate shape of raindrops.

The particle orientation is described by a canting angle (Θ) distribution which is assumed to be Gaussian with mean $\overline{\Theta} = 0°$ and standard deviation (σ) which decreases as a function of height. The profile

of σ is linear with 45° at the initial height and decreasing to 10° at the lowest height. This assumption is consistent with wind-tunnel studies which show that an increase in melt water stabilizes the particle orientation.

The dielectric constant is computed at C-band for ice, while for the water layer use is made of the water temperature computed by the melting model. The backscatter matrix is computed for each particle using the T-matrix method for both homogeneous and 2-layer cases. Computations of Z_{DR} versus height for initial hail size of 7 mm is shown in Fig. 2; the changing particle shapes and compositions are indicated. We see that Z_{DR} increases with decreasing height reaching a maximum value of $\sim 5.5\,dB$ at 1.5 km and then decreasing to $\sim 5\,dB$ at 0.5 km height. Note that the Z_{DR} values are applicable to one particle (of initial diameter 7 mm) as it falls and melts into an equilibrium shaped raindrop.

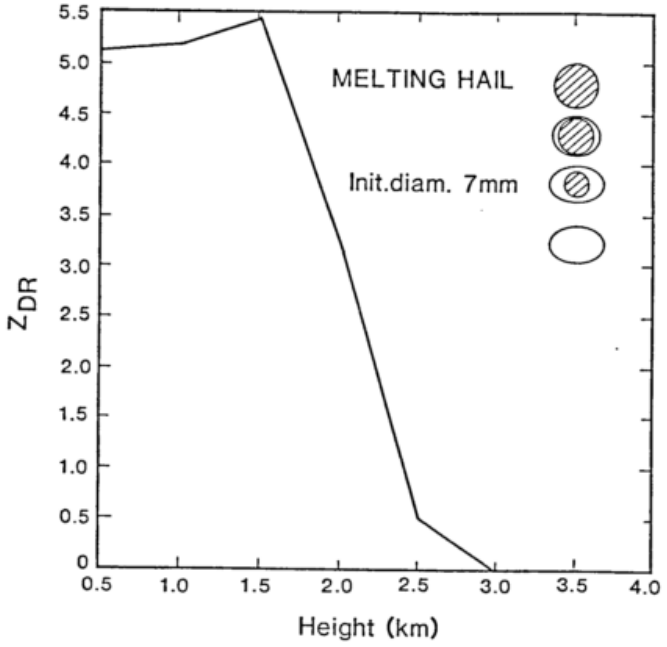


Figure 2. Z_{DR} versus height for a melting hail particle.

In order to integrate over particle sizes the size distribution must be modelled. We have chosen to model the initial hail size distribution using an exponential Marshall-Palmer form $N(D) = N_0 \exp(-3.67D/D_0)$ where $N_0 = 8000\,m^{-3}mm^{-1}$ and D_0 is chosen to give a maximum initial reflectivity of 60 dBZ for the maximum hail size of 12 mm. Figs. 3 and 4 show profiles of reflectivity (dBZ) and Z_{DR} as a function of height where integrations are performed over the spectrum of sizes, shapes, orientations and dielectric constants up to a maximum size of 7 mm. Again, we note the smooth increase in Z_{DR} as the particle melts reaching a maximum at 1.5 km height followed by a slight decrease near the surface. The enhanced Z_{DR} at 1.5 km height is due to the presence of some fraction of the particles at this level having an oblate water shell surrounding the inner ice core. This enhancement in Z_{DR} occurs eventhough the axis ratio of these partially melting oblate particles is larger (i.e., more spherical) than equi-volume, equilibrium-shaped raindrops.

Thus, we may expect radar Z_{DR} signatures in small melting hail to be perhaps significantly larger than expected for equilibrium-shaped raindrops. In Fig. 5 we show Z_{DR} versus D_0 for both exponential and Gamma size distributions of equilibrium-shaped raindrops for m-values of 0, 1 and 2. Note that the maximus Z_{DR} is 4.6 dB while typical values lie in the range 1-4 dB.

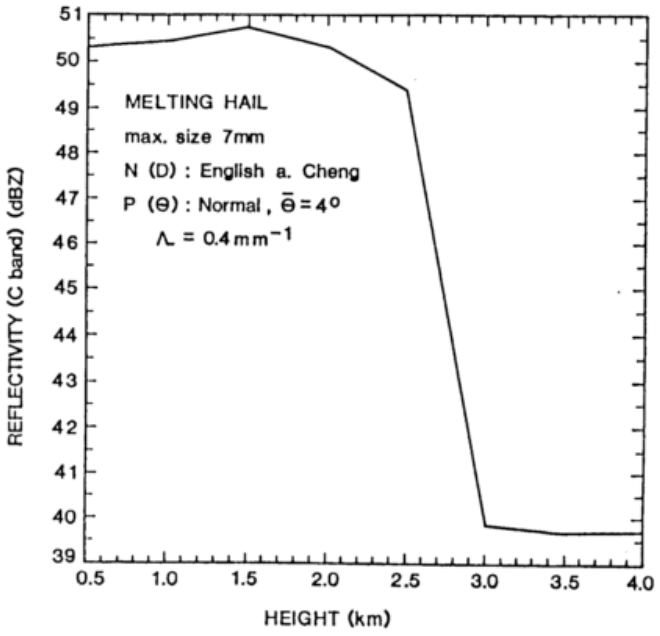


Figure 3. **Z versus height for melting hail particle distribution.**

3 Conclusions

Using a coupled microphysical-electromagnetic hail melting model and polarimetric C-band radar observations, we have shown that it is possible to detect regions of small melting hail using the vertical profile of Z_{DR}.

High values in the range 5-7 dB, were observed within the main precipitation shafts of summer-time convective storms near the area of Oberpfaffenhofen, W.Germany. The hydrometeors responsible for giving rise to the very large Z_{DR}'s are believed to be melting hailstones composed of an inner ice core surrounded by an oblate shell of melt water. Shedding of melt water is suppressed for the smaller hail sizes (diameter $\leq$ 12 mm), while the melt water significantly increases the particle stability and prevents it from tumbling. If the hail sizes are large

($> 12 - 15\,mm$), then the meltwater is shed off causing the particles to tumble and giving a Z_{DR} value close to 0 dB. This combination of small Z_{DR} and high reflectivity has been shown previously to be a reliable indicator of hailshafts, BRINGI et al., 1981.

The results of this paper show that polarimetric radar techniques can be used to distinguish between intense precipitation shafts of high reflectivity which may on the one hand be composed of rain mixed with small, melting hail, and on the other hand be composed of larger hailstones falling without significant melting.

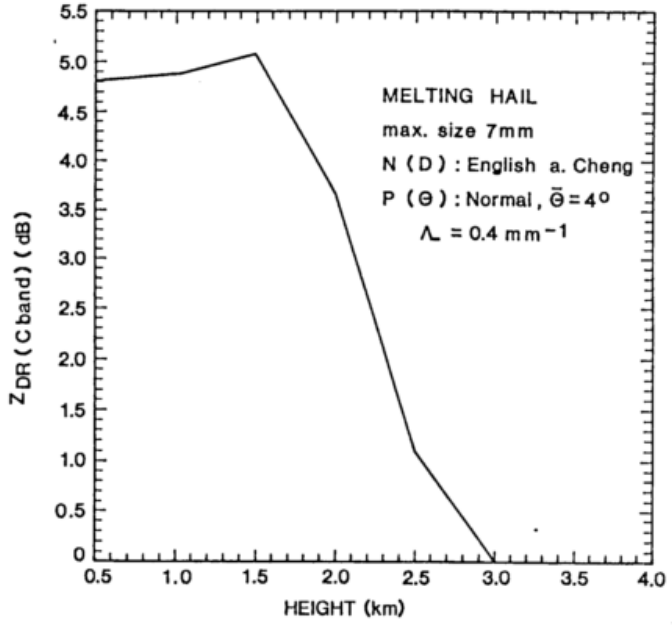


Figure 4. **Same as Fig. 3, except Z_{DR}**

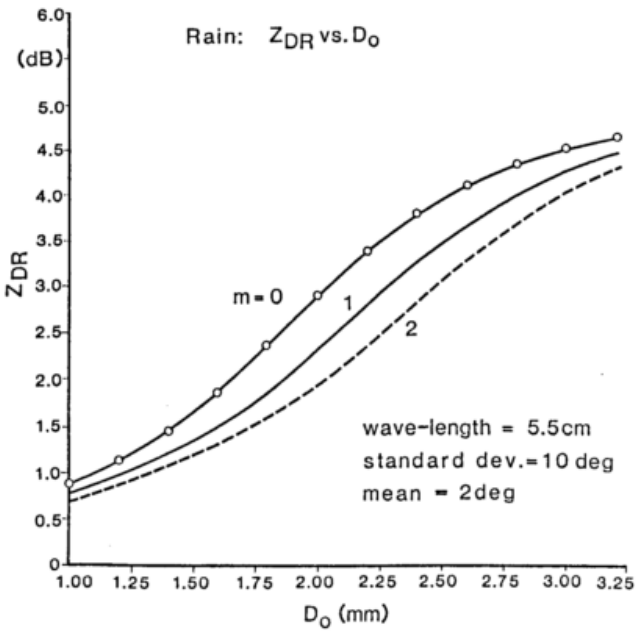


Figure 5. Z_{DR} versus D_0 for raindrop distributions, see text.

4 References

AYDIN, K.; SELIGA, T.A.; and BALAJI, V., 1986: Remote Sensing of Hail with a Dual Linear Polarization Radar. J. Climate Appl. Meteorol., 25, 1475-1484.

BRINGI, V.N.; RASMUSSEN, R.M.; VIVEKANANDAN, J., 1986a: Multiparameter Radar Measurements in Colorado Convective Storms, Part I: Graupel Melting Studies, J. Atmos. Sci., 43, 2545 - 2563.

BRINGI, V.N.; VIVEKANANDAN, J.; and TUTTLE, J.D., 1986b: Multiparameter Radar Measurements in Colorado Convective Storms, Part II: Hail Detection Studies, J. Atmos. Sci., 43, 2564 - 2577.

HALL, M.P.M.; GODDARD, J.W.F.; and CHERRY, S.M., 1984: Identification of Hydrometeors and Other Targets by Dual-Polarization Radar. Rad. Sci., 19, 132-140.

ILLINGWORTH, A.J.; GODDARD, J.W,F.; and CHERRY, S.M., 1987: Polarization Radar Studies of Precipitation Development in Convective Storms, Q.J.R. Met. Soc., 113, 469-489.

ILLINGWORTH, A.J.; GODDARD, J.W.F.; and CHERRY, S.M., 1986: Detection of Hail by Dual-Polarization Radar, Nature, 320, 431-433.

MEISCHNER, P.; BRINGI, V.N.; and JANK, T., 1988: Multiparamter Doppler Radar Observations of a Squall Line with the Polarimetric DFVLR Radar. 10th Int. Cloud Phys. Conf. 1988, Bad Homburg, F.R.G.

RASMUSSEN, R.M.; LEVIZZANI, V.; and PRUPPACHER, H.R., 1984: A Wind Tunnel and Theoretical Study of the Melting Behavior of Atmospheric Ice Particles. III. Experiment and Theory for Spherical Ice Particles of Radius > 500 μm. J. Atmos. Sci., 41, 381-388.

SCHROTH, A.; CHANDRA, M.; and MEISCHNER , P., 1988: A C-Band Coherent Polarimetric Radar for Propagation and Cloud Physics Research, to appear in J. Atm. Ocean. Techn.

TEST OF PARAMETERIZATION SCHEMES FOR CLOUD MICROPHYSICAL PROCESSES IN A 3-D MESOSCALE MODEL

L. Levkov, D. Jacob, D. Eppel, H. Grassl
Institut für Physik, GKSS-Forschungszentrum Geesthacht
2054 Geesthacht, Federal Republic of Germany

1. INTRODUCTION

In this paper a parameterization scheme for penetrative convection is presented. The influence on the large scale is investigated by incorporating the scheme into a three-dimensional mesoscale model. Results obtained from simulations using data from KonTur experiment and data from GATE are discussed.

2. MODEL

The model solves mesoscale prognostic equations for momentum, velocity components, potential temperature $\bar{\theta}$, specific humidity $\bar{q}$, in-cloud liquid water specific humidity $\bar{q}_L$, and rainwater specific humidity $\bar{q}_k$ using a grid spacing of 10 km horizontally and 500 m vertically.

The convective parameterization scheme is based on a specific one-dimensional cumulus cloud model (LEVKOV et al. 1986). The updraft is initialized by assuming a vertical velocity at cloud base computed by

$$\omega_{CB} = k\omega_* \qquad (1),$$

where ω_* is Deardorff's convective velocity scale. k accounts for partial coverage of a grid cell and clouds of different forms and sizes and development stages inside the cell. From KonTur experiment k is estimated to be $k = 1/10$.

The liquid water is divided into cloud water and rainwater. The cloud water is increased by the amount of vapor condensed in the interval ΔZ, CR, and is reduced by the autoconversion process to raindrops, A, and by raindrops collecting cloud drops. Rainwater is increased via the last two mechanisms, and is decreased by fall-out F, and evaporation E (KESSLER 1969, BERRY 1967, p. 688). The change of a cloud variable due to convection is paramaterized according to YANAI et al. 1973, p. 611. The rainfall rate R_f at a grid point is

$$R_f = 18.35\,(\bar{q}_k \cdot 1.3 \cdot 10^3)^{9/8}\ [\mathrm{mm\ h^{-1}}] \qquad (2),$$

where $\bar{q}_k$ is in kg/kg.

3. RESULTS

The calculated rainfall rate over 24 hours in the region of the intertropical convergence zone (2 September, 1974) lies between 0.1 and 12 mm/h. For the North Sea the values are between 0.5 and 3.5 mm/h for 13 October, 1981.

Additional simulations using identical initial GATE conditions were performed with different threshold values in Kessler's autoconversion formula and Berry's formula. For the Kessler case the calculated rainfall rate are smaller in case of higher threshold values (Fig. 1).

In Berry's formula no threshold value exists. The difference to Kessler's formula is most prominent for maritime clouds (drop concentration N = 100 cm^{-3} and initial radius dispersion coefficient ν = 0.25) so that the entire history of coalescence precipitation growth in a cumulus is different. In this case the model predicts more rainwater than for Kessler's original microphysical scheme (Fig.2, Fig.3).

Moreover a parameterization of ice-phase precipitation processes is included in the scheme. For the determination of active natural ice nuclei Fletcher's exponential form, Vali's observational results and Koenig's equations are used. It is shown that the production terms for snow via accretion mechanism are much larger than the autoconversion and deposition sources. The calculated transformation rates via Bergeron process are much smaller than the other snow production terms.

Simulations which include a parameterized ice-phase cloud microphysics in a 3-D mesoscale model are reported.

REFERENCES

BERRY, E.X.: Cloud droplet growth by collection. J. Atmos. Sci. 24 (1967) Nr. 6, p. 688.

KESSLER, E.: On the distribution and continuity of water substance in atmospheric circulation. Met. Monogr. 32 (1969), American Met. Soc., Boston, Mass.

LEVKOV, L., EPPEL, D., GRASSL, H: Simulation of convection over the ocean in the region of the intertropical convergence zone, GKSS 86/E/ 55.

YANAI, M., ESBENSEN, S., CHU, J.M.: Determination of the bulk properties of tropical cloud clusters from large-scale heat and moisture budgets. J. Atmos. Sc. 30 (1974) Nr.3, p. 611.

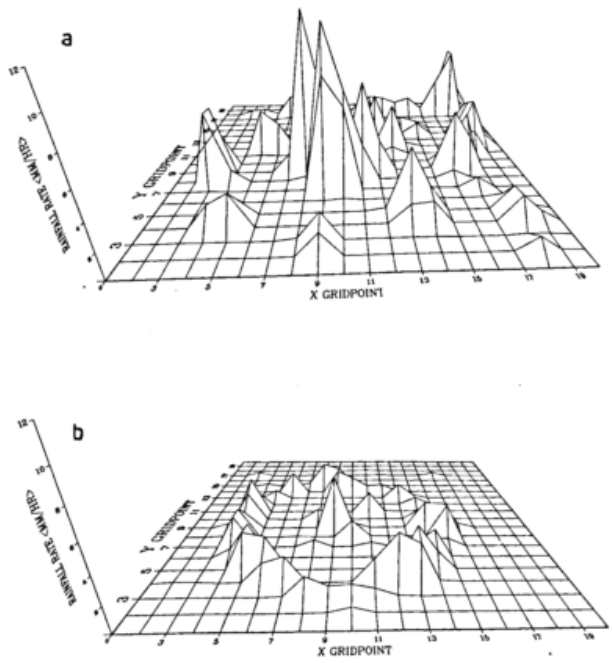


Fig. 1: Three dimensional representation of rainfall rate using different threshold values in Kessler's autoconversion formula.
a: smaller, b: higher threshold values

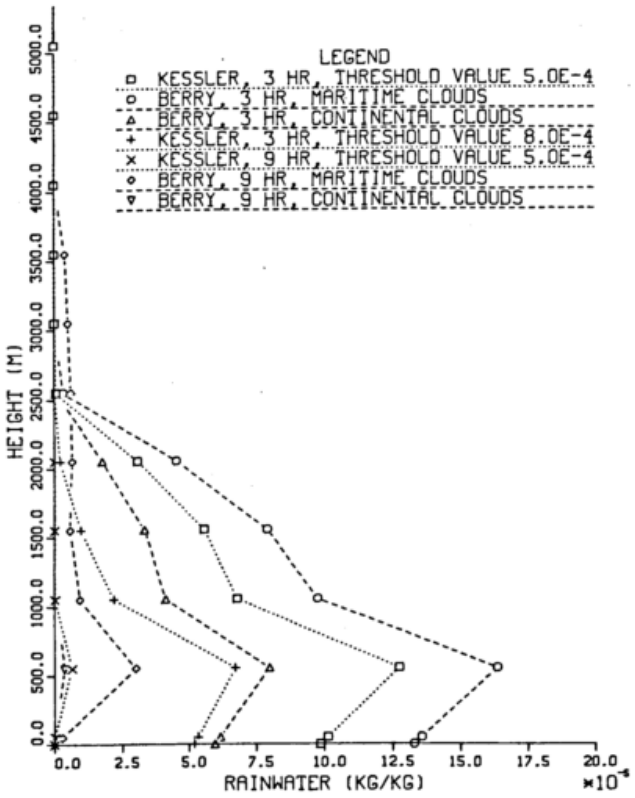
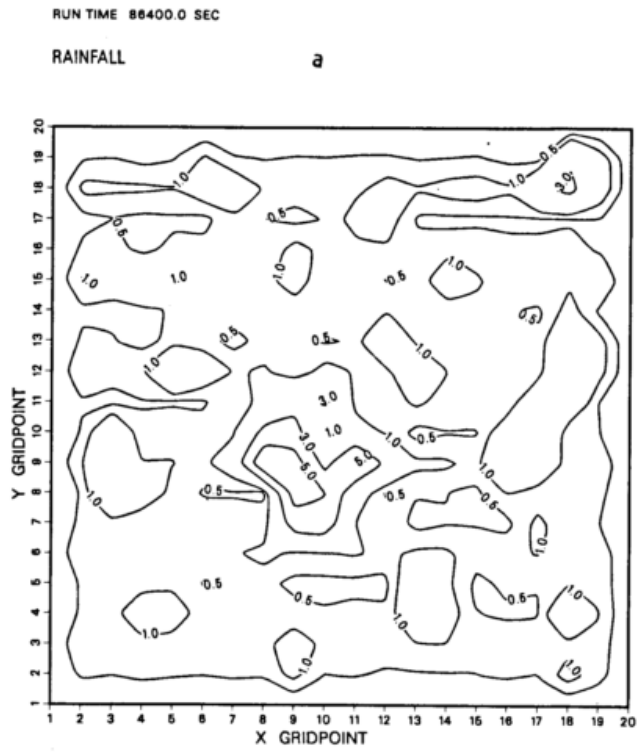


Fig. 2: Vertical profiles of rainwater above a surface grid point covered by clouds. The dotted curves were obtained with Kessler's formula, the dashed ones with Berry's formula.



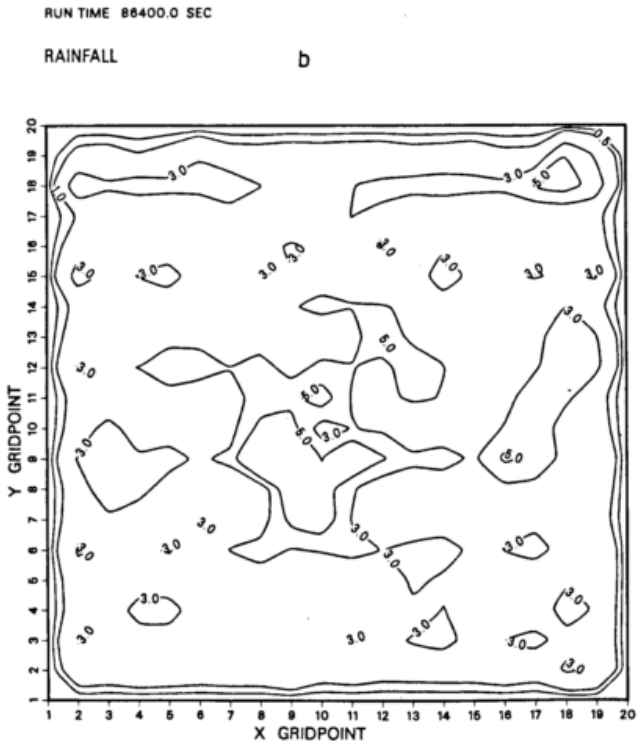


Fig. 3: Comparison of rainfall (mm) for different parameterization
a) Kessler's autoconversion formula
b) Berry's formulation for maritime environment.

DEVELOPMENT OF ANALYTICAL METHODS FOR THE INVESTIGATION OF CLOUDS, FOG AND RAIN TOGETHER WITH THE GASEOUS PHASE AND RESULTS OF FIELD MEASUREMENTS

K. Bächmann, U. Sprenger, G.R. Fuchs-Pohl, W. Schmied, P. Zeißler
Technische Hochschule Darmstadt, Fachbereich Anorganische Chemie und Kernchemie
D-6100 Darmstadt

1. INTRODUCTION

To understand chemical reactions and transport processes in hydrometeors it is necessary to obtain profound knowledge on the concentrations of inorganic and organic compounds in the liquid phase (clouds, fog and rain), in particles and in the gasphase. Therefore, analytical methods for species of interest must be developed with the aim to reach high time resolution of sampling. This is only possible with very low limits of detection.

2. DEVELOPMENT OF ANALYTICAL METHODS

2.1. AMMONIUM AND GASEOUS AMMONIA

Flow injection analysis with a gas diffusion technique and conductivity detection is used for the determination of ammonium (VAN SON 1983, p. 271). According to the acceptor used (H_2O or H_3BO_3), the limit of detection is 0.23 ng or 0.5 ng (abs.),respectively. Gaseous ammonia is sampled with a scrubber technique. It is possible to analyse continuously or discontinuously (60 samples per hour).

2.2. PROTONES

Flow injection analysis based on a reaction of an adequate acid/base indicator (kongo red or methyl red) followed by UV-photometric dedetction is used for the determination of the H^+-concentration in a continuous mode (ISHIBASHI 1986, p. 224).

2.3. ALCALINE AND EARTHALCALINE METALIONS

Alcaline and earthalcaline metalions (Na^+, NH_4^+, K^+, Ca^{2+}, Mg^{2+}) are measured with indirect UV-spectroscopy or indirect fluorescence with Ce^{3+} as eluent (SHERMAN 1987, p. 490). This methods allows a sample volume of 50 µl for the analysis of all ions.

2.4. BROMIDE

Ion chromatography with conductivity detection or amperometric detection can be used for the determination of bromide. The bromide concentrations are much lower than those of chloride, nitrate and sulfate. When conductivity detection is employed, the bromide signal is disturbed by the nitrate signal if the nitrate/bromide ratio exceeds 1600. When amperometric detection is used existing sulfite must be oxidated by Co^{3+}/oxygen before analysing.

2.5. NITRITE

Excess of chloride effects that the nitrite peak is overlapped by the chloride peak in the analysis of nitrite with ion chromatography and conductivity detection. In this case, chloride can be separated by using a column packed with silver nitrate which is connected in front of the separation column. This allows the determination of concentrations in the lower ppb-level.

2.6 ORGANIC ACIDS

Organic acids as formic acid, acetic acid, methane sulfonic acid (degradation product of reduced sulfur compounds) and pyruvic acid (degradation product of isoprene) are measured using ion exchange chromatography or ion exclusion chromatography (ANDREAE 1987, p. 6635). The acids are pre-concentrated by a solid phase extraction in which the acids are retained on a column with quarternary amine groups.

2.7. ALDEHYDES AND KETONES

Normally, aldehydes and ketones are analysed with HPLC after derivatisation DNPH (KUWATA 1979, p. 264; STEINBERG 1984, p. 253). To improve this method, a solid phase derivatisation and extraction with DNSH (HARTMANN 1987; JOHNSON 1981, p. 7) is used for pre-concentration. The separation is carried out with HPLC and gradient elution after extraction, and subsequent fluorescence detection. This method can be applied to the liquid as well as to the gaseous phase.

2.8. CHLOROACETATE/DICHLOROACETATE

To determine these compounds (degradation products of chlorinated hydrocarbons) in hydrometeors or in aerosols, an ion chromatographic pre-concentration and separation technique was developed (FUCHS 1987, p. 126, FUCHS 1987, p. 205). The detection limits for chloroacetate are 0.1 ng/ml, for dichloroacetate 0.4 ng/ml, respectively

3. FIELD MEASUREMENTS

Field measurements were taken in Darmstadt (rain, gasphase, aerosols), Kolmbach/Odenwald (rain, fog), during a meteor cruise from Palermo to Hamburg (rain, gasphase, aersols) and on Sylt (clouds, gasphase, aerosols). Additionally, cloud samples from Whiteface mountain (N.Y., USA) were analysed. The results will be presented.

LITERATURE

ANDREAE, M.O., TALBOT, R.W., LI, S.M.: Atmospheric measurements of Pyruvic and Formic Acid, J. Geophys. Res. 92 (1987), p. 6635-6641.

FUCHS, G.R., BÄCHMANN, K.: Evaluation of Analytical Methods for the Determination of Degradation Products of Chlorinated Hydrocarbons, In: Physico-Chemical Behaviour of Atmospheric Air Pollutants, Reidel, Dordrecht: G. Angeletti, G. Restelli (1987).

FUCHS, G.R., BÄCHMANN,K.: Ionenchromatographische Bestimmung von Chloracetat und Dichloracetat in Niederschlagswasserproben, Fres. Z. Anal. Chem. 327 (1987),p.205-212.

HARTMANN, W.R.: Entwicklung einer Methode zur Bestimmung von Carbonylverbindungen und Carbonsäuren in der Atmosphäre, Diplomarbeit, Darmstadt (1987).

ISHIBASHI, N., IMATO, T.: Flow Injection Analysis by Using acid Base or Metal-Ligand Buffers and Color Indicators, Fres. Z. Anal. Chem. 323 (1986), p. 224-228.

JOHNSON, L., JEFFERSON, B., MARSTOP, P.: Determination of Carbonyl Compounds in Automobile Exhaust Samples, Intern. J. Environm. Anal. Chem. 18 (1981), p.7-26.

KUWATA, K., VEBORI, M., YAMASAKI, Y.; Determination of Alphatic and Aromatic Aldehydes in Polluted Air as their 2,4-Dinitrophenyl-hydrazones by HPLC, J. Chromtogr. Sci. 17 (1979), p. 264-268.

SHERMAN, J.H., DANIELSON, N.D.: Comparison of Inorganic Mobile Phase Counterions for Cationic Indirect Photometric Chromatography, Anal. Chem. 59 (1987),p.490-493

STEINBERG, S., KAPLAN, I.R.: The Determination of Low Molecular Weight Aldehydes in Rain, Fog and Mist by Reversed-Phase Liquid Chromatography of the 2,4-DNP-Hydrazone Derivates, Intern. J. Environm. Anal. Chem. 18 (1984), p. 253-266.

VAN SON, M., SCHOTHORST, R.C., DEN BOEF, G.: Determination of total Ammoniacal Nitrogen in Water by Flow Injection Analysis and a Gas Diffusion Membrane, Anal. Chim. Acta 153 (1983), p. 271-275.

"RAIN-AEROSOL COUPLING IN MARITIME, URBAN AND RURAL AREAS : SCAVENGING RATIO MEASUREMENTS IN RELATION WITH TRANSPORT".

J.L. COLIN and J.L. JAFFREZO

Laboratoire de Physico-Chimie de l'atmosphère. Université PARIS VII, 2, place Jussieu - 75251 PARIS Cedex 05, FRANCE.

1. INTRODUCTION

The relationship between a wet deposition and the aerosol which enriches it can be evaluated for each element by means of a simplified coupling constant, the scavenging ratio (CHAMBERLAIN A.C., 1960) defined as the dimensionless ratio of the concentrations in the two phases. However, available studies show a wide range of values for these constants, the reasons for which are difficult to identify because of the very different experimental techniques employed. We have undertaken a comparative study with 3 sampling campaigns, in a coastal maritime site (Brittany), in an urban area (Paris) and in the country (Vosges), using identical sampling techniques. Moreover, these three campaigns were carried out during the same winter months so as to minimize seasonal variations.

2. EXPERIMENTAL WORK

The conditions for sampling the rain and the associated aerosol were designed so as to optimize collection of the two interacting phases: wet-only event-by-event collection of rain, while aerosols are sampled continuously for 6 hours. This short time makes it possible to relate precisely each rain event to the associated aerosol. The sampling sites were chosen at the same latitude from one side of France to the other. This situation corresponds to the general West/East air flow patterns. It is thus possible to observe the effect of transport on the interphase exchanges processes. Furthermore, the urban site, unlike the others, has a very high aerosol concentration which should maximize the role of local scavenging.

The elements chosen (Na, Mg and Cl; marine source) ; (Al, Si, Fe, Ca and K; crustal source) ; (Zn and S; anthropogenic source) have well differentiated physicochemical characteristics as regards both the size of the particles which bears them and their intrinsic hygroscopic properties. Those two factors are of primordial importance in the scavenging processes.

3. RESULTS - DISCUSSION

The scavenging ratios are calculated

by the following equation :

$W = [C]_{water} * \rho / [C]_{aerosol}$

with $[C]_{water}$ in µg*g-1, $[C]_{aerosol}$ in µg*m-3 and ρ = 1200 g*m-3, the density of air.

3.1. EFFECT OF THE RECEPTOR SITE

The values found in rural areas are higher than those of the town. This tendency is especially marked for the insoluble, crustal elements (Fig. 1).

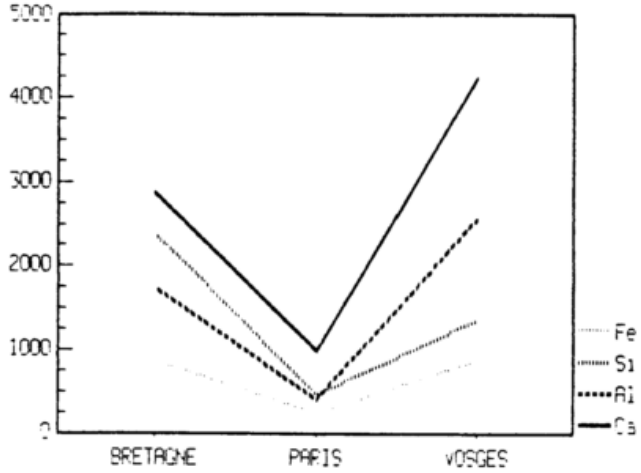


Fig. 1: Dependence of W on receptor site for insoluble elements.

For these elements, the aerosol at the Paris site is characterized by concentrations an order of magnitude greater than those in the country. The reduction of the scavenging ratios could be attributed to a limitation in the interphase exchange processes. For the soluble elements (Fig. 2), this kind of effect in the urban atmosphere is much less marked. Only the species typical of anthropogenic activity follow this trend, that is SO4= and Zn, present in the aerosol at levels much higher than in the rural area. The scavenging ratios for elements of marine origin, Na and Mg, decrease continuously across France, while that of Cl- increases considerably. This is attributed to an increase in the degasing of HCl from the aerosols as the acidity increases (ERIKSSON E., 1960) across the country. This gaseous fraction is not taken into account by our measurements but would be effectively scavenged by the precipitations.

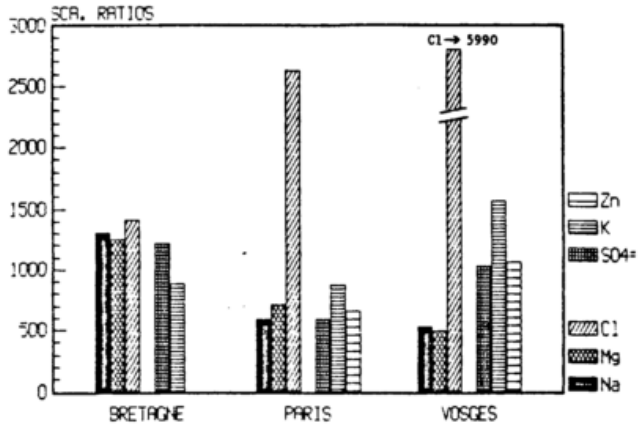


Fig. 2: Dependence of W on receptor site for soluble elements.

3.2. EFFECT OF PARTICLE SIZE

Figures 3-5 show the dependence of the scavenging ratios on the mass-median-diameter (MMD) of the elements, for the different sites. The scavenging ratios found on the coast (Fig. 3) reveal no particle-size dependence, in agreement with previous results obtained in marine areas (BUAT-MENARD P. and DUCE R.A., 1986). On the other hand, the curves obtained for the other sites (Fig. 4-5) indicate an increasing dependency with the distance from the coast (i.e. longer transport times). Those curves are similar

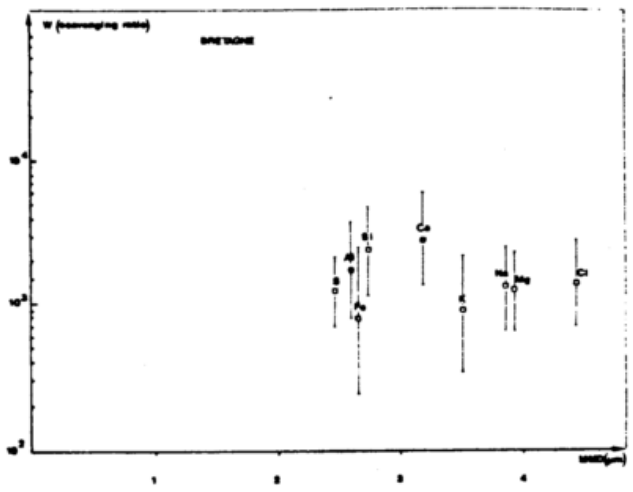


Fig. 3 : Scavenging ratios (Brittany)

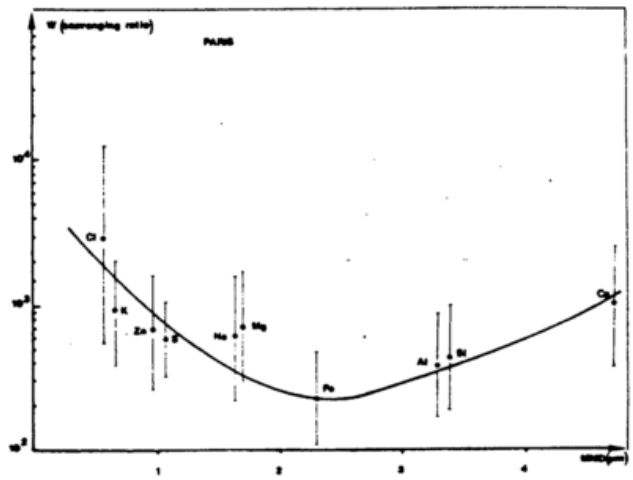


Fig. 4 : Scavenging ratios (Paris)

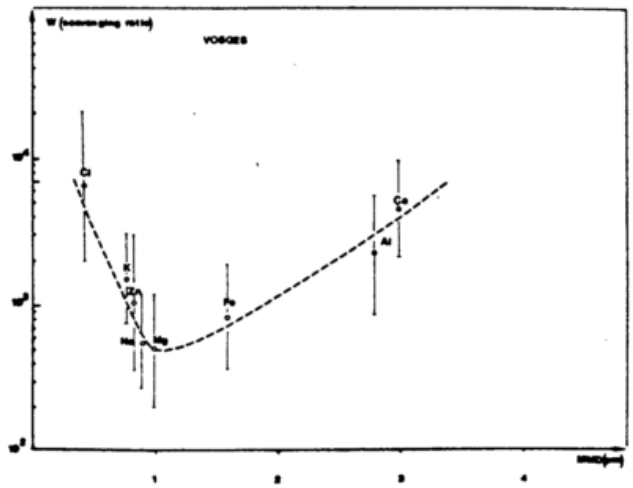


Fig. 5 : Scavenging ratios (Vosges)

to results of theoretical studies (SLINN W.G.N., 1983) which predict an increase in collection efficiency with the MMD for values above 1 µm. On the other hand, a greater increase of experimental values for submicron particles can be attributed to the high solubility of the species involved (JAFFREZO J.L. and COLIN J.L., 1988).

4.CONCLUSION

The scavenging ratio is practically the only geochemical tool available for the prediction of flux due to wet deposition. These coefficients have been shown to depend markedly on the location of the receptor site. They provide however information about incorporation mechanisms. The experimental pattern approaches theoretical curve of collection efficiency, for long transport times. There is a clear distinction between soluble and insoluble elements which suggests different incorporation processes.

REFERENCES

BUAT-MENARD P. and DUCE R.A.(1986) Precipitation scavenging of aerosols particles over remote marine regions. Nature, 321, 508-510.

CHAMBERLAIN A.C.(1960) Aspects of the deposition of radioactive and other gases and particles. Int. J. Air Poll. 3, 63-88.

ERIKSSON E.(1960) The yearly circulation of chloride and sulfur in nature. Meteorological, geochemical and pedological implications. Part II. Tellus, 12, 63-109.

JAFFREZO J.L. and COLIN J.L.(1988) Rain-aerosol coupling in urban area: scavenging ratio measurements and identification of some transfer processes. Atm. Env., in press.

SLINN W.G.N.(1983) Air to sea transfer of particles. In air-sea exchange of gases and particles, P.S. Liss and W.G.N. Slinn (eds), D. Reidel, 455-532.

THE RAINOUT REMOVAL OF SULFUR DIOXIDE AND ACIDIFICATION OF PRECIPITATION FROM STRATIFORM CLOUDS

Qin Yu

Department of Geophysics, Peking University
Beijing, China

1. INTRODUCTION

The rainout removal of SO2 and the acidification of precipitation from stratiform clouds are simulated with a one-dimensional, time-depandent and parameterized microphysical model, in which the dissolution and dissociation of the gaseous SO2 and oxidation reaction in aqueous phase are considered. The dynamic effects, updraft flow and turbulent transport, on pH value of the rainwater and on the wet deposition rate of SO2 are discussed.

2. MODEL

On the definite thermo-dynamic background,the parameterized microphysical processes of three water contents, i.e. water vapor, cloud water and rainwater, are considered as condensation, autoconversion and collection. The balance equations are written as following.

$$\frac{\partial Q}{\partial t} + (W-V)\frac{\partial Q}{\partial z} = K\frac{\partial^2 Q}{\partial z^2} + S$$

where Q represents mixing ratio of water contents, also other species. W is the updraft velocity and V is the average terminal fall velocity of raindrops. K is the turbulent transfer coefficient. S are source or sink terms. The discription in detail can be find in the paper (Qin and Chameides 1986). The sensitivity test indicated that the updraft flow controled the evolution of the clouds and precipitation and the effect of turbulent transfer on the evolution was insignificant.

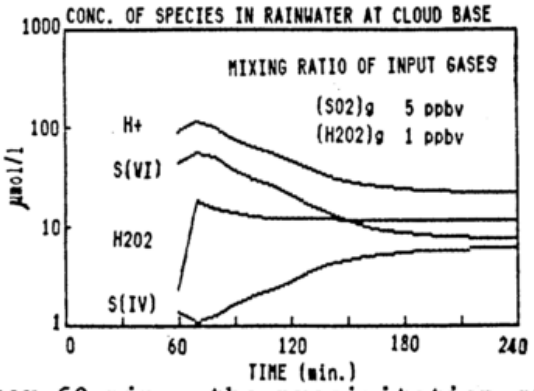
The dissolution of SO2 and H2O2 or O3 into cloudwater and rainwater and dissociation are considered as scavenging of gases by water drops. The production rates of S(VI) in cloudwater and rainwater through the oxidation reaction of S(IV) by H2O2 or O3 are from Martin (1983). The transfer of species in aqueous phase from cloudwater into rainwater with autoconversion and collection processes are also included in the source and sink terms.

At initial time, the satuation state of water vapor at every level is supposed. The mixing ratio of SO2 has a damped exponential profile with 2 km. scale height. A finite-difference method is used to resolve the equations.

3. RESULTS

3.1 The time variation of the species in rainwater at cloud base.

A 'standard case' is given in following figure, where the parameters are taken as W=0.1m/s, K=20m*m/s, cloud depth= 3000km and initial pH of cloudwater is 5.6. The input values of SO2 and H2O2 at cloud base are 5 and 1 ppbv., respectively.



After 60 min., the precipitation start at cloud base. At 70 min., the pH and concentration of S(IV) in rainwater are minimum, then the values increased with time and trend to steady values. The concentration of S(VI) and H2O2 correlate with prescribed values inversely. This first 60 min. is long enough to dissolve SO2 and H2O2 into cloudwater and form S(VI),then they are transfered to rainwater in autoconversion and collection processes. During the steady state, the duration that the cloudwater

and rainwater stay in the cloud is not longer enough to transfer S(IV) to S(VI). The concentration of H2O2 in rainwater is higher than 10 μmol/l. These results are consistent with some field observation.

3.2 THE EFFECTS OF W AND K

For numerical tests, various values are taken as 0.1, 0.05m/s for updraft and 20, 40 mxm/s for turbulent transfer coefficient. The comparison of results are listed in the following table. In the table, there is a remaval rate of SO2 by the cloud system,Vwd, is defined as the fallout flux of whole sulfur in rainwater divided by mixing ratio of gaseous SO2 at cloud base.

TABLE. CONCENTRATION OF SPECIES IN RAINWATER AT CLOUD BASE (240 min.)

Input values and rain intensity

case	1	2	3
W m/s	0.1	0.05	0.1
K mxm/s	20	20	40
SO2g ppb	5	5	5
H2O2g ppb	1	1	1
I mm/hr	2.4	1.1	2.3
Conc., pH of rainwater and Vwd of SO2			
S(IV) μmol/l	5.85	3.37	4.43
S(VI) μmol/l	7.40	16.30	11.44
H2O2 μmol/l	11.12	14.30	12.55
pH	4.67	4.43	4.55
Vwd cm/s	5.3	3.6	6.0

From the table, it can be found that the weaker updraft verocity is, the smaller intensity of rainfall, the higher concentration of whole sulfur, the lower of H2O2 and smaller pH in rainwater will be, although the removal is still higher in the case of stronger updraft flow.

Effects of the turbulent transport are different from the updraft flow. The larger value of K can enhance the acidity of rainwater and the removal of SO2 by rainwater. It can be explained that H2O2 is a highly soluble, so that the gas-phase concentration would be lower in the middle part of the cloud. The turbulent transport could increase the inflow flux of gaseous H2O2 into the cloud system, therefore, the oxidation reaction of SO2 in water could be enhanced. It would be natural that the larger K is, the lower pH values of rainwater and the higher removal of SO2 will be. The similar numerical experiment of O3 has be done. Effects of K on pH and the removal rate has not been found. Turbulent processes are likely to be variable in time and space and we know that only a little. Uncertainty will be significant.

REFERENCES

MARTIN, L.R.: Kinetic studies of sulfite oxidation in aqueous solution. "Acid precipitation: SO2, NO2 and NO oxidation mechanism: atmospheric considerations", edited by J.Calvert. Ann Arbor Sci. Pub., Ann Arbor, Mich. 1983.

QIN, Y.; CHAMEIDES, W.: The removal of soluble species by warm stratiform clouds, Tellus, 38B (1986) 285-299.

STRUCTURAL AND TEXTURAL CHARACTERISTICS OF CIRRUS CLOUDS

K. S. Kuo, R. M. Welch, and S. K. Sengupta

Institute of Atmospheric Sciences
South Dakota School of Mines and Technology
Rapid City, South Dakota 57701-3995

Department of Computer Science
South Dakota School of Mines and Technology
Rapid City, South Dakota 57701-3995

1. INTRODUCTION

Low resolution meteorological satellite sensors often give the impression that cirrus are structurally featureless. However, the LANDSAT high spatial resolution sensors reveal that even cirrostratus formations have significant structural detail. The first portion of this study examines representative cirrus structural characteristics.

The second portion of this study is concerned with determining the textural characteristics of cirrus clouds. Texture may be interpreted as a set of statistical measures of the spatial distributions of gray levels in an image. The present study is restricted to the co-occurrence statistical model (HARALICK, 1979; CONNORS and HARLOW, 1981).

Twelve LANDSAT MSS scenes were used for this study, including representative cirrus, cirrocumulus, and cirrostratus scenes. Band 3 (0.7-0.8 μm) digital data were used, with 57 m spatial resolution.

2. STRUCTURAL CHARACTERISTICS

The Reflectance Threshold Method (WIELICKI and WELCH, 1986) is used to separate cloud pixels from background. Because of their semi-transparent nature, cirriform clouds can be difficult to detect and segment from the background in satellite imagery. Analysis of various threshold approaches is given by WIELICKI *et al.* (1986) and WELCH *et al.* (1988a).

The "cloud cover threshold" segments cloud regions from the background. However, should this threshold value be used to determine cloud structure for these scenes, large regions of the cloud field would be classified as single clouds, providing little or no insight into the underlying cellular cloud structure. Therefore, we define the "cloud cell threshold" to be the median cloud reflectance, separating the brightest half of the cloud pixels from the darkest half of the cloud pixels. Pixels then can be grouped into individual cells (WELCH *et al.*, 1988a).

Figure 1A shows cell size distributions for four cirrostratus cases. Note that these cloud fields do not have a simple power law distribution. Rather, these curves show concavity, with one slope for cloud cells of diameter D <1.5 km and a different slope for cloud cells of larger diameter. For a power law size distribution given by

$$n(D) = n_D D^{-\alpha} \quad , \qquad (1)$$

the slopes α range from $\alpha \simeq 2.5$-2.9 for the small cells of diameter 0.1-1.5 km and from $\alpha \simeq 1.5$-1.9 for the larger cells. This behavior is opposite to that found in stratocumulus and cumulus clouds (Fig. 1B). Stratocumulus clouds have

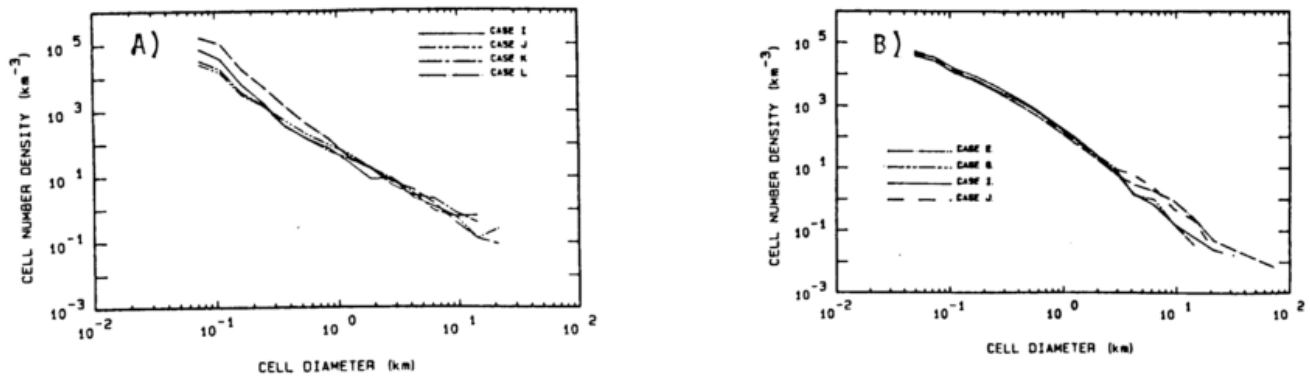


Fig. 1: Cloud size distributions vs. cloud diameter for selected cases of A) cirrus; and B) stratocumulus. Values are given as the number of clouds per (100 km)^2 surface area per 1 km cloud size interval.

slopes ranging from $\alpha \simeq 1.5$-1.9 for the smaller cells of $D < 1.5$ km and from $\alpha \simeq 2.5$-2.9 for the large cells (WELCH et al., 1988a). Therefore, the size distribution shows convexity in stratocumulus (and cumulus) instead of the concavity in cirrus.

Closed convection patterns in stratocumulus clouds are strongly influenced by long-wave radiative cooling near cloud top (e.g., RANDALL et al., 1984). Solar heating tends to counteract the infrared cooling, potentially acting to destabilize and dissipate the layer. In contrast, solar heating in convective thin cirrus increases the vigor of circulation and produces longer lasting cells (STARR, 1987). The shapes of the size distribution curves support these interpretations.

Cloud perimeter p and cloud area A are related by

$$p = c\, A^{d/2} \quad , \qquad (2)$$

where d is the fractal dimension (LOVEJOY, 1982). Stratiform cirrus appear to be bi-fractal. There is a distinct change in fractal dimension from $d \simeq 1.5$ for cloud cells of $D < 1.5$ km to $d \simeq 1.2$-1.4 for larger cloud cells. Other cirrus types have only a single fractal dimension ($d \simeq 1.2$-1.5) for all cloud sizes.

3. TEXTURAL CHARACTERISTICS

It is assumed that textural information is characterized by a set of co-occurrence matrices $P(i,j)_{d,\phi}$ where the $(i,j)^{th}$ element is the relative frequency with which two pixels separated by distance d in direction ϕ occur in the image, one with gray level i and the other with gray level j. The textural features of contrast, correlation, angular second moment, entropy, local homogeneity, contingency, difference cluster shade and difference cluster prominence are computed from the co-occurrence matrices (HARALICK, 1979; CONNORS and HARLOW, 1981; WELCH et al., 1988b).

Contrast is the measure of local variation between pixel pairs separated by distance d at angle ϕ. Correlation measures the gray level linear dependencies in the cloud fields. Figure 2 shows the measures of contrast and correlation for the two cirrus scenes as a function of distance d at angles of 0°, 45°, 90°, and 135°. Generally, convective-type cirrus cloud fields (Case C) have higher contrast values than do cirrostratus (Case F). Also, the smaller, highly convective elements show a large variation in contrast over short distances (large initial slopes), whereas the larger more uniform stratus elements have much more gradual slopes. Macrotexture is a descriptor of the textural components of the cloud field as a whole, as described by asymptotic values of texture. Clearly, asymptotic values are not reached even at a distance of 25 km for Case F. This is a clear indication that Case F consists of large sheets of relatively solid cirrus.

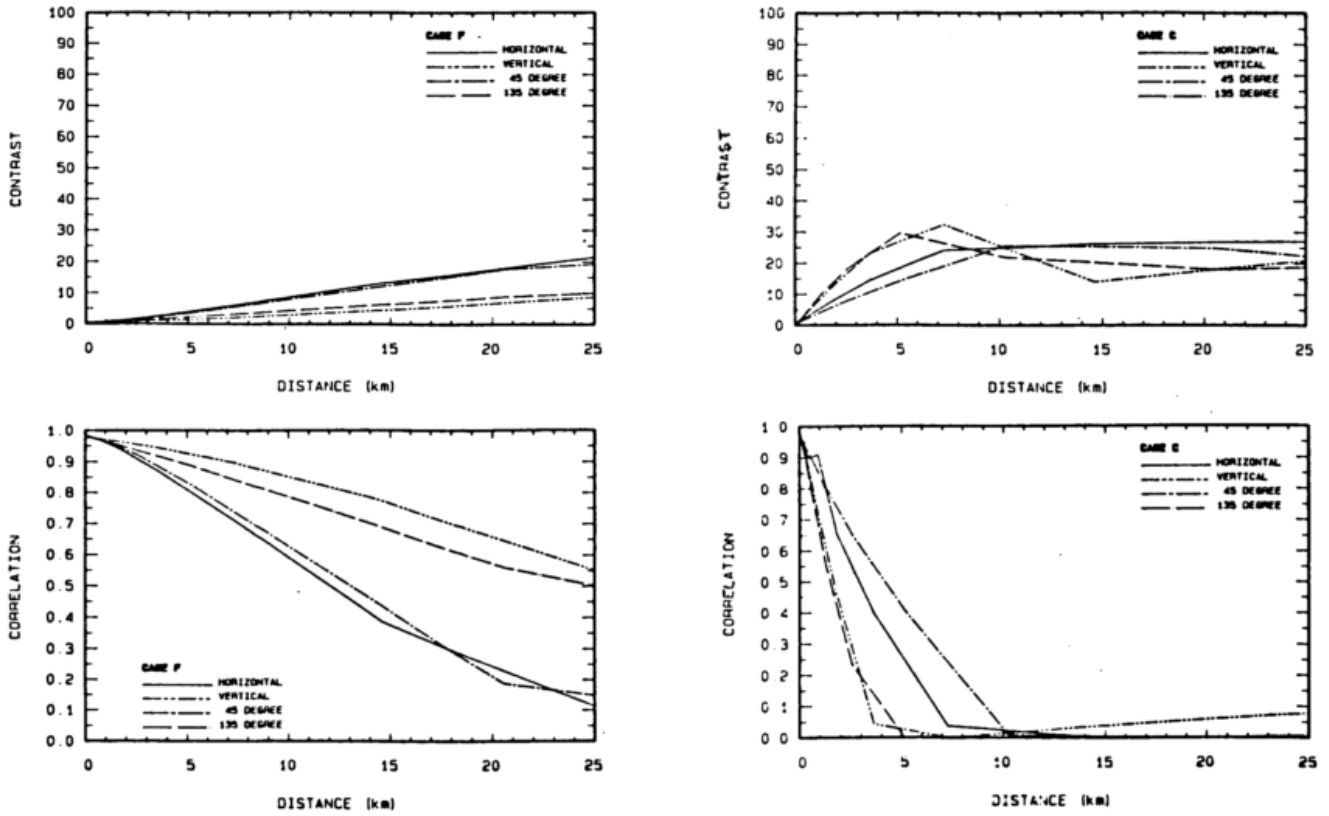


Fig. 2: Directional contrast and correlation measures for cirrostratus (Case F) and cirrocumulus (Case C) clouds.

Cloud fields composed primarily of small elements show a rapid decrease in correlation coefficient over short distances. Convective cirrus such as Case C have this behavior. As the size of the cloud elements increases, the correlation coefficients show increasingly more gradual slopes (Case F).

Directionality is also determined from the texture measures. Case F has very high values of correlation and low values of contrast at angles of 90° and 135°. Image processing reveals cloud alignment at an angle of about 120°.

These results suggest that textural features can be used effectively to classify cloud types. On the basis of this work, Welch et al. (1988c) show that cumulus, stratocumulus, and cirrus clouds can be classified with an accuracy of 95% using only a single visible channel. It is significant that textural measures are capable of distinguishing cirrus clouds from low clouds solely on the basis of spatial brightness patterns.

REFERENCES

CONNORS, R. W., HARLOW, C. A.: Toward a structural textural analyzer based on statistical methods. A. Rosenfeld (ed.), Image Modelling. New York: Academic Press, (1981) 29-61.

HARALICK, R. M.: Statistical and structural approaches to textures. Proc. IEEE, Vol. 67, (1979) No. 5, 786-804.

LOVEJOY, S.: Area-perimeter relation for rain and cloud areas. Science, 216, (1982) 185-187.

RANDALL, D. A.; COAKLEY, J. A., JR.; FAIRALL, C. W.; KROPFLI, R. A.; LENSCHOW, D. H.: Outlook for research on subtropical marine stratiform clouds. Bull. Am. Met. Soc., 65, (1984) 1290-1301.

STARR, D. O'C.: Effects of radiative processes in thin cirrus. J. Geophys. Res., 92, (1987) 3973-3978.

WELCH, R. M.; KUO, K. S., WIELICKI, B. A.; SENGUPTA, S. K.; PARKER, L.: Marine stratocumulus cloud fields off the coast of southern California observed using Landsat imagery. Part I: Structural characteristics. [Accepted by J. Climate Appl. Meteor., 1988a]

WELCH, R. M.; SENGUPTA, S. K.; KUO, K. S.: Marine stratocumulus cloud fields off the coast of southern California observed using Landsat imagery. Part II: Textural analysis. [Accepted by J. Climate Appl. Meteor., 1988b]

WELCH, R. M.; SENGUPTA, S. K.; CHEN, D. W.: Cloud field classification based upon high spatial resolution textural features. [Submitted for publication. 1988c]

WIELICKI, B. A.; WELCH, R. M.: Cumulus cloud field properties derived using Landsat digital data. J. Climate Appl. Meteor., 25, (1986) 261-276.

WIELICKI, B. A.; MINNIS, P.; PARKER, L.: The effect of spatial resolution on satellite derived cloud cover. Preprints Sixth Conf. Atm. Rad., (1986) Williamsburg, VA, AMS, 301-306.

CIRRUS CLOUDS AND MESOSCALE ATMOSPHERIC PROCESSES

Borisenkov E.P., Bazlova T.A.

Main Geophysical Observatory, Leningrad, USSR

1. Introduction

Cirrus clouds have a significant impact on the atmospheric thermal and dynamic structure (e.g., Borisenkov et al., 1981; Borisenkov and Efimova, 1986; Liou, 1986). They may promote precipitation in meso- and large-scale atmospheric systems by seeding lower level supercooled clouds (e.g., Rutledge and Hobbs, 1983). For this reason, investigations including numerical simulation of cirrus clouds and their role in the formation of weather and climate have received increased attention.

2. Brief model description

To study cirrus clouds-atmosphere interaction a 3-D time-dependent model is developed based on the paper by Borisenkov and Bazlova, (1986). The simulated cloud is considered a two-phaze system. The model incorporates advection, vertical motion, turbulent diffusion, phaze changes, cloud crystal growth (or evaporation) and precipitation. Parameterization of the cloud particle size spectrum in terms of the temperature and ice water content is used according to Heymsfield and Platt (1983).

3. Results

The results of numerical experiments simulating the effects of various meteorological processes on cirrus formation and evolution indicate that vertical motion is particularly important. The calculated time-dependent behavior of specific ice-water content and crystal concentration with the vertical motion effect is presented in Fig. 1, wherein their maximum magnitudes at various updraft speeds are plotted against time.

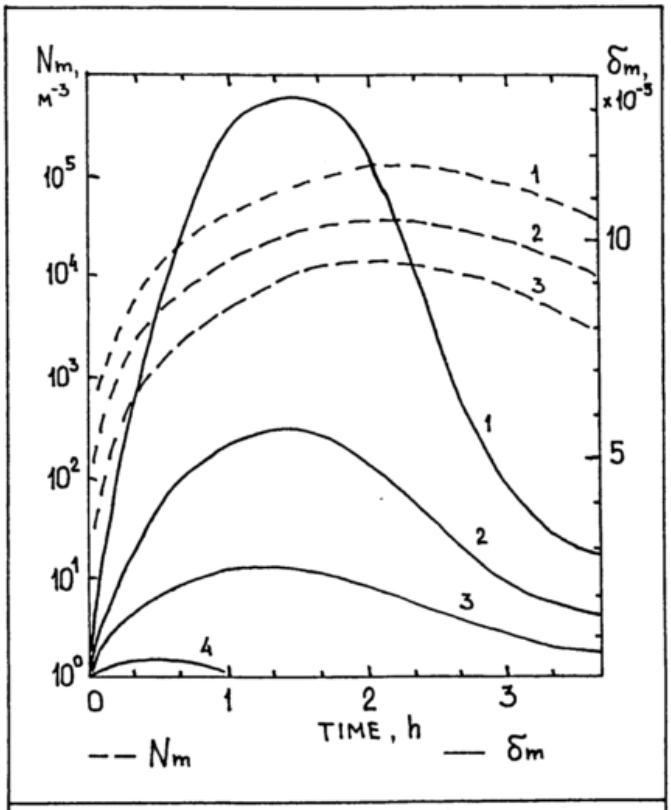


Fig. 1. Temporal behavior of maximum specific ice water content and crystal concentration during cirrus simulation at updraft speeds: 1 - 20 cm s^{-1}; 2 - 10 cm s^{-1}; 3 - 5 cm s^{-1}; 4 - 1 cm s^{-1}.

Typical updraft speeds in cirriform clouds have been found to be 10-20 cm s^{-1} at temperatures from -20 to -40°C and 1-5 cm s^{-1} at temperatures from -40 to - 60°C (Heymsfield, 1977). Variations of updraft speed from 1 cm s^{-1} in simulations leads to a two-order increase in ice water content. Such depe

ndence is associated with the supersaturation increase due to updrafts and consequent ice nuclei activation and ice crystal growth.

Radiative properties dependence on the ice water content changes during cloud lifecycle is noted. For example, an effective flux emittance, absorptance and albedo of midlatitude cirrus with mass absorption coefficient 500 $cm^2 g^{-1}$ and updraft speed 1 cm s^{-1} are calculated to be 0.62, 0.06, 0.3, respectively, during the cloud growth stage, and 0.22, 0.01, 0.17 during the decay.

Cirrus cloud dissipation is connected with ice crystal sedimentation, which, in turn, appears to promote precipitation in lower supercooled clouds by seeding. To evaluate the role of cirrus in precipitation the evolution of gravity-induced downward flux of ice water is calculated depending on humidity in subcloud layer. Simulations result in the conclusion that cirrus cloud with updraft speed ~10 cm s^{-1} (or more) provide typical mid-levelsupercooled clouds with ice crystals in sufficient amount ($\sim 10^3 m^{-3}$) if mean humidity between cloud layers is greater than 70% over ice.

With a view to study cirrus influence on weather of a limited area numerical experiments are carried out using large-scale forecast model and mesoscale cirrus cloud model by grid telescoping method.

3. Conclusions

1). Bulk properties of cirrus clouds are the result of interdependence of dynamical, thermodynamical, radiative and microphysical processes with feedbacks.

2). Large-scale vertical motion is the main factor, controlling cirrus e evolution. The turbulent diffusion is the main factor operating under weak forcing.

3). Cirrus clouds have an impacton atmospheric thermal structure and circulation through their radiative and phaze effects, depending on cloud stage. These clouds may act as a trigger for precipitation in lower clouds.

References

BORISENKOV E.P., MELESHKO V.P., SOKOLOV A.P. 1981: The effect of high clouds on the thermal regime and the circulation of the atmosphere. Meteorology and Hydrology, 11, p.5-17.

BORISENKOV E.P., EFIMOVA L.K. 1986: Peculiarities of the effect of cirrus cloud localization on the atmospheric temperature and dynamics. Trudy GGO, 503, p.76-82.

LIOU K.-N. 1986: Influence of cirrus clouds on weather and climate processes: a global perspective. Mon. Wea. Rev., 114, p. 1167-1199.

RUTLEDGE S.A., HOBBS P.V. 1983: The mesoscale and microscale structure and organization of clouds and precipitation in midlatitude cyclones. VIII: A model for the "seeder-feeder" process in warm-frontal rainbands. J. Atmosph. Sci., 40, p. 1185-1206.

BORISENKOV E.P., BAZLOVA T.A. 1986: Model of cirrus cloud evolution. Izv. Academii Nauk SSSR, Fizika Atmosph. and Ocean, 1, p.36-43.

HEYMSFIELD A.J., PLATT C, M.R. 1984: A parameterization of the particle size spectrum of ice clouds in terms of the ambient temperature and ice water content. J. Atmosph. Sci., 41, p.846-855.

HEYMSFIELD A.J. 1977: Precipitation in stratiform ice clouds: a microphysical and dynamical study. J. Atmosph. Sci., 34, p.367-381.

MESOSCALE AND MICROSCALE STRUCTURE OF CIRRUS CLOUDS: THREE CASE STUDIES

Kenneth Sassen and Michael K. Griffin

Department of Meteorology, University of Utah
Salt Lake City, Utah 84112, U.S.A.

1. INTRODUCTION

Cirrus clouds, which normally cover about 20% of the globe, are receiving increased recognition for their role as a modulator of the planet's radiation balance (for a recent survey, see Liou, 1986). However, it has only been relatively recently that instrumentation appropriate for the study of these high, cold clouds has become available, and key questions still remain to be resolved. In the United States, the First ISCCP Regional Experiment (FIRE) has been established to address basic uncertainties in our knowledge of cirrus, with the aim of improving satellite-based observing methods.

The measurements reported here are derived from three cirrus cloud case studies observed by the type of modern research instrumentation that is integral to the FIRE project. The observing techniques involved ground-based polarization lidar and Doppler radar, and aircraft operations. A variety of cirrus types are represented, including a multilayered orographic cirrus, a 6-km deep cirrostratus overcast, and a group of fibrous cirrus cloud bands associated with tropopause generating cells. The datasets describe the structure and composition of these common cirrus cloud types, and the findings provide insight into the microphysical processes and characteristic physical scales involved in the generation of cirrus cloud particles.

2. FIELD EXPERIMENTS

The data were collected during three projects involving the University of Utah mobile polarization lidar (0.7 μm wavelength) and NCAR aircraft. Two pre-FIRE field experiments supported by the NCAR Sabreliner, Lidar Cirrus I and II, were performed in October 1983 near Boulder, Colorado, and in March 1985 from near Beaver in southern Utah. Coordinated radar observations were collected in each case. The third study is comprised of lidar observations gathered from Wausau, Wisconsin on 30 October 1986, as part of the FIRE Intensive Field Observation (IFO) program.

The primary data quantities used here to describe cirrus cloud structure and composition are lidar relative (range-normalized) returned power and the lidar linear depolarization ratio δ, respectively. The lidar returned power Height versus Time (HTI) displays are not corrected for the effects of attenuation, and so the data are contoured in the relative units of dB of the maximum returned signal. Intervals of lidar δ values in the Range versus Height (RHI) and HTI displays are shaded and assigned a number, where, e.g., the lightly hatched areas labeled .4 represent $\delta = 0.4 \pm 0.05$.

3. CASE STUDIES

3.1 Orographic Cirrus (17 October 1983)

On this occasion cirrus displaying strong orographic enhancement were clearly evident in satellite imagery just downwind of the Rocky Mountain Front Range. Strong westerly flow associated with an advancing jet stream generated lee wave lenticular cirrus clouds over the site. Under these conditions the cirrus were initially comprised of a number of discrete layers, although, as synoptic-scale forcing began to dominante, the layers merged into a more vertically continuous cloud.

Figure 1 provides an RHI display (top) from coordinated lidar and NCAR CP-2 radar elevation angle scans (at 0° azimuth, approximately orthogonal to the cirrus level flow), and aircraft flight leg data. The radar reflectivity factor contours and lidar δ values both show the presence of two discontinuous cirrus layers centered at heights of ~9 and 10 km, but a lower layer containing particles too small to be detected with microwaves is also present. The near-zero δ values at portions of cloud base (filled-in) reveal the presence of highly supercooled cloud droplets, as was confirmed by aircraft probes. As shown in the bottom two panels, vertical velocities $W > 1.0$ m s^{-1} and droplet concentrations >100 cm^{-3} were encountered by the aircraft. The gradient of increasing lidar δ values above cloud base indicates that the liquid layer was rapidly glaciating at the -35°C cloud base temperature, and model simulations have shown that the 5 μm-diameter droplets froze through the homogeneous nucleation mode (Sassen and Dodd, 1988). Moreover, the convective cells embedded in the cloud base layer appear to be responsible for exchanging cloud particles between the lowest two layers, an important process in the development of this cirrus.

3.2 Widespread Cirrostratus (8 March 1985)

The extensive cirrus cloudiness was associated with an amplifying subtropical jet pattern in

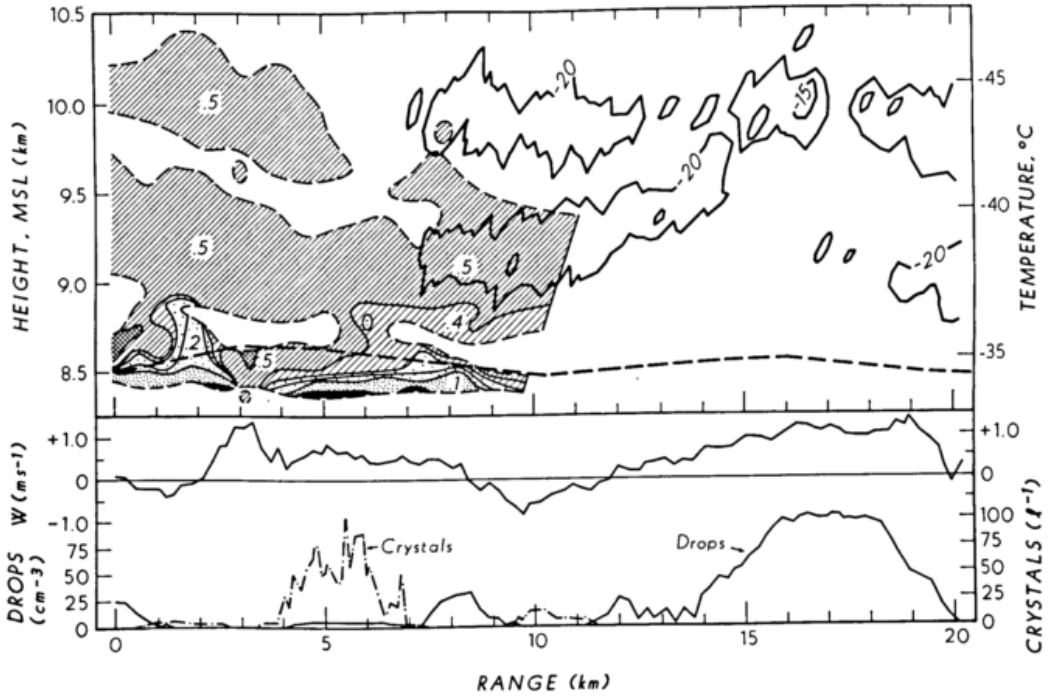


Fig. 1 RHI display of lidar δ values and radar reflectivity factors (solid lines contoured in dBZ_e for ranges ≳8 km free from ground clutter). Given in the bottom panels are vertical velocities W and FSSP cloud droplet and 2D-C probe ice crystal concentrations measured by the Sabreliner along the flight track shown as the dashed line at ~8.5 km in the RHI display.

this case. Although the cirrus over the site is quite visible in infrared satellite imagery, it is not readily apparent in visible imagery. At the field site, the cirrostratus overcast appeared thin and consistently displayed a 22° halo. However, as shown by the lidar HTI displays in Fig. 2, the cirrus had an actual thickness of ~6.0 km.

The 2.5-h segment of lidar observations shown in Fig. 2 was collected during an aircraft refueling period, but is quite interesting in that the patterns of returned laser power (top) and δ values (bottom) reveal the passage of three mesoscale generating regions. The maximum lidar returns corresponding to the generating regions and their precipitation trails are shown by the dashed lines. The upper portions of the generating cells have dimensions on the order of 100 km at 11-km altitude. When viewed at the highest available temporal resolution, such structures often display a branched appearance suggestive of complexes of convective cells (e.g., the middle generating cell at 2000 GMT), presumably on the ~1.0 km scale of cirrus uncinus. Hence, they are referred to as Mesoscale Uncinus Complexes (MUC).

The relatively low δ values (stippled regions) in the generating cells, which range from ~0.35 to 0.20, can be attributed to the scattering properties of newly-formed cloud particles, including small ice crystals, and haze or cloud droplets that reside briefly in updrafts before freezing homogeneously. Values of $\delta \simeq 0.3$ also occur sporadically in the lower cloud (outside of the precipitation trails) in the form of parcels that appear to ascend through the sheared cloud environment, and that sometimes rise from cloud base (e.g., at 1920). Positive vertical velocities

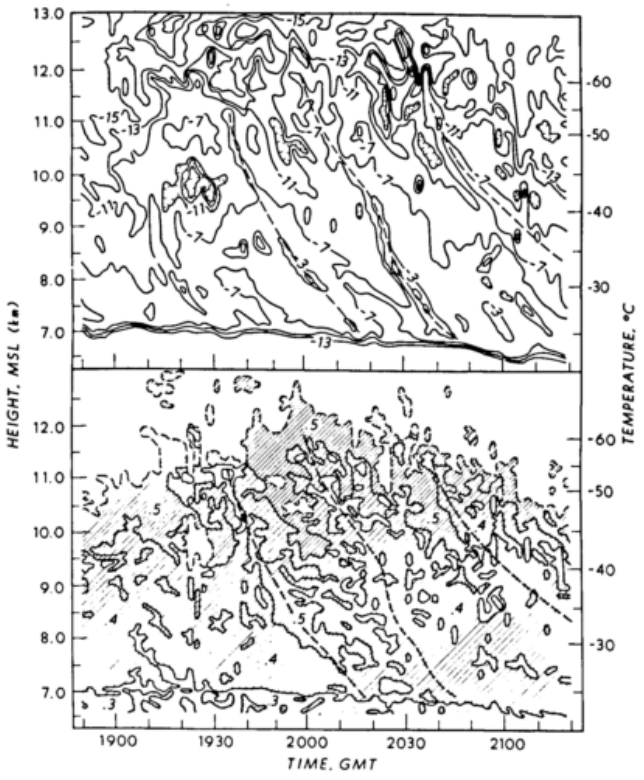


Fig. 2 HTI displays of lidar relative returned power (top) and δ values (bottom) showing the passage of the three mesoscale generating regions.

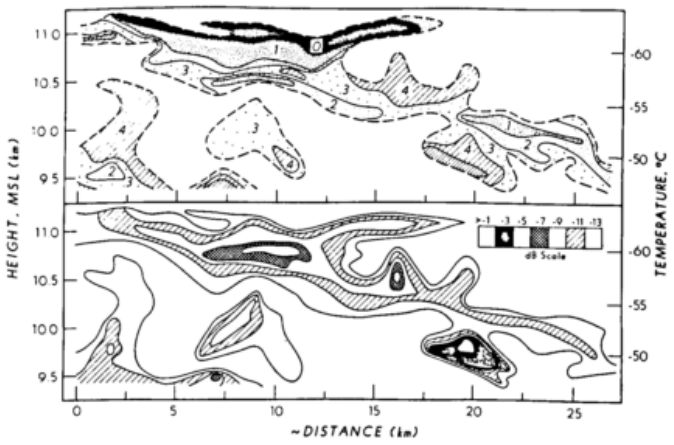


Fig. 3 Expanded view of a mesoscale uncinus complex derived from lidar depolarization (top) and returned power (bottom) measurements.

measured by the NOAA Doppler K_a-band (0.86 cm) radar were often present in these regions. These findings indicate that convective impulses embedded within the lower cloud are associated with the MUC structures observed near cloud top. The discontinuous nature of the updrafts and laser depolarization patterns would indicate a loose organization of relatively strong (~1 m s^{-1}), but intermittent vertical motions.

3.3 Cirrus Cloud Bands (30 October 1986)

Jet stream cirrus were present within the FIRE IFO area on this day, but over Wisconsin the cirrus tended to dissipate in response to a shortwave ridge. However, satellite imagery revealed that some very narrow bands, or filaments, of cirrus developed over central Wisconsin. Zenith lidar data show that the four, ~10 km-wide cloud bands present in visible satellite imagery corresponded to cloud-top mesoscale generating regions located just below the tropopause. Sheared ice crystal fallstreaks from the generating cells gradually lowered the cloud base (yielding a maximum cloud depth of 3.5 km) and also spawned new convective generating regions at lower levels, producing a visually more uniform-appearing cloud.

An expanded view of the most prominent cloud-top generating region, observed from 2215-2245 GMT, is given in Fig. 3. The time scale has been converted to distance based on the 15 m s^{-1} rate at which the bands propagated over the site, according to sequential satellite imagery. The top of the structure contains near-zero δ values, and $\delta \leq 0.15$ values are also evident in portions of the sheared fallstreak. Such low δ values could represent spherical particles, or horizontally-oriented plate crystals. In contrast, $\delta \approx 0.4$ values are found in an embedded aircraft contrail, seen as the strongly scattering region (at 20 km) just below the crystal fallstreak, and in the new convective turrets, which rise from the fallstreak in the same area. The overall structure is similar to that proposed by Heymsfield (1975) for "long-lasting" cirrus uncinus, but is here of mesoscale proportions. This is most likely due to cell spreading at the stable tropopause and to merging of individual convective elements into a MUC, where the characteristic cell scale is presumably that of the newly-formed cells seen in the trail (~1 km).

4. CONCLUSIONS

Remote sensing findings have illustrated the mesoscale organization, ranging over scales of ~10 to 100 km, of cirrus generating cells. These regions appear to be composed of complexes of cirrus uncinus cells, and so are referred to as Mesoscale Uncinus Complexes (MUC). Precipitation trails emanating from such structures have been associated with convective impulses. The evidence for ice particle generation in this fashion has implications for the "seeder-feeder zone" concept for frontal rainbands (Herzegh and Hobbs, 1980). Clearly, it is of great importance to better understand mesoscale generating structures.

The question of the frequency of occurrence of supercooled water in cirrus is also extremely important. Liquid water has been detected at cloud base from -20 to -36°C. As shown by radiative transfer simulations (Sassen et al., 1985), even relatively small amounts of liquid water can significantly alter cirrus radiative properties. The presence of water also affects the dynamic and microphysical properties of clouds. Moreover, small solution droplets can exist at very cold temperatures, as lidar depolarization data suggest, and reactivate to produce crystals under the proper conditions. The nucleation of ice particles is of fundamental concern for cirrus cloud modeling efforts.

5. ACKNOWLEDGMENTS

This research has been supported by Grant ATM-85 13975 from the National Science Foundation.

REFERENCES

Herzegh, P.H. and P.V. Hobbs, 1980: The mesoscale structure and organziaton of clouds and precipitation in midlatitude cyclones. II. Warm frontal clouds. J. Atmos. Sci., 37, 597-611.

Heymsfield, A.J., 1975: Cirrus uncinus generating cells and the evolution of cirriform clouds. II. The structure and circulations of the cirrus uncinus generating head. J. Atmos. Sci., 32, 809-819.

Liou, K.N., 1986: Influence of cirrus clouds on weather and climate processes: A global perspective. Mon. Wea. Rev., 114, 1167-1199.

Sassen, K. and G.C. Dodd, 1988: Homogeneous nucleation rate for highly supercooled cirrus cloud droplets. J. Atmos. Sci., 45 (in press).

Sassen, K., K.N. Liou, S. Kinne, and M. Griffin, 1985: Highly supercooled cirrus cloud water: Confirmation and climatic implications. Science, 411-413.

VERTICAL VELOCITIES WITHIN A CIRRUS CLOUD FROM DOPPLER LIDAR AND AIRCRAFT MEASUREMENTS DURING FIRE: IMPLICATIONS FOR PARTICLE GROWTH

Ismail GULTEPE and Andrew HEYMSFIELD
National Center for Atmospheric Research[1]
P.O. Box 3000
Boulder, Colorado 80307

1. INTRODUCTION

This paper uses a large and comprehensive data set taken by the NOAA CO_2 Doppler lidar, the NCAR King Air, and rawinsondes on 31 October 1986 during the FIRE (First International Regional Experiment) field program which took place in Wisconsin. Vertical velocities are determined from the Doppler lidar data, and are compared with velocities derived from the aircraft microphysical data. The data will be used for discussion of particle growth and dynamical processes operative within the cloud.

2. SYNOPTIC DISCUSSIONS

There was no large scale disturbances over the experimental area on 31 October 1986. The 1800 GMT surface map showed that there was a cold front 600 km to the west of the experimental area. At 1200 GMT, there was a weak upper level trough at the 200 mb level. The jet stream, with maximum wind speeds of about 45 m s^{-1}, was situated north of Wisconsin. Cirrus cloud formation occurred to the south of the jet stream in a warm air zone. There was not a direct relationship between the cirrus cloud location and the jet stream. A sounding from Green Bay at 11 CST (Figure 1) shows a moisture increase at upper levels where later the cirrus cloud formed. The base of the moisture zone is at about 450 mb with an isothermal layer just under the base. The cloud studied extended over an area of 45×20 km.

3. DISCUSSION OF AIRCRAFT AND LIDAR MEASUREMENTS

The NCAR King Air collected data within the cirrus cloud using six horizontal penetrations from 7.6 km (−29.6°C), cloud base, to 9.2 km (−42.6°C), cloud top. The King Air sampling period for each penetration was about 5 minutes, corresponding to 30 km horizontal legs. The time for total sampling through cloud layer was approximately 30 minutes.

The principal equipment used for cloud particle spectra measurements were Particle Measuring System (PMS) 2D-C and 2D-P probes, although only the size spectra from the 2D-C probe were used. The 2D-C probe sized in the range 25 μm to 1400 μm.

The velocity azimuth display (VAD) technique is used to calculate vertical velocities from the Doppler lidar measurements. This technique was first proposed by LHERMITTE and ATLAS (1961), and later developed by BROWNING and WEXLER (1968). In the VAD scanning mode, the beam is scanned continously in azimuth angles while the zenith angle is held constant. Backscatter power and azimuth angle are digitized in real time and stored on magnetic tape. The radial velocities are measured at intervals of 300 m along the beam.

4. VERTICAL VELOCITY CALCULATIONS FROM AIRCRAFT MEASUREMENTS

In order to calculate vertical velocities from aircraft measurements, the precipitation rate, ice water content and terminal velocity were calculated from 2D-C probe size spectra measurements. HEYMSFIELD (1977) presented equations for calculations the above parameters. A mean size spectrum was obtained for each sampling pass. Particle habits observed in the 2D-C probe and from direct collections on oil coated slides were predominantly columns and bullet rosettes although some plates were detected (N. Knight, private communication). We then calculated the vertical velocity distribution with altitude.

4.1 STEADY-STATE TECHNIQUE

The basis of this technique is the conservation equation for total vapor, liquid and solid substances in a rising parcel of air (HEYMSFIELD, 1975). The assumption is made that ice supersaturation (S_i) remains constant with time (t) at any given level. Thus, the crystal growth and resulting depletion of vapor are balanced

[1]The National Center for Atmospheric Research is sponsored by the National Science Foundation

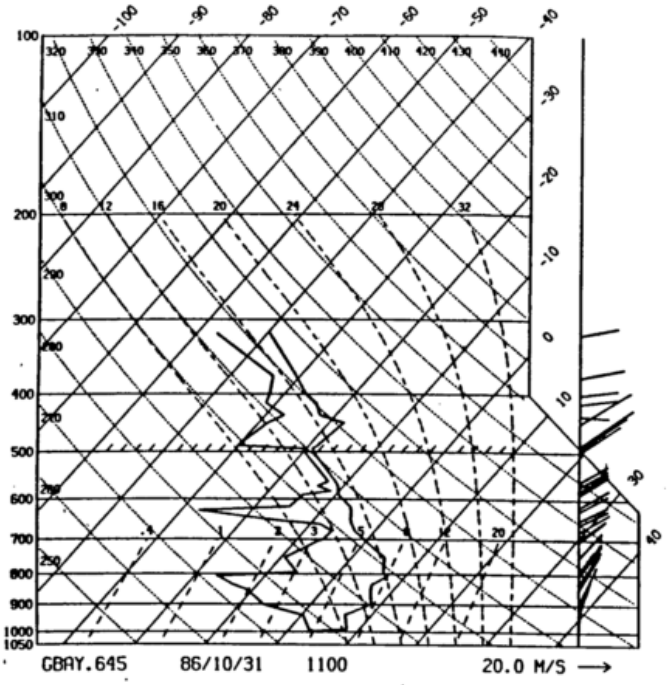


Figure 1: A skew T–log P diagram from Green Bay at 1100 CST on 31 October 1986. The moisture increase is seen approximately between 400 and 300 mb.

due to the updraft. The vertical air velocity is then derived from

$$U_A = \frac{\phi_2}{\phi_1}\frac{dw_i}{dt} , \qquad (1)$$

where U_A is the air velocity, and ϕ_1, ϕ_2 are coefficients (HEYMSFIELD, 1977). $\frac{dw_i}{dt}$, the cumulative growth rate of the particle size spectrum, is not known until the supersaturation with respect to ice (S_i) is obtained (see discussion below).

4.2 FLUX TECHNIQUE

The second technique employed in calculating the vertical air velocity from the size spectra measurements is the flux method (HEYMSFIELD, 1977). In this technique, the vertical velocity was calculated by equating the decrease in moisture between a lower and upper sampling levels to the increase in the precipitation rate between the same levels. The velocity is calculated from

$$U_A = \frac{\Delta R}{\Delta IWC + \frac{RH}{100}\Delta\rho_s} \qquad (2)$$

where ΔR is precipitation rate difference between level 1 and 2, ΔIWC is ice water content difference between the two levels, RH is the mean relative humidity, and $\Delta\rho_s$ is the vapor difference between level 2 and 1. Equations (1) and (2) can be solved simultaneously to yield U_A, RH and S_i (HEYMSFIELD, 1977).

5. VERTICAL VELOCITY CALCULATIONS FROM DOPPLER LIDAR MEASUREMENTS

Conically scanning Doppler lidar measurements were used to compute the mean divergence field, the horizontal wind speed, and direction. The VAD technique is based on a least squares technique for obtaining Fourier coefficients. Using the anelastic continuity equation, the vertical velocities are calculated at different altitudes through the cloud layer. Assuming that the particle velocity is equal to the terminal velocity, the zeroth order Fourier coefficient is given as (SRIVASTAVA *et al.*, 1986)

$$a_o = \overline{DIV}\frac{r cos\alpha}{2} - \overline{V_t} sin\alpha . \qquad (3)$$

$\overline{DIV}$ is mean divergence, r is the horizontal range, $\overline{V_t}$ is mean backscatter–weighted terminal velocity, and α is the elevation angle. The mean horizontal divergence can be calculated from a_o, $\overline{V_t}$, r and α. According to BROWNING and WEXLER (1968), inhomegeneities in the particle fall speed is a primary source of error for the divergence calculation. From concurrent DMSP satellite infrared images, it is reasonable to assume that the cirrus cloud had formed a homogenous structure.

Mean backscatter–weighted terminal velocities ($\overline{V_t}$) are estimated from the particle size spectrum. $\overline{V_t}$ is found from:

$$\overline{V_t} = \frac{\sum_{j=1}^{m}\sum_{i=1}^{n} N_{i,j} D_{eq_{i,j}}^2 V_{t_{i,j}} \Delta D}{\sum_{j=1}^{m}\sum_{i=1}^{n} N_{i,j} D_{eq_{i,j}}^2 \Delta D} \qquad (4)$$

where $N_{i,j}$ is number concentration in size class i with habit j. The physical diameter (D), which is used to calculate V_t, is converted to an equivalent diameter (D_{eq}) (HEYMSFIELD, 1972; 1975). Then, using the anelastic continuity equation and assuming vertical air velocities are zero at cloud top and base, the vertical air velocities are calculated. A variational adjustment technique is used to correct the divergence field. Vertical air velocity corrections are made following LIN *et al.* (1986).

6. RESULTS AND CONCLUSIONS

The aircraft vertical velocity and temperature measurements showed that the cirrus cloud formed in considerably stable atmospheric conditions on 31 October 1986. Maximum vertical shear of the horizontal wind

was only 1.5×10^{-2} s^{-1} (at about 8.8 km). The cirrus cloud may be formed because of a weak wave pattern or large scale lifting.

The ice crystal habits were predominantly columns and bullet rosettes at altitudes between 7.6 (−29.6°C) and 9.2 (−42.6°C) km. The total ice crystal concentration changed from 5.5 l^{-1} (7.6 km) to a maximum of 22.5 l^{-1} (8.8 km) where peak vertical velocities are found from the calculations based on aircraft and rawinsonde measurements. The ice water content values of 10^{-3} to 10^{-2} g m^{-3} through the cloud layer are significantly lower than found in convective cirrus, obviously as a result of weaker vertical motions.

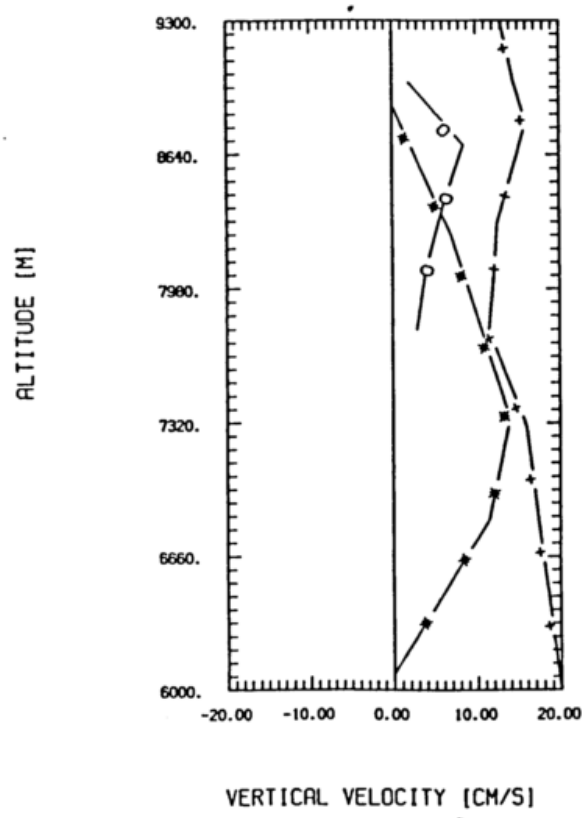


Figure 2: The calculated vertical air velocities from aircraft (o), rawinsonde (+) and lidar (*) measurements on 31 October 1986.

The peak velocity from the VAD technique with 60 degree elevation angle was about 34 cm s^{-1} at about 7.4 km but with 30 and 40 degree elevation angles was only about 14 cm s^{-1} at 7.3 km ASL (see Figure 2) while vertical velocities changed from 9 cm s^{-1} at the cloud base to 0 cm s^{-1} at the cloud top. The calculated air velocities from the aircraft in-situ measurements showed a peak (10 cm s^{-1}) at about 8.8 km where the highest calculated ice crystal growth rates (about 0.2×10^{-4} g m^{-3} s^{-1}), ice supersaturation 42% and relative humidity with respect to water of 94% were found. The calculated vertical velocities are similar to that are found by HEYMSFIELD (1975), in thin ice clouds, ranging from 2–10 cm s^{-1} in frontal overrunning systems to 25–50 cm s^{-1} in clouds associated with closed lows aloft, longitudinal rolls and isolated convective cells. Maximum vertical air velocity derived from the triangle technique (BELLAMY, 1949) using three rawinsondes along baselines of approximately 200 km was found of about 15 cm s^{-1} (at 8.8 km) in the cirrus cloud layer (see Figure 2). Differences in derived vertical velocities between the triangle, Doppler lidar, and aircraft techniques can be attributed to scale effects.

REFERENCES

BELLAMY, J.C., : Objective calculations of divergence, vertical velocity and vorticity. *Bull. Amer. Meteor. Soc.*, **30** (1949) 45–49.

BROWNING, K.A., and WEXLER, R.: The determination of kinematic properties of a wind field using Doppler radar. *J. Atmos. Sci.*, **7** (1968) 105–113.

HEYMSFIELD, A.J.: Ice crystal terminal velocities. *J. Atmos. Sci.* **29** (1972) 1348–1357.

HEYMSFIELD, A.J.: Cirrus uncinus generating cells and the evolution of cirriform clouds. Part I: Aircraft measurements of the growth of the ice phase. *J. Atmos. Sci.* **32** (1975) 789–808.

HEYMSFIELD, A.J.: Precipitation development in stratiform ice clouds: A microphysical and dynamical study. *J. Atmos. Sci.* **34** (1977) 367–381.

LHERMITTE, R.M., and D. ATLAS: Precipitation motion by pulse Doppler. *Proc. Ninth Weather Radar Conf.*, Boston, Amer. Meteor. Soc. (1961) 43, 2302–2327.

LIN, *et al.*: Pressure and temperature perturbations within a squall line thunderstorm derived from SESAME Dual-Doppler radar data., *J. Atmos. Sci.*, **43, 21** (1986) 2302–2327.

SRIVASTAVA, R.C., T.J. MATEJKA, and T.J. LORELLO: Doppler radar study of the trailing anvil region associated with a squall line. *J. Atmos. Sci.*, **43** (1986) 356–377.

HYDROMETEOR DEVELOPMENT IN COLD CLOUDS IN FIRE

Andrew J. Heymsfield and Nancy C. Knight

National Center for Atmospheric Research
Boulder, Colorado 80307, USA

1. INTRODUCTION

The role of cirrus clouds, particularly in weather and climate processes, has been increasingly investigated. Numerical models have demonstrated the importance of the solar reflectivity and infrared radiation of cirrus clouds in the earth's radiation budget and climate. These properties depend upon the cloud microphysical characteristics, density, and altitude and hence justify investigation. The results reported herein were obtained from cold clouds (–20 to –46°C) in the mid to upper troposphere, obtained from ten flights of the NCAR King Air during the First ISCCP Research Experiment (FIRE) in Wisconsin.

2. LIQUID WATER CONTENT MEASUREMENTS

The number of seconds during which liquid water was observed in FIRE clouds between –25 and –35°C, is given in Fig. 1 as a function of amount detected. Data were obtained from a Rosemount Icing Detector (RICE), a Particle Measuring Systems' Forward Scattering Spectrometer Probe (FSSP), and two hot wire probes, the Johnson–Williams (J–W) and the King. Although the J–W and the King hot–wire probes have been the instruments of choice in past investigations of liquid water in cold clouds, they are limited by detection thresholds of 0.02 to 0.05 g m^{-3}, an order of magnitude higher than the RICE or the FSSP. The results given in Fig. 1 are taken from the FSSP data and illustrate the importance

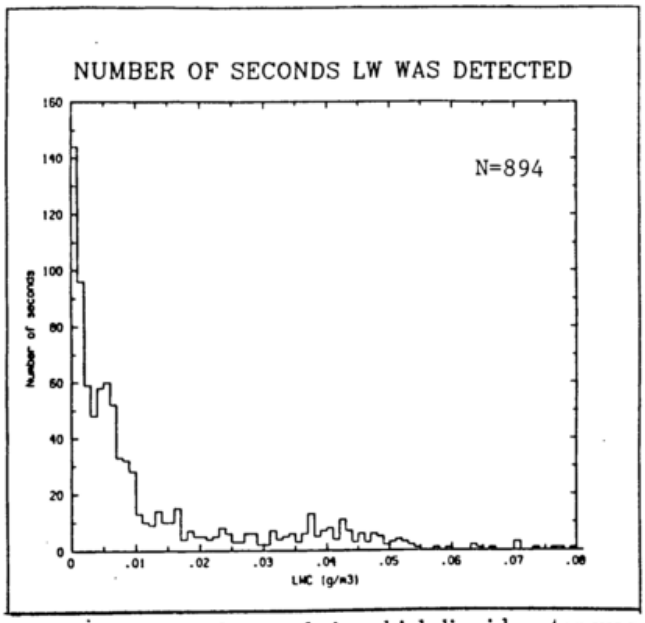


Fig. 1: Number of seconds in which liquid water was detected during FIRE flights as a function of LWC (g m^{-3}) in temperatures between –25 and –35°C. Bin widths are 0.001 g m^{-3}.

of measurements at smaller LWC; most of the liquid water observed at temperatures colder than –20°C was below the detection limits of the hot–wire probes. The data from which Fig. 1 was derived show the largest amounts of liquid water between –30 and –35°C, indicating that in this range, meteorology is more important than temperature.

The operating principles and calibration procedures of all but the RICE have been reported in the formal literature. The RICE collects water droplets and measures corresponding changes in the frequency of a vibrating cylinder. The upper noise limit was determined by examining all output obtained from the instrument at temperatures lower than –40°C where all water is assumed to be frozen. At the true air speed appropriate for the King Air, ~ 100 m s^{-1}, the limit was found to be 3 mV s^{-1}.

The National Center for Atmospheric Research is sponsored by the National Science Foundation.

FSSP spectra of the same temperatures were used to determine ice particle contamination in the data from that instrument, resulting in a conservative threshold of 1.5 cm^{-3} particles per each size bin (3 to 45 μm). Examination of the data taken at warmer temperatures indicated that the RICE and FSSP corrections were valid to -20°C.

3. ICE PARTICLE EVOLUTION

The types of ice crystals in the cold clouds and their size and number were determined from data obtained from two PMS imaging probes, 2D-C and P, and from collecting actual crystals *in situ* on slides coated with silicone fluid.

The evolution of ice particles in the cloud layers was examined using patterns in which the aircraft performed Lagrangian spirals, slowly descending through the layers while drifting with the ambient wind. The particle-size spectra derived from the imaging probes during one such Lagrangian spiral are given in Fig. 2a. Inhomogeneities have been removed by averaging each spectrum over the entire spiral. Measurements taken from the aircraft during the flight showed a zone of ice subsaturation between 7.4 and 8.8 km msl and ice supersaturations from 10 to 20% at other altitudes, all below the top of the cloud layer which the aircraft was unable to reach. In broadening with decreasing altitude the spectra shown are typical of those obtained in all of the flights. Again, typically, much of the growth occurs in the larger sizes. Examples of the particles, primarily bullet rosettes, collected during the same descent are also shown in Fig. 2b.. Bullet rosettes were predominant in many of the collections and columns or plates in others.

4. ICE PARTICLE AGGREGATION

At all temperatures the imaging probe data from

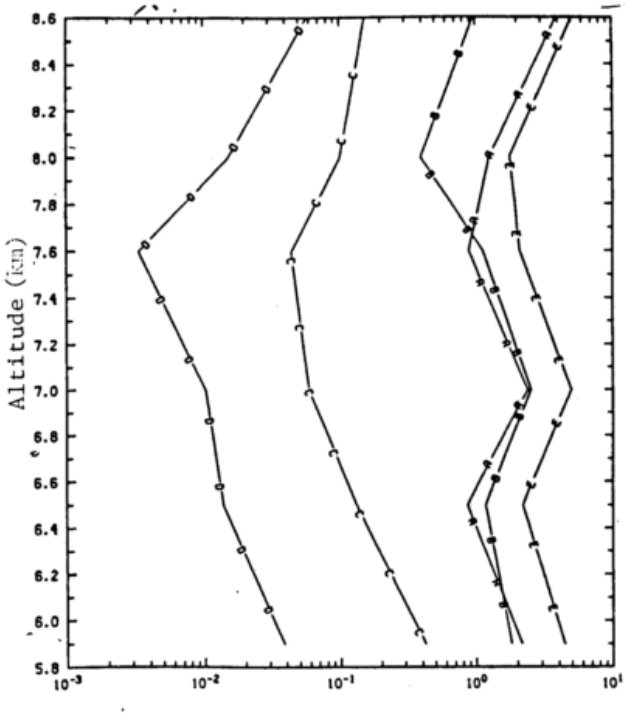


Fig. 2a: LAGRANGIAN SPIRAL, 2 November 1986. Particle concentration (number per liter) as a function of altitude. Size range (microns): a) 75 - 200; b) 200 - 500; c) 500 - 800; d) > 800; e) total.

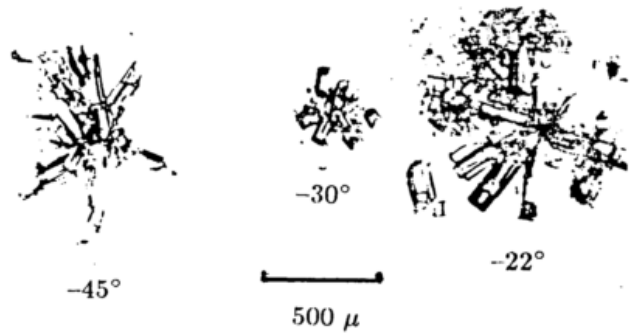


Fig. 2b: Particles collected *in situ* at temperatures given (°C).

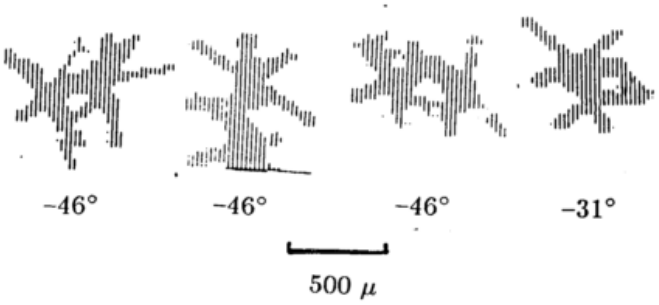


Fig. 2c: 2D-C probe images at temperatures given (°C).

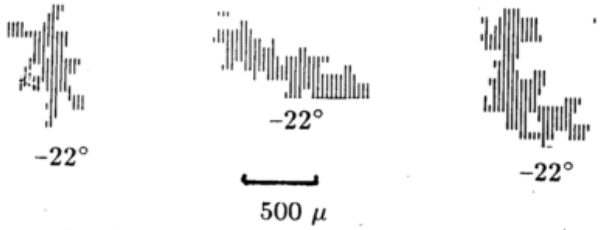


Fig. 2d: 2D-P probe images at temperatures given (°C).

every flight gave evidence of particle aggregation; usually of bullet rosettes joined at their tips, as is illustrated in Fig. 2c and d. Aggregations of plates and columns were also observed, the former joined at edges and the latter end-to-end. At temperatures lower than -25°C the aggregations were almost always of two, equi-dimensional particles with concentrations unvaried with altitude, typically 0.1 to 0.5 ℓ^{-1}. As temperatures warmed above -25°C, the number of aggregates increased as did the number of particles comprising them, their size, and their concentration in the total number of particles.

5. CONCLUSIONS

During the FIRE experiment, the microphysical characteristics of cold clouds have been examined, using the NCAR King Air. The clouds investigated ranged in temperature from -20 to -46°C. Liquid water was detected in these clouds at -35°C and may exist at even colder temperatures. Evaluation of the conditions under which it exists at such low temperatures is continuing in cooperation with the co-principal investigator, Ken Sassen of the University of Utah.

Aircraft patterns in the form of Lagrangian spirals were used to interpret particle growth processes. Significant broadening of the particle size spectra was observed with minor changes in the spectra at small sizes. Virtually all of the broadening observed was attributable to ice particle aggregation which occurred at all temperatures. The crystals comprising the aggregates were of comparable size, joined either at tips or edges, and were usually two in number at temperatures lower than -25°C, increasing to three or more at warmer temperatures. The data strongly suggest that sintering is the mechanism through which the crystals aggregate.

Aggregation appears to be important in the transfer of water mass from upper to lower levels in clouds. Investigation of the aggregation process is continuing in greater detail.

ACKNOWLEDGEMENT

The participation of the authors in FIRE was funded in part by NASA project order #L-98100B. The authors are grateful for Larry Miloshevich's contribution in the preparation of Fig. 1.

THE EMPIRICAL MODEL OF THE STRUCTURE OF CIRRUS CLOUDS IN MIDDLE LATITUDES

Kosarev A.L., Mazin I.P., Nevzorov A.N.

Central Aerological Observatory,
Dolgoprudny, Moscow Region, USSR

1. MACROSTRUCTURE

The proposed parameterization of upper cloud macrostructure is based on civil pilots reports generalization, made by some authors (ZAK, 1962, ZAK, 1964, BARANOV, 1964).

Let x_i be one of the macrocharacteristics of Ci-clouds. $x_1 = H_b$ is the height of its cloud base, $x_2 = H_t$ is the height of the cloud top, $x_3 = \Delta H$ is cloud thickness, $x_4 = |T_b|$ and $x_5 = |T_t|$ are the absolute values of cloud base and top temperatures, respectively. If $F(x_i)$ is cumulative frequency of occurrence x_i (i.e., in F% of cases $x < x_i$), then the gathered empirical data may be described by simple polynoms:

$$F(x_i) = C_{io} + C_{i1}x_i + C_{i2}x_i^2 \quad (1)$$

The values of factors C_{ij} and the range of x_i variations where the relation (1) is true, are given in Table 1.

Table 1

i	C_{io}	C_{i1}	C_{i2}	range of variable X_i
1	-90	20	0	5... 9 km
2	-143	21	0	7...11 km
3	0	36,5	-3,5	0... 5 km
4	-43	2,67	0	-17...-50°C
5	-88	3,20	0	-32...-57°C

The parameterization proposed for European territory of the USSR is useful for that of middle latitudes (ML). (See, for example, the data for Canada and Great Britain (JAMES,1957; MURGATROYD, 1956; CLODMAN, 1957).

2. MICROSTRUCTURE

Aircraft investigations carried out in cloud physics laboratory of the CAO (KOSAREV ET. AL.,1986) some years ago, made a basis for developing the empirical model (EM) of the microstructure of cirrus clouds in ML. The upper clouds (UC) there, are generally of ice structure. But even at rather low temperatures (up to $T \approx -40°C$) small liquid or frozen droplets may occur. Ice water content, as a rule, does not exceed 0,02 g/m^3, and visible light attenuation α is not over 2... 3 km^{-1}. But sometimes observed water content reached even 0,2 g/m^3 and $\alpha > 40$ km^{-1}.

Let us denote IWC as Y_1 and α as Y_2. Then for Y_{in} (n is a per cent of quantile, i.e., in n% of cases IWC< Y_{in} and $\alpha < Y_{2n}$) in temperature range T_1... T_2, the polynom (2) is quite exceptable for parameterization. Y_{in} at different temperature T°C.

$$Y_{in} = b_{io} + b_{i1}|T| + b_{i2}T^2 \quad (2)$$

For T in °C, Y_{in} in g/m^3 and Y_{2n} in km^{-1}, factors b_{ij} are given in Table 2.

Particle size spectra in relatively small cloud volumes (local spectra) are satisfactorily described by the sum of 3 terms, which perhaps implies the existence of different spectra forming mechanisms (KOSAREV ET AL.1986)

Table 2

n	b_{i0}	b_{i1}	b_{i2}	$T_1 \ldots T_2$ (°C)
		$i = 1$ (IWC)		
50	$3.81 \cdot 10^{-2}$	$-1.23 \cdot 10^{-3}$	$1.13 \cdot 10^{-5}$	-15...-55
75	$9.59 \cdot 10^{-2}$	$-3.11 \cdot 10^{-3}$	$2.86 \cdot 10^{-5}$	-15...-55
90	$1.55 \cdot 10^{-1}$	$-4.76 \cdot 10^{-3}$	$4.08 \cdot 10^{-5}$	-15...-55
		$i = 2$ (α)		
50	2.85	- 0.05	0	-15...-35
75	5.78	- 0.105	0	-15...-45
90	9.20	- 0.16	0	-15...-50

$$n(a) = n_0(a)+n_1(a)+n_2(a) \qquad (3)$$

Here a is an effective diameter of crystal shadow projection (i.e., the diameter of a circle, which area equals to the mean area of occasional shadow).

Practically, in 70-80% of cases $n_0(a)=0$. Term $n_1(a)$ characterizes particle size spectra in the range of $a < 60$ μm, term $n_2(a)$ - in the range of $a > 150$ μm. In intermediate interval (60... 150 m) both terms are significant. In the overwhelming majority of cases these terms are well described by gamma-distribution (in particular "exponent").

$$n_1(a) = \frac{N_1}{\lambda_1^2} a \exp(-a/\lambda_1) \qquad (4)$$

$$n_2(a) = \frac{N_1}{\lambda_2} \exp(-a/\lambda_2) \qquad (5)$$

Concerning the spectra averaged over the great amount of experimental data term $n_2(a)$ may be better approximated with the power function (see also HEIMSFIELD and PLATT, 1984).

The dispersion of parameter λ_1 is relatively small. $\lambda_{1\,mod} \approx \lambda_{1\,med} \approx \lambda_1 \approx$ ≈ 14 μm and standard deviation $\sigma_{\lambda_1} \approx 4$ μm. The dispersion of particle concentration in visible UC is also comparatively small. Namely, $N(a > 20)$ in 70... 80% of cases is in the limits of 0.1...1.0 cm^{-3}, $N_1 \approx \beta(\lambda_1) N(a > 20)$, where $\beta(\lambda_1) = \exp(20/\lambda_1) \cdot (1+20/\lambda_1)^{-1}$, and it varies from 0.12 to 2.5 cm^{-3}.

Thus, for EM we recommend the values of $\lambda_1 = 14 \pm 4$ μm, $N_1 = (1.1 \pm 0.9)$ cm^{-3}. Parameters N_1 and λ_1 are weakly, if any, correlated. No marked correlation between λ_1 or N_1 and temperature was revealed. Concentration $N(a > 200)$ and parameter $N_2 = N(a > 200) \cdot \exp(200 / \lambda_2)$, on the average, are notably decreased with increasing λ_2. Both N_2 and λ_2 are slightly decreased, on the average, with decreasing T. Table 3 represents median values of N_2 and λ_2, as well as 10- and 90-% quantiles $N_{10}(a > 200)$ and $N_{90}(a > 200)$. In 70...80% of cases λ_2 differs from the median value $\lambda_{2,med}$ not over than 1.5 times.

Table 3

temperature range, °C	-20...-30	-30...-40	-40...-50
Curve number in Fig.1	1	2	3
$\lambda_{2,med}$ (μm)	90	70	55
$N_{med}(a > 200)$ (L^{-1})	3,4	2,0	0,7
$N_{10} \ldots N_{90}$ (L^{-1})	1,0... 6,6	0,2... 6,0	0,05... 3,6

In 20... 30% of cases particle concentration in UC exceeds 10 cm^{-3} and the majority of particles does not exceed 20 μm in size. In such situations $n_0(a) \neq 0$. We think that $n_0(a)$ may be described by

$$n_0(a) = \frac{N_0}{2\lambda_0^3} a^2 \exp(-a/\lambda_0) \qquad (6)$$

where λ_o= 3... 5 μm, N(a > 3)=10... 20 cm^{-3}. Fig.1 graphically represents the suggested parameterization of $N(a) = \int_a^\infty n(a)da$ for a > 3 μm. Here, $N_o = \begin{cases} 0 & \text{case (a)} \\ 10.9\ cm^{-3} & \text{case (b)} \end{cases}$, λ_o=3μm. In case "b" N(a > 3)=10 cm^{-3}, N_1=1.1 cm^{-3}, λ_1 = 14 μm. Curves 1,2 and 3 correspond to parameters λ_2,med and $N_{med}(a > 200)$ listed in Table 3.

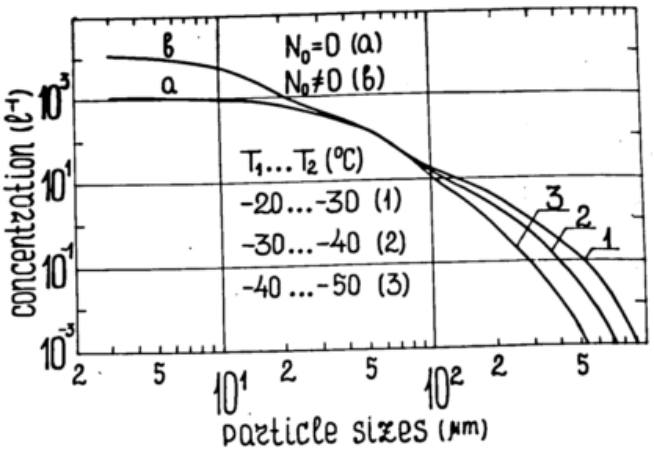


Fig. 1.

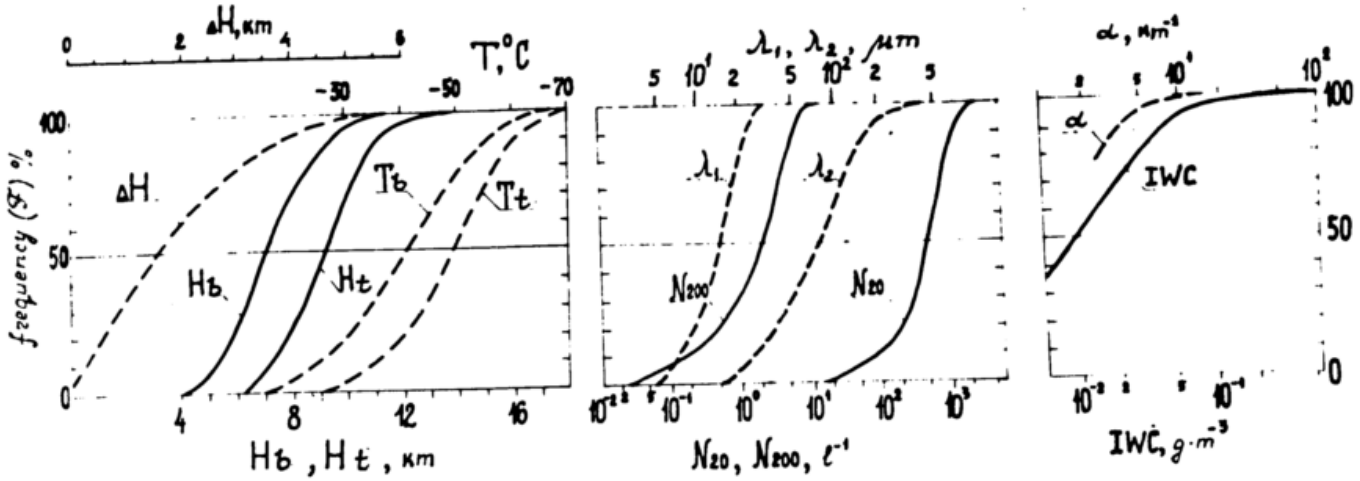


Fig.2. Distributions (cumulative frequencies) of some parameters in ULC derived from empirical data obtained over the European territory of the USSR.

REFERENCES

BARANOV, A.M.: Frontal clouds and conditions for flights within them. In Russian. Leningrad, Gidrometeoizdat, 1964, 238.

CLODMAN, J.: Some statistical aspects of cirrus clouds. Month. Wea. Rev., 1957, v.85, N 2, 37-41.

HEYMSFIELD, A.J.; PLATT, C.T.R.: A parameterization on the particle size spectrum of ice clouds... J.Atmos.Sci., 1984, 41, 5, 846-855.

JAMES, D.G.: Investigations relating to cirrus clouds. Met. Mag., 1957, N 105, 1-12.

KOSAREV, A.L.; MAZIN, I.P.; NEVZOROV, A.N.; SHUGAEV, V.F.: Microstructure of cirrus clouds. In Russian. In: Coll. Papers Some Problems of Cloud Physics. Leningrad, Gidrometeoizdat, 1986, 160-186.

KOSAREV, A.L., NEVZOROV, A.N., SHUGAEV, V.F.: On the microstructure and ice water content of high clouds. Proc. 9th Intern. Cloud Phys. Conf., Tallinn, 1984, v.1, 73-76.

MURGATROYD, H.J.; GOLDSMITH, P.: High cloud over Southern England. Prof. Notes, 1956, Air Ministry, Meteor. Office, London, 11-19.

ZAK, Ye.G. Vertical distribution of upper layer clouds. In Russian. Proc. CAO, 1962, issue 39, 13-23.

ZAK, Ye.G.: Temperature characteristics of upper layer clouds. In Russian. Proc. CAO, 1964, issue 55, 32-53.

MODELLING THE INITIAL ICE CRYSTAL SPECTRUM IN CIRRUS CLOUD

A.G Darlison

U.K Meteorological Office

1. INTRODUCTION

One striking feature of all in-situ cirrus microphysical observations is the low concentration of ice crystals compared to a) concentations of cloud condensation nuclei; and b) ice nucleus concentrations estimated from the Fletcher distribution ($N=10^{-2}\exp(0.6\,\Delta T)$. eg Rangno and Hobbs (1986) find a concentration of about 10^4 m^{-3} in stratiform cloud representiong a depletion relative to the Fletcher distribution of 10^{-6} at -45 deg C.

They suggest that ice nuclei might be scarce at cirrus altitudes and also point out that counts might be depressed by small crystals going undetected. One might also envisage dilution of the nucleation region (Heymsfield and Knollenberg (1972)) by differential sedimentation and turbulent diffusion.

It is important to understand this initial stage in the life-cycle of cirrus. In this paper we present a model which simulates the freezing process using plausible IN and CCN distributions, enabling us to distinguish between the above explanations of ice crystal depletion.

2. THE MODEL

It is a closed parcel model in which moist air containing hygroscopic nuclei (described by the maritime distribution of Junge et al 1971) is cooled at a rate corresponding to a constant updraught. The CCN/droplet spectrum is represented by a set of discreet size bins, each obeying the usual growthrate equation.

Total water is conserved, so as ascent procceds the saturation ratio rises due to cooling until the haze droplets reach a critical size, near the condensation level. The larger haze particles grow into mature cloud droplets whose radius is determined by the supply of vapour. The parcel temperature is weakly affected by the condensation because total heat is conserved. So far the model resembles that of Howell(1949) for example.

In addition we include three ice nucleation processes, charecterising the model as cirrus:

i)Homogeneous nucleation.
The probality per unit time of a droplet freezing is calculated using the classical formula (eg Fletcher (1962 p39ff)). This is proportional to volume and increases rapidly with falling temperature. In addition each droplet contains a certain mole fraction of solute from the nucleus upon which it condensed, which suppresses nucleation. This term prevents the nucleation of small haze droplets but does not inhibit the freezing of cloud droplets.

ii) Condensation-freezing.
The rate of freezing of droplets in the i'th size bin is given by:

$$\frac{dn_i}{dt} = -\left(n_i v_i \Big/ \sum_j n_j v_j\right)\left(N(T) - \sum N\right) S \rho$$

where v_i is droplet volume, S is a solute suppression term like the above, ρ is a rate constant (which is set to the 'reasonable' value of $0.1s^{-1}$), $\sum N$ is the number of condensation freezing nucleations to date, and N(T) is the Fletcher distribution. This model yields N(T) crystals in time ρ^{-1} when vapour

supply is unlimited, representing the behaviour of laboratory determinations of IN. Larger drops have a greater probability of containing an insoluble nucleus.

iii) Deposition nucleation. Ice crystals are nucleated at a rate given by:

$$\frac{dn_i}{dt} = -0.6\, N(\tilde{T})\, \frac{d\tilde{T}}{dt}$$

where $\tilde{T}$ is the temperature at which the prevailing ice saturation ratio would correspond to water saturation. The model reduces to the Fletcher distribution if water saturation is assumed, but nucleation rate is a function of ice saturation ratio, corresponding to the behaviour of deposition nuclei observed by Huffmann (1973).

Once ice crystals have been nucleated they grow at a rate proportional to the usual growthrate formula for ice crystals.

The above formulation reduces to a set of coupled non-linear differential equations which are solved numerically, paying due attention to convergence and stability. For further details see Darlison (1988).

3. RESULTS

i) Homogeneous freezing

Some sample results are shown in Figure 1. The left-hand part of (a) shows the familiar pattern of haze growing rapidly into cloud droplets at the condensation level, with smaller CCN remaining inactive and the rest of the spectrum narrowing. Thereafter ascent proceeds at slight water supersaturation, around 0.6%, with the LWC growing approximately adiabatically. As the droplets grow and cool the homogeneous nucleation rate increases rapidly and the number of crystals rises. Eventually these crystals grow fast enough to bring down the saturation ratio. Droplets evaporate and nucleation stops.

Results for the final number of crystals, N_x, nucleated under various conditions, are shown in Figure 2 and are fitted by:

$$N_x = 6.7 \times 10^6\, w^{1.6} \quad (m^{-3})$$

Surprisingly N_x depends mainly on updraught, and not on temperature or CCN concentration. For a typical cirrus updraught of 0.5 ms^{-1} homogeneous nucleation yields approxiately 10^6 crystals m^{-3}. Only one in 10^2 droplets freeze.

Beceause the nucleation process occurs rapidly (in a few 10's seconds) the spectrum of ice crystals is sharply peaked. After nucleation ceases the initial ice crystals continue to grow rapidly until ice supersaturation is close to zero. This occurs on a timescale of a few minutes. Further growth may only occur by sedimentation (which is not considered) or continued ascent. Typical sizes and timescales are shown in Table 1.

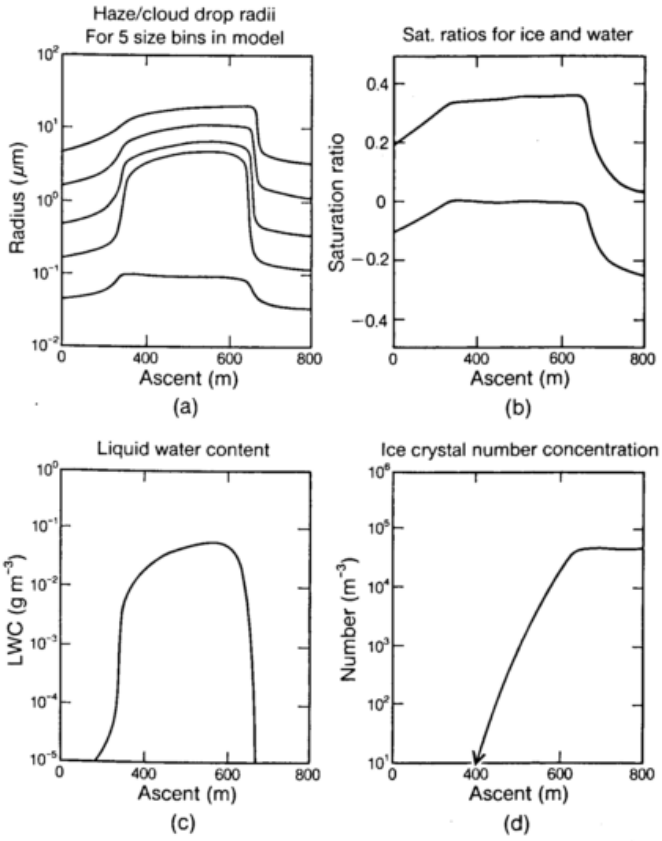


Figure 1. Various model parameters for air at dew-point −30 °C ascending at 0.1 m s^{-1} as a function of ascent above starting altitude (taken to correspond to the frost point).

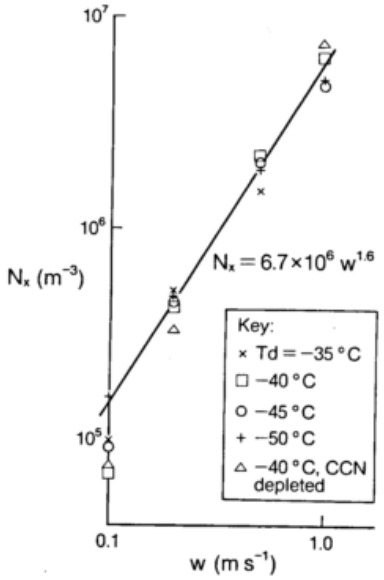


Figure 2. Number of ice crystals nucleated homogeneously as a function of updraught velocity for parcels with various dew-points, assuming a Junge (1971) maritime CCN distribution. Also shown are some points for runs with the CCN depleted by a factor of 10.

VERTICAL VELOCITY ($m\ s^{-1}$)	DEW POINT −35°C	DEW POINT −50°C
0.1	$r = 60\ \mu m$ $\tau = 600$ sec	$r = 39\ \mu m$ $\tau = 400$ sec
1.0	$r = 17\ \mu m$ $\tau = 55$ sec	$r = 11\ \mu m$ $\tau = 20$ sec

Table 1. Average radii, r, of initial ice crystals nucleated homogeneously, and the timescale, τ, of the freezing process.

ii) Heterogeneous nucleation

Condensation freezing yields

$$N_x = 4.5 \times 10^6\ w^{1.35}\ (m^{-3})$$

which is very similar to (2) despite the nucleation model being quite different. Only one in 10^3 nuclei produce ice crystals. Once again the result is insensitive to nucleus concentrations and to temperature.

Deposition nucleation yields rather fewer crystals:

$$N_x = 6.0 \times 10^5\ w^{1.45}\ (m^{-3})$$

Invariance with respect to nucleus concentratons is very pronounced: typically a thousandfold change in IN concentration yielded a 10% change in N_x.

4. SUMMARY AND DISCUSSION

The main result is that the final number of crystals nucleated depends on the updraught velocity and not on the nucleus concentration or temperature. This occurs because the factor limiting nucleation is the rate at which crystals already formed consume available vapour. Thus depletion of ice crystals in cirrus results from the physics of the nucleation process. We do not need to invoke depletion of nuclei.

However our model does yield somewhat higher concentrations than those frequently measured. Table 1 shows that the initial ice crystals are likely to be less than 100 microns and so we agree with Rangno and Hobbs that instrumental limitations may cause undercounting.

REFERENCES

Darlison,A.G (1988) submitted to Q J Royal Met Soc.

Fletcher,N.H 1962 The Physics of Rainclouds. C.U.P

Heymsfield,A.J and Knollenberg,R.G 1972 J.Atmos.Sci 29 1358-1366

Howell,W.E 1949 J.Met 6 134

Huffmann,P.J 1973 J.App.Met 12 1080-1082

Junge,C and McLaren,E 1971 J.Atmos.Sci 28 382-390

Kuhns,I.E and Mason,B.J 1968 Proc. R. Soc. A302, 437

Rangno,A and Hobbs,P.V 1986 Conf. Cloud. Physics 2 20-23 Boston AMS

EFFECTS OF CIRRUS COMPOSITION ON ATMOSPHERIC RADIATION BUDGETS

Stefan Kinne

Space Science Division, NASA Ames Research Center
Moffett Field, California 94035, U.S.A.

Kuo-Nan Liou

Department of Meteorology, University of Utah
Salt Lake City, Utah 84112, U.S.A.

1. INTRODUCTION

Cirrus clouds have been identified as presenting one of the major unsolved problems in weather and climate research (Liou, 1986). Unlike water clouds, cirrus clouds are semi-transparent with respect to incoming solar radiation and, at the same time, can significantly trap outgoing thermal infrared radiation. The greenhouse effect of cirrus clouds, however, depends not only on the cloud geometric configuration and temperature stratification, but also on the microphysical composition, including ice crystal size distributions, shapes, and concentrations. To investigate the importance of the particle size and shape on the radiation budget of the earth-atmosphere system, we have performed a number of sensitivity experiments based on radiative transfer calculations.

2. METHOD

We have developed an accurate radiative transfer model that can be used to determine the changes in solar and infrared fluxes caused by variations in the composition of cirrus clouds. In the present calculations, cirrus clouds are placed between 9 and 11 km, and the standard atmospheric temperature and humidity profiles are used. The nonspherical shape of ice crystals is taken into account by imposing "nonspherical corrections" on the single-scattering parameters for equivalent spheres. This is done by comparisons between results calculated from Mie theory and those from geometric optics. These corrections generally reduce absorption and forward scattering for spheres of equivalent surface. Thus, the importance of the particle shape may be assessed. To study the effect of size, two different ice crystal size distributions were chosen (Heymsfield, 1975). The cirrostratus (Cs) represents a nonconvective ice cloud composed of a large number of small ice crystals, while the convective cirrus uncinus (Ci) has a bimodal size distribution composed of large particles.

3. RESULTS

Figure 1 shows the increase in the solar planetary albedo caused by placing cirrus of various optical depths ranging from 0.1 to 10 into a clear atmosphere. For the same optical depths, nonconvective clouds with smaller particles display about 25% larger albedo changes than convective clouds. A similar increase, indicated by the shaded area, is related to the use of nonspherical corrections in scattering and absorption calculations.

The downward effective emissivity for cirrus clouds, as a function of the optical thickness, is shown in Fig. 2. We see that the liquid water content for the convective cloud is almost three times that of the nonconvective cirrus for the same optical depths. Thus, broadband emissivity parameterizations based on the liquid water column would depend significantly on the particle size.

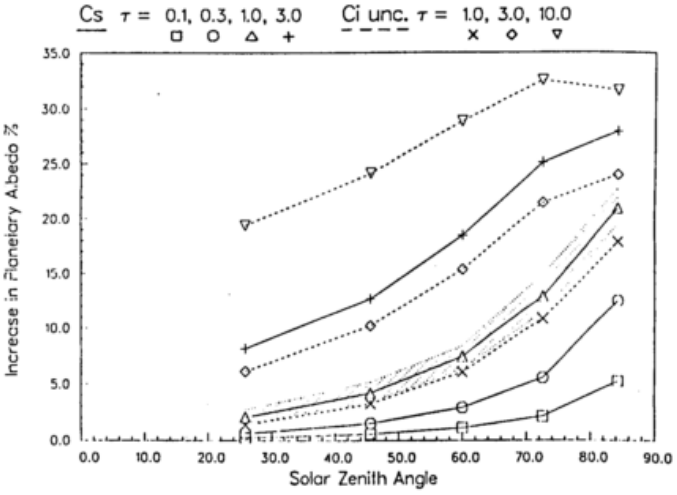


Fig. 1 Effects of cirrus clouds on the solar planetary albedo.

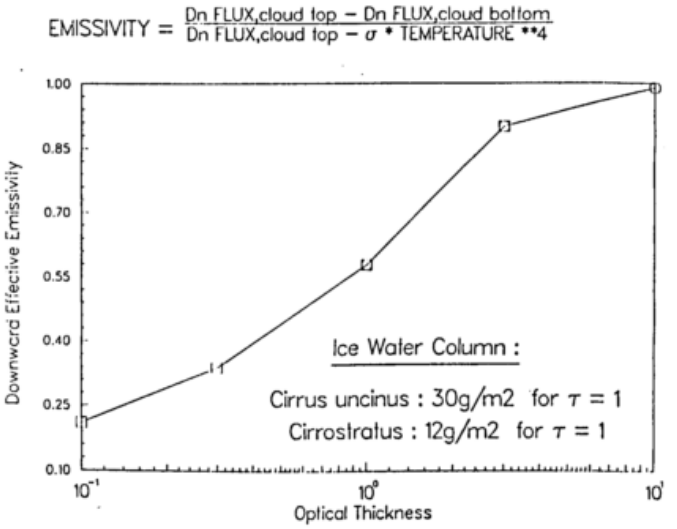


Fig. 2 Effects of cirrus clouds on the broadband effective infrared emissivity.

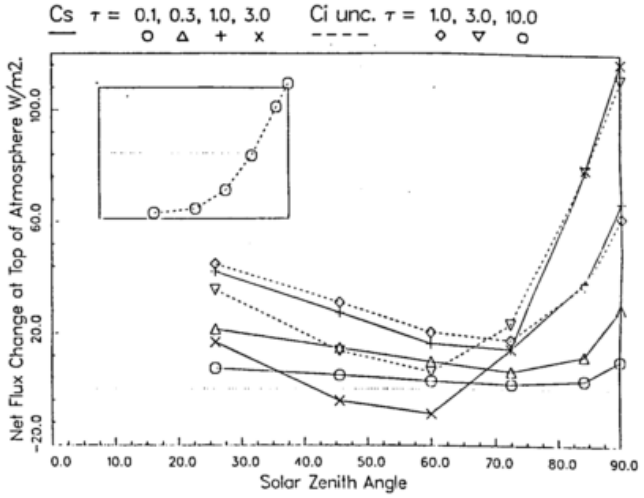


Fig. 3 Effects of cirrus clouds on the atmospheric radiation budget.

Figure 3 displays the combined net flux changes for the entire solar and infrared spectra. Only the optically thick, convective cirrus cloud shows strong cooling of the earth-atmosphere system for high solar zenith angles, a behavior typical of water clouds. All cirrus clouds with an optical depth of less than or equal to one increase the net flux at the top of the atmosphere and thus would contribute to a warming of the system. This warming depends on the ice crystal sizes and shapes in cirrus clouds through the dependence of these parameters on the transfer of solar fluxes.

4. CONCLUSIONS

Even though the cloud optical thickness dominates the radiative properties of ice clouds, the particle size and nonsphericity of ice crystals are also important in calculations of the transfer of near-IR solar wavelengths. The present results show that, for a given optical thickness, ice clouds composed of larger particles would produce larger greenhouse effects than those composed of smaller particles. Moreover, spherical particles with equivalent surface areas, frequently used for ice crystal clouds, would lead to an overestimation of the greenhouse effect.

5. ACKNOWLEDGMENTS

This research was supported, in part, by NASA Grant NAG-732 and the Air Force Office of Scientific Research Grant AFOSR-87-0294.

REFERENCES

Heymsfield, A.J., 1975: Cirrus uncinus generating cells and the evolution of cirriform clouds. J. Atmos. Sci., 32, 798-808.

Liou, K.N., 1986: Influence of cirrus clouds on weather and climate processes: A global perspective. Mon. Wea. Rev., 114, 1167-1199.

A RADIATION-FOG MODEL WITH DETAILED MICROPHYSICS

Andreas Bott, Uwe Sievers and Wilford Zdunkowski
Institut fUr Meteorologie der Johannes Gutenberg-Universität
D 6500 Mainz

1. THE MODEL

A one-dimensional numerical model is presented to simulate the development and the life-cycle of radiation fog. The model includes dynamic processes, radiative transfer and microphysics of droplets and condensation nuclei since fog formation is the result of interactive processes of these components. The dynamic part of the model consists of the atmospheric equation of motion, heat equations for the atmosphere and the soil, as well as budget equations of water vapour and the droplet spectrum for the redistribution by turbulent exchange. Radiative fluxes are calculated by means of a two-stream method including multiple scattering, absorption and emission on the basis of sthe actually simulated droplet spectrum.

2 MICROPHYSICS

The microphysics of the model is characterized by a unique description of the aerosol and droplet spectrum by means of a two-dimensional particle distribution function. Co-ordinates are the dry mass of the aerosol particle of a given constitution and the accumulated water mass. Considered is the diffusional growth of particles as well as their size-dependent sedimentation. The equation of droplet growth is extended to include radiative effects as suggested by DAVIES (1985) and others. This means that the growth rate of an individual particle is calculated from the assumption of stationary equilibrium between the fluxes of sensible and latent heat and the net radiation at the droplets surface. The diffusional growth is simulated by solving the complete budget equation for all, even the smallest particles. Test calculations show that the inclusion of radiation in the droplet growth equation is of importance and should not be neglected by any means in fog modelling.

3 ADVECTION SCHEME

The unique description of the particle spectrum does not qualitatively distinguish between humidified condensation nuclei and droplets, and therefore includes the direct simulation of the activation process. However, realizing this concept requires an efficient numerical scheme for integration of the budget equation of the spectrum which has the form of a conservative advection equation. In order to enable moderate timesteps of about 15s, the scheme must be adequate also for Courant numbers greater than one, where customary methods fail in general. In order to avoid this difficulty an algorithm was developed which is not based on a difference approximation of the differential equation but on its integral solution: The distribution function represented by mean values over the numerical grid cells is approximated by a piecewise linear function with nodal points at the walls and midpoints of the cells. The nodal values are obtained from cubic interpolation and the requirement that the mean values over the cells should be reproduced correctly by approximation function. Additionally, the discrete velocity values are extended to a continuous function by linear interpolation. Within this field the Lagrangian equation of motion for the individual particles is integrated backwardly in time from t_{n+1} to t_n in order

to obtain the original positions of particles at time t_n as function of their new positions at t_{n+1} . These calculations are carried out analytically for all particles at cell-wall positions. New cell mean values then are obtained by integrating the piecewise linear approximation of the old distribution over the region between the original positions of the two walls of each grid cell.

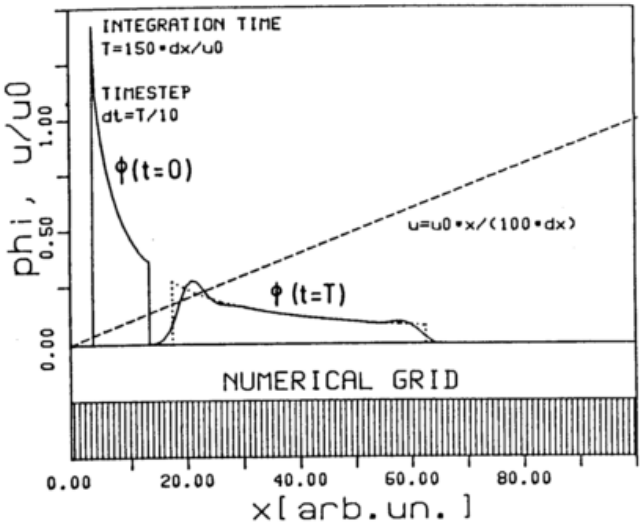


Fig.1: Result of a numerical advection experiment.

The accuracy of the resulting scheme is demonstrated in Fig.1 for the case of a linearly increasing velocity field by comparison with the exact analytical solution (dotted line). The quantity T is the total integration time which is subdivided in 10 timesteps dt, u0 is a scale velocity and dx the grid distance.

4 RESULTS

The complete fog model was applied to an early October situation in the midlatitudes of the northern hemisphere. The simulation starts at 14:00h with a temperature at shelter height of 12°C. The specific humidity is 6g/kg and the geostrophic wind 2m/s. The aerosol consists of 56% ammonium sulfate, 24% quartz and 20% soot, while the particle spectrum is subdivided into 8 aerosol and 35 water classes. The model results show fog formation at 23:00h increasing to a height of 44m at sunrise. Fig.2 displays the simulated droplet spectrum at 07.00h. The two peaks at the left part of the distribution are numerical artifacts. They represent unactivated particles and are due to the coarse resolution of the aerosol.

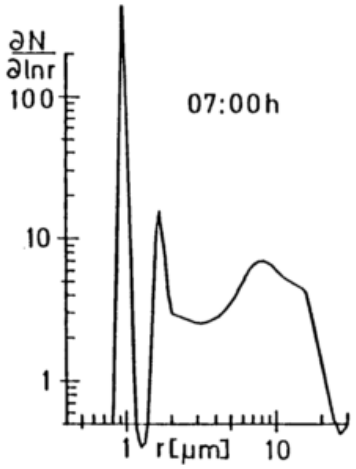


Fig.2: Simulated droplet spectrum $\partial N/\partial \ln(r)$ in cm^{-3} at 07:00h.

After sunrise the fog height increases further to its maximum value of 64m at 09:00h with a maximum liquid water content of $0.38 g/m^3$. At 11:00h fog dissipation begins at the ground and is complete at 12:30h. Fig.3 shows the remarkable reduction fo the larger aerosol particles by the fog due to nucleation scavenging and droplet settling.

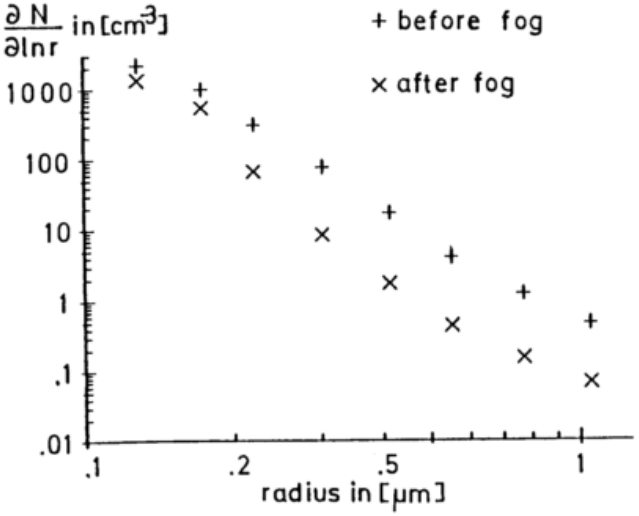


Fig.3: Distribution of aerosol particles before fog formation and after its dissipation.

Simulation results are quite encouraging and seem to indicate that the physical basis of the model is quite realistic.

5 REFERENCES

DAVIES, R.: Response of cloud supersaturation to radiative forcing. J. Atmos. Sci.42 (1985), 2820-2825.

SMALL SCALE STRUCTURE OF A RADIATIVE FOG. A NUMERICAL STUDY

Piotr K. Smolarkiewicz
National Center for Atmospheric Research[1]
Boulder, Colorado, U.S.A.

David Fitzjarrald
State University of New York at Albany
Albany, New York, U.S.A.

1. INTRODUCTION

Despite a number of fog field programs and numerous modeling studies during the last half-century, there is still no satisfactory explanation of the formation and growth of radiative fog. There is considerable controversy concerning the role of small scale dynamic activity, traditionally attributed to turbulence, in the radiation fog development. One set of observations, e.g., ROACH et al. (1976), suggests that fog forms during a lull in turbulence, while another set of observations, e.g., LALA et al. (1982), suggests that intensified turbulence stimulates fog development. Modeling studies show similar discrepancies. For instance, the calculations of BROWN and ROACH (1976) produced earlier and thicker fog formation due to reduction in a parameterized turbulent diffusion, while WELCH et al. (1986) demonstrated that turbulence generation leads to more rapid fog development and to larger liquid water contents. The traditional approach to the radiative fog evolution emphasizes microphysics and infrared radiation transfer where the internal dynamics of the fog is heavily parameterized using $K-$theories (see, WELCH et al., 1986, for a review) or methodology of higher-order closures (OLIVER et al., 1978). In spite of the disagreement on the role of turbulence in the fog evolution, there is little doubt that the event is sensitive to the dynamic activity in the surface layer. Thus, parameterization of the fog dynamics may strongly influence model results. To minimize turbulence parameterizations we adopted a direct simulation approach of the small scale fog motions.

2. MODEL SUMMARY

We hypothesize that fog evolution is fundamentally a Bénard convection problem, determined primarily by dynamics of the stratified fluid subject to imposed wind shear and *volume* cooling due to the bulk properties of the radiation transfer. We have performed a series of numerical experiments using the nonhydrostatic, anelastic model of Clark (CLARK, 1979; CLARK and FARLEY, 1984; SMOLARKIEWICZ and CLARK, 1986). Microphysics and radiation physics were parameterized. A modified SOMMERIA (1976) radiation scheme was implemented. The dynamics was treated explicitly using spatial resolution from 4 to 10 m in both 2- and 3-D. Domain dimensions of 400 m were used for the main experiments. These choices were dictated by the $\sim$ 100 m deep fog layer occurring on the 30 September – 1 October 1982, at Albany, N.Y.. The assumed conditions represent an idealization of the tethered balloon sounding at 1800 LST: $u(z) = 0.0$; $v(z) = .0122z$ if $z \leq 50$ or $v(z) = 0.00354(z-50) + 0.61$ if $z > 50$; $\Theta(z) = 289.28 + 0.0715z$ if $z \leq 20$ or $\Theta(z) = 290.71 + 0.0019(z-20)$ if $z > 20$; $q_v(z) = -0.048z + 10.2$ if $z \leq 25$ or $q_v(z) = 9$ if $z > 25$, where u, v, Θ, q_v, and z are wind velocity components, potential temperature, water vapour mixing ratio and height above the ground, respectively (*all quantities are expressed in SI units*). Based upon rawinsonde sounding, $c = \int_L^\infty \rho q_v dz = 1.8_{[CGS]}$ (an important constant for the upper boundary condition in radiation scheme) was used. Since the radiative cooling alone was insufficient to result in condensation, we have specified, based on available data, a surface

[1]The National Center for Atmospheric Research is sponsored by the National Science Foundation

turbulent heat flux, $F_H = -10$ W/m^2, randomly perturbed with equal amplitude white-noise to initiate condensation. After condensation occurred, the sign of the heat flux was reversed (roughly to simulate the observed upward soil heat flux). Subsequent fog evolution was not sensitive to the surface flux imposed, and was controlled by the infrared radiative transfer and the environmental structure. When no surface heating was imposed underneath the model fog, downward convective motions were too weak to remove the surface layer inversion.

3. DISCUSSION OF THE RESULTS

The 2- and 3-D experiments produced similar fog evolutions, which were in the rough agreement with observations. After $\sim$ 2 h of a shallow patchy fog, the fog grows to $\sim$ 100 m depth with the convective eddy structures (with vertical vs. horizontal aspect ratios evolving from $\sim 1/2$ in the early stage to $\sim 1/1$ after six hours) and spatial scale determined by the depth of the fog. A characteristic strong inversion forms at the top of the fog layer, with thermodynamic model variables resembling the Heaviside function. Similarity between the 2- and 3-D simulations (the 3-D fog was somewhat shallower and colder than the 2-D one) and insensitivity of the fog growth to the weak random surface heating (described earlier) suggests that the evolution of the fog layer is not necessarily related to the surface layer turbulence but rather to the dynamics of the fog top interface which in turn depends on the environmental structure (stability, shear, moisture) evolving continuously due to imposed volume sources/sinks of heat related to the infrared radiative transfer and water phase exchange.

To assess the role of explicit dynamics we performed 1-D experiments equivalent to the multidimensional simulations. Without introducing a diffusive term into the thermodynamic equations, the fog layer did not grow. This result has a simple interpretation. It is easy to show (assuming simple radiation scheme parameterization) that at the interface of the two-layer fluid, with zero liquid water content in the upper layer, the divergence of the radiative flux is not well defined, i.e., $\frac{\partial F_R}{\partial z} \sim \delta(z - H)$ (where H is height of the interface and δ is the Dirac delta distribution). As a result of this discontinuity, in an initially stable, idealized two-layer fluid, the condensation in an arbitrarily small distance above the interface is effectively prevented and the interface becomes an infinitesimal thin layer of unstable stratification. Developing instability will disperse the interface and consequently cool the adjacent layer aloft. This in turn would lead to the condensation and rise of the interface. Certainly, one-dimensional models are incapable to render this process, and, in order to do so, they require specification of some diffusive mechanism. Naturally, the results will be strongly dependent on the diffusion rate specified. Figure 1, shows the depth of a one-dimensional fog after six hours of evolution versus the mixing coefficient, K. The dashed line represents the mixing length scale, $l_m = (K \cdot t_{6h})^{\frac{1}{2}}$. It is apparent that the increasing weak mixing, which results in the mixing length scale comparable to the depth scale of the interface (grid interval in a low resolution numerical model), stimulates fog development, whereas the increasing strong mixing, which results in the mixing length comparable to the depth of the entire fog layer retards and finally inhibits fog development. This apparent sensitivity of the fog growth to the diffusion rate assumed does not necessarily imply leading role of the surface layer turbulence in the fog evolution. In the direct simulation experiments discussed earlier, the eddy mixing coefficient was $\sim 10^{-3}$ m^2/s throughout the fog layer with a distinct peak at the interface. Similarly, the resolved Reynolds fluxes of heat, moisture, and liquid water were on the order of unity when expressed in W/m^2 throughout the fog layer, with characteristic jump at the fog interface. Thus, in the cases considered here it is not a surface layer turbulence, but rather instability at the fog top

interface, which drives the fog and produces internal fog convective circulations similar to those in the classic Bénard problem.

One should realize that the $h(k)$ curve has no universal character and will be strongly dependent on the environmental conditions and the infrared transfer formulation. On the other hand it may help to explain the controversy on the role of turbulence in the fog evolution. It is apparent from Fig. 1 that both results are possible. The local variability in the environmental conditions due to a variety of external forcings may both enhance and retard growth of fog, depending upon the evolution of the fog interface. Also, in a case of strongly turbulent fog, increase in turbulence intensity may lead to fog dissipation, whereas in a weakly turbulent or effectively laminar fog, an increase of turbulence may lead to faster fog development. Further progress in understanding radiative fog processes requires systematic studies relating internal fog dynamics to the environmental conditions. It is highly unlikely that one-dimensional models can offer any substantial information on this issue, however, they may help to establish important sensitivities to the formulations of the microphysics and the infrared radiative transfer.

4. REFERENCES

BROWN, R; ROACH, W. T.; The physics of radiation fog: II - a numerical study, *Quart. J. R. Met. Soc.* (1976) **102**, 335–354.

CLARK, T. L.; Numerical simulations with a three-dimensional cloud model: Lateral boundary condition experiments and multicellular severe storm simulations. *J. Atmos. Sci.* (1979) **36**, 2191–2215.

CLARK, T. L.; FARLEY, W. R.; Severe downslope windstorm calculations in two and three spatial dimensions using anelastic interactive grid nesting: A possible mechanism for gustiness. *J. Atmos. Sci.* (1984) **41**, 329–350.

LALA, G. G.; JIUSTO, M. B.; KORNFIELD, M; Mechanisms of radiation fog formation on four consecutive nights. Preprints Conf. Cloud Physics, Chicago (1982) Amer. Meteor. Soc., 9–11.

OLIVER, D. A.; LEWELLEN, W. S.; WILLIAMSON, G. G.; The interaction between turbulent and radiative transport in the development of fog and low-level stratus, *J. Atmos. Sci.* (1978) **35**, 301–316.

ROACH, W. T.; BROWN, R.; CAUGHEY, S. J.; GARLAND, J. A.; REDINGS, C. J.; The physics of radiation fog. Part I: A field study, *Quart. J. R. Met. Soc.* (1976) **102**, 313–333.

SOMMERIA, G.; Three-dimensional simulation of turbulent processes in an undisturbed trade wind boundary layer. *J. Atmos. Sci.* (1976) **33**, 216–241.

SMOLARKIEWICZ, P. K.; CLARK, T. L.; The multidimensional positive definite advection transport algorithm: Further development and applications, *J. Comput. Phys.* (1986) **67**, 396–438.

WELCH, R. M.; RAVICHANDRAN, M. G.; COX, S. K.; Prediction of quasi-periodic oscillations in radiation fogs. Part I: Comaprison of simple similarity Approaches, *J. Atmos. Sci.* (1986) **43**, 633–651.

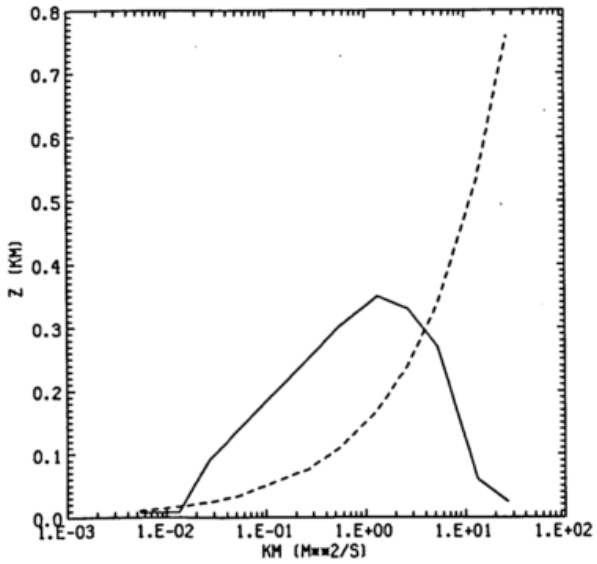


Figure 1. See description in text.

NUMERICAL STUDIES ON THE EVOLUTION OF RADIATION FOG

Wolfram Wobrock

Institut für Meteorologie und Geophysik, Universität Frankfurt a.M., FRG

1. INTRODUCTION

Recent investigations in fog modeling have the objective to predict the meteorological parameters as well as the micrometeorological data, i.e. droplet spectra and the pollutants in the droplets. Correct simulations of the uptake of trace constituents through a cloud system involve a detailed microphysical concept for the liquid water phase. The inclusion of detailed microphysics in a fog model is also reasonable in order to describe the physical processes as precise as possible.

The main purpose of this study is thus to use a detailed microphysics in a dynamic framework in order to verify the model results against field observations and to investigate the reasons for the formation of dense fog. As even today there is doubt about the conditions for the formation of dense fog. Jiusto and Lala (1983) stated, that turbulence can favor fog formation, Roach et al. (1976), however, concluded from field observations, that turbulence inhibits fog formation.

2. THEORETICAL CONCEPT

The dynamic model simulates the atmospheric boundary layer up to a height of 1000 m. As radiation fog is considered a one dimensional phenomenon, the model only describes vertical exchange processes. Herein the turbulent mixing is very effective and is formulated with the so called K-theory of boundary layer meteorology. For a detailed description of the model see e.g. Kramm (1986). Besides the components of horizontal wind speed, the specific humidity and the potential temperature the model predicts a so-called two dimensional number density distribution for aerosol particles and droplets. This treatment allows to simulate a continuous transition from dry to wet aerosol particles like haze and finally to droplet (Wobrock et al, 1986). The time rate of changes of the particle or droplet spectrum is determined by the turbulent mixing, the sedimentation and the diffusional growth. The properties of the ground and the surface are considered through a one dimensional soil model (Kramm, 1986), predicting soil temperature and volumetric liquid water content in several soil layers. To calculate the heating and cooling rates in the atmosphere and at the earth surface by solar and thermal radiation, the two-stream approximation of Zdunkowski et al (1982) is used.

3. RESULTS

To verify the model results against field observations, the data of the fog night October 19./20. recorded during the Bologna Fog Experiment 1986 in Italy (Beltz et al, 1987) were used. As the wind-, temperature- and humidity profiles at the beginning of the night were not known the model was initialized with three different soundings, which are displayed in Fig. 1 for the lower 100m of the atmosphere. The simulations start at 5.40p.m., around 1 hour after sunset. The numerical integration of the model yields a persistent and dense fog for initial sounding A. This was also recorded by the observers. For case B the model produces an unsteady, short fog and for case C a light fog starting 2 hours before sunrise.

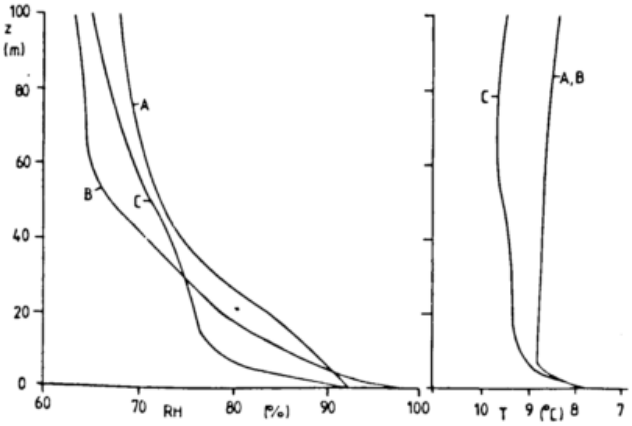


Fig.1: Initial profiles of rel. humidity RH and temperature T for the model cases A,B and C

During the first two hours of the simulations the characteristic evolution in the so-called sundown stage is nearly identical in

all three cases: The temperature near the ground decreases around 3°C/h (see Fig.2a), the relative humidity increases near 100% and the very stable stratification results in the formation of a low level jet. With the beginning of the adjacent stage, the so-called conditioning stage, the evolution of the three simulations differs significantly.

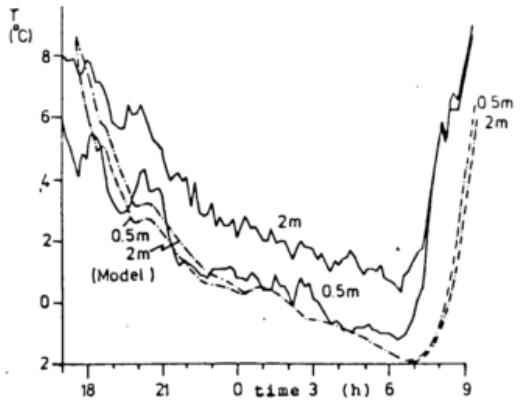


Fig.2a: Time evolution of observed and calculated temperature for case A

In case A, which resembles a typical dense radiation fog, the temperature decrease drops to 1°C/h (Fig.2a), in agreement with the observation (after 8p.m.) and the classification of Jiusto and Lala (1983). The atmosphere near the ground exceeds saturation for short periods, consequently a brief and weak fog in the lower 2m was observed (Fig 2b). The model reproduces the increase of rel. humidity at 8p.m., although the atmosphere remains subsaturated and thus only haze forms. The temperature curves (Fig.2a) show that both observed short fog formations at 6.30p.m. and 8p.m. are coupled with significant warming. Since these fog events were very shallow and light, this warming was obviously not caused by the latent heat of the condensation process nor by the emission of thermal radiation from the fog itself. The illustration for the calculated moisture fluxes (Fig.2c) shows, that the mixing of humid air from above results in the increase in rel. humidity at 8p.m.. As the eddy moisture flux is always associated with a turbulent heat flux (see Fig.2c) the turbulent mixing of warm air from above produces the temperature increase around 8p.m..

In the course of time low temperatures and high rel. humidities extend to higher levels and the stable stratification in the lower atmosphere weakens significantly. In case A the onset of the turbulent fluxes of heat and

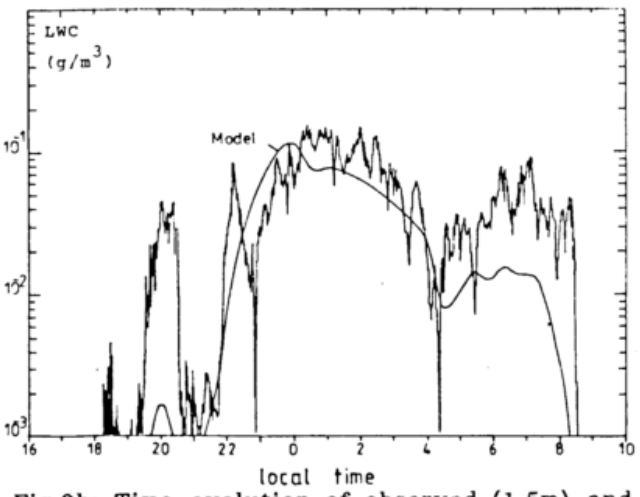


Fig.2b: Time evolution of observed (1.5m) and calculated (2m) LWC for case A

moisture from the layer 17-35m results in the formation of fog. The fog rapidly becomes dense with a LWC of more than 0.1g/m³ and a height of around 25m. Hereby it is most important, that the dense fog only develops when the moisture flux from above is not exceeded by the moisture transport to the ground. This is illustrated again by the results of case B.

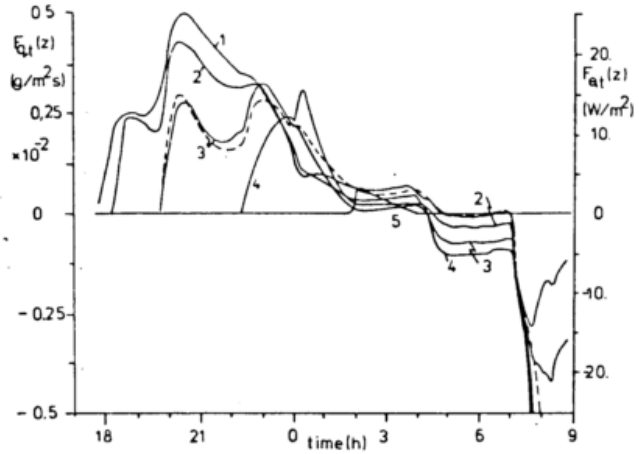


Fig.2c: Calculated moisture fluxes (case A) between the layers 0.5-2m (1), 2-7m (2), 7-17m (3), 17-35m (4) and 35-57m (5), ---is the heat flux between 7-17m

Due to the higher rel. humidity in the first 7m for case B the simulation shows a shallow fog at 7.20p.m. (Fig.3a). The onsetting moisture flux from above at 7.40 p.m. (Fig.3b) cannot exceed the transport into the ground. The associated heat flux helps to dissipate the shallow ground fog (Fig.3b). The lower layers dry out and only haze forms again shortly before sunrise.

In case C the conditions for fog were reached very late at night, since the initial humidities were significantly lower (Fig.1).

During the mature stage, which starts with the formation of dense fog, the cooling of the surface and the lower layers ends.

The simulation for case A shows a light warming of the air (Fig.2a), (mainly caused by the heat fluxes), which is typical for the beginning of the dense period. The observation only noted constant temperatures. The persistent dense fog dissipates near the ground at around 4p.m.. This decrease in LWC is due to the heat transport from above, which is mainly caused by the thermal radiation of the dense upper part of the fog layer. The simulated fog has reached now a height of around 45m. The temperature profile in the lower part of the fog becomes isothermal and finally slightly superadiabatic, thus a new cooling starts near the ground associated with a small increase in rel. humidity and LWC. The fog dissipates around two hours after sunrise, when the incident solar radiation causes a heating of the surface and the upgoing heat flux dissolves the fog from below.

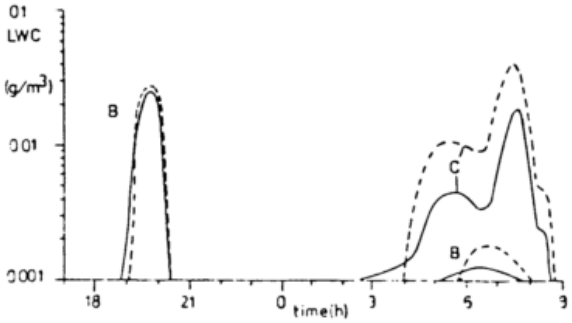


Fig.3a: Time evolution of calculated LWC for case B and C in 2m (—) and in 7m (---)

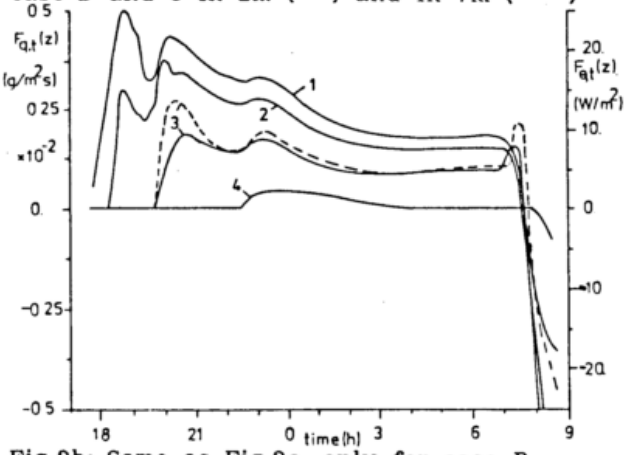


Fig.3b: Same as Fig.2c, only for case B

The various results show, that the formation of fog was essentially influenced by the turbulent fluxes in the surface layer. These results are in principal agreement with those of Jiusto and Lala (1983), ("turbulence early in the evening may inhibit fog whereas later in the evening, turbulent mixing can intensify fog"). Their observations of turbulence, however, were only based on the increase in wind speed when fog forms. In contrast, the model in most cases predicts high wind speeds prior to the fog (caused by the LLJ), which weaken considerably with the onset of fog. On the other hand own model results, which are not displayed here, have shown that during long persistent fog nights when wind speeds in the lower 20m are less than 1.5 m/s further fog enhancement results in higher turbulence and an increase in wind speed of 0.5–1 m/s.

4. CONCLUSION

The simulations have shown that the eddy transport of heat and moisture mainly determines the wind structure of a fog field. Considering this thermodynamic forcing of turbulence and not only its dynamical impact, the statement of Roach et al. (1976) that "turbulence inhibits fog formation" has to be reviewed. This statement resulted from their frequent observations that windspeeds of 1–2 m/s prior to a dense fog event decreases to 0.5 m/s when the fog evolves. The model results suggests, however, that this is an effect of an increase and not a decrease in turbulence during the fog formation. Future theoretical and experimental investigations should thus consider in particular the influence of thermodynamic turbulence on the formation of fog.

5. REFERENCES

Beltz N., K. Enderle, W. Jaeschke and H. Obenland, 1987: Measurements of sulfur species during the 1986 field experiment in S. Pietro Capofiume. Heterogeneous atmospheric chemistry project; Collection of reports of participants to the fog field project November 1986 at field station of S. Pietro Capofiume in the Po Valley, S. Fuzzi, ed., 16–21.

Kramm, G., 1986: Modellrechnung zur Bestimmung der trockenen Deposition atmosphärischer Spurenstoffe. IABG-Bericht B-TD 9003/02, München.

Jiusto, J.E., and G.G. Lala, 1983: Radiation fog field programs – recent studies. ASRC-SUNY, Publ.No.869.

Roach, W.T., R. Brown, S.J. Caughey, J.A. Garland and C.J. Readings, 1976: The physics of radiation fog: I – a field study. Quart. J. R. Met. Soc. 102, 313–333.

Wobrock W., G. Kramm and F. Herbert, 1986: The influence of aerosol particle distribution and composition on the evolution of radiation fog. Aerosols: Formation and Reactivity, 426–429; 2nd Int. Aeorosol Conference in Berlin, Pergamon Journal Ltd., Great Britain.

Zdunkowski W.G., W.G. Panhans, R.M. Welch and G.J. Korb, 1982: A Radiation scheme for circulation and climate models. Beitr. Phys. Atmosph. 55, 215–238.

A Numerical Study of Mesoscale Perturbations in Stratiform Boundary Layer Cloud Fields

Michael Tjernström

Department of Meteorology, Uppsala University
Uppsala, Sweden

1. INTRODUCTION

Development of stratified clouds in the atmospheric boundary layer (ABL), as well as the related turbulent structures and its interactions with other processes, has been studied in some detail over the last decades. Such studies have been based on observations (Brost et. al., 1982a and b) or numerical simulations. These numerical studies have been performed both with ordinary higher order closure models (Oliver et.al., 1978) and "Large Eddy models" (Deardorff, 1980). Important knowledge has, in this way, been gained on the different processes in such clouds. Most such studies are, however, performed with basically one dimensional models. On the other hand, much work has, during the same time, been devoted to studies related to so called mesoscale phenomena (cf. e.g. Atkinson, 1981), and a number of such circulations has been identified and studied, also both through observations and numerical simulations.

In the present work, the aim has been to develop a model that combines the detailed description of the ABL processes vital to stratified boundary layer clouds, from a higher order closure ABL model, with a mesoscale model. This is done in order to investigate the influence of mesoscale circulations or perturbations on such clouds.

It is believed that some of the difficulties in the validation the existing ABL models may be ascribed to the influence of such mesoscale systems, caused by the fundamental three-dimensionality of meteorological problems and the scarcity of basically homogeneous areas. The use of a model capable of describing both vital ABL properties and mesoscale circulations should be able to give valuable insights into the physics of the interactions between different processes and different scales.

2. THE MODEL

2.1 A Brief description

The model used for this study is a hydrostatic 2D or 3D mesoscale model with terrain following coordinate system (Pielke and Martin 1981), using a higher order parameterisation for ABL turbulence ("Yamada-Mellor level 2.5", Yamada and Mellor, 1979). Other parameterisations included are a radiation parameterisation for both shortwave and longwave radiation, a sub-grid scale condensation scheme and a simple energy balance scheme for the lower surface (optional). The model has been tested against measured data from an area in south-western Sweden, featuring terrain forcing on the meso-γ -scale (Tjernström, 1987a and Enger, 1988a) giving encouraging results. For a detailed description of the model, see Tjernström (1987d).

2.2 The condensation parameterisation

Both the temperature (Θ_l) and humidity (R) variables in the prognostical equations are chosen so that they are invariant to phase changes between vapour and liquid water. It is then assumed that the instant value of the saturation deficit, expressed with these invariant variables, is distributed around its gridvolume mean value according to a Gaussian probability density function (PDF). The volume containing liquid water and the mean amount of liquid water, inside such a gridvolume, is then calculated by integration of every possible saturation deficit contributing to liquid water, using that PDF, as

$$Cf = 0.5\cdot\left(1-erf\left(\frac{\Delta R}{\sqrt{2}}\right)\right)$$

$$\frac{R_l}{\sigma_f \lambda_l} = Cf\cdot\Delta R + \frac{\exp\left(-\frac{(\Delta R)^2}{2}\right)}{\sqrt{2\pi}}$$

where

$$\Delta R = \frac{(R-R_{sl})}{\sigma_f}$$

and the parameters λ_l and δ_l relates the invariant and the ordinary thermodynamical variables and erf is the error function.The standard deviation of the saturation deficit can be expressed with the variance of R and Θ_l and their covariance.The calculation is done prognostically, adding the prognostical equations for these moments from the "level 4" closure these variables.

3. THE EXPERIMENT

3.1 Terrain height differences

A great number of simulations where carried out for a cloud capped ABL with different upstream cloud base and cloud top heights. Three types of terrain geometries

were studied, i.e. an escarpment, a ridge (both 2D simulations) and a hill (3D simulations). The maximum height of the hill/ridge top was at 150 m and a the halfwidth was 2 km. It was found that the variations in local cloud base heights could be very much larger than what is motivated by the terrain geometry only. When the stratification was stable, it was found that the cloud base heights were reduced, also in heights above sea level and vice versa for unstable stratification. Fig. 1 shows one typical example of such a cloud base descent.

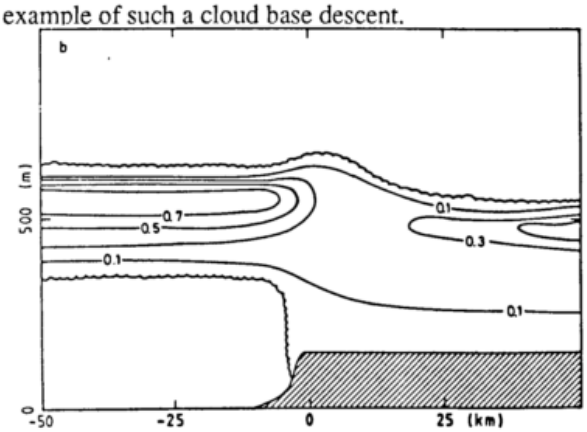


Fig. 1 A cross section showing an example of the cloud base descent, when the cloud capped ABL approaches higher terrain.

This behavior was analysed in terms of the effect of adiabatical lifting, for cases with stable stratification. It was found that the magnitude of the maximum cloud base height descent from the model agreed well with what would be expected from this simple theory.

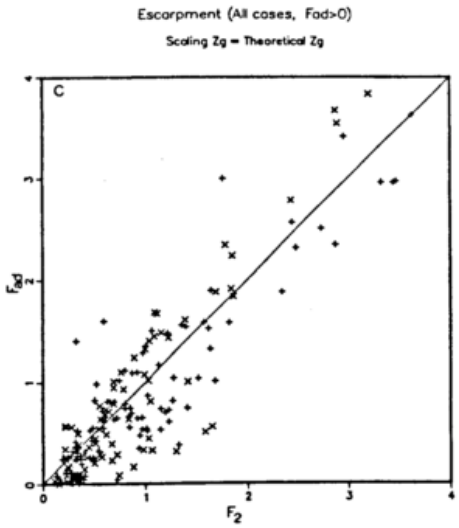


Fig 2. Scatter-plot showing the scaled adiabatic cloud base descent (Fad) plotted versus the scaled cloud base descent from the numerical model

Some deviations from this conclusion was evident. It was found that for less stable cases, the increased mixing due to the increase in TKE, when the air approaches the terrain obstacle, was more important than adiabatic lifting. It was also found that higher upstream clouds suffered less reduction in cloud base heights, than was expected from the simple theory. A wave in the lee of the hills/ridges was also present in practically all cases. The amplitude of this wave was found to agree well with "hydraulic jump" theory for some of the cases, with linear analytic wave theory for other cases, but a large number of cases could not be accounted for by any of these theories. The most striking feature of this wave is its ability to increase the height to the cloud base and, at times to dissolve the cloud completely. The magnitude of these phenomena could, however, not be explained with any simple model. The three dimensional simulations was found to reveal a more complex pattern in the cloud field. When the stratification was increased, the airflow chooses to move around the hill, rather than above it, below some point along the slope. This causes divergency above the hill and subsequent subsidence. The lowest cloud base for these cases was thus found to be "hanging down" on the upstream side of the hill, agreeing relatively well with the reduction in cloud base heights expected from adiabatic lifting, but the cloud base heights above the hill was higher than otherwise expected.

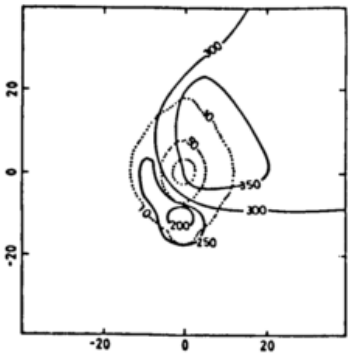


Fig. 3 Isolines showing spatial variation of the cloud base height for the case of a hill. Thick lines are cloud base height above sea-surface and dashed lines is the topography

3.2 Shore line effects

3.2.1 Advection out over warm water

In these simulations, a cold or cool ABL was advected out over warm water. In the first set of simulations, the upstream ABL was cloud capped and only slightly stable (near neutral), with a typical surface temperature difference of 5-6°C. It was found that for these cases, the cloud base practically always descended when advected out over water. The cloud base height reduction took place in two stages, one first stage, close to the shore line, were the cloud base descended rapidly, and differently for different cases and in a "rugged" manner, and a second stage, further downstream, were the clouds

descended more orderly, smoothly and in a similar manner for the different cases.

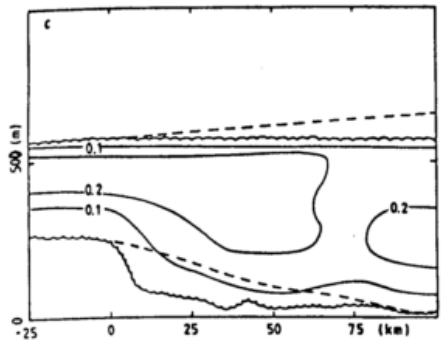


Fig. 4 Cross section of a cloud that is being advected out over warm water

This two stage behavior is believed to be the effect of a coupling between the drastic increase in low level buoyancy production of TKE and the higher level absence of stability. There is no stability present in the ABL to prevent this increase in turbulent production to propagate up through the ABL and to mix the high levels of ABL humidity close to the surface through the whole ABL readily. Further downstream, the ABL turbulence fields become more balanced, thus the smoother second stage.

This picture was changed if the upstream ABL was stable, i.e. with a surface inversion. These test were performed for upstream cloud free conditions. Here, the surface temperature differences was 15-18^{o}C and the upstream ABL temperature increased 10^{o}C within the lowest 200m. For these cases, the ABL stability tends to damp the growth of a new ABL and the transition to a convective marine ABL is much more smooth. Clouds will or will not form in this new ABL mostly depending on the humidity in the upstream ABL.

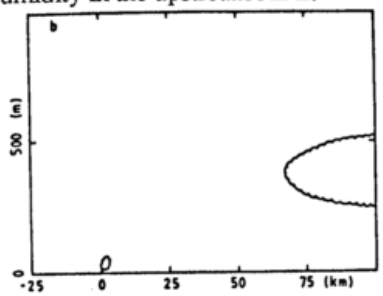


Fig. 5 Same as fig. 4, but for a case with a stable cloud free upstream ABL, and a larger difference in sea-surface temperature

These cases, also, were re-modelled using a simple "mixed layer" model, which was partially successful in simulating these features (Tjernström, 1987c).

3.2.2 Sea-breeze driven fog recirculation

When the annual minima in sea surface temperature coincides with a time of year with frequent radiation fogs, and the solar elevation angles at the same time begins to be hight enough that solar radiation may disperse these radiation fogs relatively rapidly, the surface heating may also result in a weak sea-breeze system that may "re-advect" the fog, still present out at sea in over the shore line again. The simulations show this to be a very delicate balance between optical thickness of the fog, time of year and synoptic situation. This type of weak sea breeze have winds of only 2-4 m/s and a vertical thickness of only a couple of hundred meters, so the presence of even moderate synoptic forcing will effectively preventing the circulation. If the initial radiation fog is to thick, no dispersion will occur, or it will occur to late in the day for any recirculation to develop. If the initial fog is to thin, there will be a quick dispersal of the fog and a circulation development, but the solar heating will strong enough to disperse the recirculated fog right at the shore line. Sometimes, however, the fog may be just thick enough to prevent emediate dispersal, but be lifted into stratus and be totally dissolve by mid-morning. In these cases the circulation will advected the sea fog back in over the coastal areas (fig.5) and the new fog may be dissolved later in the day or remain the whole day.

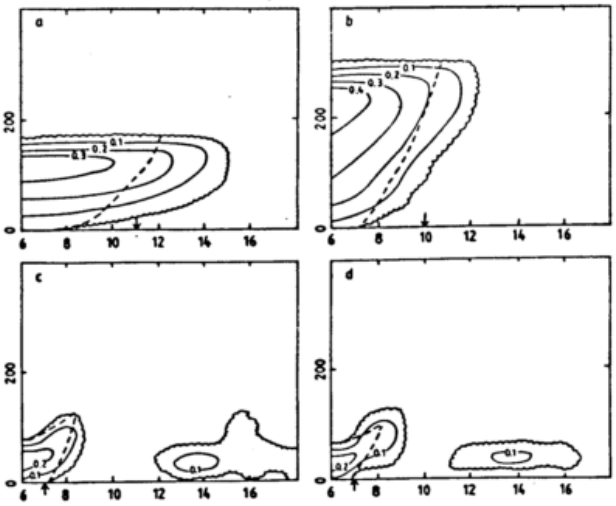


Fig. 6 Time-height cross section showing a "re-advected fog/stratus cloud.

3.2.3 The effect of internal boundary layers.

The simulations for this type of flow was carried out for a moist marine, slightly stable, ABL being advected in over a land surface that is heated during the day.

For the formation of ABL clouds it is concluded that the sea surface temperature is vital. To low surface temperature will lead to a less moist ABL and no, later or less cloud formation. The convergency zone set up by the reduction in airspéed over the rougher surface, at least in

stable or moderately unstable conditions, is also important to cloud formation. Another factor that proved very important, to cloud formation, and development is the synoptic scale subsidence rate. This is critical in view of the difficulty in obtaining an accurate estimate of this variable from routine measurements.

The formation of a IBL is also important for the development of a cloud field. It was found that the IBL in temperature was the most critical for a stratified cloud cover being advected inland. When this new ABL grew up through the clouds they were dissolved. This causes the leading cloud edge to back downstream as the slope of the temperature IBL grows during the day. It also has the effect that a shallow , low cloud or a sea fog will be dissolved close to the shore line, while a higher cloud deck will continue to be advected some distance inland, regardless of the amount of solar heating.

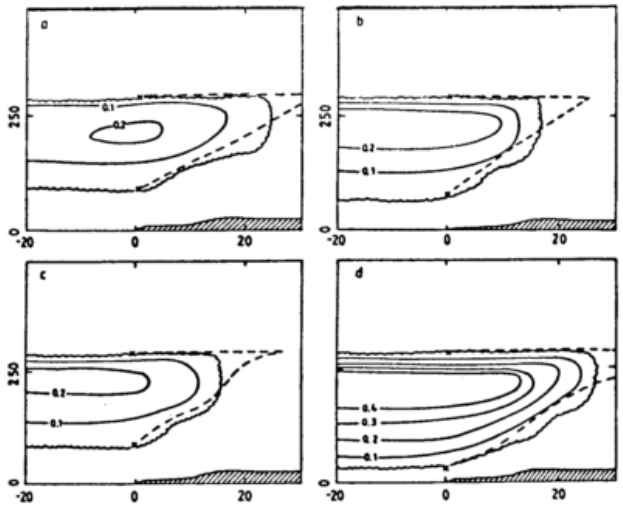


Fig. 7 Cross section of a marine cloud layer that is advected in over a land area with a growing convective IBL.

4.CONCLUSIONS

The simulations show the, often drastic, impact on stratiform ABL clouds of mesoscale perturbations in the flow field. Such effects has to be taken into account in local cloud forecasting. A large part of such work is based on synoptical cloud observations, and there is a bias, at least in Sweden, in the location of such stations to lower areas (e.g. valleys etc), specially in hilly terrain. In a survey of all the synoptical stations in Sweden performed by the Military Weather Service it was found that practically all stations had higher terrain at least in some direction, within a 30 km radius. For southern Sweden, the typical height difference was 100 m, ranging between 50 and 250 m. Also, for the case of the shore line effects, upstream observations do not always reveal what will happen downstream and the downstream observations, out at sea, may be very sparse.

The use of complex mesoscale models for prognostical purposes is probably still many years away, mostly due to their demands on computer facilities. Simpler physical models and accumulated knowledge (experience and statistics), will because of this, continue to play a major role in local forecasting. This study shows that a complex numerical model may be an effective "test bench" for such simpler models. A word of caution is, however, motivated in this context. A model is but a model and, as such, always an over simplification of the real atmosphere, and any final conclusions should be based on comparisons with real data, obtained from the atmosphere.

References

Atkinson, B.W., 1981.: Meso-scale atmospheric circulations.,Academic Press, pp 478.

Brost, R.A., Wyngaard, J.C. och Lenschow, D.H., 1982a.:Marine stratocumulus layers. Part I: Mean conditions., JAS, 39, 800-817.

Brost, R.A., Wyngaard, J.C. och Lenschow, D.H., 1982b.:Marine stratocumulus layers. Part II: Turbulence budgets., JAS, 39, 818-836.

Deardorff, J.W., 1980.:Stratocumulus capped mixed layers derived from a three dimensional model., BLM, 18, 596-627.

Enger, L. 1987a.: Simulation of dispersion in complex terrain. Part A. The fluid dynamic model., Submitted to Atmos. Environ.

Oliver, D.A., Lewellen, W.S. and Williamson, G.G.:The interaction between turbulent and radiative transport in the development of fog and low level stratus., JAS,35, 301-316.

Pielke, R.A. and Martin C.L.:1981, The Derivation of a Terrain following Coordinate System For Use in a Hydrostatic Model.,JAS,38,1707-1713.

Sommeria, G. and Deardorff, J.W.,: 1977, Subgrid-scale Condensation in Models of Nonprecipitating Clouds.,JAS,34,344-355.

Tjernström, M., 1987a.: A study of flow over complex terrain using a three-dimensional model. A preliminary model evaluation focusing on fog and stratus., Ann. Geophysicae, 5B, (5), 469-486.

Tjernström, M., 1987b.: Numerical simulations of stratiform boundary layer clouds on the meso-γ-scale. Part I. The influence of terrain height differences., Accepted for publication in BLM.

Tjernström, M., 1987c.: Numerical simulations of stratiform boundary layer clouds on the meso-γ-scale. Part II. The influence of a step change in surface roughness and surface temperature., Accepted for publication in BLM.

Tjernström, M., 1987d.: A three-dimensional meso- γ -scale model for studies of stratiform boundary layer clouds. A model description., Rep. No. 85, Dep. of Meteorology, Uppsala University, Sweden.

Yamada, T. and Mellor, G.L., 1979.: A numerical simulation of the BOMEX-data using a turbulence closure model coupled with ensemble cloud relations.,QJRMS, 105, 915-944.

A Numerical Study of Radiation Fog Over the Yangtze River

Qian Min-wei Lei Xiao-en

Institute of Atmospheric Physics, Chinese Academy of Sciences,
Beijing, China

List of Symbols

C_p specific heat of air at constant pressure
C rate of condensation per unit mass of air
F_N net radiative flux
g acceleration of gravity
G gravitational settling flux of liquid water
K_H horizontal exchange coefficient
$K_z^m, K_z^\theta, K_z^q, K_z^M$ vertical exchange coefficients
K_s soil heat diffusivity
L latent heat
M liquid water mixing ratio (kg/kg)
P pressure
P_∞ reference pressure
q water vapour mixing ratio (kg/kg)
q_s saturation mixing ratio (kg/kg)
R gas constant
U, W component of velocity (m/s)
W^* vertical (Z^*) component of velocity (m/s)
X, Z coordinates
Z^* transformed height coordinate
Z_G ground elevation
Z_H height of the top of the model
π Exner's function
θ potential temperature
ρ air density

1. Introduction

Along upper reaches of the Yangtze River, the terrains of the banks are very complex. One hill after another sits along the river. Some hills are very high and steep and some are low and flat.

The fog haunts in this area very frequently, especially in winter. Some people there say that almost every morning in winter, they find that they have been surrounded by fog. They will be free nearly at noon. In fact, the fog in this area does not appear everywhere. Some drivers have the experiences that they might meet heavy fog at one place and at the same time there is no fog at all at another place only several kilometers away. Another interesting phenomenon is that fog never appears in the Yangtze Gorges where the span of the river is very small and the hills of the banks are very steep. Captains need not worry that fog will rise when their ships are sailing along the gorge which stretches more than 200 kilometers. All these characters of the fog in this area are closely related to the water surface and the terrains of the river banks. The purpose of this paper is to study their interactions.

2. The Model

We use a transformed height coordinate system in order to put the geographical features into our model easily. The vertical coordinate is defined by

$$Z^* = (Z - Z_G) / (Z_H - Z_G) \cdot Z_H$$

The equations in the Z^* - coordinate system are given below

$$\frac{du}{dt} = -\theta\frac{\partial \pi}{\partial x} + g\frac{Z^* - Z_H}{Z_H}\cdot\frac{\partial Z_G}{\partial x} + \frac{\partial}{\partial x}\left(K_H\frac{\partial u}{\partial x}\right) + \left(\frac{Z_H}{Z_H - Z_G}\right)^2\frac{\partial}{\partial Z^*}\left(K_z^m\frac{\partial u}{\partial Z^*}\right) \quad (1)$$

$$\frac{d\theta}{dt} = \frac{\partial}{\partial x}\left(K_H\frac{\partial \theta}{\partial x}\right) + \left(\frac{Z_H}{Z_H - Z_G}\right)^2\frac{\partial}{\partial Z^*}\left(K_z^\theta\frac{\partial \theta}{\partial Z^*}\right) - \left(\frac{Z_H}{Z_H - Z_G}\right)\frac{1}{\rho C_p}\frac{\partial F_N}{\partial Z^*} + \frac{L}{C_p}C \quad (2)$$

$$\frac{dq}{dt} = \frac{\partial}{\partial x}\left(K_H\frac{\partial q}{\partial x}\right) + \left(\frac{Z_H}{Z_H - Z_G}\right)^2\frac{\partial}{\partial Z^*}\left(K_z^q\frac{\partial q}{\partial Z^*}\right) - C \quad (3)$$

$$\frac{dM}{dt} = \frac{\partial}{\partial x}\left(K_H\frac{\partial M}{\partial x}\right) + \left(\frac{Z_H}{Z_H - Z_G}\right)^2\frac{\partial}{\partial Z^*}\left(K_z^M\frac{\partial M}{\partial Z^*}\right) + \left(\frac{Z_H}{Z_H - Z_G}\right)\frac{\partial G}{\partial Z^*} + C \quad (4)$$

$$\frac{\partial u}{\partial x} + \frac{\partial W^*}{\partial Z^*} - \frac{1}{Z_H - Z_G}\left(u\frac{\partial Z_G}{\partial x}\right) = 0 \quad (5)$$

$$\frac{\partial \pi}{\partial Z^*} = -\left(\frac{Z_H - Z_G}{Z_H}\right)g/\theta \quad (6)$$

where

$$\pi = C_p\left(\frac{P}{P_\infty}\right)^{R/C_p} \quad (7)$$

$$W^* = \left(\frac{Z_H}{Z_H - Z_G}\right)\cdot W + \frac{Z^* - Z_H}{Z_H - Z_G}\left(u\frac{\partial Z_G}{\partial x}\right) \quad (8)$$

$$\frac{d}{dt} = \frac{\partial}{\partial t} + u\frac{\partial}{\partial x} + W^*\frac{\partial}{\partial Z^*} \quad (9)$$

Since the scale we study only covers 20 kilometers, the Coriolis force is omitted. Of course, we have assumed that all physical factors along the river are homogeneous. For the soil layer we have

$$\frac{\partial T_s}{\partial t} = \frac{\partial}{\partial Z}\left(K_s\frac{\partial T_s}{\partial Z}\right)$$

Some data the model needs at the initial time, e.g. the data of wind, humidity, air temperature, soil temperature, water temperature, etc., are obtained from the two cross sections that we select for simulating the fog there. One section is in Chong-qing, the other is in Fu-lin.

Because the trends of the river at the two sections are from west to east, the trends of the two sections are from north to south. The prevailing winds at the two places in winter are N coincidentally. Considering that the river is only about 1000 m wide, we choose 200 m horizontal grid interval. In the vertical we use 20 layers with variable grid space. The first grid space is 10 m and the others increase at a rate of 1.2 . The top of our model is at about 1800 m. In soil we use 10 levels with constant grid spacing of 5 cm. The time step is 30 s.

We only care for the fog in winter there. The simulating time is from 20:00 to 06:00 .

At the initial time we specify M=0.

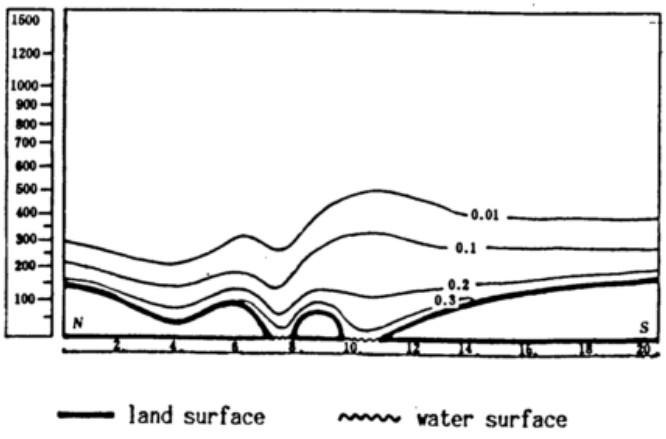
3. The Results

After sunset, the soil surface temperature begins to decrease. However, the water temperature varies very slightly in a short time due to large heat capacity of water. At the initial time (20:00) , the soil surface temperature is about 3 degrees lower than the water temperature . This difference of temperature generates a circulation similar to that of the sea breeze. Furthermore, another circulation is caused by differential cooling between the air over the top of hill and that over the valley. Thus the local wind consists of the two circulations. Because the prevailing wind in this area is very weak (about 0.5 m/s below 10 m and 3.6 m/s above 1500 m), the local wind certainly play a main role in affecting the fog. In other words, both the Yangtze River and the terrain of the banks play important roles.

3.1 The Role of the Terrain

The effect of the terrains on forming and developing of fog is secondhand through the wind field. The wind partly controlled by the terrain makes main contribution to the forming and developing of fog.

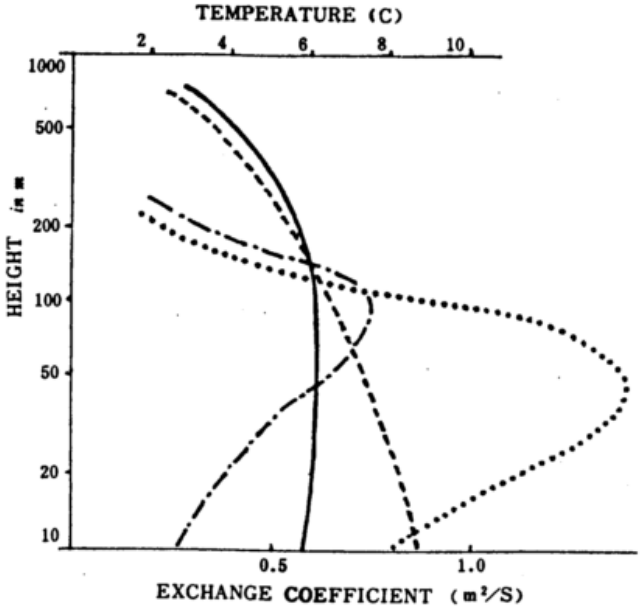
Fig(1) shows the distribution of liquid water content in Chong-qing at 06:00.



Fig(1) Distribution of liquid water content (g/kg) in Chong-qing at 06:00

The top of fog is specified by the 0.01-isoline of liquid water content. There is another river called the Jia-lin River at the north of the Yangtze River. From Fig(1), we can get a general picture of the fog there. Noticeable feature is that the height of fog over the banks far from the river is only about 150 m to 250 m, while that over the river is more than 500 m. We think that there are three factors which should take the responsibility for the result we mentioned above.

The first factor is the different stability between the air over the river and that over the banks. Fig(2) shows the temperature profiles and the exchange coefficient profiles over both the river and the banks. Obviously, there is a inversion layer above the banks. On the contrary, there is no inversion layer over the river due to the higher temperature of the water. Thus the moisture and liquid water over the river can diffuse up easily. The exchange coefficient profiles also reflect the different stability over the two places.

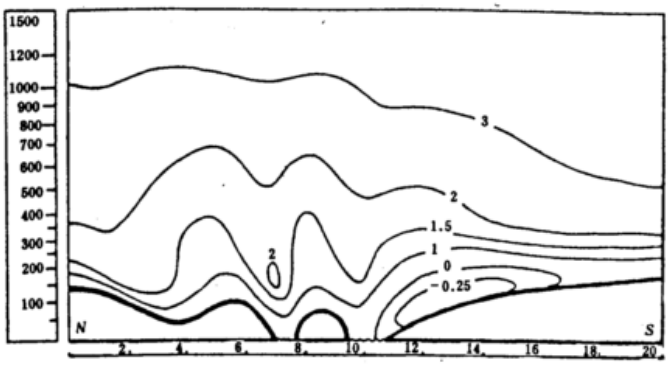


Fig(2) Temperature and exchange coefficient profiles above the river and the banks in Chong-qing at 06:00
—— temperature over the bank
----- temperature over the river
—·— exchange coefficient over the bank
····· exchange coefficient over the river

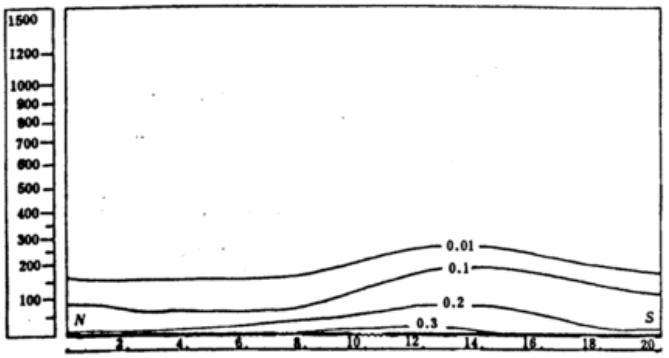
The second factor is the plenty of moisture coming from the river that makes it possible that fog can reach a higher level. About how the river affects fog in this area will be discussed later.

The third factor is the terrain which plays an important role because the local wind there partly relys on it. Fig(3) shows the horizontal wind field. Generally speaking, there are two circulations on both sides of the Yangtze River. They converge at lower level over the river. Of course, they will diverge at a higher level. At the convergent area, there is a strong updraft which might reach more than 0.2 m/s at some level. It is the updraft that would carry the moisture and liquid water to higher level. If the terrain in this section is totally flat, the circulations and the updraft might not be so strong and the situation of fog might be different.

Fig(4) shows the distribution of liquid water for content the flat terrain. The height of the fog above the river can only reach 260 m instead of 500m.



Fig(3) Distribution of horizontal wind (m/s) in Chong-qing at 06:00



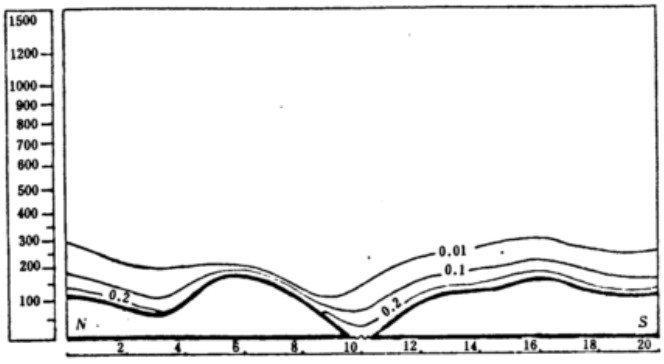
Fig(4) Distribution of liquid water content (g/kg) for the complete **flat** terrain at 06:00

Up to now, we may have a conclusion that the **mountain slopes** on both sides of the river are very favorable for the fog to reach a higher level. But things can be changed to the opposite direction if the slopes are too steep.

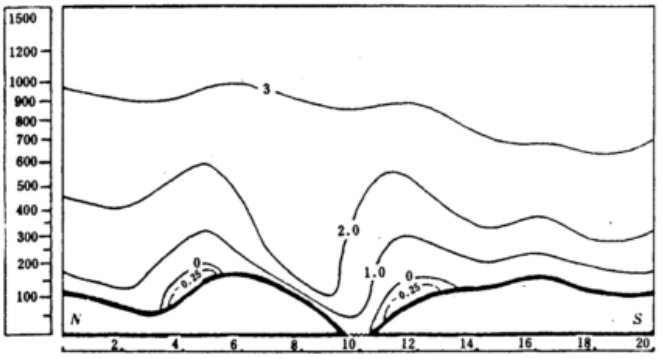
Fig(5) and (6) show the distribution of liquid water content and horizontal wind field in Fu-lin at 06:00. The mountain slope at the north of the Yangtze River is steeper and longer. Noticeable feature is that the fog in this slope is sparse and the height of the fog is very low. The liquid water content in this slope does not exceed 0.2 g/kg and the height of fog is only about 30 m, while at other places, it is more than 150 m. Fig(6) can give the explanation that why fog at this slope is different from that at other places. Because of the steeper and longer slope, the wind in this slope is much stronger than that in any other places. It is well known that the strong wind is disadvantageous for the fog to form and develop. Therefore it is possible that fog may form at one place but could not form at another place only short distance away.

Now it seems that the effects of the terrains on fog are not exposed completely. Let's double the height of the terrain in Fu-lin and see what will happen.

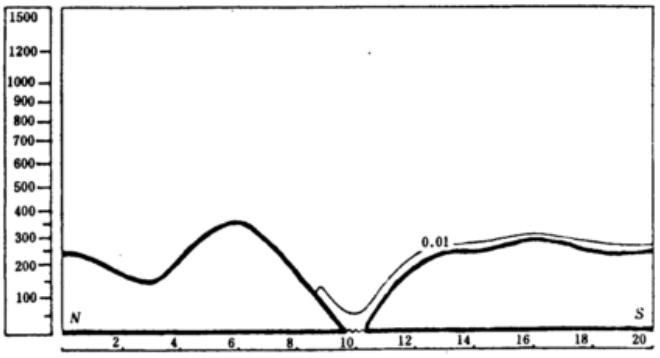
Fig(7) and (8) show the distribution of liquid water content and horizontal wind field in Fu-lin at 06:00 under the condition of doubling the height of terrain.



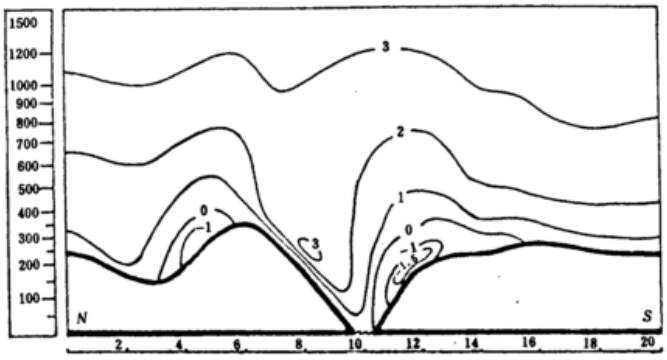
Fig(5) Distribution of liquid water content (g/kg) in Fu-lin at 06:00



Fig(6) Distribution of horizontal wind(m/s) in Fu-lin at 06:00



Fig(7) Distribution of liquid water content (g/kg) under the conditions of doubling the height of terrain in Fu-lin at 06:00



Fig(8) Distribution of horizontal wind (m/s) under the conditions of doubling the height of terrain in Fu-lin at 06:00

From Fig(7), we can see that nearly no fog appears there. This result can easily be understood after looking at the distribution of the horizontal wind field. The circulations are much stronger than those in normal terrain. We can use this result to explain the phenomenon that why fog never appears in the Yangtze Gorges. Of course, under the actual conditions, the circulations are not the only reason for the phenomenon. The component of the wind along the river also takes the responsibility for that. The component sometimes is really strong. Anyway, the circulations are very important.

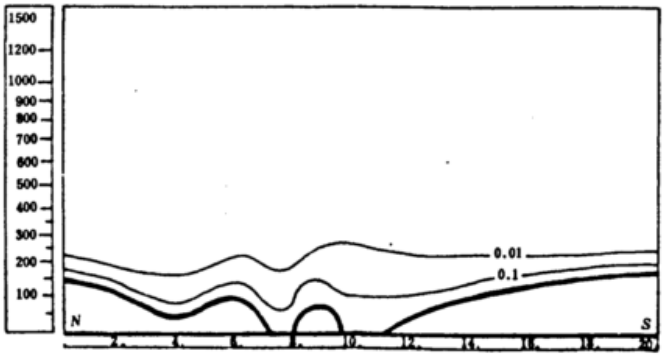
3.2 The Role of the River

The effects of the Yangtze River on fog include two parts. One is the circulation caused by the differential heating between the air over the river and that over the banks. The circulation, like the circulation of mountain and valley, affects fog secondhandly through the wind field. If the difference between the water temperature and the soil surface temperature is not very big, the circulation might not be important. The other is that the Yangtze River provides necessary moisture .

Making a comparison between Fig(1) and Fig(5), we can find that the fog near the river in Fu-lin does not reach the height which it can reach in Chong-qing. The height of fog over the river is only about 150 m instead of 500 m. Also, the fog is sparser in Fu-lin.

The noticeable difference between the two sections is the span of the river. The span of the river in Fu-lin is only about half of that in Chong-qing. It is certain that the moisture coming from the river in Fu-lin is much less than that in Chong-qing. Therefore the fog near the river in Fu-lin does not reach a higher level and is not so heavy.

It is no doubt that fog will be sparser and lower if there is no moisture coming from the river. Assuming that it is not water but soil covering the area of the river, the situation of fog will be greatly different. Fig(9) shows the result.



Fig(9) Distribution of liquid water content(g/kg) under the assumption of no water in the river in Chong-qing at 06:00

The fog only reaches about 50 m over the banks far from the river and 260 m over the river. The content of liquid water does not exceed 0.2 g/kg. This situation of fog is not due to the strong wind , but the lack of moisture coming from the river.

Comparing with Fig(1), we can realize the importance of the river.

Actually, we have overestimated the content of the liquid water. If there is no water, at the initial time the vapour mixing ratio there can not reach the value we observed at the section of Chong-qing. In this case, the fog will be much sparser and lower than that showed in Fig(9) and even can not form.

References

[1] Brown, R., and W.T. Roach, 1976: The physics of radiation fog:II- a munerical study. Quart. J.R. Met. Soc., 120, 335-354

[2] Estoque, M.A., and C.M. Bhumralkar, 1969: Flow over a local heat source. Mon. Wea. Rev., 97, 850-859

[3] Mahrer, Y., and R.A. Pielke, 1977: A Numerical Study of the Airflow over Irregular Terrain. Beitrage zur Physik der Atmosphare, 50, 98-113

[4] McDonald, J.E., 1963: The Saturation Adjustment in Numerical Modelling of Fog. J. Atmos. Sci., 20, 476-478

[5] Nnbutaka Mannouji, 1982: A Numerical Experiment on the Mountain and Valley Winds. J.Meteor. Soc. of Japan, 60(5), 1085-1104

[6] Roach, W.T., and R.Brown etc.,1976: The Physics of Radiation Fog: I-a field study. Quart. J.R. Met. Soc., 102, 313-333

[7] Zdunkowski, W.G., and B.C. Nielsen, 1969: A Preliminary Prediction Analysis of Radiation Fog. Appl. Geophys., 75, 278-299

[8] Zdunkowski, W.G., and A.E. Barr, 1972: A Radiative-Conductive Model for the Prediction of Radiation Fog. Boundary-Layer Meteor., 3, 153-177

[9] Zdunkowski, W.G., and F.G. Johnson 1965: Infrared Flux Divergence calculations with Newly Constructed Radiation Tables. J.Appl. Meteor., 4, 371-377

PRECIPITATION MECHANISM OF PRECIPITUS STRATIFORMIS OVER JILIN PROVINCE IN SPRING

Wang Xue-lin Jin De-zhen Li Yong-zhen Zheng Chun-ri
Meteorological Institute of Jilin Province

1. INTRODUCTION

Jilin Province was the first to do artificial precipitation experiment in the mainland of China since 1958. From 1963 till 1986 there are 660 sorties for cloud seeding experiment, among them 130 times for research with special designs. The great amount of data about the structure and precipitation mechanism of precipitus stratiformis were obtained by aircraft, satellite, Radar, radiosoundings and surface equipments [1]. The principal objects of research were precipitus stratiformis in rain band of weather system. Their precipitation rate ranges from 0.1mm/hr to 3.0mm/hr, and the temperature of cloud top is about -10℃—20℃.

2. SOURCE OF ICE CRYSTALS

Comprehensive analysis reveal three principal source of ice crystals in As—Ns.

2.1 Activization of Ice Nuclei

The number of activized ice crystal from ice nuclei presents exponential distribution with temperature. We may write,

$$N = N_* \times EXP(-2T)$$

Fig1. illustrates distribution of active ice nuclei with temperature in BEIJING AND BAICHENG [2], [3]. The temperature of cloud top As-Ns over Jilin province normally is the range of -10℃—20℃. So the concentration of ice crystal should be 1.0/L —5.9/L.

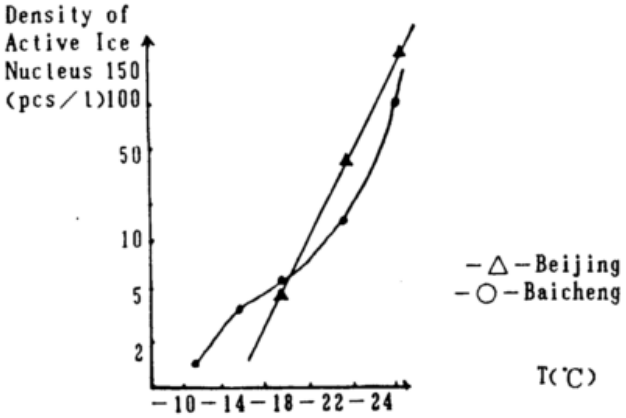


Fig 1. Variation of ice nuclei concentration with temperature

2.2 Seeding of Upper Layer Cirrus

From paper [4] we can see that the concentration of ice crystal may increases by one order magnitude.

2.3. Multiplication of Ice Crystal

According to the condition of Mossops experiment [5], the amount of secondery ice generation is about 16.0/L in our province. Further analysis shows that ice crystal multiplication may occur in deep As op.

3. Growth of Ice Particles in Supercooled Layer

We have analysed and calculated mass contribution by sublimation, riming and collision of ice crystal with snow crystal [6]. The calculated results are shown in Fig 2 and Fig 3.

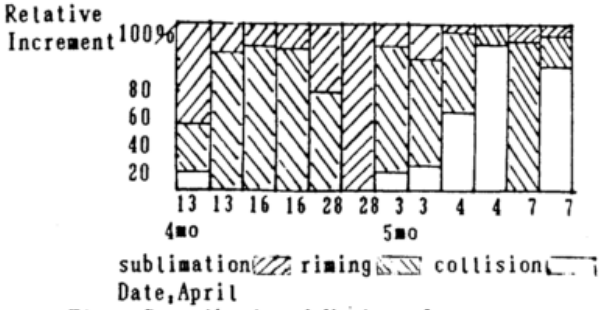


Fig. 2. Contributio of Various Increment to Total Increment of Precipitation Element.

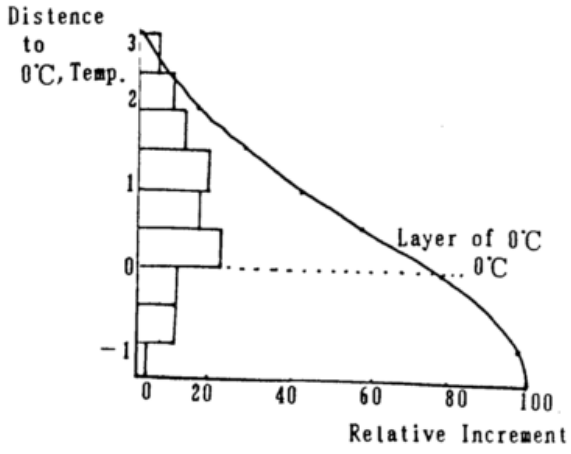


Fig. 3. Distribution of Different Layers with Altitute.

It is seen in the figures,

a) In supercooled layer of precipitus stratiformis over Jilin province, the principal increments of precipitation elements are sublimation and riming. Great differences exist increasing conditions of different increasing process due to differences of weather system and cloud layers

b) Relative contribution of riming processes to precipitation element increments is the greatest, 55% in average, relative contribution of sublimation process to precipitation element increment is important only for individual cases and its average is about 25%.

c) Icreases of precipitation element mass is most rapid at the sector about 1 km above the layer of 0℃, the relaive increment reaches 40% there.

4. CONVERSION OF PRECIPITATION ELEMENTS IN MELTING LAYER AND INCREMENT IN WARM LAYER

Most of solid precipitation elements are melted and converted into liquid drops in melting layer[7]. Their relative increment in warm layer depends on depth and liquid water content of warm layer. The contribution of mass increment may be very little if condition is unfavourable. But the maximum increment may reach 70%–90% if conditions favourable. The average increment is about 20%。

REFERENCES

[1] Wang Xue-lin et. al. 1987, Synthetic Analysis of Macro and Microscopic Properties of Precipitus Stratiformis over Jilin Province in Spring. Collected Papers of Clouds and Rain Physics, P1–16.

(2) Wang Xue-lin et. al., 1965, Ice Nuclei over Baicheng Area in Spring. Acta Meteorological Sinica, Vol. 35, 273–279.

(3) You Lai–guang et. al., 1964, The Measurement and Analysis of Ice Nuclei Concentration in Beijing during the Period from March 18th. to April 30th in 1963. Acta Meteorologica Sinica, vol. 34, 548–553.

(4) You lai–guang et. al., 1965. The Formation and Growth of Snow Crystals in Cold Stratiform Clouds over JiLin in Spring. Acta Meteoprologica Sinica, Vol. 35, 423–438.

(5) Mossop, S.C., 1978. The Influence of Drop Size Distribution on the Production of Secondary Ice Particles during Graupel Growth. Quart. J. Roy. Met. Soc., Vol. 104, 323–330.

(6) You Lai–guang, 1982, Study on the Conditions for Precipitation Element Increment in Stratus in Spring over Jilin Province. Collected Papers of Meteorolgical Science and Technology. NO. 2, 1–9.

(7) Wang Xue–lin et. at., 1987, Conversion of Precipitation Particles in Melting Layer of Stratus over JiLin. Collected Papers of Clouds and Raining Physics, 287–292.

AIRCRAFT OBSERVATIONS AND SIMULATIONS OF ARCTIC STRATUS CLOUDS

Jörg E. Finger and Peter Wendling

Intitut für Physik der Atmosphäre, DFVLR Oberpfaffenhofen, 8031 Weßling, F.R.G.

1. Introduction

During summer the arctic planetary boundary layer (APBL) is often modulated by low level stratus clouds. The high persistence and large extension of stratiform clouds has an important influence on the radiation budget of the arctic basin during summer and on the climate in lower latitudes. The mechanisms that lead to the formation, persistence and break up of arctic stratus clouds as well as the interactions with the tubulence structure of the APBL are not fully understood. In order to understand these interactions better we will report on results of measurements collected on several flights with the DFVLR aircraft 'Falcon 20' during MIZEX 84 (Marginal Ice Zone Experiment 1984) in the area of the Fram Strait and of simulations for one day with a statistical turbulence model of second order closure.

2. Observations

The 'Falcon' was equipped with standard meteorological sensors to determine windvector, temperature, humidity and pressure with a frequency of 100 Hz (Hauf, 1984). The high sampling rate combined with a flight speed of 100 m/s leads to a spacial resolution of 1 m. This is sufficient in order to measure small scale effects and to apply statistical evaluation methods. In addition, low resolution measurements (10 Hz) have been performed of cloud microphysical parameters such as cloud droplet size distribution and concentration (size range: 2 ...600 μm Knollenberg-Probes FSSP and OAP-230X) and of shortwave and longwave radiative fluxes (Eppley pyranometer and pyrgeometer). During the whole experiment seven flights have been carried out, one of them will be discussed here. In order to get detailed information on the vertical cloud structure seven horizontal legs of 12 to 60 km length have been flown. A descent made before this sampling pattern gives information on the boundary layer structure. The stratus cloud layer observed on June 26, 1984 formed at the western side of a high pressure system with center at Novaya Zemlya and extended over an area of about 800 x 400 km^2. Its persistence was two days.

3.Simulations

The applied model consists of three main parts: a statistiscal turbulence model with second order closure (SOC-model), that describes the dynamics of the APBL; the cloud mircophysics are represented by a simple condensation scheme; the radiative transport is calculated by an improved two-stream method developed by *Zdunkowski et al.(1982)* . The SOC-model solves prognostic equations for the horizontal wind components, potential liquid temperature and total water mixing ratio as well as for all their second moments, that means variances and fluxes. The turbulent diffusion of these second moments is parameterized with a downgradient approximation. For the time integration of the equations the *Adams Bashforth* scheme with a time step of $\Delta t = 0.05\ s$ has been used due to the choice of the vertical resolution $\Delta z = 5m$ (*Finger(1988)*).

4.Results

The measurements demostrate that the cloud topped APBL is to a large degree horizontally homogeneous as it is shown in the small variability of the first moments (Figure 1) and second moments (Figure 2) on the horizontal flight legs. The profiles of liquid water content, droplet concentration and mean diameter indicate that cloud droplet growth by condensation dominates, as suggested by *Tsay and Jayaweera (1984)* . A deviation from the adiabatic liquid water content is only given in the region near cloud top, where dry and warm air is entrained, see profile of liquid water flux in (Figure 2).

The evaluation of the data and the numerical simulation show both that the cloud topped APBL is well mixed up to the inversion (Figure 1) caused mainly by two different processes: 1. at the surface the wind shear is the dominating effect that produces a large amount of turbulence kinetic energy (TKE). The contribution of the turbulent heat and moisture fluxes is small due to the small difference in air and seasurface temperature. 2. At cloud top TKE shows a secondary maximum due to stong windshear and destabilization by radiative cooling. The resulting large entrainment transports cool and moist air parcels from the PBL to the free antmosphere against the thermal stability. The radiative cooling is identified to be the most important physical prozess of the stationary APBL that produces up to 90 % of

the TKE and therefore the mixing in the whole cloud layer.

5. *References*

Finger, J.E., 1988: Turbulenzstruktur arktischer Stratuswolken aus Messung und Berechnung. Dissertation an der Universität München.

Hauf, T., 1984: Turbulenzmessungen mit dem Forschungsflugzeug 'Falcon'. Meterol. Rdsch. 37, 163 - 176

Tsay, S.C. and Jayaweera, K., 1984: Physical characteristics of arctic stratus clouds. Jour. of Climate and Appl. Meteor., 23, 584-596

Zdunkowski,W., Panhans,W. Welch,R. and Korb,G., 1982: A radiational scheme for circulation and climate models. Beitr. Phys. Atmos., 55, 215-237

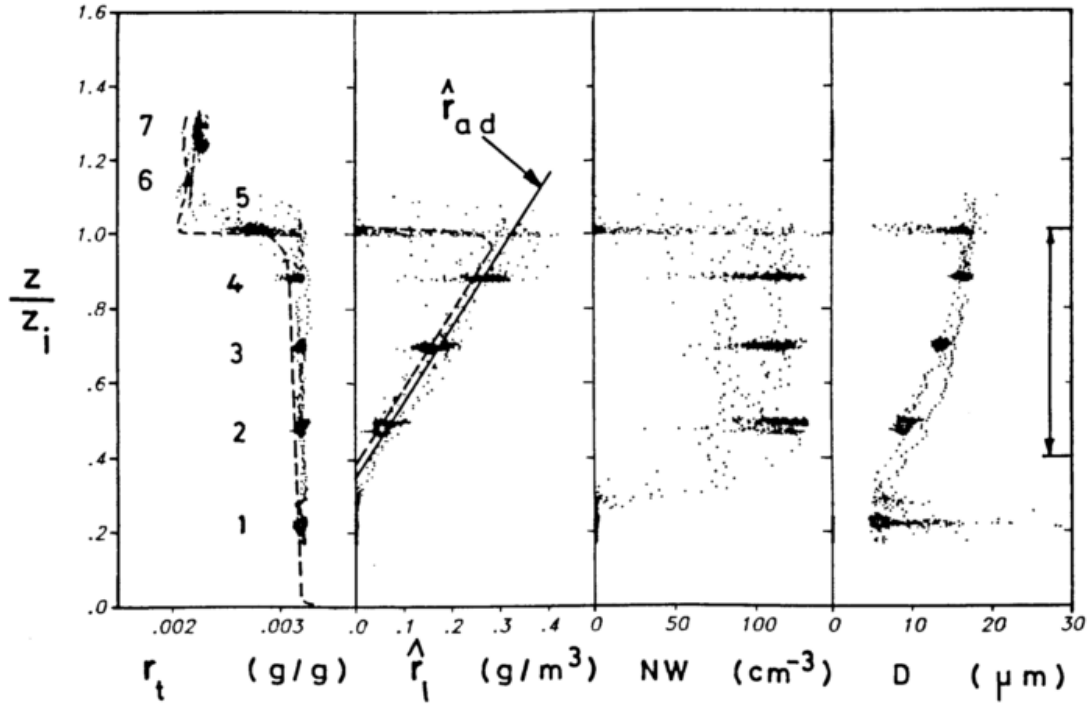


Figure 1. Profiles of water mixing ratio r_t, liquid water content $\hat{r}_l$, droplet concentration NW and mean droplet diameter D, dashed line: simulations, dots: measurements,1 s means, $z_i = 410\,m$

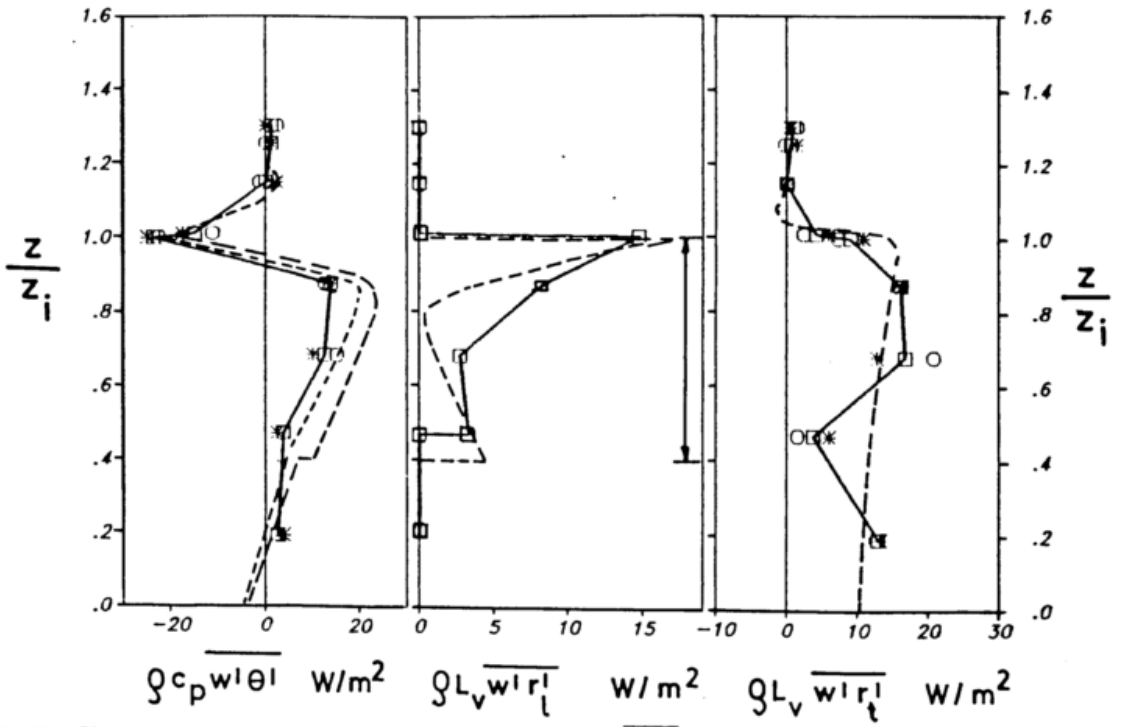


Figure 2. Profiles of turbulent fluxes of sensible heat $\rho\, c_p \overline{w'\theta'}$, latent heat $\rho\, L_v \overline{w'r_l'}$ and liquid water content $\rho\, L_v \overline{w'r_t'}$, dashed line: simulations, full line: measurements

DIURNAL VARIATION OF A STRATOCUMULUS-TOPPED ATMOSPHERIC BOUNDARY LAYER OVER SEA

Peter G. Duynkerke
Royal Netherlands Meteorological Institute
P.O. Box 201
3730 AE De Bilt, The Netherlands

1. INTRODUCTION

In a horizontally homogeneous stratocumulus deck the evolution of the cloud depends upon the combined effect of many different physical processes such as, longwave radiative cooling at cloud top, shortwave radiative heating inside the cloud layer, windshear at the surface and at cloud top, a buoyancy flux at the surface, latent heat release due to condensation and subsidence (Driedonks and Duynkerke, 1988). Improved understanding of the cloud-topped atmospheric boundary layer (ABL) has been gained from detailed observational studies (Brost et al., 1982; Nicholls, 1984; Nicholls and Leighton, 1986). The observations have shown that different combinations of physical processes may lead to a totally different turbulent structure of the ABL. In this paper we give a brief description of the model and present simulations of the diurnal variation of marine stratocumulus layer over the sea at mid-latitudes.

2. MODEL

A one-dimensional ensemble averaged model has been developed (Duynkerke and Driedonks, 1987) in which we have prognostic equations for the horizontal velocities (u,v), wet equivalent potential temperature (θ_q), and total water content (q_w). The vertical velocity is prescribed. Turbulence closure is formulated by using an equation for the turbulent kinetic energy (E) and viscous dissipation (ε). The radiation model consists of an emissivity model for the longwave radiation (Garrat and Brost, 1981) and a two-stream model for the shortwave radiation (Fouquart and Bonnel, 1980).

We have used the model to study various combinations of physical processes in a cloud-topped ABL and their combined effect on the turbulent structure. The model has been successfully applied to the datasets of Brost et al. (1982) and Nicholls (1984) in Duynkerke en Driedonks (1987) and to data from flight 564 of Nicholls and Leighton (1986) in Duynkerke and Driedonks (1988).

3. RESULTS

Using the model we have made a 48 h integration with conditions appropriate to 1 July, starting at 0000 GMT. The initial conditions are the same as those used in Turton and Nicholls (1986) except for that we have set the gradient of q_w above the boundary layer top equal to zero. The simulation is made at a latitude of 56°N, divergence of $3\times10^{-6}s^{-1}$, albedo = 0.05 and a roughness length $z_o = 2\times10^{-4}$m. The sea-surface temperature $T_S = 284.5$ is only slightly higher than the air temperature just above it. Further details on initial and boundary conditions can be found in a forthcoming paper.

The simulated variation of cloud base and cloud top height are shown in Figure 1. Initially the longwave radiative cooling at cloud top is the most important process for the production of turbulence. It destabilizes the whole ABL and produces mixing down to the sea-surface. Shortly after sunrise the shortwave absorption becomes of the same order as the longwave cooling (Figure 2). The combined effect of longwave cooling, shortwave heating

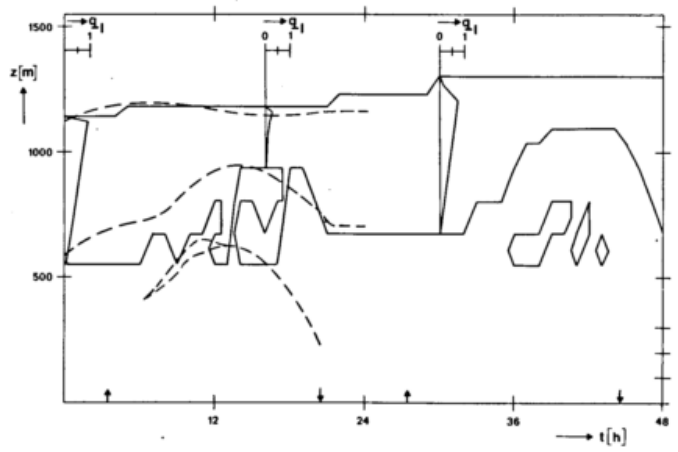


Figure 1. Variation of simulated cloud-top and cloud-base height as a function of time (full line) compared with results of Turton and Nicholls (1986) (dashed line). Also the liquid water content (q_l) is indicated.

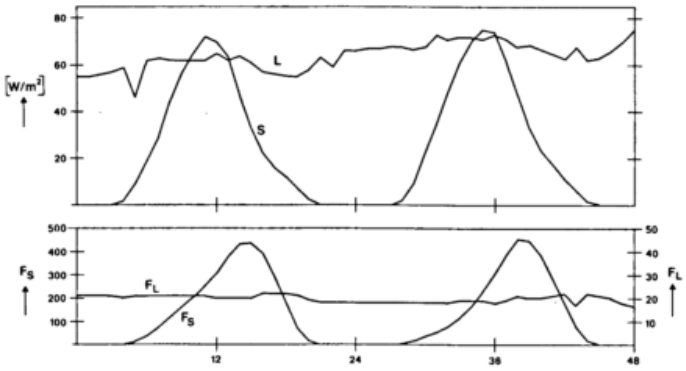


Figure 2. The simulated net longwave (L) and shortwave (S) radiative flux over the whole cloud layer (upper) and at the surface (lower) for 1 July.

and entrainment of warm air from above the ABL is that the cloud layer is heated, whereas the temperature in the sub-cloud layer remains nearly the same. As a result a stable layer is formed near cloud base and the cloud layer and sub-cloud layer become decoupled. The decoupling can be clearly seen from the minimum in the turbulent kinetic energy (E) near cloud base at t = 16 h in Figure 3. The decoupling can also be diagnosed from the total moisture flux at t = 16 h (Figure 4) which is nearly zero near cloud base. Moreover the gradient of the total moisture flux is negative in the sub-cloud layer and thus q_w increases, whereas in the cloud layer the gradient is positive so that q_w decreases. The increase of q_w in the sub-cloud layer is due to the moisture input from the sea-surface, whereas in the cloud layer q_w decreases due to entrainment of dry air from above the inversion. In the late afternoon the shortwave heating in the cloud layer gets smaller than the longwave cooling (Figure 2) as a result the whole ABL is destabilized again. Therefore the moisture which was brought in the sub-cloud layer during daytime will be redistributed over the whole ABL and as a result the cloud thickness increases again (Figure 1).

We have also made simulations with the same initial and boundary conditions but then during different seasons. As such we investigated at which time of the year the decoupling is most likely to happen. We had two criteria to diagnose the decoupling: the first is when the moisture flux deviates significantly from being linear throughout the ABL, the second is

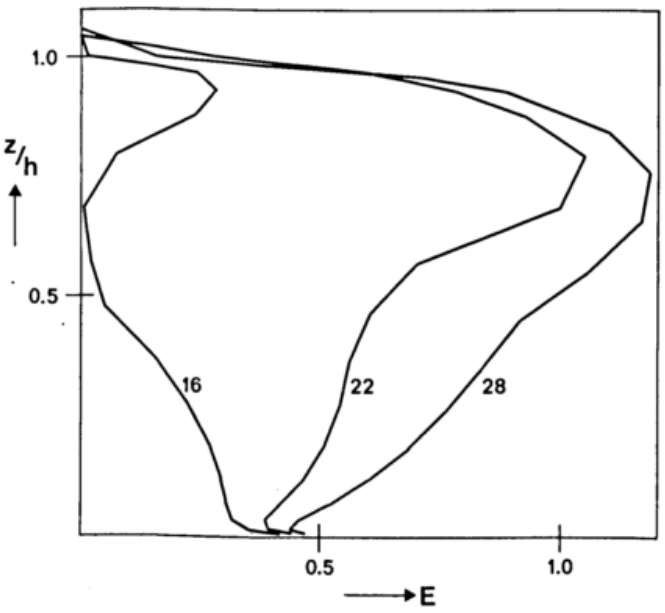


Figure 3. The turbulent kinetic energy as a function of dimensionless height at t = 16, 22 and 28 h.

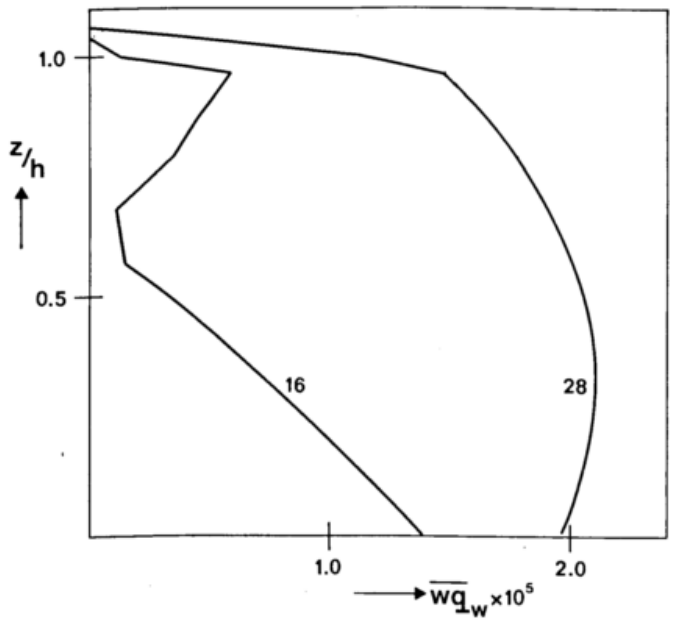


Figure 4. The total moisture flux at t = 16 and 28 h as a function of dimensionless height.

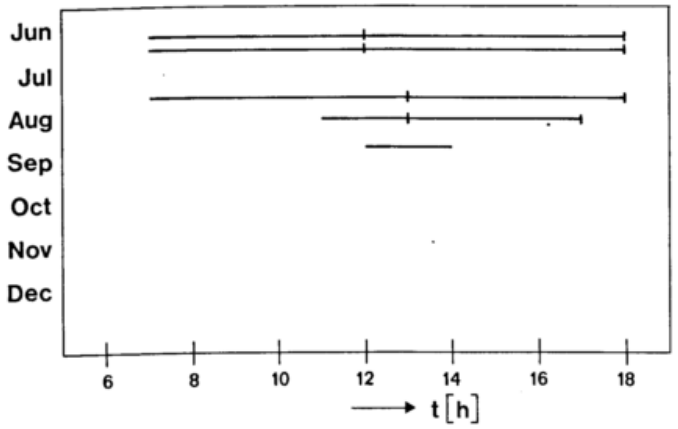


Figure 5. The presence of decoupling as a function of time of the day during different months: full line from moisture flux criterion; ⟝⟞ E at cloud base less than 20% of maximum in cloud layer.

when the TKE at cloud base is less than 20% of the maximum TKE in the cloud layer. The results are shown in Figure 5. The model confirms the intuitive expectation that at mid-latitudes the decoupling is most likely to happen in summer during the afternoon due to the influence of the shortwave radiation.

The decoupling of the cloud layer can have important consequences for the surface energy budget because a thinner cloud is much more transmissive at short wavelengths but is still optically thick at longer wavelengths. This can be seen in Figure 2 where we have shown the net longwave (F_L) and net shortwave (F_S) radiative flux at the sea-surface. Due to the decoupling, the net longwave radiative flux at the sea-surface hardly changes, whereas the net shortwave flux increases significantly. The surface energy budget is thus drastically changed due to the decoupling. This is one reason why it is important to resolve the diurnal variation of ABL clouds in large scale (climate) models.

4. REFERENCES

Brost, R.A., D.H. Lenshow, and J.C. Wyngaard, 1982. J. Atmos. Sci., 39, 818-836.

Duynkerke, P.G., and A.G.M. Driedonks, 1987. J. Atmos. Sci., 253, 43-64.

Duynkerke, P.G., and A.G.M. Driedonks, 1988. Accepted in J. Atmos. Sci.

Driedonks, A.G.M., and P.G. Duynkerke, 1988. Submitted to Mon. Weath. Rev.

Fouquart, Y., and B. Bonnel, 1980. Beitr. Phys. Atmosph., 53, 35-62.

Garratt, J.R., and R.A. Brost, 1981. J. Atmos. Sci., 38, 2730-2746.

Nicholls, S., 1984. Quart. J. R. Met. Soc., 110, 783-820.

Nicholls, S., and J. Leighton, 1986. Quart. J. R. Met. Soc., 112, 431-460.

Turton, J.D., and S. Nicholls, 1986. Quart. J. R. Met. Soc., 969-1009.

INTEGRATED FOG WATER SAMPLING SYSTEM

L. Schütz, M. Krämer, B. Friederich and F. Franken

Institute of Meteorology, University of Mainz, Saarstr. 21, D-6500 Mainz, F.R.G.

Intercomparison of a large number of fog and cloud water sampling devices showed clearly that the impactor principle is superior to all other active collection principles. This is due to the sharp cut-off of the collection efficiency curve and known effective flow rate. If care is taken that the collected droplets are quickly removed from impaction surfaces and transferred into storage vials in order to prevent evaporation, this type of instrument can be addressed as an almost ideal collector for fog and cloud water.

Low liquid water content values of the order 0.01 g/m³ require a high flow rate in order to guarantee reasonable sampling periods and a good time resolution. This can be achieved by applying the wide stream impaction principle. Based on this principle rotating arm collectors have qualified in the past. Morover, these types of instruments collect droplets isokinetically.

This device has been modified in order to guarantee constant cut-off fog droplet radii under variable wind conditions. Even during high winds on mountain top stations, samples of cloud water can be taken for longer time intervals. This will be achieved by automatic control and adjustment of constant flow conditions at the impaction surfaces. According to the actual wind speed and direction the whole instrument and its collectors will constantly be directed against the flow. A microcomputer together with a datalogger controls the collection parameters such as the motor speed, alignment of the samplers with the wind direction, and the angle of impaction of the collection surfaces. Cut-off radii for fog and cloud droplets between 5 µm and 10 µm radius can be selected within average of wind speeds between about 0.5 ms^{-1} and 15 ms^{-1}. First experiments under field conditions will be presented at the conference.

USE OF LIDAR DATA IN SHORT-TERM FORECAST OF STRATIFORM CLOUDINESS BASE HEIGHT

S.I. Kolev*, O.P. Parvanov**, L.A. Kostadinov***, I.N. Kolev**

* Institute of Hydrology and Meteorology, Sofia

** Institute of Electronics, Sofia

*** Hydrometeorological Service, Sofia

1. INTRODUCTION

The aim of this work is to study the behaviour of stratiform cloudiness base height (SCBH) through the established conventional methods and its parallel investigation by the use of lidar equipment, in order to evaluate the capabilities of the latter with a view to its future use in the practice as well as to describe the space and time dynamics in the vicinity of the cloud base. It was incited by the growing attention recently paid to the description of stratiform cloud dynamics in various space and time scales when developing numerical prediction schemes. The unsatisfactory state of this problem is due first of all to the insufficient accuracy and resolution of the methods of measurements of meteorological parameters.

2. FORMULATION OF THE PROBLEMS. MEANS OF SOLUTION

The conditions of formation of stratiform cloudiness are extremely variable and its base height depends on a very large number of factors. SCBH, variable in time and space, is an important parameter in weather forecasting. We shall consider SCBH as the condensation level determined from upper-air sounding. The following expressions will be used in the computations: $Z_k = (\gamma, w, k, ...)(T - T_d)$, where T is surface air temperature, T_d - surface due-point temperature, γ - variable coefficient, depending on the temperature lapse rate γ, vertical velocity w, turbulent coefficient K, etc. Expressions of this kind allow to evaluate SCBH averaged over an area of 50 x 50 km and for a time interval not less than 1 hour (MATVEEV, 1981, p. 310).

Lidar data used cosist of back-scattered laser pulses (λ = 0,533 nm) shot by a triple-beam sounding equipment , bringing information about the optical properties of the aerosol. A sequences of pulses allow to obtain the time changes of aerosol at several heights simultaneously. The elevation of SCBH is determined with height accuracy of 7,5 m and time resolution 0,1 sec, using the technique described in KOLEV (1987, p.366). The absence at present of an unambiguously grounded theory of such small-scale dynamics justifies the use of statistical time-series processing. This fully complies with the requirement that the measurement error should be less by an order of magnitude than the most frequently encountered changes of measured value. The comparison between the model and experimental results is used for investigation of instant deviations (fluctuations) of SCBH. The meteorological conditions and the statistical characteristics of SCBH inhomogeneities are determined.

3. EXPERIMENTAL DATA

Experiments were carried out on 11 Nov. 1983 (02h,08h), 18 July 1984 (02h, 08h) and 18 Sept. 1984 (02h,08h) Synoptic situations were as follows:

10 - 11 November 1983 - intensively developing ridge of high pressure. Continuous layer of St and Sc develops over the region of Sofia during the night and in the early morning hours.

17 - 18 July 1984 - cold front passage over the region in the afternoon hours of July 17. From 00h to 03h on July 18 the cloud cover is 10/10 Sc without precipitation. Unstable air mass.

17 - 18 September 1984 - cold front from west moves over the region in the afternoon hours of September 17, associated with the occluding cyclone over the Carpathians, developing thunderstorm activity withot precipitation. Broken St are observed in the early morning of 17.

Under these conditions we can apply the techniques described in BOGATKIN (1987, p. 183) for calculation of SCBH, based on upper-air sounding. The results are shown in Table 1.

Lidar information is obtained in several sounding sequences of 400 sec each, conducted near the time of radiosonde launching in close proximity to the tracking radar. The results of statistical processing of

sounding sequences of SCBH are presented as autocorrelation functions and histograms of measured heights (Figs. 1 and 2). The velocity and the direction of the drift of SCBH inhomogeneities are determined by the technique described in KOLEV et al. (1987, p.37) and are compared with upper-air sounding data.

4. ANALYSIS OF RESULTS

In spite of the great variability of SCBH the selected sounding durations are suitable for recording the stationary changes in SCBH. At the same time several types of variations of measured parameter are observed. The spectral characteristics (Fig. 1) show the distribution of the variation in time and space frequences. It is close to the distribution of inhomogeneities originating from dissipation of turbulent vortices in the inertial range (Kolmogorov-Obuchov's spectra). It is also seen that the variations range from rapid small-scale random changes, followed by medium-scale variations (with correlation radiuses determined from the standardized autocorrelation function $R(\tau)$ at the level $0,5 - \tau_{0,5} = 20 \div 30$ s) and arriving to their quasi-periodic alternation (appearing as occurrence of periodic secondary maximums in $R(\tau)$, thus breaking the monotony of the spectrum around 80 s.

The displacements of the maximums of correlation functions corresponding to the three sounding tracks allow to measure the drift velocity of SCBH inhomogeneities. Space-averaged dimensions are determined on the basis of time-averaged ranges of height changes. For short-living formations they are of the order of 5 - 15 m, while the most typical horizontal extension of SCBH inhomogeneities, averaged over all sounding sequences, is in the range between 100 - 150 m. The wave structure has an average period of 300 - 400 m.

The distribution of measured heights, as shown in Fig. 2, can be interpreted as a posteriory probability of occurrence of cloudiness at certain height. From the series of measurements the persistence in time of these distribution can be assessed and associated with the stage of cloud development. Besides, a characteristic variation of the statistical parameters of signals from different heights (sections of cloud vertical structure) was observed, associated with the different entry of the sounding pulse into the cloud. This was theoretically predicted by MATVEEV (1981, p. 315).

5. CONCLUSIONS

SCBH data obtained by conventional numerical prediction methods and from lidar measurements are in good agreement, thus prooving the possibility of reliable lidar determination of this cloud characteristic.

The incomparably high resolution of lidar measurements allows to notice that in small-scale terms SCBH is in constant change and the surface of the cloud base has characteristic structure.

Lidar measurements indicate, that the adjacent to the cloud base layer of big supersaturations varies in the range of 30 - 50 m, corresponding to the theoretical concepts.

Lidar measurements of stratiform cloudiness reveal the existence of inhomogeneities with horizontal dimensions determined by the present state of the underlaying surface and the surface layer of the atmosphere, orography, turbulent fluctuations, etc.

Lidar measurements can be used for testing the numerical models of short-term SCBH variations due to short-term changes of meteorological parameters and turbulent disturbances.

Lidar sensing can be used as a means of statistical nowcasting for aeronautical purposes.

REFERENCES

BOGATKIN, O.G.; GOVERDOVSKII, V.F.; ENIKEEVA, V.D.: Manual on aeronautical meteorology (in Russian), 1987, Leningrad, Gidrometeorizdat, 183 pp.

KOLEV, I.; PARVANOV, O.; KAPRIELOV, B.; NABOKO. V.: Lidar Measurements of the Drift Velocity of Cloud Formations. Bulgarian Geophysical Journal, XI, (1987) Nr. 4, p. 37 - 44.

KOLEV, I.; PARVANOV, O.; KAPRIELOV, B.; NABOKO, V.: Lidar Measurements of the Cloud Base Height. Proc. of III National Conference (with international participation) "OPTICS - 87", 18 - 20 May 1987, Varna, p. 366 - 369.

MATVEEV, L.T.: Cloud Dynamics. 1981, Leningrad, Gidrometeoizdat, 310 pp.

TABLE 1

DATA	HOUR	Hm_1	Hm_2	Hm_3	Hm_4	LIDAR
11.11.1983	02	244	416	462	340-427	470
	08	232	334	440	190-278	303
18.07.1984	02	647	843	814	706-794	911
	08	476	777	770	638-727	613
18.09.1984	02	195	228	352	258-346	327
	08	--	--	--	--	--

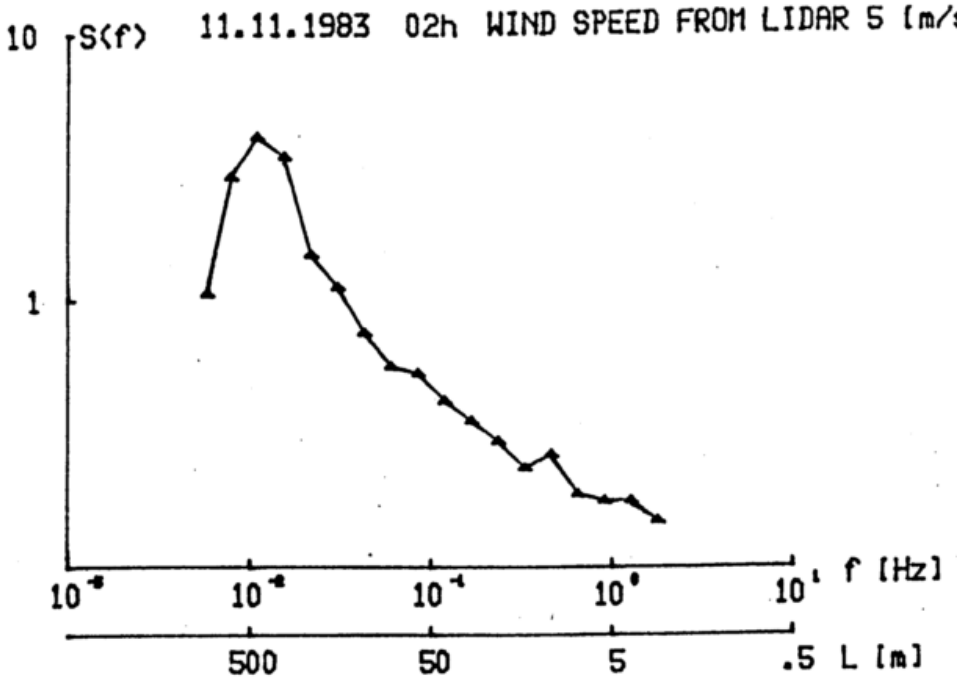


FIG 1

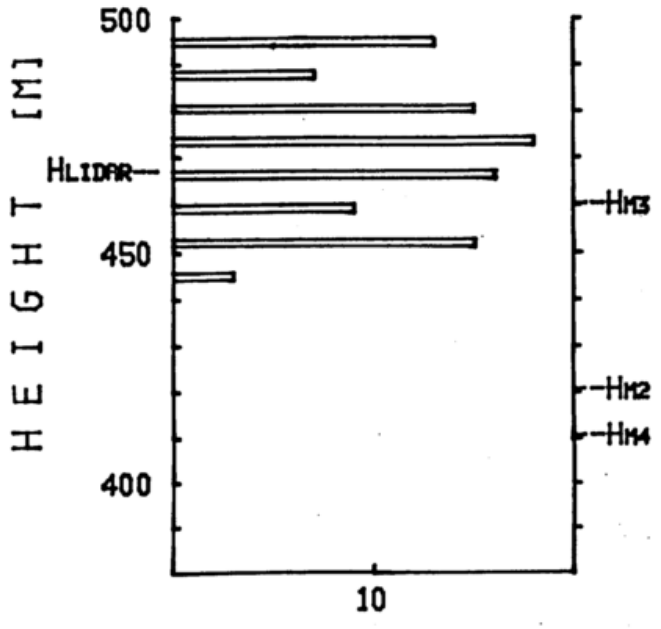


FIG 2

WATER CONTENT OF WINTER CLOUDS OVER ETS

A.S.Azarov, N.A.Bezrukova, N.F.Buranbaev,
A.V.Koldaev, A.A.Chernikov

Central Aerological Observatory (USSR)

1. INTRODUCTION

The development of models of precipitation formation in winter are largely complicated by the lack of experimental data on the water content of winter clouds (MAZIN,1983,p.246). In solving the problem of the redistribution or initiation of precipitation at middle latitudes, winter clouds modification might play an important role. However, no reliable assessment has been made by now of winter clouds liquid water content, which could be a sure indicator of the effectiveness and expedience of cloud modification. This is caused by the lack of systematic measurement data on the spatial distribution of cloud water content.

The routine methods of studying supercooled liquid water, consisting in the aircraft sounding of clouds using in situ probes, have a serious disadvantage of not permitting continuous observations during several thousand hours, i.e. obtaining a seasonal set.

For the remote sensing of liquid water content a microwave radiometric method has gained recognition. Nevertheless, the early seasonal measurements of winter clouds water content were only conducted in 1984 (HEGGLY, 1985) in a mountainous locality. For a plain locality, such as ETS, the data on liquid water content of winter clouds are not available.

The first aim of this work is the development of a technique for the long-term measurements and carrying out such measurements during a winter season. The second aim is the estimate of potential for weather modification in winter condition.

2.MICROWAVE RADAR/RADIOMETER SYSTEM

Ground-based radar/radiometer system were developed at the Central Aerological Observatory, which comprised: microwave radiometers operated at 22.2 and 37.5 GHz, X-band Doppler radar, an automated complex of data collection and processing based on a computer Elektronika-60 (AZAROV et al.,1983). The radiometers were installed in a room with a constant (+22°C$\pm$0.5°C) temperature. Through a MILAR-film window the radiometers antenna were directed at a passive reflector made of a flat sheet of metal. The reflector was equipped with a mechanical scanning unit permitting the pointing of the antenna beams to the zenith and conducting the absolute calibration of radio-brightness temperature using a method of angular altitude sounding in a cloudless atmosphere. Every 20 minutes automatic calibrations were performed against the reference heat load and noise generator.

The radar was also pointed to the zenith and during the radiometers calibration, with a 20-min. interval, it obtained conical azimuth sections at a 30° elevation for the determination of speed and direction of cloud drift. The radiometer and radar data were simultaneously feeded to the computer for subsequent joint processing. Radar data were obtained from 16 distance channel with a 0.5-km spatial reso-

lution and a 750-m initial distance. Main characteristics of the radiometers is: antenna main lob-3°, temperature resolution-0.1K, integration time-1 S, absolute accuracy-2 K. The radar has the following characteristics: antenna beam width (3dB)-47', transmitter peak power-150 kW, PRF-2kHz, pulse width - 0.3 μs.

Information about precipitation was provided by MRL-2 radar (one from the standard weather network of USSR).

3. RESULTS

The above complex was operated in Dolgoprudny, Moscow Region, in a 24-hour regime during 3 months, from December 4,1985 through February 28, 1986. For technical reasons the measurements were interrupted several times for not longer than 4 days. The total measurement time made 1812 hours. During the data processing, all cases with wet snow precipitation (the total of $\simeq$ 31 hours) were excluded due to interpretation difficulties. Mean kinetic temperatures of cloud lay were calculated from the data of radio sounding in Dolgoprudny.

Monthly and mean seasonal cumulative distributions of liquid water content (LWC) are given in Fig.1, were time percentage is taken with respect to the whole observation period.

Thus, the average water content in the supercooled liquid fraction of winter clouds, estimated from these data, made 0.11 kg/m^2. The existence time of liquid water zones in winter clouds made 18% of the total observation period. With marked anticyclonic situations observed during 600 hours in this period, the existence time of liquid water zones in clouds were estimated to make 30%.

The spatial distribution of liquid water content in winter clouds is specific, i.e. mainly observed are extended zones with rather sharply outlined borders and slight water content variations within. However, along with such typical situations, encountered are zones with liquid water content having sharp maxima and minima, which may testify to the existence of latent convection in winter precipitable clouds. In the synoptic situation of 22-29 January,1986 such zones occure most frequently, the maximum for all season liquid water content measured on 26 January being 0.9 kg/m^2.

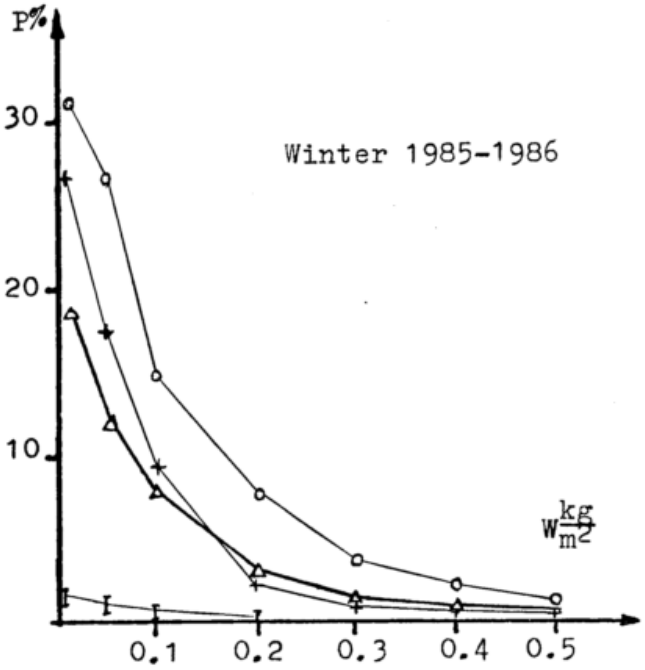


Fig.1. Cumulative distributions of LWC; +- December, o - January, I - February, Δ -mean seasonal.

Also typical is the anti-correlation between precipitation and the presence of water zones in clouds.

4. DISCUSSION

The data obtained make it possible to assess the potential of winter clouds for modification by seeding of supercooled water zones. From a single measurement of liquid water content in clouds one can try and assess their

water resources and, finally, the amount of precipitation which will be obtained by modification.

One can agree with (LEONOV,1967) that the role of the water content in supercooled frontal clouds is similar to that of a catalyst, i.e. due to the crystallization of a supercooled part of a cloud resulting from seeding, precipitation increase due to the sublimation of supersaturated vapor as well as weaker vaporization to above-cloud layers and acceleration of water vapor inflow as a result of an intensified precipitation-forming process.

From the data on the mean temperature of a cloud layer one can approximately estimate the amount of gaseous supersaturation moisture. In (LEONOV, 1967), the part of the gaseous moisture of clouds, corresponding to a difference between saturation over liquid water and saturation over ice, was called an additional supersaturation water reserve. Considering this water reserve as an additional water content realized through modification, one should multiply the values of supersaturation water content ($0.2 g/m^3$ under average conditions in winter) by the mean thickness of supercooled liquid layer of clouds, which may be assumed to be 1 km. The resulting value in LWC terms is $0.2 kg/m^3$.

The average spatial extention of liquid water zones, estimated from radiometer and Doppler radar data, is 60 km. Using this value as an extention of modification seeding zone and the data of Fig.1, the layer of additional precipitation D can be estimated as:

$$D = \frac{T \cdot P \cdot V \cdot W}{L}$$

where T=1812 hours is the total measurement time; P=18% is the time percentage of LWC zones existence; V = 30 km/h is the average speed of cloud drift; $W = 0.3 kg/m^2$ is the measured LWC value plus additional water content of supersaturation; L=60 km is the average spatial extention of LWC zone. Thus, D is about 48 mm.

The season layer of precipitation in winter 1985-1986, calculated from the data of weather stations near Dolgoprudny, is equal 169 mm, thus the additional layer for this season is 30%. Obviously, the estimate is upper from overall, because in discussion 100% efficiency of seeding implied.

Besides that, radiometers data with connection to synoptic situations were analysed. This analysis have shown a good correlation between synoptic-scale features of atmosphere and distribution of LWC in winter clouds.

REFERENCES

AZAROV, A.; ZHERDEV, Yu.; KOLDAEV, A.; MIRONOV, A.: Radiophysical complex for the investigation of precipitable clouds. Manuscript Dep. in VINITI N 2680-83 dep., 1983. (In Russian).

HEGGLY, M.: The role of microwave radiometry in weather modification research. WMO Rept. N 2. Technical Document WMO/TD N 53, Geneve 1985.

LEONOV, M.; PERELET, I.: Cloud modification in the cold season of the year. Leningrad: Gidrometeoizdat 1967 (In Russian).

MAZIN, I.; SHMETER, S.: Clouds: Structure and Physics of Formation. Leningrad: Gidrometeoizdat 1983 (In Russian).

MICROPHYSICAL STRUCTURES OF JAPANESE WARM-FRONTAL CLOUDS OBSERVED WITH A NEW TYPE SONDE (HYVIS)

Masataka Murakami ,Takayo Matsuo,
Hakaru Mizuno, and Yoshinori Yamada

Meteorological Research Institute,
Tsukuba, Ibaraki 305, Japan

1. INTRODUCTION

In the temperate zone, cyclones and fronts frequently form, and clouds associated with them produce precipitation over the broad area. Recently, needs for improvements in short range forecasting of precipitation have increased, and a better understanding of precipitation formation processes is required.

However, observational data on microphysical and thermodynamical structures of warm fronts are not complete yet although the Cloud Physics Group at the University of Washington has made a great progress in understanding precipitation processes through observational studies on the meso- and micro-structures of warm fronts (Herzegh and Hobbs,1980; Houze *et al.*,1981; Locattelli and Hobbs,1987).

The Cloud Physics Section of MRI in Japan has made observational studies of stratiform clouds associated with warm fronts and stationary fronts (Baiu front) in Tsukuba, Japan since 1985, using a balloonborne special sonde (HYVIS) developed by Murakami and Matsuo (1988) and its prototype named a Cloud Particle Video Sonde (Murakami *et al.*,1987). In this paper, observed microphysical structures of warm-frontal clouds and precipitation formation processes operating in these clouds are described.

2. DATA COLLECTION AND SYNOPTIC SITUATION

Two HYVIS observations were made in a warm-frontal cloud system which passed over the Tsukuba Area, Kanto Plain, Japan on 20 June 1987. A Doppler radar of 5 cm wavelength was located within 500 m from the HYVIS observation site and was operated in three modes during the observation period; PPI, RHI, and vertically pointing modes. Before the HYVIS sounding, the radar was operated in PPI scanning mode and RHI scanning mode to observe mesoscale features of warm-frontal clouds. During the HYVIS sounding, emphasis was placed on obtaining RHI's of refractivity and Doppler velocities in the direction of the ascending HYVIS. Also, the spectra of fallspeed of precipitation particles were occasionally measured in the vertically pointing mode.

A surface weather map for 0900 JST 20 June 1987 and the study area are shown in Fig.1. Also shown are the positions of the surface warm fronts at 0600 and 1200 JST. The warm-frontal system was moving east-northeast along the south coast of the Japanese Islands at a speed of 40 km/hr. The first sounding was made at around 0600 JST when the observation site was located 350 km north of the surface warm front. The radar measurements suggested that the HYVIS penetrated a weakly convective region embedded in thinner upglide clouds.

The second sounding was made five hours after the first one (i.e., at around 1100 JST) when the observation site was located 200 km north of the surface warm front. The radar measurements suggested that the HYVIS penetrated non-convective, deep upglide clouds.

In the next section, data of hydrometeor concentration were averaged over 250 or 500 m in depth in order to minimize the statistical sampling errors, although the HYVIS provides a fine vertical resolution (~50 m) of microphysical measurements.

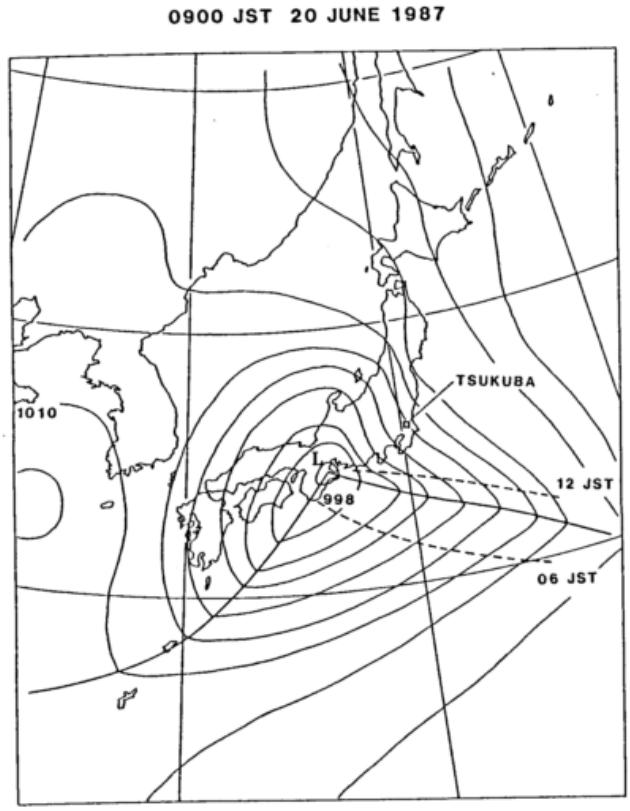


Fig.1. Surface weather map for 0900 JST 20 June 1987.

3. RESULTS OF OBSERVATIONS

3-1. THINNER UPGLIDE CLOUDS

The HYVIS observation showed that the cloud top was at a height of ~10 km although patches of sparse clouds existed up to ~12 km.

A well-defined warm front with a strong temperature inversion layer (where temperature increased by 6.5°C) was at a height of ~5 km.

A significant growth of snow crystals was seen below a height of ~8 km, and the snow water content and precipitation rate reached their maximum values of 0.4 g/m^3 and 2 mm/hr in the lower part of the upglide clouds. Below the frontal surface, snow crystals rapidly evaporated in a dry air (~30 % R.H.). Therefore, no rain drops were observed during the ascent of the HYVIS except for a sparse drizzle layer (less than 100 drops/m^3 in number) observed in a region between heights of 4.5 and 6.0 km.

The major shape of the snow crystals was columnar type crystals throughout the whole cloud layer. Capped columns and hexagonal plates were also observed below the -17°C level. These crystals hardly showed any riming on their surfaces and they did not aggregate. This means that snow crystals grew by vapor deposition alone in the slightly convective region embedded in the thinner upglide clouds.

3-2. DEEP UPGLIDE CLOUDS

Vertical structures of deep upglide clouds are shown in Fig.2. According to the HYVIS measurements, the cloud top was at a height of ~12 km. Although the warm front was not clearly defined from the temperature profile in Fig.2A, profiles of wind and equivalent potential temperature suggested that the warm front was at a height of ~2 km. Surface precipitation rate ranged from 4 to 8 mm/hr during the HYVIS sounding. Radar and surface rainfall measurements suggested that the HYVIS measured the deep, stratiform upglide clouds above a height of 2.5 km although, below this height, it was under the influence of precipitation core embedded in these clouds. As seen from Figs.2 and 3, snow crystals gradually grew while they fell down to a height of ~6.5 km. At this height, the snow water content and precipitation rate were only 0.15 g/m^3 and 0.8 mm/hr, respectively. They then grew rapidly in a shallow region (2 km deep) directly above the 0°C level. In this region, a low concentration (less than 50 drops/m^3) of drizzles coexisted with snow crystals as seen from Fig.3 and the air was considered to be almost water-saturated. The snow water content and snowfall rate just above the 0°C level had their maximum values of ~0.5 g/m^3 and ~5 mm/hr, respectively.

The HYVIS observation showed that columnar type crystals predominated throughout the whole cloud layer and capped columns and hexagonal plates existed below the -18°C level. These crystals hardly showed any riming on their surfaces. Such features of snow crystal distribution aloft were very similar to those observed in the thinner upglide clouds, and demonstrating that the snow crystals grew by vapor deposition.

In the melting layer, as seen from Fig.4c, moderate aggregations occurred unlike the thinner upglide clouds mentioned in the previous

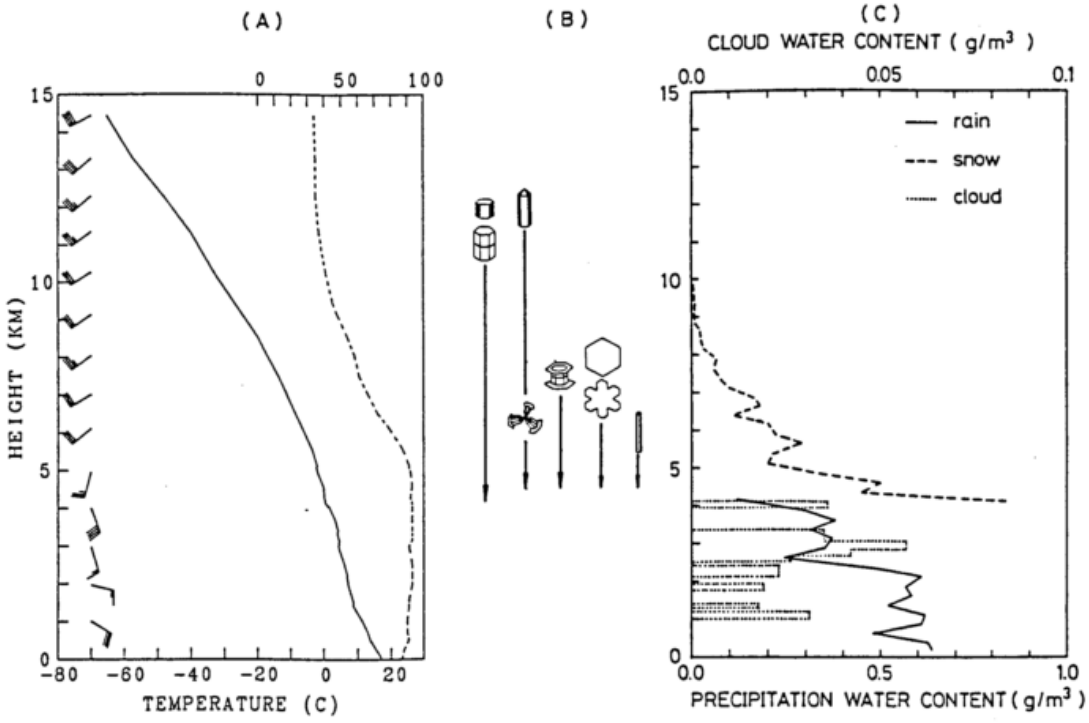


Fig.2. Vertical structures of deep upglide clouds: (A) temperature (solid line), relative humidity (broken line), and wind; (B) snow crystal types observed aloft; (C) rain water content (solid line), snow water content (broken line), and cloud liquid water content (dotted line).

sub-section. Below the melting layer, the air was moist (R.H.≥90 %) and patches of sparse clouds (less than 10 droplets/cm^3 in number and less than 0.06 g/m^3 in amount) existed. Therefore, rain drops did not show any rapid growth nor any intense evaporation while they fell down to a height of 2.5 km.

Change in size distributions of cloud droplets along the ascent of the HYVIS are shown in Fig.4. Figures 4a-4c and Figures 4d-4g show the size distributions of cloud droplets in sparse stratocumulus clouds beneath the warm front and in clouds associated with warm-frontal upgliding, respectively. Figure 4h shows the size distribution of cloud droplets just below the melting layer. Most of these clouds consisted of larger droplets ($D \geq 16\mu m$) while smaller droplets ($D < 16\mu m$) were only observed just above the warm front.

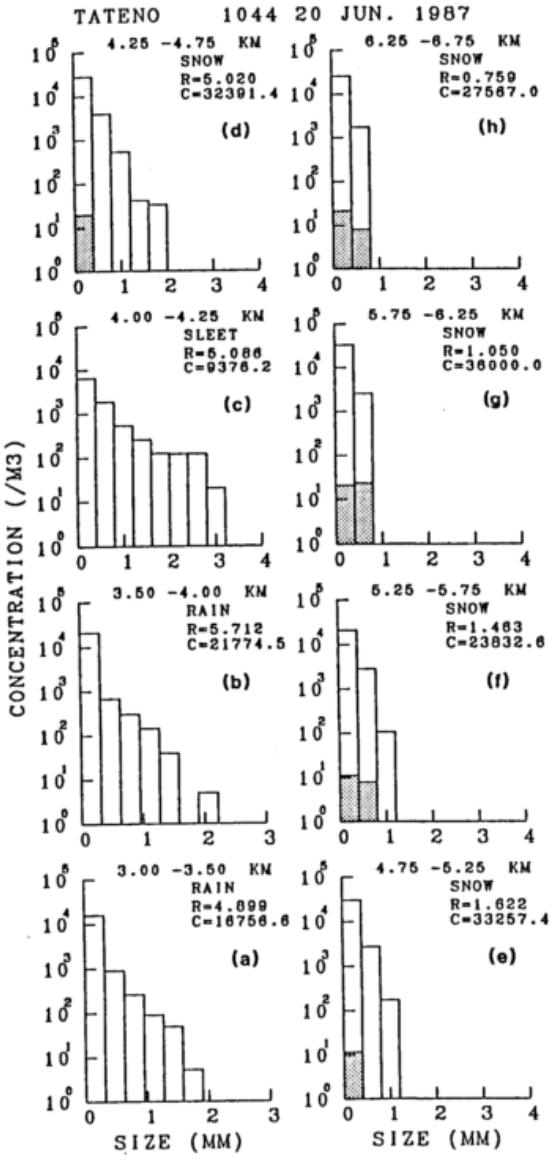


Fig.3. Change in size distributions of precipitation particles along the ascent of the HYVIS. Shaded bars represent supercooled drops. At the upper right of each figure shown are precipitation rate (R; mm/hr) and total concentration of precipitation particles (C; particles/m^3).

An increase in rainfall rate due to the collection of cloud droplets is estimated to be less than 0.5 mm/hr, corresponding to the HYVIS measurements which also showed no significant increase in rainfall rate. This means that the contribution of collectional growth below the melting layer to the total precipitation was negligibly small (less than 10 %). Most of the precipitation mass reaching the ground came from the depositional growth of snow crystals above the 0°C level although ~80 % of precipitation mass actually came from the depositional growth in a shallow (2 km deep), almost water-saturated region directly above the 0°C level.

4. CONCLUSIONS

The HYVIS observations showed the following microphysical structures and precipitation formation processes in the warm-frontal

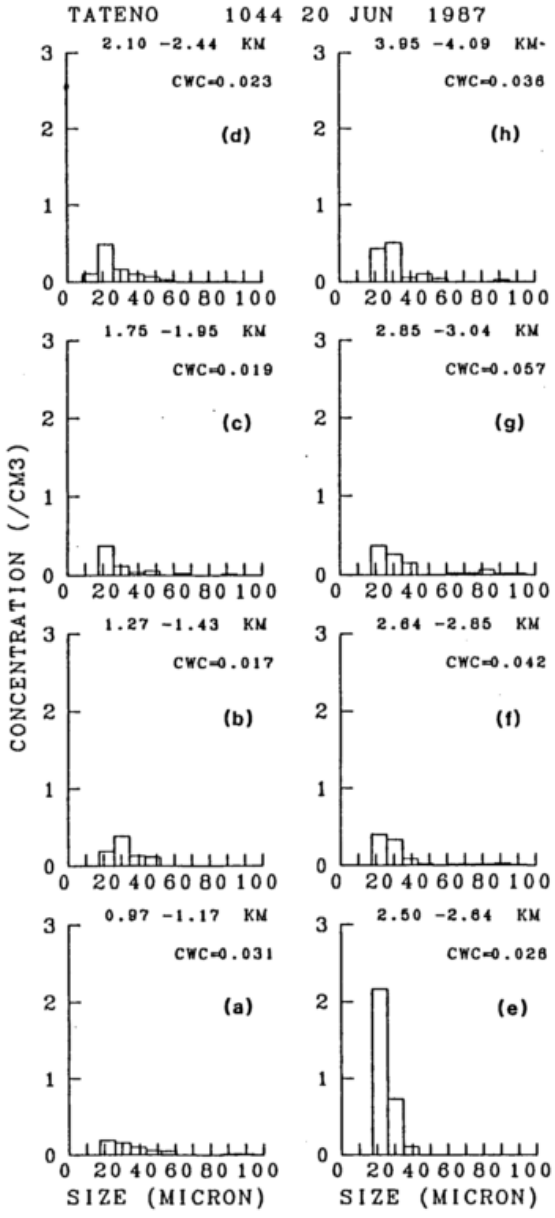


Fig.4. Change in size distributions of cloud droplets along the ascent of the HYVIS. At the upper right ishown is cloud liquid water content (CWC; g/m^3).

clouds.

Columnar type crystals predominated throughout a whole cloud layer, and some capped columns and hexagonal plates were also observed below the -17°C level. These crystals hardly rimed nor aggregated. Only in the melting layer, wet aggregates of these crystals were found. No supercooled cloud water existed in the clouds. These observational results demonstrated that the dominant mechanism of precipitation formation in these warm-frontal clouds was the depositional growth of snow crystals above warm-frontal surfaces.

Between the 0°C and -10°C levels, a low concentration (less than 100 drops/m^3) of drizzles coexisted with snow crystals, and the air was almost water-saturated. In this region, snow crystals rapidly grew by vapor deposition.

ACKNOWLEDGEMENTS

The authors would like to thank the staff members of the Aerological Observatory for their cooperation in the balloon observations.

REFERENCES

Herzegh, P. H. and P. V. Hobbs, 1980: The mesoscale and microscale structure and organization of clouds and precipitation in midlatitude cyclones. II: Warm-frontal clouds. *J. Atmos. Sci.*, **37**, 597-611.

Houze, R. A. Jr., S. A. Rutledge, T. J. Matejka and P. V. Hobbs, 1981: The mesoscale and microscale structure and organization of clouds and precipitation in midlatitude cyclones. III: Air motions and precipitation growth in a warm-frontal rainband. *J. Atmos. Sci.*, **38** 639-649.

Locattelli, J. D. and P. V. Hobbs, 1987: The mesoscale and microscale structure and organization of clouds and precipitation in midlatitude cyclones. VIII: Structure of a warm front. *J. Atmos. Sci.*, **44** 2290-2309.

Murakami, M., T. Matsuo, T. Nakayama and T. Tanaka, 1987: Development of Cloud Particle Video Sonde. *J.Meteor.Soc.Japan*, **65**, 803-809.

Murakami, M. and T. Matsuo, 1988: Development of Hydrometeor Video Sonde. *Preprints 10th International Cloud Physics Conference*, Bad Homburg, FRG, 1988.

COLD FRONTAL PASSAGE OVER THE SIERRA BARRIER

John D. Marwitz

Department of Atmospheric Science, University of Wyoming
Laramie, Wyoming

1. INTRODUCTION

A well defined narrow cold frontal rainband (Fig. 1) passed over the California Valley and moved up the Sierra barrier. The Sierra barrier is two dimensional and oriented ∿25 deg CCW from the rainband.

The NCAR CP-4 Doppler radar recorded 3-D volume scans at ∿5 min intervals. The Doppler radar was located at the upwind edge of the Sierra. The PPI volume scans have been processed using the box velocity processing (BVP) program developed by Johnston (1984). The critical assumptions for the BVP program to be valid is the airflow must be two dimensional ($\partial\Phi/\partial Y \simeq 0$) and the Doppler data must be symmetrically distributed on either side of the radar (Y=0). In spite of the presence of the two mesoscale vortex circulations, the flow was tested and both assumptions were found to be valid.

For the airflow through the rainband to remain steady-state and two-dimensional there has to be a quasi-balance between the mass and velocity fields. When the rainband began its ascent up the Sierra barrier the balance between the mass and velocity fields was severely upset. The purpose of this paper is to examine the temporal variations of the kinematic flow field as this transient rainband interacts with the Sierra topography. The kinematics of the velocity field have been calculated using the Doppler velocity fields.

2. KINEMATIC STRUCTURE OF AIRFLOW

The BVP results are presented for 1243 (Fig. 2) when the band was 37 km west of the radar, and for 1441 (Fig. 3) when the band was 36 km up the Sierra barrier. The mean reflectivity along the center of the band was 27 to 33 dBZ for each volume scan. The dominant structure in the airflow kinematics is the helical right hand circulation (Fig. 2b & 3b). The updrafts and downdrafts were variable in width and magnitudes. The widths varied from 2 to 4 km and the magnitudes varied from 1 to 5 m/s.

One important characteristic of the airflow which appeared to be steady over the valley and highly variable over the Sierra barrier was the band parallel low level jet (LLJ). Over the valley a LLJ with a core velocity of 27 to 29 m/s was present in the inflow region at 1 km and extended up into the rainband (Fig. 2d). At 1441 (Fig. 3d) the band parallel wind component (V) and the low level inflow had slowed to 23 m/s. The jet was near 3 km and in the updrafts at 1423 (18 minutes earlier). At 1441 the "jet" had changed to a region of minimum speeds (18 m/s).

An obvious conclusion is that the quasi-balance in the mass and velocity fields which was present in the rainband while it was over the California valley was severely upset when the rainband began to move up the Sierra barrier. The mass-velocity adjustment process appears to operate on at least a time scale of one hour.

References

Johnston, B., 1984: The kinematic structure of cold frontal rainbands. Ph.D. dissertation, University of Wyoming, AS Rpt # 146, 129 pp.

Acknowledgements: This research was sponsored by the Department of Interior's Bureau of Reclamation under Contract 2-07-81-V0256. The CP radar was provided by the Field Observing Facility of the National Center for Atmospheric Research.

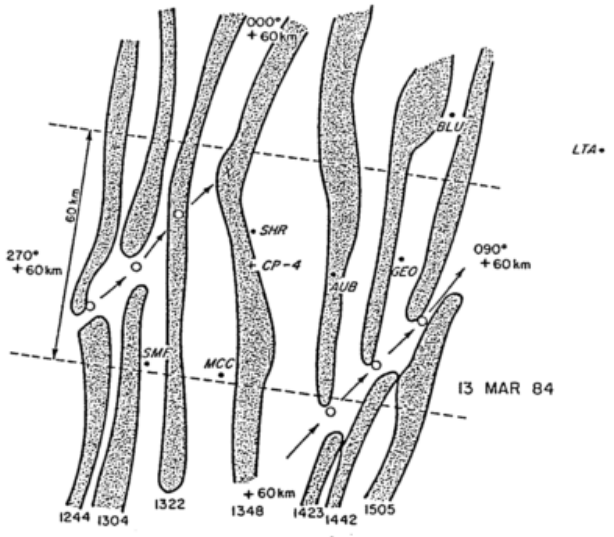


Fig. 1. The location of the 35 dBZ echo associated with the narrow cold frontal rainband/cold front is shown at various times. The vortex over the valley and its track, as well as the vortex over the barrier and its track, are shown.

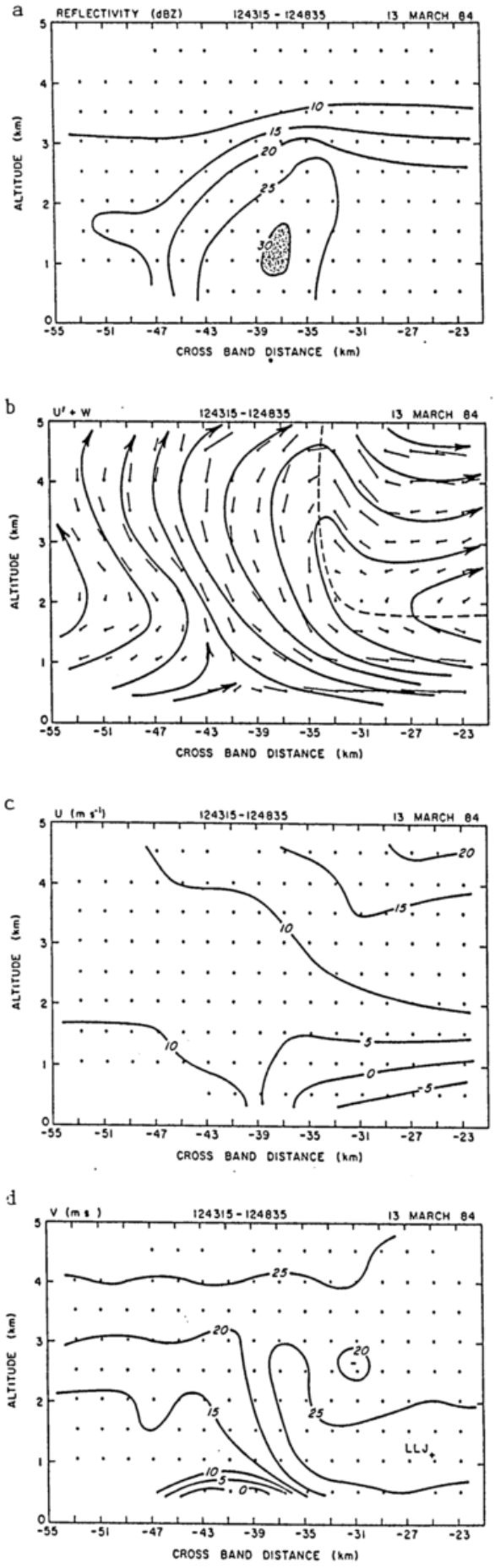


Fig. 2. X-Z cross sections from the BVP analysis.

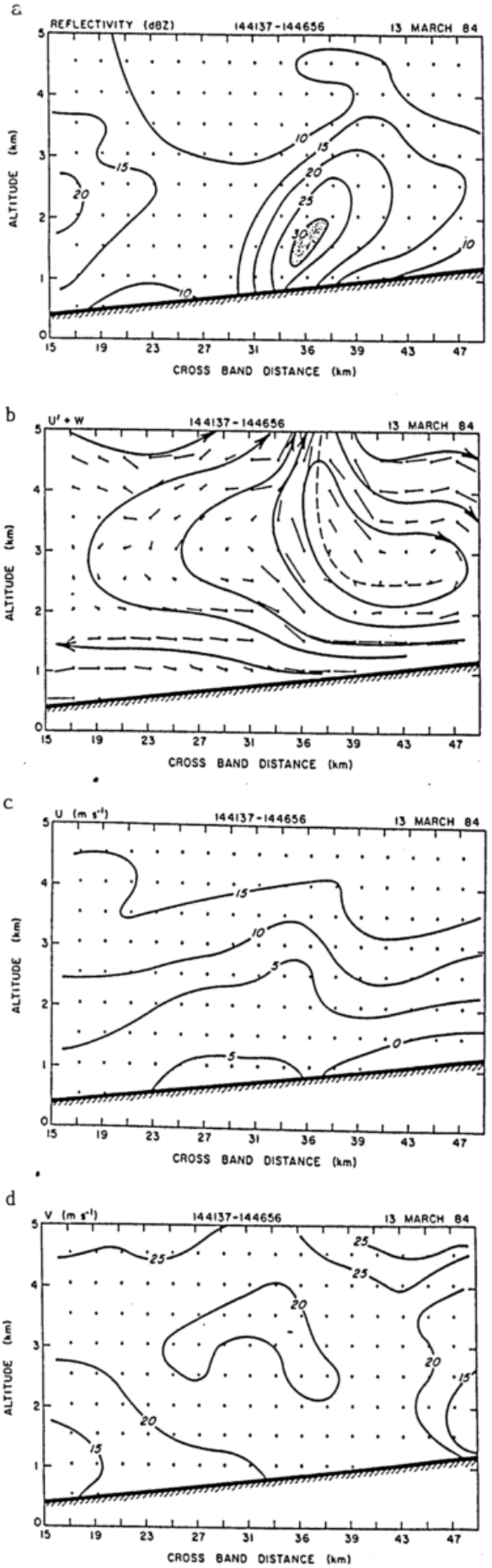


Fig. 3. X-Z cross sections from the BVP analysis.

A NUMERICAL MODELING STUDY OF COLD-FRONTAL RAINBANDS

David J. Knight and Peter V. Hobbs
Atmospheric Sciences Department, University of Washington, Seattle, Washington 98195 USA

1. INTRODUCTION

A two-dimensional, hydrostatic, primitive-equation model has been used to investigate the dynamics of frontogenesis in a moist atmosphere. The model has a medium resolution planetary boundary layer and uses an explicit scheme for the prediction of water vapor, cloud water and rain water. The development of a cold front is forced by shear-deformation associated with the non-linear evolution of an Eady wave. Simulations are performed with 5, 10, 40 and 80 km horizontal resolutions and fourteen levels in the vertical (four in the boundary layer).

The specific purpose of this numerical modeling study was to increase understanding of the mesoscale circulations associated with cold fronts and the rainbands that can accompany them. Field studies have revealed three types of rainbands associated with cold fronts, each of which is oriented nearly parallel to the front: wide cold-frontal, narrow cold-frontal, and warm-sector rainbands (Hobbs 1978). However, the dynamical mechanisms responsible for these rainbands have not been determined.

In this study, particular attention is paid to the dynamics of wide cold-frontal (WCF) rainbands. These rainbands form behind the surface cold front and above the cold-frontal zone and they move toward the surface front. We wished to determine if WCF rainbands can be simulated in a numerical model, and, if so, to determine under what conditions they form in the model. Parsons and Hobbs (1983) suggested that conditional symmetric instability (CSI) is the most likely mechanism for the formation of WCF rainbands. Although CSI has received some attention in the past (e.g., Bennetts and Hoskins, 1979; Bennetts and Sharp, 1982), CSI forced by vertical motions due to frontogenesis has not been treated quantitatively. Because upright convection complicates analysis of the results, care was taken to avoid convective instability.

2. RESULTS

Compared to the dry case, the inclusion of moisture in the model produced a stronger low-level jet ahead of the front, a stronger upper-level jet, and stronger temperature gradients at mid-levels. Moisture also produced a stronger ageostrophic circulation across the front and a more concentrated updraft just ahead of the surface front.

In the presence of a region of negative equivalent potential vorticity (i.e., a region of CSI), the inclusion of moisture also produced updrafts with a banded structure above and behind the surface cold front. These bands had a wavelength of about 70 km. They formed near the back edge of the cloud shield and moved with the winds at the top of the rainband. Therefore, they propagated toward the surface front with a relative velocity of about 1 m s^{-1}. The location, movement and spacing of the bands in the model agreed well with observations of WCF rainbands.

The banded structures in the model formed in a convectively *stable* region. The first band that appeared formed and intensified in a region of negative equivalent potential vorticity. Subsequent bands formed behind the first and intensified as they moved into the region of negative equivalent potential vorticity, indicating that CSI also played an important role in their formation and intensification. The slope of the updrafts and the spacing of the bands agreed well with the theory of CSI. While in the region of CSI, the vertical air velocities in the bands increased exponentially with time, although the growth rate was smaller than that predicted by linear SI theory. The bands were poorly resolved when the horizontal resolution (Δx) of the model was 40 km, and they are absent with $\Delta x = 80$ km. However, the strength and horizontal scale of the bands was about the same in simulations with Δx of 5 and 10 km. The WCF bands disappeared when the vertical stability was increased to the point that

equivalent potential vorticity was everywhere positive (i.e., CSI was not present).

Frictional convergence in the boundary layer forced a narrow cold-frontal rainband (NCFR) just above the surface front. The horizontal dimension of this band was greater than that for observed NCFR, presumably because of limited resolution in the model.

We are left with the following picture for the formation of WCF rainbands. During the early stages of cyclone development, a region of CSI is produced near the surface in the warm sector of the cyclone (Fig. 1a). This region of CSI is lifted by the ageostrophic circulation associated with frontogenesis. When the air in the region of CSI becomes saturated, the instability is released and this results in the formation of a WCF rainband (Fig. 1b). Subsequent WCF rainbands form behind the first and intensify as they move into the region of CSI (Fig. 1b,c).

For further details on this study the reader is referred to Knight and Hobbs (1988).

3. REFERENCES

Bennetts, D. A.; Hoskins, B. J.: Conditional symmetric instability - a possible explanation for frontal rainbands. *Quart. J. Roy. Meteor. Soc.*, 105 (1979), 945-962.

Bennetts, D. A.; Sharp, J. C.: The relevance of conditional symmetric instability to the prediction of mesoscale frontal rainbands. *Quart. J. Roy. Meteor. Soc.*, 108 (1982), 595-602.

Hobbs, P. V.: Organization and structure of clouds and precipitation on the mesoscale and microscale in cyclonic storms. *Rev. Geophys. Space Physics*, 16 (1978), 741-755.

Knight, D. J.; Hobbs P. V.: The mesoscale and microscale structure and organization of clouds and precipitation in midlatitude cyclones. XV: A numerical modeling study of frontogenesis and cold-frontal rainbands. *J. Atmos. Sci.*, 45 (1988) (in press).

Parsons, D. B.; Hobbs P. V.: The mesoscale and microscale structure and organization of clouds and precipitation in midlatitude cyclones. XI: Comparisons between observational and theoretical aspects of rainbands. *J. Atmos. Sci.*, 40 (1983), 2377-2397.

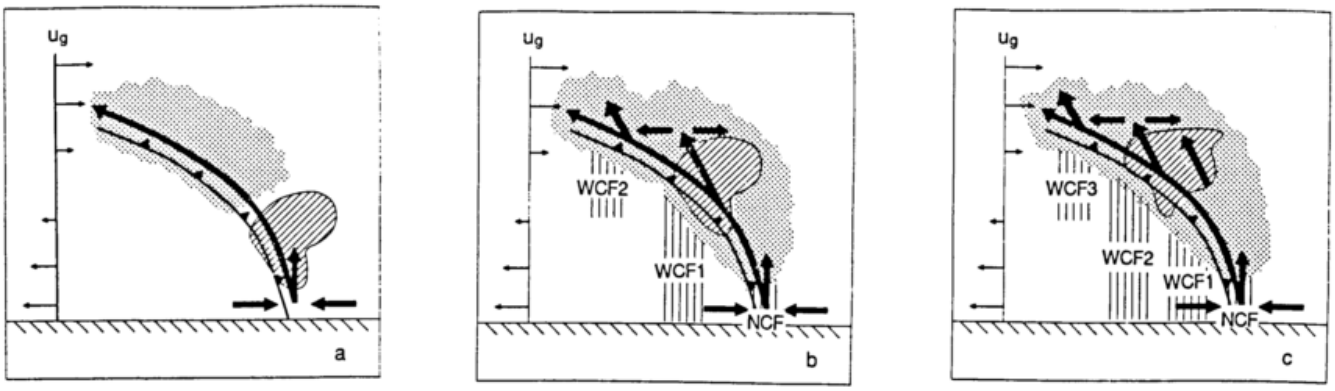


Figure 1. Schematic of the processes leading to the formation of cold-frontal rainbands. The cross hatching shows the region of CSI and light, shading shows the region of cloud water. Vertical hatching below cloud base represents precipitation. The geostrophic wind in the plane of the cross section (u_g) is indicated on the left hand side of the figure. Broad arrows shown ageostrophic air motions in the plane of the cross section. All winds shown are relative to the motion of the Eady wave. a) A region of CSI that forms in the warm air is advected toward then up along the frontal surface by the ageostrophic motions. b) When the region of CSI becomes saturated the instability is released, resulting in a wide cold-frontal rainband (WCF1). A second rainband (WCF2) is forced by convergence behind WCF1. Convergence in the planetary layer forces a narrow cold-frontal rainband (NCF). c) WCF1 moves toward the warm air, WCF2 moves into the region of CSI and intensifies, a third band (WCF3) is forced by convergence behind WCF2.

NUMERICAL SIMULATION OF RAINBANDS CAUSED BY MESO-β SCALE POTENTIAL VORTICITY ANOMALIES

Han-Ru Cho and Douglas S.T. Chan
Department of Physics, University of Toronto
Toronto, Ontario, Canada

1 INTRODUCTION

The formation of precipitation in the midlatitudes is usually associated with dynamical systems at the synoptic scale; but the distribution of precipitation often show pronounced organization at the meso-β scale in the form of rainbands (Hobbs, 1978). The dynamics involved in the formation of these rainbands is not yet well understood.

We propose in this study that pre-existing potential vorticity in the air masses may be a possible cause for the formation of rainbands in the development of midlatitude cyclones. A two-dimensional moist frontogenesis model is used to examine in detail the dynamics which can lead from potential vorticity anomalies to the formation of rainbands.

2 A NON-UNIFORM POTENTIAL VORTICITY MODEL

The model is based on the two-dimensional semi-geostrophic frontogenesis model forced by a deformation flow (Hoskins and Bretherton, 1972). The moist dynamics are described in the geostrophic coordinates (X,Z) by

$$\frac{D\theta}{Dt} = E \tag{1}$$

$$\frac{Dq}{Dt} = \zeta\frac{\partial E}{\partial Z} \tag{2}$$

$$\frac{DQ_v}{Dt} = -\frac{c_p\pi}{L}E \tag{3}$$

where θ is the potential temperature, q the potential vorticity, Q_v, the mixing ratio of water, ζ, the vertical component of the absolute vorticity, E the rate of condensational heating, π the dimensionless pressure, c_p the heat capacity at constant pressure and L the latent heat of water.

We assume as the background a constant potential vorticity q_o and a baroclinic field $\theta_s(X,Z)$ at the synoptic scale. If anomalies exist at the mesoscale, we have

$$q = q_o + q_m(X,Z) \tag{4}$$

$$\theta = \theta_s(X,Z) + \theta_m(X,Z) \tag{5}$$

where q_m and θ_m give the mesoscale structures of the potential vorticity and potential temperature field. q_m and θ_m are not independent, as θ and q are related through the elliptic equation

$$\frac{1}{f^2}\frac{\partial^2\theta}{\partial X^2} + \frac{\partial}{\partial Z}\left[\frac{f\theta_o}{gq}\frac{\partial\theta}{\partial Z}\right] = 0 \tag{6}$$

where f is the Coriolis parameter, g the gravitational acceleration and θ_o a typical surface potential temperature. Thus a mesoscale anomaly may be specified either in terms of q_m, or in terms of θ_m, provided they are consistent with equation (6).

3 RESULTS AND DISCUSSION

Results of two simulations are compared here to show mesoscale anomalies as possible causes for rainbands. In the first simulation, no mesoscale anomalies are introduced; the initial conditions are simply given by the uniform potential vorticity field

$$q = q_o = 5\times10^{-7}Km^{-1}s^{-1}$$

and the potential temperature field is specified on the boundaries to be

$$\theta = \theta_s = \theta_o + \frac{q_o}{f}Z + \Delta\theta_s \tanh(X/L_s)$$

with $\Delta\theta_s = 12°C$ and $L_s = 700$ km.

This is the case of a simple moist frontogenesis. In the second simulation, an anomaly in the potential temperature field is introduced at the initial time:

$$\theta_m = \Delta\theta_m\left[\frac{(X-X_o)}{L_m}\right] \exp\left[\frac{-(X-X_o)^2}{L_m^2}\right] h(Z)$$

with $\Delta\theta_m = -1°C$, $L_m = 200$ km, $X_o = 600$ km, and h(Z) being equal to unity from 0 to 2.5 km, then decreasing linearly to zero at 5 km. The corresponding q_m field can be determined from equation (6). This mesoscale perturbation corresponds to a low level jet in the along-front direction centered at X_o. The same initial moisture field is used in both simulations; in terms of mixing ratio, it is given by

$$Q_v(X,Z) = Q_{vs}(X,Z)\ H(Z)$$

where Q_{vs} is the saturation mixing ratio, and H(Z) has value 0.75 from 0 to 5 km, then decreasng linearly to 0.5 at 10 km.

Figure 1a shows the vertical cross section of the vertical velocity field for the basic frontogenesis case with no perturbations. The result corresponds to an early stage of frontal development at 1 hr model time. Figure 1b shows the vertical velocity field obtained from the second simulation at the same model time. Strong perturbations in the vertical velocity field were induced over the region where the temperature inhomogeneity was introduced.

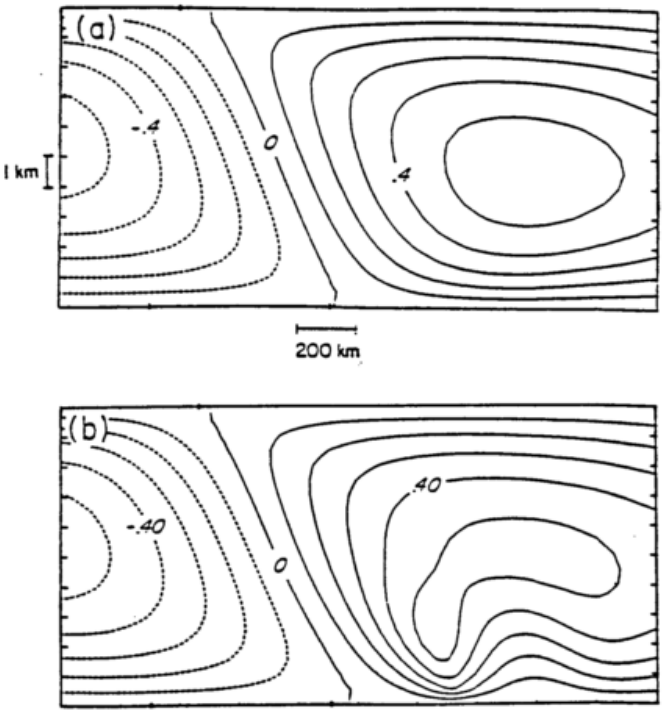


Fig. 1: Contours of vertical velocity. (a) Basic frontogenesis case. (b) Frontogenesis with a mesoscale anomaly. The domain is 2000 km in x and 10 km in z (common for all figures). Contour interval is 0.1 cm s^{-1}, dashed contours represent negative velocity.

Condensation commenced at about 16 hours of model time in both simulations. Figure 2 shows the contours of E, the instantaneous condensational heating field in units of the maximum of E (unity = E_{max}) at 25 hours model time: (a) the simple frontogenesis case, and (b) the case with mesoscale anomaly. In the basic frontogenesis case $E_{max} = 9\times10^{-5}Ks^{-1}$. A single frontal rainband with a narrow base was simulated. The narrow base is the result of the positive feedback betwen the diabatic heating and the ageostrophic convergence at the lower levels. Figure 2b shows the

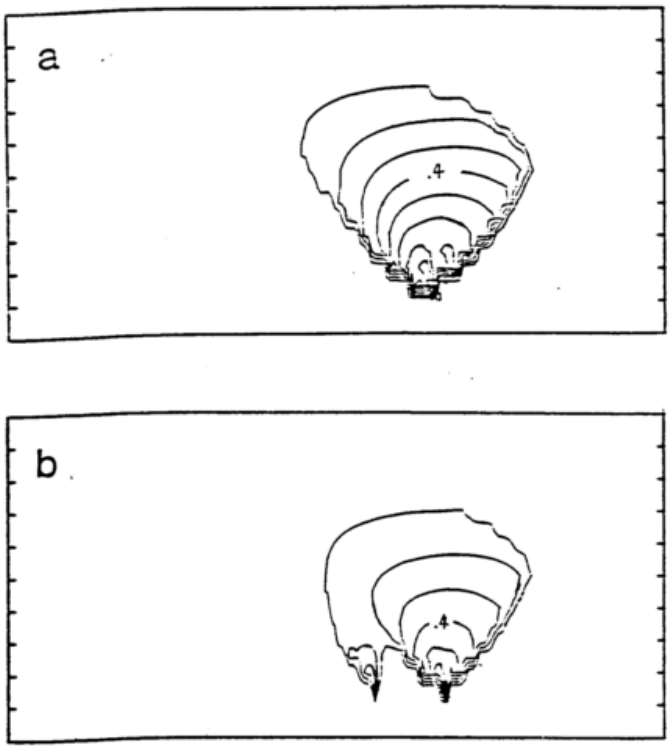


Fig. 2: Contours of the instantaneous heating field (E) in units of the maximum of E (unity=E_{max}) at intervals of 0.1. (a) Basic frontogenesis case, $E_{max}=9x10^{-5}$ Ks^{-1}. (b) Frontogenesis with a mesoscale anomaly, $E_{max}=1.4x10^{-4}Ks^{-1}$.

mesoscale anomaly has induced the formation of two distinct rainbands at the lower levels. Each rainband has a narrow base indicating that a positive feedback mechanism is working on each band. The bands are separated by about 200 km. The right band is more intense, it has $E_{max} = 1.4x10^{-4}Ks^{-1}$, the left band has $E_{max} = 8x10^{-5}Ks^{-1}$.

These results indicate that when mesoscale anomalies are present in the atmosphere, complex patterns in the vertical velocity field were induced, which resulted in the formation of middle level rainbands. When proposing mesoscale anomalies as the cause of rainbands, the question naturally arises as to the origin of the anomalies themselves. One important source is diabatic heating. Equations (1) and (2) indicate that diabatic heating generates anomalies in the θ and q fields. Thus in a moist atmosphere which has undergone many precipitation cycles, the θ and q fields may become highly non uniform on the mesoscale. So the basic assumption of this study (at the initial stages of frontogenesis, the atmosphere may contain mesoscale anomalies) appears to be a reasonable one. The natural variability of the atmosphere on the mesoscale is an important problem to be studied in the future.

REFERENCES

Hobbs, P.V. : Organization and structure of clouds and precipitation on the mesoscale and microscale in cyclonic storms. Rev. Geophys. Space Phys., **16** (1978), 741-755.

Hoskins, B.J.; Bretherton F.P. : Atmospheric frontogenesis models : Mathematical formulation and solution. J. Atmos. Sci., **29** (1972), 11-37.

SIMULATION OF FRONTAL CLOUDS AND PRECIPITATION USING A MESOSCALE WEATHER PREDICTION MODEL

E. Müller, U. Wacker
Deutscher Wetterdienst, Offenbach, FR Germany

1 INTRODUCTION

Cloud physical processes play an important role in the development of frontal systems, since a feedback to the dynamics takes place through diabatic heating by phase transitions. A better understanding of these processes can be achieved by extended field observations (e.g. Hobbs et al., 1980) and/or by numerical simulation within a complex 3D dynamical framework. Weather prediction models, confined as yet to the synoptic scale, begin to include the meso-α scale (e.g. Bell and Dickinson, 1987). But the treatment of cloud physical processes remains nevertheless very simplified. At the Deutscher Wetterdienst a regional numerical weather prediction (NWP)model - the "Europa-Modell" (EUM; Müller et al., 1987) - was developped as experimental precursor of a later operational version. In this model meso-α structures of cloud and precipitation coupled with fronts and orography are resolved; on the other hand, the hydrometeorological processes in stratiform clouds are parameterized in relative detail.

This has been done

- to properly include physical mechanisms as phase transitions or cloud/radiation interaction,
- to improve the forecast of weather parameters like type and amount of cloudiness and surface precipitation,
- to provide a suitable meteorological basis for air pollution modelling,
- to investigate cloud physical processes in a realistic dynamic environment.

2 MODEL DESCRIPTION

The computational domain of EUM covers Europe and the Eastern North Atlantic with a mesh size Δs = 63.5 km. In the vertical, the atmosphere is resolved by 18 layers of upward increasing thickness in a terrain following coordinate system. The time step is 75 s. In addition to the grid-scale equations for the prediction of the flow and mass fields, EUM contains a complete parameterization package related to horizontal diffusion, vertical turbulent fluxes, soil processes, stable precipitation, moist convection and radiation.

Concentrating on the aspect of specific interest, prognostic variables are total heat h ($= c_p T + L_v q_v$) and total water content q_{vc} ($= q_v + q_c$; q_v, q_c: specific content of vapor, cloud water). T, q_v, q_c follow diagnostically from h, q_{vc}, if saturation equilibrium within clouds is supposed. The adjoint parameterization scheme of stable precipitation (Fig. 1) includes the ice phase. It is of Kessler-type and allows for interactions between two precipitation phases rain and snow (ice), cloud water and water vapor by: autoconversion of cloud water to rain (AUT) and to ice ("nucleation" NUC), deposition (DEP), riming (RIM), shedding (SHED), melting (MELT), accretion (ACC), evaporation of raindrops (EVAP). The precipitation rates P_R, P_I result from vertical integration, assuming stationarity and neglecting advection (equilibrium in columns):

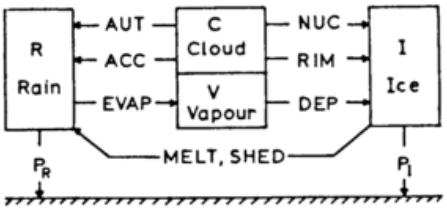


Fig. 1: Schematic diagram of processes involved in the precipitation parameterization.

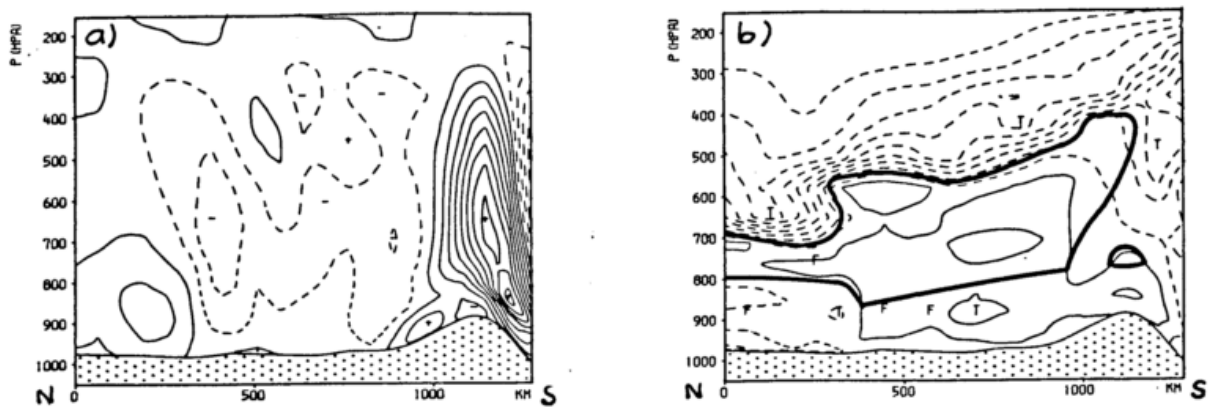


Fig. 2: Vertical cross sections from 1.5E, 54.1N (north of Strait of Dover; left) to 3.6E, 43.5N (Lion Gulf; right). Forecast valid at 23 January 1986 09 UTC.
a) Vertical motion ω. Isoline distance $\Delta\omega = 0.2$ Pa/s. ——: $\omega \geq 0$; ----: $\omega < 0$.
b) Relative humidity RH. Isoline distance $\Delta RH = 0.1$. ----: $RH < 1.$, ——: $RH \geq 1.$, i.e. cloud area. Thick solid line marks ice saturation.

$$\frac{\partial P_R}{\partial t} = S_{AUT} + S_{ACC} + S_{SHED} + S_{MELT} - S_{EVAP}$$

$$\frac{\partial P_I}{\partial t} = S_{NUC} + S_{RIM} - S_{SHED} - S_{MELT} + S_{DEP}$$

with

$$S_{AUT} = [1-\varepsilon(T)]q_c/\tau_{AUT}, \quad \tau_{AUT} = 10^4 \text{ s}$$

$$S_{NUC} = \varepsilon(T)q_c/\tau_{NUC}, \quad \tau_{NUC} = 10^3 \text{ s}$$

$$S_{ACC} = a_1 P_R^{7/9} q_c$$

$$S_{RIM} = a_2 P_I q_c$$

$$S_{SHED} = H(T-T_0)S_{RIM},$$

$H(x)$: Heaviside function

$$S_{MELT} = a_3 P_I^{5/8.6}\{1+b_3 P_I^{1.8/8.6}\}(T-T_0)$$

$$S_{DEP} = a_4 P_I^{5/8.6}\{1+b_4 P_I^{1.8/8.6}\}(q_v - q_{vs}^{(I)})$$

$$S_{EVAP} = a_5 P_R^{4/9}\{1+b_5 P_R^{1/6}\}(q_{vs}^{(w)} - q_v)$$

By choosing different time constants for AUT, NUC and a function ε(T) increasing from 0 at T_0 = 0°C to 1 at T = -38°C, the formation of ice is favoured as temperature decreases. The coefficients a_2, a_4, a_5, b_4 are temperature dependent reflecting the varying crystal growth habit and the temperature difference between hydrometeor and air. Considering also the effect of different saturation values $q_{VS}^{(W)}$, $q_{VS}^{(I)}$ over water and ice, resp., we see: the role of the ice phase in precipitation formation is clearly accentuated, particularly the Bergeron-Findeisen process.

3 A CASE STUDY

The forecast starting from 23 January 1986 00 UTC is selected for a case study. The synoptic situation shows a cold front moving rapidly southward from the British Isles/North Sea over France to the Mediterranean. According to the 9h-forecast the front lies over southern England. In the cross-section (Fig. 2) it is indicated by maximum rising motion and deep cloudiness between 400 and 500 km. A second prominent cloud system (700 to 900 km) is orographically influenced by the Massif Central. Strong down winds cause a well-marked cloud edge; only low clouds with relatively high water content cover the summit. The 0°C-isoline rises from 900 hPa (N) to 750 hPa (S). Fig. 3 provides additional information about the contribution of the different microphysical processes participating in the production of precipitation. In deep clouds, most precipitation is generated via the ice phase. Concerning the frontal cloud system vertical profiles of the conversion rates show an effective seeder-feeder mechanism. Here we find the highest surface precipitation rate though the integrated cloud water is essentially lower than in the orographic cloud system. This is brought about by depositional growth in layers supersaturated with respect to ice (indicated in Fig. 2b), and by riming in lower layers. Cloud water is

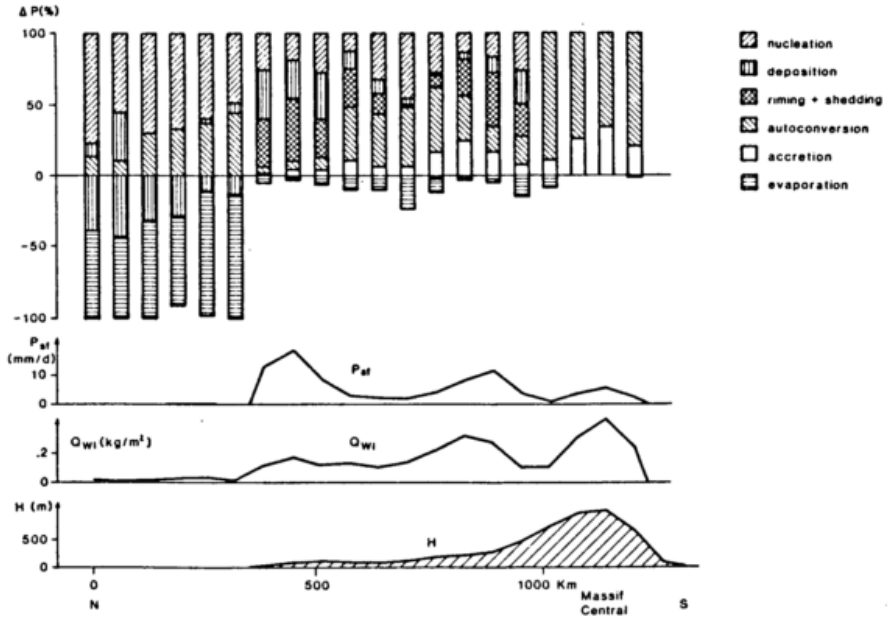


Fig. 3: Characteristics of cloud physical processes: Vertically integrated contributions of conversion rate ΔP in % of total precipitation, surface precipitation rate P_{sf}, vertically integrated cloud water content Q_{WI}, and orographic height H. Cross section as in Fig. 2

therefore removed very effectively. On the contrary, high q_c-values are generally found in shallow clouds in the lower troposphere, e.g. over mountains.

Due to the lack of adequate observations this plausible picture of simulated cloud physics cannot be verified in detail. Compared with synoptic observations for the period 6-18 UTC the model is in reasonable overall agreement with respect to accumulated precipitation.

4 CONCLUSION AND OUTLOOK

It is the intention of this work to formulate the hydrologic cycle in NWP models as realistic as possible. Certainly, the elaborated parameterization scheme applied gives some insight into the hydrometeorological process. The increased computational amount, however, is not easily justified. Comparative experiments with simplified parameterizations reveal that surface precipitation is essentially determined by the dynamics of the system via the water budget and shows very limited sensitivity to the details of the parameterization. Rather the model atmosphere tends to an equilibrium between dynamically forced gain and any precipitated loss of condensate. In this sense, the stable and convective component of precipitation also supplement each other.

Accordingly, expectations are mainly directed to 3 aspects: spatial and temporal precision of precipitation forecast, especially in connection with meso-β models; quality of cloud prediction; provision of information necessary to calculate wet deposition (rainout, washout).

Future work is necessary, to adapt and possibly supplement (cloud ice phase!) the physical scheme and its numerical realization for use in meso-β models, to take into account partial cloudiness, mainly in vertical respect, to improve the field analysis of atmospheric water variables.

ACKNOWLEDGEMENT

The authors gratefully acknowledge the valuable assistance of their colleagues of the mesoscale modelling group of the DWD. Parts of this work are supported by the SFB 233 sponsored by the DFG.

REFERENCES

BELL, R.S.; DICKINSON, A.: Meteor.Office (UK), Scient. paper No.41, Met.O. 979 (1987).

HOBBS, P.V.; MATEJKA, T.J.; HERZEGH, P.H.; LOCATELLI, J.D.: J.Atmosph.Sci., 37 (1980), 568-596.

MÜLLER, E,; FRÜHWALD, D.; JACOBSEN, I.; LINK, A.; MAJEWSKI, D.; SCHWIRNER, J.U.; WACKER, U.: J.Meteor.Soc. Japan, Spec.Vol. (1987), 533-546.

LONG LASTING TRADE WIND RAINBANDS

Tsutomu Takahashi

Physics Department, Kyushu University
Fukuoka, Japan 812

1. INTRODUCTION

The study of rain in Hawaii that was conducted using aircraft has revealed many findings (TAKAHASHI 1977, p. 1773; 1981, p347; 1986 p. 575). These include observation of raindrops near the cloud top, long-lasting rainfall from certain types of rainbands, and a high rain-water accumulation rate in multicell clouds. Both a three-dimensional cloud model with microphysics and the 1985 Joint Hawaii Warm Rain Project data were used to confirm and extend the previous observations and to investigate the physical concepts.

2. RESULTS

a. Drop size distribution

On July 24, 1985, two rainbands developed upwind of Hilo, Hawaii in parallel to the coastal line (Fig. 1). The rainband closer to the coast (first cloud band) showed a strong low level convergence and produced heavy rainfall, while the rainband further from the

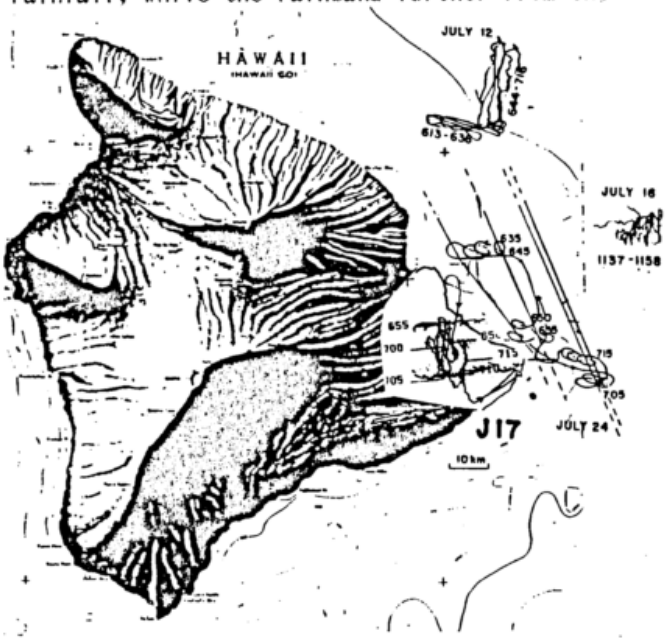


Fig. 1. Flight pathes at the island of Hawaii.

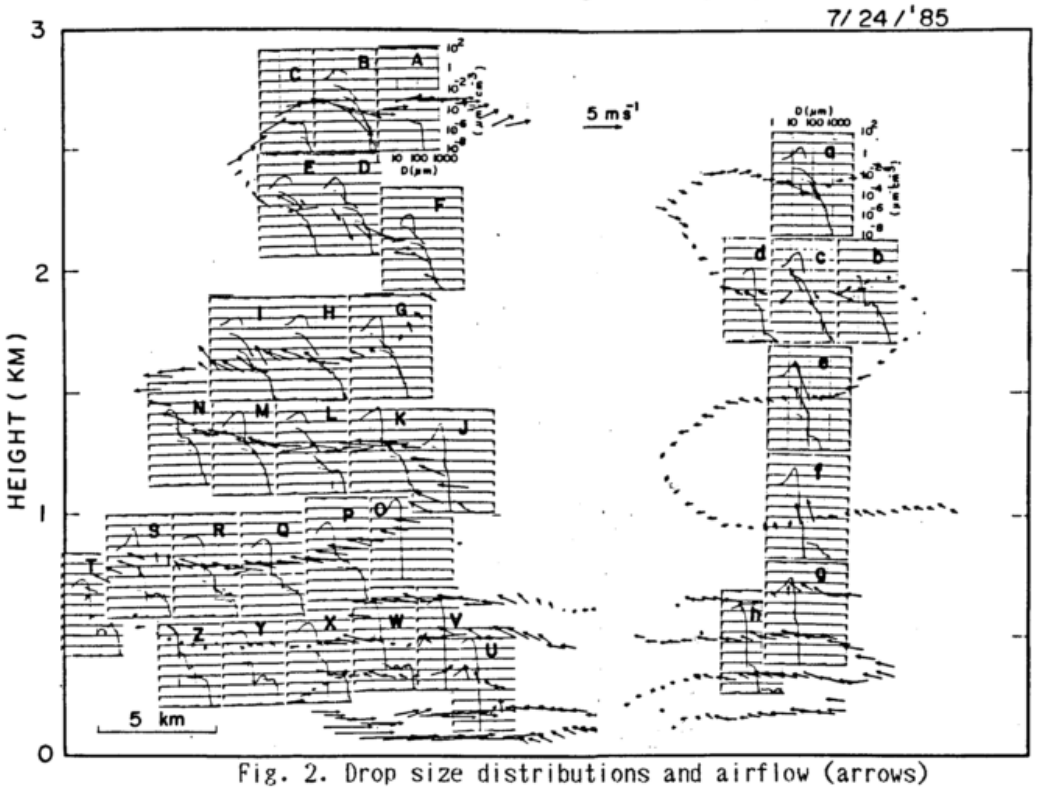


Fig. 2. Drop size distributions and airflow (arrows)

coast (second cloud band) had no low level convergence and did not produce rainfall. In the second band (cloud top, 2.7 Km and cloud base 0.5 Km), maximum updraft (5 ms^{-1}) was observed near the cloud top and a downdraft was seen along the cloud boundaries, suggesting a "developing stage".

In this second cloud band, the modal size of cloud droplets increased with height, and the drop size distribution abruptly became broader when the modal size grew to 25μm in diameter near the cloud top (Fig. 2). Raindrops (1 mm in diameter and in the concentration of 10 $mm^{-1}m^{-3}$) were observed near the cloud top. In this area, both cloud droplets and drizzle showed maximum mixing ratios.
In the first cloud band the cloud drop growth rate was higher than in the case of the second band. The preliminary growth that occurs in the feeder cloud cells seems to be the reason for the observed large cloud drops even at low levels. Small particles among precipitating particles falling from cloud top are recycled at the middle of cloud. Raindrop formation is thus be enhanced. Further raindrop growth is seen at the lower part of cloud by collecting low-level large drops. The 3D model demonstrates that the fast raindrop formation is due to the low cloud muclei concentration and drop recirculation.

b. Long-lasting rainband
On July 12, 1985, a very broad band (about 50 Km in width) developed along a north-to-south direction (Fig. 3). Winds had a parabolic profile with strong low-level wind twists. The radar echo lasted for about two hours at maximum. Updraft in the cloud was sloped to the upshear (maximum speed about 7 ms^{-1}). Gentle downdrafts were seen at both east and west cloud boundaries. Equivalent potential temperature profiles showed the lifting of air at very low levels from the west.

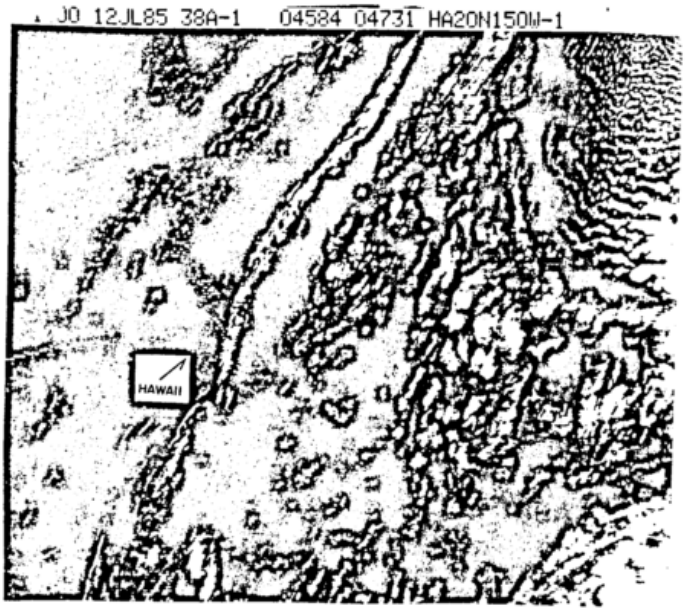


Fig. 3. Long-lasting rainband (July 12, 1985).

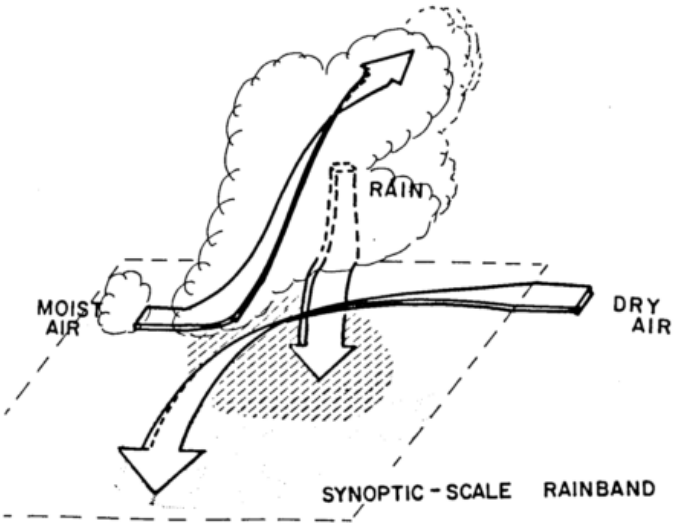


Fig. 4. Model of long-lasting rainband.

Thermodynamic profiles projected at the horizontal levels of 500 m and 170 m showed the inflow of moist air from the northwest at low levels. Dry air descended from east of the rainfall area at the 500 m level and stretched to the western and southern part of the rainfall area at the 170 m level. Temperature was about 1℃ warmer at the western side than at the eastern side of the rainband (Fig. 4).
The 3D model which produce long lasting rainfall shows sloped updraft where raindrops do not interfere with the updraft. Dry air which acts as a dissipating effect on cloud development in the trade wind layer is not intruded and raindrops do not block the low-level reverse flow.

c. Precipitation processes in multicell clouds

On July 19, a band cloud developed over the land in nearly an east-west direction. The cloud size was about 15 Km wide and two cloud cells were identified across the cloud band. A strong temperature difference (4℃) was measured at low levels. The heavy precipitation area coincided with the area of the maximum horizontal temperature gradient at low levels. Both cells were located at the northern (warmer) side of the precipitation area. The updraft sloped from the north to the south with increasing height. Analysis leads to the following conclusions about drop growth processes (Fig. 5).

In the northern cloud cell, cloud drops grow by condensation during upward movement. At the upper part of the cloud cell, drizzle is formed and raindrops grow, falling at the southen part. At low levels, downdraft due to rainfall forms a convergence and creates a second cloud cell between the first cloud cell and the rainfall column. Due to the supply of low-level moist air, the drop growth rate is high in the second cell, even at low levels. The recirculation of large cloud drops by the downdraft also helps to grow drizzle earlier. Raindrops falling from the first cloud cell capture the drizzle and increase in size. Thus rainwater becomes maximum at the lower part of the cloud.

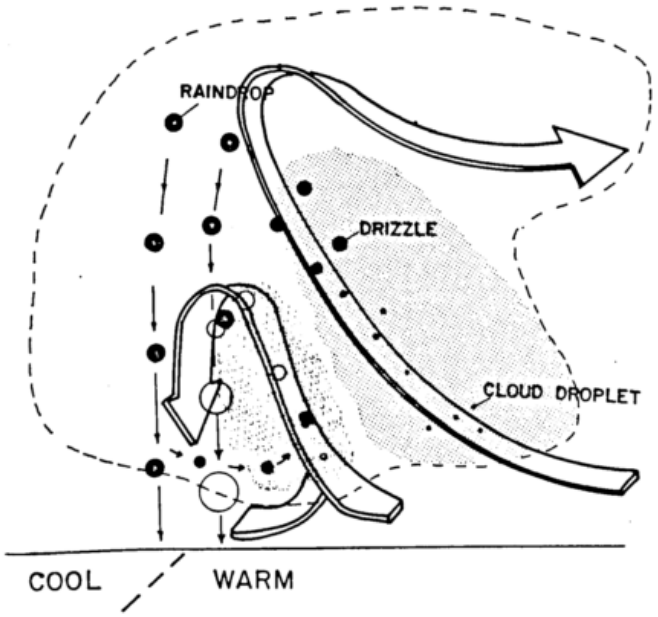


Fig. 5. Model of cell-cell interaction for precipitation.

3. Conclusions

(1) In the trade wind cumulus clouds raindrops are formed efficiently by drop recirculation.

(2) Trade wind cloud bands producing long-lasting rain showers are characterized by a special airflow pattern where dry air does not intrude.

(3) Cells in the multicell cloud interact microphysically with each other to produce an efficient precipitation process and maintenance of the rainband.

ACKNOWLEDGMENTS

The author would like to express his sincere appreciation to Dr. A. Copper, Mr. W. Sand, Mr. D. Baumgardner and the crews who helped to make the 1985 Hawaii project a success. The project was supported by the National Science Foundation (ATM 8602957).

REFERENCES

TAKAHASHI, T.: A study of Hawaiian warm rain showeres based on aircraft observation. J. Atmos. Sci. 34 (1977) 1773-1790

TAKAHASHI, T.: Warm rain in Hawaii - rain initiation. J. Atmos. Sci. 38 (1981) 347-369.

TAKAHASHI, T.: Wind shear effects on water accumulation and rain duration in Hawaiian warm clouds. J. Meteor. Soc. Japan 64 (1986) 575-584.

CHARACTERISTICS OF CUMULUS BANDCLOUDS OFF THE COAST OF HAWAII

G. Raga [a], J. Jensen [b], J. Wettlaufer [c] and M. Baker [c]

[a] University of Washington
Atmospheric Sc. Dept.
Seattle, Wa. 98195

[b] National Center for
Atmospheric Research [+]
Boulder, CO 80303

[c] University of Washington
Geophysics Program
Seattle, Wa. 98195

1. BACKGROUND

The Joint Hawaii Warm Rain Project (JHWRP) in 1985 was a collaborative aircraft experiment designed to explore the processes leading to warm rain evolution in cumulus clouds off the east coast of Hawaii. The site was chosen because of the regularity and relative simplicity of the clouds and the fairly extensive documentation on the meteorology in the region.

In the present study we have investigated the interactions of the clouds and the near-cloud environment. Specifically, we addressed the following questions:

i) What generates the clouds?

ii) Can we estimate entrainment rates as functions of cloud parameters?

iii) Which are the preferred regions of entrainment? Which are the important mechanisms of transport of the entrained air within the clouds?

iii) How do detrained parcels modify the environment surrounding the clouds?

2. FIELD PROJECT AND DATA ACQUISITION

During 6 weeks (July-August 1985) the University of Wyoming King Air sampled the bandclouds that develop off the east coast of Hawaii. The measurements included thermodynamic, dynamic and microphysical variables. For a detailed description of the instrumentation we refer the reader to Cooper (1978). The dataset was analyzed to detect inconsistencies and the methods used to correct them are described in Jensen et al. (1988).

The results presented in this paper represent a subset of the total dataset. It includes sixteen of the clouds sampled during July 10, 11, 12 and 13.

The sampling of the clouds usually started around 6 am local time, with a clear air sounding (during take-off), followed by penetrations at different levels, almost always starting at cloud top. The studies ended with the determination of conditions at cloudbase and in some cases, there were passes underneath cloudbase through precipitation. The radar on board was used to avoid the regions of strong echoes during the penetrations.

3. ENVIRONMENTAL CHARACTERISTICS

The island of Hawaii represents an obstacle to the incoming stratified tradewinds. The flow is governed by the Froude number, which in this case is very low (≈ 0.25). Smolarkiewicz et al. (1987) have simulated the flow around Hawaii with a 3D model. They find that for such small Froude number, a region of low level convergence develops upwind of the coast and bandclouds develop above that region. A surface map with the location of the clouds included in this study clearly shows that these clouds were aligned in an arc-like pattern following the coastline.

Typical thermodynamic soundings show the presence of very moist subcloud and cloud layers (80% RH) and very dry (20% RH) above the trade inversion. The horizontal wind below the inversion is typically from the East or ENE. The change in equivalent potential temperature from below to above the inversion ranges between -10 and -16 K. At the inversion level there is usually a change in wind speed and direction, and above it, we observe either northerly or southerly winds. A typical example of an environmental sounding obtained during take-off ($\approx$ 6 am local time) from Hilo on July 11 is shown in Fig. 1. Notice the return flow and the characteristic dry and cool air associated with it. Cloud base height was typically 500 to 600 m and tops ranged between 2500 and 3000 m, depending on the height of the trade inversion.

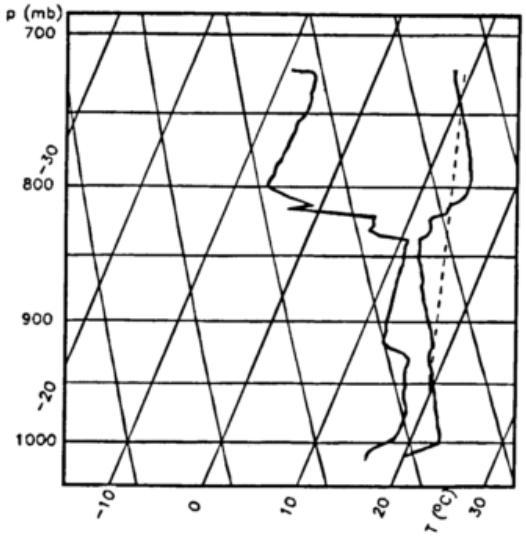


Figure 1. Sounding (skew-T diagram) observed during 55000-55812 on July 11, 1985.

4. CLOUD EVOLUTION

4.1 *Cloud Generation*

We have computed the buoyancy of incloud parcels as a function of the height above cloudbase. Although the buoyancy should be interpreted with caution given that it is the result (usually small) of the difference between two large numbers, we find that the average buoyancy is negative just above cloudbase. From this result, the fact that there is a

[+] NCAR is sponsored by the National Science Foundation

region of convergence and the observation that the clouds form in bands, we conclude that these clouds are dynamically forced. The forced ascent produces negatively buoyant parcels.

The level of free convection for these clouds is usually only a few hundred meters above cloudbase. Once the ascending parcels go beyond this level, they become positively buoyant and the effect of latent heat release takes over the cloud dynamics.

4.2 *Rate of entrainment*

The total water content Q(kg/kgair), is found, in average, to decrease with height, indicating that dilution is occurring. We have estimated a bulk entrainment rate that corresponds to a scale of $\approx$ 1km, which is of the order of cloud scale. We have used this rate in a simple plume model and obtained fairly good agreement with observations for the equivalent potential temperature and the number concentration of cloud droplets.

We have computed the ratio between the liquid water content and the adiabatic liquid water content. We observe that this ratio varies widely at all levels. In average we obtain higher values than those reported by Warner (1970) for Australian cumuli.

4.3 *Undiluted parcels*

The analysis of individual case studies reveals the presence of what we believe are undiluted parcels, defined (Jensen, 1985) by the following criteria:

i) $\left|T - T_{ad}\right| \leq 0.5°$

ii) maximum in vertical velocity

iii) minimum in turbulence intensity

Fig. 2 shows an example of the parcels that we have classified as undiluted. The top box (thick line) shows a maximum in the vertical velocity between 72502 and 72504. The middle box has the departure of the temperature from the adiabatic value (thick line), showing a 'plateau' during those same seconds. The bottom box shows a big drop (more than a decade in logarithmic scale) in the turbulence intensity (thick line). The liquid water content also has a maximum for this period. We have found these parcels at all levels, even above the trade inversion. Their typical sizes are a few hundred meters, only a small fraction of cloud volume (typical horizontal dimension: 3-5 km).

4.4 *Sources of entrainment*

We investigated the sources and rates of entrainment in the manner which has become standard, using Paluch (1979) and saturation point (Betts, 1982) diagrams. Fig. 3 show typical saturation point diagram for a penetration below the inversion. In Fig. 3, all the cloudy parcels are buoyant with respect to the environment at the observation level. Mixing cloudbase air with environmental air from levels above the inversion would produce even more positively buoyant parcels at the penetration level. It does not appear likely that air from above this level has actually descended within cloud to

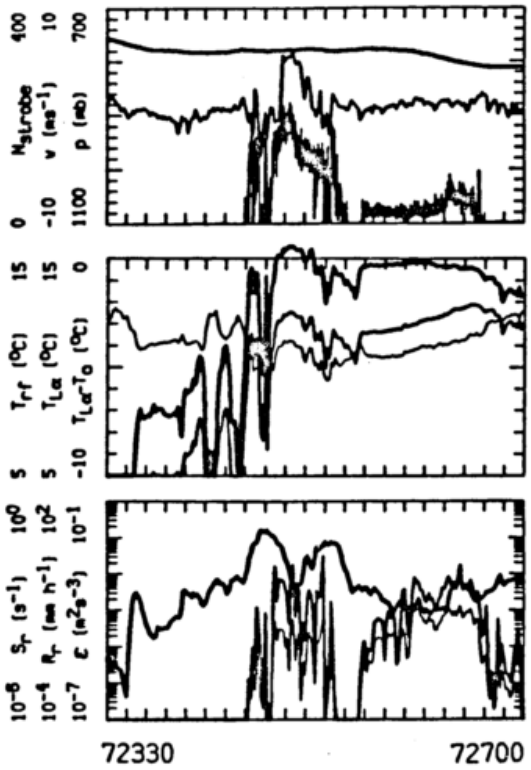


Figure 2. Time series for 72330-72700 on July 12. The penetration was made above the trade inversion at 2100 m. The top box shows the 50 Hz N_{strobe}, FSSP droplet count (thin line). All other parameters are 1 Hz values. The medium line shows the vertical velocity, w and the bold line shows the pressure p. The middle box shows the reverse flow temperature, T_{rf} (thin line), the Lyman-α temperature, $T_{L\alpha}$ (medium line), and the cooling due to entrainment, $T_{L\alpha} - T_a$ (bold line). The bottom box shows the scavenging rate, S_r (thin line), the rain rate, R_r (medium line) and the turbulent energy dissipation rate, ϵ (bold line).

862 mb. The fact that negative vertical velocities were seldom observed below the inversion is consistent with this thermodynamic conclusion. The buoyancy pattern shows negatively buoyant parcels concentrated in a localized region near the inversion. We conclude that penetrative downdrafts are not an important transport mechanism, at least not on the scale of the cloud. Downdrafts were usually observed around the edges of the turrets (both up and downwind), bringing down air from above the inversion that then entered the cloud.

Our analysis suggests that continuous entrainment is occurring and that buoyancy sorting (Jensen, 1985) does not play a role in the determination of the composition of incloud air.

4.4 *Incloud fluxes*

We have computed incloud vertical fluxes of total water, heat and momentum (vertical and horizontal) and obtained average values as functions of height. Leaving segments with precipitation out of this study, the average value of the fluxes (over the trade layer) increase to about 150% of cloudbase values and then decrease to about 50% of cloudbase values, suggesting that there is entrainment in the trade layer and detrainment at the level of the inversion (also con-

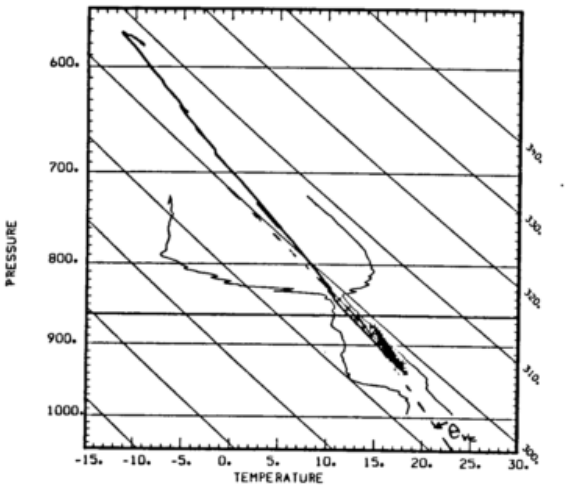


Figure 3. Saturation point diagram for a study on July 11. Cloudbase was determined at 71412, the environmental sounding (thin line) was observed during 64830-70130 and the incloud samples (small +) were sampled during 70900-71030 at a flight level of 862 mb.

sistent with picture from buoyancy considerations of parcels oscillating around that level).

5. MODIFICATION OF THE ENVIRONMENT

Fig. 4 shows the sounding taken on July 12 during take-off, on the downwind side of the bands. The characteristic points of parcels resulting from the mixture of two air sources would appear as a straight line in this diagram. Notice how the sounding shows a distinct break around 870 mb, within the trade layer. Betts and Albrecht (1987) find a similar pattern in soundings from FGGE. They suggest that precipitation falling and evaporating into the dry air near the inversion produces negatively buoyant parcels that sink down to midlevels, producing the break.

We have computed vertical fluxes of moisture in the surrounding clear air, both up and downwind of the clouds,

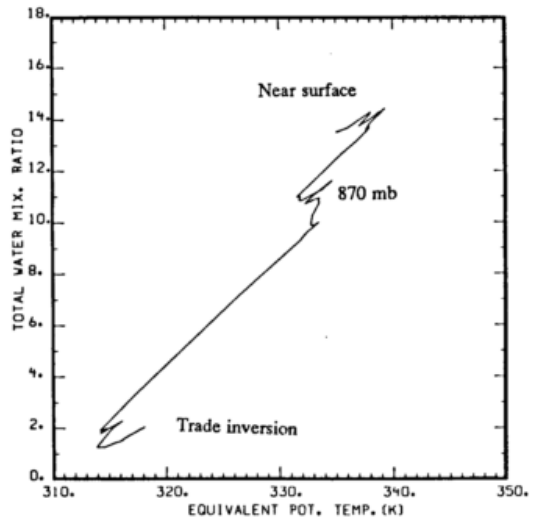


Figure 4. Environmental sounding observed during 60054-60754 on July 12, downwind of the clouds.

using the approach legs before the aircraft penetrated the clouds. There is evidence of moisture flux convergence around midlevel within the trade layer on the downwind side.

This is consistent with preliminary analysis of the results of 3D simulations (Smolarkiewicz et al., 1987) which suggest that the clouds process the air in such a way as to generate regions with relative maxima of Q and θ_e and minimum vertical velocity within the trade layer.

The mechanism of Betts and Albrecht requires the evaporation of precipitation into the dry inversion air. This implies strongly sheared clouds, which were usually not observed. Precipitation was usually observed falling through cloudbase. We suggest that air detrains from the clouds at upper levels, mixes with the clear air and then finds its level of neutral buoyancy to form the top sublayer.

6. DISCUSSION

Our results suggest that the bandclouds are dynamically forced by a region of low level convergence. This convergence determines the location of the onset of convection, but the incloud dynamics above the level of free convection is governed by the release of latent heat of condensation.

There appears to be continuous, lateral entrainment, with some unmixed parcels reaching cloudtop. A simple lateral entraining plume produced fairly good agreement with the observations. We find this interesting, given the fact that the clouds are still under the influence of the sources of momentum and buoyancy and are certainly not self-similar.

We find that buoyancy sorting and penetrative downdrafts originated at cloudtop (by evaporative cooling) are not important mechanisms of incloud transport of entrained air, as contrated to results from continental cumuli (Jensen, 1985). The explanation for these different results is linked to the humidity of the environment. In our case, the environment is very moist and mixtures of incloud and clear air parcels are positively buoyant and keep moving upwards.

We observe a marked moisture flux convergence in the clear air downwind of the clouds, at midlevel within the trade layer. This is consistent with the increase in Q and θ_e observed at midlevel in the clear air soundings, suggesting that the clouds play an important role in the development of two sublayers.

Betts, A. K., 1982: Saturation point analysis of moist convective overturning, *J. Atmos. Sci.*, **39**, 1484-1505.

Betts, A. K. and B. Albrecht, 1982: Conserved variable analysis of the convective boundary layer thermodynamic structure over the tropical oceans, *J. Atmos. Sci.*, **44**, 83-99.

Cooper, W. A., 1978: Cloud physics investigations by the University of Wyoming in HIPLEX 1977, *Rept. #AS119, Univ. of Wyoming* , 321 pp.

Jensen, J. B., 1985: Turbulent mixing, droplet spectral evolution and dynamics of continental cumulus clouds. *Ph. D. Thesis, Univ. of Washington*

Jensen, J., B., D. Baumgardner and G. B. Raga, 1988: *Proceedings of 10th International Cloud Physics Conference, Bad Homburg.*

Paluch, I.R., 1979: The Entrainment Mechanism in Colorado Cumuli, *J. Atmos. Sci.*, **36**, 2467-2478.

Smolarkiewicz, P., R. Rasmussen and T. Clark, 1988: On the dynamics of the Hawaiian cloud bands: Island forcing, *J. Atmos. Sci. (in press)*

Warner, J., 1970: On steady-state one-dimensional models of cumulus convection, *J. Atmos. Sci.*, **27**, 1035-1040.

STRUCTURE OF LAYER CLOUDS AS OBSERVED SIMULTANEOUSLY BY A MICROWAVE RADIOMETER AND AN 8.6 mm-RADAR

Guosheng Liu and Takao Takeda

Water Research Institute, Nagoya University
Nagoya 464-01 Japan

1. INTRODUCTION

Middle-level layer clouds associated with subtropical cyclones near Japan were observed in spring of 1985 simultaneously by a microwave radiometer and an 8.6 mm-radar. In this paper observational results will be analysed, especially paying attention to their glaciation degree which is defined by the ratio of ice-water amount to the sum of liquid-water and ice-water amounts.

2. DATA

Vertically-integrated liquid-water amount (L) is estimated by analysing the data of a 19.35 GHz microwave radiometer together with upper-air sounding data. The error of estimation is expected to be within 10 mg/cm^2. Since the formation of large water drops can be hardly expected at middle-level layer clouds above freezing level, it is concluded in consideration of the detectable limit of our radar that radar echoes above freezing level resulted mainly from large ice particles. For this reason we estimated ice-water amount in the cloud on the basis of its radar-echo intensity. Data of the microwave radiometer and the 8.6 mm-radar were available only before the initiation of rainfall.

3. CASE STUDY (6-7 APRIL 1985)

Clouds in this case were associated with a warm-front. Fig.1 shows a time-height section of radar-echo intensity (upper) and vertically-integrated liquid-water amount (lower) in the period of 5.10 to 9.00 on the 7th. Vertically-integrated radar-echo intensity (R), which would reflect the amount of ice particles, is also shown in arbitrary unit in the lower figure. Radar echoes were observed between 3 and 6 km levels and exhibited clearly a cellular pattern. L exceeded 40 mg/cm^2 sometimes after 6.00. Interestingly, peeks in L were observed well consistently with cellular radar echoes.

As shown in Fig.2, radar echoes in the period of 17.10 to 20.50 were intensive in comparison with those in Fig.1 and they existed at upper levels as well as middle levels. Echo top defined by -6 dBZ was as high as 8 km. L was less than 10 mg/cm^2 before 19.00 when radar echo was intensive, and it increased as radar echo became weaker. Vertically integrated ice-water amount (I) is 4 mg/cm^2 on an average in the period of 6.00 to 8.00 on the 7th and 31 mg/cm^2 in the period of 18.00 to 19.00 on the 6th. Total amounts of condensed water (T=L+I) are 41 mg/cm^2 and 36 mg/cm^2, respectively, in the above two periods. That is, their glaciation degrees are about 10% and 85%, respectively. Upper air soundings at 21.00 on the 6th and 9.00 on the 7th showed the existence of middle-level clouds around 4 km where relative humidity were larger than 80%. Freezing level was about 2.5 km.

4. TWO DIFFERENT TYPES OF CLOUDS

Though total water amounts are not so dif-

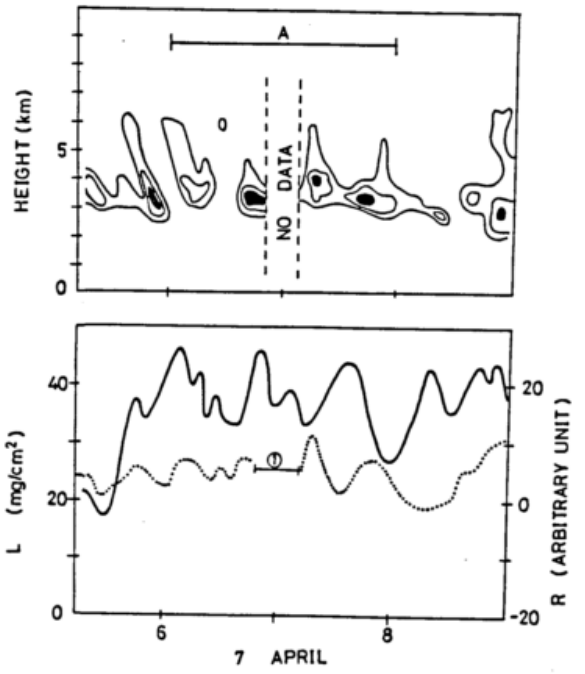


Fig.1 Upper: Time-height section of radar echo intensity. Contours are drawn every 3 dBZ from -6 dBZ. Lower: Variations of L (solid line) and R (dotted line).

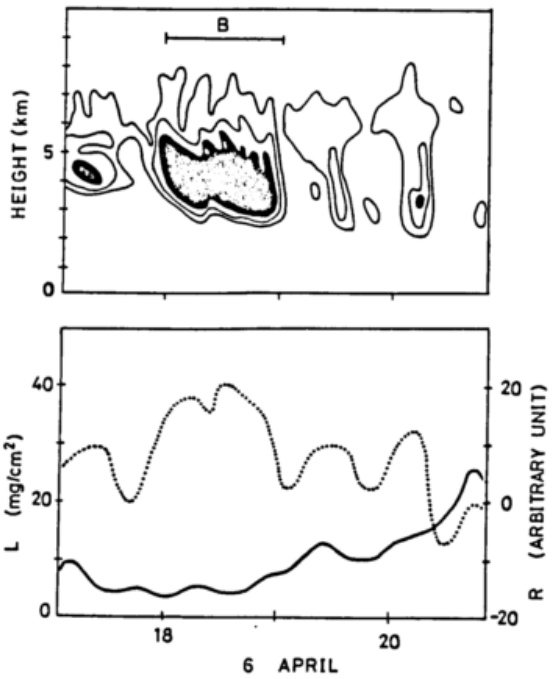


Fig.2 Same as Fig.1 except for 17.10 to 19.50 on 6 April.

ferent, clouds in the period of 6.00 to 8.00 on the 7th had low echo-top and low glaciation degree, and clouds in the period of 18.00 to 19.00 on the 6th showed high echo-top and high glaciation degree. Hereafter, these two different types of clouds will be called type-A and type-B, respectively. Both types of clouds were often observed in spring of 1985. Some examples are shown in Table 1. The relationship between T and I are shown in Fig.3. Glaciation degree is less than 10% in type-A clouds and larger than 50% in type-B clouds.

On the basis of observational data their structure and precipitating formation process are described as follows:

A type-A cloud is a one-layer middle-level cloud and ice particles form near its top. Since air temperature at the top is not so low as to allow a sufficient amount of nuclei to be activated, ice-water amount in the cloud is low in spite of abundant liquid-water. Glaciation degree is low (7% on an average for 3 cases). Radar echo exhibits cellular structure in a spatial scale of several-ten kilometers and a peek in L corresponds to each cell. On the other hand, a type-B cloud is a two-layer cloud system. Ice particles are initiated in an upper-level cloud and grow due to falling through a middle-level cloud. Ice particles are abundant, and glaciation degree is high (63% on an average for 3 cases). Spatial variations of L and I are not correlative, and sometimes they are in an inverse relation.

The significiant difference in glaciation degree between type-A and type-B clouds would result mainly from the existence of an upper-level seeding cloud ("seeder-feeder" process) and the intensity of an updraft at middle levels. Upper-level clouds in type-B must have played an important role in promoting the glaciation in middle-level clouds by supplying much more ice particles than in type-A clouds. It is also shown by both observations and numerical computations that the growth of ice particles at middle levels is faster in

Table 1 Examples of two different types of clouds

CASE	DATE	H_f	H_{top}	T_{top}	TYPE
1	7 Apr.	2.5	6.0	-15	A
2	5 May	4.0	5.0	-6	A
3	10 May	3.5	7.5	-23	A
4	6 Apr.	2.5	8.0	-30	B
5	26 Apr.	3.5	9.5	-35	B
6	7 Jun.	4.0	9.5	-28	B

NOTES: H_f: height of freezing level (km). H_{top}: height of echo top (km). T_{top}: air temperature at H_{top}.

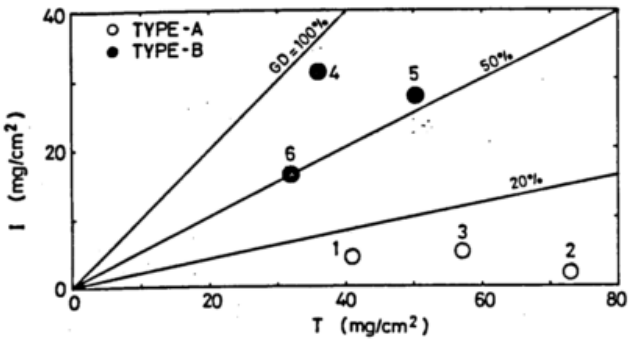


Fig.3 Relationship between T and I in each case (1 to 6 in Table 1).

type-A clouds than in type-B clouds. This implies that the middle-level updraft is stronger in type-A clouds. Accordigly, the present study showed quantitatively that a middle-level cloud could not efficiently produce solid precipitation even though it forms by a strong updraft, unless an upper-level cloud supplies sufficient amount of ice particles to it.

Statistical results on vertical radar-echo distribution in a layer cloud is summarized in Fig.4, in which a type-A cloud results in a small value of $\sqrt{Z_{e1}}$ and a large value of $(\sqrt{Z_{e2}} - \sqrt{Z_{e1}})$ and a type-B cloud results in a large value of $\sqrt{Z_{e1}}$ and a small value of $(\sqrt{Z_{e2}} - \sqrt{Z_{e1}})$. It can be seen that most of non-convective precipitation in spring

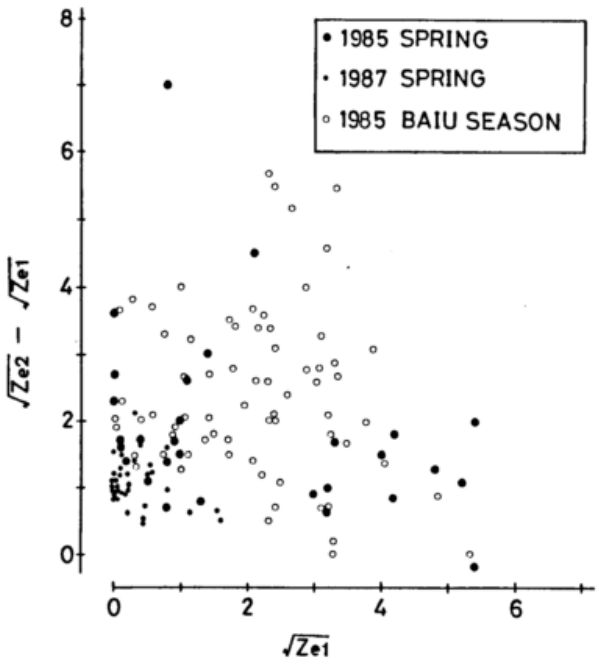


Fig.4 Relationship between $\sqrt{Z_{e1}}$ and $(\sqrt{Z_{e2}} - \sqrt{Z_{e1}})$. Here, Z_{e1} and Z_{e2} are one-hour averaged radar-echo intensities at 2.5 km and 0.5 km levels above the central level of bright band.

around Nagoya (35N,137E) can be produced by type-A or type-B clouds, though other types of precipitation are frequently observed during Baiu season (from middle of June to middle of July).

ANALYSIS OF SINGLE DOPPLER RADAR DATA: WIND FIELD AND PRECIPITATION OBSERVATIONS DURING A FRONTAL PASSAGE

Martin Hagen

Institut für Physik der Atmosphäre, DFVLR, 8031 Oberpfaffenhofen, Fed. Rep. of Germany

1 INTRODUCTION

Various techniques have been developed for mesoscale wind field estimations by single Doppler measurements (KOSCIELNY et al., 1982, WALDTEUFEL and CORBIN, 1979). These techniques give the wind vector, divergence and deformation from single Doppler data within large sector elements. If only the horizontal wind vector is of interest, it is sufficient to apply simpler methods to smaller sectors such as the uniform wind technique (PERSSON and ANDERSSON, 1987). To reduce the sector size and to increase the accuracy the ECUW method was developed (ECUW = equation of continuity combined uniform winds).

The ECUW method is applied to the Doppler data of the new DFVLR radar at Oberpfaffenhofen (SCHROTH et al., 1988). The retrieved wind fields are compared with wind profiles obtained by the VAD technique (BROWNING and WEXLER, 1968) and with rawinsonde data. Additional information on the structure of the cold front is given by vertical cross sections of the reflectivity and of the spectral width of the Doppler velocity. A case study is performed with the data of December 19, 1987 when a cold front, associated with a strong frontal rainband, approached the Alps. The data suggest an orographic influence on the formation of the rainbands.

2 THE COMBINED WIND VECTOR METHOD

The uniform wind technique is based on the fact that if the wind field is constant within a limited region the unknown tangential wind component v_ϕ can be computed from the measured radial velocity v_r by

$$v_\phi = -\frac{\partial v_r}{\partial \phi}. \qquad (1)$$

The horizontal equation of continuity in polar coordinates is

$$\rho \frac{\partial r v_r}{\partial r} + \rho \frac{\partial v_\phi}{\partial \phi} = 0, \qquad (2)$$

where ρ is the density of air (a function of the height only), and ϕ the azimuth. Within a horizontal sector of 5° in azimuth and 5km in range, the average v_r, $\partial v_r/\partial r$ and $\partial v_r/\partial \phi$ are computed from the measured Doppler data. v_ϕ is derived from (1), and $v_\phi/\partial \phi$ from (2). This is repeated for all the sector elements of a PPI scan. It is assumed that the error of the directly measured v_r and $\partial(rv_r)/\partial r$, is less than the error of the estimated v_ϕ and $\partial v_\phi/\partial \phi$. Velocity v_ϕ and $\partial v_\phi/\partial \phi$ are therefore adjusted until they are in accordance with the results of the adjacent sector elements along the same circle. $\partial(rv_r)/\partial r$ and the final adjusted $\partial v_\phi/\partial \phi$ give an estimation of the horizontal divergence. Finally the results of the sector elements from PPI scans at different elevations are interpolated to a cartesian grid system.

The ECUW technique has been tested with simulated as well as with measured radar data. The results of these tests show that this method give a more accurate solution in those cases where the uniform wind technique fails due to strong tangential gradients of v_r. The ECUW technique therefore, allows the use of smaller sectors elements, which is essential to retrieve discontinuities, as they occure along fronts.

The maximum elevation for reliable results from the ECUW method is estimated to be below 10° (BROWNING and WEXLER, 1968, PERSSON and ANDERSSON, 1987). The elevation angle is limited by the influence of the particle fall-speed on v_r, and the influence of $\partial v_r/\partial z$ on $\partial v_r/\partial r$. Within the accuracy of the ECUW method ($\approx 2 ms^{-1}$), however, no systematic error was found up to an elevation of 20°. Figure 1 shows a comparison between a rawinsonde ascent and the ECUW-analysis for the launching site of the rawinsonde at Munich.

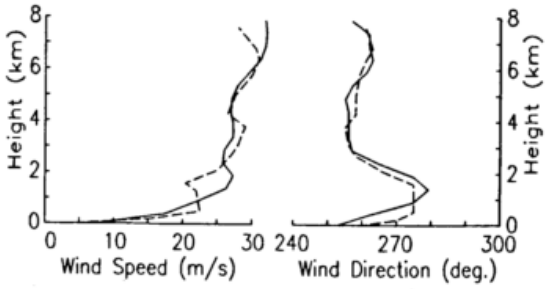


Figure 1. Rawinsonde Munich (dashed) and ECUW winds (solid) at 23:00 UTC on Dec. 18, 1987.

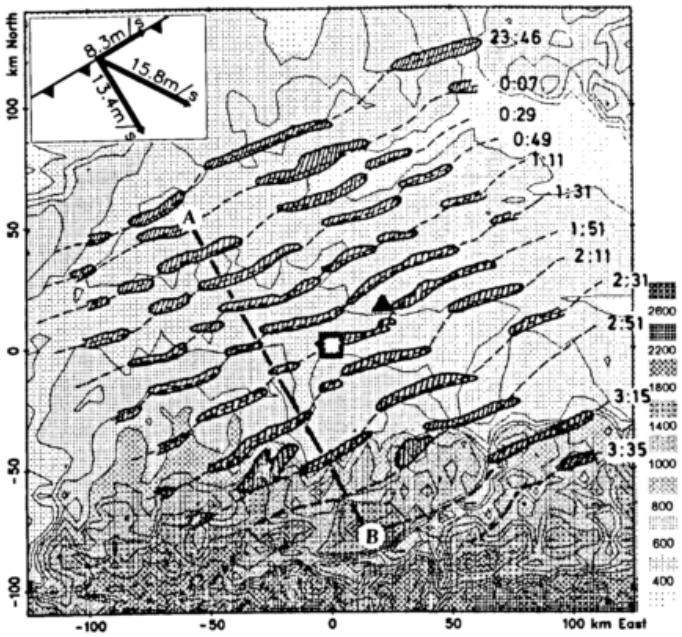


Figure 2. Position of high reflectivity cores ▨ and wind-shear zone (----) at the indicated times (UTC) on Dec. 18/19, 1987. PPI-scans at 1.5° elevation. ■ Radar (Oberpfaffenhofen), ▲ Rawinsonde (Munich), smoothed orography (Meter MSL). Inset shows propagation of the front. A – B base line for Fig. 4 and 5.

3 ANALYSIS OF A COLD FRONT

During the German Front Experiment 1987 (HOINKA and VOLKERT, 1987) cold fronts were observed in order to study the influence of the Alps on frontal systems. On December 19, 1987 an ana-type cold front approached the Alps from north-west (Fig. 2). This front was accompanied by a severe rain band embedded in a wide area of moderate rain.

3.1 WINDFIELD

Doppler data were analysed with the ECUW technique and interpolated to a cartesian grid. The x axis is orientated normal to the front (150°), y parallel to the front (60°), corresponding velocities are u and v. Figures 4a, b and 5a, b give examples of vertical cross sections parallel to the x axis.

The v component (Fig. 4b) can be compared with Figure 3 when assuming stationarity. A low level jet, also termed as *conveyor belt* is located at the pre-frontal edge whereas behind the front weaker parallel velocities are observed. The u component (Fig. 4a) of the flow shows low ($\approx 5 ms^{-1}$) prefrontal and high ($\approx 15 ms^{-1}$) postfrontal velocities which exceed the propagation speed of the front $c \approx 13 ms^{-1}$. This feature is often observed at narrow cold-frontal rainbands (e.g. HOBBS and PERSSON, 1982). The convergence leads to the strong line convection (i.e. rainbands) along the front. According to this observations the front can be classified as an ana-type cold front.

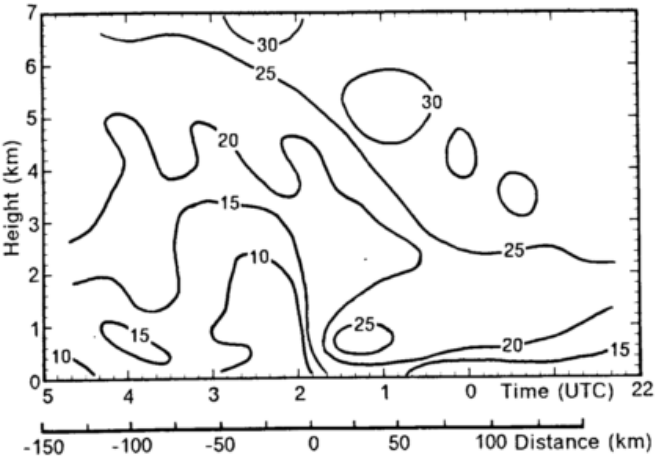


Figure 3. Time-height cross section of velocity parallel to the front (v), computed by the VAD technique from PPI scans every 20 minutes. Distance scale corresponding to $c = 13 ms^{-1}$.

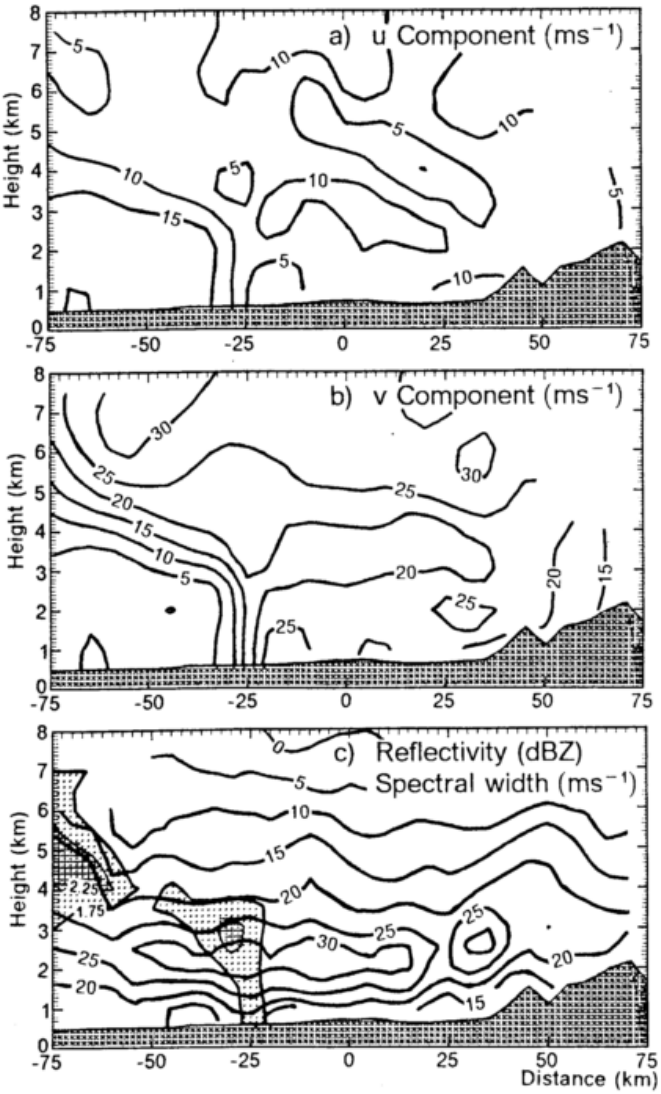


Figure 4. Vertical cross sections along A – B (Fig. 2) at 1:21 UTC, front position at $x = -25$km. a) u component, and b) v component computed by the ECUW method, c) reflectivity (contour lines) and spectral width (hatched $\geq 1.75 ms^{-1}$).

3.2 RAINBANDS

Narrow cold frontal-rainbands have been described in detail by HOBBS and PERSSON (1982) or PARSON and HOBBS (1983). The core structure of the forced line convection is affected by the barotropic instability produced by the strong wind shear within the flow parallel to the front. The precipitation cores slightly change in size and shape during their passage through the Alpine foreland (Fig. 2). The propagation is closely connected to the postfrontal wind speed and direction.

The reflectivity data (Fig. 4c) show an extended region of high reflectivity. The edge of one precipitation core is embedded in the high reflectivity of the melting layer, but smoothed by the interpolation to the cartesian grid. The spectral width of the Doppler velocity indicates the zone of maximum wind shear and turbulence.

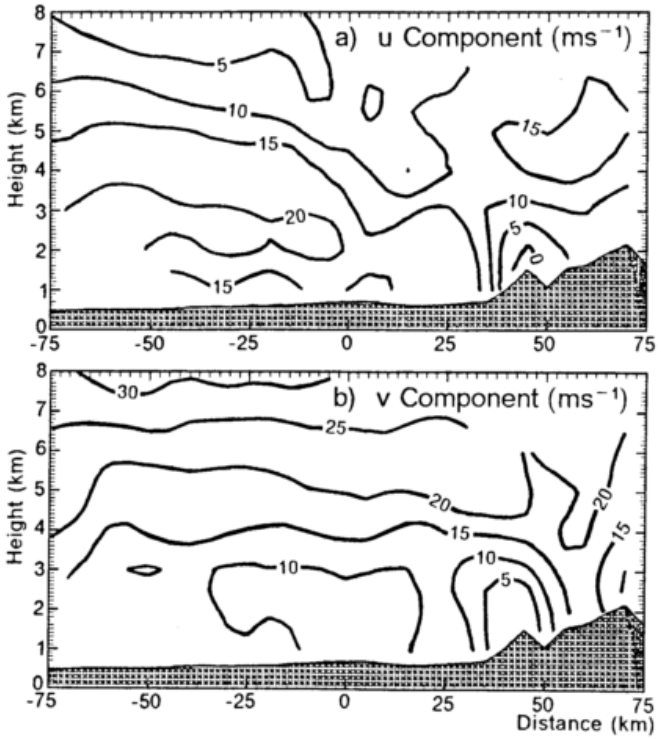


Figure 5. Vertical cross sections along A – B (Fig. 2) at 2:32 UTC, front position at x = 40km. a) u component, and b) v component computed by the ECUW method.

3.3 INFLUENCE OF OROGRAPHY

Figure 5 shows the influence of the Alpine mountains on the frontal air flow. When reaching the first ridge of the Alps ($\approx$ 1500m at Fig. 2) the rainbands are retained and their size propbably enlarged due to the orographic lifting of the cold air. According to the reflectivity data, no rainbands associated with the front, can be located within the Alps. Surface observation at Innsbruck (10km SSW of point B at Fig. 2) indicated the frontal passage at 3:10 UTC.

The u component (Fig. 5a) has maintained its typical structure with low prefrontal and high postfrontal velocities. The v component (Fig. 5b), however, has changed completely in the region of the front at x = 40km. It is now impossible to locate the prefrontal low level jet.

It is assumed that the dense cold air may enter the North - South orientated Alpine valleys, while the strong parallel prefrontal flow has to be lifted or retarded. Such effects are expected to rearrange and weaken the internal circulation along the low altitude frontal-zone.

4 CONCLUSION

The ECUW technique is shown to be an appropriate method to retrieve the mesoscale wind field from single Doppler radar data. This method was used to study the influence of the Alps on the frontal air flow. Within the Alps the prefrontal low level jet has disappeared. The band type precipitation cores along the front has changed into widespread precipitation at the windward side of the Alps, while the front continues propagating.

5 REFERENCES

BROWNING, K.A. and T.W. HARROLD (1970): Air motion and precipitation growth at a cold front. Quart. J. R. Meteorol. Soc., **96**, 369-389.

BROWNING, K.A. and R. WEXLER (1968): The determination of kinematic properties of a wind field using Doppler radar. J. Appl. Meteor., **7**, 105-113.

HOBBS, P.V. and P.O.G. PERSSON (1982): The mesoscale and microscale structure and organization of clouds and precipitations in midlatitute cyclones. V: The substructure of narrow cold-frontal rainbands. J. Atmos. Sci., **39**, 280-295.

HOINKA, K.-P. and H. VOLKERT (1987): The German front experiment. Bull. Amer. Meteor. Soc., **68**, 1414-1427.

KOSCIELNY, A.J., R.J. DOVIAK and R.RABIN (1982): Statistical considerations in the estimation of divergence from single-Doppler radar and application to prestorm boundary-layer observations. J. Appl. Meteor., **21**, 197-210.

PARSON, D.B. and P.V. HOBBS (1983): The mesoscale and microscale structure and organization of clouds and precipitations in midlatitute cyclones. IX: Some effects of orography on rainbands. J. Atmos. Sci., **40**, 1930-1949.

PERSSON, P.O.G. and T. ANDERSSON (1987): A real-time system for automatic single-Doppler wind field analysis. Proc. Symp. Mesoscale Analysis & Forecasting, Vancouver, ESA Publication **SP-282**, 61-66.

SCHROTH, A., M. CHANDRA and P. MEISCHNER (1988): A C-band coherent polarimetric radar for propagation and cloud physics research. To appear in J. Atmos. Ocean. Techn.

WALDTEUFEL, P. and H. CORBIN (1979): On the analysis of single-Doppler radar data. J. Appl. Meteor., **18**, 532-542.

THE OCCURRENCE OF ICE IN CLOUDS ASSOCIATED WITH EXTRATROPICAL CYCLONES

Roelof T. Bruintjes

South African Weather Bureau
Pretoria, South Africa

1 INTRODUCTION

Measurements of ice crystal habits and concentrations in clouds associated with a cold-frontal passage and in post-frontal cumulus clouds were collected as part of the Western Cape Precipitation Research Project (WCPRP), conducted during July 1983, near Cape Town, South Africa. The objective of the research was to investigate the microphysics of precipitation mechanisms operating in the dominant cloud systems. Weather in the Southwestern Cape in winter is dominated by eastward moving extratropical cyclones. The centres of these frontal systems move south of the continent and, consequently, precipitation is associated with the passage of a cold front.

The Southwestern Cape is affected by a considerable relief change especially over the peninsula. Traversing it from west to east, the altitude increases from sea-level to 1000 m over Table Mountain within a horizontal distance of just 2.4 km. The larger mountain ranges further inland (~50 km), to the east and Northeast of Cape Town show increases in precipitation on their windward side. These ranges are generally oriented in a NNW to SSE direction and about 20 to 40 km broad with some mountain tops going up to 2000 MSL. As the frontal system crosses the larger mountain ranges they tend to dissipate rapidly with a sharp drop in precipitation.

It is well established that mesoscale rainbands are an important organised component of the precipitation associated with extratropical cyclones (Browning, 1974, and Matjeka et al., 1980). Generally the rainbands associated with the passage of a cold front tended to dissipate fairly quickly moving inland. However, on several occasions it was observed, especially in the post-frontal airmass, that showers were initiated by the topography.

On two occasions, extensive aircraft studies were conducted in cold-frontal systems passing over the Southwestern Cape. The data discussed in the following sections will primarily be from these flights.

2 DATA COLLECTION

Ice crystals were collected on oil-coated slides exposed in a decelerator on the research aircraft (Aerocommander 690A). A detailed description of the instrumentation package installed on the Aerocommander and the measurement techniques is discussed in Krauss et al. (1987). Liquid water contents were measured by a JW probe while the the aircraft was also equipped with two Particle Measuring Systems (PMS) probes: a forward scattering spectrometer probe (FSSP), to count and size particles with diameters between 2 and 47 µm, and a two-dimensional optical array probe (2DC-OAP), which images particles from 25 to 800 µm diameter. Ice particles concentrations were measured by an ice particle counter (IPC).

3 FRONTAL CASE STUDY 21-7-1983

3.1 PRE-FRONTAL WARM-SECTOR CLOUDS

The data presented in this section was collected during a circular descent in the rear half of a warm-sector pre-frontal rainband.A research flight in a warm-sector pre-frontal rainband was conducted on July 21, 1983. Most of the cloud deck consisted of seperate layers. However, within the rainbands the cloud deck was one continuous deck. The lowest layer consisted of a stratus deck between 300 and 1400m MSL, while the second layer consisted of alto- and nimbostratus clouds between 2000 and 5000m MSL. The top layer, above 5000m MSL, consisted of cirrus-stratus. Within the rainbands, the cloud tops went up to about 6700m MSL.

The circular descent started at an altitude of 5500m MSL at the top of the deck with a temperature of -17.5°C. The descent was terminated at an altitude of 2800m MSL. The images collected from the 2D-C probe at the -11.4°C and -6.6°C levels are displayed in figures 1 and 2. The images shown in figure 1 collected in the top part of the cloud deck indicate that columns and capped columns are the dominant crystal type observed in these clouds. Little or no riming is evident from the images, and the only larger particles observed are

aggregates. Note that two capped columns stuck together in figure 1. The images collected around the -6.6°C level are displayed in figure 2. The growth of the particles by aggregation from the previous level is clearly evident. The liquid water content measured at this level showed a peak of 0.2 g m^{-3} and growth by riming might also have occurred.

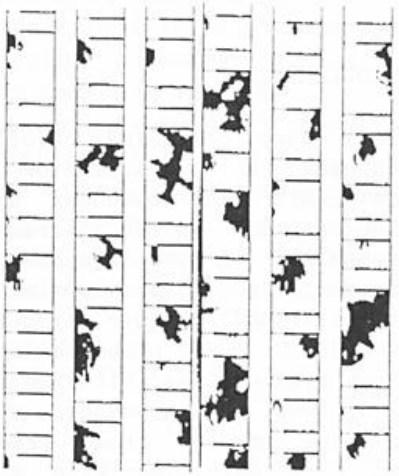


Fig. 1. Particle images collected with the 2D-C probe at the -11.4°C level.

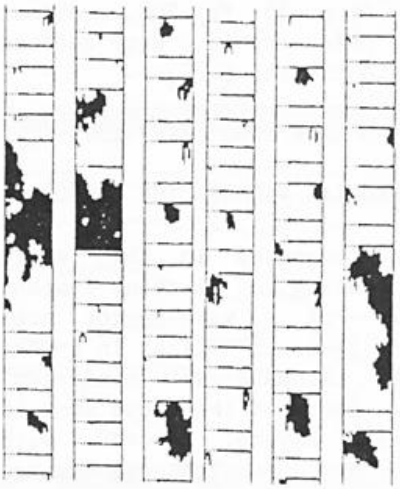


Fig. 2. Particle images collected with the 2D-C probe at the -6.6°C level.

The cloud droplet concentrations measured by the FSSP, and liquid water content measured by the JW probe, stayed low during the descent except near the 0°C level where a maximum value of 0.65 grams per cubic meter (g m^{-3}) was encounterd. The existence of liquid drops near the 0°C level could be explained by the airmass with maritime characteristics. This was reflected in the cloud droplet spectra measured by the FSSP which were typical maritime in nature, with concentrations around 100 cm^{-3} and mean diameters around 20 µm. At colder temperatures these drops were quickly depleted via the riming process.

The concentrations of ice particles by both the 2D-C probe and the ice particle counter, decreased downward in the cloud during the descent. This is consistent with previous studies in rainbands in frontal systems (Hobbs et al,1980). The reason for the decrease in average particle concentrations with decreasing altitude observed in the clouds is due to the aggregation of ice particles. The aggregation of ice particles was evident on the two-dimensional images collected with the 2D-C probe. The occurrences of liquid water contents greater than 0.2g m^{-3}, as measured by the JW probe, for one second time intervals during the descent, totalled 63 seconds. This implies that supercooled water in quantities greater than 0.2g m^{-3} occurred less than 5% of the time during the descent. Liquid water contents greater than 0.4g m^{-3} were only detected on 7 occasions, mostly near the 0°C level.

The development of the precipitation via the "seeder-feeder" mechanism (Hobbs et al 1980), was clearly evident in these clouds. Particles falling from the "seeder" part developed via the aggregation process before entering the "feeder" clouds. With low quantities of supercooled water detected above the 0°C level, little or no riming was observed. The "feeder" clouds were maintained by a low level jet of moist air. One possible reason for not observing higher amounts of supercooled water might be because the descent was done in the rear side of the rainband. Higher amounts of supercooled water are usually associated with convection on the leading edges of these rainbands (Hobbs et al.,1980).

3.2 PRE-FRONTAL COLD SURGE CLOUDS

The passage of an occluded front around 10h00 SAST on July 21, brought a surge of cold air, producing potential instability in the middle levels (800 to 400 hPa). The maximum amount of cooling occurred around the 600 hPa level where the temperature dropped 8.5°C between 01h30 and 12h30 SAST on July 21. This resulted in convective clouds within rainbands moving over the Southwest Cape. The relief seems to act as a triggering mechanism for some of the convective elements, as was the case on post-frontal days. A research flight was conducted between 14h21 and 16h42 SAST concentrating on the convective elements in the clouds and rainbands, to the east and northeast of False Bay.

Convective elements were growing, embedded in altostratus and cirrostratus clouds with tops up to 6km and bases around 2km MSL within the rainbands. High amounts of supercooled water (1 to 2 g m^{-3}) were

present in the newly growing convective elements. The concentrations of ice particles ranged between 10 and 100 L^{-1} in convective parts of the rainbands. The high amounts of liquid water were depleted within 5 to 8 minutes which might be indicative of an ice multiplication being active in these clouds. Ice particle concentrations between 10 and 100 L^{-1} were detected simultaneously with supercooled water around 1g m^{-3}. A photograph taken from the oil coated slides collected in the high liquid water region at -9.0°C is displayed in figure 3. It is evident that the dominant ice crystal habit in these clouds consisted of columns and capped columns. Rimed and graupel particles are clearly visible together with large cloud drops (~100μm).

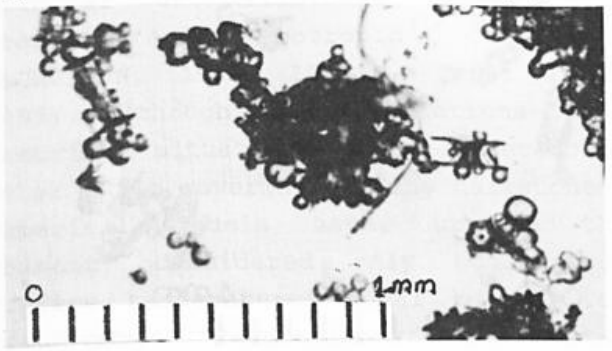


Fig. 3. Photograph from an oil-coated slide collected at the -9°C level.

Needles were also observed on numerous occasions in these clouds. A picture of an oil coated slide collected at the -8°C level where needles were observed together with a graupel particle is shown in figure 4. More examples of the crystal habits and graupel particles are displayed in figure 5a to b. Figure 5a shows an multiple capped column. A heavily rimed column is displayed in figure 5b.



Fig. 4. Needles together with a graupel particle from an oil-coated slide collected between the -5 and -8°C level.



Fig.5. Examples of crystal habits collected in pre-frontal cold surge clouds.

Although the "seeder-feeder" mechanism has an influence on the precipitation development in these clouds, the dominant precipitation feature was the convective cells. Although aggregation of ice particles still attributed to particle growth, aircraft observations showed that particle growth within the convective elements was dominated by the riming of ice particles. Convective elements also seem to be important sources of ice particles in frontal clouds. The concentrations observed in the surge rainbands ranged between 10 and 100 L^{-1}, while in rainbands with little or no convection, it ranged between 1 and 20 L^{-1}. This suggests that in convective elements secondary ice particle producing mechanisms are possibly operative such as the mechanism suggested by Hallet and Mossop (1974).

4 POST-FRONTAL CLOUDS

Convective clouds developing in the post-frontal airmass formed in moderately unstable air shortly after the passage of a cold front. The average cloud base temperatures on post-frontal days was +1.8°C with cloud top temperatures around -13°C which agrees well with studies in other parts of the world (Mossop et al.1970, and Hobbs and Rangno, 1985). In young developing cumulus clouds quantities of supercooled water between 1 and 2g m^{-3} were frequently observed especially at temperatures warmer than -8°C. Clouds with their summit temperatures colder than -7°C contained ice on more than 80% of the cases studied, while all clouds contained ice with summit temperatures colder than -15°C. No ice crystals were observed in clouds with their summit temperatures warmer than

-4°C. The cloud droplet spectra measured in the clouds were of a typical maritime origin with concentrations between 100 and 150 cm^{-3} and a mean diameter around 18µm near cloud base. Water drops with diameters up to 250µm were also detected by the 2D-C probe in these clouds on several occasions. Light drizzle was observed on a few occasions simultaneously with or even preceding the first precipitation through the ice phase. These drops disappear as glaciation proceeds, either by falling out or by being incorporated in the solid precipitation particles.

Once ice was detected in the post-frontal clouds, a very rapid conversion from water to ice was observed. The available supercooled water exponentially decayed to 1/e its original value within 5 minutes. Ice crystal concentrations varied between 10 and 100 L^{-1}, independant of temperature over the range -5 to -15°C. Such concentrations are greater than the concentrations of ice nuclei by a factor of about 10^3 at -15°C and correspondingly higher at warmer temperatures. The multiplication of ice crystals thus appears to be a regular process.

In airborne observations within 300m of the cloud top of growing cumulus clouds with their summit temperatures near the -5°C level, it was found that needles were the dominant crystal type as displayed by a photograph taken from an oil-coated slide in figure 6. Clouds with their summit temperatures warmer than -10°C also contained columns while clouds with colder summit temperatures contained these ice crystal types together with capped columns and plate-like crystals. However, capped columns comprised more than 90% of all crystals observed and were thus by far the dominant crystal habit in this region of clouds. An example of the crystal habit collected with the oil-coated slides is displayed in figure 7.

A microphysical ice growth model developed by Heymsfield (1982), was used to determine the time it would take an ice crystal nucleated at -5°C to grow to riming and precipitation size. A maritime cloud droplet spectra, a constant updraft velocity of 1m s^{-1} were used as input for the model runs. The results show that a column nucleated at the -5°C level takes 4.5 minutes to grow to riming size, which corresponds to the -6.7°C level, whereafter it would be classified as a graupel particle. After about ten minutes it would start falling against the updraft when it reached the -8 to -9°C level. This indicates that even without the presence of large drops for coalescence, clouds with their summit tempereatures warmer than -10°C are able to produce precipitation via the ice process.

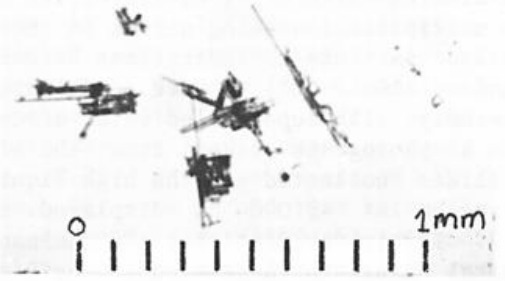


Fig. 6. Needles collected on an oil-coated slide at the -5°C level.



Fig. 7. Example of ice crystal habits observed on the oil-coated slides in post-frontal convective clouds.

5 ACKNOWLEDGEMENTS

This research was sponsored by the Weather Bureau of the Department of environment Affairs and by the Water Research Commission

REFERENCES

BROWNING,K.A.: Mesoscale structure of rain systems in the British Isles. J. Met. Soc. Japan, 50 (1974), 314-327.

HALLET,J.;S.C.MOSSOP: Production of secondary ice particles during the riming process. Nature, 249 (1974), 26-28.

HEYMSFIELD,A.J.: A comparitive study of the rates of development of potential graupel and hail embryos in High Plains storms. J.Atmos.Sci., 39 (1982), 2867-2897.

HOBBS,P.V.; T.J.MATJEKA; P.H.HERZEGH; J.D. LOCATELLI; R.A.HOUZE,JR: The mesoscale and microscale structure and organization of clouds and precipitation in mid-latitude cyclones. Part I: A case study of a cold front. J.Atmos.Sci.,37 (1980), 568-596.

HOBBS,P.V.;A.L.RANGNO: Ice particle concentrations in clouds. J.Atmos.Sci., 42 (1985), 2523-2549.

KRAUSS,T.W;R.T.BRUINTJES;J.VERLINDE; A.KAHN: Mycrophysical and radar observatios of seeded and non-seeded continental cumulus clouds. J.Clim.Appl.Met.,26 (1987), 585-606.

MATJEKA,T,J.;R.A.HOUZE,JR; P.V.HOBBS: Mycrophysics and dynamics of clouds associated with mesoscale rainbands in extratropical cyclones. Quart.J.Roy.Meteor. Soc., 106 (1980),29-56.

MOSSOP,S.C.;A.ONO; E.R.WISHART: Ice particles in maritime clouds near Tasmania. Quart.J.Roy.Met.Soc., 96 (1970),487-508.

THE SUPERCOOLING OF SURFACE WATER SKINS OF SPHERICAL AND SPHEROIDAL HAILSTONES

Roland List, F. García-García, R. Kuhn and B. Greenan

Department of Physics, University of Toronto
Toronto, Ontario. M5S 1A7, Canada

1. INTRODUCTION

Existing theories on the heat and mass transfer of hailstones assume bulk growth and isotropic conditions (SCHUMANN, 1938; LUDLAM, 1958; LIST, 1963). Although such formulations could describe situations with supercooled water skins covering growing hailstones, numerical models have, up to the present, considered only homogeneous surface temperatures equal to 0°C for "wet" growth. Recent laboratory results, however, revealed water skin supercoolings as low as -5.5°C, even in the presence of underlying spongy ice deposits (GARCIA and LIST, 1986). New experimental results further indicate that surface conditions and temperatures are not homogeneous and vary from one region of the particle to another.

2. EXPERIMENTAL

Hailstone growth in the form of incremental layers of ice was studied in a simulated atmospheric environment using the University of Toronto wind tunnel facility (LIST et al., 1987). Air speed, temperature, pressure and liquid water content were selected, and both spherical and spheroidal smooth ice particles were used as initial models.

The ice spheres (2 cm initial diameter) were rotated about a horizontal axis in the vertical airflow of the measuring section, at frequencies $f_1 \leq 20$ Hz, at laboratory pressure (100 ± 1 kPa) and at an air speed of 19.8 ± 0.5 m/s (equivalent to the calculated initial terminal speed). The surface temperatures of the growing particles were measured at or close to the equator and pole using two infrared (IR) radiometric microscopes (Barnes Engineering Co., model RM-2B; and Optikon, model Microrad 100) with measuring spot sizes of 1.8 and 1.0 mm, respectively. Both IR radiometers have an absolute accuracy of ± 0.5°C.

The oblate spheroids (2 cm major axis diameter, 0.67 aspect ratio) were forced to gyrate around a horizontal main axis with a nutation/precession amplitude of 30° at three different sets of gyration frequencies (spin, f_3, and nutation/precession, f_0, rates in opposite senses of up to 30 and -14 Hz, respectively). The air speed V was set equal to the calculated terminal speed of the gyrating initial model (LESINS and LIST, 1986). One group of experiments was performed at laboratory pressure, whereas in a second group the tunnel pressure p was set according to soundings taken on hail days in Colorado (BECKWITH, 1960). In the latter cases, only the surface temperature at the equatorial region of the spheroid was measured due to the lack of an air-tight mount for the second radiometer.

The droplet mean volume diameter of the injected water was 28 μm, averaged over the range from 2.3 to 80 μm. This spectrum was preferred over narrower distributions with smaller mean volume diameters because hailstone growth rates would have been unrealistically slow. [Some experiments performed with mean volume diameters of 14 μm and maximum diameters of 25 μm revealed growth rates of about 6 mg/s, with net collection efficiencies as low as 25%, at air temperatures of -15°C and liquid water contents of 4.5 g/m³.] A detailed account of the experimental apparatus and procedure can be found in LIST et al. (1987) and in GARCIA and LIST (1986).

3. RESULTS AND DISCUSSION

The results from three particular sets of experimental conditions, characterized by an air temperature of -15°C, are summarized in *Figure 1*. It displays the measured surface temperature of the growing hailstones t_s as a function of the liquid water content W_f. The general behavior of the data for both spheres and spheroids is similar to that of previous results presented by GARCIA and LIST (1986). Note that all surface temperatures are below 0°C for the whole range of W_f investigated. Experimental results at other air temperatures and rotation and gyration frequencies showed similar trends. For the case of low tunnel pressure, the decrease in equatorial t_s at higher W_f is more pronounced than for the cases at laboratory pressure. This seems to be related to the larger air speed and consequent shedding associated with lower pressures, and thus to the shorter residence time of the accreted droplets on the hailstone surface.

The trends in t_s for both spheres and spheroids at laboratory pressure are similar. The maximum difference between equatorial and polar temperatures is more pronounced for the case of spheres *(Figure 2)* because the poles are more

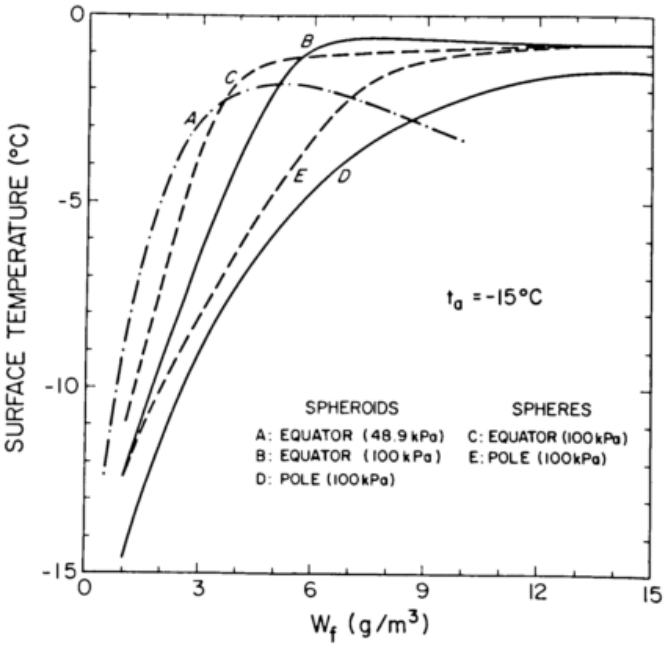


Figure 1. Equatorial and polar surface temperatures of spherical and spheroidal hailstones as functions of the liquid water content, W_f, for an air temperature of -15°C. Experimental conditions: A: p = 45.9 kPa, V = 29.8 m/s, f_3 = 9.5 Hz, f_o = -14 Hz. B and D: p = 100 kPa, V = 19.8 m/s, f_3 = 9.5 Hz, f_o = -14 Hz. C and E: p = 100 kPa, V = 19.8 m/s, f_1 = 10 Hz. For clarity, experimental points have been omitted.

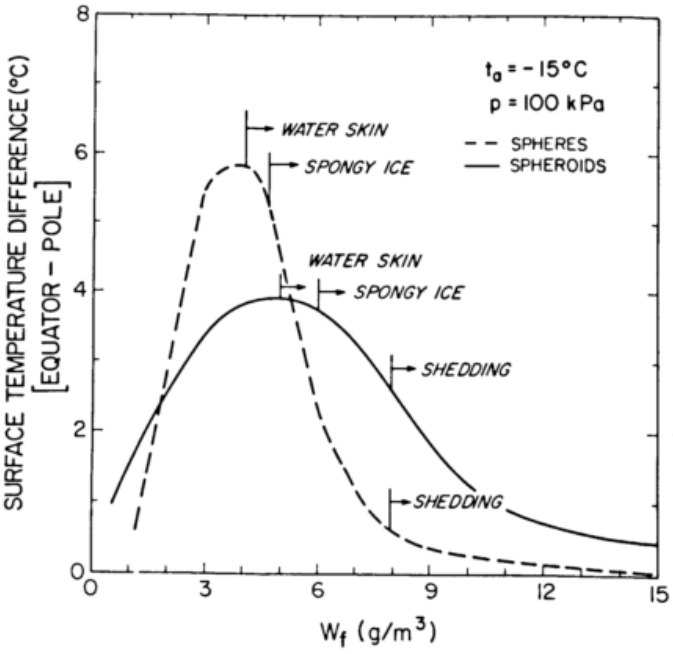


Figure 2. Difference between equatorial and polar surface temperatures as functions of liquid water content, for experiments at laboratory pressure displayed in *Figure 1*. Water skins, shedding and spongy ice deposits observed as indicated.

shielded from accretion (no wobbling). At higher W_f, the difference becomes smaller as the accreted, unfrozen water is able to move poleward. Note that maximum differences as large as 5.8°C coincide with the lowest W_f at which a water skin, partially covering the hailstone, is observed. This W_f value is 1 g/m^3 lower than the minimum W_f at which spongy ice deposits are observed, and at least 3 to 4 g/m^3 lower than that at which shedding occurs. The observed equator to pole temperature differences are also consistent with unpublished results by LIST et al. (1972/74, personal communication).

The growing hailstones often did not preserve their initial symmetries but became more oblate or tended towards a solid wheel-like shape, since the main growth region occurred around the equator.

The above results indicate that the heat and mass transfer of hailstones has to be treated as non-homogeneous and non-isotropic. Furthermore, the assumption of 0°C surface temperatures for water skins of growing hailstones needs to be abandoned, even more so since the poles, which mostly show solid ice deposits, are even colder than the equatorial regions.

Acknowledgements. This work was sponsored by the Natural Sciences and Engineering Research Council of Canada. One of the authors [FGG] is indebted to Consejo Nacional de Ciencia y Tecnologia (Mexico) for financial support.

REFERENCES

BECKWITH, W.B., 1960: Analysis of hailstorms in the Denver network, 1949-1958. *Physics of Precipitation, Geophys. Monogr. No. 5.* Amer. Geophys. Union, 348-353.

GARCIA-GARCIA, F., and R. LIST, 1986: Surface temperature of gyrating hailstone models during accretional growth. *Prepr. Conf. Cloud Phys., Sept. 22-26, Snowmass, Colo.* Amer. Meteor. Soc., **2**, 129-132.

LESINS, G..B., and R. LIST, 1986: Sponginess and drop shedding of gyrating hailstones in a pressure-controlled icing wind tunnel. *J. Atmos. Sci.*, **43**, 2813-2825.

LIST, R., 1963: General heat and mass exchange of spherical hailstones. *J. Atmos. Sci.*, **20**, 189-197.

LIST, R., G.B. LESINS, F. GARCIA-GARCIA and D.B. McDONALD, 1987: Pressurized icing tunnel for graupel, hail and secondary raindrop production. *J. Atmos. Oceanic Technol.*, **4**, 454-463.

LUDLAM, F.H., 1958: The hail problem. *Nubila*, **1**, 12-96.

SCHUMANN, T.E.W., 1938: The theory of hailstone formation. *Quart. J. Roy. Meteor. Soc.*, **64**, 3-21.

MICROPHYSICAL CONCEPT OF HAILFORMATION

Tlisov M.I., Khorguani V.G.
High Mountain Geophysical Institute Nalchik

Study of microphysical hail parameters and estimation of quantitative relationships with conditions for hail generation in clouds are one of the easily available and most informative sources for learning the hail formation mechanism. In this report the analysis results of elemental and isotopic embryo composition and layers of hail sampled during Complex Hail Experiment are given. The measurements of the main elements definding the mineral hail structure may give useful information about hail formation processes. But at the present time it is not yet clear what elements can give this information. That's why it is necessary to choose such a method that helps to identify a maximum number of elements. Such unique technique is the mass-spectrometer method with double focusing and ion optics used in our investigation. Ice samples extracted from embryos and hail layers were placed on gallium pads (superpure sample of gallium with certificate pureness of 99.9999%) under the vacuum glass cap in refrigerator at the temperature -15°C. It was taken into account that the loss of the identified elements is possible due to evaporation of volatile compounds, if the evaporation rate is more than 0.2 ml/g cm^2. Teflon mould (1 × 15 mm) was filled with liquid gallium. The method was tested on some salt solutions with known concentrations. Transparent sand particles were observed in many samples. Under optical microscope the inhomogenious cover of these particles was observed easily which contained alluminium, iron, calcium, potassium and other elements. This cover is assumed to be a silicon alluminium (a clay). In all samples bright coloured circles attracted our attention that showed high contents of chlorine and sodium as well as calcium, potassium and aluminium. Twenty five hailstones from 8 hailfalls were analysed. It is shown that the ratio of chlorine to sodium for salt water is approximately 1.8 but for precipitation is 0.5 - 2. But in aerosol deposits of hail this ratio fails. It is typical that during the elemental composition analysis of soil in region under study NaCl is not found in 15-20 representative samples. A considerable content of Na and Cl was found in hailstone aerosol deposits. Hardly we can say that the sources are of local soil origin. In some studies a high content of Na in individual series of hygroscopic aerosols of sea origin was found.

As it was stated chloride component of precipitation was of sea origin (GITLIN 1978, p. 64). Taking into account measurement errors relative content of Al/Si in hail is characterized by very high stability and is one of the characteristic features of atmospheric aerosol of local origin. However the analysis shows that hailstones in the hailfalls of June, 26, 1985 and June, 5, 1986 are characterized by presence of lime origin aerosols as it was defined in the region under study the

Table

Relative element content in hail and snow embryos versus magnium.

Sample type	elements					
	K/Mg	Al/Mg	Ca/Mg	Mn/Mg	Fe/Mg	Zn/Mg
1 graupel	14	3.7	9	0.17	1.3	0.5
2 drop	0.55	0.7	1.25	0.3	2.9	1.8
3grauple	21.6	1.1	9.4	0.11	1.3	2.0
4 drop	3.3	0.9	1.3	0.4	10.6	10.6
5 drop	0.56	0.16	5.8	-	0.2	1.5
6 snow	195	4.4	23.4	0.11	0.9	1.0

1,2 - 13.09.84, 3,4 - 5.06.84, 5 - 5.06.86, 6 - snow, December, 1984.

soil of which contained lime as one of the main elements. Clay particles of the smaller size contain more Al and K than the larger aerosol particles. Comparing K/Si and Al/Si we can see that the content of K is greater than that of Al. The same we can say about aerosol precipitation of hail embryos and snow in 1984 and 1986, shown in Table. Usually K is converted into high dispersion aerosol which may penetrate to the highest layers of low troposphere where the cloudiness is formed. It is shown in the Table, that large embryos and snow are formed in aerosol medium, the great part of which contains potassium particles, while in drop embryos of hailstones their number is much less. Such heavy elements as Mn, Fe, Zn are the components of large aerosol particles in drop embryos of hailstones. These conclusions confirm the results of previous investigations on dispersity of aerosol deposits of hail embryos and layers. In these investigations it was shown, that different crystal structure of hailstones forms in its aerosol medium with specific dispersity (TLISOV M.I., KHORGUANI V.G., 1984, p.287). Found agreement between crystal structure of hail embryo different types and their aerosol structure and element composition can indicate the absence of single mechanism of hail embryo formation.

Graupel embryos are formed in relatively weak drafts and in the small-drop medium when there is a substantial exchange with the surrounding air where the aerosol particles are of relatively small size and specific elementary composition. Drop embryos are formed in strong drafts, which lift supergiant aerosol particles into the cloud from the surface layer.

As to the problem of hail study the main advantage of isotopic method is that the isotopic content of D and O_{18} in ice layers of hailstones is defined by medium temperature (hight), primarily, while the interpretation of bubble and crystal hailstone structure is hindered with an ambiguous dependence on many hailforming parameters, particularly on cloud water content.

The applied technique consists of cutting off sections of hailstones, extracting the embryo and adjacent layers sealing the melted ice in a capillary, removing the sample from the capillary into the ampoule with gas-free zinc under vacuum conditions, restoring hydrogen on hot zinc and entering the sample in the mass-spectrometer analyser.

Temperature values of formation of hailstone embryos and layers, obtained

from the results of relative content deuterium measurements and adiabatic model (MACKLIN et.al., 1970, p.472) were adjusted by comparing with radar data, crystal and bubble hailstone structure and used for deducing the thermodynamic conditions of hailstone growth and plotting the path of their movement in a cloud.

It is known that critical liquid water content q_{cr} is such a quantity of liquid water in a cloud under which a hailstone grows in dry regime, and in opposite case - in wet. As the changes in growth type usually correspond to the changes in transparency and polycrystallinity of ice layers, the calculation of q_{cr} for radii, gives the estimation of cloud liquid water content. For the calculation of q_{cr} we use the following formulae:

$$q_{cr} = \frac{4(1+0{,}24Re^{1/2})(D_n L_2 \Delta\rho + \lambda_2 T_\infty)}{R V_R E (L + C T_\infty)}$$

where Re - Reynolds number; D_n - a factor of molecular diffusion of vapor in the air; $\Delta\rho$ - difference between vapor density at the hailstone surface and the environment; λ_2 - air heat conduction; L and L_2 - the heat of freezing and evaporation of water, respectively; T_∞ - environment temperature (°C); R - hailstone radius; V_R - hailstone fall velocity; E - collection efficiency; C - specific heat of water.

In hail clouds liquid water content, calculated on the base of measurement data on the isotopic hydrogen content of hailstones in 1983-1985 hailstorms, took on values up to 7.5-8 g/m^3. It is noteworthy the sequence of vertical movement of hailstones on different type embryos. This sequence can be represented as a scheme, shown in the figure. The most frequent hailstone growth temperature levels, defined on isotopic composition, range between -12 ÷ -25°C. The scheme clearly shows, that different type embryos move in opposite directions after their generation on various levels. If drop embryos move upwards after their generation, then forming large embryos continue to descent into the hail growth zone. The above phenomenon typical of several super cell storms is one more important verification of the absence of a single mechanism of formation and growth of different-type hail embryos that was shown using another investigation methods. We can say that two precipitation mechanisms can work in one supercell hailstorm creating both types of embryos.

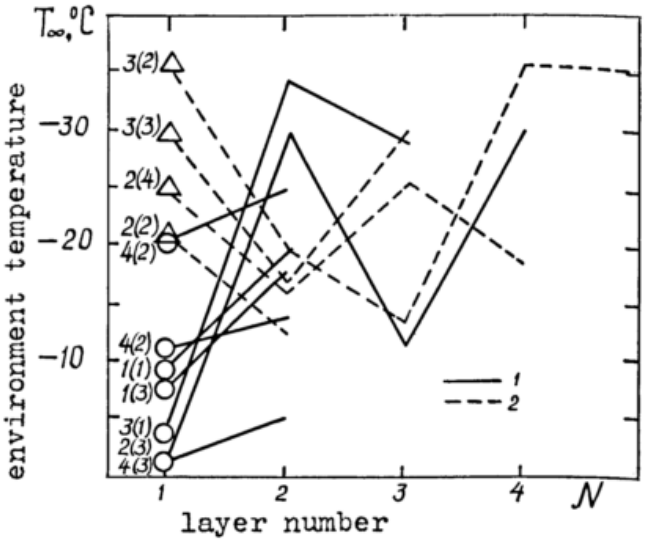


Fig. The scheme of hailstone movement since their generation using data on isotopic measurements. 1 - drop embryos 2 - graupel embryos; 1(1),1(3) - hailstones 1,3 from hailfall on 4.05.83; 2(2), 2(3), 2(4) - on 5.05.83; 3(1), 3(2), 3(3) - on 21.06.83; 4(2), 4(3) - on 14.07.83.

GITLIN,S.:Microprobe Analysis of Project Duststorm Hailstone Samples. J. Appl.Met.,1978,v.17,Nr.1,p. 64-72.

TLISOV,M.;KHORGUANI,V.:Microphysical Conditions of Hail Formation in Clouds Proc.9th Int.Cloud Phys.Conf.,1984,v.1

MACKLIN,W.;MERLIVAT,L.;STEVENSON,C.: The Analysis of a Hailstone.Quart.J. Roy.Met.Soc., 1970, v.96, p.472-486.

STUDIES OF ARTIFICIAL HAILSTONES UNDER DIFFERENT EXPERIMENTAL CONDITIONS

Franco Prodi
Dipartimento di Fisica, Università di Ferrara, 44100 Ferrara, Italy
Istituto FISBAT-CNR, 40126 Bologna, Italy
and
Wang Ang-Sheng
Institute of Atmospheric Physics, Academia Sinica,
Beijing, The People's Republic of China

1. INTRODUCTION

An important part of the research on hail and hail suppression have been the studies on artificial hailstones performed in the last thirty years (KIDDER and CARTE 1964; MACKLIN et al 1977; LEVI and PRODI 1978; ASHWORTH and KNIGHT 1978; PFLAUM 1984; PRODI et al 1986 a, b, c, among others). They have explored several processes and conditions in the growth of natural hailstones, mostly through experiments of ice accretion on cylinders to simulate the natural processes.

These studies then formed the basis for work on the growth of artificial hailstones from embryos having stationary, or vertically and horizontally rotating axes in the hail tunnel.

2. EXPERIMENTAL CONDITIONS

All the experimental work was done in the Istituto FISBAT-CNR's (Bologna, Italy) cold room and warm laboratory. The basic experimental facility included a vertical hail tunnel built beside a cold room of about 13 m^3, a working cold room (21.6 m^3, at -8°C) and an open refrigeratory (0.78 m^3). The growth experiments were performed in this tunnel and its cold room. The square-section (30 cm wide), vertical wind tunnel (2m high) is connected at the lower and upper ends to the cold room; the working section is reduced to 7 cm per side (PRODI et al 1986 a). The water droplets were produced by a sprayer in which the pressure is exerted directly on the air of the water bottle. Thus different liquid water contents (LWC) from 0.3 to 3 g m^{-3} were produced by using different pressures and updraft velocities. In our experiments mean volume radii were obtained in the range 8-12 μm, and median volume radii in the range 12-18 μm.

Different types of hail embryos replaced the cylindrical embryos of previous experiments. The ice embryo is fixed or rotating around a horizontal or vertical axis.

In our experiments the conditions tested were:

1. Rotation condition:
   A. Not rotating;
   B. Rotating around a horizontal axis
   C. Rotating around a vertical axis.
2. Air temperature: 1.: -25°C; 2.: -15 °C; 3.: -5°C and 4.: -10°C.
3. Size of embryo: 1.: 1.5 cm; 2.: 1.0 cm and 3.: 0.5 cm.
4. Form of ice embryo: 1.: Sphere; 2.: Drop; 3.: Cone; 4.: Peach; 5.: Disk; and 6.: Half-sphere.
5. LWC and vertical velocity together define the total liquid water (TLW) which passes through the working section; in turn the LWC is determined by the pressure of the sprayer and the vertical velocity.

   Therefore we define the cases: 1.: (v = 5 m s^{-1}; p = 0.2 kg cm^{-2}, resulting in LWC=2.42 g m^{-3}), the total liquid water through the working section, TLW, being taken as 1 in these conditions; 5.: (v=15 m s^{-1}, p=0.4 Kg cm^{-2}), TLW=1.77; 9.: (v=25 m s^{-1}, p=0.8 kg cm^{-2}) TLW=2.95 and case 0.: (v=25 m s^{-1}, p=1.2 kg cm^{-2}) where TLW is larger than 4.
6. Rotation rate:
   (*): 1.67 Hz (for C), or 2.67 Hz (for B);
   ( ): 8.33 Hz (for C) or 8.88 Hz (for B)
   0.: i.e. fixed embryo.

With combinations of the above conditions several thousand experiments could in principle be planned. 128 cases were chosen as typical for hail growth in our experiments.

A sequence of symbols Xabcd* represents the above mentioned six items. X can become A, B or C; a can become 1, 2, 3 and 4, representing different environmental temperatures (e.g. 2 represents -15°C, and so on). In item b, 1, 2, 3 represent embryo size,

etc. For example, in deposit C2145*, C represents the rotation around a vertical axis; 2: -15°C air temperature; 1: 1.5 cm ice embryo; 4: peach embryo shape; 5. TLW case 5; *: rotation rate 8.33 Hz.

Growth time in the tunnel was 5 min for all deposits. For each deposit the following were made:

-measurement of the surface temperature;
-photography of the external appearance;
-sawing and sectioning in slices of 0.3 - 0.5 mm thickness;
-photography of section under reflected, transmitted and crossed polarized light;
-X ray contact micrograph of the slice;
-formvar replica of the ice surface.

3. FORMS OF ARTIFICIAL HAILSTONES

Protruding icicles were found in several natural hailstones. In our experiments icicles were found in C2165, C2160, C2145. A case with 5 extending icicles is shown in Fig. 1. Twenty of the total 128 deposits showed protruding icicles, all obtained with vertical rotation axis and environmental temperatures around -15°C. Other shapes: concavity in the stagnation area (A1155, Fig.2), disk (C3155, Fig.3), spherical, ellypsoidal, conical (A1119, Fig.4, and C2315, Fig.5), were obtained.

4 SIZE AND VOLUME OF ARTIFICIAL DEPOSITS

Rotation rate was found to affect the final size of the deposits. Rotation around a vertical axis is a favorable condition to larger growth, especially when icicles are formed. Of all the experiments, 10% grew to about 3 cm and another 10% from 2.8 to 3 cm. The maximum dimension attained by one deposit was 5.2 cm (C2165). Higher LWC and stronger vertical velocities are important factors too. Since the size is measured in the plane of largest growth, the volume of the deposit must be considered to account for three dimensional characteristics. For example, C3110* (Fig.6) had 1.67 times greater volume than C2165, the deposit of largest size. Since the density of the large deposits is the maximum one, the values of the artificial deposits represent their mass.

5. INTERNAL STRUCTURE OF THE DEPOSITS

All morphological features confirm data derived by cylindrical deposits. Large ice crystals are formed at warmer air and deposit temperatures. Protruding icicles are formed by larger crystals. Sections, formvar replicas and microphysical studies were used to attain quantitative data on ice crystals in our experiments. Results of microphysical data are presented in Table 1. In the Table, T is the environmental temperature of the hail tunnel, T_s the surface temperature of hailstone growth, D the surface concentration of ice crystals (number per mm^2), L and W are mean maximum length and width of ice crystals. The letters a and b indicate the region near the embryo and the outer region respectively.

6. SUMMARIZING CONCLUSIONS

Although the free fall natural growth conditions are not simulated by fixed rotation axis control, significant information in the understanding of growth processes can be achieved. Shapes, sizes and volumes of the deposits are discussed. Microphysical parameters such as average grain size, surface area and width were also determined and compared to results from cylindrical accretions. The effects of the growth parameters, rotation condition and speeds, growth temperatures, LWC and updraft velocity are examined.

7 REFERENCES

ASHWORTH, T.; KNIGHT, C.A.: Cylindrical ice accretions as simulations of hail growth. J.Atmos.Sc. 35 (1978), 1987-2000.

KIDDER, R.E. and CARTE A.E.: Structures of artificial hailstones. J.Res.Atmosph., 1, (1964), N.4, 169-181.

LEVI, L. and PRODI, F.: Crystal size in ice grown by droplet accretion. J.Atmos.Sc., 35 (1978), 2181-2189.

MACKLIN, W.C.; KNIGHT, C.A.; MOORE, H.E.; KNIGHT, N.C.; POLLOCK W.H.; CARRAS, J.N.; THWAITES, S.: Isotopic, crystal and bubble structures of hailstones. J.Atmos.Sc, 34 (1977), 961-967.

PFLAUM, J.C.: New clues for decoding hailstone structure. Bull. AMS, 65, (1984), 583-593.

PRODI, F.; SANTACHIARA, G.; FRANZINI, A.: Properties of ice accreted in two-stage growth. Quart.J.Roy.Met.Soc., 112, (1986a), 1057-1080.

PRODI, F.; LEVI, L.; LEVIZZANI, V.: Ice accretions on fixed cylinders Quart.J.Roy.-Met.Soc., 112 (1986b), 1091-1109.

PRODI, F.; LEVI, L.; PEDERZOLI, P.: The density of accreted ice. Quart.J.Roy.Met.-Soc., 112 (1986c), 1081-1090.

Table 1 MICROPHYSICAL RESULTS ON ARTIFICIAL HAILSTONES

Cases	T ,°C	T_S,°C	D,(n cm^{-2})	(mm^2)	L, mm	W, mm
A1111	-25	-6.0	85.9	0.0116	0.155	0.101
A1112	-25	-7.4	79.7	0.0126	0.151	0.104
A1119	-25	-12.1	94.8	0.0106	0.148	0.081
C1119a	-25	-8.2	94.8	0.0106	0.125	0.073
b			14.9	0.0673	0.535	0.161
B2119*	-15	-2.3	9.9	0.101	0.529	0.196
C2165a	-15	-3.1	6.4	0.156	0.542	0.299
b			4.4	0.226	0.674	0.472
C4155a	-10	-2.0	9.2	0.109	0.467	0.322
b			2.2	0.455	1.187	0.553
B3119*	-5	-2.3	4.9	0.206	0.677	0.351
C3169*	-5	-0.8	0.7	1.512	1.994	1.308

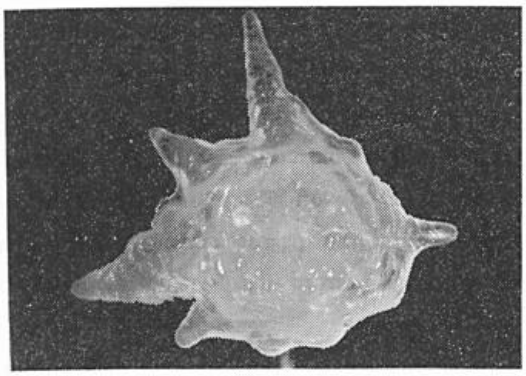


Fig. 1 Deposit C2145, showing 5 icicles

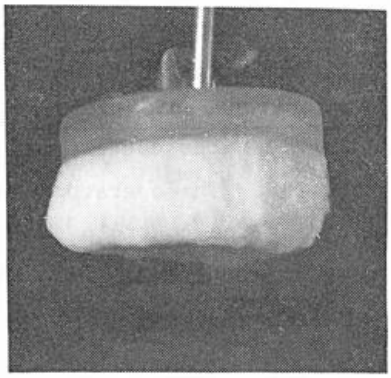


Fig. 2 Deposit A1155, with concavity in the stagnation zone.

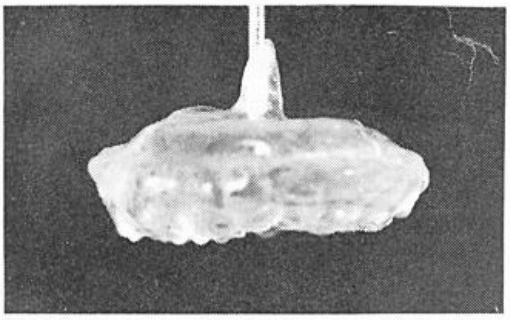


Fig. 3 Deposit C31155



Fig. 4 Deposit A1119

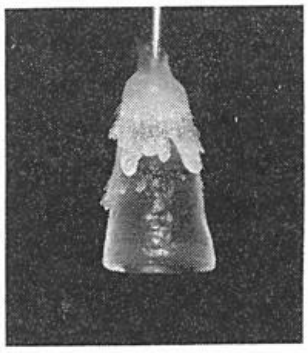


Fig. 5 Deposit C2315

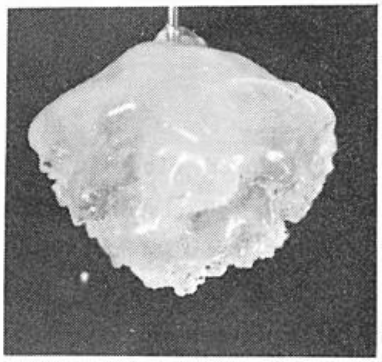


Fig. 6 Deposit C3110*

WIND TUNNEL HAILSTONE GROWTH USING DOPPLER RADAR DERIVED TRAJECTORIES

Glen B. Lesins

School of Meteorology, University of Oklahoma
Norman, OK 73019, U.S.A.

1. INTRODUCTION

There are three basic methods used in studying hailstone growth: analysis of natural hailstones, numerical model simulations using heat and mass transfer equations, and controlled growth of artificial hailstones in a laboratory setting.

The use of dual Doppler radar analysis to recover the three dimensional wind field within the precipitation volumes of thunderstorms has provided the means of predicting hailstone trajectories (HEYMSFIELD ET AL. 1980; NELSON 1983; ZEIGLER ET AL. 1983; FOOTE 1984). Microphysical retrieval techniques (ZEIGLER 1985) has improved the determination of the thermodynamic and water fields within the thunderstorm.

In spite of this progress there remain important uncertainties such as the effect of hailstone shape and roughness during growth, the rotational behaviour of the hailstone which affects the sponginess and net collection efficiency (LESINS and LIST 1986), the density of the deposit (PFLAUM 1980) and the fractional range of liquid water content with respect to adiabatic values.

The cloud physics wind tunnel facility at the University of Toronto is capable of recreating the time dependent environmental conditions that the Doppler analyses and thermodynamic retrievals have deduced along predicted hailstone trajectories. Hailstone trajectory A, analyzed by Zeigler et al. (hereafter referred to as ZRK) was used to grow artificial hailstones and is discussed here.

2. WIND TUNNEL EXPERIMENTS

The University of Toronto cloud physics wind tunnel is a closed circuit design with controllers for the fan blower, refrigerator elements, vacuum pump and water flow meters. Further details can be obtained in LIST ET AL. (1987). A Particle Measuring System's FSSP measured a mean volume diameter of 28 μm with the peak in number concentration occurring at 15 μm diameter.

The hailstone growth took place in a measuring section with a cross section of 17.8 cm by 17.8 cm. A gyrator, on which 1 cm diameter ice spheres were mounted, forced the hailstone to execute symmetric gyration (KRY and LIST 1974) where the spin axis of the hailstone nutates and precesses with an amplitude of 30 degrees about a fixed horizontal vector.

In a typical trajectory experiment a time series of air temperature, air pressure, dynamic pressure and liquid water content was prepared using data from ZRK. The operator was responsible for adjusting the controls so that these parameters were reproduced in the wind tunnel in the proper sequence. The effects of time lags in depressurization and thermal response was particularly critical, however, the wind tunnel was able to vary the environmental conditions in close concert with the time series from ZRN. During the growth a video tape recorded the hailstone shape, size and surface characteristics.

After the time series, which was about 10 minutes long, had been completed the tunnel was repressurized, the hailstone was removed and

photographed, and then a thin section was prepared for further photographs in transmitted light. The thin section was produced by slowly melting the hailstone down to a disk with a thickness of 2 to 3 mm which maximized the contrast between the various growth rings.

3. HAILSTONE A AND ITS TUNNEL SIMULATION

A complete description of Hailstone A is found in ZRK, with only a brief summary given here. The time series starts when the hailstone is 1 cm in diameter which occurs after the hailstone encountered its first strong updraft which lifted it to 9.5 km AGL at a temperature of -31°C (Figure 1). It then falls out of the first updraft into a weak downdraft of -2.4 ms^{-1} to 6 km AGL and -7.5°C in about 5 minutes. At this point it encounters a second updraft of up to 38.5 ms^{-1} and adiabatic LWC of 8 gm^{-3} which carries it to 7.6 km AGL and -20°C in about 2 minutes. Finally, the hailstone falls out of the updraft and reaches the melting level in about 3 minutes.

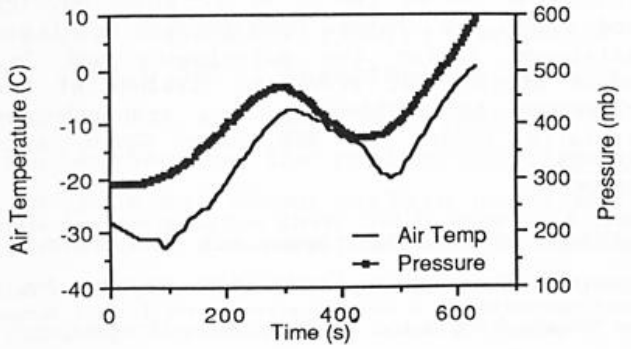


Figure 1: Air temperature and pressure time series for Hailstone A from ZRK.

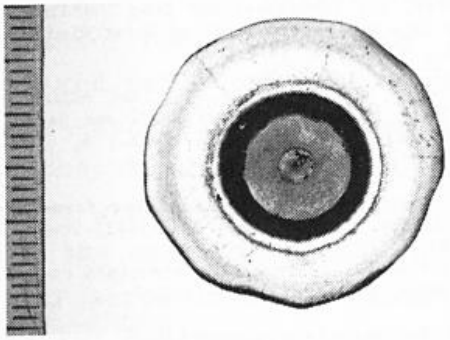


Figure 2: Photograph of a thin section of the artificial hailstone from Experiment 12 in transmitted light. The 1 cm embryo is the grey circle within the black, opaque ring. The lines on the scale to the left are 1 mm apart.

Two different rotation settings were used: in experiment #12 the spin frequency fluctuated from 0.5 to 1 Hz and the precession/nutation frequency was 2.5 to 3.0 Hz whereas in experiment #14 a much higher rotation rate was used with a spin of 5 to 6 Hz and a precession/nutation frequency of 14.0 Hz. All other conditions including the air temperature, pressure, velocity and LWC time series were nearly identical.

The final hailstone thin sections photographed in transmitted light are shown in Figures 2 and 3. The slow rotation case produced nearly symmetric circular growth layers whereas the fast rotation case produced a completely different shape with large lobes in the outer layer. The final aspect ratios were 0.90 and 0.52 for the slow and fast cases, respectively. The 1 cm, grey center of both photos is the original hailstone embryo. Five distinct growth zones can be identified in Figure 2. The zones are numbered 1 to 5 starting from the inner most zone next to the embryo. Zone 1 is complete opaque indicating a larger air bubble concentration. Zones 2 and 4 are clear while zones 3 and 5 are grey and speckled in appearance. In Figure 3 a similar classification can be used except that zones 4 and 5 are indistinguishable.

4. DISCUSSION

The diameter growth is shown in Figure 4 for the actual tunnel hailstones and their model

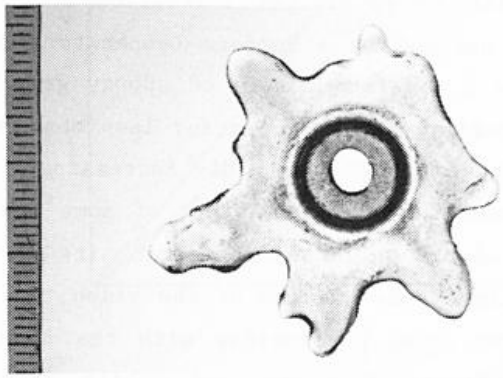


Figure 3: Same as Figure 2 but for Experiment 14, the fast rotation case. The central hole indicates the position of the supporting rod which is removed.

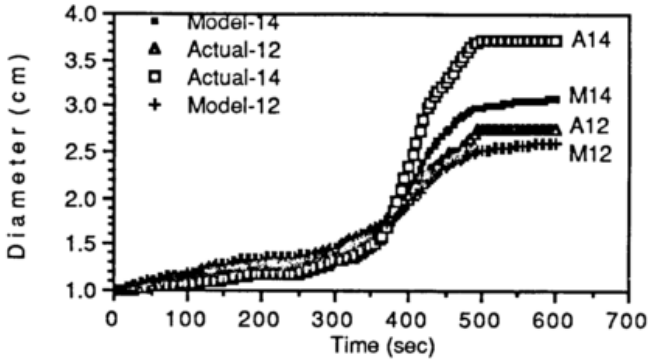


Figure 4: Time series of the diameter growth for Experiments 12 and 14, denoted by A12 and A14, respectively, and for model simulations of Experiments 12 and 14, denoted by M12 and M14, respectively.

predictions. In the slow rotation the model underestimates the final diameter by only 0.15 cm, but is 0.7 cm too small for the fast rotation. This is caused by the large lobes that developed in fast rotation and the measured diameter extended to the lobe tips. If a simple smoothening out of the lobes and valleys is done from the final photograph, a diameter of 3.2 cm is obtained which is only 0.1 cm larger than the model prediction. It appears that the model is making reasonable predictions of the hailstone growth.

In an attempt to interpret the growth zones, the model-predicted hailstone surface temperature and net collection efficiency is plotted as a function of the hailstone diameter in Figure 5 for experiment 12. Also shown are the boundaries of the growth zones as determined from Figures 2 and 3. The outer boundary of zone 1, the completely opaque ice, coincides with the predicted initiation of wet growth as defined by a surface temperature of 0°C. Zone 2 consists mostly of spongy growth with no shedding which occurs for less than 30 seconds since the LWC is rapidly increasing. Zone 3 appears to be a transient of some sort occurring as the hailstone is nearing its maximum shedding rate. Review of the video tapes reveals that zone 3 coincides with the first visual evidence of a wet and mobile water skin. This is verified by close examination of Figure 3 which indicates that the thickness of zone 3 varies, being largest under a lobe and smallest under a valley. Zone 4 is clear ice occurring during wet and shedding growing. In experiment 12 the beginning of zone 5 coincides with predicted spongy without shedding growth. Note, however, that the opacity of zones 5 and 3 are different and that no zone 5 can be found in experiment 14.

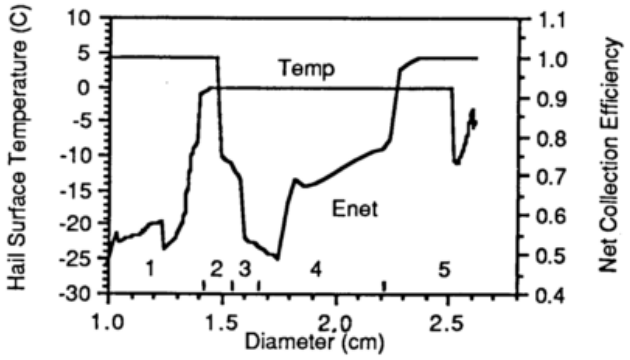


Figure 5: The surface hailstone temperature and the net collection efficiency as calculated by the heat and mass transfer model is plotted as function of the diameter of the hailstone for Experiment 12. At the bottom of the graph, vertical ticks indicate the diameters at which a boundary occurs between the growth zones as identified in Figure 2.

ACKNOWLEDGEMENTS

I wish to thank Prof. Roland List for providing the use of the U. of T. cloud physics wind tunnel, Ms. Marion Dove for her excellent assistance during the experiments and Dr. Conrad Ziegler for providing listings of his trajectory calculations. This research was partially funded by NSF under Grant ATM-8500792.

REFERENCES

FOOTE, B.: A study of hail growth utilizing observed storm conditions. **J. Climate Appl. Meteor., 23,** (1984) 84-101.

HEYMSFIELD, A.J.; JAMESON, A.R.; AND FRANK, H.W.: Hail growth mechanisms in a Colorado storm. Part I: Hail formation processes. **J. Atmos. Sci., 37,** (1980) 1779-1807.

KRY, P.R. and LIST, R.: Angular motions of freely falling spheroidal hailstone models. **Phys. Fluids, 17,** (1974) 1093-1102.

LESINS, G.B. and LIST, R.: Sponginess and Drop Shedding of Gyrating Hailstones in a Pressure-Controlled Icing Wind Tunnel. **J. Atmos. Sci., 43,** (1986) 2813-2825.

LIST, R.; LESINS, G.B.; GARCIA-GARCIA, F.; and MCDONALD, D.B.: Pressurized Icing Tunnel for Gaupel, Hail and Secondary Raindrop Production. **J. Atmos. Ocean. Tech., 4,** (1987) 454-463.

MACKLIN, W.C.: The density and structure of ice formed by accretion. **Quart. J. Roy. Meteor. Soc., 88,** (1962) 30-50.

NELSON, S.P.: The influence of storm flow structure on hail growth. **J. Atmos. Sci., 40,** (1983) 1965-1983.

PFLAUM, J.C.: Hail formation via microphysical recycling. **J. Atmos. Sci., 37,** (1980) 160-173.

ZEIGLER, C.L.; RAY, P.S.; and KNIGHT, N.C.: Hail growth in an Oklahoma multicell storm. **J. Atmos. Sci., 40,** (1983) 1768-1771.

ZIEGLER, C.L.: Retrieval of Thermal and Microphysical Variables in Observed Convective Storms. Part I: Model Development and Preliminary Testing. **J. Atmos. Sci.,** (1985) 1487-1509.

THE EFFECT OF SUPERCOOLED DROPLET ELECTRICAL CHARGE ON THE HAIL GROWTH COAGULATIVE PROCESS

T.G.Bliadze, A.I.Kartsivadze, A.M.Okudjava, T.N.Saliashvili

Institute of Geophysics of the Georgian Academy of Sciences

It is natural that the study of ice accumulation on the substrate in flow of charged water aerosols provokes a great interest, it is conditioned by the fact that the growth of hydrometeor particles, including large hailstones, in cumulus congestus occurs in charged droplets environment. The theoretical evaluations of the electrostatic effect influence on the rate of large particle growth reveal its small significance, as the inertial forces in the range of Reynolds numbers, corresponding to hail stone sizes, considerably exceed electrostatical ones (LEVIN 1961, p.105; SMIRNOV 1980, p.111; KHORGUANI 1984, p.187). Nevertheless we have started our experimental study of the problem because the preliminary investigations had shown certain peculiarities in the character of ice accumulation on the spherical substrate blown round by the stream of charged supercooled droplets (OKUDJAVA et al, 1988, p. 38).

The experiments have been carried out in the cloud chamber 200m^3 by volume. A fixed hailstone model representing a brass sphere, 20mm in diameter is placed in the axial part of the wind tunnel where a necessary negative temperature and the updraft of 8ms^{-1} are maintained. Water aerosols are obtained using a jet nozzle of "tube in tube" type. The modal value of droplet sizes is 20μm in diameter and 80 per cent of total droplet quantity ranges from 15μm up to 25μm. For droplet charging a voltage is supplied to a ring with a diameter of 8mm arranged 2mm above the nozzle outlet. The evaluation of droplet charge value is conducted by measuring a current from the model. We get an avarage charge of one droplet of about 10^{-13}C. Droplet charges in cumulus congestus can be by some orders of magnitude greater comparing with the obtained value (CHALMERS 1974, p.216-240). Figure 1 shows the depenaence of accreted ice mass upon time at ambient temperature -8°C. Upper curve corresponds to 2kv-voltage on the charging ring. Lower curve is obtained when a model is blown round by neutral drop-

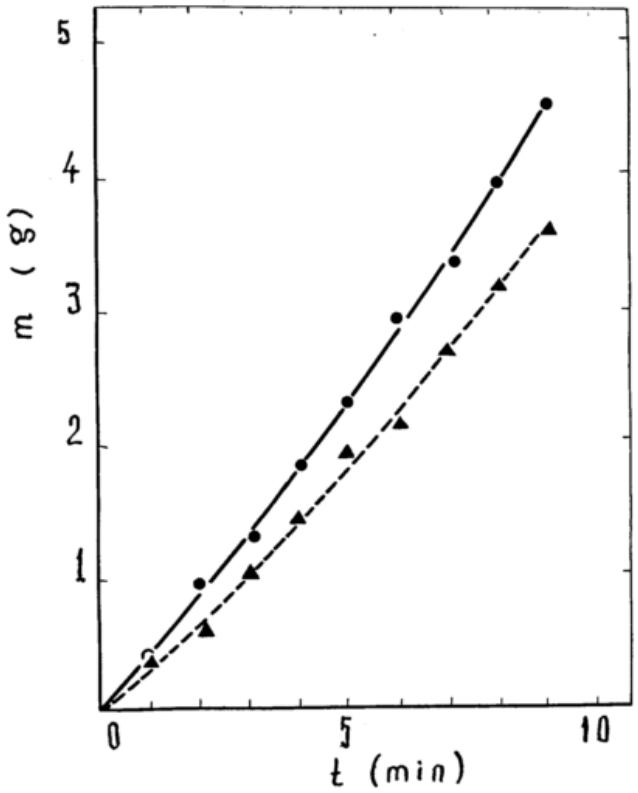


Fig.1: The fixed ice model mass increase M plotted as a function of growth time T. Solid line belongs to the case of charged impacting droplets.

lets. As we see the difference in mass reaches 25 per cent by the end of the ninth minute. As we expected the deposition rate in "dry" growth conditions was in proportion to water discharge from the injector. A charge of potential difference from 2 to 3kv increases deposition rate 1.5 times by the end of the third minute.

The experiments have shown that water aerosols electrization leads not only to collection efficiency increase but also to changes in geometrical pattern of ice accumulation and in structure of ice formation. Non-charged aerosols deposit only on the frontal side of a growing model (Fig.2).

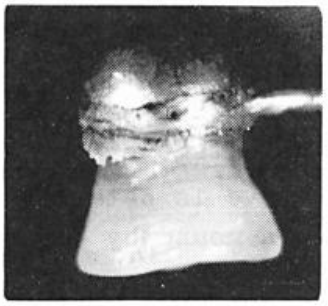


Fig.2: Photograph of the ice model growing in a current of neutral droplets.

When a model is in a current of charged droplets we observe in all cases a white thick coating on its back side (Fig. 3).

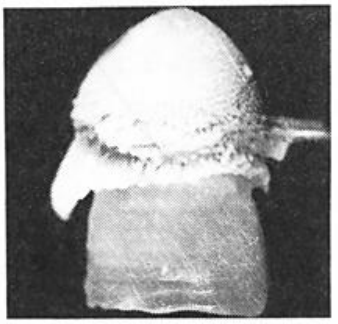


Fig.3: Photograph of the ice model growing in a current of charged droplets.

Curves shown in Fig.1 can be described as well by empirical expressions of the following type:

$$m = 0.306\, t^{1.12}; \quad m = 0.385\, t^{1.11};$$

It is known from laboratory tests (WALLACE, HOBBS 1977,p.176) that if the impacting droplets carry an electric charge in excess of about 10^{-14}C their coalescence with water surface enhances. The analogous phenomenon can take place when a charged droplet comes into collision with a hailstone. So the total increase of ice accretion rate can be stipulated by the coalescence efficiency increase at the expense of the droplets the collision of which ends in rebound if an electrostatic attraction is absent. "Dry" growth zone of the hailstone back side could arise owing to intensive convective heat exchange in the vortex range behind a spherical model. Only small droplets can fall into this region.

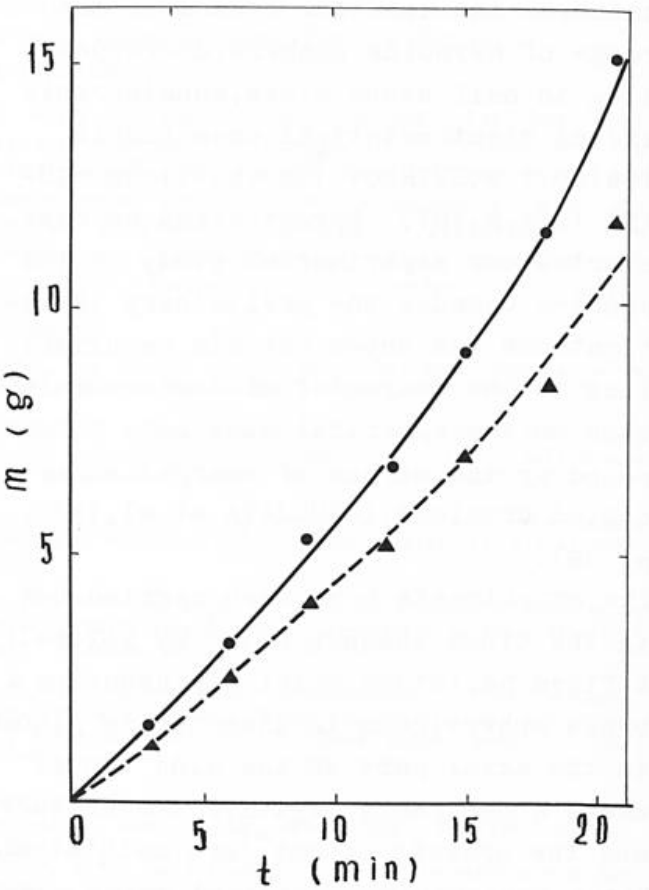


Fig.4: The suspended ice model mass increase M plotted as a function of growth time T. Solid line belongs to the case of charged impacting droplets.

Experiments with a fixed model described above don't give a full picture of

a large hailstone growth. Nevertheless they point at necessity to take electrical effects in account and give a possibility to reveal certain growth peculiarities difficult to be discovered on a freely growing model.
Further investigations have been carried out on the experimental facility allowing to suspend a hailstone in a blowing airstream (OKUDJAVA et al. 1982, p.90). Preliminary tests have shown (Fig. 4) that in case of freely suspended model the growth rate is higher in the presence of charged aerosols than in neutral environment.

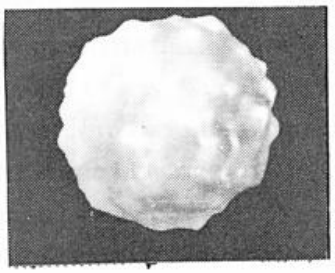


Fig. 5: Typical picture of knobby ice model surface.

It should be mentioned that for the relatively high water content of suspending medium the spherical surface of a growing ice model, as a rule, becomes knobby, as is easily seen from Fig. 5.

References.

CHALMERS,J.A.: Atmospheric Electricity (in Russian),Gidrometeoizdat,Leningrad 1974.

KHORGUANI,V.G.: The microphysics of hail nucliation and growth (in Russian),Gidrometeoizdat,Moscow,1984.

LEVIN,L.M.: Investigations on the physics of rough disperse aerosols (in Russian),Moscow,Ed.by the Acad. Sci. USSR, 1961.

OKUDJAVA,A.M.; BLIADZE,T.G.; LOMINADZE,D.R.; SALIASHVILI,T.N.: Hailstone growth and melting processes modeling device (in Russian),Tbilisi:Trudy Inst.Geoph.Acad.Nauk Gruzinskoi SSR, 19, 1982.

OKUDJAVA,A.M.; BLIADZE,T.G.; SALIASHVILI,T.N.: Ice deposition in the stream of charged water aerozol (in Russian), Fizika obrazovania gradovikh protsessov i aktivnikh vozdeisvii na nikh, Gigrometeoizdat,Moscow, 1988.

SMIRNOV,V.B.: Electrostatic probe in poorly ionized polycomponent plasma (in Russian), Gidrometeoizdat,Moscow: Tr.IEM, 24(89), 1980.

WALLACE,J.M.; HOBBS,P.V.: Atmospheric Science, Academic Press, New York, 1977.

GROWTH OF HAILSTONES IN CONVECTIVE CLOUDS. RESULTS OF MEASUREMENTS AND NUMERICAL EXPERIMENTS

S.Stoyanov
Hydrometeorological Service,blvd."Lenin"66, Sofia,Bulgaria
M.Tlisov
High Mountain Geophysical Institute,360030,Nalchik, USSR
I.Geresdi,Cs.Zoltán,Cs.Székely,K.Molnár
Meteorological Service,7811,Szalánta,Pf.1,Hungary

1. INTRODUCTION

The aim of the paper is to present some results from a comparative analysis of the microphysical conditions of hailstones formation and growth. The results are obtained by means of model computations and data from crystalline,bubble and isotope analyses of hailstones. The basis of the theoretical estimates is the idea of the jet character of convective clouds development(STOYANOV 1975), which is evolved into models for computation of hailstone growth in the cloud(ZOLTÁN et al. 1982;GERESDI et al. 1984). The methods for laboratory study of microphysical conditions of hail formation in convective clouds (TLISOV and KHORGUANI 1984) is the basis for the analysis of the results from the measurements of hailstones.

2. METHODS OF STUDY

2.1 NUMERICAL MODELLING

The numerical estimates are done in two stages. During the first stage the thermodynamical characteristics of a stationary cloud jet averaged by each horizontal cross-section of the jet are computed. They correspond to the stage of maximum development of the convective cloud and they are obtained by means of a system of ordinary differential equations derived from the basic equations of convective dynamics. During the second stage by means of empirical dependences quasi-three-dimensional space in relation to updraught velocity is introduced in which the movement and growth of hailstones are computed.

2.2 LABORATORY ANALYSIS

The analysis of the crystalline structure is applied to the examination of the hailstone type and their clear distinction as well as the distinction of the other layers in the hailstones.

On the basis of laboratory experiments of water drops crystallization an empirical relation between the temperature of the air medium of drops and the mean arithmetic diameter of bubbles is derived. This relation enables the determination of frozen hail nuclei temperature.

The isotope analysis includes procedures for conservation of hailstones and examination of samples by means of mass-spectrometer. The amount of hydrogen and oxygen isotopes in ice deposition of hailstones is determined mainly by the temperature of the cloud medium. Thus, on definite assumptions conserning condenzation,sublimation and coagulation processes and at certain initial values of the isotope composition, the temperature of partial cloud humidity condenzation could be restored by the isotope composition in ice samples of hailstones.

3. RESULTS AND DISCUSSIONS

The described methods of numerical and laboratory experiments have been used for the examination of the hail process on June 5,1986 developed over

the territory of the complex hail experiment - North Caucasus (USSR) . Data from the radiosounding of the atmosphere at 15,00hrs local time are shown(Fig.1).Results from computation of some cloud characteristics are also shown on Fig.1. These numerical estimates show the development of a powerful convection - the velocity of updraught could reach 45-50m/s.The upper limit of clouds exceeds 13km, which is confirmed by radar measurements done that day.

The laboratory analysis of hailstones, which has been possible for the time being, shows that the interpretation of the results is difficult due to the close relation between the crystalline and bubble structure of hailstones and some cloud characteristics like liquid water content in the cloud, which are very important for the process of hail-formation. According to theoretical evaluations the freezing temperature of water drops with radius 0,1cm in a cloud having liquid water content 4 g/m^3 is with 1-2°C higher than in the process of isolated crystallization. Thus, in the present study the crystalline and bubble analyses of hailstones are used for specification of nuclei borderlines as well as the borderlines of the different layers, while the isotope analysis is used for the determination of thermodynamical conditions for hailstones formation and growth by measuring the relative amount of deuterium.

Fig.2 shows a scheme of a thin cross-section of one of the hailstones (Number 76), typical for the examined process.A nuclei is a frozen spherical drop with radius 0,2cm, growing first in wet regime and after that in dry regime. The thickness of the first layer is 0,4cm, while the extreme radius of the hailstone is 0,7cm.The freezing temperature of the nucleus drop is -3°C according to the bubble method evaluated without accounting for the liquid water content in the surroundings.On the assumption that hail is formed and grows in the cloud within the temperature interval -5°C and -30°C, the freezing temperature of the nucleus drop obtained by the isotope method is -7°C. The isotope analysis enables the evaluation of the transition temperature from wet to dry regime of hailstones growth.In the examined case this transition is done at cloud temperature -16°C.Yet again, on the basis of the isotope analysis the liquid water content-3g/m^3 by our estimates - at which the change of the regimes of hailstones growth occurs may be evaluated by the critical liquid water content and the well-known Schumann-Ludlams' curves.

Some results of the numerical modelling of hailstones movement and growth in the analyzing situation are presented on Fig.3. The output data of the model includes results of the laboratory measurements: the nuclei cloud drops radiuses obtained on the basis of structural and bubble analyses as well as the values of the freezing temperature of these drops. An example is shown for hailstone growth with a change of the wet and dry regime and the corresponding trajectories in two projections. The time for this movement is 990s.

The comparative analysis on Fig.1,2, 3 shows that the results from the computation of in-cloud characteristics and hailstones growth in various regimes and the results from the laboratory analyses are satisfactory.

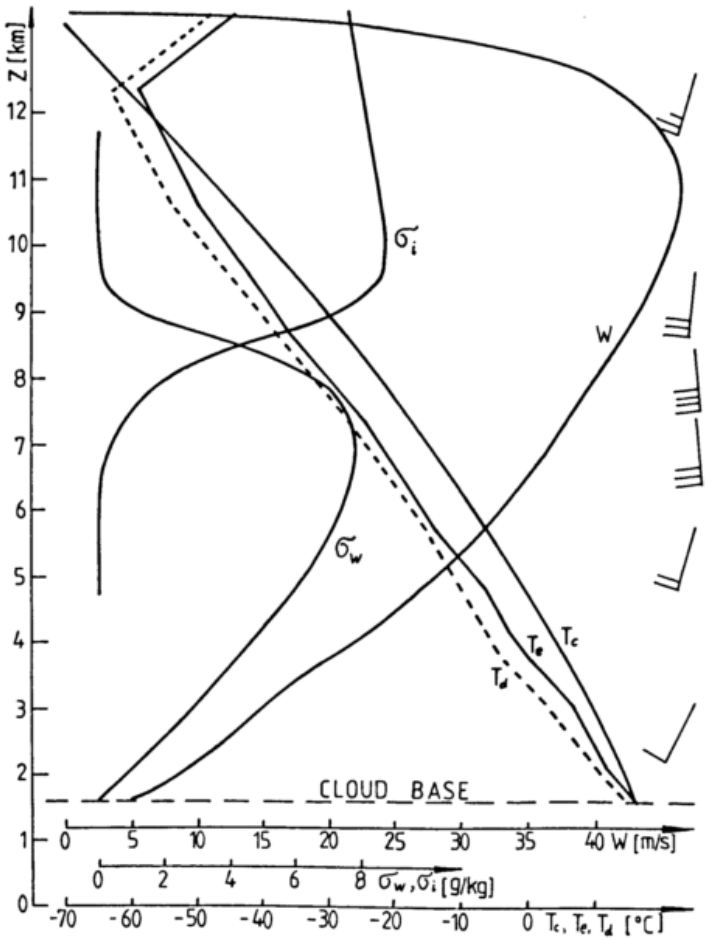


Fig.1:Cloud characteristics: mean vertical velocity W ,liquid water mixing ratio σ_w ,ice mixing ratio σ_i and temperature T_c (computation).Data from radiosounding of the atmosphere: temperature T_e ,dew-point T_d and wind (the flag means 4-6m/s).

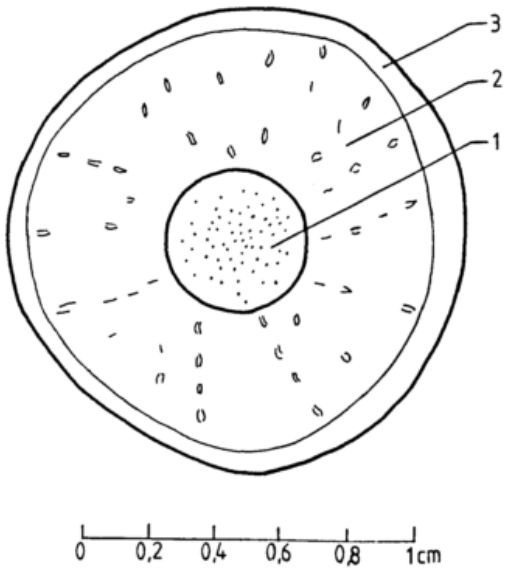


Fig.2: Thin cross-section of a typical hailstone with freezing water drop nuclei (1).Layers of wet(2) and dry(3) growth (laboratory analysis).

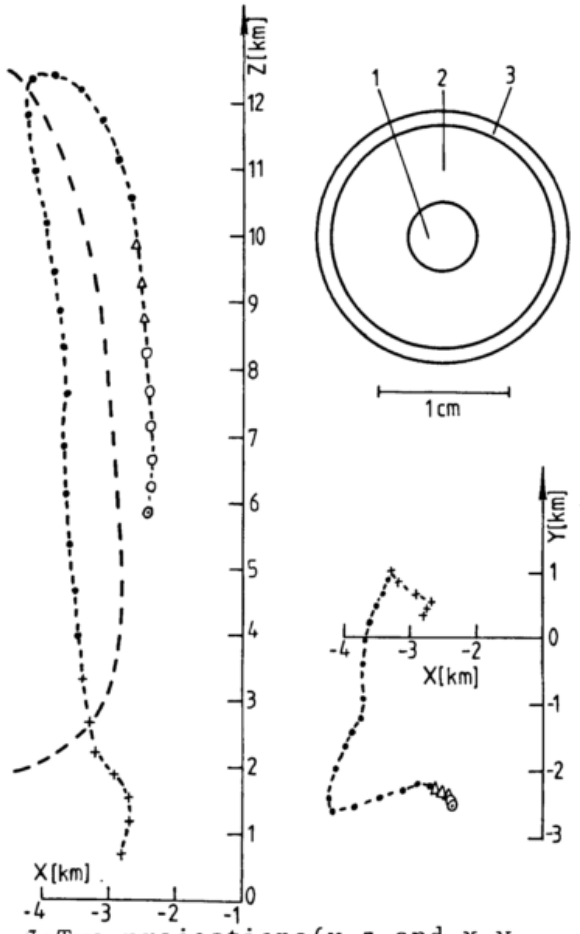


Fig.3:Two projections(x-z and x-y planes) of a typical hailstone trajectory and hailstone growth.Symbols: 1 - freezing water drop, o-starting point, o and 2 - wet growth, Δ and 3 - dry growth, + -melting, • -no growth.

4. REFERENCES

GERESDI, I.;ZOLTÁN, Cs.;SZÉKELY, Cs.; MOLNÁR, K.;STOYANOV, S.: A Numerical Model of Hailstone Growth.Proc. of the 9th Int.Cloud Phys.Conf., Tallin 1984 vol.II,p.493-496.

STOYANOV, S.: Jet Model of Convective Clouds(in Russian).Hydr. i Met., vol.XXIV(1975),No.3,p.3-12.

TLISOV, M.I.;KHORGUANI, V.G.: Microphysical Conditions of Hail Formation in Clouds.Proc. of the 9th Int.Cloud Phys.Conf.,Tallin 1984,vol.I,287-290.

ZOLTÁN, Cs.;SZÉKELY, Cs.;GERESDI, I.; MOLNÁR, K.;STOYANOV, S.: A Model of Hailstone Growth.Papers pres.at the II Int.Conf. on Hailstorms and Hail Prevention, Sofia 1982,p.607-612.

HAIL IMPACTS, HAIL NETS AND DAMAGE

Danie Roos
Council for Scientific and Industrial Research, P.O.Box 395, Pretoria, South Africa

Steve Durrant
Current address: Dept. of Chemistry, University of Surrey, Guildford, U.K.

1 HAIL INTENSITY AND ECONOMY

Hailfalls are mostly light: for example, 80% of the areal impact energy densities of hailfalls recorded in Switzerland, Canada and South Africa has values of less than 25 $J.m^{-2}$ and most swaths are smaller than 25 km^2. Heavy hailfalls, of total impact energies exceeding ~10^9 J, are rare but those storms, perhaps 10% of the total, cause 90% of all crop damage (Admirat *et al.* 1985).

In the 1986/87 season crops in S.A. insured with a major hail insurance company amounted to S.A. Rand 1760 x 10^6 ≙ US \$880 x 10^6 (Sentraoes 1987), which represented some 37% of all crop farming in the country. Farmers of maize, tobacco, wheat and other crops subsequently claimed \$49 x 10^6 for hail losses, in the ratio of 37:27:17:19 (per cent).

Cities are also vulnerable: for example, on 12 July 1984 a hailstorm destroyed insured property in München to the value of \$500 x 10^6 (Munich Re 1984). Hail in Pretoria on 1 Nov. 1985 caused damage of \$20 x 10^6 to motor cars alone (Beeld 1985). CSIR hailpads indicated widespread high intensities on this day:

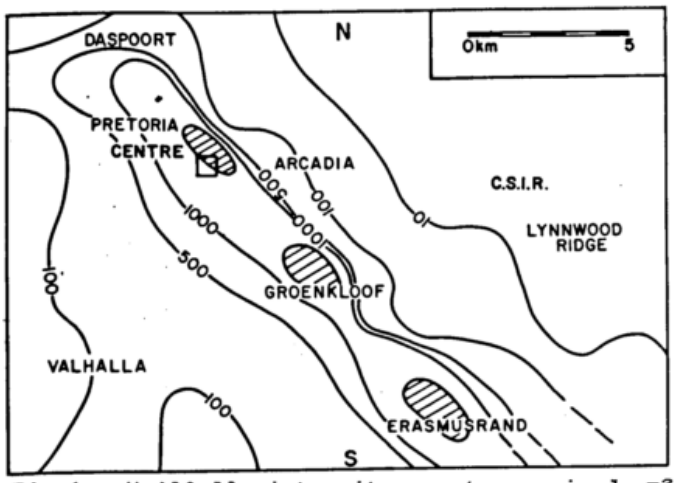


Fig.1: Hailfall intensity contours in $J.m^{-2}$ over central and S.E. Pretoria, 1 Nov. 1985.

values exceeding 100 and 1000 $J.m^{-2}$ occurred over 180 and 50 km^2, respectively (Fig 1).

Efforts to reduce damaging hail have a strong economic incentive and include protecting property with stretched nylon nets. Aspects of the dynamics of impacting hailstones and damage caused by them are discussed below.

2 MODELLING OF HAIL IMPACTS ON NETS

2.1 GEOMETRY OF THE NET

The common hail net considered has a regular hexagonal pattern, with braiding width 2d and unit cell 'half-width' R (Fig. 2). If A1, A2 and A3 are the areas, in mm^2, of the unit cell, the opening and the hexagonal annulus (dotted), respectively, then

$$A1 = 6\,R^2.\tan 30° = 139.68$$

$$A2 = 6(R - d)^2.\tan 30° = 99.15$$

and $A3 = 6 \tan 30° [R^2 - (R - d)^2] = 40.53$

for R = 6.35 mm and d = 1 mm, which are idealised values for the net used.

2.2 PROBABILITIES OF INTERACTIONS

In theory, a sphere of diameter ϕ would be stopped by the net if $\phi > 2(R-d) = 10.7$ mm. For a smaller sphere falling vertically on a horizontal net, three possibilities exist: (a) the sphere penetrates the net unrestrictedly and retains its energy with probability P = Pu for this to happen; or (b) net contact occurs at the lowest point of the sphere, its impact energy is transferred to the net and it recoils, P = Pr; or (c) contact occurs away from the lowest point of the sphere, where some of its energy is lost, and it deflects, P = Pd. For $\phi < 2(R - d)$, Pu + Pr + Pd = 1.

Hailstone sizes from CSIR hailpads are given in intervals of 3 mm (Roos 1978) and characterised by mean diameters $\bar{\phi}$ = 4.5, 7.5, 10.5 mm, etc. (Table 1). P (Fig. 2) then becomes:

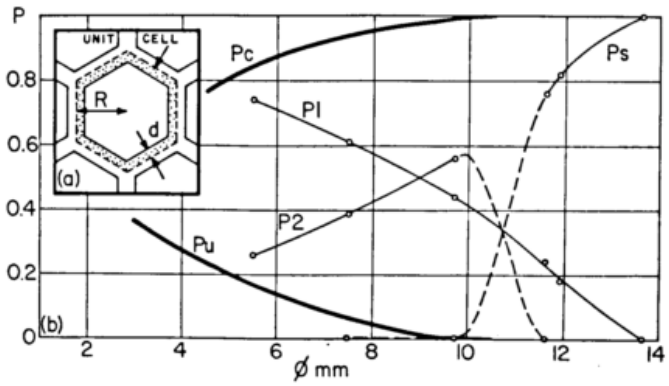


Fig. 2: (a) Hail net unit cell, 'half-width' R and d (see 2.1). (b) Probabilities of various net interactions as function of ø: bold lines are theoretical (see 2.2) and thin lines experimental results (see 3.2)

$$Pu = \frac{6[R - (d + r)]^2.\tan 30°}{A1} \qquad (r = 0.5 \times \phi)$$

$$= \frac{[R - (d + r)]^2}{R^2} = \frac{(5.35 - r)^2}{40.32}$$

which decreases rapidly as ø increases.

$$Pr = \frac{A3}{A1} = 0.29 = \text{constant, and}$$

$$Pd = 1 - Pr - Pu = 0.71 - \frac{(5.35 - r)^2}{40.32}$$

which increases steadily with ø. The probability of net contact, Pc = Pr + Pd = 1 - Pu, increases from 0.76 to 1 for size group i = 1 to 3. Table 1 also shows P-values for the size groups considered together.

Table 1: Hailstone sizes in mm and probabilities of net interactions, per cent.

ø-intervals	(3-6]	(6-9]	(9-12]	(3-12]
Size group i	1	2	3	1+2+3
Mean diam. $\bar{\phi}$	4.5	7.5	10.5	-
Pu (unrestr.)	23.8	6.3	0.02	10.0
Pr (recoiled)	29.0	29.0	29.0	29.0
Pd (deflected)	47.2	64.7	71.0	61.0
Pc (contacted)	76.2	93.7	100	90.0

3 HAIL NET EXPERIMENTS

3.1 FIELD WORK

Hailpads were erected in the open and under a horizontal net, 3 m above ground, to record hailstone size distributions. Table 2 shows some results in terms of hailstone number density, N m^{-2}; areal mass density, M $g.m^{-2}$; and areal impact energy density, E $J.m^{-2}$.

The fraction of E registered under the net appeared to be nearly 50% of the 'exposed' value for the light hailfall of 5 $J.m^{-2}$ and only 20% for the heavy fall of 260 $J.m^{-2}$. In both cases about one half of the hailstones, all relatively small, did penetrate the net. For the heavy fall, 361 of the 983 hailstones recorded in the open exceeded ~1 cm in size (maximum diameter = 18 mm), while the protected pads showed 66 dents characteristic of hailstones > 1 cm. Indications were that the net held back approximately one half of the ice mass for the light fall and three-quarters for the heavy fall.

Table 2: Effect of net on parameters defined above for hailfalls of two intensities.

	Parameter	Hailpad position: Exposed	Hailpad position: Protected	Protected ÷ Exposed
Light	N	2880	1390	0.48
	M	139	65.4	0.47
	E	5.3	2.5	0.45
Heavy	N	8970	4800	0.53
	M	3085	730	0.24
	E	260	52.4	0.20

3.2 LABORATORY STUDIES

Hail impacts on stretched nets were simulated by firing ice, plastic and wooden spheres of various diameters (masses), using a mechanical hail gun, at appropriate terminal speeds to keep the impact energies true to nature. Fig. 2 shows results from 440 shots of spheres of ø (arbitrary) = 5.5, 7.5, 9.7, 11.6, 11.9 and 13.6 mm. P1, the probability of penetration on first impact, decreases from 70% through 7% to zero as ø increases from 6 through 13 to 13.6 mm while Pu (theoretical) was 14% for ø = 6 mm and zero for ø = 10.7 mm. The finding that P1 is much larger than Pu (Fig. 2) relates to hailstones which penetrated the net on first impact although they did not pass through unrestrictedly.

The probability P2 for penetration on second (or further) impact increases with ø for ø < 10mm, such that P2 = 1 - P1. For ø > 10mm, the probability Ps of hailstones stopped

by the net increases rapidly from zero, while Ps = 1 - (P1+P2). P2 rapidly decreases to zero as $\phi \rightarrow 11.6$ mm; thereafter, Ps = 1 - P1 until, for $\phi \geq 13.6$ mm, Ps = 1. This threshold exceeds by 2.9 mm the theoretical value in Sect. 2.2 and shows the degree of net stretching that may accompany penetration.

3.3 PROBABILITIES OF IMPACT DAMAGE

The threshold value of hailstone diameters for impact damage to occur, ϕ^*, is important to know, especially for hail net manufacturers and users. Relevant data were obtained by firing spheres of 10 different diameters of between 5 and 50 mm, at proper terminal speeds, 100 times from the hail gun at hail-sensitive ripe tomatoes and more hardy sections of motor car bodywork. ϕ^* for these objects in windstill conditions was found to be 7.5 and 23 mm, respectively (Fig. 3), with a 50% chance of damage at ϕ=11 and 30 mm and certain damage at ϕ=13.5 and 44 mm. ϕ^* represents impact energies e of approximately 0.01 and 1 J.

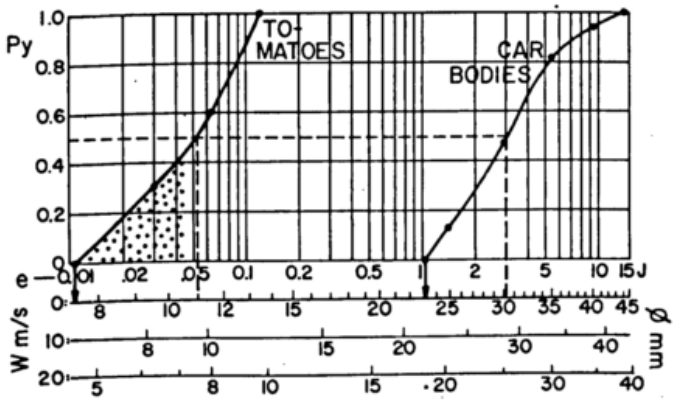


Fig. 3: Probability of immediately visible damage Py as function of hailstone kinetic energy e for objects indicated. Appropriate ϕ-scale depends on wind speed W. ϕ^* values are arrowed. Dotted region, showing potential for damage under net for W=0, extends to $\phi \doteq 2(R-d)$.

Note that a given e can be attained by a smaller hailstone if driven by wind, which explains the different ϕ-scales in Fig. 3. In principle, motor cars are well protected under the hail net, while tomatoes may be damaged by hailstones falling through the 10.7 mm net opening (see dotted region in Fig. 3). The contribution of deflected hailstones to damage under the hail net is not known.

4 CONCLUSIONS

•Hail intensity relates to hail damage and economic forces (Sect. 1) may be employed to promote research in this field. At the same time scientific foresight is needed to complement such studies with pro-active research on the growth of hail and measures to counter it.

•Interactions of hailstones with nets depend, apart from the factors in Sect. 2, on impact angle (determined by wind), the net slope, and the relationship between them. These could best be investigated on an *ad hoc* basis.

•Field and laboratory studies provided encouraging results on the efficiency of hail nets (Sect. 3). However, it proved that under a hail net many hailstones impact at subterminal speeds, which may lead to underestimates of ϕ and M but perhaps not of E and N. Hailpad data interpretation under these conditions needs to be fine-tuned.

•The finding that hail damage can occur under a net suggests further experiments to determine Ps (Fig. 2) for different net types and correlating those with ϕ^* (Fig. 3) for selected hail-sensitive products.

•Secondary effects like sagging and tearing caused by large quantities of hail and the various micro-climates created under nets of different densities need particular attention.

5 ACKNOWLEDGEMENT

The field work, partly reported here, was done on a farm of Transvaal Kiwi Orchards (Pty) Ltd. who partially sponsored this research.

REFERENCES

ADMIRAT, P.; GOYER, G.; WOJTIW, L.; CARTE, E.; ROOS, D.; LOZOWSKI, E.: A comparative study of hailstorms in Switzerland, Canada and South Africa. J. Climatol. 5 (1985) 35 - 51.

BEELD Newspaper, Pretoria, 8 Nov. 1985, p. 8.

MUNICH Reinsurance Company, München: Hailstorm (1984) 56 pp.

ROOS, D. vdS.: Hailstone size inferred from dents in cold rolled aluminum sheet. J. Appl. Meteor. (1978) 1234 - 1239.

SENTRAOES Annual Report: Sentraoes (Co-op.) Limited, Ficksburg, S. Afr. (1987) 28 pp.

COMPARISON OF THE SHAPE AND SIZE DISTRIBUTIONS OF RAINDROPS AND HAILSTONES

Pao K. Wang

Department of Meteorology
University of Wisconsin
Madison, WI 53706 U.S.A.

1. INTRODUCTION

The size and shape of cloud and precipitation particles are of central importance to the physics of cloud developments. It is therefore desirable to be able to describe them in a quantitative way. In the past, only the size factor was better understood and was often expressed in "numbers". If shape factor, on the other hand, was usually expressed in words. Recently WANG (1982), WANG AND DENZER (1983), and WANG (1987) developed some simple mathematical expressions that can describe the sizes and basic shapes of raindrops, grauple, hailstones, and ice crystals. Using this technique, WANG ET AL. (1987) analyzed the shape and size distributions of a group of 679 hailstones. The same technique can be applied to study the raindrops. In the following, we will explain the method and then compare the results between hailstones and raindrops.

2. METHOD OF ANALYSIS

The following equation generates shapes resembling conical hailstones and raindrops (WANG, 1982):

$$x = \pm a[1 - (z^2/c^2)]^{1/2} \cos^{-1} (z/\lambda c) \quad (1)$$

where x and z are horizontal and vertical coordinates, $a(=L/\pi)$ is the horizontal semi-axis of the generating ellipse, L is the width along the x-axis, c is 1/2 the vertical dimension, and λ (range from 1 to ∞) is a dimensionless shape factor. Each individual raindrop or hailstone can be fitted by Eq. (1) with proper choice of a, c, and λ. The statistics of these three parameters form the shape and size distributions.

3. COMPARISONS OF THE SHAPE AND SIZE DISTRIBUTIONS OF HAILSTONES AND RAINDROPS

Figs. 1-3 show the distributions of a, c, and λ obtained from fitting 679 hailstones (WANG ET AL., 1987). Figs. 4-6 show the corresponding distributions for a group of hypothetical raindrops. The raindrops are assumed to have a Marshall-Palmer size distribution (PRUPPACHER AND KLETT, 1978) and have shapes described by BEARD AND CHUANG (1987).

It is seen that the hailstones have size (a and c) parameters described by gamma distribution and the shape (λ) parameter by exponential distribution. The raindrops, on the other hand, have size and shape distributions all described by exponential distributions. The raindrop distributions, of course, depend highly on the assumed Marshall-Palmer distribution. Different assumptions may result in different characteristic distributions.

Acknowledgments. This study is partially supported by NSF grants ATM-8317602 and ATM-8718221.

References

BEARD, K. V. AND C. CHUANG: A new model for the equilibrium shapes of raindrops. J. Atmos. Sci., 44, (1987) 1509-1524.

PRUPPACHER, H. R., AND J. D. KLETT: Microphysics of Clouds and Precipitation. Reidel, 714 pp. 1978.

WANG, P. K.: Mathematical description of the shape of conical hydrometeors. J. Atmos. Sci. 39 (1982) 2615-2622.

WANG, P. K.: Two dimensional characterization of polygonally symmetric particles. J. Colloid. Interf. Sci. 117 (1987) 271-281.

WANG, P. K., T. J. GREENWALD, AND J. WANG: A three parameter representation of the shape and size distributions of hailstones- A case study. J. Atmos. Sci. 44 (1987) 1062-1070.

Fig. 1 a-Distribution - Hail

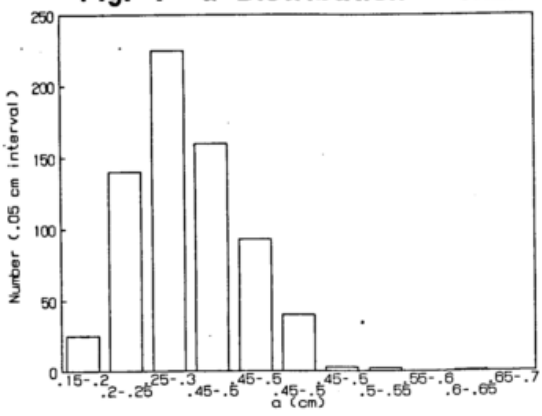


Fig.2 c-Distribution - Hail

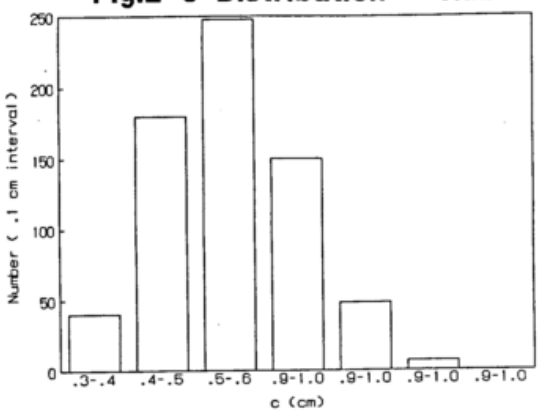


Fig.3 Lambda-Distribution - Hail

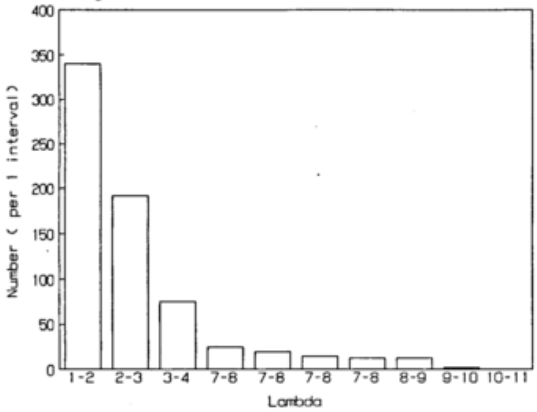


Fig.4 a-Distribution - Raindrops

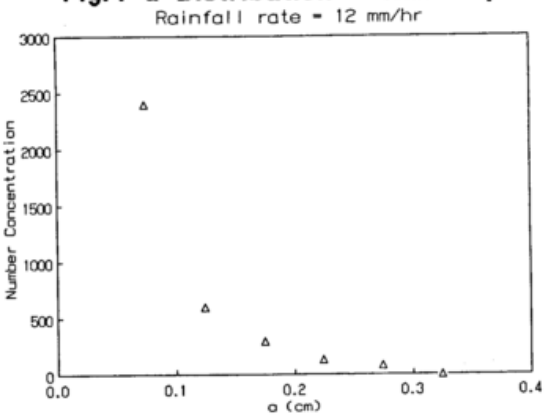


Fig.5 c-Distribution - Raindrops

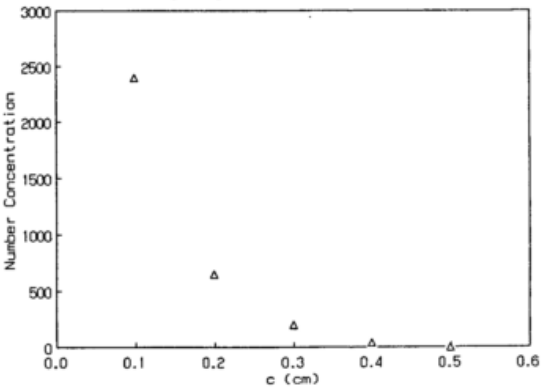
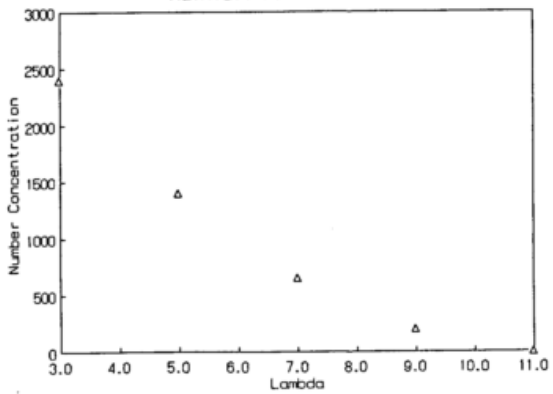


Fig.6 Lambda-distribution Raindrops



TWO STAGE HAILSTONE GROWTH IN THE AUGUST 1, 1981 CCOPE STORM

John C. Pflaum and Roy M. Rasmussen

CIMMS, University of Oklahoma, Norman, OK 73019
Bureau of Reclamation, Denver, CO 80225

1. INTRODUCTION

The two stage process of low density riming followed by wet growth soaking and freezing has received increased attention in recent years as a mechanism of hailstone growth. It has been demonstrated that hailstones can accrete and freeze water at lower densities than previously thought (PFLAUM, 1980) and that such accretion can alter growth trajectories (PFLAUM et al., 1982) as well as overall hail production (FARLEY, 1987). In addition, our ability to simulate internal hailstone structure in laboratory accretions has improved as a result of two-stage growth experiments (PFLAUM, 1984; PRODI et al, 1986).

In describing past attempts at growth simulations, ORVILLE (1977) separated models into those with coupled and those with uncoupled microphysics-dynamics. FARLEY (1987) has discussed in detail the role of low density riming in a coupled model. Aspects of low density riming growth have been incorporated into uncoupled models with varying degrees of completeness (e.g. PFLAUM et al., 1982; HEYMSFIELD, 1983; MILLER AND FANKHAUSER, 1983), but a detailed discussion on the role of low density riming has not appeared. This is the purpose of the current study.

2. MODELING FRAMEWORK

The dynamical framework is a time averaged 3-D wind field derived from multiple Doppler analysis of a hailstorm which occurred on Aug. 1, 1981, during the Cooperative Convective Precipitation Experiment (CCOPE). A general description of the storm has been presented by TUTTLE et. al. (1987) with additional discussion by RASMUSSEN AND HEYMSFIELD (1987b). During the time period between 1630 and 1650 Mountain Daylight Time, the storm became quasi-steady state, with a nearly vertical updraft structure co-located with regions of strong reflectivity.

The microphysical model is that of PARISH and HEYMSFIELD, 1985, with modifications by RASMUSSEN and HEYMSFIELD (1987a). This model allows for variable riming densities and also calculates impact velocities of impinging droplets after RASMUSSEN and HEYMSFIELD (1985) rather than assuming impact at the terminal velocity of the collector.

3. DISCUSSION

RASMUSSEN and HEYMSFIELD (1987b), hereafter referred to as RH, were interested in the potential role of shed drops from hailstones growing in the wet regime and during subsequent melting. Consequently, the emphasis of their focus was on a region of the storm where 1 mm drops could grow into hail larger than 1 cm in diameter. As a first step, these results were examined for indications of low density growth. Fig. 1 shows a composite of two illustrative trajectory types from their discussion. Note that in both cases, hailstones grew to approximately 2 cm in diameter at densities less than 0.9 g-cm^{-3}.

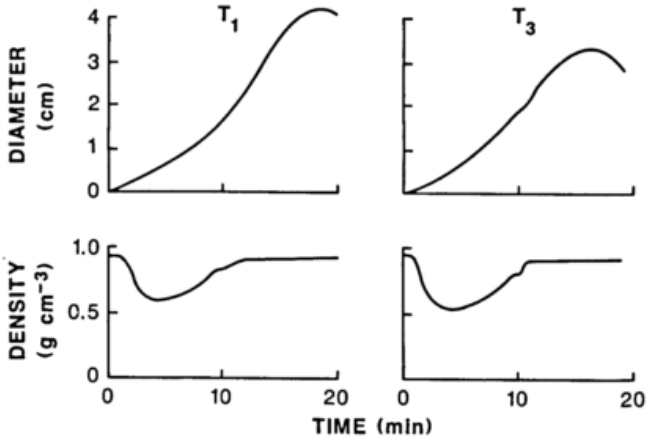


Fig. 1: Density-diameter plots for illustrative trajectories.

To explore this tendency further, 1 mm embryos were released every 500 m throughout the region identified by RH as the important source region for hail formation. Fig. 2 shows maximum hailstone size as a function of initial starting position for embryos released at the 5 km level. Regions where lower density accretion is a factor during growth are stipled. Panel 2A shows the results obtained by RH, who used the following partitioning of water in

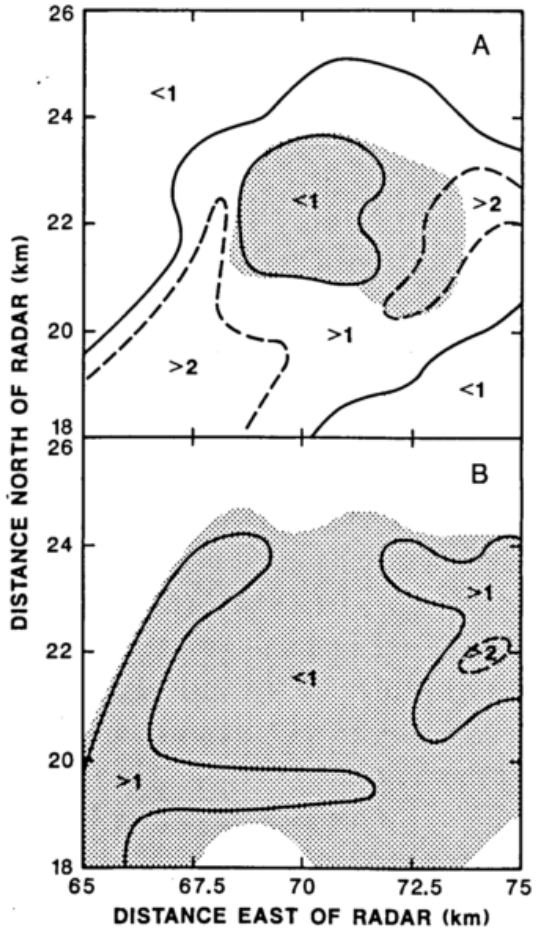


Fig. 2: Maximum hailstone sizes as functions of initial starting locations for the 5 km. level. See text for explanation.

their calculations: 1) above 10 m-s^{-1} adiabatic liquid water is assumed, below 10 m-s^{-1} liquid water is decreased linearly to zero at zero updraft; 2) below -25 C liquid water is linearly depleted to zero at -40 C. Panel 2B shows results for an alternative distribution of liquid water using T-28 data for partial guidance: 1) above 15 m-s^{-1}, 0.65 of adiabatic liquid water is assumed, below 15 m-s^{-1} liquid water is decreased linearly to zero at zero updraft: 2) below -35 C liquid water is linearly depleted to zero at -40 C.

As would be expected, lowered water contents lead to an increased frequency of lower density growth. However, associated with this is an overall reduction in hail size, for the region under consideration. There is a general recession away from the area of strongest updraft. The lower density particles, having slower fall velocities, are carried away from the prime growth locations before they can reach comparable sizes to those grown in more intense cloud environments. If comparable source regions at this level exist for scenario B, they must lie outside the source regions for scenario A.

At the time of preprint deadline, this investigation was just in its very initial stages. Additional material will be available at the conference.

ACKNOWLEDGEMENTS

The authors wish to thank John Tuttle, Jay Miller and Andy Heymsfield of NCAR for their helpful cooperation.

REFERENCES

FARLEY, R.D., 1987: The role of low density riming growth in hail production. J. Cimate Appl. Meteor., 26, 234-254.

HEYMSFIELD, A.J., 1983: Graupel and hail growth mechanisms deduced through particle trajectory calculations. J. Atmos. Sci., 40, 1482-1509.

MILLER, L.J. and J.C. FANKHAUSER, 1983: Radar echo structure, air motion, and hail formation in a large stationary multicellular thunderstorm. J. Atmos. Sci., 40, 2399-2418.

ORVILLE, H.D., 1977: A review of hailstone-hailstorm numerical calculations. Hail: A review of hail science and hail suppression, G.B. Foote and C.A. Knight, Eds., Meteor. Monogr., No. 38, 49-61.

PARRISH, J.L. and A.J. HEYMSFIELD, 1985: A user guide to particle growth and trajectory models. NCAR Tech. Rep. NCAR-TN-259+1A,.

PFLAUM, J.C., 1980: Hail formation via microphysical recycling. J. Atmos. Sci., 37, 160-173.

_____, 1984: New clues for decoding hailstone structure. Bull. Amer. Meteor. Soc., 65, 6, 583-593.

_____, S.P. Nelson and M.P. Foster, 1982: Hail growth studies within a Doppler- radar reconstructed supercell. Preprints, 12th Conference on Severe Storms, San Antonio, Texas, Amer. Meteor. Soc., 1-4.

PRODI, F., G. SANTACTIARA AND A. FRANZINI, 1986: Properties of ice accreted in two stage growth. Quart. J. Roy. Meteor. Soc., 112, 1057-1080.

RASMUSSEN, R.M. and A.J. HEYMSFIELD, 1987a: Melting and shedding of graupel and hail: Part I. Model physics. J. Atmos. Sci., 44, 2754-2763.

_____, and _____, 1987b: Melting and shedding of graupel and hail. Part III. The role of shed drops as hail embryos in the 1 August CCOPE severe storm.

_____, and _____, 1985: A generalized form for impact velocities used to determine graupel accretional densities. J. Atmos. Sci., 42, 2275-2279.

TUTTLE, J.D., G.B. FOOTE AND L.J. MILLER, 1988: Hail growth trajectories in a steady, unvaulted Montana storm. (to be submitted)

ON SOME CHARACTERISTICS DETERMINING THE DEVELOPMENT OF HAIL PROCESSES IN BULGARIA

Petio Simeonov and Dimitar Sirakov

Hydrometeorological Service
blvd.Lenin 66, Sofia, Bulgaria

Department of Meteorology
Sofia University,Bulgaria

1. INTRODUCTION

Studies of various meso- and local-scale atmospheric characteristics associated with the development of severe hail storms, are still topical. This is due to the remaining problems of hail forecasting and evaluation of hail supression effect, discussed in the review papers of ABSHAEV et.al. (1984,p.23),DIRKS (1983,p.1065). The present study is based on a long-term complex of data from days with development of hail processes. The area is about 1500 sq.km in Northwest Bulgaria.

2. DATA AND INITIAL CHARACTERISTICS

Data from 120 days with hail and crop damages, covering the period 1961-1972 without seeding and denoted as BG1-sample, and from 178 seeded days with hailstorms (with and without damages), covering the 1974-1984 period and denoted as BG2-sample, are treated. Surface data for p, T, T_d, $\vec{V}$ and diurnal precipitation total Q are taken from 4 meteorological stations in the region. The closest to the commencement of the process synoptic charts and upper-air soundings at CAO-Sofia are used. The hail crop damage data are obtained from the State Insurance Institute and its representativeness is discussed in SIMEONOV(1984, p.21).Radar data (1974-1984) are used to determine the duration and the path of the hail process.

A set of characteristics has been computed by the use of a specially created program for upper-air sounding processing, applying the particle method and, in case of air-mass situations, the method with the mean humidity in the layer surface - 850 hPa. A total of more than 40 different characteristics has been studied. Here we show the following: TMAX and TD - surface maximum air temperature and dew-point temperature, averaged over the 4 stations; DT7,6,5,4 and DTM - temperature differences between sounding and adiabatic curves at 700, 600, 500 and 400 hPa levels and the maximum differences; SDT75 and SDT74 - sums of corresponding DT; WM - the maximum vertical velocity; DHW>15 - depth of the layer with W>15 m/sec; ETOT - total positive energy of instability; $\bar{q}$ - mean specific humidity in the first 100 hPa over the surface;SW - precipitable water; CCL - cloud condensation level; TTI and KI - instability indices; HO - height of $0^{o}C$ isoterm; SD-total humidity deficit from 850,700 and 500 hPa levels;V7,5,3 and DD7,5,3 - wind velocity and direction at the corresponding pressure levels, as well as their differences V37,DD37, etc.; DH85, DH7, DH5,DOT - indices of the Laplacians over the geopotentials at AT850,700, and 500 hPa and OT1000-500; VF and DTF - speed of the front and the temperature contrast around it,TGR and SGR - total duration and path of registered cells in hail-dangerous stage. The following parameters are

treated as response variables: DA and RDA - hail damaged area and this one reduced to 100% loss area; SQ4 - total diurnal precipitation measured at 4 stations.

3. RESULTS AND DISCUSSIONS

Eighty four percent of the storms in BG1 and 85% in BG2 have commenced between12 and 20 hours LT. The parameters of sample distributions, shown in Table 1, indicate similarity between BG1 and BG2 of TMAX, TD,SDT75, DTM,SW,KI,CCL,DD5,V5 and VF. More significant differences are observed in RDA, because all days in the control sample BG1 are with damages area, while in BG2 only 32% of the days have RDA. Closest to Gaussian distribution are TMAX,SDT75,SW,CCL and KI. Asymmetric are the distributions of RDA, DHW > 15, DTM,V5,DD5,TGR and SGR.

Attached to the characteristics of BG1 and BG2 are the tests of Kolmogorov-Smirnov (KS),Mann-Whitney (MW) and Student (t) used to test the zero hypotjesis H_o for belonging to the same general population. H_o is not rejected at acceptable significance levels for SDT75, CCL, KI, SD(Table 2) H_o is rejected for DOT and the related parameters DH85 and DH7. For DHW > 15 significance levels are small.

A stepwise multivariate regression analysis with orthogonal transformation of variables is applied. Computations are made with 42 predictors and 3 response variables (DA,RDA and SQ4),after many variations and transformations of variables and 25 tests selections with respect to the correlation coefficient r_{y/x_i} , residual variance ΣS^2 and distribution symmetry $(Y_i-\hat{Y}_i)$ in appropriate intervals. The Fisher criterion for adequacy of the regression is also checked. The best regression equations are:

$$\hat{DA} = a_o + a_1(DT5)^3 + a_2(SDT74)^3 + a_3(DTM) + a_4(DT5)^2 + a_5(DTM)^2 + a_6(V37)^3 \qquad (1)$$

$$\hat{RDA} = a_o + a_1(DT5)^3 + a_2(DT5)^2 + a_3(DT74)^3 + a_4(DTM)^2 \qquad (2)$$

The values of a_i and part of estimate parameters are shown in Table 3.

No strong and significant correlations have been obtained between the precipitation and the thermodynamic predictors (r_{y/x_i} not greater than 0,65 when including 12 different predictors, and only in frontal cases). In this respect certain extention of the study is required, including more stations. As preliminary result a linear regression is obtained between DA and (SGR x TGR) with r = 0,86, but only on 21 cases, selected from BG2-sample as more vigorous.

4. CONCLUSION

These statistical studies on relatively large information on hailstorm situations allowed to test distributions and inter-relations between thermodynamic characteristics of the atmosphere, some cloud parameters, hail damages and precipitation.The attempt to evaluate the seeding effect in BG2 by the use of Eqs.(1) and (2) leads to interesting results, which are subject to further publications.

TABLE 1. Basic statistics for some variables from BG1 and BG2 samples.

variable	BG	TMAX	TD	SDT75	DTM	DHW>15	SW	CCL	KI	HO	SD	V5	DD5	DOT	VF	RDA	TGR	SGR
statistic	N°	°C	°C	°C	°C	km	g/kg	km	°C	km	°C	m/s	°	gpm	km/h	ha	min	km
minimum	1	15,6	6,7	3,0	1,6	0,50	6,0	0,52	20	1,64	1,0	0	0	-68	8	1	-	-
	2	17,6	8,0	3,0	2,6	0,10	5,8	0,51	20	2,09	0,4	1	3	-42	9	6	7	3
average	1	26,9	15,6	8,4	6,0	7,23	10,6	1,64	31	3,37	18,2	12	216	-7	34	539	-	-
	2	26,9	15,9	8,6	6,2	7,67	10,9	1,60	31	3,42	19,3	12	216	4	36	609	90	41
maximum	1	37,3	20,9	15,6	14,1	11,00	14,1	3,28	44	4,53	41,1	30	352	60	67	10326	-	-
	2	37,3	20,2	16,9	12,1	11,75	14,8	2,60	45	4,45	49,6	35	365	83	95	12546	332	316
std. dev.	1	4,1	2,5	2,4	2,2	2,23	1,8	0,47	5	0,55	8,5	7	82	25	13	1336	-	-
	2	3,6	2,1	2,5	1,8	2,16	1,7	0,40	5	0,47	9,1	7	87	22	14	1786	69	41
median	1	27,2	15,7	8,5	5,6	7,87	10,7	1,65	32	3,44	18,8	10	230	-10	33	139	-	-
	2	27,4	16,2	8,5	6,1	8,00	10,9	1,62	31	3,49	17,6	10	240	1	33	88	69	30
asymmetry	1	-0,2	-0,5	0,1	1,0	-1,0	-0,2	0,3	-0,0	-0,4	-0,2	0,7	-0,9	0,2	0,6	5,2	-	-
	2	-0,3	-0,9	0,2	0,8	-1,0	-0,3	-0,3	-0,1	-0,5	0,7	0,9	-0,9	0,6	0,9	5,7	1,4	2,8

TABLE 2. Comparison of variables from samples BG1 and BG2 at H_o: equality of distributions and means.

test	KS - test		MW - test			Two-tailed t-test at α = 0,05		
variable	max. distance DN	level of significance p	average rank 1st group	average rank 2nd group	prob. z for (=) or (>)	computed t	level of significance p	H_o rejected
SDT75	0,098	0,50	145	151	0,46	-0,699	0,48	no
DHW>15	0,268	$0,67.10^{-4}$	139	156	0,10	-1,678	0,09	no
CCL	0,099	0,48	152	147	0,67	0,805	0,42	no
KI	0,230	0,001	149	150	0,94	0,014	0,99	no
SD	0,109	0,36	146	152	0,52	-1,096	0,27	no
DOT	0,317	$0,11.10^{-5}$	127	165	$0,16.10^{-3}$	-4,104	$0,53.10^{-4}$	yes

TABLE 3. Regression coefficients in Eqs. 1 and 2 and some statistics of the sample BG1 from 120 cases.

N°	coefficients a_o	a_1	a_2	a_3	a_4	a_5	a_6	statistics r_y/x_1	-S/2 %	S/2 %	ΣS^2	F
1	-3,6	19,3	0,764	396	-143	-62,2	0,019	0,90	15	62 | 11	$0,18.10^7$	5,0
2	576	11,6	-86,6	0,264	-12,9	-	-	0,92	13	63 | 12	$0,27.10^6$	6,5

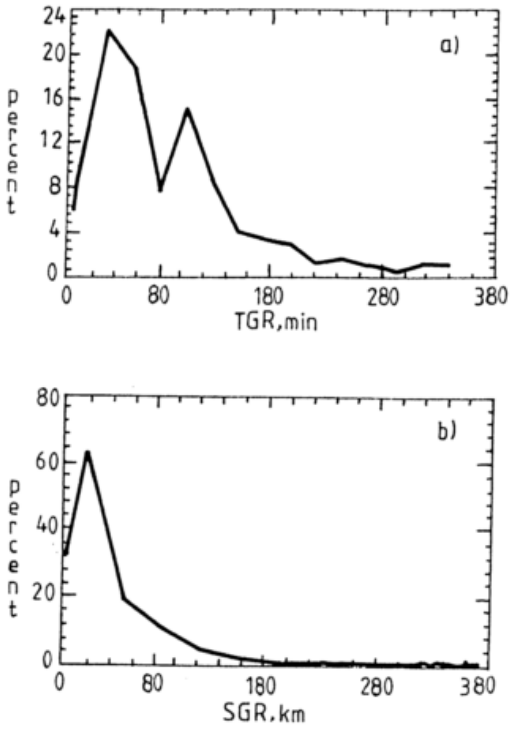


Fig. 1. Relative frequency polygon:
a) total daily lifetime and
b) total daily path covered by hail cells

5. REFERENCES

ABSHAEV, M.T.; BIBILASHVILI, N.S.; BURTZEV, I.I.; FEDCHENKO, L.M.; KHORGUANI, V.G.: Results of hail-storm studies and hail suppression activities in USSR. Proceedings of the 9th Int. Cloud Phys. Conf., Tallin, August, 1984, 393-396.

DIRKS, R.A.: Progress in weather modification research 1979-1982. Reviews of Geophysics and Space Physics, Vol.21, No.5, (1983), U.S.Nat. Rep. to IUGG, 1065-1076.

SIMEONOV, P.: Information on Bulgarian hail suppression activities and crop hail insurance. Report of the Meeting of Experts, Nalchik, Sept. 1984, WMO Re. No.5/TDN°97 (1986), 21-35.

MEASUREMENTS OF CLOUD DROPS, THEIR AEROSOL CONTENT AND CLOUD INTERSTITIAL NUCLEI NEAR THE BASES OF CONVECTIVE CLOUDS IN ISRAEL

Zev Levin, Eli Ganor, Colin Price, Doron Pardess

Department of Geophysics and Planetary Sciences,
Tel Aviv University, Ramat Aviv, 69978, Israel

1. INTRODUCTION

It has been shown by many investigators that formation of acid rain is a complex process which depends on the origin of the air masses forming the clouds, the aerosol particles that are incorporated into the cloud and into rain drops and the microphysics of the cloud (eg. PARUNGO et al 1987). In Israel, rain is formed mostly by convective cold continental clouds within frontal and post frontal systems. These systems approach the coast from the West, Southwest and Northwest bringing with them air from varying origins and carrying aerosols of different compositions. LEVIN and LINDBERG (1979) showed that the aerosol particles in Israel can be characterised as desert particles superimposed with particles of maritime and pollution sources. The concentrations of these non desert particles strongly depend on the directions of air trajectories and contain sea salt particles as well as sulfate and fly ash.

The purpose of this study was to investigate the role of sulfate particles in the acidification of rain in Israel with a special emphasis on the role of desert particles in neutralizing it.

For this purpose a field station on the top of mount Meron (1120 m ASL) was used. During the winter months and during the passage of cold fronts the top of this mountain and the measuring station are often covered by convective clouds whose bases are often at around 1000m ASL. Measurements were conducted before, during and after the passage of the cloud. On some occasions measurements were carried out just below cloud base to help determine the characteristics of the aerosol particles entering the cloud.

2. METHOD OF SAMPLING

The method of sampling consisted of collecting aerosols or drops directly on carbon coated electron microscope (EM) grids which were placed in a cascade impactor. It was possible to determine whether the particles were dry or wet based on the imprints they left on the surface. The imprints were used to determine drop sizes using a laboratory calibration conducted with known drop sizes. A constant ratio of 0.9 was found between drop and imprint size for the size range of the cloud drops. After determining the size of the drops, the samples were postcoated with $BaCl_2$ (BIGG et al. 1974; MAMANE and DE PENA 1978). When sulfate was present in the particles, a reaction with the $BaCl_2$ occured after exposure to 75% relative humidity for two hours creating $BaSO_4$. These reactions appeared as halos when again viewed through an EM.

Fig. 1a presents an example of aerosols after impaction on carbon as seen using the Scanning Electron Microscope SEM. Fig. 1b presents the same aerosols and the reactions which are produced after postcoating with $BaCl_2$.

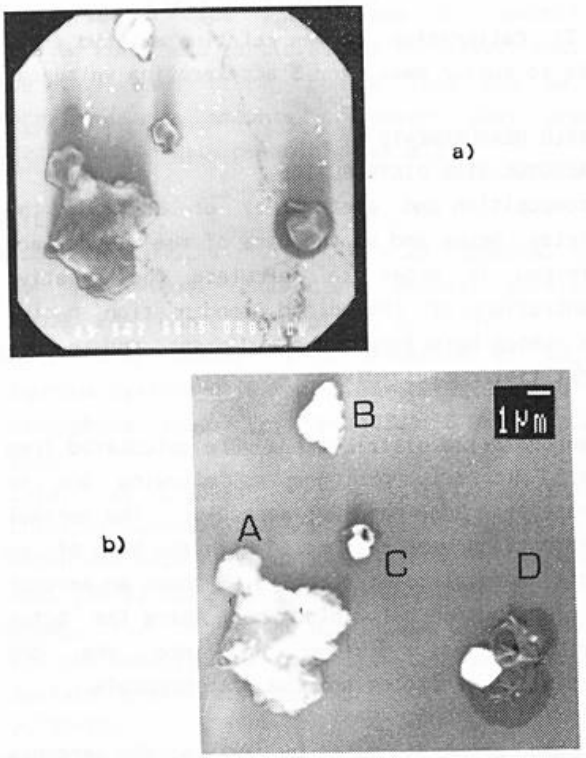


Fig. 1: SEM photograph of a) individual aerosols sampled on carbon, and b) of the same particles after coating with $BaCl_2$ and exposure to 75% relative humidity.

Two of the particles, marked A and B, are desert particles which remained as dry interstitial nuclei in the cloud. Since no reaction with $BaCl_2$ occured these particles did not contain hygroscopic sulfate. On the other hand, the droplets marked C

and D both reacted with the $BaCl_2$ indicating the presence of hygroscopic sulfate. The amount of sulfur was determined by counting the X-ray radiation emitted by the excited sulfur atoms at the 2320 eV wavelength, compared to that emitted by a standard sample of Cobalt at the 6920 eV wavelength. This measurement was then compared with calibration curves which had been previously obtained in the laboratory using $(NH_4)_2SO_4$ particles of known sizes (Fig. 2). As an example, the sulfur masses in the droplets C and D are marked on the 15KeV acceleration voltage line in Fig. 2.

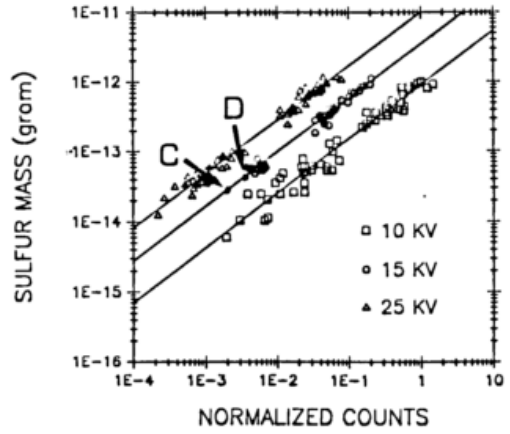


Fig. 2: Calibration curves relating emitted x-ray counts to sulfur mass, for 3 accelerating voltages.

3. FIELD MEASUREMENTS

3.1 AEROSOL SIZE DISTRIBUTION

The composition and state (wet or dry) of the particles below and at the base of the clouds were determined in order to calculate the relative concentrations of the cloud condensation nuclei (CCN) which help form the cloud drops, and the dry interstitial nuclei (CIN).

The aerosol size distributions were calculated from electron microscope photographs, allowing one to seperate the dry and wet aerosols. The aerosol concentrations were calibrated with the help of an optical aerosol counter. Fig. 3 shows an aerosol size distribution below cloud base where the total distribution was divided up into the dry interstitial particles and the haze droplets.

The haze droplets make up 79% of the aerosols sampled, and the remaining 21% are the dry CIN. The total concentration of aerosols in this distribution is 392 cm^{-3}. Within the cloud base a concentration of 712 cm^{-3} was measured, suggesting that those Aitken nuclei not detected by our optical counter below cloud base grew to their haze size within the cloud base, entering the range of detection.

The CIN are mainly desert aerosols containing Mg, Al, Si, Ca, and K. The CCN, on the other hand, are mainly sulfates as well as salts such as NaCl, and MgCl.

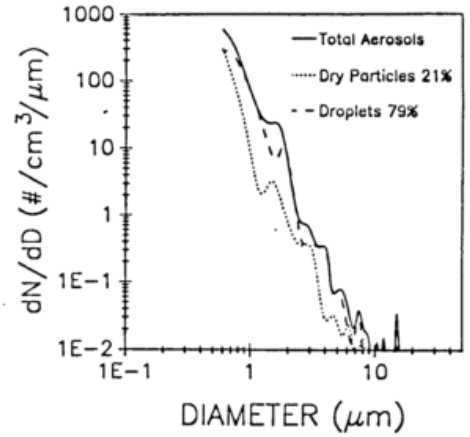


Fig. 3: Aerosol size distribution below cloud showing the distributions of CIN and droplets which make up the total distribution.

3.2 SULFATE CONCENTRATION IN CLOUD DROPLETS

Using the sulfur calibration curves in Fig.2 one can calculate for each drop size, the appropriate sulfur mass. In this way the sulfur mass distribution can be determined (Fig.4). From the volume distribution of the droplets which can be found using the size distribution in Fig. 3, and the sulfur mass distribution in Fig. 4 one can obtain the average sulfur concentration in the cloud droplets. For the example shown in the figures, about 33 mg of sulfur per cm^3 of cloud water is found. Assuming that all the sulfur contained within the CCN is in the form of sulfate, one can determine the concentration of sulfate in the cloud water.

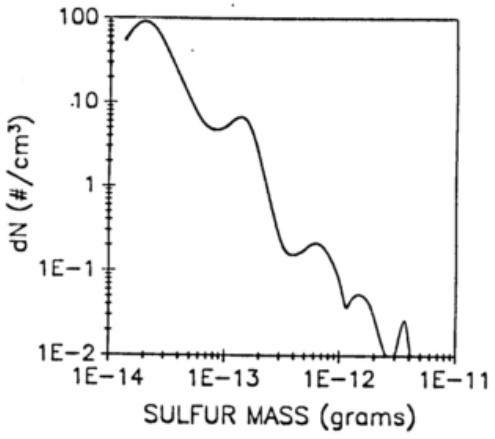


Fig. 4: The concentration of droplets according to their sulfur mass.

The above calculations were carried out both below and above cloud base, for airmasses of different origins. The sulfate concentration in the airmass and in the cloud water is shown for each case in Table 1.

Even though the hygroscopic sulfate concentration in the air increases in the cloud, it is most

probably due to inaccuracies in our measurements, and not from the oxidation of SO_2 in the drops. The life time of drops in the cloud base is too short to allow for SO_2 oxidation to occur (HEGG and HOBBS 1978). However, the sulfate concentration in the drops decreases by 30-50% within the cloudbase. This is a result of dilution of the sulfate in the drops as they grow by condensation in the early stages of the cloud development.

	Below Cloud Base	Within Cloud Base
Northerly winds	A=7.1 µg/m³ C=56.1 mg/cm³	A=22 µg/m³ C=38.4 mg/cm³
Westerly winds	A=8.2 µg/m³ C=172.2 mg/cm³	A=33 µg/m³ C=99.75 mg/cm³
South westerly winds	A=6.7 µg/m³ C=33.3 mg/cm³	- -

Table 1.: The concentration of sulfate in air (A) and in cloud water (C) below and within clouds as a function of the wind direction

3.3 pH OF CLOUD DROPLETS

The pH of cloud droplets was measured by sampling droplets on pH paper placed in each stage of the cascade impactor. This provides some information on the variation of the pH with drop size. Even though these measurements were carried out at different dates, they provided clues to the changes of pH during the early stages of cloud growth, and can be compared with that measured during rain. During this measurement the airflow was mostly from the west and the results, which are shown in Fig. 5, show a decrease in acidity with increase in drop size. As the drops grow by condensation, the sulfate in solution is diluted, increasing the pH. The rain produced by this cloud had a pH of 4.8.

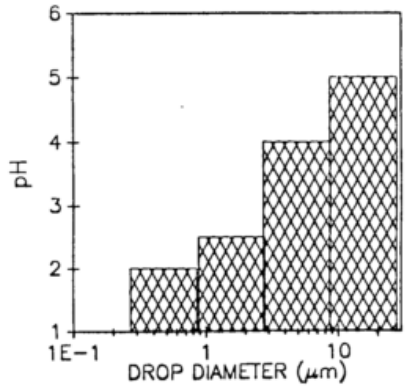


Fig. 5: pH of cloud drops as a function of size

3.4 ALKALINE RAIN

One set of measurements was carried out during a storm accompanied by winds from the SW carrying large amounts of desert dust. The clouds on this day produced rain which had a pH as high as 8.2. This corresponds to 121 µg/l of sulfate in the rainwater. However, the amount of sulfate in the haze particles below cloud base was 33 mg/cm^3. As shown in section 3.3, measurements during another field expedition to Mt. Meron showed that the pH of the haze and cloud droplets is very acidic (2.5). Therefore, the fact that the cloud droplets contain high concentrations of sulfate and no carbonatious particles, while the pH of the rain is very high, suggests that these CIN are scavenged by the rain and neutralize the acidity caused by the sulfate. It seems that part of the Ca found in the CIN neutralizes the sulfate in the droplets by forming gypsum ($CaSO_4$). The extra $CaCO_3$ remains dissociated in solution causing the high pH value. Alkaline rain associated with SW air flow in Israel has also been measured by MAMANE (1987).

4. CONCLUSIONS

We found that the source of sulfate in cloud droplets is predominantly from nucleation scavenging. As the drops grow by condensation the sulfate concentration decreases due to the dilution of the droplets.

The pH of the rain in Israel resulting from these clouds depends on the source of the aerosols. Northerly and westerly flows produce acidic precipitation (pH 4.8), since the amounts of calcium carbonate particles are relatively low. On the other hand storms coming from the SW and carrying large amounts of desert dust produce precipitation with pH as high as 8.2.

REFERENCES

BIGG, E.K.; ONO, A.; WILLIAMS, J.A: Chemical tests for individual submicron aerosol particles. Atmos. Environ. (1974) Vol. 8, p. 1-13.

HEGG, D.A; HOBBS, P.V.: Oxidation of SO_2 in Aqueous Systems with Particular Reference to the Atmosphere. Atmos. Environ.(1978) Vol.12,p.241-253.

LEVIN, Z; LINDBERG, J.D.: Size Distribution, Chemical Composition and Optical Properties of Urban and Desert Aerosols in Israel. J. Geophys. Res. (1979) Vol. 84, p. 6941-6950.

MAMANE, Y.; DE PENA, R.G.: A Quantitative Method for the Detection of Individual Submicrometer Size Sulfate Particles. Atmos. Environ. (1978) Vol. 12, p. 69-82.

MAMANE, Y.; DAYAN, U.; MILLER, J.M.: Contribution of Alkaline and Acidic Sources to Precipitation in Israel. Sci. Tot. Environ.(1987) Vol.61, p. 15-27.

PARUNGO, F.; NAGAMOTO, C.; MADEL, R.: A Study of the Mechanisms of Acid Rain Formation. J. Atmos. Sci. (1987) Vol. 44, p. 3162-3174.

ACKNOWLEDGEMENTS

We would like to thank the National Council for Research and Development, Israel and the G.S.F., Munchen, F.R.G. for supporting this research.

Microphysical Characteristics of Convective Clouds over the South-Central United States

Michael R. Poellot[1] and John C. Pflaum[2]

[1] University of North Dakota, Grand Forks, ND
[2] CIMMS, University of Oklahoma, Norman, OK

1. INTRODUCTION

As part of an effort to evaluate the potential for rain enhancement over the south-central United States, the University of North Dakota instrumented Citation II aircraft was used to penetrate developing convective clouds during the period September 9 through September 28, 1987. This measurement program, in support of the Bureau of Reclamation Southwest Cooperative Program, represents the second year of an investigation into the microphysical characteristics of these cloud systems. A previous study (POELLOT, 1987) focused on the persistence of supercooled liquid water and used data collected during a brief field program in 1986. The present study will attempt to characterize the 1987 clouds in terms of their cloud water and ice particle content and possible precipitation formation mechanisms.

2. FIELD OPERATIONS

During the data collection program the aircraft was based in Norman, Oklahoma, and cloud systems were sampled over the western 2/3 of that state. The Citation was configured with the following measurement capabilities: state parameters (pressure, dewpoint, reverse flow and total temperature sensors); three-dimensional winds (inertial platform and flow angle probe); cloud microphysics (PMS FSSP, 2D-C and 1D-P probes and a JW liquid water content meter); and forward-looking video. We were fortunate to have encountered a very active period of convection, given the length of the program. Data from 60 clouds sampled during 7 missions were analyzed for this study.

Cloud sampling legs were flown generally in the vicinity of either the -5°C or -12°C level. These levels were selected in order to study the availability of supercooled liquid water and to investigate the ice process in these clouds in consideration of potential cloud modification activities. Cloud candidates were selected visually based on an appearance of positive vertical growth and a "hard" or sharp boundary at cloud top. These are characteristics of clouds typically chosen as potential seeding candidates. The initial penetrations were normally made within about 300-600 m of cloud top shortly after the top climbed through the sampling level.

Repeated sampling of the cloud continued until liquid water was nearly depleted at the sampling level or operational or safety considerations precluded further measurement. During each mission the aircraft made a descent sounding to below cloud base to determine the thermodynamic cloud environment and to measure conditions near cloud base. On several occasions passes were made through growing towers at several levels from just above cloud base up to cloud top.

3. DATA

There are many possible stratifications of the data. As a first look, it was decided that two basic stratifications are penetration temperature and cloud diameter. It is important to keep in mind that cloud diameter

Table 1. Summary of Measurements

length	W (m s^{-1})	-5°C N	-5°C peak LWC (g m^{-3})	-5°C frac. adia. LWC	-5°C peak FSSP conc. (cm^{-3})	-5°C FSSP MVD (μm)	-5°C peak 2D conc. (ℓ$^{-1}$)	-12°C N	-12°C peak LWC (g m^{-3})	-12°C frac. adia. LWC	-12°C peak FSSP conc. (cm^{-3})	-12°C FSSP MVD (μm)	-12°C peak 2D conc (ℓ$^{-1}$)
<2 km	< 0	25	.56	.14	178	25.6	6.9	9	.99	.22	199	26.3	7.5
	0-2	19	1.09	.29	274	24.4	1.7	5	.98	.20	203	25.1	5.3
	2-4	9	1.33	.37	279	25.0	0.2	7	1.29	.29	350	23.5	0.3
	≥ 4	11	1.97	.44	358	23.5	2.4	4	1.53	.30	510	22.1	0
≥2 km <4 km	< 0	15	1.03	.24	324	22.4	9.2	1	.70	.16	203	25.9	13.0
	0-2	11	1.27	.31	292	24.7	37.5	5	1.24	.32	397	23.1	9.1
	2-4	13	1.70	.44	340	24.3	11.4	1	1.20	.35	321	23.8	94.0
	≥ 4	14	2.77	.72	398	24.2	6.9	4	2.50	.47	392	22.9	0.5
≥4 km	< 0	12	1.13	.29	347	20.5	22.1	0	–	–	–	–	–
	0-2	9	1.90	.47	372	24.2	30.8	3	1.63	.43	439	23.9	108.5
	2-4	6	2.63	.59	312	25.6	26.7	4	1.53	.34	553	23.8	41.1
	≥ 4	4	2.23	.49	434	23.0	37.3	2	2.85	.66	388	25.1	24.9

is really penetration length. In some cases this corresponds to a path through the middle of the cloud and is a good approximation of cloud diameter. In other cases, the penetrations consisted of a glancing path through the edge of a more mature system. Thus, cloud penetrations of similar length do not necessarily imply similar dynamical and microphysical conditions. As an effort to sort out this complexity, a further stratification was made by average vertical motion during the penetration.

A subset of measured parameters was chosen for summary in this report and is shown in Table 1. The penetration length corresponds to the distance in cloud with detectable liquid water. The liquid water contents (LWC) are those measured by the JW probe. The FSSP data have been corrected for known instrument errors according to DYE and BAUMGARDNER (1984). Droplet diameters are represented by the mean volume weighted diameter at the time of peak number concentration. The 2D data have been processed to reject artifacts by a method similar to that of COOPER (1978). All values have been averaged over the number of samples (N) indicated.

In general the clouds were found to have relatively high cloud liquid water contents. The positively buoyant cloud regions had average peak LWC of 1.0 to 2.9 gm^{-3} with individual values as high as 4.4 gm^{-3}. The peak LWC was directly related to updraft velocity. The cloud water was contained in relatively large droplets (mean volume diameter of 22-26 μm). In addition, the average peak droplet concentrations were fairly low (180-550 m^{-3}). This shows the influence of the maritime tropical air mass which dominates the south-central states in the summer months.

As one would expect, the longer samples and those with stronger updrafts had peak LWC values which were more nearly adiabatic. Four updraft regions with peak LWC greater than 90% of the adiabatic value were encountered. At -5°C, the stronger updraft samples also had higher droplet concentrations and somewhat smaller drops on the average.

The peak concentrations of larger hydrometeors at the -12°C level (as detected by the 2D-C) were not very different from those measured near -5°C. This suggests that the nucleation and growth of ice particles to detectable sizes was not significant between these levels. However, the peak 2D concentrations

were typically greater in the larger clouds. This was expected because the larger clouds were generally older.

4. PRECIPITATION FORMATION MECHANISMS

It is a challenging problem to identify precipitation development mechanisms using only occasional line measurements through a developing cloud. Most of the time, either no precipitation-sized particles were present or else the precipitation process was already well under way and it was difficult to separate what was observed from possible paths of formation. However, on September 14, the timing of the penetrations in relation to cloud development and the associated microphysical data allowed for a clearer picture to evolve. (A short film will be shown at this time).

The clouds sampled on this mission were associated with but visually separate from a very strong convective complex (tops > 17 km). The surface dewpoint temperature was greater than 22°C in the area. The droplet spectra were broad as seen in Fig. 1, and the larger particles detected by the 2D-C were predominantly liquid drops (Fig. 2). Since the towers were sampled early in their lifetimes, shortly after passing through the -5°C level, and they were isolated from the mature system, recycling of melted ice particles as a source of large drops was unlikely. Thus, it seems highly probable that these clouds were developing precipitation initially through the warm rain process.

Although it is not as certain as in the above case, there are indications that this is a primary mode of initial precipitation development in the clouds studied during this project. Drops grew in the updrafts and were carried to colder temperatures as the clouds developed. Here, they froze and rimed into graupel and were carried back down to lower levels by downdrafts. During many of the

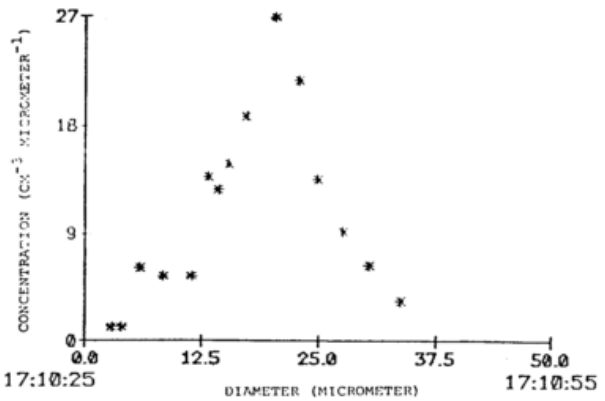


Fig. 1. Sample FSSP droplet spectrum from September 14.

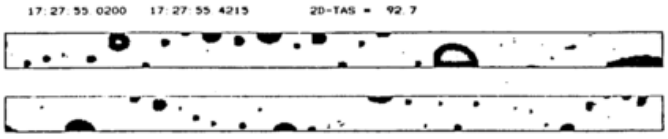


Fig. 2. Sample of 2D images from September 14. Vertical dimension of bar represents 1 mm.

penetrations, graupel was first observed in the downdrafts. There is evidence that some of these particles were being recycled upwards at the edges of updraft regions. Later contributions to the precip process may have come from graupel grown on depositionally formed crystals from ice nuclei or as a result of secondary ice particle production via the Hallett-Mossop mechanism. However, during the early stages of development, it appears that most of the larger graupel evolved from frozen drops.

ACKNOWLEDGEMENTS

This work was supported by Bureau of Reclamation Grant No. 4-FC-81-03780.

REFERENCES

DYE, J. E. and D. BAUMGARDNER, 1984: Evaluation of the forward scattering spectrometer probe. Part I: Electronic and optical studies. J. Atmos. and Oceanic Tech., 1, 329-344.

COOPER, W. A., 1978: Cloud physics investigations by the University of Wyoming in HIPLEX 1977. Final Report, University of Wyoming, Laramie, 320 pp.

POELLOT, M. R., 1987: Observations of liquid water persistence and the development of ice in Oklahoma convective clouds. Prepr. 11th Conf. on Weather Modification, Edmonton, Alta., 79-82.

INVESTIGATION BY TRACER METHOD OF THE CONVECTIVE CELLS OF CUMULONIMBUS CLOUDS

L.A. Dinevich
Hail Suppression Services of State Hydrometeorological Committee of U.S.S.R.
S.S. Šalavėjus
Institute of Physica of Academy of Sciences of Lithuanian S.S.R.

1. INTRODUCTION

Experiments on the convective cells investigation by tracer methods are conducted since about two decades. Natural and artificial radionuclides as well as non-radioactive substances are used as tracers (GATZ 1977, ŠALAVĖJUS 1984). Theory and practice of the active actions on clouds shows that broader knowledge on processes occuring in the Cumulonimbus clouds are necessary.

2. INVESTIGATION METHODS

In our experiments the ^{32}P, ^{210}Po, heavy water, metallic indium and ice-making reagents AgI and PbI_2 were used as tracers. They were injected into a cloud by the hail-suppressing rockets. The tracer spraying was carried out by the explosions in a determined part of the cloud. The ice-making reagents AgI and PbI_2 were injected into a cloud by the burning of a pyro-mixture along the rockets trajectory. Experiments were carried out on the polygone of the area 400 km^2. The meteorological, radar, rocket,radio-communication and automobil services interacted in course of the experiments which allowed to conduct successfully the complex experiments. The radar information arrived from the meteorological radar location point. For evaluation of the variability of the precipitation intensity and their total amount a dense pluviometric network was constructed on the polygone. The sampler for the precipitation sampling during the separate time intervals was made from a firm material and was of an upturned pyramide shape with the base equal to 2x4 m. For the separate raindrops collection the plane-tables were used. Their exposition lasted from 1 to 30 s depending on the precipitation intensity. The plane-tables were covered by the chromatographic paper on which a dye was spred. The raindrops fallen on the paper let bright coloured spots on it. After their radii the raindrops parameters were determined. The dried paper was put into the contact with a special photoemulsion. The ^{210}Po was determined in precipitation samples after its spontaneous deposition on copper or silver discs. For the determination of the chemical yield the ^{208}Po was used.

3. RESULTS OF THE FIELD EXPERIMENTS

The development of clouds on the day the experiment was carried out (17^{th} July 1972) was conditioned by a cold front. The tracer ^{210}Po was injected at the altitude of 4 km into the frontal part of a convective cell being in a quasi-stationary state. The cloud into which ^{210}Po was injected consisted of the two cells. After the radar data the altitude of the upper boundary of the both cells reached 10 km. The cells were registered by the attenuation of the radiosignal up to 48dB. /For conveniency, the cell into which the tracer was injected we call the ex-

perimental cell E and the other cells - the background ones F. The analysis of the data of the pluviometric network and of the precipitations amount in sampling points showed that the most voluminous precipitations fell from the background cell. The distance between the cells which contours were determined by the isolines 48 dB was about 5-6 km. As it is clear from the Fig.I, the distribution of the tracer high fallout densities on the polygone coincides with the experimental cell moving trajectory.

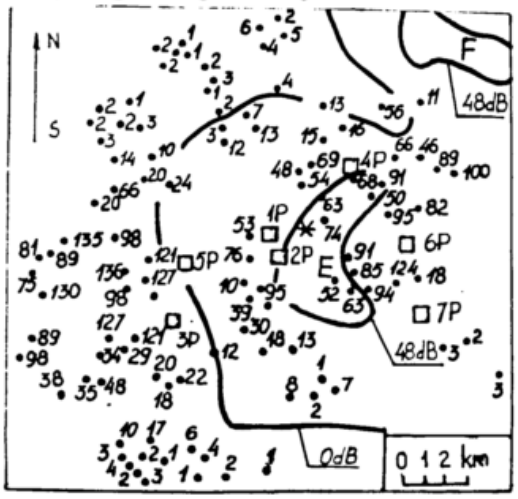


Fig.1. The ^{210}Po fallout field

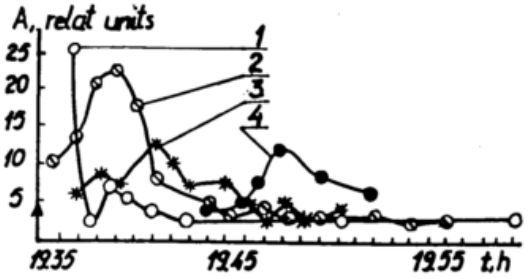


Fig.2. The ^{210}Po concentration change in the raindrops on sampling points

At the same time, in regions above which the cell F of the same cloud moved, the fallout density exceeded not the background values despite of the fact that from this cell 5-6 times more precipitation fell than from the cell E. The arriving of ^{210}Po on the cloud displacement front coincides in time with the displacement trajectory of the cells E back part. In several points of the polygone the α-radioactivity of separate raindrops during the rain was measured. On the Fig. 2 the variation of the specific α-activity of ^{210}Po in points Nos. 4,5,6,7 (the corresponding curves 1,2,3,4) is shown. From Fih.2 follows that α-activity in precipitation decreased up to the background values in point No.4 after 3 min, in points Nos.6,7 - after 6 and 7 min, respectively. The background specific α-activity of ^{210}Po ranged from 3 to 10 relative units. On the curve 2 (Fig.2) a maximum is seen which arose 13 min after the tracer injection moment. This maximum coincides in time with the displacement of the back part of the cloud. Thus a conclusion can be made that in the sampling points the ^{210}Po was measured in precipitations falling from the experimental cell.

On the 18th July 1977 the clouds development was conditioned by a cold front. Its displacement velocity was about 40-50 km h^{-1}. The convective cloudiness development was promoted by the great instability energy. The convections upper level reached 11 km. ^{210}Po was injected into a cell being in a back part of the cloud. At the injection moment a rain with ice-graupel falling from this cell was observed at the ground level. The cell E was in a quasi-stationary state. The ^{210}Po injection height was about 4 km, air temperature at this level was equal to 0^0 C. At the tracer injection moment close to the cell E an another cell was observed which was registered by the radiosignal attenuation up to 48 dB as well, the distance between the centers of the cells was about 6 km. Unlike to the previous experiment the

^{210}Po fallout density maximum is observed here in the region of its injection but the tracer spreaded throughout the entire cell. In points Nos.1,2 the tracer arrival to raindrops was registered already 3 min after the injection. This may be explained, apparently, by the existence of downdraugh flows with velocity 25-30m s^{-1} in the tracer spreading zone inside the cell. The ^{210}Po transport with precipitation droplets velocities in points Nos. 1,2 are 25 and 23 m s^{-1}, respectively. At the ^{210}Po injection moment the point No.3 was under the cell F. In the raindrops fallen out only the background α-radioactivity of ^{210}Po was found.It is evidence of that, firstly, the tracer is washed out on the small area in the injection epicentre region and, secondly, ^{210}Po spreads only inside of the experimental cell.

On the 27th July 1985 the cold front moved above the polygone from SW. At the distance of 17 km from the radar on the asimuth 196° a raining cell was revealed. To the right of it on the asimuth 175° at the distance of 13 km an another cell selected by us as an experimental one was observed. At the moment of maximal development the cells parameters were: the upper boundary height - 11 km, the maximal radar reflectivity height ($\eta = 10^{-9} cm^{-1}$) -6,5 km. On the level of the updraught flow maximal velocity (H=5 km) the ^{210}Po was injected. At the tracer injection moment the distance between the centers of the cells limited by the isocontours $\eta = 10^{-9}$ cm^{-1} was equal to 2-3 km, and the isoecho contour by $\eta = 10^{-10}$ cm^{-1} united the both cells into the one zone. Despite of the fact that rain fell out from the both cells, ^{210}Po was found only in precipitation falling from the experimental cell.

The ground level measurements showed that ^{210}Po is distributed in the cell non-uniformly. Its maximal concentrations are registered in the centre of the cell, the minimal ones - at its borders. The ^{210}Po removal from a cell being in dissipation stage occurs mainly on its displacement trajectory above the polygone. The field experiments conducted by us showed that a substance injected into the convective cell being in the quasi-stationary stage spreads mainly in this cell and is not carried to the other cells. We made a conclusion that between the cells a hydrodynamical bond exists and the transport of a substance is not observed. The conclusion has a practical value (besides the pure scientifical value). By the active action for the hail formation prevention on the multi-cellar processes using cooling- or ice-creating reagents we must form the calculated reagent concentrations in the every cell depending on its development stage and not to take into account the active actions on the other cells. Moreover, from the conclusion follows that by the identical development conditions the neighbour cells (not acted upon) may be taken as control ones for evaluating the active actions effect.

CATZ D.F.: A review of chemical tracer experiments on precipitation systems. Atmos. Environ.11,(1977),Nr.10. P. 945 -953.

ШАЛАВЕЮС С.С.: Исследование конвективных облаков при помощи химических трассеров. Физика атмосферы. 3(1977). С. 15-35.

INVESTIGATING MIXING AND THE ACTIVATION OF ICE WITH GASEOUS TRACER TECHNIQUES

J. L. Stith[1], M. K. Politovich[2], R. F. Reinking[2],
A. G. Detwiler[3], and P. L. Smith[3]

[1]University of North Dakota, Grand Forks, ND; [2]NOAA/ERL, Boulder, CO
[3]South Dakota School of Mines and Technology, Rapid City, SD.

1. INTRODUCTION

Fast response analyzers for insoluble tracer gases, such as sulfur hexafluoride (SF_6), make real time measurements of tracers possible in small clouds (STITH and BENNER, 1987). Some applications of these relatively new techniques to studying mixing and activation of AgI cloud seeding aerosols in cumuli are reported here. One objective of these studies is to compare the effects from releases directly into the mid to upper supercooled cloud regions with releases into updrafts at the cloud base. It is assumed that, during typical sampling periods (~20 min.), the AgI aerosols disperse with the SF_6 until nucleation scavenging removes the particles. Within these periods any ice produced by the aerosol should become detectable by optical sizing instruments, such as Particle Measuring Systems 2DC probes.

2. INSTRUMENTATION AND METHODOLOGY

Previous SF_6 tracer experiments are reported in STITH et al., (1986) and STITH and BENNER (1987). In the present work, airborne releases of gaseous SF_6 along with AgI-AgCl aerosols from acetone burners were performed on 22 and 28 June, 1987, near Dickinson, ND. Release rates of SF_6 were 0.5 and 0.3 kg km^{-1} for 22 June and 28 June, respectively. In addition to a release aircraft, the University of North Dakota Cessna Citation and the South Dakota School of Mines T-28 research aircraft were used for sampling. Details on the instrumentation, calibration procedures, and aerosol characteristics are given in STITH et al., (1986) and STITH and BENNER (1987).

Measurements of SF_6 from releases directly into ice-free supercooled clouds at temperature levels warmer than -7°C (the approximate activation point of the AgI aerosol) have not revealed the formation of ice (e.g., STITH et al., 1986). This suggests that neither the SF_6 release method, nor the treatment aircraft itself produced ice particles (e.g., as suggested by RANGNO and HOBBS 1984), at least at these relatively warm temperatures. Further tests, using SF_6 only, are planned to confirm these results over a broader range of temperatures.

3. OBSERVATIONS OF MIXING AND ICE ACTIVATION

On 22 June, the upper region of a small cumulus congestus cloud was treated by a single pass at -11.5°C. The cloud base was at +11°C. The measurements obtained during the sampling passes at -13.5°C (300 m above the treatment altitude) are shown in Fig. 1. The cloud was free of ice (Fig. 1 a) at the time of treatment. On the second sampling pass (Fig. 1 b) small ice particles developed in three regions which together comprised about half of the cloud width. The boundaries and shapes of these regions correlated well with those of the tracer regions; this is rather convincing evidence that the ice was formed by the AgI treatment and did not develop naturally in the cloud. However, the amounts of ice observed per unit amount of tracer varied somewhat from region to region; this may be a result of slightly different growth

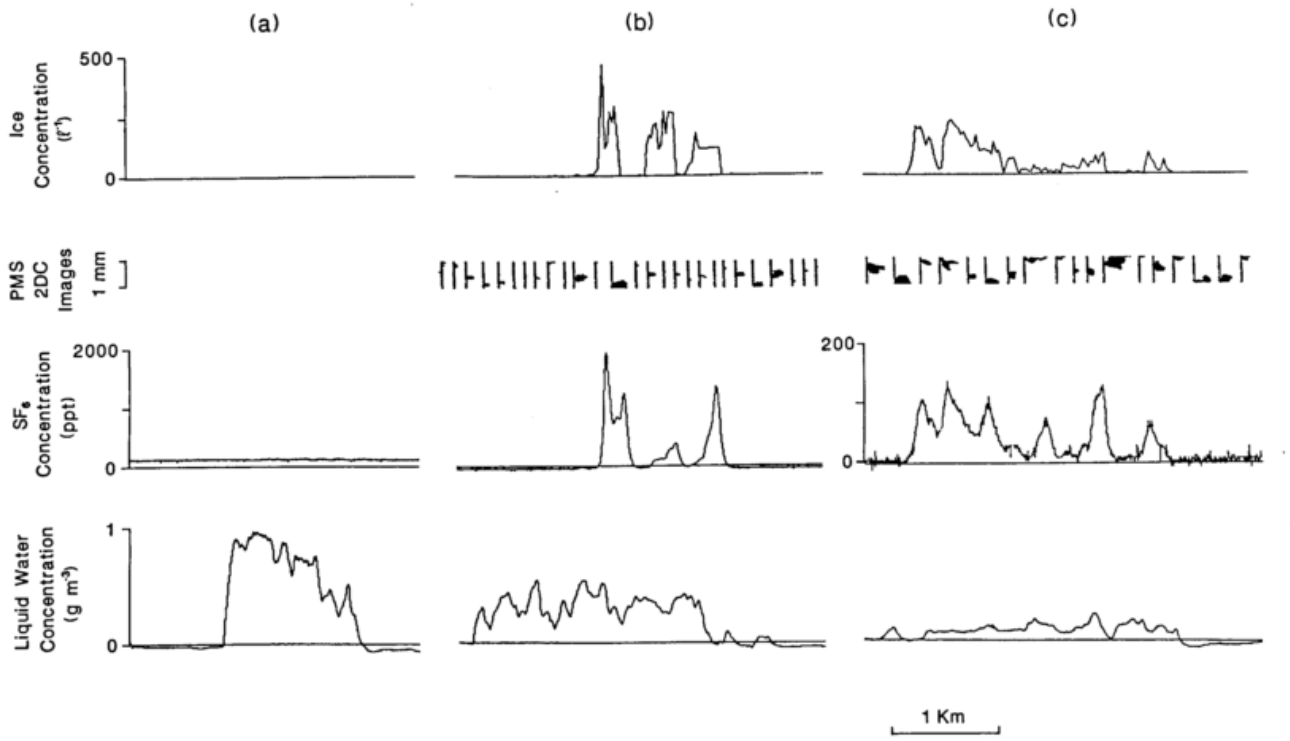


Fig. 1 Concentrations of ice particles (from 2DC shadow - or), 2DC images, SF_6 concentrations, and liquid water (from JW) on 22 June, 1987, 300 m above treatment altitude (at a temperature of -13.5°C at: (a) the time of treatment, (b) 4 min after treatment, and (c) 7 min after treatment.

conditions present in these regions during the 4 min between treatment and sampling. On the third pass, some 7 min after treatment, the ice, liquid water, and SF_6 were well mixed throughout the cloud top and the ice particles had grown larger (Fig. 1 c); as before, the amounts of ice per unit amount of SF_6 in the cloud varied with location.

On 28 June, a cumulus cloud of similar size was treated for 15 min by a continuous release during orbits across the horizontal wind shear axis in updrafts at cloud base (2.2 km MSL and 5.8°C). Sampling was done along the horizontal wind shear axis at various altitudes. Early in the sampling period, at lower levels of the cloud, the tracer region was quite narrow and concentrated (Fig. 2 b), as found in other clouds from our earlier studies (STITH et al., 1986). In contrast, near the top of the cloud, 8 min later, the tracer was well mixed (Fig. 3). Some 2.5 min prior to the pass at the cloud top, relatively concentrated tracer was found at midlevels of the cloud, mixed through about half the updraft on the upshear side; more dilute tracer was found downshear in downdraft (Fig. 2 a). Small ice particles were well mixed throughout the cold (-12°C) cloud top region and were found only in downdrafts at warmer (-7°C) midlevels.

These results confirm the expectation that, at a given level in a cloud, the ice concentrations are closely related to the history of the air. For example, at the -12°C cloud top region (Fig. 3), ice had only begun to develop in the upshear portion of the cloud. On the downshear side higher ice concentrations were observed in the downdraft region, which was bringing air down from colder temperatures. At the -7°C level of the cloud the updrafts with concentrated tracer had not yet developed measurable ice, while the downdrafts with more dilute tracer had appreciable ice.

These and our earlier studies indicate that the tracer, whether directly released into cumuli or carried up from cloud base, mixes

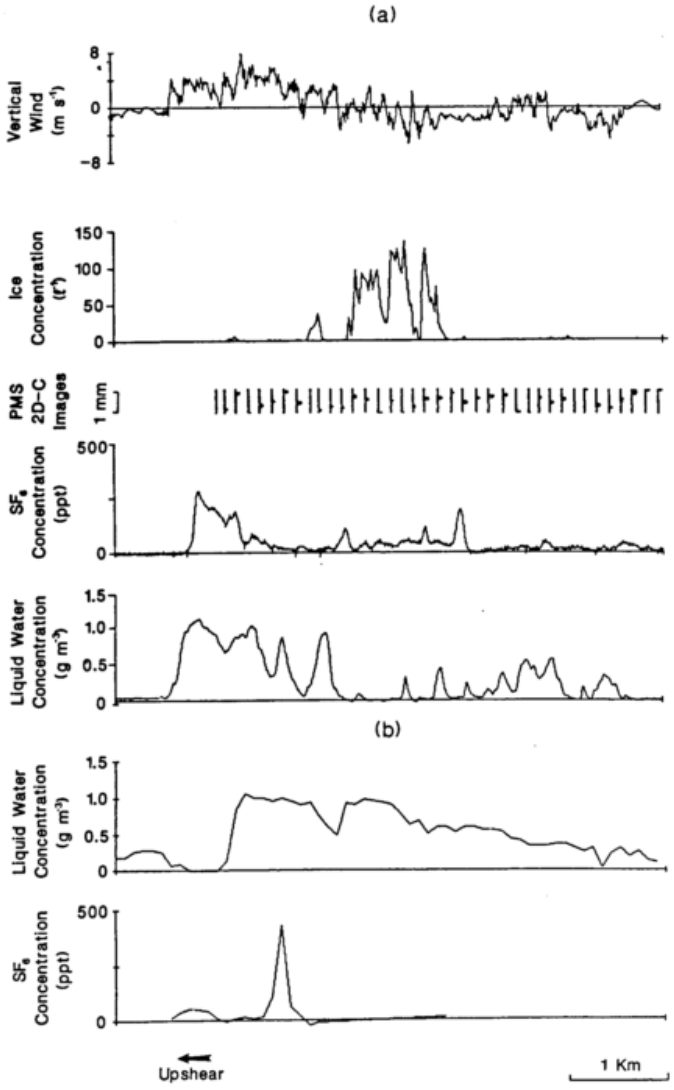


Fig. 2 (a) Vertical wind, 2DC images, and the concentrations of ice, SF_6 and liquid water on 28 June, 1987, at cloud midlevels (3.5 km altitude and -7°C) 17 min after the start of treatment. The cloud was treated for 15 min at the cloud base. (b) Concentrations of liquid water and SF_6 at lower levels of the cloud (3.0 km altitude) 11.5 min after the start of treatment.

completely through the upper regions of the cloud. As far as the concentration of ice is concerned, the history of the air found at a given location in the cloud may be at least as important as the amount of ice forming nuclei present, at least in the early stages of ice development.

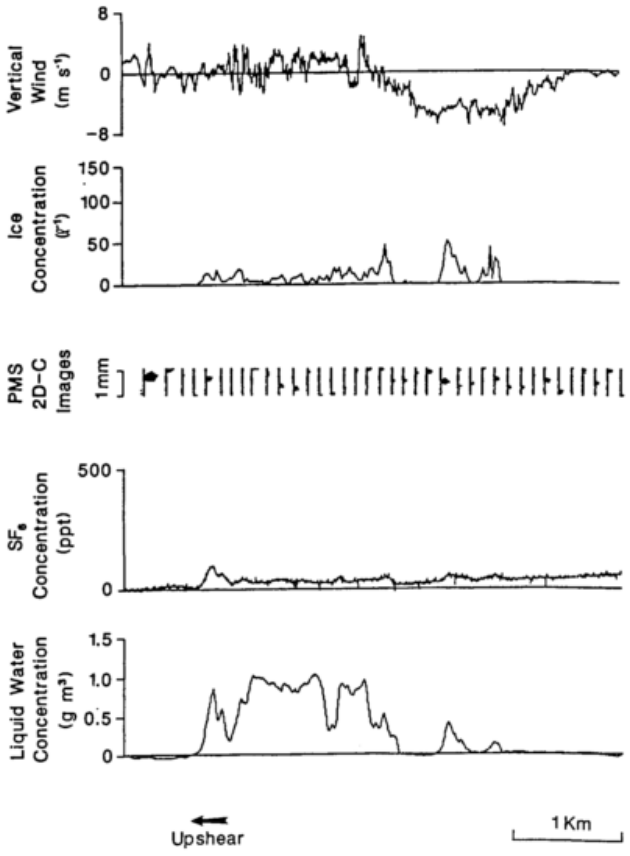


Fig. 3 As in Fig. 2a, except near the top of the cloud at an altitude of 5km (-12°C) 19.5 min after the start of treatment.

ACKNOWLEDGEMNETS

Support was provided by the North Dakota Atmospheric Resource Board through contract number NDARB-UND-NOAA-87 and by NSF grant ATM-8620145.

REFERENCES

STITH, J.L., D.A. GRIFFITH, R.L. ROSE, J.A. FLUECK, J.R. MILLER, Jr. and P.L. SMITH, 1986: Aircraft observations of transport and diffusion in clouds. J. Climate Appl. Meteor., 25, 1959-1970.

STITH J.L., and R.L. BENNER, 1987: Applications of fast response continuous SF_6 analyzers to in situ cloud studies. J. Atmos. Oceanic Technol., 4, 599-619.

RANGNO, A.L., and P.V. HOBBS, 1984: Further observations of the production of ice particles in clouds by aircraft. J. Climate Appl. Meteor., 23, 985-987.

FIRST FORMATION OF PRECIPITATION IN AN ISOLATED CONVECTIVE CLOUD

Charles A. Knight

National Center for Atmospheric Research*
Boulder, Colorado 80307, USA

1. INTRODUCTION

In a previous study, a Lagrangian-style precipitation growth model was applied to a small, relatively steady-state thunderstorm, assuming that all precipitation was formed by primary ice nucleation and subsequent growth (Knight, 1987). The resulting, modelled field of ice particle size distribution was many orders of magnitude deficient in the smaller particles needed to produce the observed rain from the storm, leading to the conclusion that the primary ice process was not a large, direct contributor to the precipitation. The style of modelling of the precipitation field lends itself well to interpreting field data in terms of mechanisms of ice-phase precipitation initiation, and is applied here to a very well-observed case of first echo formation in a cold-based, continental cloud.

The first purpose is to see whether there is a compelling need to invoke some "exotic" process like ice multiplication or accretion on giant aerosols to explain the first-echo formation. The general philosophy is as before: in view of the several serious approximations involved, the model results have to be very different from the observations before the need will be compelling. Second, the treatment is planned as a test for the category model treatment of precipitation. Category models have the potential for numerical spreading problems arising from the rather coarse categorization of particle size and fall velocity. The seriousness of these can be assessed by comparison with the present treatment, which avoids those particular problems at the expense of some other serious limitations.

*The National Center for Atmospheric Research is sponsored by the National Science Foundation.

2. THE STORM AND THE DYNAMIC MODEL

The CCOPE case of 19 July 1981 is used: a brief, isolated cumulonimbus with a cold cloud base and a lot of microphysical measurements (Dye *et al.*, 1986), and with a numerically modelled wind field (Helsdon and Farley, 1987).

The radar reflectivity and visual cloud-top history are shown in Fig. 1 along with aircraft penetration times and heights. This was essentially a fairly large, single-impulse convective turret that rose to about 10 km and developed a radar echo briefly to 45 dBZ_e as high as 8 km. Cloud base was at +1°C and droplet concentration was about 600 cm^{-3}.

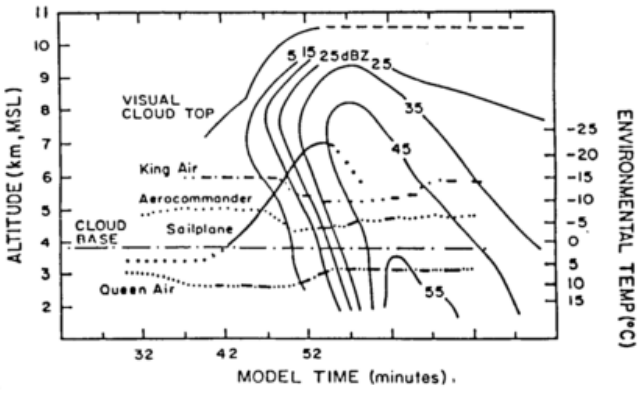


Fig. 1. The radar visual cloud top, and aircraft penetration history of the 19 July 1981 cloud, from Dye *et al.* (1986), using model time from Helsdon and Farley (1987).

The two-dimensional, time-dependent model used for the wind and cloud water fields was originally run for electrification studies and has been compared with the observations in some detail by Helsdon and Farley (1987). It employs both ice and coalescence processes using exponential size distributions and an eddy diffusion entrainment scheme, and reproduces the time history of cloud size and radar echo development rather well. Since its cloud base is about 1 km lower than that observed, here the wind and cloud-water fields are shifted up 1 km, the liquid water content is reduced by 2 g kg^{-1} and the updraft multiplied by 0.7 to bring the maximum values close to those observed in the storm. The model resolution is 200 m. The updraft in the model is about 2 km in diameter, the cloud top increases from 5 km at 21 min to 11 km at 51 min and the first echo at 5 dBZ_e was at 43 min.

3. PRECIPITATION MODEL PERFORMANCE AND RESULTS

Here we assume the "standard" ice nucleus population $n(\ell^{-1}) = 10^{-(0.25T+5)}$, with T in C°. The bins used to collect the numbers of growing ice particles were always 1 km square (x,z) with 15 sizes, the largest of which was "greater than 10 mm diameter". Three starting resolutions used were $(x = z,t)$ = (0.25 km, 0.5 min), (0.5 km, 1 min), and (1 km, 2 min). The coarsest was unsatisfactory, but the finest was little more than a smoothed version of the middle one, so most runs used the 0.5 km, 1 min resolution.

As in previous work (Knight, 1987), the philosophy is to use very simple microphysics and test the sensitivity. The initial attitude is that the assumed wind and cloud-water fields are so approximate that few if any microphysical subtleties are justified. Density/drag coefficient specifications were from previous work. Case 4: ρ_{ice} (g cm^{-3}) = 0.3D + 0.1, with C_D = -5D + 4 for R< 0.6 cm and = 1 otherwise. Case 2: ρ_{ice} = 0.125D + 0.45, with C_D = 0.75. Case 4 is just about the lowest ice density that is at all reasonable, and gives very low terminal velocities. Case 2 goes to extremes in the other direction, for this cloud. (At 7 km and 1 g m^{-3} of cloud water, a case 2 particle reaches 1 m s^{-1} in about 3 min while a case 4 particle takes 11 min.) A five minute time delay before the start of growth was imposed or not, giving four "runs".

Table 1 shows the first echo times and the maximum dBZ_e at 7.5 km for the observed storm, the Helsdon and Farley treatment and the four cases herein.

Table 1

	first echo time (min) at 5 dBZ_e	max dBZ_e at 7.5 km
observed	45	47
Helsdon and Farley	43	50
a) Case 4, 5 min	43	17
b) Case 4, no delay	38	36
c) Case 2, 5 min	41	28
d) Case 2, no delay	37	38

Figure 2 shows the observed concentrations of total ice and mm ice during the early echo stage at

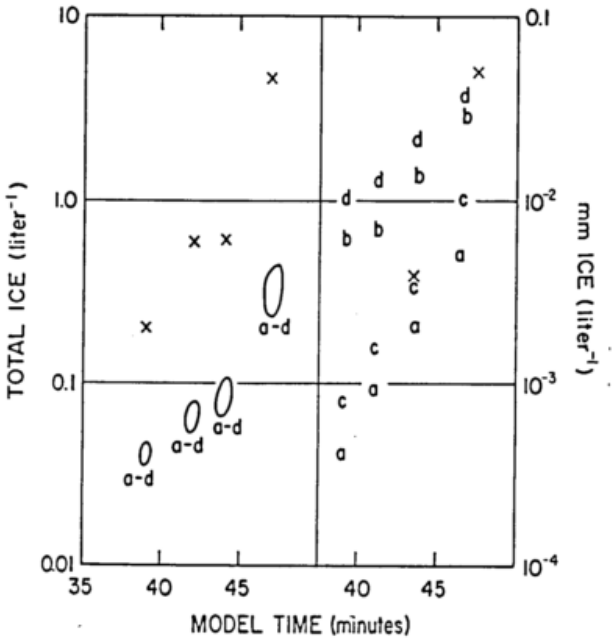


Fig. 2. Observed (x) and calculated (a – d; see Table 1) maximum 1-km-average total ice and mm ice concentrations.

6 km (–15°C) compared with the four modelled cases. Considering the major model uncertainties (the 2-D wind field, the very crude representation of the time to the start of rapid riming, and the cloud water field), the agreement is not bad. Furthermore, the maximum ice particle sizes observed in the storm were approximately those modelled. No compelling need for additional mechanisms is revealed.

In the later stages the observed maximum total ice rose to about 50 ℓ^{-1} at –15°C. The model results never approach that, but the modelled updraft does not decay as abruptly as the observed one evidently did, and the model was not run past 60 minutes.

It is interesting that nearly all of the mm-sized ice produced in this model nucleated at –15°C or above. There were 808 trajectories that produced mm ice at model time 57 minutes within the strongest radar echo region (x = 13 to 17, z = 4 to 9 km), adding all four cases together, at 0.5 km resolution. Of these, one started with nucleation at 7.0 km (–20°C), 23 at 6.5 km (–17°C), 68 at 6.0 km (–13°C), and the remaining 716 from 5.5 to 4.0 km. The warm ice nucleation totally dominates the first echo formation, and in fact nearly all of the formation of precipitation-sized particles. If real, this would have obvious implications not only for weather modification, but for the sensitivity of the time history of radar reflectivity and the precipitation to the "most active" — that is the warmest — ice nuclei, whose natural concentration is very poorly known and probably quite variable.

4. CONCLUSION AND DISCUSSION

This study does not reveal a strong need for any other mechanism than the ordinary ice process to explain the first precipitation formation in the 19 July CCOPE cloud. In the writer's view, a three-dimensional wind field with better correspondence to observation, and a better-verified cloud water field would be needed to justify a more sophisticated microphysical treatment for comparison of results to observations. Two main shortcomings of the present, very simple model are the exclusion of the strong temperature-dependence of the vapor growth stage before riming starts and the exclusion of melting and evaporation. Nevertheless, in combination with the previous results on the 12 June 1981 storm, the present results are consistent with the hypotheses that explain the highly anomalous ice concentrations often observed in terms of multiplication processes that require the presence of precipitation-sized ice in order to operate.

The strong dominance of the early and warm nucleation events in the formation of the largest ice particles appears to be due to the need for "embryos" of these particles to be introduced into the updraft in the mature phase of this cloud. Nucleation within the mature updraft leads only to small ice that is ejected into the anvil.

5. ACKNOWLEDGEMENTS

Richard Farley kindly furnished the model results that were used here for the wind and cloud water fields. Joanne Parrish programmed and ran the precipitation model.

6. REFERENCES

DYE, J. E., J. J. Jones, W. P. Winn, T. A. Cerni, B. Gardiner, D. Lamb, R. L. Pitter, J. Hallett, and C. P. R. Saunders, 1986. Early electrification and precipitation development in a small, isolated Montana cumulonimbus. *J. Geoph. Res.*, **91**, D1, 1231–1247.

HELSDON, J. H. Jr., and R. D. Farley, 1987. A numerical modelling study of a Montana thunderstorm: 1. Model results versus observations involving nonelectrical aspects. *J. Geoph. Res.*, **92**, D5, 5645–5659.

KNIGHT, C. A., 1987. Precipitation formation in a convective storm. *J. Atmos. Sci.*, **44**, 2712–2726.

RETRIEVAL OF DYNAMIC VARIABLES IN DOPPLER-OBSERVED CONVECTIVE CLOUD SYSTEMS

Carl E. Hane

National Severe Storms Laboratory, NOAA
Norman, Oklahoma U.S.A.

1. INTRODUCTION

For more than a decade multiple Doppler radar observations have been analyzed by various investigators to produce the three wind velocity components within convective storms. Efforts have been made in the last decade to use this velocity information to retrieve perturbation pressure and buoyancy fields over the same three-dimensional volume where wind information is available. Development and testing of these techniques are described by Gal-Chen (1978), Hane et al. (1981), Roux et al. (1984), Brandes (1984), and others. This paper briefly describes one retrieval method and presents some examples of retrieved fields from several case studies that the author has carried out as a part of either past or current work.

2. EXPLANATION OF METHOD

The retrieval method is described in detail by Hane et al (1981). A two-dimensional Poisson equation for pressure is formed from the horizontal momentum equations and solved using velocity measurements from Doppler radar to specify forcing terms. The vertical momentum equation is then solved for buoyancy using pressure analyses on successive horizontal planes and the velocity measurements. Pressure and buoyancy solutions are in the form of deviations from horizontal averages.

3. EXAMPLES OF RETRIEVED FIELDS

The first example comes from the case study of a tornadic thunderstorm. Fig. 1 shows perturbation pressure deviations (hPa or mb) and velocity vectors on a horizontal plane 500 m above the ground about seven minutes prior to the appearance of the tornado. Velocity information is available over a network of grid points spaced at 1 km in both horizontal directions. The tornado developed coincident with the left-most of the two vorticity maxima (circled plus signs). Low pressure coincident with the left-most vorticity maximum (the mesocyclone) results primarily from the strong vorticity. Perturbation pressure also has a hydrostatic component in all solution fields as is exemplified by the relatively high pressure in the rain-cooled area in the north-central portion of the domain.

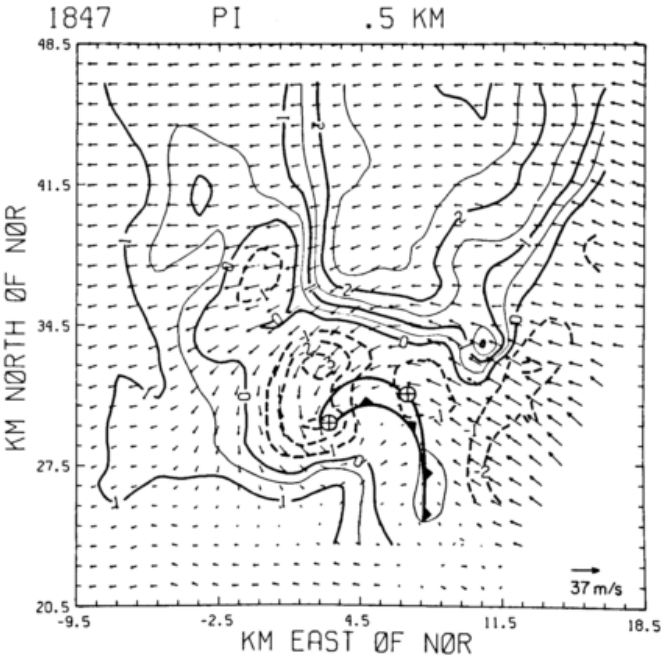


Fig. 1. Perturbation pressure and vector wind in tornadic storm case at z=500 m. Pressure in hPa (mb); gust front labeled by cold frontal symbols; ⊕ marks vorticity maxima; solid line, arc-shaped updraft area.

A second example comes from analysis of thunderstorms embedded within a mesoscale convective system (MCS). Rotunno and Klemp (1982) have shown that based on linear theory a pressure gradient should be present across deep convective updrafts with high pressure on the upshear side and low pressure on the

downshear side. The shear referred to here is the vertical shear of the horizontal wind characteristic of the storm environment. In the tornadic storm case referenced above this relationship held true in the middle and upper levels of the storm where there were pressure differences of 3-6 hPa across the updraft at all levels. In the example shown in Fig. 2 the same relationship holds quite well for the convective region of an MCS (only 20% of the analyzed domain is shown). Three strong updrafts are in the area shown, which is located along the eastern edge of a north-south line. In the northernmost and easternmost updrafts the pressure falls across the updraft in an east-northeasterly direction, in good agreement with the orientation of the shear vector at this level from an environmental sounding. In the southwest updraft the pressure decreases proceeding northward through the updraft; a valid question here is how one defines the environmental shear in the case of a convective cell embedded within a larger-scale rain area.

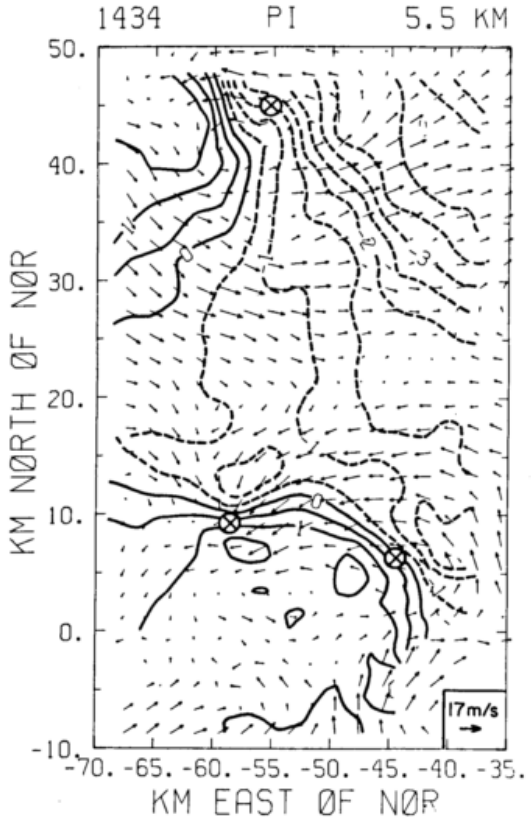


Fig. 2. As in Fig. 1, but for MCS case at z=5.5 km; ⊗ =updraft maxima.

A third example results from analysis of a large multicellular thunderstorm that occurred over the High Plains of the United States. This data set is unique in that an attempt was made to use aircraft and sounding data in the storm environment along with the in-storm Doppler winds to produce a complete set of wind components in a regularly bounded three-dimensional region within and surrounding the storm. The two previous examples, in contrast, produced solutions within irregularly bounded regions characterized by the presence of rainwater. The pressure field in the upper portion of the storm is shown in Fig. 3. Coincident with the strongly positive pressure anomaly is a region of pronounced divergence marking the center of the storm's upper level outflow. The updraft maximum is coincident with the high pressure center in this case; the linear theory relation seems to break down due to very weak environmental shear at this altitude and highly perturbed flow. The buoyancy field at this time (not shown) contains a warm plume in the strong updraft region, most pronounced between 3 and 10.5 km. The maximum deviation buoyancy is 9-10°K at z=9 km, in good agreement with undilute parcel calculations from a nearby sounding. The updraft top is very cold owing to localized ascent through a stable environment. It is clear that the

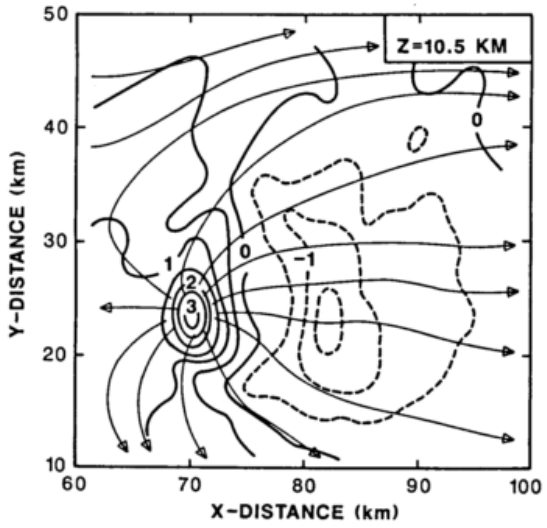


Fig. 3. As in Fig. 1, but streamlines drawn rather than wind vectors for High Plains multicell storm at z=10.5 km.

positive pressure anomaly in Fig. 3 is in large part hydrostatically produced.

4. EFFECTS OF ERRORS AND LACKING DATA

The accuracy of retrievals is entirely dependent upon the quality of the analyzed velocity field. A parameter can be calculated following the retrieval of pressure that provides a measure of the input velocity quality. This parameter is essentially a normalized integral of the difference between the retrieved horizontal pressure gradients and those gradients calculated directly from the individual momentum equations.

$$E_r = \frac{\int\int [(\pi_x - F)^2 + (\pi_y - G)^2]\, dxdy}{\int\int [F^2 + G^2]\, dxdy}$$

Here, F and G are the terms in the horizontal momentum equations other than pressure gradients. The larger E_r is, the greater the mismatch between the best-fit pressure field and the gradients calculated from the individual equations; these mismatches are due to velocity errors.

Mismatches are also affected by a lack of data. In particular, velocity analyses are often too infrequent to calculate time derivatives of velocity components in the momentum equations. Under such conditions a steady state is assumed in a reference frame moving with the most dynamically active elements of the system (the only reference frame for which a steady state is possible). This motion can only be estimated, and less than optimal estimates used in the retrieval calculations result in larger values of E_r. This fact can be used in a reverse sense however, in that an optimal reference frame in the steady state case can be determined by trial and error through repeated guesses at reference frame motion until the minimum E_r value is found. Fig. 4 shows the result of a series of trials for the convective region of the mesoscale convective system discussed earlier. The resulting optimal reference frame motion matches fairly closely with the motion of reflectivity cells tracked by radar in this case.

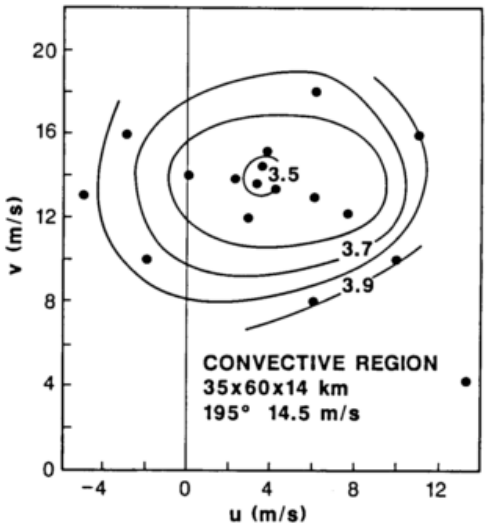


Fig. 4. Height-summed E_r as a function of assumed reference frame motion. Each dot represents a trial.

5. FUTURE WORK

Several directions are planned for continuation of this work. Potential exists for application of this technique and microphysical retrieval methods (Ziegler, 1985) to common data sets since the retrieved variables are largely complementary. Also, extension of this work will seek to take into account information in the environment of convective storms and to use time-dependent model calculations in various ways to enhance the quality and utility of retrieved fields.

ACKNOWLEDGMENTS: Peter Ray, Cathy Kessinger, and John Tuttle carried out various portions of the Doppler analyses cited in this paper. Ms. Sandy McPherson and Ms. Joan Kimpel helped prepare the manuscript.

REFERENCES

BRANDES, E. A.: Mon. Wea. Rev., 112 (1984), 1033-1052.

GAL-CHEN, T.: Mon. Wea. Rev., 106 (1978), 587-606.

HANE, C. E.; WILHELMSON, R. B.; GAL-CHEN, T.: Mon. Wea. Rev., 109 (1981), 564-576.

ROUX, F.; TESTUD, J.; PAYEN, M.; PINTY, M.: J. Atmos. Sci., 41 (1984), 3104-3121.

ROTUNNO, R.; KLEMP, J. B.: Mon. Wea. Rev., 110 (1982), 136-151.

ZIEGLER, C. L.: J. Atmos. Sci., 42 (1985), 1487-1509.

THE EFFECTS OF THE EXISTENCE OF STRATIFORM CLOUD ON THE DEVELOPMENT OF CUMULUS CLOUD AND ITS PRECIPITATION

Huang Meiyuan, Hong Yanchao, Xu Huaying and Zhou Heng
Institute of Atmospheric Physics, Academia Sinica, Beijing

1. INTRODUCTION

It has been noted that the interaction of cumulus clouds may play an important role in the cloud development and its precipitation. One type of interaction of clouds is the influence of stratiform cloud on cumulus cloud embedded in it. The observation pointed out that the convective clouds developing in the stratiform cloud have a longer lifetime, higher rainfall rate and larger rain amount than isolated convective clouds, and heavy rain and gush rain often exist in the mixed cloud to be composed of cumulus clouds and stratiform clouds (Hong et al., 1987, P.56). In this paper,we shall calculate and discuss the problem about the influence of stratiform cloud on growth of the cumulus cloud using a two-dimension slab-symmetric model of cumulus cloud by the author's (Xu et al., 1983, p.403).

2. CALCULATION

2.1 THE CONSIDER IN CALCULATION

In calculation, we only consier liquid water content and without regard for the stream field and the microphysical processes in the stratiform cloud. The boundary conditions are taken in such a way that airflow velocity, cloud water content et al. are zero at the boundaries. The temperature and humidty at the boundaries are taken as those in the environment. The initial condition and initial disturbance condition are same as that given in author's paper with the addition of initial cloud water content of 0.2 g/m^3.

2.2 THE RESULTS

The main parameters of cumulus cloud developing in the stratiform clouds with various thicknesses and heights are give in table 1. It follows from table 1 that, in general, whether the top of the stratiform cloud is with an inversion layer or not, the stratiform clouds play a significant role in development of the cumulus clouds and their precipitation, the values of the cumulus cloud are obviously larger than that of the isolated cumulus cloud.

Table 1. Development of the cumulus cloud in the stratiform cloud

cumulus parameters	isolated cumulus cloud	heights and thicknesses of the sratiform clouds (km) 1.5 - 3.5	3.0 - 5.0	5.5 - 7.5	1.5 - 5.0	1.5 - 7.5
w(m/s)	2.1	2.2/1.2*	2.6/2.2	2.1/2.1	3.8/2.2	4.3/4.0
qc(g/m^3)	1.2	1.6/1.4	1.7/1.6	1.2/1.2	1.7/1.6	1.7/1.7
qr(g/m^3)	0.2	1.0/0.4	1.2/0.9	0.2/0.2	1.8/1.3	2.1/2.0
z(dbz)	29	42/35	43/42	29/29	47/44	48/48
PA(mm/h)	1.3	12.7/4.5	13.9/10.1	1.3/1.4	24.0/17.2	28.1/27.7
sqc(t/m)	291	2115/2698	2069/2994	291/291	3744/4327	5235/5824
SR(t/m)	70	1311/824	1436/1176	70/70	2841/2232	3982/3875
Pe(%)	24	64/31	69/39	24/24	76/52	76/67

Noted: (1) w is updraft speed, qc cloud water content, qr rain water content, z radar reflectivity, PA rainfall rate, Sqc total condensation amount, SR total rainfall amount and Pe precipitation efficiency, in which w, qc, qr, z and PA are maximum values on axis of the cumulus cloud, respectively; (2) * in case of existing an inversion layer.

Especially, total rainfall amount may increase for sereval to tens times, and under the stratiform cloud, precipitation efficiency of the cumulus clouds rises greatly from 24% to 64%-67% (without the inversion layer) and 31%-67% (with the inversion layer). The maximum rainfall rate increase from 1.3 mm/h to 7.0-28.1 mm/h and 4.5-22.7 mm/h, too.

3. THE ANALYSIS

3.1 THE INFLUENCE ON GROWTH OF CUMULUS

The maximum updraft speed (w) on axis of cumulus cloud is an important parameter in showing development of cumulus cloud. In table 1, w = 2.1 m/s for the isolated cumulus cloud, w increases for cumulus cloud developing in the stratiform cloud in the middle level (3.0-5.0 km) and the whole level (1.5-5.0 km; 1.5-7.5 km), and the thicker stratiform cloud, the larger w. From the changes of w with time, it can been seen that the form of distribution of the updraft speed with time are different. The updraft in the isolated cumulus cloud increases sharply, and the maximum lasts for a short time; but in case of existing the stratiform cloud, the stronger updraft may remain stably for a longer time, and it is obvious that the lifetime of cumulus cloud is prolonged by a factor of two. The rainfall may increase for several to tens times.

Because, the cumulus cloud embedded in stratiform cloud is in a saturation environment, the water-vapour and heat in the cloud or enery needing for the development can not be losed by effects of turbulence exchange and entrainment through the lateral boundary. There is no evaporation of cloud droplets to decrease bouyancy force near the top of the cumulus cloud; the existence of stratiform cloud humidifies the inflow air of cumulus cloud. All of these factors result in increase in condensation water and release of more condensation latent heat in the cloud, as a result, the updraft velocity and moisture content in the inflow are increased, which is follow by quickening further condensation and increasing cloud water and rain water content. The cumulus cloud develops vigorously to enhance rainfall amount under this processes of pasitive feeback.

3.2 THE INFLUENCE ON THE STRUCTURE AND STREAM FIELD OF CUMULUS

To discuss this problem, a case is given in Fig.1. At 4 min, the neights noted by the maximun of stream function are much the same, the heights of upper boundary of the rise-decent circulation and the distribution of liquid water content in the cloud are different under the influence of the inversion layer. It can be seen from Figs.1a1, 1b1 and 1c1 that, as compared with the cumulus cloud developing in the stratiform cloud, at first, the maximum of cloud water content in the isolated cumulus cloud is a little larger but at lower height and with smaller range, while existing stratiform cloud, the zone with a maximum water content is situated higher level and has extended to 4 km height (see the isotimic of 0.3 g/m^3); under condition of the inversion layer, the water-vapour being transferred upward and followed condensation water are suppressed below it, as a result, the cloud water is accumulated to form a zone of high water content, with maximum of above 0.5 g/m^3 (Fig.1c1). At 12 min, by compare

Fig.1a2 with Fig.1b2, we can see that the difference between the two cumulus clouds is remarkable; the top of cumulus cloud developing in stratiform cloud has reached up to level of 6 km, showing vigorous vertical growth. The cores of cloud water and rain water content appear in the middle part of the cumulus cloud, which values are much larger than that of the isolated cumulus cloud. The updraft extend to a layer in 5-6 km. Out of the cloud, the compensation dowmdraft appeared in the middle and upper part. Moreover, the inversion layer has an effect on cloud structure, too. Because the divergence of the updraft owing to suppression below the base of inversion layer, the streamlines are horizontal and straight, the stratiform cloud there becomes gradually a cloud anvil (Fig.1c2). At 24 min, the isolated cumulus cloud, in which the downdraft dominates, has been in the dissipation stage (Fig.1a3); but the cumulus cloud developing in the stratiform cloud (Fig.1b3) grows to reach up to 8 km level, produces rainfall with high rate and the counter-circulation in the lower level; this is not the case in condition of the inversion layer (Fig.1c3), the top height of the cumulus cloud is much less than that in Fig.1b3, only about 5.5 km, the centre with 0.9 g/m³ of cloud water content is limited under the inversion layer and the cloud anvil is intensified. But the rain water content here is very low which implicates low conversion rate of rain from cloud water. This example shows that stratiform cloud promotes powerfully development of the cumulus cloud and increase of rainfall, and the inversion layer has an effect on structure of the cumulus cloud.

REFERENCES

Xu Huaying et al.: Numerical simulation of cumulus precipitation seeded by salt power, Scientia Atmospherica Sinica, 7(1983), 403-410.

Hong Yanchao et al.: The echo structure of mesoscale system and its relation with heavy rain in Mei-yu frontal cloud system. Acta Meteorologica Sinica, 45(1987), 56-64.

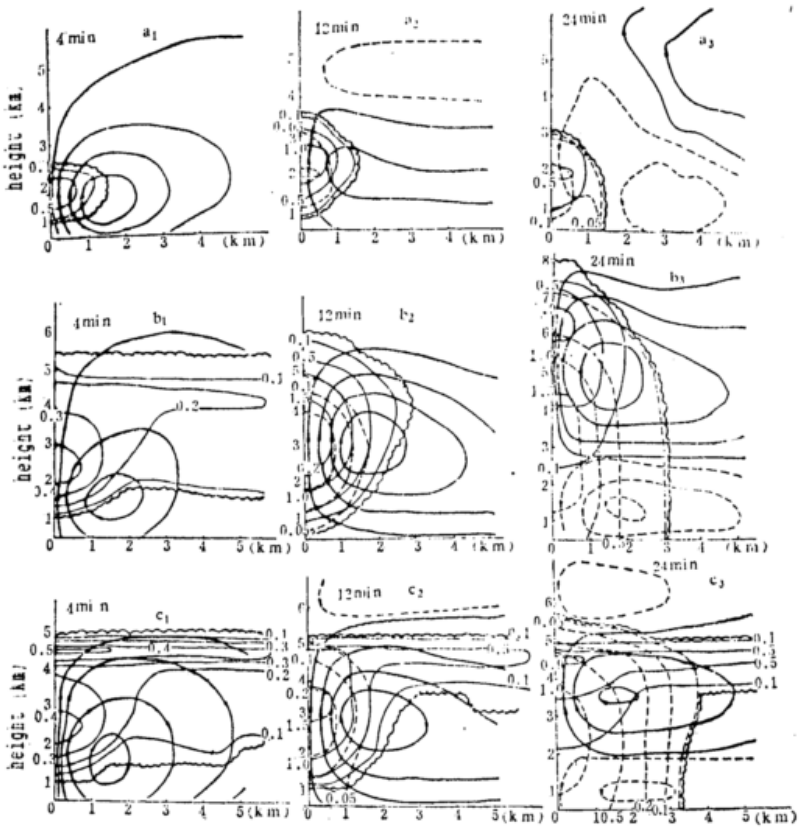


Fig.1. The vertical section charts of cloud water content (thin full curves), rain water content (dotted lines) and stream line (full curves and dotted line with arrows) at 4, 12, and 24 min, respectively, in the isolated cumulus cloud (a1-a3) and the cumulus cloud developing in the stratiform cloud in 1.5-5.0 km without the inversion layer (b1-b3) and with the inversion layer (c1-c3).

A CASE STUDY OF A SLOW-MOVING CONVECTIVE BAND OBSERVED BY A DOPPLER RADAR

Kenji Akaeda, Masahito Ishihara, Akira Tabata, Tatsuo Yokoyama and Hitoshi Sakakibara

Meteorological Research Institute
1-1 Nagamine, Tsukuba, Ibaraki, 305 JAPAN

1. INTRODUCTION

Midlatitude squall lines have been investigated mainly in the central United States. Smull and Houze (1985, 1987) analyzed a rapidly moving squall line that passed over central Oklahoma using Doppler radars. They showed the importance of a jet of maximum front-to-rear flow at midlevels. But there have been very few reports on midlatitude squall lines except those in the United States. A slow-moving convective band in a subtropical maritime region was observed by the X-band Doppler radar of MRI on 6 June 1987. The internal flow features of this band in a mature stage were similar to that of squall lines. A primary objective of this paper is to compare the structure of radar echo and characteristics of internal flow between the initial stage and the mature stage of this convective band.

2. DATA

The principal data used in this study were collected at Okinawa island (27N, 128E) in 1987 Special Observations (Ishihara et.al., 1988). The Doppler radar was situated at Naha. This radar measured in the range of 64km with RHI and PPI modes. Reflectivity data within 200km were obtained at 5 min intervals by Yaedake radar which was located about 50km north-northeast from Naha. The various surface data and upper-air data at 6 hour intervals at Naha were also used.

3. ENVIRONMENTAL CONDITIONS

Neither cyclone nor fronts were present around Okinawa island. Figure 1 indicates the vertical distribution of equivalent potential temperature (θe), relative humidity and wind. A potentially unstable layer was present below 3.5km level. The whole layer was moist. Wind direction veered with height but the wind shear was not so strong.

4. EVOLUTION OF THE RADAR ECHO PATTERN

The horizontal distribution of radar echo detected by the Yaedake radar is shown in Fig.

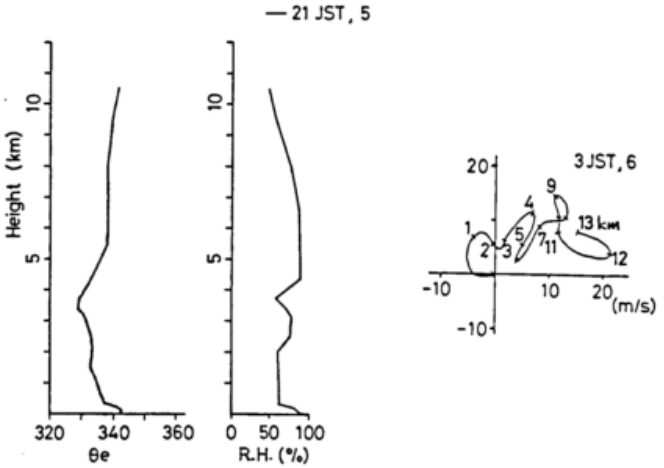


Fig.1 The vertical distribution of θe, relative humidity and wind at Naha.

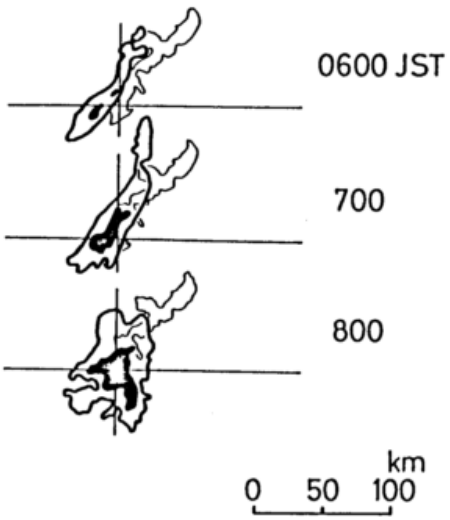


Fig.2 Time variation of horizontal distribution of radar echoes. Thick line indicates 20dBZ contour and black area indicates more than 45dBZ. Thin line indicates the coast line of Okinawa island. Intersection shows the position of Naha.

2. The convective system originated at about 0530 JST as a group of isolated echoes located west of Okinawa island. Convective areas developed in a NE/SW orientation by 0600 JST. The orientation of the band was parallel with the direction of Okinawa island and its length was about 100km. By 0700 JST, the convective band had intensified but the position of the line remained essentially unchanged. The size

of the strong echo incresed and moved southeastward after 0700 JST.

The detailed horizontal echo structures obtained at 10 min intervals are shown in Fig.3. The band consisted of two cells between 0600 and 0650 JST. Each cell remained almost stationary during this period. After 0700 JST, the shape of convective band changed into bow shape. With this change of shape, the convective band started moving southeastward at the speed of 5m/sec. The most intense part of the echo passed over Naha between 0710 and 0740 JST. The gradual temperature drop, pressure rise and abrupt change in wind were observed at Naha around 0700 JST. The maximum 10 min rainfall was 13mm between 0710 and 0720 JST.

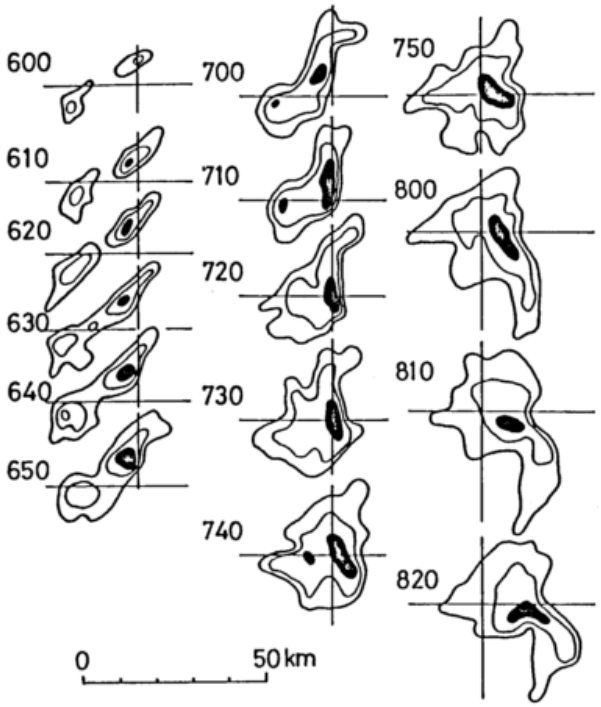


Fig.3 Time variation of horizontal distribution of radar echoes. Contours are at 5dBZ intervals beginning at 45dBZ. Black area indicates more than 55dBZ. Intersection shows the position of Naha.

5. CHARACTERISTICS OF EACH STAGE

The evolution of the system was divided into two stages, due to the aforementioned changes in the features and movements of the band. Stage 1 was prior to 0700 and stage 2 after 0700 JST.

A vertical cross section in stage 1 from the Naha Doppler radar is shown in Fig. 4. It was taken along a line normal to the orientation of the convective band. The main convective cell was identified by a core of high reflectivity near -6km range in Fig. 4a. Anvil cloud extended on the right side of this

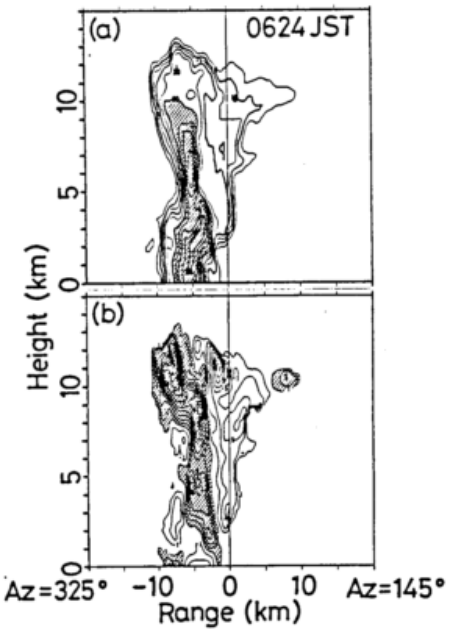


Fig.4 Vertical cross section of (a) reflectivity (b) Doppler velocity. (a) Contours are at 5dBZ intervals beginning at 5dBZ. Hatched area indicates more than 30dBZ. (b) Contours are at 2m/sec intervals beginning at ±1m/sec. Hatched area indicates more than 1m/sec. Negative Doppler velocity indicates the velocity toward the radar.

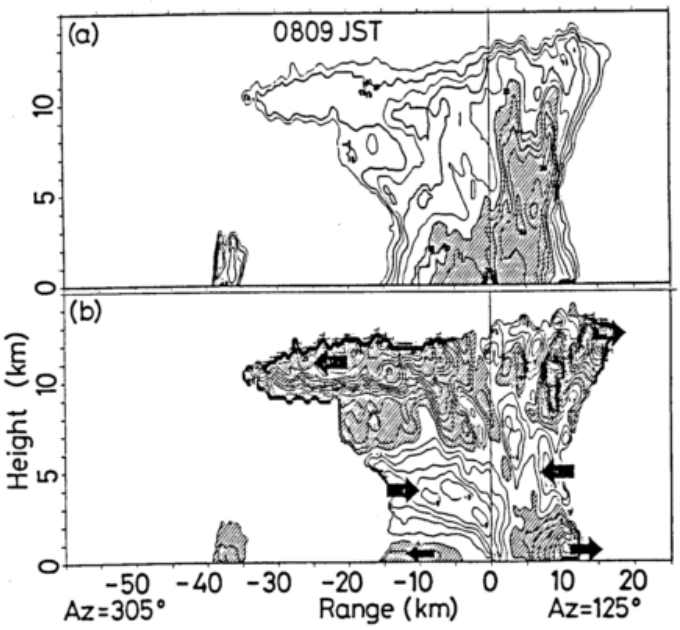


Fig.5 The same as in Fig.4 except at 0809JST.

core. The cross section of Doppler velocity (Fig. 4b) showed a pair of positive and negative velocity areas. The positive area was tilted to the up-shear side. Since this area was observed near 0km range, the positive velocity area indicated the updraft region. Negative velocity area extended below the anvil cloud at about 0km range. Low-level divergence was seen at about -7km range. This divergence

was caused by a downdraft due to heavy rainfall. The positions of updraft and downdraft in this convective cell corresponded to the down-shear and up-shear side of the vertical wind shear, respectively. These characteristics of internal flow were similar to that of supercell storms. In this way, convective scale circulation was predominant in stage 1.

A typical vertical cross section in stage 2 is shown in Fig. 5. A convective core was seen around 5km range in Fig. 5a. The anvil cloud extended to the left side of the core. Bright band, which is a good sign of stratiform precipitation, was not observed under the anvil cloud. There were several strong flows in the system (Fig. 5b). At the middle-levels, inflows were present both from the front and from the rear. The inflow from the rear was more clearly identified by Doppler radar. At the upper-levels, strong outflows which exceed 20 m/sec were present both to the front and to the rear. Surface gust front which exceeds 15 m/sec was observed at 12km range. These characteristics of internal mesoscale flows are similar to that of tropical and midlatitude mature squall lines (Zipser, 1977; Newton and Newton, 1959).

6. CONCLUDING REMARKS

The characteristics of stage 2 were much different from those of stage 1. The differences were as follows: 1) The anvil cloud extended more widely and to the opposite side of that in stage 1. 2) Mesoscale circulation predominated in stage 2. The formation of gust front and the extension of the anvil cloud against the environmental flow began after the middle-level inflow became stronger. These differences between stage 1 and stage 2 imply the importance of the middle-level inflow to form the structure of the mature system. The convective band began to move after 0700 JST, as the middle-level inflow became stronger. Therefore, the strong inflow at the middle-level was also important for the movement of the system.

The differences between this system and Smull and Houze's squall line were as follows: 1) The scale of this system was rather small. 2) The area of stratiform precipitation was not seen below the anvil cloud. 3) The speed of this system was rather slow. 4) Middle-level jet of front-to-rear flow was not clear in this case.

7. ACKNOWLEDGEMENTS

The authors are grateful to the members of Okinawa Meteorological Observatory for their various support to our observation. We also grateful to Okinawa Northern Dam Consolidated Supervision Office for providing data of Yaedake radar.

8. REFERENCES

Ishihara,M., A.Tabata, K.Akaeda, T.Yokoyama and H.Sakakibara, 1988: Characteristics of mesoscale cloud systems developed in the maritime subtropics. Preprints of 10th Int. Cloud Physics Conf. at Bad Homburg.

Newton,C.W. and H.R.Newton, 1959: Dynamical interactions between large convective clouds and environment with vertical shear. J.Meteor., 16, 483-496.

Smull,B.F. and R.A. Houze,Jr. 1985: A midlatitude squall line with a trailing region of stratiform rain: Radar and Satellite observations. Mon.Wea.Rev., 113,117-133.

Smull,B.F. and R.A. Houze,Jr. 1987: Dual-Doppler radar analysis of a midlatitude squall line with a trailing region of stratiform rain. J.Atmos.Sci., 44, 2128-2148.

Zipser,E.J., 1977: Mesoscale and convective scale downdrafts as distinct components of squall-line structure. Mon.Wea.Rev., 105, 1568-1589.

ANALYSIS OF DIFFERENT APPROACHES TO MATHEMATICAL DESCRIPTION OF CONVECTION

M.V. Buikov

Ukrainian Regional Research Institute, Kiev, USSR

In modelling of convective clouds different equations to describe convection are applied: I) one-dimensional Lagrangian and Eulerian equations; 2) two-dimensional equation for updraft and continuity equation in cylindrical coordinates neglecting pressure perturbation; 3) the system of equations of convection. In this paper new approaches for the description of entrainment of environmental air into cloud for one-dimensional equations and the derivation of one-dimensional equation from two-dimensional ones and the last - from convection equations are discussed.

I. Stommel's formula for entrainment of environmental air results in increasing of cloud radius with height; this is confirmed by laboratory experiments, but is not in accordance with the fact that cloud jet is flowed round as a rigid body. Approximately the influence of turbulent exchange of cloud with environment on liquid water content may be estimated by the solution of the equation of eddy diffusion for $q_L(r, z)$. (CARSLAW, JAEGER, I959). This results in the following formula for entrainment coefficient:

$$\mu_{entr} = \frac{a\,k}{w\,R^2} \cdot \qquad (I)$$

a is a number. This entrainment coefficient is more sensitive to cloud radius and depends on w. It may lead to more fast vanishing of liquid water content where $w \approx 0$.

The turbulent exchange of cloud and environment is valid for both Lagrangian and Eulerian equations but an additional not-turbulent entrainment due to acceleration of updraft appears in Eulerian description. Because entrainment of dry air is equivalent to that of undersaturation the rate of change of liquid water content with height due to ordered entrainment is:

$$\left.\frac{\partial q_L}{\partial z}\right|_{entr} = -\frac{\partial \ln w}{\partial z}\left[q_m(T) - q_e\right]. \qquad (2)$$

2. The Lagrangian equation of motion may be strictly applied only to infinitly thin slice of cloud. The equation for cloud of finite thickness may be derived by averaging of Eulerian equation of motion over height:

$$\frac{\partial w}{\partial t} + w\frac{\partial w}{\partial z} = \frac{g\theta'}{T_e} \cdot \qquad (3)$$

As a result the equation for averaged over height updraft is:

$$\frac{\partial \overline{w}}{\partial t} = \frac{g\overline{\theta'}}{T_e} - w(H, t)\frac{dH}{dt} \cdot \qquad (4)$$

The right hand part of this equation depends on mean overheating and on negative contribution due to cloud thickness increase.

3. The one-dimensional equation (3) is considered to be derived from two-dimensional equation of motion for updraft and continuity equation by averageing them over cloud cross-section (KUO, RAYMOND, I980; OGURA, TAKAHASHI, I97I). But in this procedure two prob-

lems are confused: the averageing over cloud cross-section and over eddy pulsations. In order to separate these problems the solution of two-dimensional equation of motion and continuity equation are expanded in the series of Jacobi's polynomials as the functions of radial coordinate (MORSE, FESHBACH, I953). The transformed equations are:

$$\frac{\partial w_l}{\partial t} + \sum_{l=0}^{\infty}\left[\alpha_{lmn}\, w_m\, u_n \frac{}{R} + \beta_{lmn}\, w_m \frac{\partial w_n}{\partial z}\right] = \frac{g\,\theta'_l}{T_e}\,. \qquad (5)$$

$$\frac{\partial w_l}{\partial z} + \frac{I}{R}\sum_{m=0}^{\infty}\sigma_{lm}\, u_m = 0\,. \qquad (6)$$

α_{lmn}, β_{lmn}, σ_{lm} are number matrices and depend only on $G_n(x)$. Average values of $\tilde{w}$ and $\tilde{u}$ are proportional to w_o and u_o. For w_i and u_i may be adopted zero initial conditions and due to this the solutions of homogeneous equations (5) for $l \geqslant I$ are equal to zero too. Then Eqn. (5) in the case $\theta'(x, z, t) = \theta'(z, t)$; $\theta'_i = 0$ when $i \geqslant I$ for $l = 0$ turns to be usual one-dimensional equation like Eqn. (3). If overheating θ' depends on r it is necessary to solve more complicated equations for w_i and u_i but Eqn. (3) may have wide enough applicability because buoyancy of cloud depends on total weight of air and does not depend on its distribution over horizontal cross-section.

4. Two-dimensional equation for updraft (8) in which pressure perturbation is neglected may be derived from the set of equations of convection for velocity and overheating using the above - applied expansion in the series of Jacobi's polynomials of horizontal coordinate ($x = r/R_\infty$). In order to eliminate pressure perturbation all functions are represented as time series. For every power of time (the second index of pressure perturbation) may be derived the following equation:

$$\frac{d^2\Pi_{ik}}{dz^2} - \frac{I}{R^2}\sum_{i=0}^{\infty}\gamma_{il}\Pi_{lk} = \frac{g}{T_e}\frac{d\theta'_{ik}}{dz} + F_{ik}\,. \qquad (7)$$

where γ_{ik} is number matrix and F_{ik} does not directly depend on θ'_{ik}. For given i and k fixed the set (7) can be solved under the boundary conditions: $\Pi = 0$ at the ground and tropopause and Π, can be expressed as a some functional of θ''. Therefore the right hand part of the equation for updraft may be presented in the following way:

$$-\frac{\partial \Pi}{\partial z} + \frac{g\theta'}{T_e} = \frac{g}{T_e}\lambda(r,z)\left[\theta(r,z) - \theta^*_e(r,z)\right]. \qquad (8)$$

So the two-dimensional equation for updraft may be derived from the set of equations of convection but with modified overheating. This modification may be interpreted as the influence of compensating downdraft around cloud on temperature of environment. The existence of downdraft region around cloud jet follows from continuity equation. After integration over the cross-section of convective cell at the boundary of which $u(R, z) = 0$ it may be obtained:

$$\frac{d}{dz}\int_0^{R_\infty} dr\, r\, w(r, z) = 0. \qquad (9)$$

But at the ground w = 0 and then

$$\int_0^{R_\infty} dr\, r\, w(r, z) = 0. \qquad (10)$$

This equality may be true if updraft is compensated by downdraft at any height.

5. The parametrized modification of environmental temperature due to compensating downdraft was introduced into the numerical time-dependent microphysical one-dimensional cloud model. It was shown that this modification may have strong influence on the formation of precipitation, its amount and particle spectrum. It was also shown that there is the value of the dimension of convective cell at which amount of precipitation has a maximum.

References

CARSLAW H.S., JAEGER J.C. Conduction of heat in solids. Clarendon Press, Oxford, 1959.

MORSE P.M., FESHBACH H. Methods of theoretical physics. P. I, Mc-Graw Hill. N. Y. - L. - T. 1953.

KUO H.L., RAYMOND W.H. A quasi - one-dimensional cumulus cloud model and parametrization of cumulus heating and mixing. Mon. Wea. Rev. 108 (1980), No. 7, p. 991-1009.

OGURA Y., TAKAHASHI T. Numerical simulation of the life cycle of a thunderstorm cell. Mon. Wea. Rev. 99 (1971), No. 12, p. 895-911.

List of Symbols

g acceleration due to gravity

$$G_n(x) = \frac{2^{1/2}(n+1)^{3/2}}{x\quad(n+1)}\,\frac{d^n}{dx^n}\,x^{n+1}\,(1-x)^n$$

Jacobi's polynomials.

H cloud thickness.

k turbulent diffusivity.

p' pressure perturbation.

r, z radial and vertical coordinates.

R(R_∞) cloud (convective cell) radius.

q_m(q_e) saturation (environmental) mixing ratio.

T (T_e) temperature (environmental temperature).

u, w radial and vertical components of air velocity.

$u = \sum_{m=0}^{\infty} u_m(z, t)\, G_n(x)$;

$w = \sum_{m=0}^{\infty} w_m(z, t)\, G_n(x)$ the series of the expansion using Jacobi's polynomials as eigenvalue functions.

$\bar{w}$ ($\tilde{w}$) mean updraft averaged over height (cross-section).

ρ_0 environmental air density.

$\Pi = p'/\rho_0$

θ (θ_e) potential temperature.

$\theta' = T - T_e = \theta - \theta_e$ overheating.

ORGANIZATION OF CLOUD CONVECTION BY GRAVITY WAVES IN THE LOWER TROPOSPHERE

Jerzy M. Radziwill

Institute of Geophysics, Warsaw University
Pasteura 7, 02-093 Warsaw, Poland

1. INTRODUCTION

Convective clouds are often observed to develop in wave-like mesoscale patterns involving plane, circular, solitary and other forms, sometimes in complex interference structures visible on satelite images. It seems certain, that such a patterns result from interaction of gravity waves with convection. The present paper is aimed at elucidation of some mechanisms possibly involved in such an interaction. To avoid distraction we shall concentrate on the plane wave forms.

2. CONVECTIVE CLOUDS

A number of mechanisms can be involved in organization of cloud convection by the gravity waves, some of them very complex (Clark at all., 1986). In the present paper we shall consider the following three, all of relatively simple nature:

(a) changes of the ambient stratification (particularly mixed layer depth) on the time and spatial scales larger than the corresponding scales of an individual convective cloud,

(b) direct triggering of individual convective clouds,

(c) supporting the developing clouds with the wave momentum and energy.

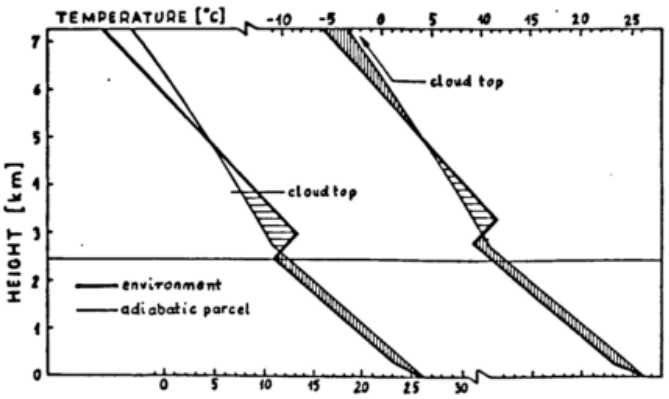


Fig.1. *Effect of vertical displacement of the inversion base on a convective cloud development in terms of the classical parcel approach.*

The first mechanism (a) may be expected in the case of long, quasihydrostatic waves. It is connected with the fact, that the development of convective clouds formed by thermals starting in the surface layer depends substantially on the mixed layer depth. To get a qualitative explanation of this phenomenon it is enough to analyse an adiabatic parcel on the thermodynamic diagram in typical fair weather stratification Such a stratification consists of the following four layers (e.g. Ludlam, 1980): (1) surface layer, (2) well-mixed boundary layer, (3) stable transition layer (sometimes even inversion) and (4) conditionally unstable convection layer, capped by stable upper troposphere and/or stratosphere. Typically, the lifting condensation level lies very close to the inversion base. Then, even slight displacement of the latter considerably reduces the amount of energy necessary to lift the thermal through the layer of negative buoyancy and achieve the free convection level (Fig.1). The net result is that greatest clouds are likely to develop in regions where the inversion layer is most elevated. This means, that the mesoscale pattern of convection is particularly sensitive to the vertical displacements at levels close to the inversion; displacements at other levels, as well as changes of water vapour content in the boundary layer are much less effective in that respect (Radziwill, 1988). Similar mechanism may work in the case of inversions more elevated with respect to the LCL. It is worth noting, that within strong inversions even relatively short and fast waves are quasihydrostatic.

Mechanisms (b) and (c) are likely to work in the case of short nonhydrostatic waves, up to few kilometers long. The mechanism (b) involves direct displacement of air to the condensation and free convection levels in the crests of the wave. In the case of mechanism (c) the wave supports the developing convective

cloud with its momentum and energy either in reaching condensation level or in passing obstacles created by layers of high stability (e.g. inversions). Effectiveness of mechanisms (a) and (b) depends on the vertical displacement, whereas that of mechanism (c) - on the vertical velocity of the wave motion.

In view of the above considerations one may speculate, that waves fulfiling the following requirements might be particularly suited for being reflected in the convection patterns:

(1) The amplitude (of vertical velocity or displacement) is sufficiently large in the vicinity of layers (LCL, inversions) important from the point of view of cloud dynamics.

(2) The horizontal wavelength and the intrinsic period at the cloud base are larger or at least comparable to the spatial and time scales of an individual convective cloud. (Otherwise the convection may have no time to react to the wave action).

(3) The wave makes the best use of the finite energy supplied by the generating mechanism. Namely, the wave should have the maximum amplitude (of vertical displacement or velocity) close to the appropriate layer, and be evanescent elsewhere.

We show in the next section, that waves with such a properties are likely to occur in many convective situations, at least for certain directions of propagation.

3. GRAVITY WAVES

Let us considere the vertical distribution of amplitude of the vertical displacement in a gravity wave propagating in a horizontally homogeneous atmosphere. It can be calculated from the simplified equation (adopted from Haman, 1962, with some modifications)

$$\tilde{\phi}'' - 2\frac{u'}{c-u}\tilde{\phi}' + \left[\frac{N^2}{(c-u)^2} - k^2\right]\tilde{\phi} = 0 \quad (1)$$

where: $\tilde{\phi} = (\rho_o/\rho_s)^{1/2}\phi$, ϕ is the amplitude of vertical displacement ρ_o - density, ρ_s - constant, c - phase velocity u - wind velocity in the direction of the wave vector, N - Brünt-Vaisala frequency, k - horizontal wavenumber, z - height, and prime (') - denotes the differentiation with respect to height.

The solution of equation (1) can be evanescent provided that the expression $\left[\frac{N^2}{(c-u)^2} - k^2\right]$ (refered thereafter as a term [A]) is negative above a certain level (or at least sufficiently small). On the other hand, the solution may have a positive maximum (or negative minimum) only in the region where [A] is positive. Since N sharply increases in inversions and stable layers, [A] is likely to become positive there and thus such a layers are likely to be connected with maxima of the amplitude.

We should notice, that such a favourable distribution of the sign of [A] (positive close to the inversion and negative elsewhere) consistent with requirements (2) and (3) of previous section may be possible only for certain soundings and certain directions of the horizontal wave vector. For other soundings and in other directions the wavelengths and frequencies of waves with desired vertical structure may be unsuitable for interaction with convection.

A special computional procedure has been developed, solving the equation (1) and automatically sweeping the (k,c) space in search for solutions fulfilling boundary conditions $\phi = 0$ at $z=0$ and $z=\infty$. Applying this procedure to real situations facilitates understanding which mechanisms were actually involved in shaping the convection pattern. Example of such an application is given in the next section.

4. WAVES AND CLOUDS

On the satelite image in Fig.2 a wave structure in cloudiness over the central Poland is visible. The cloud cover is 4/8 to 6/8, Cu med to Cu cong, according to the routine surface observations. The vertical sounding (Fig.3a) is for Poznan, 12.00 GMT, about 100 km west from the left edge of the presented image. The wavelength is about 6 km. Lines of constant phase are aligned approximately at 80° to the north. The wave period estimated from the heliographic records is about 5 min (though this estimate is not very certain). This gives the ground related phase velocity about 20 m/s.

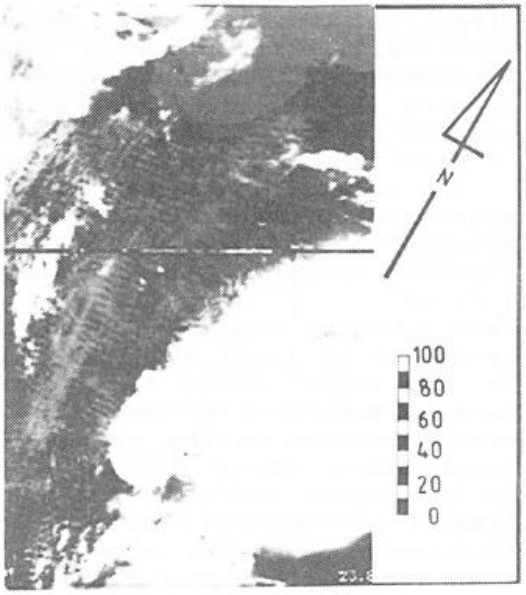


Fig. 2.

NOAA 9, 11 June 1986, 10:12 GMT, Channel 4

The height distributions of the normalized vertical displacement ($\tilde{\phi}$) and the energy density for evanescent waves of the observed length (6 km) for both possible directions of propagation (170° and 350°) are given in Figs 3c and 3d. The phase velocity for 170° is 2.9 m/s. The phase velocity for 350° is 20.9 m/s in a good agreement with the observed value (20 m/s). This suggests, that direction 350° is the actual one.

In view of the fact that the amplitude and energy distributions for the actual wave (350°) are relatively diffused when compared with other virtual directions of propagation (e.g. 170°), it looks that mechanisms (b) at the cloud base and mechanism (a) at the inversion level might be responsible for the observed wave pattern. Unfortunately the precise informations on the actual cloud base height which might help in answering some important questions in that respect are unavailable.

The above example can not be regarded as a full case study, since the available data are insufficient. Nevertheless, it encourages to continue this research for other, better documented cases.

5. REFERENCES

CLARK, T.L., T. HAUF and J.P. KUETTNER, 1986: Convectively forced internal gravity waves: results from two-dimensional experiments. *Quart. J. Roy. Meteor. Soc.*, 112, 899-926.

HAMAN, K.E., 1962: On some possible causes of clear air turbulence. *Acta Geoph. Pol.*, X, 4, 335-357.

LUDLAM, F.H.: *Clouds and Storms*. The Pensylvania State University Press, 1980. pp 141-147.

RADZIWILL, J.M, 1988: Effect of mesoscale convergence on single convective cloud development. (Submitted to *Tellus*).

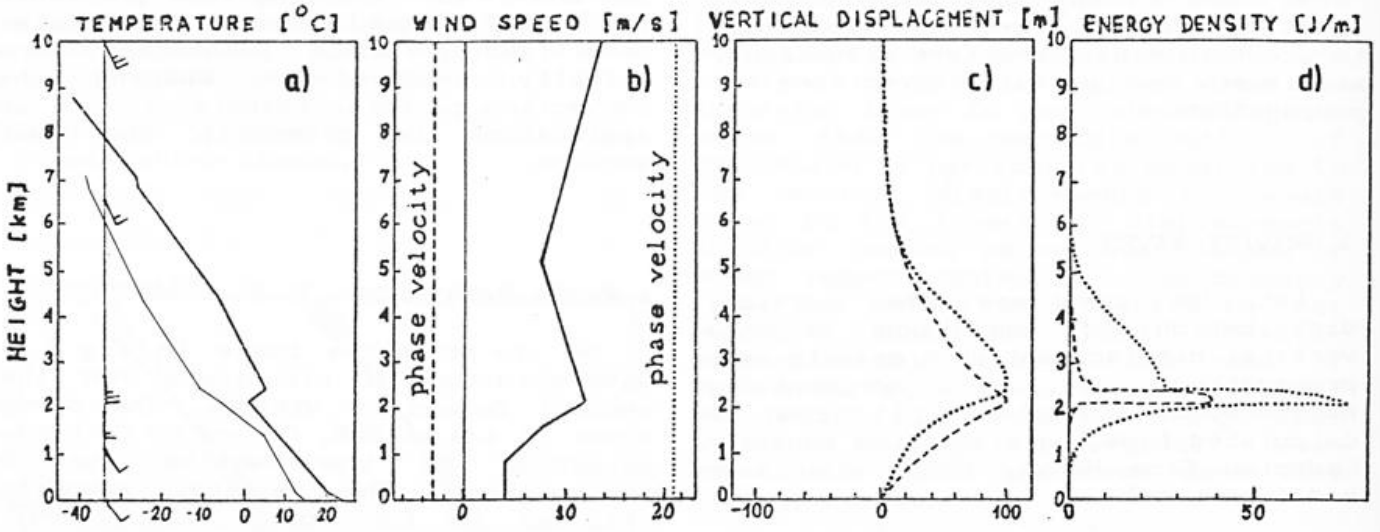


Fig. 3. *Presumable vertical structure of the wave visible on Fig. 2.: (a) wind, temperature and dew point, Poznan, 12:00 GMT, (b) wind projection on direction 350°, (c) $\tilde{\phi}$ (Eq. 1) for wave propagating in direction 350° (dots) and 170° (dashes), (d) wave energy density for waves as in c.*

DRAG EFFECTS IN CONVECTIVE DRAFTS

Krzysztof E. Haman and Szymon P. Malinowski
Institute of Geophysics, University of Warsaw

1. INTRODUCTION

In spite of the rapid development of three-dimensional numerical models for cumulus convection, the description of cumulus properties in terms of parcels, 1-D jets and thermals can still make an important contribution for understanding the basic physics of these clouds. With their simple structure, often allowing analytical treatment, 1-D models form an irreplaceable aid in conceptual work and help to provide the basis for more sophisticated modelling. Due to low computer requirements, they may also be useful as operational tools in synpotic practice. The present paper is aimed at elucidation of some problems appearing with the use od 1-D models.

2. REMARKS ON PARAMETERIZATION OF NONBUOYANT FORCES

The two most common versions of 1-D model for vertical convection in a steady environment are the self-similar entraining spherical thermal and the stationary entraining jet with axial symmetry. If only buoyancy force is allowed, both are governed formally by the same vertical momentum equation:

$$(1) \qquad w\frac{dw}{dz} = B(z) - \mu(z)w^2 \ ,$$

where: z is the vertical coordinate, B the average buoyancy per unit mass, w the average vertical velocity, and μ the entrainment coefficient defined as $\mu(z)= \frac{1}{M}\frac{dM}{dz}$, where M denotes the total mass of the thermal or vertical mass flux in the jet. The usual parameterization of entrainment is $\mu(z)=\frac{\alpha}{R(z)}$ where R(z) is the radius of a spherical thermal or of the horizontal cross-section of a jet and α is a dimensionless empirical constant. Suggested values for this constant are rather scattered, but 0.2 for jets and 0.6 for thermals are often accepted.

It has become clear, even from the earliest attempts at applying such models to real clouds, that nonbuoyant forces and particularly the vertical component of anelastic pressure gradient, may often be comparable to the buoyancy. These additional forces will affect the profiles of vertical velocity and should be accounted for, what creates some problems, different for jets and thermals. The remainder of the paper will be restricted to the latter. Some modellers (e.g. Simpson and Wiggert, 1969) have attempted to treat thermals like rigid bodies and to parametrize anelastic pressure effects by means of a virtual mass coefficient ε and an aerodynamic drag coefficient C_d. Assuming axisymmetrical flow around the thermal and disregarding density differences except in the buoyancy terms, equation (1) becomes then:

$$(2) \qquad w\frac{dw}{dz} = \frac{B}{1+\varepsilon} - \left(\frac{\alpha}{R} + \frac{3C_d}{8R}\right)w^2$$

Note that both aerodynamic drag and dilution of the vertical momentum by entrainment result in terms proportional to $^1/_R$.

When dealing with clouds the analogy with aerodynamics of a rigid body,

particularly the numerical values of coefficients, must be applied with caution. There are significant physical differences between a rigid spheres and deformable, spheroidal masses of fluid with ill-determined boundaries. Further, even in symmetrical flow, internal circulation (e.g. in the form of a spherical vortex) and turbulence may be generated, modifying the virtual mass coefficient, while the flow structure responsible for the value of C_d may be strongly affected by entrainment. Imagine, for instance, a situation in which the entraining sphere "sweeps off" air in its path with 100% efficiency. The constant α for such a situation can be found easily as 0.75, (i.e. fairly close to the empirical value 0.6), and the flow around such a thermal would be nearly undeformed except for the wake effects. C_d for such a flow can be expected to be considerably smaller than in the case of the rigid sphere. There are some suggestions that for certain bulk motions in clouds a "frontally sweeping" sphere may be a more appropriate model than the rigid one.

3. EFFECT OF WAVE DRAG

For the purposes of this section we accept the rigid body aerodynamic drag as a first approximation to nonbuoyant forces for certain forms of penetrative convection. We now consider drag due to generation of internal gravity wave by a rising convective element, the so-called wave drag. The wave drag on vertically moving bodies in the range of Froude numbers characteristic of cumulus clouds has attracted little attention till now. Warren (1959) computed (with strong simplifications characteristic for linear theory) wave drag for some axially symmetric shapes. Formulas given by Warren confirm a simple heuristic consideration based on similarity arguments that the drag force F_d in the presence of stable stratification should take the form:

$$(3) \qquad F_d = \frac{\rho w^2 \pi R^2}{2} \left(C_d + \frac{N^2 R^2}{w^2} C_w \right),$$

where ρ is the fluid density, N the Vaisala-Brunt frequency and C_w the wave drag coefficient which should be a function of the Froude number $w/_{NR}$ *) (Fig.1).

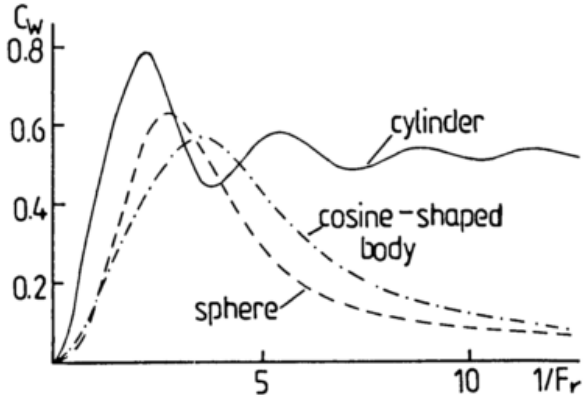


Fig.1. Cw as a function of $Fr^{-1} = NR/w$ *(adapted from Warren, 1959)*

Estimates made by Warren for atmospheric thermals brought him to the conclusion that in typical situations the wave drag is a negligible fraction of the buoyancy force. In contrast, the following examples show when and where it may become important.

4. WAVE DRAG EFFECTS IN BUOYANT PLUMES

The authors have been involved in numerical and observational investigations of a one-dimensional model of cooling tower and stack plumes ALINA (Haman and Malinowski 1987). The vertical momentum equation for a bent-over plume is in fact very similar to the equation for the elliptical two-dimensional thermal with slab symmetry and resembles equation 2. First comparisons of the model outputs with observations have shown that if

*) *In the case of nonspherical, vertically oriented objects with axial symmetry the vertical "length" of the object instead of R should be used in definition of Fr (Warren, 1959).*

wave drag is disregarded C_d between 2 and 5 must be assumed in order to get reasonabe agreement. This is a very big value when compared with typical values for rigid bodies (about 0.5 for a sphere and 1.1 for a plate).It is not easy to to estimate likely values for the wave drag correction, since we lack reliable values of C_w, but the Warren results (Fig.1) suggest the range 0.1-0.8. With w~1m/s, plume half-width R~500m and N~$10^{-2}s^{-1}$ the term $N^2R^2w^{-2}C_w$ in equation (3) may fall in the range 2.5-20, that is become great enough to explain the observed value of the drag. The hypothesis on wave origin for a considerable part of the drag experienced by the plume has been additionally confirmed by the fact, that the scatter of observed versus computed values of the plume parameters can be visibly reduced by assuming some dependence of the drag on N as a crude simulation of this effect (Fig.2).

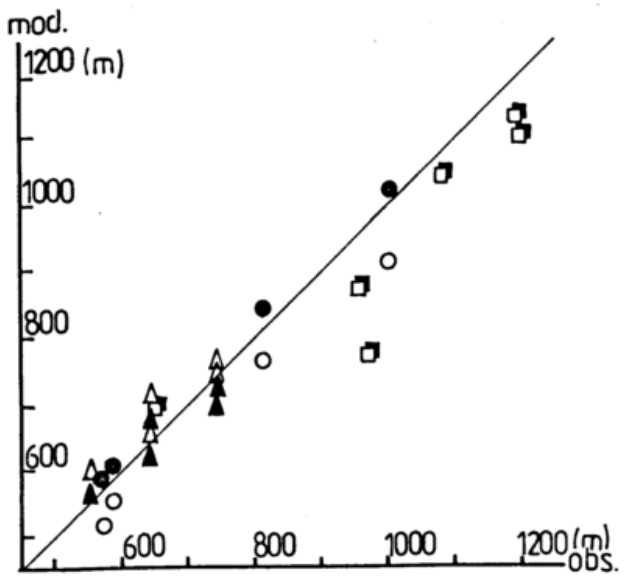


Fig.2. Observed versus computed plume elevations. Empty figures- computations with Cd=3.1 for all stratifications. Dark figures - computations with Cd=1.5 for $N<5*10^{-3}s^{-1}$ (dots), Cd=3.1 for $5*10^{-3}s^{-1}<N<10^{-2}s^{-1}$ (squares) and Cd=4.7 for $N>10^{-2}s^{-1}$(triangles). This result is a by-product of purely empirical tuning of the model. Systematic attempts at introducing the wave drag into the model are going on.

5.WAVE DRAG IN DEVELOPING CUMULUS CLOUD

A modified form of equation (3) taking account of wave drag effect becomes:

$$(4)\quad w\frac{dw}{dz} = \frac{B}{1+\varepsilon} - \left(\frac{\alpha}{R} + \frac{3Cd}{8R} + \frac{3N^2RC_w}{8w^2}\right)$$

At the moment a developing cumulus cloud crosses its condensation level and next its free convection level, its buoyancy is usually low. Thus entrainment and drag terms may become dominant in the right hand side of the equation (4). These terms (in parenthesis in Eq.4) have minimum with respect to R for:

$$(5)\quad R_{min} = \left[\left(\alpha + \frac{3}{8}C_d\right)\frac{8w^2}{3N^2C_w}\right]^{1/2}$$

Thus R_{min} may determine a scale for the "fastest growing mode" of a developing cumulus cloud. For typical values of N~$10^{-2}s^{-1}$, w~1m/s, C_d and C_w of order 10^{-1}-10^{0}, R_{min} is a few hundred meters, and this seems to be in good agreement with observation. Thus some forms of cumulus convection - gravity wave interaction, the importance of which has recently been pointed out by Clark et al.(1986) and Kuettner et. al. (1987), can in be found also in simple 1-D models.

REFERENCES

Clark,T.L.; Hauf,T.; Kuettner,J.P.: Convectively forced internal gravity waves: Results from two-dimensional numerical experiments. Q.J.R.Meteorol. Soc., 112, (1986), 899-925.

Haman,K.E.; Malinowski,S.P.: Some aspects of one-dimensional models of stack and cooling tower plumes. Proc. of an Int. Conf. on Energy Transformation and Interaction with Small- and Mesoscale atmospheric processes. Lausanne, 2-6 March 1987.

Kuettner,J. ;Hildebrand,P. ;Clark,T.: Convection waves: Observations of gravity wave systems over convectively active boundary layers. Q.J.R.Metrorol. Soc., 113, (1987), 413-444.

Simpson,J.S.;Wiggert,V.: Models of precipitating cumulus towers. Mon. Wea. Rev., 97,(1969),471-489.

Warren,F.W.G.: Wave resistance to vertical motion in a stratified fluid. J.Fl.Mech, 7, (1959), 209-229.

MOISTURE CONVERGENCE AS A SOURCE OF EXPLOSIVE GROWTH IN MODELED CUMULUS CLOUDS

J. H. Helsdon, Jr., H. D. Orville,
R. D. Farley, and F. J. Kopp

Institute of Atmospheric Sciences
South Dakota School of Mines and Technology
Rapid City, South Dakota 57701-3995

1. INTRODUCTION

When we first ran our Storm Electrification Model (SEM) to simulate the 19 July 1981 CCOPE cloud, one of the most interesting features of the simulation was that the model results duplicated the observed explosive growth phase of the cloud (see DYE et al., 1986 and HELSDON and FARLEY, 1987). Since the prime focus of our study was the evaluation of the electrification of this cloud using our model, the analysis of the nature of the explosive growth in the model results was less detailed than it should have been. Since this growth phase occurred in conjunction with the appearance of cloud ice in the upper portion of the cloud, we assumed that the release of latent heat of fusion was the energy source for the growth and made a statement to that effect in the manuscript submitted for publication. Some astute reviewer took us to task for drawing this conclusion and forced us to take a closer look at what was going on. This paper is the result of that investigation.

2. OVERVIEW

Figure 1 shows the 1400 MDT, Miles City sounding for 19 July 1981. Lifting of the 10 g/kg air near the surface yields a cloud base near 720 mb (∿2.1 km AGL). Following the pseudoadiabat from cloud base shows a moderate positive area to the tropopause. The 7.5 g/kg mixing ratio line has also been drawn for later discussion. The two sets of temperature lines below 800 mb show how the lowest layers of the sounding were made adiabatic for model input in order to promote convection early in the simulation.

Figure 2 shows the cloud top height and the

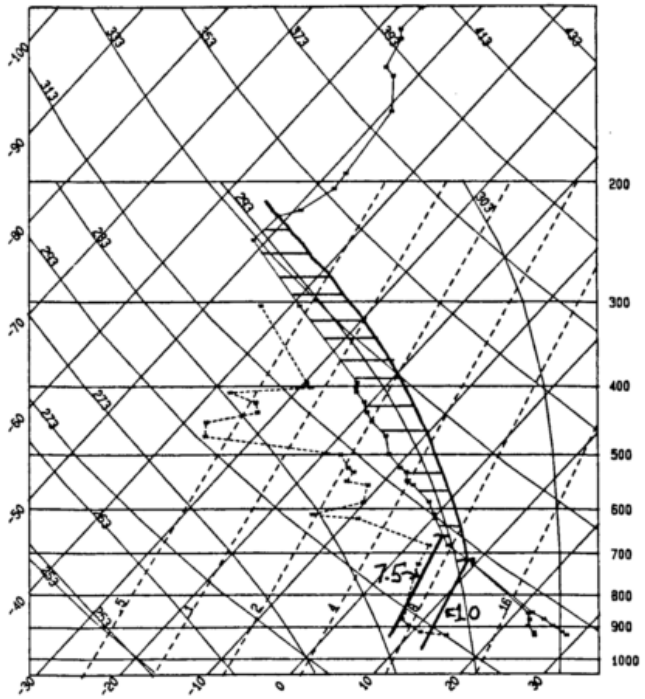


Fig. 1: 1440 MDT Miles City sounding.

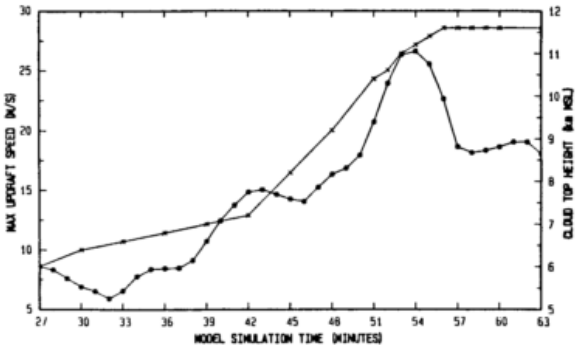


Fig. 2: Updraft speed (o) and cloud top height (x).

value of the maximum updraft speed as functions of time during the simulation. The explosive growth phase is evident as the cloud top goes from 7.2 km to 11.6 km MSL during a 14 min period from 42 to 56 min simulation time. During the previous 15 min, the cloud top increased in height by only 1.2 km. The faithfulness of the simulation to the observed growth can be seen by comparing Fig. 2 with

Fig. 3 from DYE et al. (1986) which documents the observed explosive growth occurring over a 15 min period. Also of note is the pulsating nature of the updraft in the simulation which can be seen in Fig. 2.

A simple procedure to test whether or not the initiation of the ice phase was responsible for the explosive growth was to turn off all of the ice processes in the model and rerun the simulation with only liquid processes active. This test was carried out and the results are reported below.

3. RESULTS

When the model was run in an all liquid configuration, the explosive growth was again observed to occur in identically the same manner as the simulation with the ice processes active. This indicated that the impetus for the explosive growth had to come from the relase of latent heat of condensation or possibly some computational artifact of the model itself (apparently a mechanism favored by the reviewer who called the problem to our attention in the first place). We chose to look for a physical mechanism first.

An additional release of latent heat implied an additional source of moisture to the cloud which had been growing rather unspectacularly prior to 42 min. However, since the cloud base height did not change with time during the simulation, there was no reason to believe that some new source of low level moisture was being tapped as the simulation proceeded. It would seem that the same moisture sources had to be tapped, but with a greater volume than during the initial cloud growth. Examination of the water vapor field and velocity fields supported this assumption.

Figure 3 is a time sequence of plots of the contours of water vapor in g/kg. The base of the cloud is marked with a horizontal line. At 27 min, we see that the cloud has formed

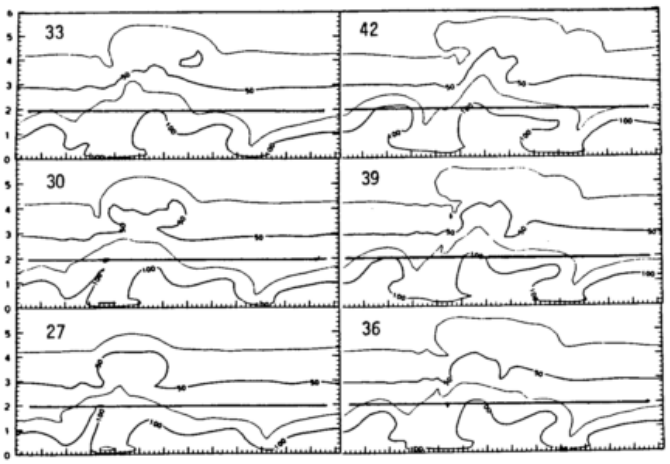


Fig. 3: Water vapor mixing ratio in g/kg contour interval 2.5 g/kg (divide labels by 10). Simulation time in upper left of each panel.

from a narrow plume of moist air of mixing ratio of ~10 g/kg. By 30 min, this plume has broken away from the cloud and the main air sustaining the cloud growth has a mixing ratio of ~7.5 g/kg. Referring to Fig. 1, we see that air with a mixing ratio of 7.5 g/kg condenses near 670 mb and follows a pseudo-adiabat which generates little thermal excess over the environment. Thus, the cloud has little energy to support further growth.

To the right of the initial 10 g/kg plume, there is a second "bubble" of 10 g/kg moist air that begins to rise and reaches cloud base by 33 min. As this moisture starts to condense and release its latent heat, an updraft begins to organize and can be seen as the updraft pulse that begins at 33 min in Fig. 2. That plume narrows and the updraft weakens by 42 min; however, the widespread lifting associated with this broader plume has lifted a larger volume of 10 g/kg air toward cloud base. By 45 min, this air has become active in releasing latent heat and the final and strongest updraft impulse is initiated pushing the cloud to its final height.

The cause of the organization of this plume of 10 g/kg air is a region of low level convergence which is depicted in Fig. 4, a time series of the horizontal velocity field.

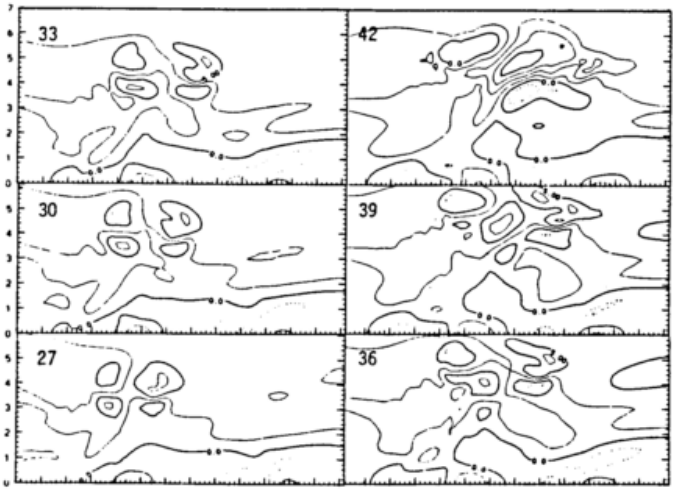


Fig. 4: Horizontal velocity. Solid lines-motion to right, dashes lines-motion to left. Contour interval 2.5 m/sec. Time in upper left corner of each panel.

At 27 min, there is a small region of flow to the right directly under the cloud with a speed >2.5 m/sec. This is embedded in a general flow from right to left, below 1.5 km, with a maximum 4 km to the right. As time passes, the two maxima approach each other. By 39 min, the two maxima are within 3 km of each other and represent an approximate convergence of 3×10^{-3}/sec. By 42 min, the two maxima are 2.5 km apart and the surface convergence is 4.2×10^{-3}/sec. The convergence zone is located directly beneath the moisture plume and creates a broad region of updraft with speeds up to 5 m/sec.

4. CONCLUSIONS

The model simulation of the 19 July CCOPE case reproduced an explosive growth phase that was observed to occur. Examination of the results from the simulation show that the cause of this explosive growth is an organized lifting of a near-surface moisture layer by a convergence zone in the horizontal velocity field which forms downwind from the cloud and intensifies with time. The updraft which results from the convergence and lifts the moist air is intensified by the latent heat released when the moisture reaches its condensation level. Whether or not this process was responsible for the explosive growth that actually occurred on that day is unknown because the cloud did not form over the CCOPE mesonetwork.

ACKNOWLEDGMENTS

Our thanks to Joie Robinson and Carol Vande Bossche for their able assistance in preparing this paper. This work was supported by the National Science Foundation under Grant Nos. ATM-8313484 and ATM-8611614. The computer time was provided by the National Center for Atmospheric Research which is sponsored by the National Science Foundation.

REFERENCES

DYE, J. E.; JONES, J. J.; WINN, W. P.; CERNI, T. A.; GARDNIER, B.; LAMB, D.; PITTER, R. L.; HALLET, J.; SAUNDERS, C. P. R.: Early electrification and precipitation development in a small, isolated Montana cumulonimbus. J. Geophys. Res., **91** (1986) 1231-1247.

HELSDON, J. H.; FARLEY, R. D.: A numerical modeling study of a Montana thunderstorm: 1. Model results versus observations involving nonelectric aspects. J. Geophys. Res., **92** (1987) 5645-5659.

THE EFFECTS OF COLD WATER SURFACE ON WARM CUMULUS CLOUDS -- NUMERICAL EXPERIMENT

Kong Fanyou Huang Meiyuan Xu Huaying
Institute of Atmospheric Physics, Academia Sinica
People's Republic of China

1. MODEL

1.1 BASIC MODEL, INITIAL AND BOUNDARY CONDITIONS

The basic equations of the 2-D, slab-symmetric numerical warm cloud model used in this study are similar to those derived by Xu Huaying et al.(1986). The integration domain has been enlarged and horizontal ambient wind has been introduced. To calculate microphysical process variables, the parameterization schemes suggested by Kessler(1969) and Berry(1968) are used. A constant eddy mixing cofficient,K, is assumed for all field variables. A finite wide cold water surface is embedded into lower boundary and both water and land surface temperatures are assumed constant over integrating period.

1.2 PROCESSING OF WATER SURFACE

Assuming that the integration domain is perpendicular to the coast lines of the finite wide water, because of heat conduct and turbulence,there is a modified layer just above the cold water surface .To maintain the form of basic equation , a new technique called 'transferring scheme' is used at initial time, which doesn't change the horizontally uniform character of the basic state temperature $\bar{T}$. With the technique the horizontal temperature difference between the air within the modified layer at each grid and that on the land is defined as the initial value of perturbed temperature T' at the same grid. This is equivalent to decomposing $T'=T_1'+T_2'$, here T_1' is the convective perturbation field of temperature, T_2' is initially overlapped negative temperature.It is obvious that T_2' remains zero outside the modified layer.

1.3 NUMERICAL TECHNIQUES

The height of the integration domain is 12 km and the width is 39 km with the space increment Δx=1 km, Δz=0.5 km and time increment Δt=10 sec. The modeling cold water surface is located downwind of the initial cloud with changable distance from the initial cloud and width of it.

The staggered grid arrangement is used for all variables with a forward time difference and central space difference on non-advective terms. The advective space differencing term is calculated by a mixture scheme.

The temperature is assumed 30 °C at land surface and 20 °C at water surface. The initial relative humidity of 90% is imposed within the modified layer which has an initial depth of 1 km. In order to keep the simulated clouds within the domain, the entire grid is translated downwind systematically with the velocity of ambient wind.

2. RESULTS

2.1 TIME EVOLUTION FEATURES

The evolutions of the affected cumulus clouds depend largely upon the water surface. Fig.1 shows a set of W_{max} -time curves, each representing a numerical run with a distance of 5 km but different water width.It is easy to find that the wider the water surface is, the

steeper the increasing part of the curves, the greater the first peek values, and in the same, the more rapid the declining process.This fact suggests that great water surface forms strong local circulation and, on the other hand, has strong restricting effect on the clouds.

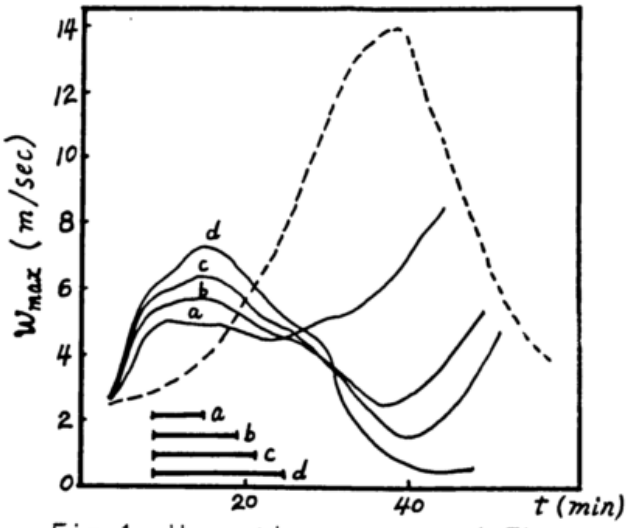


Fig.1 W_{max} -time curves of 3km (a),5km(b),7km(c), and 10km(d) wide water surface cases with ambient wind U=10 m/sec. Initial convection is 5km away from the water. Dash line is the contrast case unaffected.

Fig.2 displays another set of W_{max} -time curves with constant width but different distances. It shows that the larger the distance from cloud generating porsition to water surface, the weaker the effects water surface exerts on the

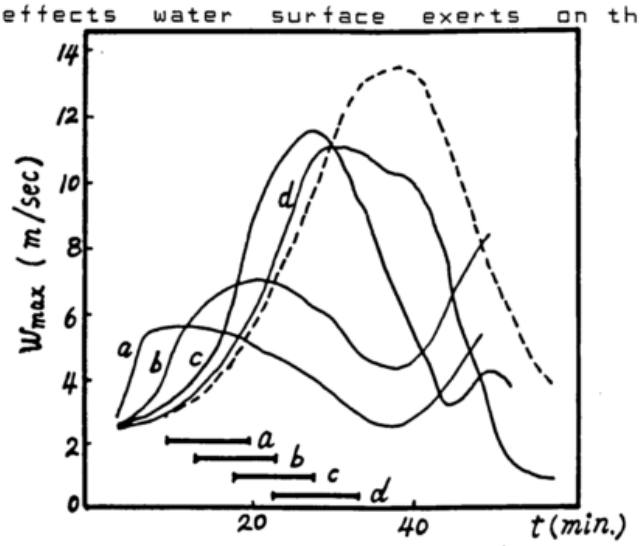


Fig.2 W_{max} -time curves of numerical runs with different distances of 5km(a),7km(b), 10 km(c),and 13km(d) from initial convection porsitions to water surface of 5km wide.U=10m/sec.

clouds. It also shows indirectly that the effects of water surface on strong moving cumulus clouds is less than on weak ones.

Some general characters of the affecting cumulus clouds can also be seen from these two figures. It is much more evident that the clouds have a three-stage evolution pattern: In the first stage, the clouds strengthen fast until moving to water surface.So,their values of W_{max} are over the contrary's; At the begining of the second stage, the rates of enhancing slow down and then begin to reduce till sometime after leaving the water surface. During this period, W_{max} tend to be smaller than that in contrast case. Later, there are different ways among the cases:For some cases (Fig.1d, Fig.2d), the updraft vanishes after leaving the water. For other ones (Fig.1b & 1c, Fig.2a & 2b), however, their W_{max} decrease first, then go up again.

In spite of the large difference of these cases appeared in the last stage, their evolution features are quite similar while the clouds are near or over the water surface.But it can be further found that the rates of W_{max}'s early enhancing and later reducing for different cases are quite different. For example, in Fig.1 line d (with wide water surface) has greater enhancing rate and declining rate than line b (narrow water surface).

2.2 RE-ENHANCING CONDITION

As mentioned above, some moving-out-water clouds intensify again, showing a second peek feature. The relation between re-enhancing and two factors, the water surface width and the distance from initial clouds, are studied, with specified other factors. Many cases

were run by changing the factors. The results are plotted in Fig.3, classified according to whether or not the re-enhancing process appears. The horizontal coordinate axis represents the time called 'negative affecting time', within which the modeling clouds move across the cold water surface. The vertical coordinate axis represents another time called 'positive affecting time', the time spent in travelling the clouds from their generating porsitions to the water surface. It is easy to see that an obvious demarcation line can be drawn

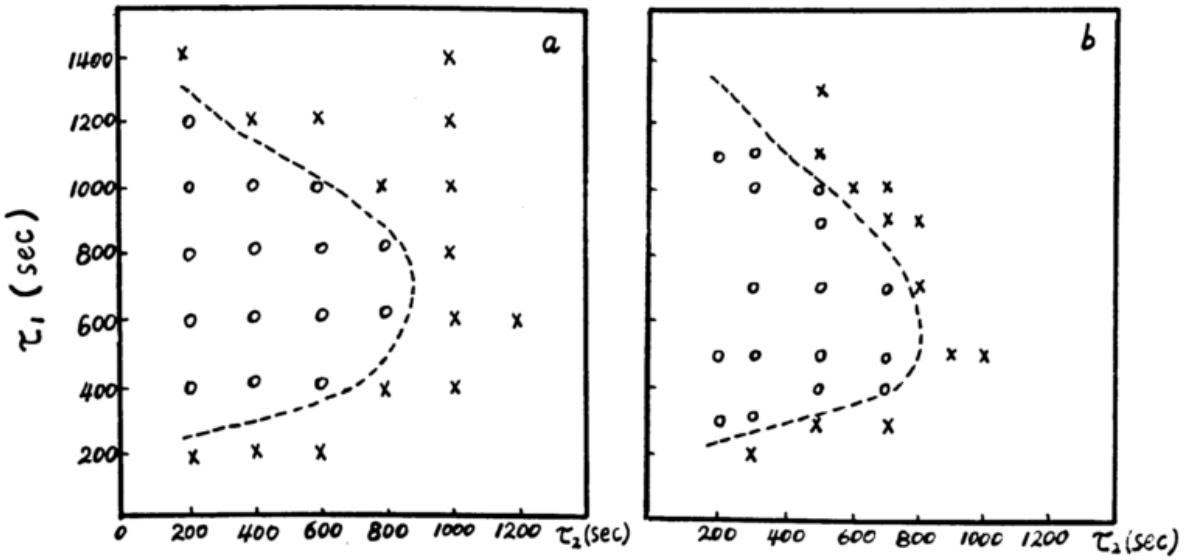


Fig.3 The statistical relations of the appearance of re-enhancing process with water width (τ_2) and distance from initial convection porsitions (τ_1). (a) U=5 m/sec, (b) U=10 m/sec.
o --- re-enhancing case x --- without re-enhancing case

between re-enhancing cases and without re-enhancing cases, and the lines corresponding to two different ambient wind speeds are largely coincident.

Two features are shown in Fig.3:

1) The wider the water surface, the less chance for re-enhancing. As the width reaches a certain value (τ_2>900 sec for these cases), all moving-out-water cumulus clouds dissipate. This feature further shows that with increasing of the water width, the increasing rate of promoting effect (dynamic mechanism) the water surface exerts on the clouds is always slower than that of restricting effect (both dynamic and thermodynamic mechanism).

2) If the generating place of the clouds are too near or too far from water surface, it is rare for them to re-enhance. There is an optimum distance range (around τ_1=600 sec for the runs). The farther deviates from this range, the smaller the critical width of appearance of re-enhancing is. When τ_1<200 sec or τ_1>1000 sec, no re-enhancing appears. This is because the cold water surface has strong restricting effect on either newborn or fully developing mature cumulus clouds.

References

Berry, E.X.: Modifi. of the warm rain process, Prec. First Natl. Conf. Weather Modifi., Albany, NY, 1968, p81-88.

Kessler, E.: Meteor. Monogr. 10(1969)-32.

Xu, H.Y. et al.: Numerical study about cumulus precipitation process, Sym. of Cloud Phy. and Weather Modif. in Southern China, Meteor. Press, Beijing, 1986.

COMPREHENSIVE RESEARCH OF CONVECTIVE CLOUD DYNAMICS FROM THE DATA OF AIRCRAFT AND NUMERICAL EXPERIMENTS

Dovgaljuk J.A., Drachova V.P., Egorov A.D., Sinkevich A.A., Stankova E.N., Stepanenko V.D.

Main Geophisical Observatory, Leningrad, USSA

1. INTRODUCTION

To estimate the seeding effect it is nesessary to carry out comprehensive numerical and aircraft experiments and subsequent joint analysis of obtained data. An example of such combined approach is described in this study.

2. THE RESULTS OF AIRCRAFT EXPERIMENTS

In April, 84, dynamics of 3 convective clouds was studied from aboard the IL-14 aircraft laboratory. Two clouds (Cb calv, Cu cong 1) were seeded. The third cloud (Cu cong 2) was chosen for reference and, therefore, left intact (V.G. BARANOV 1986, p.114). The operative flight leg was 100 km off the Crimean coast. The aircraft crossed the clouds at 3,6 km altitude (T=-11 °C) staying at the level where the reagent was introducted. LTI-11 compound was used as an ice-forming reagent. Measurement data are presented in Fig.1. Experimental data analysis was performed comparing the "reference" cloud parameters and those of seeded cloud. It was found that introduction of reagent leads to appearance of intense downdrafts in the cloud, followed by subsidence of their tops and a considerably more rapid destruction of clouds. Cloud tops crystallize earlier and intensly as compared to "reference" cloud. Electric field tension increased considerably faster after introduction of the reagent. In the "reference" cloud

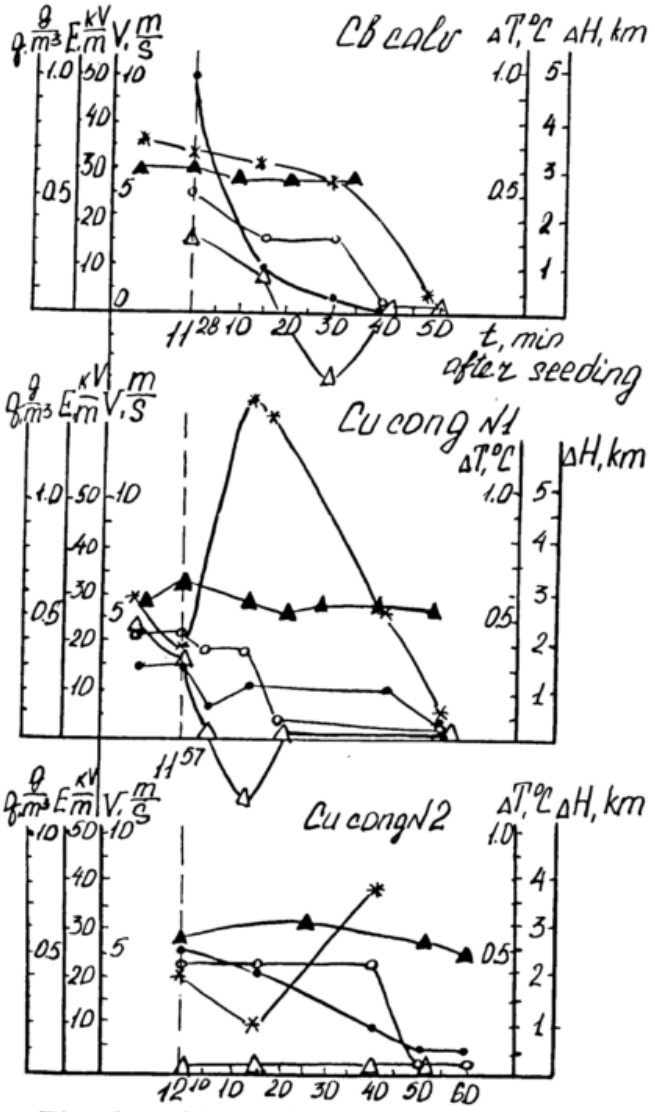


Fig.1 Aircraft measurement data
• -water content q, ∘ -overheating ΔT,
Δ -updraft and downdraft velocity V,
▲ -thickness ΔH, * -electric field tension E

the electric field tension started to increas later and built up slower. Seeded clouds produced radar echos earlier than "reference" one and these echos existed longer than under unperturbed conditions. No significant changes in water content in either seeded

or "reference" clouds could be reveled.

3. RESULTS OF NUMERICAL EXPERIMENTS

A non-stationary one-and-a-half-dimensional model with parameterized microphisics was run in the course of numerical experiments. Rawinsonde data from a location closest to the area of aircraft soundings were used as initial data for calculations. Clouds were developed by the model both in "natural" and "seeded" cycles and these results were further analyzed. Calculations showed that natural evolution of the model cloud had strongly pronounced stages of growth and stabilization. Cloud top reached 4,6 km at the 45-th minute, after which it stabilized. Downdrafts in the cloud were practically absent. Precipitation didn't reach the Earth surface. Seeding of the model cloud caused a sharp but short uplift of the top and an increase of updraft velocity. Downdrafts appeared in the cloud 10 minutes later, and it started to precipitate.

4. JOINT ANALYSES OF NUMERICAL AND AIRCRAFT EXPERIMENTS

The comparison of the "natural" model cloud with cloud Cu Cong 2 from the aircraft experiment, chosen for "reference", revealed similar features in their development. Both clouds remained stationary for a long time, they lacked downdrafts, and precipitation from both aircraft and numerical experiments didn't reach the Earth surface. In both cases seeding stimulated rapid cloud destruction and precipitation. Comparison of calculated and measured cloud parameters at flight level (Fig.2) demonstrated general similarity of their values and temporal evolution mode.

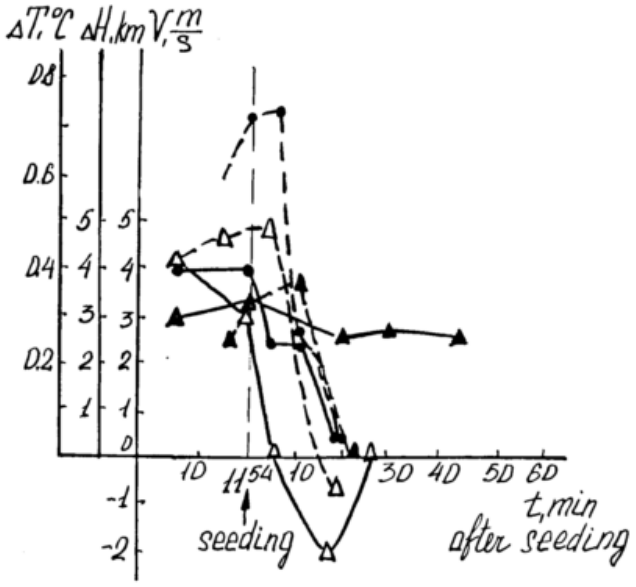


Fig.2: Comparison of natural and calculated cloud parameters

- overheating in natural cloud
- overheating in calculated cloud
- updfaft and downdraft velocity in natural cloud
- updraft and downdraft velocity in calculated cloud
- natural cloud thickness
- calculated cloud thickness

REFERENCES

BARAHOV V.G., DOVGALJUK J.A., STANKOVA E.N., STEPANENKO V.D. Surface strong overheating and its influence on convective cloud evolution and its radar reflectivity. -In: Radav Meteorology. Proceedings of the Socialist Countries Meteorology Center for Radiometeorology. -Leningrad, 1984, p.p.41-49 (in Russian).

BARANOV V.G., DOVGALJUK J.A., DRACHOVA V.P., EGOROV A.D., SINCEVICH A.A., STANKOVA E.N., STEPANENKO V.D., CHUBARINA E.V. Analyses of the effect seeding on dinamical, microphisical and electrical

characteristics of convective clouds. (From the April 84 experiment data.)- Third All-Union Simposium on Atmospheric Electricity, 1986, Tarty, p. 114 (In Russian).

A STUDY ON NUMERICAL SIMULATION OF CLOUD MERGERS AND INTERACTIONS

Huang Meiyuan Xu Huaying and Ji Wusheng

Institute of Atmospheric physics,Academia Sinica,
Beijing, People's Republic of China

I. INTRODUCTION

In the process of evolution of cumulus cloud system the cloud development and rainfall genesis are effectually influenced by the interaction and merger of two neighboring clouds, It has been clearly found from direct observations[1-3] that cloud merged shortly after it accreted rapidly. In general, the merged cloud develops more vigorously than the unmerged, and this can result in the appearance of heavy rain and hailfall.

Orville et al.[4] and Turpeinen[3] simulated the process of cloud merger, but they showed different results in the conditions of cloud merger. Here, we used a two-dimensional time-dependent and warm cumulus cloud model studying the mechanism, conditions and process of cloud mergers and interactions. The computational domain is 30km in horizontal width and 12km in vertical height. Mesh size is 600m.

A typical, conditional, unstable stratification was obtained as initial vertical distribution of temperature and humidity.

The dimensions of disturbance domain in initiation are assumed from 1.2 to 2.4km deep,4.8km wide, in which relative humidity is 100% and disturbance temperatures are from 1 to 3°C. In sumulation of evolution of two clouds we quoted symbol D(L) L(T) R(T),Where T in L(T) and in R(T) denotes the disturbance temperature of left and right edge of domain respectively, and L in D(L) denotes the edge-to-edge spacing of two disturbance sources.

II. RESULTS OF NUMERICAL EXPERIMENT

Now, we present some simulations of the merging processes and interactions of two clouds with different distances and intensities.

1. The Case of Two Clouds With Nearly Equal Intensity and at Close Distance

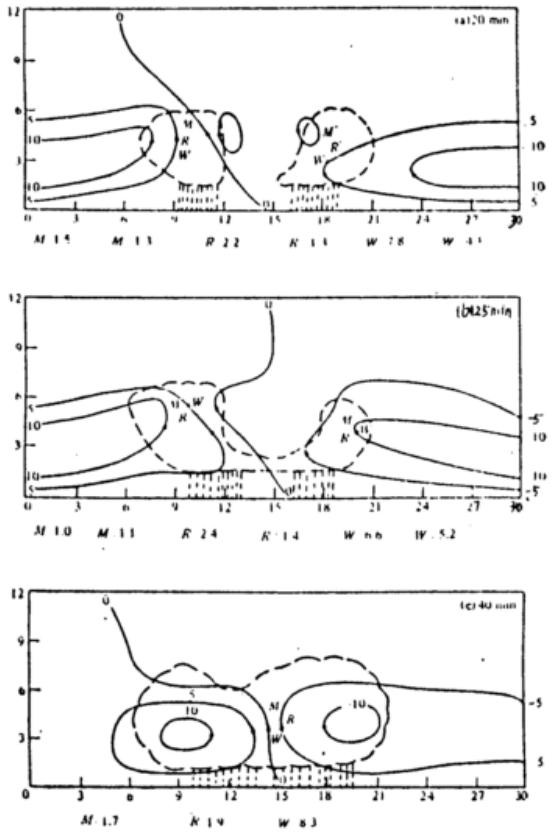


Fig.1. The map of the evolution of two clouds in case D(1.8)L(2.1)R(1.9).

Fig.1 is the case of D(1.8)L(2.1) R(1.9), it can be seen that before 15 min the two clouds developed individually, at 20 min (Fig.1a) the lower layer of the right cloud stretches to the left. At 23 min the right cloud stretches farther and the lower layer of the left cloud begins to stretch as well. At 25 min (Fig.1b) the lower layers of the two clouds link together completely. At 30 min the two clouds merge basically and are invaded by an updraft between them. At 40 min (Fig.1c) the two clouds complete a merger and become an updraft core. The maximum updraft velocity is increased violently.

The results of cloud merger processes obtained according to the numerical simulation are in good agreement with the observations made by Simpson et al.[11] They pointed out that cloud merger was initiated in the lower parts of the clouds linked up each other as a form of "bridge".

2. The Case of Two Clouds With Equal Intensity and at Far Distance

In case D(4.8) L(2.1) D(1.9) though the merging tendency of two clouds can be found, they do not merge each other. So, the two clouds disappear almost at the same time.

3. The Case of Two Neighboring Clouds With Competely Unequal Intensity

In case D(4.8) L(3) R(1) develop identically and independently at the first 5 min, Thereafter, the strong cloud develops and the weak cloud decays gradually at the next 5 min, At 18 min the weak cloud disappears completely. And by this time,the strong cloud has marked increment in lifetime and rainfall under similar conditions.

4. The Case of Two Clouds Formed With Timing Difference

As seen in Fig.2 that the right well-developed cloud absorbs the left weaker cloud in the early stage and under the action of lower layer pressure gradient force, the left weaker cloud is pulled to the right stronger cloud. So, a merger is produced with this absorption. The two clouds may merger only when they are both in the developmental stages, but cannot merger when their lifetime is longer than 20 min.

III. THE DEVELOPMENT OF MERGED CLOUD

The merged cloud develops more violently than the unmerged one. Fig.3 shows the evolution curves of the maximum vertical speed and rain water content in case D(1.8) L(2.1) R(1.9) and D(4.8) L(2.1) R(1.9) of the two pairs of convective clouds. After 30 min the clouds in case D(4.8) disperse subsequently and their maximum vertical speed drops gradually, while the clouds in case D(1.8) merge and develop violently, and thereafter the maximum vertical speed and the rain water content are

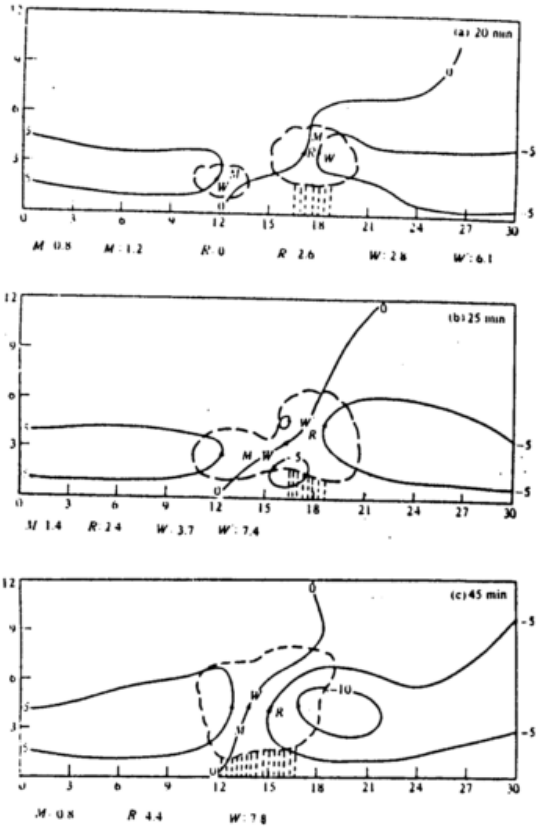


Fig.2. The evolution of the initial perturbation with timing difference in case D(1.2)L(1)R(1) (left perturbation by 11 min delay).

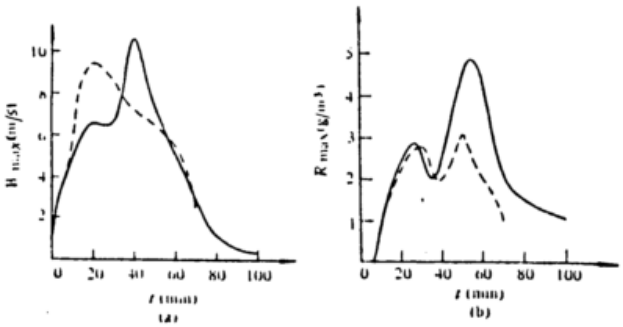


Fig.3. The variation of basic parameters of two clouds with different distance. Solid line denotes D(1.8); dash line denotes D(4.8). (a) the evolution of the maximum vertical speed; (b) the evolution of the maximum rain content.

increased by a factor of nearly 2. The cloud in case D(4.8) maintain 70 min and produce total rainfall of 102t/m. The others in case D(1.8) prolong 100 min and produce total precipitation of 220t/m.

IV. THE MECHANISM OF CLOUD MERGER

There are following two phases in cloud merger mechanism.

1. The Force of Pressure Gradient on The Cloud Merger

Fig.4 shows the distribution of pressure perturbation field in case D(1.8) L(2.1) R(1.9) of model clouds merged initially at 15 min. Their domains are controlled by updraft and the lower layer region between the two cloud transforms into a low pressure region under an associated general absorption of the two updrafts. Therefore, the two clouds close up in lower layer under the action of the force of a horizontal pressure perturbation gradient, and at last the two clouds are merged.

2. The Action of Convergence-Updraft Induced By Two Downdrafts on Cloud Merger

When the two clouds in case D(1.8) L(2.1) R(1.9) develop for over 20 min, the lower layer of the two clouds are occupied fully by downdraft due to continuous increase in precipitation. So, the amount of airflow convergence is also increased gradually at the same place and an updraft caused by convergence appears [see (b) and (c) in Fig.1]. A prolonged updraft zone forms in the two clouds, and this serves as an airflow basic domain for cloud merging.

V. CLOUD MERGER CONDITIONS

It can be seen from the above instances that two clouds, whether merged or unmerged, are related to the intensity ratio and the distance between them. For the analysis of cloud merger conditions twenty-two cases were studied and are plotted in Fig.5 by three types. The big black point denotes such a case that the weak cloud is depressed and disperses early; the circle is the case of cloud merger; the small black point is the case of the unmerged that disperse almost at same time.

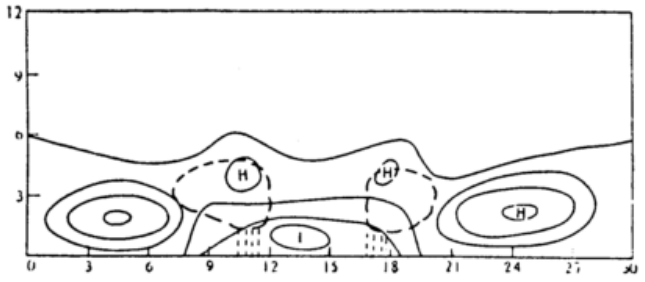


Fig.4. The size distribution of pressure perturbation field (p') before merging of the two clouds [At 15 min in case D(1.8)L(2.1)R(1.9)]. *H* and *L* represent the high and low pressure perturbation region, respectively.

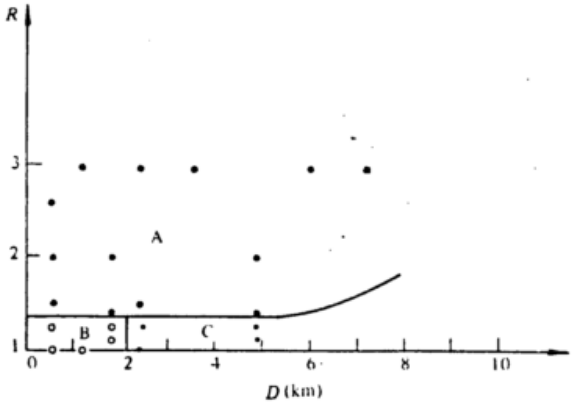


Fig.5. Cloud merger conditions. R means a ratio of initial disturbance temperature between the two clouds; *D* means an initial edge-to-edge spacing between the two clouds.

REFFERENCES

[1] Simpson, J. et al., Arch. Meteor. Geophys. Bioklim, 29(1980), 1-40.

[2] Huang Meiyuan and Wang Augsheng et al., The Introduction of Hail Suppression, Sciences Press, 1980.

[3] Turpeinen, O., Conference on Cloud Physics, Chicago,II.,1982.

[4] Orville, H.D. et al., J. Rech. Atmos., 14(1980), 449-516.

SMOOTH PARTICLE HYDRODYNAMICS AS APPLIED TO 2-D CUMULUS TYPE CONVECTION

Alan Gadian
Dept. of Pure and Applied Physics
University of Manchester Institute of Science and Technology
PO Box 88
Manchester M60 1QD, UK

1. SUMMARY

Smooth Particle Hydrodynamics is applied to two dimensional cumulus convection to gain greater comprehension of entrainment and diffusive mixing processes. Water and vapour phases are included in the calculations. The relevant advantages of the Lagrangian framework are discussed. Entrainment of elements surrounding the buoyant plume are observed; the inclusion of inter-particle mixing and diffusion processes being crucial for a realistic simulation. Simple linear diffusive transfer of particle properties between neighbouring elements (BAKER and LATHAM, 1979) is insufficient, with a velocity gradient proportionality providing more realistic computations.

2. THE LANGRANGIAN FRAMEWORK

There has been some evidence (HILL and CHOULARTON, 1985) that cumulus clouds are blobby in structure, implying that a parcel or particle approach might be applicable.

SALMON (1985) suggested a Lagrangian Hamiltonian approach to the study of shallow water waves in a rotating system. The system of ordinary differential equations has a close resemblance to the semi-geostrophic set produced by HOSKINS (1973), relying on transformation from cartesian to an elemental description. It is in this context that Smooth Particle Hydrodynamics (SPH) is applied.

In the areas of astrophysical fluid dynamics (eg. GINGHOLD and MONAGHAN, 1977) and plasma physics simulations, SPH techniques have been widely used. Two dimensional elements with a Gaussian density structure interact with each other to produce a fluid continuum. The buoyancy term provides the vertical acceleration and the horizontal pressure gradient effectively ensures continuity. Condensation and evaporation of water are the only energy sources incorporated, although it is planned to include the microphysics of droplet size distributions at a later stage.

3. MODEL DETAIL

Each element has a smooth Gaussian density structure or kernel, with the density at any particular point in space a resultant of the summation of all other neighbouring elements. The polynomial interpolant which determines this density distribution can be reasonably varied without a significant effect on the computation.

Initially, the elements reach a dynamical equilibrium, with the vertical pressure gradient balancing the gravitational force. For the model runs, the buoyancy provides the vertical acceleration, ie.

$$\frac{Dv}{Dt} = g\frac{\delta T}{T}$$

where T is the mean temperature v the vertical velocity and g the gravitational acceleration. The horizontal acceleration satisfies

$$\frac{Du}{Dt} = \frac{-1}{\rho}\frac{\partial p}{\partial x}$$

with pressure gradient calculated directly from the kernel density (ρ) structure. At each time-step the relevant phase changes alter the ambient temperatures. Mixing processes are incorporated with the change in a property (A_i). For a particle i defined by δA_i = - factor * A_i + factor * A_j, for all neighbouring particles j. Factor is a time-

scale parameter dependent on the size of model elements multiplied by the sum of the absolute differences in component velocities. The time-scale values are defined as consistent with those given in BAKER and LATHAM (1979).

A 5th order 7 stage Runke Kutta procedure is employed to iterate the differential equations (DORMAND and PRINCE, 1980). Recent advances in such o.d.e. solvers and the use of vector processes has enabled the feasibility of such computations, using a particle size of approximately 100 metres.

4. DISCUSSION

The particular simulation to be presented is based on a temperature and humidity profile (JONAS, 1987), provided by the UK Meteorological Office. The corresponding observations indicated widescale cumulus convective clouds between about 1 and 2.2 km. To initiate convection in the model all particles within a column 300 m wide by 1100 m high are given a temperature perturbation of +1°C, with a mixing ratio of 4.3 gm/kg, the ground measurement. The model atmosphere has horizontal dimensions of 4 km, with two columns on either side where the air can descend to compensate for the vertical motion, and where the vertical acceleration is a consequence of the vertical pressure gradient. Thus no mass is lost from the model and there is no interaction of the downward moving air and the buoyant column.

Results are calculated using different representations for the mixing and diffusion processes with a purely diffusive mixing relationship (ie. no velocity gradient weighting) and with an e folding time t_c of approximately 100 secs (BAKER and LATHAM, 1979), some of the cooler entrained elements unrealistically pass directly through the convective plume. Significant decreases in the rate constant t_c effectively reduces the convective strength and horizontal dissipation becomes important. The mixing resultant from the inclusion of a velocity dependent term produces much more representative flow patterns, although it is appreciated that the formulation in Section 3 is probably by no means the best.

The use of the perturbation approximation for the vertical momentum equation and the difficulties accruing in evaluating a realistic equation of state, clearly represent disadvantages of using this Lagrangian framework. Despite these limitations the results indicate that this is possibly a useful technique, especially if extended to include cloud microphysics and chemistry.

REFERENCES

BAKER, M. and LATHAM, J.: The Evolution of Droplet Spectra in Small Cumulus Clouds. J. Atmos. Sci. 36 (1979) 1612-1615.

DORMAND, J.; PRINCE, P.: A Family of Embedded Runge-Kutta Formulae. J. Computation and Appl. Maths. 6 (1980) 19-26.

GINGOLD, R.; MONAGHAN, J.: Smoothed Particle Hydrodynamics. Mon. Notices of Roy. Astr. Soc. 181 (1977) 375-89.

HILL, T.; CHOULARTON, T.: An Airborne Study of the Microphysical Structure of Cumulus Clouds. Q. J. of Roy. Met. Soc. 111 (1985) 517-544.

JONAS, P.: Private communication, Met. Office aircraft observed profile (1987).

SALMON, R.: New Equations for Nearly Geostrophic Flow. J. Fl. Mech. 153 (1985) 461-77.

CONVECTION WAVES AND THEIR STRUCTURAL IMPACT ON CLOUD FIELDS

Thomas Hauf and Terry Clark

National Center for Atmospheric Research Boulder / Colorado

1. INTRODUCTION

In the presence of shear exceeding 5 m/(s km) near the top of a convectively heated boundary layer internal gravity waves develop in the overlying stable atmosphere. These waves were first observed by gliders (Jaeckisch, 1968; Lindemann, 1972) and were called thermal or convection waves. Kuettner et al (1987) studied them using an instrumented aircraft. Clark et al (1986) performed 2-dimensional numerical simulations, whereas recent simulations by Hauf and Clark (1988) and Balaji and Clark (1988) were in 3 dimensions. These nonlinear model simulations were supplemented by linear studies (Clark and Hauf, 1986; Balaji and Clark,1988). Based on these papers we review some basic features of convection waves and as an example illustrate their organizing impact on clouds.

2. BASIC FEATURES

Waves develop as soon as boundary convection in response to surface heating penetrates into the stable layer overlying the boundary layer. Within a few hours the wave system covers the whole troposphere and extends well into the stratosphere. Depth and location of the shear layer as well as its strength and direction determine the wave generation efficiency. The structure of the wave field and of the boundary layer motions also strongly depend on the shear profile. The dominant horizontal wavelength is between 10 and 15 km and is thus significantly higher than horizontal boundary layer scales of approximately 6 km. The observed typical amplitudes of vertical wind velocity range between 1 and 3 m/s with lower values found by the numerical simulations. Horizontal phase speed is nearly uniform over the tropospheric depth and different from the phase speed of the boundary layer modes with respect to magnitude as well as direction. In the 12 June 1984 case which was investigated by Clark et al (1986) and by Hauf and Clark (1988) waves move

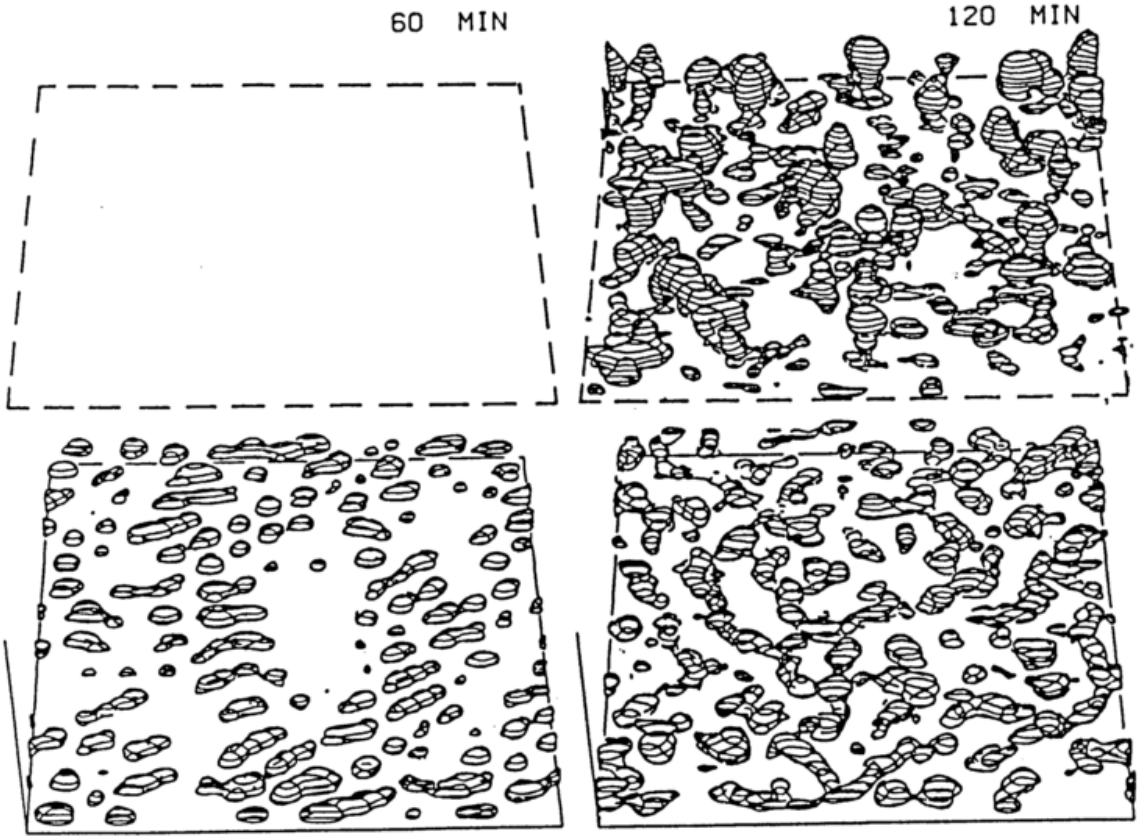


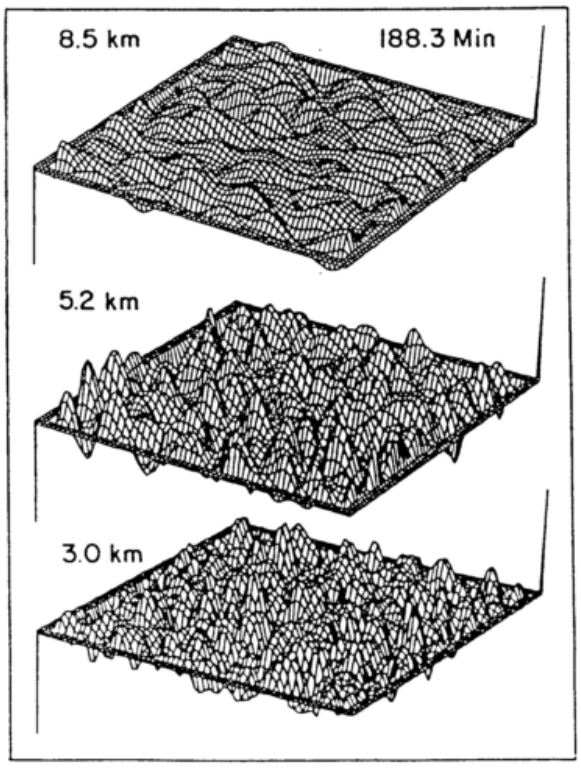
Fig. (1) Three-dimensional perspective view of vertical velocity surfaces showing volumes where w $\geq$0.5 m/s. The domain size is 60 x 60 km in the horizontal and 15 km in the vertical. Lower plate shows region between 0 - 3 km, upper plate 3 - 15 km.

in the upshear direction at a speed of about 10 m/s relative to the ground. Waves also propagate in the vertical with a vertical wavelength commensurate to the tropospheric depth.
It is suggested that convection waves belong to a fundamental atmospheric eigenmode which is comprised of convective eddies in the boundary layer and overlying waves. This also can be described in terms of an interaction between the gravity waves and the convective eddies in the boundary layer. Convective eddies in the presence of shear excitate the waves but simultaneously they are modified by the waves. As a consequence boundary layer convection is not solely governed by boundary layer parameters but depends also on the gravity wave field. Dry and moist shallow convection in the presence of shear, therefore, is a nonlocal phenomenon which requires for its understanding the full depth of the gravity wave system. For example, Clark et al (1986) compared the boundary layer solutions in the presence of waves with those of an isolated boundary layer without waves and found significantly different horizontal scales. It is concluded that convection waves are an important organizer of shallow convection and, therefore, also of clouds.
In this paper we illustrate this organizing effect of convection waves on shallow cloud populations.

3. STRUCTURAL ASPECTS

Three figures are presented in this paper which should illustrate the structure of the gravity wave field and its influence on the cloud population. The figures are taken from Hauf and Clark (1988). Similar figures are shown in a movie which also provides an impression of the wave dynamics.
Figure (1) shows in a perspective view those regions in three-dimensional space were the vertical wind velocity is greater than + 0.5 m/s. Similar pictures can be drawn for higher values or also for negative values but are ommited here. As boundary layer motions are quite different from wave motions, two plates are shown for each time. The lower refers to the lowest 3 km whereas the upper one to the region between 3 km and 15 km. The horizontal domain is 60 x 60 km. At t = 60 min after the model initiation no waves have developed yet and the boundary layer shows longitudinal rolls approximately parallel to the mean boundary layer shear in line with linear theory. One hour later waves have developed and the boundary layer structure has dramatically changed to a varicose like structure. The wave field is scattered with single and nearly vertical updraught 'towers' . These towers extend well into the stratosphere. The scatter is explained as result of gravity wave/convective eddy interaction. According to Wegener's theorem wave fronts in the stable atmosphere form perpendicular to the shear vector. In a pure speed shear case, therefore, rolls and fronts are perpendicular to each other. The fronts are modulated by the rolls which results in the broken structure of the wave field. Vice versa boundary rolls are modified by the waves yielding the varicose like structure of the boundary layer motions.
The wave updraught fields lead to a deformation of the initially horizontal isosurfaces of potential temperature as shown in Figure (2). Three theta-surfaces (304, 310, 320 K) are displayed corresponding to altitudes of 3.0, 5.2 and 8.5 km. Again the domain is 60 x 60 km whereas the peaks in the corner are 600 m high. The wave field is polychromatic with spectra narrowing with height. With increasing height the short waves disappear and the wave amplitude is lowered. The dominant wavelength in the shear direction is greater than the dominant wavelength in the direction perpendicular to it. The maximum vertical displacements of up to +/- 300 m occur at the lowest levels. They are about half of this value at 8.5 km. It is easy to imagine that such a vertical displacement field influences any cloud development.

Fig. (2) Deformation of theta-surfaces (304, 310, 320 K) at three heights. Domain size 60 x 60 km; peaks in corners scale 600 m. (shear direction parallel to x-axis, from left corner to lower right)



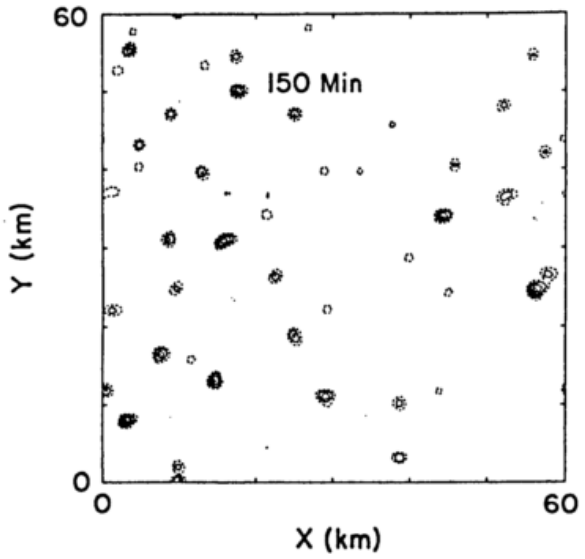
4. INFLUENCE ON CLOUD POPULATIONS

Cloud growth is necessarily linked to moisture supply from lower levels by the convective eddies. The impact of gravity waves on the convective eddies, therefore, is also identificable in the cloud field. Fair weather cumuli clouds generally form near the top of the convective boundary layer which is also the region of strong wave/eddy interaction. The dynamical interplay between supporting eddies from below and updraught resp. downdraught motions

provided by the gravity waves, together with the nonlinear character of the phase transitions itself, cause the appearant high degree of randomness of the cloud population (Fig. 3). The important parameters which govern the cloud population seem to be - the horizontal wavelength of the dominant eigenmode, - the relative phase speed difference between the waves and the eddies, - the size and lifetime of the eddies, - and the timescale of cloud dissipation.

We point out that the scatter or randomness of the cloud field is neither the result of any inhomogeneity in the surface heat flux as the latter exhibits nearly wavenumber zero, nor a result of pure boundary layer circulations alone. Rather it is explained as a result of the mutual modification of waves and convective eddies which is an internal and inherent nonlinear process. Future research has to quantify the illustrated organizing impact of convectively forced internal gravity waves on fair weather clouds.

Fig. (3) Horizontal cross-section through the liquid-water field showing cloud field at 2 km height.



REFERENCES

BALAJI, V., CLARK, T.L.: Scale selection in locally forced convective fields and the initiation of deep convection. J. Atmos. Sci. (submitted,1988).

CLARK, T. L., HAUF, T., KUETTNER, J. P.: Convectively forced internal gravity waves: Results from two-dimensional numerical experiments. Quart. J. R. Met. Soc., 112 (1986), pp. 899-925.

CLARK, T. L.; HAUF, T.: Upshear cumulus development: a result of boundary layer- free atmosphere interactions. Proc. 23rd Radar Meteor. and Conf. Cloud Phys. (1986), Vol. 3, J18-J21.

HAUF, T., CLARK, T. L.: Three-dimensional numerical experiments on convectively forced internal gravity waves. Quart. J. R. Met. Soc. (submitted, 1988).

JAECKISCH, H.: Waveflow above convection streets. OSTIV Publication X (1968).

KUETTNER, J. P., HILDEBRAND, P. A. , CLARK, T. L.: Convection waves: Observations of gravity wave systems over convectively active boundary layers. Quart. J. R. Met. Soc. (1987), pp 445 - 467.

LINDEMANN, C. : Thermal wave soaring. OSTIV Publication XI (1972).

COMPARISON BETWEEN NUMERICAL CLOUD RESULTS AND OBSERVATIONS

Rumjana Mitzeva and Vasil Andreev

University of Sofia, Bulgaria

1. INTRODUCTION

It is known that Lagrangian bulk entrainment one-thermal cloud models are unable to simulate simultaneously cloud top height and in-cloud liquid water content (LWC) of cumulus clouds.LUDLAM (1958) suggested that these clouds are composed of a succession of thermals. MASON and JONAS(1974) developed a model of a non-precipitating cumulus cloud that grows by the ascent of successive spherical thermals through the residues of their predecessors.

In this paper we shall compare the measured LWC in non-precipitating cumulus clouds with the values computed by a model of a cloud composed of a succession of thermals.

2. CLOUD MODEL

According to the model used (ANDREEV et al.1979)the convective cloud is composed of active and non-active cloud masses.It is assumed that the active mass is formed by successive ascending spherical thermals,while the non-active cloud region is formed by thermals that have previously risen and stopped at their convective level;it is motionless and expands by turbulent diffusion This region is characterise by certain temperature excess and the presence of cloud droplets and water vapor;they vary in time due to diffusion and evaporation.The microphysical processes in moving thermals are described using bulk parametrization (ANDREEV 1976). Four different categories of hydrometeors are taken into account: cloud and rain drops,cloud ice and graupel. The Marshall-Palmer distribution for rain drops are assumed.

According to the model described the ascending thermals entrain continuously air of any level from cloudless environment or from non-active cloud mass. In order to model the entrainment from the non-active part of the cloud the diffusional thermals are transformed from sphere to cylindrical layer. For the entrainment rate α_i of the ascending thermals the following expression is used $\alpha_i = 0.6/R_i(Z_i)$,where $R_i(Z_i) = R_{io} + 0.2.Z_i$,$R_{io}$ and $R_i(Z_i)$ are the radius of thermals at cloud base and at height Z_i respectively.

Differential equations describing the processes in the model cloud are numerically integrated by Runge-Kutta method. The calculations are carried out for thermals ascending from cloud base to the height where zero velocity is obtained.

3. OBSERVATIONS

The model has been run using environmental conditions on (i) 18 July 1964, Ukraina,(ii) 23 June 1981,CCOPE.

3.1 18 JULY 1964,UKRAINA

VOIT and MAZIN (1972) have made a number of aircraft measurments of the LWC at different levels in a field of non-precipitating cumulus clouds with similar cloud base and cloud depth,where the data of measurments in disipative clouds are excluded.From their results one could evaluate the change in the average in-cloud LWC with the height.

The environmental sounding (above the cloud base) for 18 July 1964 is given in Table 1. The depth of the observed clouds was approximately 3900 m.

Table 1

18 July sounding used in this paper
P - pressure, T - temperature, f - relative humidity, H - height

H [m]	P [hPa]	T [°C]	f [%]
1500	850	14.3	64
2000	801	9.8	61
3000	709	2.7	62
4000	626	- 0.4	25
5000	552	- 6.3	10
6000	485	-12.7	10

3.2 23 JUNE 1981, COOPE

The observed cloud was essentialy ice-free and non-precipitating. Cloud base was at 751 hPa($\approx$ 1500m) and cloud top was observed at approximately 480 hPa($\approx$ 5000m). The environmental sounding (taken from TAYLOR et al.1986) is shown in Fig.1. The detailed description of the microphysical observations is given by AUSTIN et al.1985.

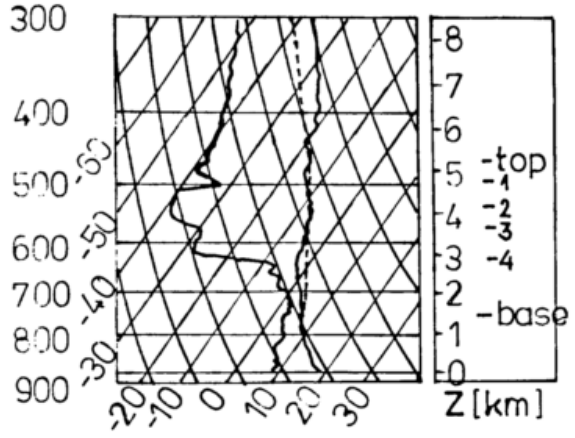


Fig.1 23 June 1981 COOPE sounding. Cloud base, cloud top and the penetration levels are noted in the box at right.

4. COMPARISON OF OBSERVATIONS AND MODEL RESULTS

mainly the measured and computed LWC will be compared here.

The following parameters have to be known in order to conduct the model computations: the thermal radius at the cloud base - R_{io}, the time interval between successive thermals - Δt, their number, and the turbulent diffusion coefficient for the non-active cloud mass - K. Their values are chosen in a way, that the model simulates correctly the height of the observed cloud top.

4.1 18 JULY 1964, UKRAINA

The computations are carried out with two different set of parameters: (i) 5 thermals with R_{io}= 500 m, Δt=5 min, K=30 m^2/sec, (ii) 15 thermals with R_{io}= 280 m, Δt = 3 min, K = 30 m^2/sec. In both cases after a certain time a cloud with depth about 3900 m is formed in the model. The LWC in moving thermals after this moment is given on Fig.2

+ for (i), • for (ii).

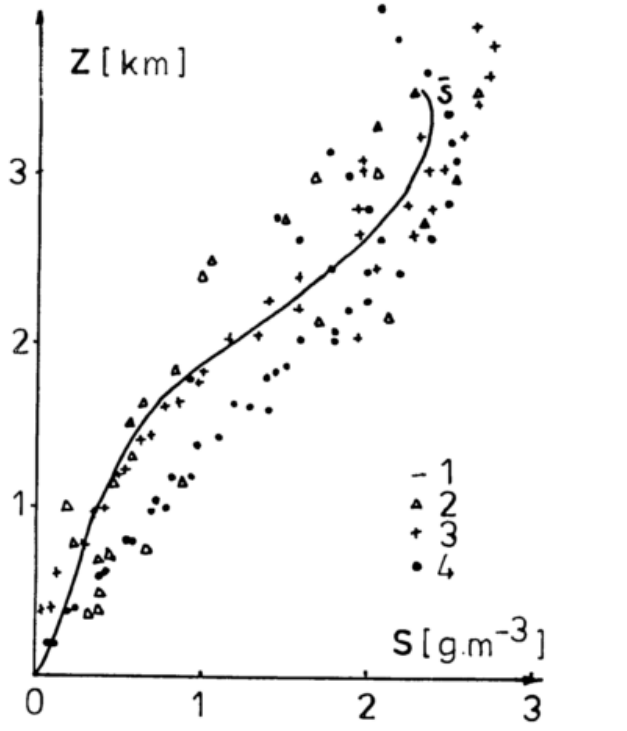


Fig.2 Mean liquid water content profile S(Z) on 18 June 1964. 1- mean experimental data curve; 2 - averaged LWC values over flight trajectories; 3 - model LWC values for (i); 4 - model LWC values for (ii)

Curve $\overline{S}$ on Fig.2 shows the average LWC measured in clouds with 3900 m depth on 18 July 1964.

4.2 23 JUNE 1981 CCOPE

The following set of parameters was used: 8 thermals with R_{io} = 750 m, Δt = 5 min, K = 70 m^2/sec. Using this parameters after a certain time the model cloud top was at 4920 m, showing a good agreement with the observed one.

Fig.3 shows the model LWC plot. The penetration level at 570 hPa (about 2000 m above cloud base) is given by dotted line. In the upper part of Fig.3 the LWC measured at 570 hPa is given (taken from AUSTIN et al.1985). One can see that the peak computed LWC for the penetration level is 1.8 g/m^3 and is comparable with the measured peak value.

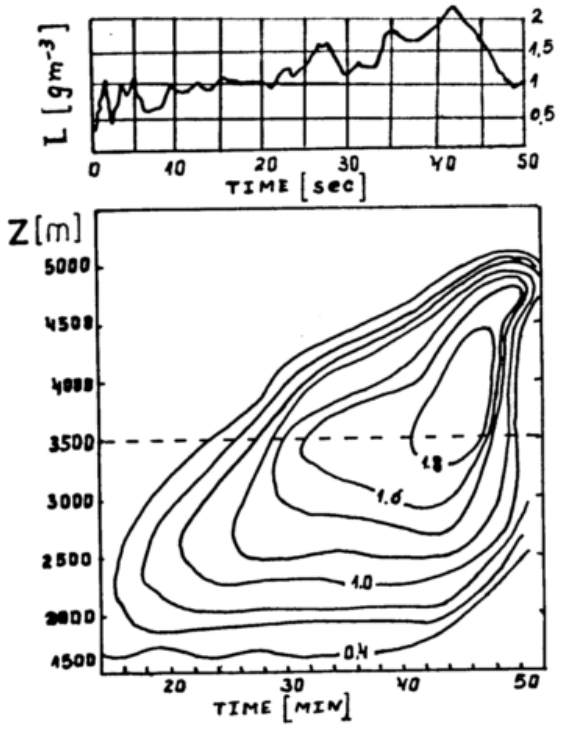


Fig.3 Contour plot of LWC for the cloud model.Contour interval is 0.2 g/m^3. The dashed line shows the penetration level (570 hPa). In the upper part of the figure the LWC measured at 570 hPa is given.

5. SUMMARY

The results show that the model simulates quite well the changes in the average in-cloud LWC with the height measured on 18 July 1964 in Ukraina. A reasonable agreement between the peak computed LWC and the one measured on 23 June 1981,CCOPE is also seen. This demostrates that the cloud model composed of active and non-active cloud mass with continuous entrainment of successive ascending thermals could simultaneously predict the values of the in-clcud LWC and cloud top height of non-precipitating cumulus clouds.

REFERENCES

ANDREEV,V.:Microphysical Effects in a Dynamical Model of an Active Isolated Element of Convection,Bulg.Geophys.J., 1976,N4,p.17-27 (in Bulgarian)

ANDREEV,V.;SYRAKOV,D.;MITZEVA,R.: Modelling of Convective Cloud Formation as Successive Ascending Thermals,Buig. Geophys.J,1979,N1,p.3-9(in Russian)

AUSTIN,P.;BAKER,M.;BLYTH,A.;JENSEN,J.: Small-Scale Variability in Warm Continental Cumulus Clouds,J.Atm.Sci.,1985, v.42,p.1123-1138.

LUDLAM,F.:The Hail Problem,Nubila,1, 1958,p.12-96.

MASON,B.;JONAS,P.:The Evolution Droplet Spectra and Large Droplets by Condensation in Cumulus Clouds,Quart.J.Roy. Meteor.Soc.,100,1974,p.23-38.

TAYLOR,G.;BAKER,M.;JENSEN,J.:Entrainment Studies of CCOPE Clouds Using an Axisymetric Cloud Model,A.M.S.,Conference on Cloud Physics SnowMass,Colorado,1986,p.149-152.

VOIT,F.;MAZIN,I.:Liquid Water Content in Cumulus Clouds,Izvestia Acad.of Sciences USSR,Atmosph. and Ocean Physics,11,1972,p.1166-1176(in Russian)

LOCAL ENVIRONMENTAL CONDITIONS INFLUENCING THE GROWTH AND INTERNAL STRUCTURE OF NON-SEVERE THUNDERSTORMS

Nancy Westcott
Illinois State Water Survey
Champaign, Illinois 61820

1. Introduction

An examination has been made of the internal structure of a number of convective storms occurring on two days in August 1986, using the CHILL 10-cm reflectivity measurements. These two days provide an interesting contrast in the way in which non-severe storms of similar intensity can form and evolve. On one day, the echoes were first detected at and below the freezing level (minimum reflectivities of 10 dBZ), and grew slowly in height. Not until very late into the life of the storm did any of the echo tops exceed 7 km. On a second day, convection occurred in two storm events, one in the morning and one in the late afternoon. The morning echoes formed above the 0°C isotherm (5-6 km) and readily exceeded 7 km, with many reaching 11 km. The afternoon echoes formed at the freezing level, and were somewhat taller and longer lasting, than those observed during the other two flights. Echoes from all three flights attained peak reflectivities of 55 dBZ. This paper will examine the manner in which these storms develop, in the context of the local meteorological conditions as determined from environmental soundings, visible satellite imagery, an objective analysis of standard surface and upper air observations, and from inferences made concerning the organization of the storms.

2. Data source and methodology

These data were collected during three randomized cloud treatment flights in Illinois as a part of the exploratory phase of 1986 PACE (Precipitation Augmentation for Crops Experiment). The overall goal of PACE is to determine whether and under what conditions summer precipitation in the central part of the United States can be enhanced by cloud seeding. In this area of the U.S., evidence to date indicates that cloud droplet growth by condensation followed by precipitation growth by coalescence is the dominant precipitation initiation mechanism (Ackerman and Westcott, 1986). Because of the importance of the warm rain processes in initiating precipitation in this area, the experiment is based on the dynamic seeding hypothesis. A total of 19 clouds were treated and studied from the 3 flights. Clouds from two of the flights were actually seeded with silver iodide and those in a third flight were treated with a placebo. The small sample size precludes comment on a seeding effect.

The PACE operations were based at the NSF/ISWS CHILL radar site at the University of Illinois Willard Airport (CMI) located in Savoy, Ill. The target area encompassed the region within 150 km of the radar. However, all cloud passes were made within 95 km of the radar on these two days. During the field program, 10-cm reflectivity data (1° beam) were collected at 512 range bins, each 300 m deep, out to a range of 150 km. The radar was operated in a 360° scan mode with the intent of topping all echoes in the area, completing a volume of 10 - 16 elevation steps within 3 - 5 minutes.

Volumes covering the history of the treated clouds were interpolated to grids with a 1 km resolution in the horizontal and vertical directions. The approximate aircraft pass locations based on the aircraft Loran C and VOR/DME systems, were plotted on these fields. A preliminary analysis determined that the treated cloud could be associated with an individual echo core. The reflectivity history of the specific echo cores associated with the treated clouds were tracked by hand, in time and height. For purposes of comparison, a minimum reflectivity of 15 dBZ was imposed on the data used in this analysis. Eighteen of the 19 cores were joined at some point in their life with an adjacent core at some reflectivity level, half within their first five minutes and the remainder within 20 minutes. For a given core, the history was stopped, not when it became joined with another but when it could no longer be distinguished from the rest of the echo with any certainty. Particular attention is given to the growth rates of the area and reflectivity characteristics of the echo cores. Because the volumes spanned 3 to 5 minutes in length, the times presented are approximations, and thus the rates calculated are only simple estimates.

3. Description of the three flights and general weather conditions

The environmental conditions were similar in several respects for the 3 flights. In particular, the days were characterized by relatively warm cloud base temperatures (16 - 20 °C) and ample moisture in the lowest part of the troposphere, (surface mixing ratios of 14-16 g/kg).

3.1 August 6, 1986 - Flight 1

The late afternoon flight (1556 - 1746 CDT) on August 6, was centered on a small line of thunderstorms. A gradually strengthening trough associated with a surface low to the north was moving in to the area. By 1800 CDT, the trough was analyzed at the surface as a cold front stretching from Chicago southward through east-central Illinois and then southwestward through St. Louis.

While scattered high-based clouds had been observed in the area since late morning, only after 1500 CDT did this convection become suitable for treatment (grow to the -10°C level). The 1514 CMI sounding was neutral with respect to the saturated adiabat above 880 mb, with adequate moisture below 600 mb, but rapid drying above. The lifted condensation level (LCL) and the convective condensation level (CCL) was nearly identical (16 °C at 1.1 km), suggesting that sufficient heating was present to initiate convection. Also low-level convergence present in the area during the afternoon (10^{-4} s^{-1}, as determined from the NWS first order stations) appeared sufficient to lift the air mass, resulting in a convectively unstable conditions and in an enhancement of the convection moving into the area from the west.

Visual observations from the aircraft indicated a cloud base of .8 km. Echoes were first observed at or below the freezing level, 4 km msl. Eight passes were made through 5 clouds concentrated in a single line of storms between 1631 and 1703 CDT, some 65 km to the southwest of CMI. New growth was occurring on the WSW end of this line. The nearest area of convection reaching to at least 6 km at this time, was 100 km to the NE.

3.2 August 26, 1986 - Flight 2

The first flight was from 0846 - 1202 CDT on this day, in an area of thunderstorms about 250 km ahead of a strong, slowly moving cold front. This area of convection had originated in southern Iowa around midnight and moved southeastward into the area in the morning. The nearby 0700 CDT SLO sounding showed conditionally unstable conditions above the shallow surface inversion to 500 mb, with substantial moisture up to 450 mb. Visual observations from the aircraft indicated multiple layers of clouds. Surface heating was inhibited by a cirrus overcast present during the morning flight. Surface wind observations indicated only weak convergence in the area. By 1145 CDT, a period of the day when convective activity is at a climatological minimum, the convective activity was moving out of the target area and diminishing rapidly in intensity.

Ten passes were made in a total of 8 clouds between 0958 and 1131 CDT. Echo formation occurred at or above the freezing level (4.4 km msl). In 5 cases, the echoes were separated from other echoes by at least 3 km; and in 3 cases new growth was immediately adjacent to an existing echo.

3.3 August 26, 1986 - Flight 3

The second flight on this day was from 1507 - 1900 CDT, in an area of developing thunderstorms more directly associated with the cold front. Frontal passage at CMI occurred at approximately 1800 CDT. The 1417 CMI sounding indicated unstable conditions below the LCL, conditional instability to 700 mb and neutrally stability above to at least 500 mb. Ample moisture was available to 450 mb. Cloud base was reported as 2 km.

Treatment occurred in 7 clouds during this flight, although only 6 were analyzed due to problems in determining the aircraft position. The echoes appeared to form near the freezing level (4.7 km). These clouds were associated with the front and generally in a broad line of activity.

4. Results and Discussion

To give an overall indication of the echo characteristics during the 3 flights, mean values of peak reflectivity, peak echo height and peak area for reflectivities equal to or exceeding 15 and 35 dBZ are presented in Table 1. Two points can be made from this table. First, while the peak reflectivities are similar for the 3 flights, the areal coverage is much smaller on the morning flight. This might be expected as the convection during this flight was generally diminishing in intensity. The second major difference lies in the height of the echoes cores during the two afternoon flights. The mean top height of the echo cores for the August 6 flight was some 2 km less than on the 26th. This may be explained by the very rapid drying of the troposphere above about 4.5 km on the 6th. Additionally, it is interesting that although all of the echoes treated on August 6, were from the same line of thunderstorms and were treated within a half-hour of each other, the variance of peak reflectivity and areal extent was larger than on the afternoon of the 26th when the flight spanned a two and a half hour period. This may suggest that not all of the echo cores were large enough or strong enough on the 6th to be sustained at a level of unfavorable moisture. On the afternoon of August 26, no such cap was present to restrict the growth of the less intense echoes.

Table 1. Mean, standard deviation and sample size for peak values for echo cores by flight

Flt. No.		Max Refl. (dBZ)	Max Top (km)	Max Area dBZ≥15 (km^2)	Max Area dBZ≥35 (km^2)	Time To Max Area>35 (min)
1	X	52.8	8.8	65.0	27.2	23
	SD	7.7	2.5	21.2	18.5	5
	N	5	5	5	5	4
2	X	53.3	9.	41.8	14.8	17
	SD	8.6	2.1	19.1	9.0	3
	N	8	7	8	8	8
3	X	55.5	11.2	64.7	28.7	23
	SD	2.0	2.1	19.0	10.8	13
	N	6	5	6	6	6

Growth rates from the time of first observation at values greater than or equal to 15 dBZ, to the time of the peak value of the particular echo parameter also were calculated (Table 2.). These indicate that the rate of increase of peak reflectivity and maximum top height on August 6 were slower than for the two flights on the 26th. While the rates for the two flights on the 26th are similar, the duration of the growth period was much shorter for the morning flight: The mean time to reach peak reflectivities were 19, 13 and 14 minutes respectively for the 3 flights; and the mean time to grow to the maximum height were 19, 11 and 20 minutes.

Table 2. Mean, std. dev. and sample size for growth rate from first detection and peak value.

Flight No.		Max Refl. (dBZ/min)	Max Top (m/s)	Max Area dBZ > 15 (km^2/min)	Max Area dBZ > 35 (km^2/min)
1	X	1.7	3.8	2.4	1.0
	SD	.9	1.7	.5	.6
	N	4	5	5	5
2	X	2.5	4.8	1.6	1.0
	SD	.9	.7	.9	.8
	N	8	7	8	8
3	X	2.5	5.0	2.1	1.5
	SD	1.4	1.7	.8	.6
	N	6	5	6	6

The randomization was such that the two afternoon flights were actually seeded with AgI and the morning flight with the placebo. Due to the nature of the local environmental conditions, it was not unexpected that the morning echoes were smaller and shorter-lived. It is common in this area of the country for nighttime storms to diminish in strength after sunrise. This may have been an overriding factor that result in the differences in echo characteristics for the morning flight rather than the treatment type. The variety of environmental conditions controlling the dimensions of the clouds from day to day and on a single day, suggests that in evaluating cloud characteristics to determine a seeding effect, it is necessary to stratify echo parameters based on these conditions. Additionally, it may be necessary to treat both a control group and a seeded group of clouds during the same period of convection. Because of the variance found even for a single thunderstorm line, a number of clouds must be treated on any given day to insure adequate sampling.

Acknowledgements. This work was supported by the PACE Federal-State Program, under grant COMM/NOAA CHANGNON A.

5. References

Ackerman, B. and N. E. Westcott, 1986: Midwestern convective clouds: a review. J. Wea. Mod., 18, p. 87-94.

Braham, R. R., Jr., 1986a: The cloud physics of weather modification. Part I - Scientific basis. WMO Bulletin, 35, p. 215-222.

Braham, R. R., Jr., 1986b: The cloud physics of weather modification. Part II - Glaciogenic seeding for precipitation enhancement. WMO Bulletin, 35, p. 308-315.

DOPPLER RADAR STUDY OF A WEAKLY SHEARED THUNDERSTORM

David J. Raymond and Alan M. Blyth

Physics Department and Langmuir Laboratory for Atmospheric Research,
New Mexico Institute of Mining and Technology,
Socorro, NM 87801

1. INTRODUCTION

During the New Mexican summertime, storms develop initially over the mountain ranges. In 1984 an experiment was performed on the cumuliform clouds which developed over Langmuir Laboratory in the Magdalena Mountains near Socorro, New Mexico. The experiment utilized 4 Doppler radars, several instrumented aircraft and other ground-based equipment. The radars were installed close to the mountains so that observations were made at high resolution and elevation angle. The high elevation angle allowed the vertical component of particle velocity to be accurately measured.

The purpose of this paper is to describe the evolution of a well-observed storm cell that occurred on 2 August 1984. Air motions and precipitation particle trajectories are presented and interpreted.

2. THE CENTRAL CELL ON 2 AUGUST 1984

The storm on this day developed in an environment with moderate instability and weak shear. The first cumulus clouds formed over the mountain at 09:10 MST and cloud base was at 3.7 km MSL. The early evolution of the system followed a pattern where the cumulus clouds alternately grew and decayed, each time ascending to a slightly higher altitude. Radar observations commenced at 10:30 when the maximum reflectivity in the storm was about 25 dB(Z) at an altitude of 5 km MSL. The top of the minimum detectable radar echo was near 8 km by this time. At about 11:00 the cloud system rapidly ascended to 13 km MSL. Several cells were distinguishable, and each rose to the same level at slightly different times. To simplify the discussions herein, we will concentrate on one cell (the *central cell*) that was located over Langmuir Laboratory.

The central cell drifted to the east at about 2 m/s. The environmental shear was to the northeast, so radar data are displayed in a vertical plane oriented 220° - 40°. This plane cuts through the center of the cell and was allowed to drift with the cell. Doppler-derived winds are displayed in a cell-relative frame. Figure 1 shows the reflectivity and wind pattern in the above-defined plane for times 11:05, 11:14, 11:23 and 11:32.

The time evolution of the cell is quite straightforward. Highest reflectivities occurred within the main updraft. The sequence illustrated in Figure 1 indicates that the 30 dB(Z) contour ascended and the maximum echo increased in magnitude as the updraft intensified. Thereafter the echoes weakened and descended as the updraft at the lower levels ceased. Outflow into an anvil cloud is quite pronounced from 11:14 onward.

The picture which emerges from Figure 1 suggests that the precipitation process is a relatively straightforward one in which graupel forms in the updraft, falls through it, and grows in the cloud liquid water. We now try to test this picture by tracing the trajectories of precipitation particles.

3. PARTICLE TRAJECTORIES

The trajectories of particles reaching 3.5 km MSL at two specified times were traced backward in time until missing velocity data terminated the calculation. This typically happened when the trajectory approached the edge of the cloud during a period of rapid evolution. Calculations employed linear interpolation between radar volumes and between grid points to find velocities on the trajectory. The calculations shown here assumed that all motion occurred in the two-dimensional plane illustrated in Figure 1, but fully three-dimensional calculations show similar results. Values of all measured fields interpolated to the trajectory were also saved.

The first set of trajectories (see Figure 2) was started at 11:15, or during the period of maximum reflectivity. They presumably represent the evolution of the most intense precipitation. It can be seen from Figure 2 that particles reaching the 3.5 km level at 11:15 originated at about 7 km where the temperature was approximately -15° C. Figure 3 shows the calculated positions of the precipitation particles at 10:56, along with the reflectivity pattern at that time. It is clear that these particles are first detected in the uppermost part of the cloud when its tops are near 8 km. (Not all particles could be traced back to this time.)

Figures 4 and 5 respectively show the mean reflectivity and the mean terminal and fall velocities of particles as a function of height along their trajectories. Note that the reflectivity increases from 20 to 45 dB(Z), and that the terminal velocity increases from 4 m/s to over 10 m/s. Simultaneously the particle fall velocity increases from 2 m/s, or a state of near-suspension, to almost 10 m/s. The difference between these two curves gives the updraft velocity, which decreases from 4 m/s to 1 m/s as the particles descend.

The second set of trajectories (see Figure 6) was started at 11:30, or during the decaying phase of the cell. These trajectories can also be traced back to near cloud top, or approximately 8 km. The only apparent difference is that these particles fell through weak to non-existent updrafts, and as a consequence, encountered little, or no growth-inducing liquid water on the way down. Most growth occurred in this case while particles were suspended by the updraft near 7.5 km. As Figure 7 shows, mean reflectivity stayed near 30 dB(Z) below 7 km. Figure 8 shows that terminal velocity remained near 6 m/s down to 5 km, the increase below that level being due most likely to melting of low density graupel into higher density raindrops. Updraft speed was 1 m/s or less below 6 km.

4 DISCUSSION

The main conclusions from these observations are as follows:

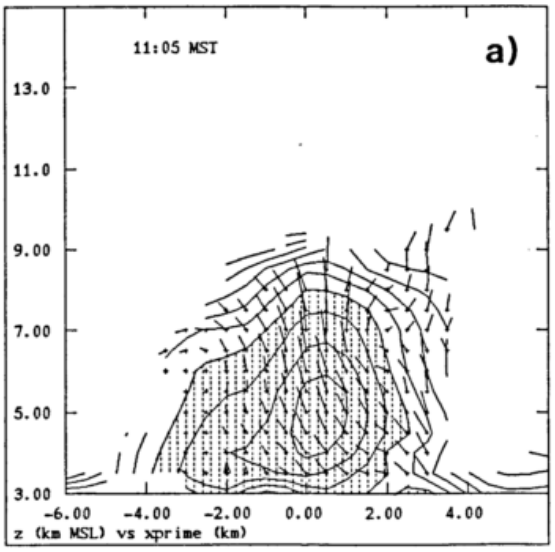
1. The studied cell exhibited a transient, thermal-like evolution.

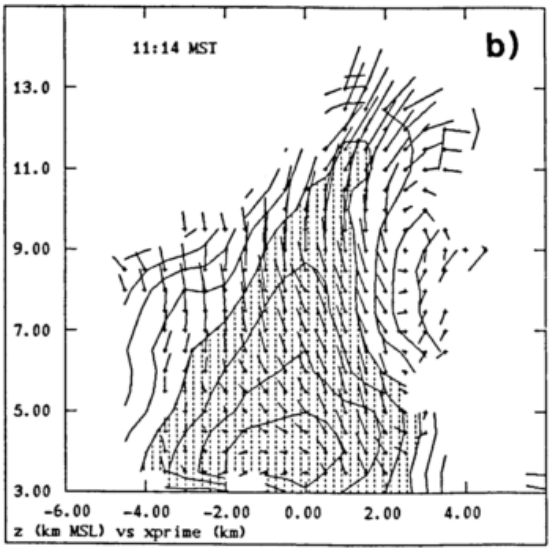
2. The heaviest precipitation came from graupel embryos that formed near cloud top in the early stages of the cell when tops were near 8 km MSL.

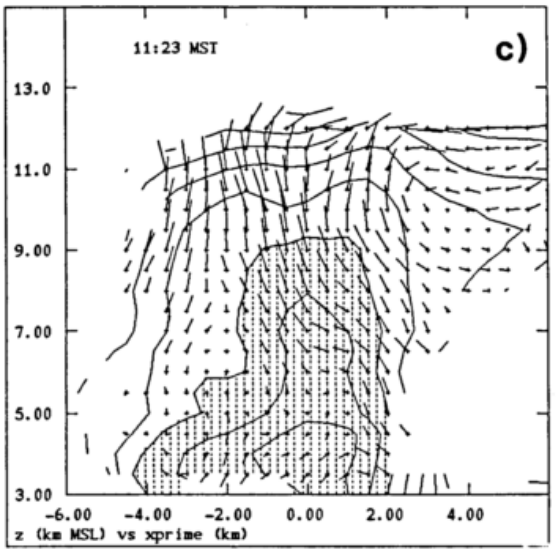
3. Reflectivity and terminal velocity of falling graupel (or small hail) increased only when the particles were falling through regions of updraft. These were presumably regions containing significant supercooled liquid water.

Based on the observed evolution of terminal velocity and educated guesses for cloud liquid water content, graupel density, and drag coefficient, we estimate that precipitation particle diameters increased at a rate consistent with the upper limits predicted by graupel and hail growth models.

We gratefully acknowledge the contributions of William Winn, Charles Moore, and Paul Krehbiel to this project, as well as those of NCAR's Atmospheric Technology Division. This work was supported by National Science Foundation Grants ATM-8311017, ATM-8611364, and ATM-8605136.







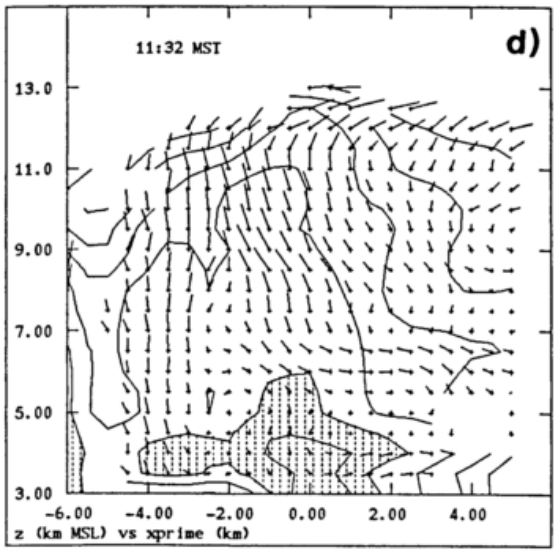


Figure 1. Vertical section through central cell oriented 220° - 40°. Reflectivity contours every 5 dB(Z), hatching above 30 dB(Z). Wind vectors have cross at tail, vector one grid interval long represents 5 m/s. a) 11:05. b) 11:14. c) 11:23. d) 11:32.

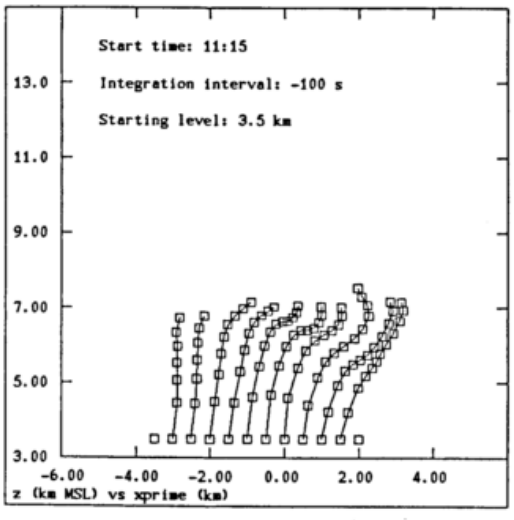


Figure 2. Trajectories of precipitation particles reaching 3.5 km at 11:15. The boxes show the positions at 100 s intervals.

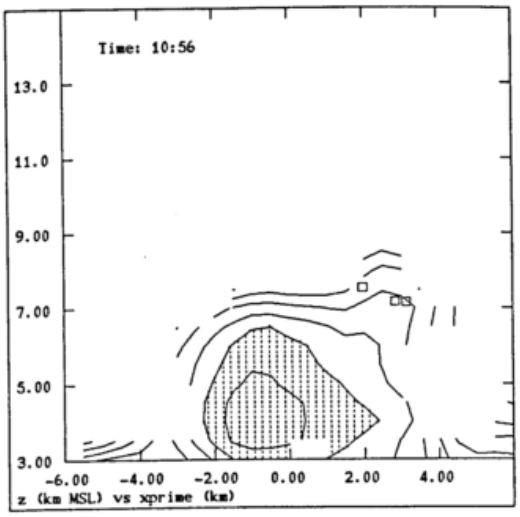


Figure 3. Reflectivity at 10:56, similar to Figure 1, along with positions of particles illustrated in Figure 2 at that time. Not all such particles could be traced back to 10:56.

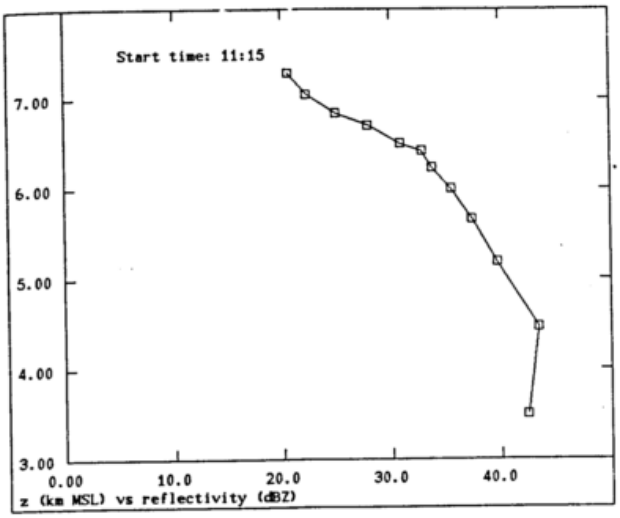


Figure 4. Mean reflectivity of particles illustrated in Figure 2 as a function of height. The boxes indicate 100 s intervals.

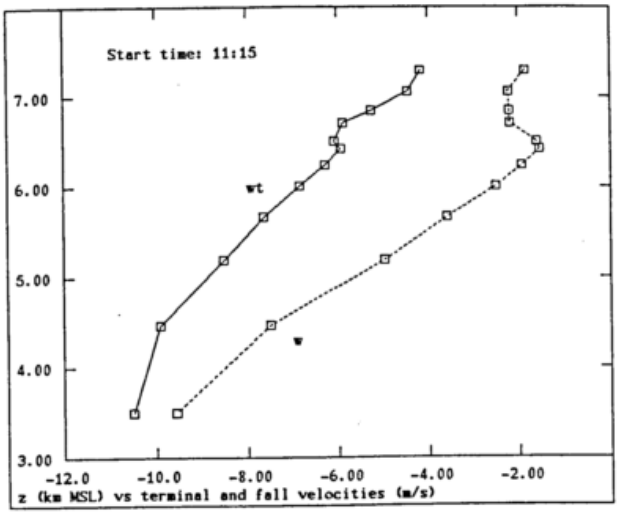


Figure 5. Mean terminal velocity (wt) and fall velocity (w) for particles illustrated in Figure 2. The boxes indicate 100 s intervals.

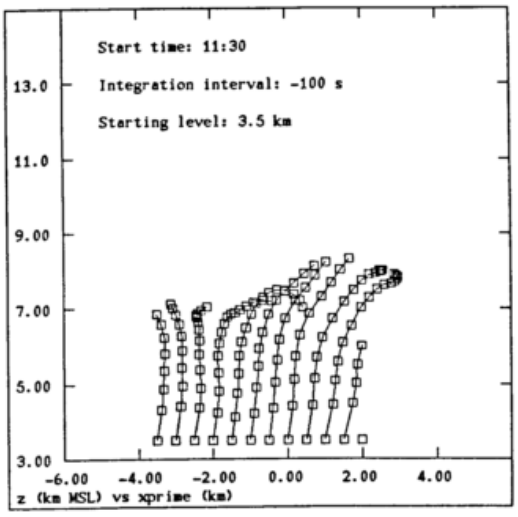


Figure 6. Trajectories of precipitation particles reaching 3.5 km at 11:30. The boxes show the positions at 100 s intervals.

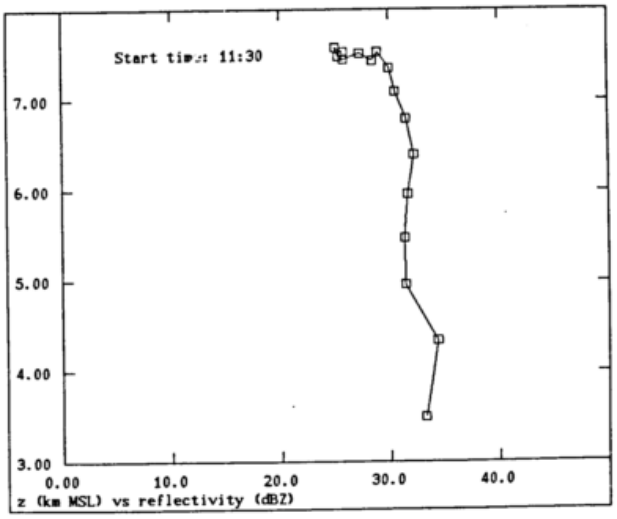


Figure 7. As in Figure 4, except referring to particles illustrated in Figure 6.

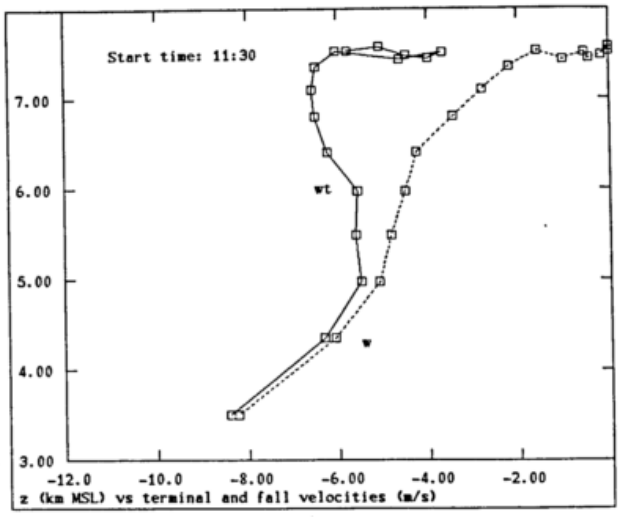


Figure 8. As in Figure 5, except referring to particles illustrated in Figure 6.

INTERIOR CHARACTERISTICS AT MID-LEVELS OF THUNDERSTORMS IN THE SOUTHEASTERN UNITED STATES

Dennis J. Musil and Paul L. Smith

Institute of Atmospheric Sciences
South Dakota School of Mines and Technology
Rapid City, South Dakota 57701-3995

1. INTRODUCTION

Data characterizing the vertical wind structure and hydrometeors within cumulonimbus clouds in the southeastern United States were collected by the armored T-28 aircraft (JOHNSON and SMITH, 1980) during the 1986 Cooperative Huntsville Meteorological Experiment (COHMEX). The data analysis has concentrated on the hydrometeor character and development, as well as the general microphysical and kinematic structure of the clouds penetrated. Longer range plans call for synthesis of the T-28 data with other observations and numerical models, with the overall goal of describing the precipitation process in these convective storms.

2. STORM CHARACTERISTICS

Typical cloud base temperatures in the COHMEX region were about +18°C. Average temperatures of the T-28 penetrations ranged between -7.5°C and +5.5°C; initially penetrations were made at the colder temperatures, but later in the season penetrations had to be restricted to warmer temperatures because of lightning damage to the propeller deicing device.

An example of data gathered during one of the T-28 penetrations is shown in Fig. 1, which illustrates some of the features found in the COHMEX storms. The updrafts shown are atypical, in that they represent some of the strongest updrafts observed during COHMEX. In fact, the updraft of about 19 m s^{-1} during this penetration is the strongest observed during the project. Usually the vertical winds, calculated according to a method by KOPP (1985), were found to be weak, the average updraft maximum being just less than 4 m s^{-1}. Downdraft minima typically ranged between -5 and -10 m s^{-1}.

The updraft regions in the COHMEX storms were generally narrow, but usually very turbulent; values of turbulence intensity greater than about 9 $cm^{2/3}$ s^{-1}, which correspond to extreme turbulence (MACCREADY, 1964), were common. Furthermore, the turbulence remained relatively strong throughout large regions of each penetration, unlike most storms of the High Plains where updraft interiors are relatively calm (MUSIL et al., 1986). As indicated in Fig. 1, the updraft regions did not exhibit the large increases in equivalent potential temperature (θ_e) often found in other geographic regions where the T-28 has penetrated thunderstorms (MUSIL et al., 1986). In the COHMEX storms, maximum values of θ_e ranged between 339-347 K and the values were usually quite uniform during each penetration. This suggests that the COHMEX storms were well mixed or that θ_e was relatively constant with height. Moisture does not drop off as rapidly with height in the COHMEX region as in the High Plains, where storms tend to show very high values of θ_e in the updraft regions, with lower values in other regions.

3. HYDROMETEORS

Cloud liquid water concentrations (LWC) were usually low, typically much less than adiabatic values. A comparison of LWC observations with adiabatic values shows that the LWC's at warmer penetration temperatures were relatively closer to adiabatic, with the average percentages being about 15 and 25% for colder and warmer penetrations, respectively. This suggests

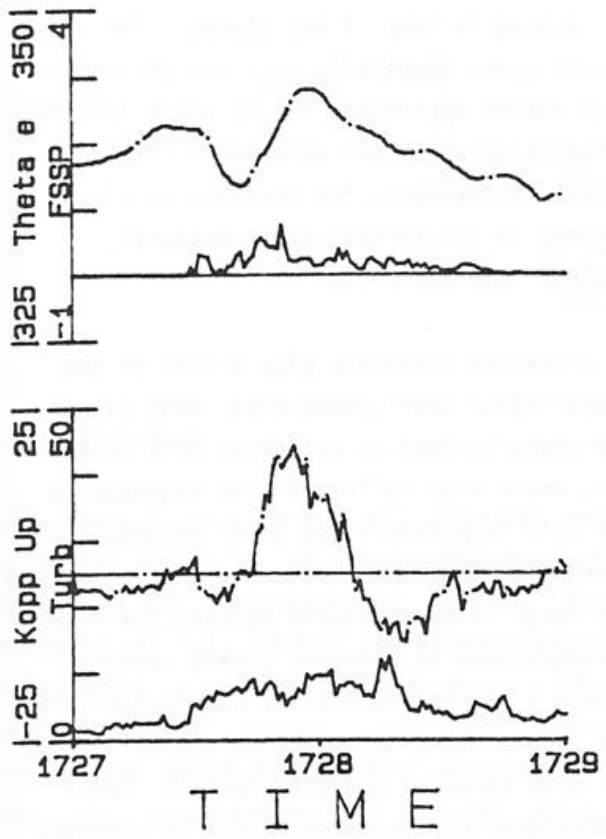


Fig. 1: Time plot of selected data from Penetration 4 on 23 June 1986. The time scale can be converted to an approximate distance scale using the nominal T-28 flight speed of 0.1 km/s. Topmost trace: θ_e (K). Second trace: LWC from FSSP (g m^{-3}). Third trace: Updraft speed (m/s). Lowest trace: Turbulence ($cm^{2/3}$ s^{-1}).

that the cloud water is being rapidly depleted during its ascent in the updraft and that coalescence may be active.

The Forward Scattering Spectrometer Probe (FSSP) obtains a cloud droplet spectrum for each second of flight. The spectra often indicated a mode droplet diameter of about 15 µm, while droplets >40 µm in diameter were often observed (the largest droplet size sensed by the FSSP is 45 µm). Aside from the large droplets, the droplet spectra were rather continental in character.

Large numbers of particles >1 mm in diameter appear in the foil impactor data from the T-28. The sample shown in Fig. 2 corresponds to about 30 m^{-3} of particles >5 mm, which is about three times more than were observed in a similar case in Switzerland (WALDVOGEL et al., 1987). The concentrations for these size ranges are the highest ever observed with the T-28 system.

Comparisons with particle size distributions from other regions (Fig. 3) substantiate this observation. The COHMEX storms tend to have many more particles in the 1-5 mm range, while storms in other places tended to have more particles at the larger sizes. In fact, the COHMEX spectra often appeared truncated, with an absence of particles larger than about 7-8 mm.

Hail was infrequent in the COHMEX storms, occurring in less than 25% of the penetrations, and the observed sizes were usually <1 cm. Particles larger than about 1 cm were observed very infrequently, despite reflectivities between 50-60 dBz. Larger hail was observed in only 2 of the 74 penetrations made by the T-28 during COHMEX.

Concentrations of particles >1 mm and >5 mm typically ranged up to 300 m^{-3} and 30 m^{-3}, respectively, with mass concentrations corresponding to about 6 g m^{-3}. The total mass concentrations for the larger hydrometeors,

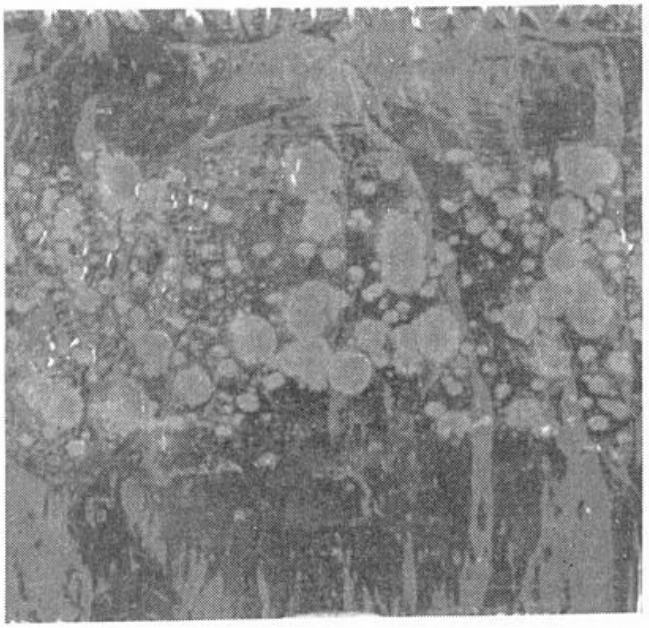


Fig. 2: Example of foil data from T-28 Penetration No. 4 on 23 June 1986; T = -7°C. Width of the foil is 7.6 cm.

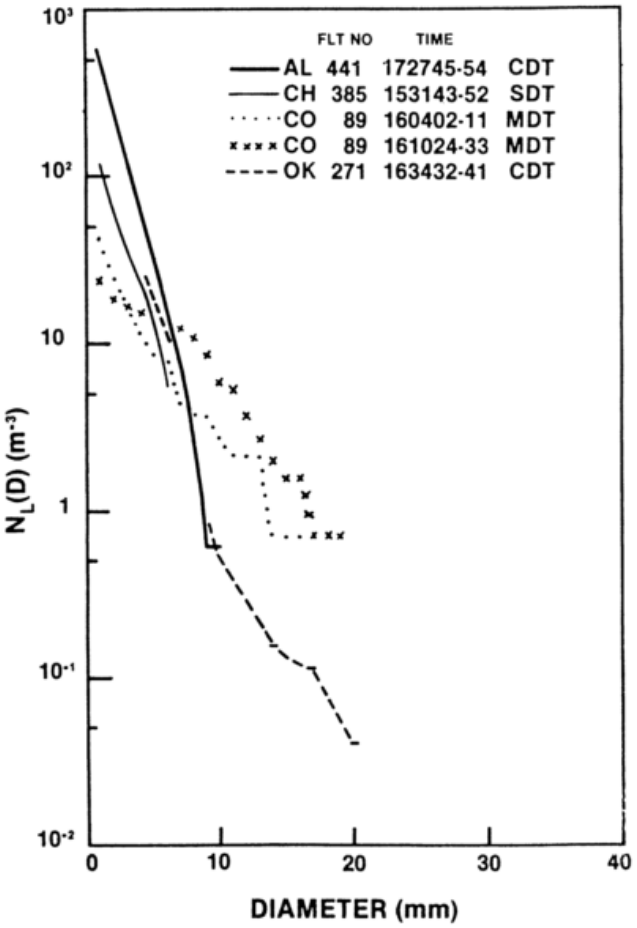


Fig. 3: Comparison of particle size distributions from T-28 penetrations in Alabama (AL), Colorado (CO), Oklahoma (OK), and Switzerland (CH). Ordinate shows number concentration of particles larger than the size indicated on the abscissa. All data came from penetrations at about -7°C.

added to typical observed cloud water concentrations of about 1 g m^{-3}, compare quite favorably with adiabatic values. The particle phases are not known with certainty, but at least some were surely liquid at the warm temperatures of some of the penetrations (about +5°C).

4. SUMMARY AND CONCLUSIONS

The high reflectivities, which sometimes exceeded the usual 55 dBz limit set for the T-28, are not necessarily related to hail in the COHMEX storms. Instead, large numbers of millimeter-size particles were found, while the hail infrequently encountered was generally small. The fact that the larger hydrometeors were usually found in narrow and weak updrafts that appeared to be well mixed suggests that a coalescence mechanism may have been active in many of the storms. The depth of warm cloud (typically ∿3.5 km) present in these storms apparently allows ample time for particles to reach the observed millimeter sizes. Furthermore, the presence of cloud droplets in the largest sizes measured supports this mechanism.

Ice processes certainly play a role in the precipitation development also; most clouds were characterized by extremely deep convection, where high reflectivities extended to very cold temperatures at great heights. Nevertheless, hail was probably unable to grow very large in these storms because the high concentrations of observed growth centers suggest a natural beneficial competition process. This would tend to keep the hail small even with stronger updrafts (DENNIS, 1980). Furthermore, particles would not be expected to remain in the updrafts long enough to develop into large hail and the updrafts would become loaded due to the high precipitation mass concentrations.

Acknowledgment. Support for this research was provided by NASA Grant No. NAG8-633 and NSF Grant No. ATM-8602861.

REFERENCES

DENNIS, A. S.: Weather Modification by Cloud Seeding. New York: Academic Press, Inc., 24, 267 pp, 1980.

JOHNSON, G. N.; SMITH, P. L., Jr.: Meteorological instrumentation system on the T-28 thunderstorm research aircraft. Bull. Amer. Meteor. Soc., **61** (1980) 972-979.

KOPP, F. J.: Deduction of vertical motion in the atmosphere from aircraft measurements. J. Atmos. Ocean Tech., **2** (1985) 684-688.

MACCREADY, P. B., Jr.: Standardization of gustiness values from aircraft. J. Appl. Meteor., **3** (1964) 439-449.

MUSIL, D. J.; HEYMSFIELD, A. J.; SMITH, P. L.: Microphysical characteristics of a well-developed weak echo region in an intense High Plains thunderstorm. J. Climate Appl. Meteor., **25** (1986) 1037-1051.

WALDVOGEL, A.; KLEIN, L.; MUSIL, D. J.; SMITH, P. L.: Characteristics of radar-identified Big Drop Zones in Swiss hailstorms. J. Climate Appl. Meteor., **26** (1987), 861-877.

ELECTRIFICATION OF THE 31 JULY 1984 NEW MEXICO MOUNTAIN THUNDERSTORM

C.L. ZIEGLER
NATIONAL SEVERE STORMS LABORATORY
NORMAN, OKLAHOMA 73069

P.S. RAY AND S.L. LANG
FLORIDA STATE UNIVERSITY
TALLAHASSEE, FL 32306

1. INTRODUCTION

This study focuses on the microphysical and electrical evolution of a thunderstorm over the Magdalena Mountains of central New Mexico on 31 July 1984. The storm history is revealed by multiple Doppler and in-situ data collected during the TRIP field program, in which two of the authors (CLZ and PSR) participated as Doppler radar coordinators. The relative importance of various charge separation mechanisms is evaluated by comparing electric field measurements from a penetrating aircraft with corresponding fields derived from a numerical cloud model at the specified times and locations of a particular aircraft observation. The detailed verification of forecast cloud properties provides an objective basis for evaluating the charge separation mechanisms and their numerical representation.

2. METHOD

A kinematic numerical cloud model (Ziegler, 1985) assimilates the three-dimensional, time-spaced multiple Doppler wind analyses and retrieves the distributions of temperature, vapor, cloud water and ice, rain, snow, and graupel/hail in the storm. A simultaneous set of continuity equations are solved for the hydrometeor space charge densities (Ziegler et al, 1986; Helsdon and Farley, 1987).

The charge separation mechanisms are modified form of the Helsdon and Farley (1987) parameterization. The current study focuses initially on the non-inductive mechanisms involving rebounding collisions of graupel with ice crystals. Additional numerical experiments to evaluate the role of induction charging between graupel and cloud droplets are being conducted. Three model sensitivity tests have been performed with charging sign reversal temperatures of 0, -10, and -20°C. The latter case is represented using the Ziegler et al (1986) parameterization. A charge of 10^{-13}C is separated by rebounding collisions involving snow crystals when the inductive mechanism is assumed to be inactive: the corresponding value for cloud ice crystals is 10^{-16}C. In a fourth sensitivity test which combines inductive and non-inductive charging, a graupel/snow non-inductive charge transfer of 10^{-14}C is assumed.

3. RESULTS

Measurements of temperature, hydrometeor content, vertical motion, and electric field strength within the storm are provided by coordinated penetrations by the NCAR/NOAA sailplane and the New Mexico Institute of Mines and Technology SPTVAR powered glider. The NCAR Multiple Aircraft Positioning System (MAPS) provides (x,y,z) aircraft coordinates accurate to within several hundred meters. Additional electric

field information is available from a surface field mill at Langmuir Laboratory.

Radial particle velocity and reflectivity data from the NCAR CP3, NCAR CP4, and NOAA D Doppler radars are used to synthesize the three-dimensional airflow field at 3 min intervals over the period of greatest storm growth between 1134 and 1152 MST. Fields of reflectivity and updraft at 1152, depicted in Fig. 1a, indicate that three horizontally distinct regions of precipitation and updraft are present. Good agreement is noted between analyzed and measured updraft strength along the sailplane penetration (Fig. 1b). Inspection of the time-spaced analyses shows that the small eastern cell is in a state of gradual decay, while the western cell is vigorously intensifying from extremes of 35 dBZ and 5 m s^{-1} to about 50 dBZ and 15 m s^{-1}.

The cloud model has been integrated forward in time with assimilation of the time-spaced three-dimensional wind analyses from 1134 to 1152. The initial fields are a steady-state model solution using fixed graupel content estimated from measured reflectivity. The modeled western cell intensifies from 35 dBZ to nearly 50 dBZ, while the modeled eastern cell gradually decays. Modeled and observed peak reflectivities are within 5 dBZ over the course of integration. Fig. 2 reveals modeled and observed electrical parameters, both within the vertical cross-section A-B (located in Fig. 1a) and along the sailplane flight path. In this test with non-inductive, negative graupel charging only, the modeled vertical electric field locally approached -100 kV m^{-1}. Negative charge, which resides on graupel and graupel meltwater, predominates below the penetration temperature of about -18° C, while positive charge on snow and cloud ice crystals predominates above that level. The sensitivity tests reveal that the charge and electric field dipole rises with the assumed reversal temperature. When the reversal temperature is -20°C, the modeled vertical electric field becomes positive during the first min of the sailplane penetration. Provided that other charging mechanisms are not important, this contradiction of observations suggests that the actual reversal temperature may be warmer.

4. DISCUSSION

Comparison of the modeled and observed vertical electric field component along the sailplane traverse suggests that a strong non-inductive charge separation mechanism, characterized by a relatively large charge separated per collision and a uniform sign of charging, is capable of explaining the cell-scale electric field without recourse to inductive or other mechanisms. The existence of significant localized differences between the observed and (non-inductively) modeled vertical electric field component over horizontal distances of 500-1000 m suggest that additional mechanisms may become significant on these fine scales. Such small scale space charge and electric field structures could conceivably arise by unresolved flux convergence of existing space charge, variability of the non-inductive charge reversal temperature, or the superposition of the inductive and non-inductive mechanisms. Preliminary sensitivity tests with combined charging suggest that the non-inductive mechanism provides a cloud-scale dipole, which the induction mechanism locally intensifies to produce realistic fine-scale structure.

5. ACKNOWLEDGMENTS

The authors gratefully acknowledge the contribution of NCAR/NOAA sailplane data by

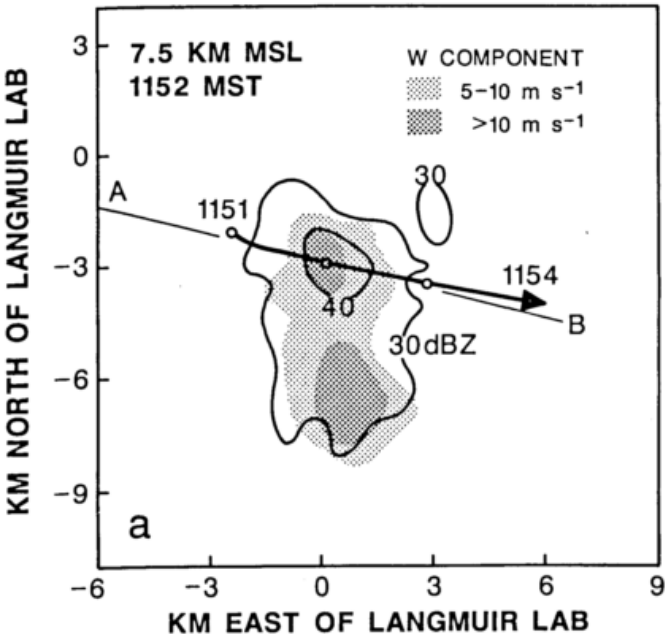
Dr. J. Dye and Ms. R. Vaughn of NCAR. The cloud model calculations are performed on the NOAA/NBS CYBER 205 supercomputer. The Research Aviatiion Facility of NCAR instruments and operates the NCAR/NOAA sailplane, while the CP3 and CP4 radars are operated by the NCAR Field Observing Facility. NCAR is sponsored by the National Science Foundation.

6. REFERENCES

Helsdon, J.H., Jr. and R.D. Farley, 1987: A numerical modeling study of a Montana thunderstorm: 2. Model results versus observations involving electrical aspects. J. GEOPHYS. RES., 92, 5661-5675.

Ziegler, C.L., 1985: Retrieval of thermal and microphysical variables in observed convective storms. Part 1: Model development and preliminary testing, J. ATMOS. SCI., 42, 1487-1509.

_____, P.S. Ray, and D.R. MacGorman, 1986: Relations of Kinematics, microphysics, and electrification in an isolated mountain thunderstorm, J. ATMOS. SCI., 43, 2099-2114.



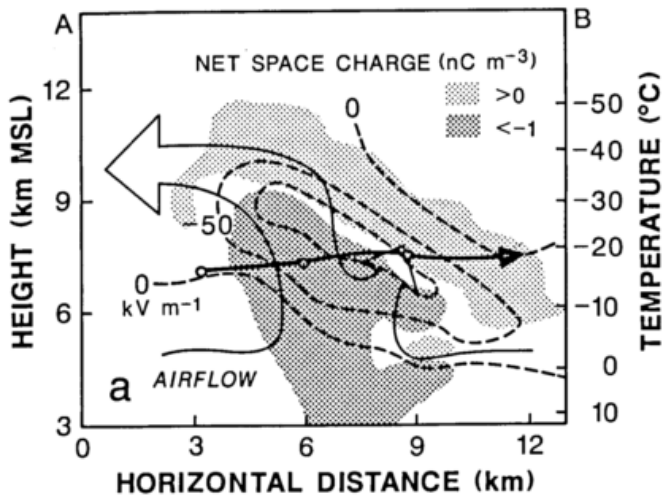
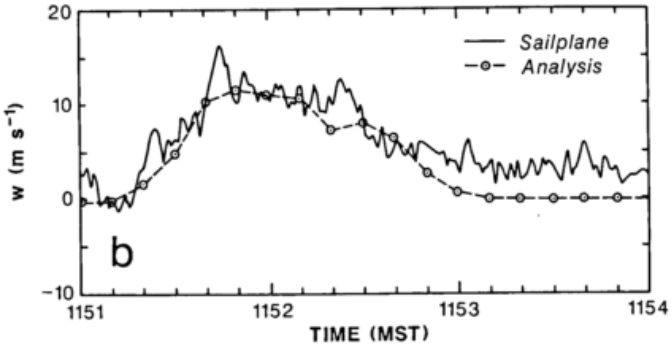


Fig. 1. Analysis and measurements of updraft and reflectivity from the 1152 Doppler analysis and NCAR/NOAA sailplane traverse from 1151 to 1154. (a) Reflectivity, updraft strength, and sailplane track at 7.5 km MSL. (b) Measured and analyzed updraft interpolated to sailplane position.



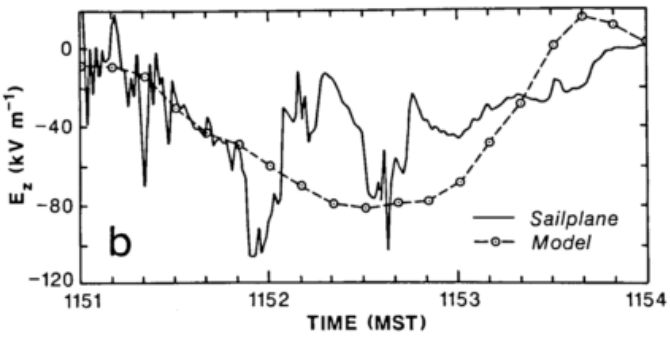


Fig. 2. Modeled and observed storm electrical structure at 1152. (a) Vertical electric field, net hydrometeor space charge, and airflow in vertical cross-section approximately along 1151-1154 sailplane traverse. (b) Observed versus modeled and interpolated vertical electric field.

RETRIEVAL OF MICROPHYSICAL VARIABLES IN NEW MEXICAN MOUNTAIN THUNDERSTORMS FROM DOPPLER RADAR DATA

Peter S. Ray[1], Conrad L. Ziegler[2], and Steven L. Lang[1,3]

[1]Florida State University
Tallahassee, Florida 32306 USA

[2]National Severe Storms Laboratory
Norman, Oklahoma 73069 USA

1. INTRODUCTION

During the summer of 1984, extensive observations were made on thunderstorms that formed in the vicinity of Langmuir Laboratory, near Socorro, New Mexico. Langmuir Laboratory is located at 3222 m MSL in the Magdalena Mountains, surrounded by a plain that is about 1500 m MSL. During the summer months storms frequently form over the mountain, making it an ideal laboratory for the deployment of fixed facilities needed to study the properties of small thunderstorms, including the generation of electrical fields. Two of the authors, Ray and Ziegler, were radar coordinators during this period.

A storm that occurred over the mountain in 1979 has been studied by ZIEGLER *et al.* (1986) using observations from a single Doppler radar. The wind field was deduced and employed in a one-dimensional microphysical model to produce the time varying temperature, water substance, space charge density, and axial electric field in the updraft region.

Among other noteworthy papers on these storms, DYE *et al.* (1988) discusses data from the NCAR sailplane and the New Mexico Institute of Mining and Technology SPTVAR aircraft from a storm that occurred on 3 August, 1984, one of the days reported in this study. They found a narrow (500 m) region of charge near cloud top. They found this region to be composed of supercooled liquid water and ice, including graupel. Because initial electrification coincided with regions where ice-particle concentrations, sizes and collision rates were large, it was suggested that charge generation occurred through a precipitation-based mechanism.

The observation that charging may be due to a precipitation-based mechanism clearly indicates the value of having an accurate description of the wind field and a three-dimensional description of the precipitation field in which there is phase discrimination. A method that shows promise of being able to provide such a description, which uses wind fields derived from Doppler radar data, is described below.

[3]Present affiliation: General Sciences Corporation, Laurel, Maryland 20707

2. OBSERVATIONS

The principal observation we discuss is of the winds that are derived from data taken from four Doppler radars. The two NCAR radars operate at a wavelength near 5 cm, and the two NOAA radars use a wavelength near 3 cm. The radar locations are given in Fig. 1, with the local topography contoured.

On 31 July, storms formed shortly after 1000 MST and on 3 August, they formed shortly after noon MST. In both cases, storms persisted until about 1330 MST. The radar observations are synthesized as described in Ray *et al.* (1980), with downward integration used and no variational adjustment employed. This is because the mountaintop terrain provided no reliable lower-boundary condition. Wind fields were synthesized every three minutes for a period of about 45 minutes on 31 July and 1.25 hours on 3 August. This is a total of 45 separate analyses. The time-height cross section of maximum reflectivity and maximum vertical velocity for each day is given in Figs. 2 and 3, respectively. For both days the maximum reflectivities exceeded 45 dBZ.

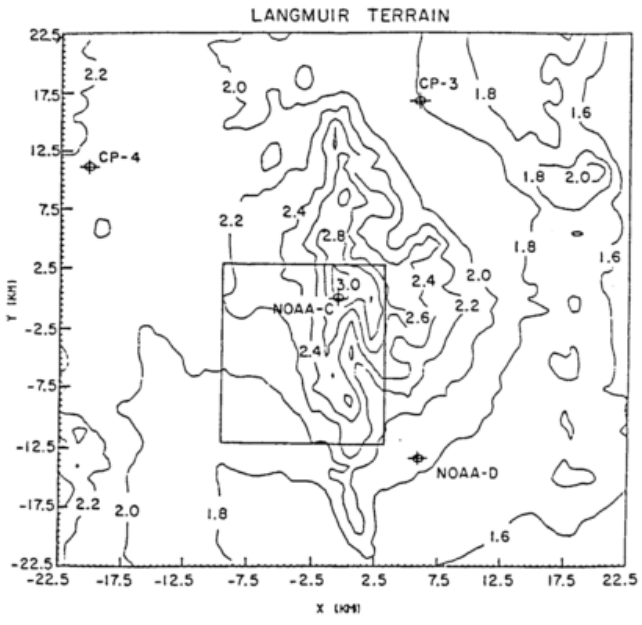


Fig. 1. Radar locations surrounding the Magdelana Mountains where Langmuir Laboratory is located. Elevation is contoured in km MSL. Box represents sample analysis region to illustrate analysis domain size.

The reflectivity and vertical velocity patterns in Fig. 2 contain maxima at 1134, 1155, and 1209 for an average period of 15 minutes. Fig. 3 reveals at least two readily-discernable updrafts, one near the time of 1230 and the other near 1242. The peaks in the 35 dBZ contour are separated by 15 minutes, similar to the observations of ZIEGLER *et al.* (1986) for another storm over Langmuir. In this storm there was a periodic enhancement of the reflectivity field and a deduced corresponding updraft that occurred nearly every 12 minutes. It is apparent that these storms persist by a nearly continuous redevelopment.

Maximum storm tops (defined by the 15 dBZ contour) were 9.5, 9.5 and 8.0 km above Langmuir for the 7 August (1979), 31 July, and 3 August cases, respectively. Using single Doppler radar, maximum vertical velocites between 15 and 20 m s^{-1} were inferred for the the 1979 case studied by ZIEGLER *et al.* (1986). During the nominal 1155 analysis time the radars were in a RHI scanning mode that did not include the storm core. Therefore, the properties over this important interval

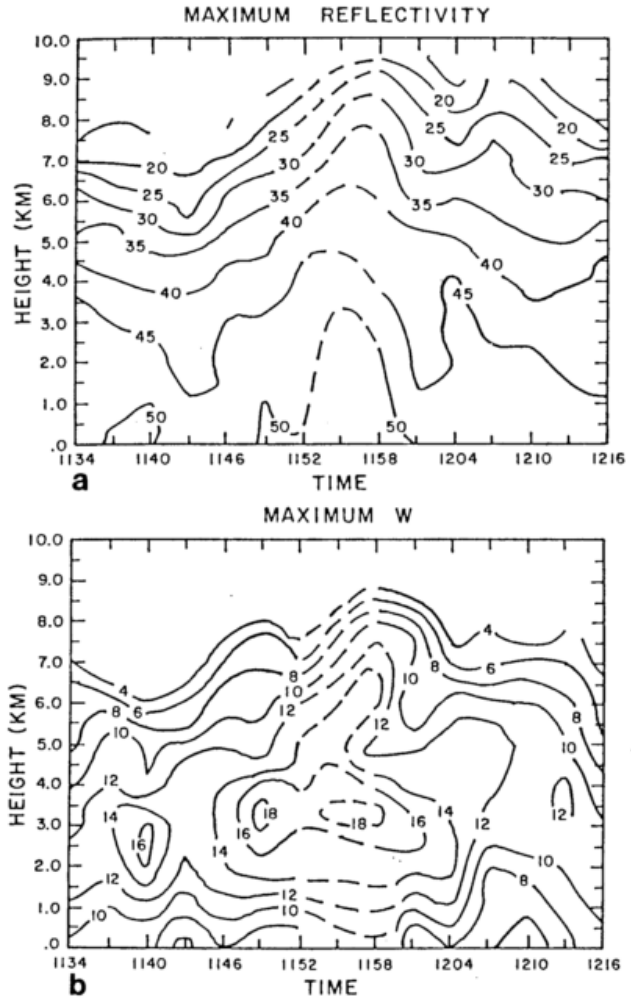


Fig. 2. Time height cross section of (a) maximum reflectivity and (b) vertical velocity for a storm that occurred on 31 July, 1984. The time interval extends from 1216 to 1331 MST. Reflectivity is contoured in 5 dBZ increments and the vertical velocity in 2 m s^{-1} intervals.

were subjectively estimated and are represented by dashed lines in Fig. 3. On 31 July, the maximum vertical velocities were about 17 m s^{-1}, while they were only 10 m s^{-1} on 3 August, demonstrating a consistent relationship between storm top and updraft speed. The multiple-Doppler radar derived horizontal wind fields displayed divergence patterns at the storm top similar to those inferred for the 1979 storm. The reflectivity maxima with height in the 3 August case, propagate at an implied speed of about 10 m s^{-1}, as also deduced for the 1979 case. Given the similarities between the inferred wind fields for the 1979 storm and those that were deduced in the 1984 storms, it is expected that many of the conclusions reached for the earlier storm will also be valid in the more recent data.

To illustrate some of the evolution aspects of this convection, a vertical reflectivity and wind cross sections for 1243 MST is presented in Fig. 4. The cross section transects the reflectivity core and is oriented in an east-west direction, with the view from the south. From Fig. 3, it is clear that this

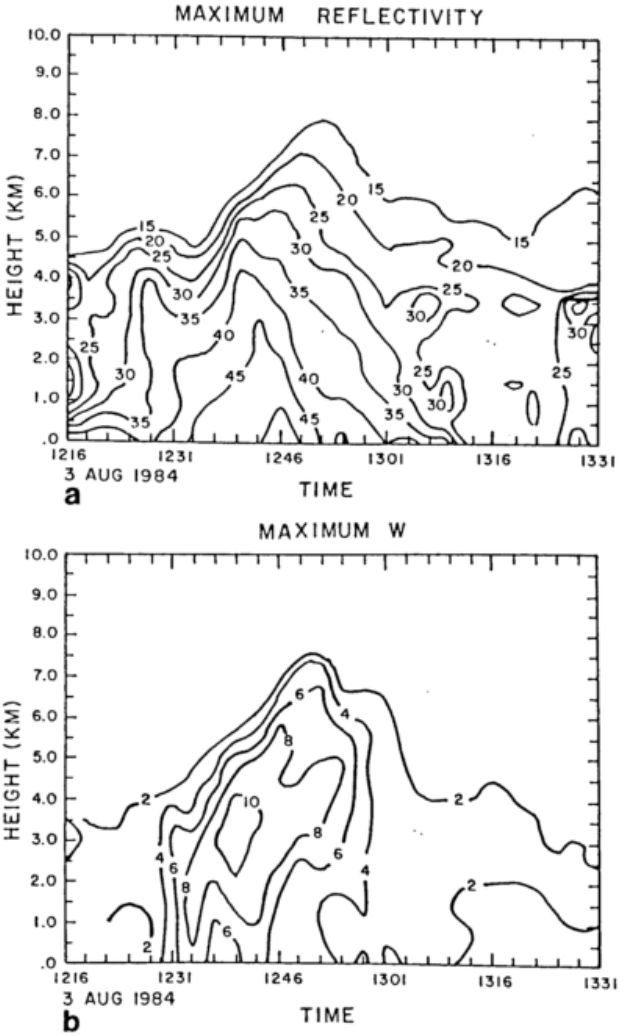


Fig. 3. Time height cross section of (a) maximum reflectivity and (b) vertical velocity for a storm that occurred on 3 August, 1984. The time interval extends from 1134 to 1216 MST. Reflectivity is contoured in 5 dBZ increments and the vertical velocity in 1 m s^{-1} intervals.

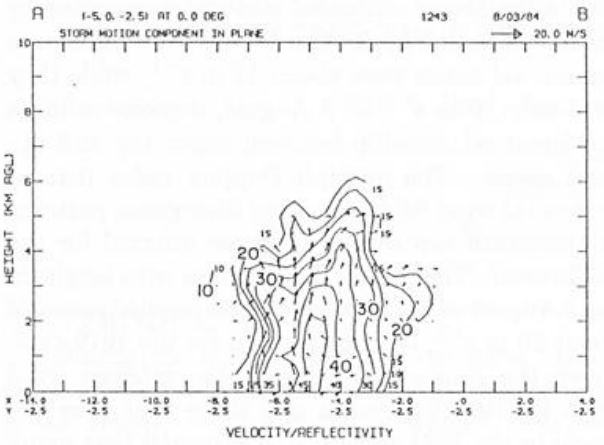


Fig. 4. East-West vertical cross section through 3 August storm at 1243 MST. Reflectivity is contoured in 10 dBZ increments, and the winds are storm relative.

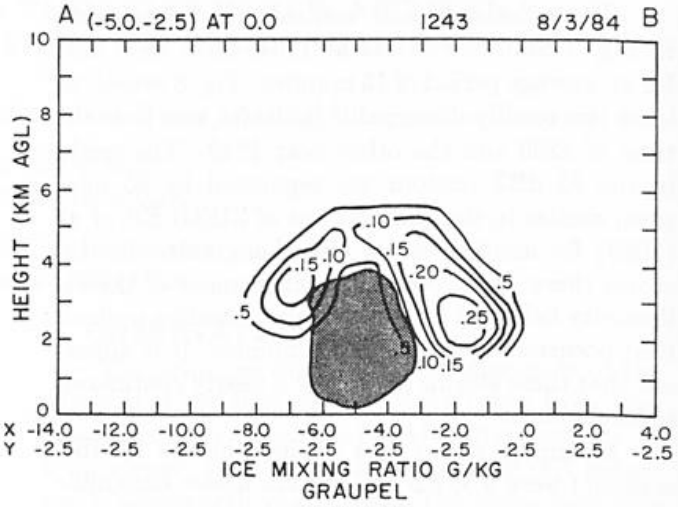


Fig. 5. East-West vertical cross section depicting the mixing ratios of snow (ice) in gm kg^{-1} and graupel. Mixing ratios of graupel greater than 0.1 gm kg^{-1} are shaded.

is during the period of maximum growth, and near the time reported in Dye *et al.* (1988). Over the preceding three-minute period the storm grew 500 m in the vertical as the low-level reflectivity maximum grew and expanded. Three minutes later the maximum reflectivity increased to 50 dBZ. Velocity fields such as these will be used to derived the consistent fields of water.

3. MICROPHYSICAL RESULTS

The microphysical model is based upon that formulated after ZIEGLER (1985). A system of continuity equations is solved for the temporal and spatial changes in the model variables. The model domain spans 30 gridpoints in the horizontal directions, and 20 in the vertical, with a grid spacing of 500 m in all directions. To initialize the model, local soundings were used to derive the conditions that were believed to exist at the time of the convective activity. A cloud and precipitation-free environment was initially assumed, with the microphysical fields allowed to develop to a condition of balance with the prescribed wind field. Additional model details can be found in ZIEGLER (1985), and ZIEGLER *et al.* (1986).

The mixing ratios of snow and graupel are shown in an east-west cross section in Fig. 5. Liquid water is present in the region where snow and graupel coexist. There is some evidence that these conditions promote rapid electrification (DYE *et al.* (1988)). The evolution of these fields in three dimensions can provide the basis for a more systematic assessment of active precipitation and electrical processes within storms.

4. DISCUSSION

The combined use of *in situ* and remote sensors is required to adequately describe the microphysical and electrical state of convection. The promise of fields derived from the synthesis of multiple-Doppler radar data to lend insight into the details of microphysical and electrical processes, is just being realized. Key to the eventual success is the active intercomparison between different sensors, each of which is characterized by a unique set of capabilities and limitations.

ACKNOWLEDGEMENTS

Assistance in figure preparation and discussions on analysis procedures by Dr. Kenneth Johnson is appreciated. Partial support for the preparations was provided by NSF Grants ATM 8604143 and ATM 8619957 to Florida State University, and by the Department of Energy Contract No. DE-Fco5-85ER250000 to the Florida State University Supercomputer Computations Research Institute.

REFERENCES

DYE, J. E., J. J. JONES, A. J. WEINHEIMER, and W. P. WINN: Observations within two regions of charge during initial thunderstorm electrification. *J. Atmos. Sci.*, **45** (1988).

RAY, P. S., C. L. ZIEGLER, W. BUMGARNER, and R. J. SERAFIN: Single- and multiple-Doppler radar observations of tornadic storms. *Mon. Wea. Rev.*, **108** (1980), 1607–1625.

ZIEGLER, C. L.: Retrieval of thermal and microphysical variables in observed convective storms. Part I: Model development and preliminary testing. *J. Atmos. Sci.*, **42** (1985), 1487–1509.

ZIEGLER, C. L., P. S. RAY, and D. R. MACGORMAN: Relations of kinematic, microphysicals, and electrification in an isolated mountain thunderstorm. *J. Atmos. Sci.*, **43** (1986), 2098–2114.

ON THE ROLE OF PRECIPITATION IN MAINTENANCE OF DOWNDRAFTS IN CUMULONIMBUS CLOUDS

Hanna Pawlowska-Mankiewicz

Institute of Geophysics, Warsaw University

1. INTRODUCTION

The physics of downdraft has been a subject to many investigations. First measurements were conducted during the Thunderstorm Project, when Byers and Braham (1949) identified a cold downdraft (i.e. colder than environment) as a distinct and important entity in the life of the thunderstorm, observable in the middle and lower parts of the cloud. They attributed the development of a downdraft to the precipitation drag and its evaporation as well as entraiment of environmental air with low equivalent - potential temperature.

Kamburova and Ludlam (1966) showed however that cooling of downdraft by evaporation of relatively large raindrops usually prevailing in heavy rains is not sufficient to maintain conspicuous downdrafts in Cumulonimbus, except when stratification is close to dry adiabatic. Thus some effective sources of fast evaporating small droplets had to be found in order to give adequate explanations for intensive cold downdrafts. Looking for such sources Haman (1973) and Haman and Niewiadomski (1980) found that in a certain range of aerological situations entrainment of an updraft air rich in small droplets can sustain an intensive and cold downdraft, but only in the middle region of a cloud. Pawlowska (1987) showed that evaporation of liquid water entrained from the updraft in the presence of air with low equivalent- potential temperature entrained from environment may lead to sufficient cooling. Furthermore Srivastava (1987) draw attention to the role of ice melting in the process of cooling of a downdraft. In numerical models the precipitation is often treated in parameterized form. The most common parameterization is due to Kessler (1969). Since this parameterization overestimates the number of small droplets, one might fear that it may also overestimate evaporative cooling and lead to development of artificial downdrafts in the models.

This paper attempts to check if evaporation of small droplets present in the precipitation can cool the downdraft strongly enough to sustain a negative buoyancy. We would like also to answer the question if Kessler parametrization can be safely used in numerical models.

2. NUMERICAL EXPERIMENTS

In order to investigate the effect of precipitation on the dynamics of downdrafts a number of numerical experiments with one dimensional steady-state model was performed. To make the analysis of physical mechanisms responsible for the development of downdraft as clear as possible we simplified the starting point for our experiment and assumed that the only forces acting on downdraft were buoyancy and precipitation drag. We neglected the entrainment of mass from environment, but it was checked that considering it makes little difference to the main conclusions. The rainwater was described in two different ways. The first referred later as "bulk model" is the well known Kessler parameterization assuming that coalescence and breakup are quick enough to maintain the Marshall-Palmer type distribution, i.e. that

$$n(D) = N_0 \exp(-\lambda D) \tag{1}$$

where $n(D)\,dD$ is the number of drops of diameter between D and $D + dD$ per unit volume of space, N_0 and λ are parameters of the distribution. λ is held constant during each run of experiments. This assumption is considered appropriate for heavy rainfall (see Hodson (1986)). Another approach is a model of non-interacting raindrop classes called further "detailed model". All raindrops in each class have the same size which can change only due to evaporation and condensation. One can expect that these two models represent two limits of what can occur in a real

cloud. The calculations with the detailed model were performed for 15 raindrop classes with initial concentrations resulting from the same Marshall-Palmer distribution (1), as in the bulk model at the starting level of the downdraft. The additional experiments showed that increasing the number of classes does not change significantly the conclusions but raises the computational costs.

The concentration $N(D)$ (expressed as number of particles per unit volume of air) in each class of drops changes with height z according to the equation

$$\frac{dN}{dz} = \frac{N}{w - \nu(D)} \left(\frac{w}{\rho} \frac{d\rho}{dz} + \frac{d\nu(D)}{dz} \right) \tag{2}$$

where w - vertical velocity of a downdraft (negative), $\nu(D)$ - free-fall velocity of drop of diameter D, ρ - density of air. Let us notice that this equation includes the effect of three-dimensional convergence on the droplet concentration.

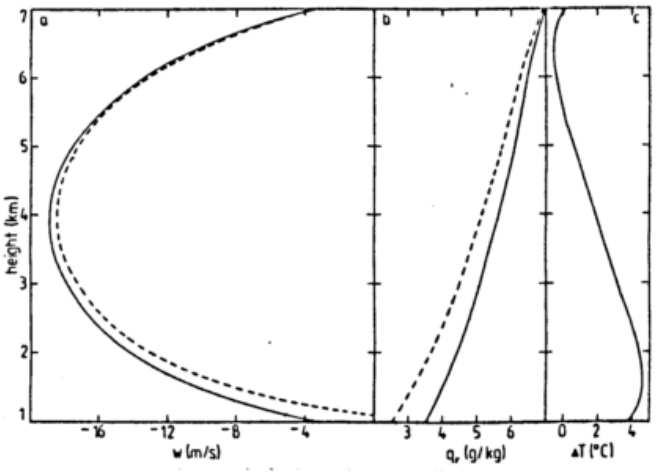


Figure 1: Profiles of downdraft velocity (a), rainwater mixing ratio (b) and temperature deficit (c) as predicted by the detailed model (solid line) and bulk model (dashed line). Environmental stratification parameter $k = 0.3$. The parameters of initial Marshall-Palmer distribution: $N_0 = 26 \cdot 10^6 m^{-4}$ and $\lambda = 2100 m^{-1}$ correspond to rainfall rate equal 170 mm/h at the top of the downdraft column. The initial relative humidity in the downdraft is equal to zero.

A typical example of experiment is given below. The downdraft develops in steady hydrostatic environment with relative humidity 70% and temperature stratification T computed in centigrade from the following formulae

$$T(z) = 17.5 + \int_{1000m}^{z} \Gamma \, dz \tag{3}$$

$$\Gamma = \Gamma_w + k(\Gamma_d - \Gamma_w) \tag{4}$$

where Γ_d, Γ_w, Γ are dry adiabatic, wet adiabatic and environmental temperature lapse rate respectively and k is an assumed constant. Pressure at 1000m equals 900hPa. The downdraft starts at 7000m with initial velocity $w = -3m/s$, with no liquid water and the temperature T_0 the same as in the environment.

On figs. 1 and 2 the profiles of downdraft velocity, precipitation mixing ratio and temperature deficit from two runs of the bulk and detailed model are compared. The temperature deficit is very similar in both models so only the result for the detailed model is shown. Both models give nearly the same shapes of downdraft velocity profiles although the bulk model gives slightly smaller values. In the bulk model the precipitation mixing ratio diminishes during the process of evaporation i.e. downstream the draft. In the detailed model the droplets also evaporate, even to disappearance of some classes.

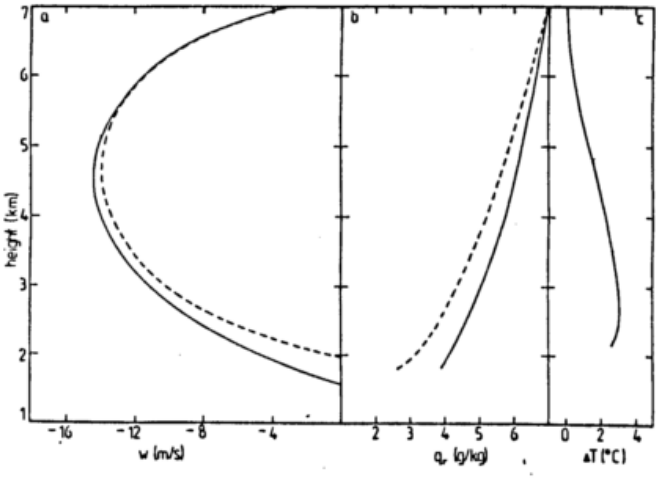


Figure 2: Similar to fig. 1 except the relative humidity is equal to 70%.

However a convergence of free-fall velocity (second term in the parenthesis of eq.2) causes an increase of concentration particularly in the small-size side of the spectrum. This effect of gravitational sorting is omitted in the Kessler parametrization. Because of the convergence of free-fall velocity in the detailed model the resulting drop spectrum deviates less from the Marshall-Palmer type than it would occur in the absence of grav-

itational sedimentation. The decrease of the precipitation mixing ratio downstream is smaller than in the bulk model (see figs. 1b and 2b).

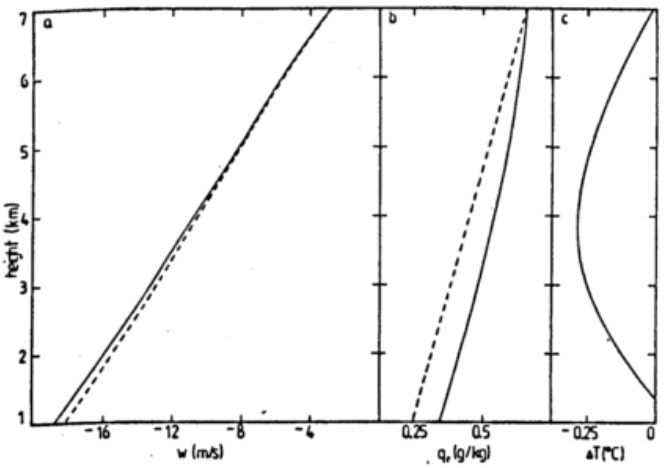


Figure 3: Profiles of downdraft velocity (a), rainwater mixing ratio (b) and temperature deficit (c) as predicted by the detailed model (solid line) and bulk model (dashed line). Environmental stratification parameter $k = 0.9$. The parameters of initial Marshall-Palmer distribution: $N_0 = 25 \cdot 10^5 m^{-4}$ and $\lambda = 2100 m^{-1}$ correspond to rainfall rate equal 15 mm/h at the top of the downdraft column. The initial relative humidity in the downdraft is equal to zero.

This in turn gives stronger evaporative cooling in the detailed model despite of seemingly less convenient structure of the droplet spectrum (i.e. relatively fewer small droplets). As a result the downdraft that develops under the buoyancy and precipitation load is more intensive in the detailed model. Nevertheless it seems that neither Kessler parameterization nor detailed description do not produce the cold downdraft unless the stratification is close to dry adiabatic (see fig.3) although warm downdrafts may develop also in more stable conditions under drag of sufficiently heavy rainfall (100- 200 mm/h) (see figs. 1 and 2).

3. SUMMARY AND CONCLUSIONS

We carried out some numerical experiments for one-dimensional steady- state downdraft with two different descriptions of precipitation: Kessler parameterization and discrete description of non-interacting raindrop classes. Both models give fairly similar shapes of downdraft velocity profiles but velocity is slightly greater in the second model. It results from greater precipitation mixing ratio in this case. The main reason for it is the convergence of free- fall velocity which affect the droplet concentration in the detailed model but it is absent in the Kessler parameterization. Thus the fear mentioned in the introduction that Kessler parameterization may overestimate evaporative cooling and produce false downdrafts in the model seems baseless. The numerical experiments show that in that respect this parameterization is fairly safe in modeling of Cb downdrafts. However in neither parameterization cold, precipitation driven downdraft can persist unless the stratification is close to dry adiabatic. This confirms once more the earlier suggestions (see Haman (1973), Haman and Niewiadomski (1980), Pawłowska (1987), Srivastava (1987)) that cold, persistent downdraft observed above the base of Cumulonimbus cloud have yet other reasons than rainfall evaporation and drag.

REFERENCES

BYERS, H.R; BRAHAM, R.R.: The Thunderstorm. U.S. Department of Commerce. Washington DC. (1949) 287pp.

HAMAN, K.: On the updraft - downdraft interaction in convective clouds. Acta Geophys. Pol. XXI (1973), 215-253.

HAMAN, K.E.; NIEWIADOMSKI, M: Cold downdrafts in Cumulonimbus Clouds. Tellus. 32 (1980), 525-536.

HODSON, M.C.: Raindrop size distribution. J. Climate Appl. Meteor. 25 (1986), 1070-1074.

KAMBUROVA, P.L.: LUDLAM, F.H.:Rainfall evaporation in thunderstorm downdraughts. Quart. J. Roy. Meteor. Soc. 92 (1966), 510-518.

KESSLER, E: On the distribution and continuity of water substance in atmospheric circulations. Met. Monograph. 10. No32 (1969), American Meteorological Society, Boston.

MARSHALL, J.S.; PALMER, W.,McK.: The distribution of raindrops with size. J. Meteor., 5 (1948), 165-166.

PAWLOWSKA-MANKIEWICZ, H: On the mechanisms of downndraft maintenance in cumulonimbus clouds. Tellus. 39A (1987), 266-270.

SRIVASTAVA, R.C.: A model of intense downdrafts given by the melting and evaporation of precipitation. J. Atmos. Sci. 44 (1987), 1752- 1773.

INFLUENCE OF THUNDERSTORM-GENERATED ACOUSTIC WAVE ON COAGULATION

Mladjen Ćurić and Zlatko Vuković*

Institute of Meteorology, University of Belgrade, Yugoslavia
*Hydrometeorological Institute of Serbia, Belgrade, Yugsolavia

1. INTRODUCTION

Although many microphysical processes causing the precipitation are known (Langmuir, 1948, Robertson, 1974, Whelpdale and List, 1971), causal and consequent connection between strong thundering and intensity of rain is not completely known.

A great number of modern researchers have paid their full attention to explain the observed sequences. Thus they have investigated the influence of electric forces in a cloud to the rainfall occurrence or enhancement (Vonnegut and Moore, 1960, Moore et al., 1964, Paluch, 1970, Dayan and Gallely, 1975, etc.). Both theoretical and experimental results show a more efficient collision in cloud electrical field. However, the sequences of events are not uniformly determined.

The objective of this paper is to formulate a procedure that can be used to calculate the contribution of the acoustic waves generated by electrical discharges to the occurrence or enhancement of rain. Thus the coagulation acoustic coefficient will be found.

2. PROBLEM FORMULATION

The lightning channel will be considered vertical in shape of a cilinder with a base radius d. The cloud characteristics are axial-symetrical refering to the lightning channel. It will also be assumed that a cloud is composed of still water drops. An energy is released in the lightning channel that is further consumed for the liquid water evaporation as well as for the increase of air temperature. The rest of the energy is consumed for spreading the over-pressure front. Further spreading of the front causes the energetic transformation in the relation front - medium. The final result is that beside air cloud drops receive a certain amount of the kinetic energy. Because of that, the drops will obtain some velocities that are proportional to the drop sizes. Faster drops will come across the slower ones and this will create the conditions for coagulation growth. This growth will be called acoustic coagulation.

3. EQUATIONS OF CLOUD DROP MOTION IN ACOUSTIC FIELD

In order to describe the cloud drops motion, it is necessary to consider the motion under the direct influence of the over-pressure front as well as the motion after the front passage. The final movement velocities of the first type will be the initial velocities for the second type of movement.

Under the above mentioned conditions, the equation of spreading the density of wave front energy in horizontal direction r is given by:

$$E = \frac{E_o}{2\pi r} e^{-k(r-d)} \qquad (1)$$

where E_o is the initial front energy

while k is the acoustic attenuation coefficient by the cloud medium through which the front is spreading.

The cloud represents a composition of gaseous and liquid phase. The gaseous phase is refered to as the saturated air while the liquid one is composed of cloud drops. In this case, the attenuation coefficient k can be presented as a sum of coefficients of gaseous and liquid phase: $k=k_g+k_t$. By differentiation (1) we get:

$$dE = -\frac{E}{r}\,dr - kgE\,dr - k_t dr \qquad (2)$$

The left side refers to the changes of front energy density, while the right one concerns the terms causing a decrease in energy density. The first term comes from volume spreading within which the frontal exists, the second and the third concern the attenuation by liquid and gaseous phase. The last two terms describe the increments of the kinetic energy of the saturated ensemble of cloud drops because of the front passage.

We presume that

$$k_g E = \frac{\rho U^2}{2} \qquad (3)$$

and

$$k_t E = \int_{m_o}^{m} \frac{mV_m^2}{2} f(m)\,dm \qquad (4)$$

where S is the air density, U the air velocity immediately after the front passage at the distance r from the lightning channel axis; V_m velocity of cloud drop mass m immediately after front passage; m_o and m the smallest and the largest mass in cloud drop spectrum; f(m) number of drops of a given mass.

In order to establish the form of dependence of the drop velocity V_x to its mass (dimension) and distance r, we should consider the spherical drop of the mass x with corresponding radius R in unit air volume at the distance r. The approach of the acoustic wave front to the zone where the drop is located causes the change in initial pressure field. This may be described by the empiric formula

$$P(r,t) = p(r)\left(1-\frac{t}{t_o}\right) e^{-\frac{t}{t_o}} \qquad (5)$$

Thus we describe the existance of the over-pressure at the distance r lasting to a certain moment t_o after which there is the under-pressure having an irrelevant small value refering to the over--pressure amplitude.

The equation of a single drop motion under the acoustic wave front is given by the relation

$$m\frac{dV_m}{dt} = S\,P(r,t) \qquad (6)$$

where S is the cross-section area of the spherical drop with radius R. Using the integration from the zero moment when the drop is moved from the static phase up to the moment t_1 after which there is no effect of the pressure disturbance force when the drop has the velocity $V(t_1)$, we get

$$V_m(t_1) = \frac{S}{m} G \;;\; G = p(r)t_1 e^{-\frac{t_1}{t_o}} . \qquad (7)$$

To solve the equation (7) it is necessary to known the product value G which is achieved by replacing (7) in (4) with the choice of Khrgian-Mazin distribution of drop masses (Edwin and Chin, 1972). Then it follows the expression for cloud drop velocity immediately after the acoustic front passage

$$V_m = A_m B(r)\, m^{-1/3} \qquad (8)$$

where A_m and B_r are some defined values.

After the front passage, the following motion equation will be valid for the cloud drops

$$m \frac{dV_m}{dt} = 6\pi\eta R \frac{C_d \, NR_e}{24} (U - V_m) \qquad (9)$$

where: η coefficient of dynamic viscosity; C_d coefficient of resistance force; N_{Re} Reynolds number.

In order to determine the velocity changes of the surrounding air, the law of energy conservation is used:

$$kE = \frac{1}{2} \rho U^2(t) + \int_{m_o}^{m} \frac{mV_m^2(t)}{2} f(m,t)\,dm + E_d(t) \qquad (10)$$

The system of equations (8)-(10) is closed so we can get velocities of the drops of different masses and distances r in time function t.

4. EQUATION OF CLOUD DROP COAGULATION GROWTH IN ACOUSTIC FIELD

To describe the cloud drop growth we use the modified equation of stochastic growth (Berry, 1967) given by

$$\frac{\partial f(m,t)}{\partial t} = \frac{1}{2} \int_o^m f(m,t) f(m-y,t) K_a(y,m-y)\,dy - f(m,t) \int_o^\infty f(y,t) K_a(m,y)\,dy - f(m,t) P(m) + \int_m^\infty f(y,t) Q(y,m) P(y)\,dy \qquad (11)$$

The collection kernel is symetrical function of its arguments and is given by the expression (Berry, 1967)

$$K_a(m,y) = \pi (m^{1/3} + y^{1/3})^2 \left(\frac{3}{4\pi\rho_L}\right)^{2/3} E_a [V_m - V_y] \qquad (12)$$

where m,y and V_m, V_y are the masses and corresponding drop velocities, respectively, E_a is collision efficiency of the acoustic coagulation given by the product of collision coefficients E' and coefficients of drop joining efficiency that were in collision E_c

$$E_a = E' \, E_c \, .$$

REFERENCES

Berry, E.X., 1967: Cloud droplet growth by collection, J.Atmos. Sci., 24, 688-701.

Dayan, N., and I.Gallily, 1985: On the collection efficiency of water droplets under the influence of electric forces I: Experimental, charge-multiple effects, J.Atmos.Sci., 32, 1419-1429.

Edwin, H.C. Chin, 1972: A numerical simulation of the gravitational coagulation process for cloud droplets, J.Atmos.Sci., 29, 718-727.

Langmuir, I., 1948: The production of rain by chain reaction in cumulus clouds at temperature above freezing, J. Meteor., 5, 175-192.

Moore, C.B., et.al., 1964: Gushes of rain and hail after lightning, J. Atmos.Sci., 21, 646-665.

Paluch, I.R., 1970: Theoretical collision efficiences of charged cloud droplets, J.Geophys.Res., 75, 1633--1640.

Robertson, D., 1974: Monte Carlo simulations of drop growth by accretion. J.Atmos.Sci., 31, 1344-1350.

Vonnegut, B., and C.B.Moore, 1960: A possible effect of hightning disscahrge on precipitation formation process. Monogr. of Am. Geophys. Un., No.5, 287-290.

Whelpdale, D.M., and R.List, 1971: The coalescence process in raindrop growth. J.Geophys. Res., 76, 2836--2856.

SATELLITE-SURFACE LINKAGE TO ESTIMATE MID-LATITUDINAL PRECIPITATION FEATURES

Margit Scholl
Institute for Geophysical Sciences
Freie Universität Berlin

ABSTRACT:
Preliminary results will be presented of a combination of surface-observed cloud properties and METEOSAT-based VIS, IR, WV spectral-band information accomplished to derive the distribution of precipitation in more detail. The concept bases on help from a-priori bottom-up actual weather reports in order to get thresholds for the top-down low-resolvent retrievals. The scheme is applied to Western Central Europe during an acid wet deposition episode in 1982; insufficiencies and possible improvements of the method will be discussed.

1. THE IDEA

Surface observations are the main source of accurate meteorological information on lower tropospheric levels. Therefore surface-observed weather informations should be exploited to gain general a-priori-knowledge for combination and comparison with data from other observational methods. Especially METEOSAT satellite imagery seems to be usable with its multispectral channels scanning the earth disc every half an hour. It is a common characteristic of both bottom-up and top-down observational methods that cloud parameters cannot be derived completely from either source: Higher cloud systems may be masked by lower cloud decks in surface reports whereas lower-layer information may be unobtainable from satellite images due to occultation by higher clouds. Thus, to examine the complex dynamics of multi-layered clouds, both data-sets should actually be used to supplement each other.

The utilization of further indirect meteorological information (like radar or NOAA-channel-3 radiances) might be useful or even necessary in order to get most possible insight into weather phenomena. However, besides human visual and computer system capacity, the coordination of "as much information as possible" depends on the availability of those data in digital form for the investigated period and on significant cross-linked integration techniques. Therefore, as a first step, the work sketched in this paper bases only on linkage of surface observations and METEOSAT data. Actual thresholds are obtained from the direct linkage and are then applied to regions with sparse surface reports.

2. THE APPLICATION

Background of the investigated time period (20.2.-1.3.1982) and area (Western Central Europe) is a project supported by the Umweltbundesamt, dealing with a tropospherical long-range transport model of acidifying substances with grid cell sizes of 63.5 * 63.5 km² (STERN et. al., 1987). Within the analysed episode, air pollutants are accumulated over Western Central Europe, dispersed and transported during high pressure periods,

and were rained out and/or washed out by frontal precipitation (SCHERER and SCHOLL, 1986a and 1986b). Besides mist and fog, type and intensity of precipitation are important components which influence the distribution and efficiency of acid wet deposition. Precipitation features admit great spatial and temporal variability. Two main questions in this study are: How do actual precipitation patterns change in the vicinity of an observed report representing a "point-information"? And, in comparison with model results, which predications can be made for grid cell precipitation?

3. THE CONCEPT

The first main aspect is to discriminate precipitating cloud areas and non-precipitating clouds. To do this for complex mid-latitudinal weather situations including frontal passages, it seem to be an advantage to exploit all three METEOSAT channels simultanously in order to determine a "threshold-tripel" for a specific meteorological situation indicated by a surface report. As can be seen from Fig. 1, mid-latitudinal rain observed at the ground is not necessarily associated with IR-cloud-top-temperatures colder than 0°C. Hence, a one-channel threshold is not sufficient (SCHOLL, 1986A). While for surface observations a "radius of included information" depends on the observed cloud base heights, METEOSAT pixel resolution varies according to the satellite viewing angle. Thus, multispectral radiance information of only the nearest pixel may mostly correspond with a surface report. However, such observed "point-information" may also be usable for the neighbourhood of the station report. Therefore also the nearest 3*3

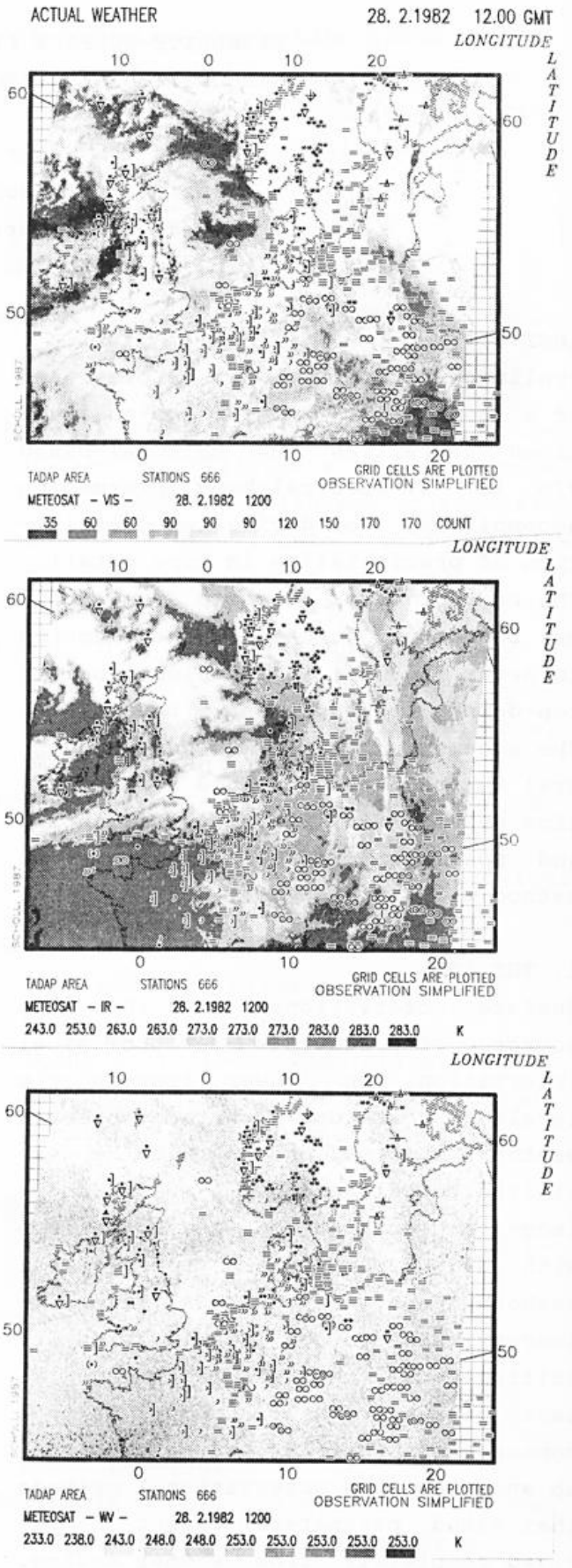


Fig. 1 Plotted parts of the VIS-, IR- and WV-images and surface-observed actual weather reports.

pixels are used to derive a multispectral mean radiance. The deviation then characterizes this pixel-area as cloud-free, partly cloudy or overcast. It is obvious that this combination needs correctly located picture elements which was done by utilizing the Interactive System Meteorology (ISM) of the DFVLR (SCHOLL, 1986b). However, even with optimal navigation there exists a geometrical "mispositioning" of clouds (ERIKSSON, 1987) which has to be corrected for a ground "truth" comparison. Moreover, the VIS-radiances are normalized to eliminate the solar zenith angle. Atmospheric correction is neglected for this case of mid-latitudinal clouds in a winter atmosphere.

In a first simple step, total cloud cover observations N=0 and N=8 as well as actual weather codes (ww) greater than 50 are used to mark pixel characteristics. The procedure is then subdivided according to further surface-observed cloud properties. Plots of selected, three-hourly cloud properties for the whole period are summarized in SCHOLL (1987). For grid cell estimations, an objective vertical analysis is available (REIMER, 1980). Additional a-priori knowledge like topography, coastal effects, influence of wind as well as vorticity may be included furtheron.

4. REFERENCES

ERIKSSON, A.: Qualität von Winden aus manipulierten METEOSAT-Bildfolgen zwischen 52° N und 72° N. Diplomarbeit, Freie Universität Berlin, Fachbereich Geowissenschaften, 1987.

REIMER, E.: A test of objective analysis with optimum utilization of the radiosonde network in Central Europe. Contr. Atm. Phys., 1980, 53, 311-335.

SCHERER, B.; SCHOLL, M.: Analyses of an acid deposition episode and preparation of meteorological input data for an Eulerian longrange transport and deposition model. Proceedings of the 4th European Symposium on Physico-Chemical Behaviour of Atmospheric Pollutants held in Stresa, Italy, 1986 (a), 667-676, published by D. Reidel Publishing Company.

_____: First results of the analysis of an acid deposition episode. Proceedings of the 6th ESA METEOSAT Scientific Users' Meeting held in Amsterdam, the Netherlands, 1986 (b), Vol. II, published by EUMETSAT/Darmstadt.

SCHOLL M.: The use of METEOSAT data within the analysis of an acid deposition episode. Proceedings of the 6th ESA METEOSAT Scientific Users' Meeting held in Amsterdam, the Netherlands, 1986 (a), Vol. II.

_____: "Cookery book" to navigate METEOSAT imagery utilizing ISM (in german), 1986 (b). In: **GRANT, KÖNIG, KONJACK, OLESEN and RATTEI:** ISM-Manual. DFVLR-report, Oberpfaffenhofen, 1986.

_____: Surface-observed cloud properties of an acid deposition episode within ALPEX, Part I: TADAP-modeling area. Annotated edition of meteorological data, 1987, pages 455. FU Berlin, Geophysical Sciences.

STERN, R.; SCHERER, B.; PANKRATH, J.: Application of a regional model for the transport and deposition of acidifying pollutants to Central Europe. Proceedings of the 16th International Technical Meeting on Air Pollution Modeling and its Applications held in Lindau, F.R.G., 1987, in print.

RESULTS FROM THE RAINFALL ESTIMATION STUDIES BASED ON METEOSAT DATA

Olli M. Turpeinen (*)

European Space Operations Centre
6100 Darmstadt, FRG
(*) Present affiliation: Recherche en Prévision Numérique
Dorval, PQ., CANADA H9P 1J3

1. INTRODUCTION

In recent years rainfall estimation studies have been carried out at the European Space Operations Centre (ESOC) using the ESOC Precipitation Index (EPI) (TURPEINEN ET AL., 1987; TURPEINEN AND DIALLO, 1988).
The purpose of this paper is to report the main results of the studies on (i) the geographical applicability of the EPI and (ii) the seasonal behaviour of the precipitation estimates.

2. DATA AND METHOD USED

Both, satellite and ground truth data, have been collected for two test periods:

(i) October 1985 - December 1985 from Côte d'Ivoire, Kenya, Morocco, Senegal and Tunisia to study the geographical applicability.
(ii) October 1985 - September 1986 from Burkina Faso to study the seasonal variations of the accuracy of the estimates.

Burkina Faso, Côte d'Ivoire, Kenya and Senegal lie in the tropical region, exposed to convective rainfall from ITCZ. Morocco and Tunisia are located in the subtropical zone, where frontal passages are fairly frequent in winter.

2.1 DATA

The satellite data consist of the precipitation indices EPI, based on a cloud indexing technique assuming that the larger the cold cloud core, the heavier the rainfall. The detailed description of the EPI, given by TURPEINEN ET AL. (1987), will not be repeated; only the main features will be summarized briefly:

(i) A fractional cloud cover for the effective black-body temperature colder than 235 K, in each Meteosat segment (150 x 150 km^2 at the sub-satellite point) is counted.
(ii) The upper tropospheric humidity (SCHMETZ and TURPEINEN 1988) based on the 6.3 µm-channel is incorporated into the EPI by segregating the index into three classes according to the upper tropospheric humidity. The sum of all the three indices, the non-segregated index, is called EPI-all.

The above calculations are performed every three hours and the results are summed for five days.

The ground truth data consisted of daily records from all regularly operating rain gauges from the countries considered. The rain-gauges were allocated among the segments according to their geographical coordinates. The daily mean of observed precipitation was calculated for all the segments considered, and summed over 5 days to render the observed precipitation compatible with the EPI.

2.2 METHOD USED

The EPI was evaluated by correlating it to the observed precipitation. As the linear correlation coefficient characterizes the dependence between two variables, the EPI was converted into rainfall, only if a fair correlation existed between the index and ob-

served rainfall. In the study of the geographical applicability of the method one single regression line was used based on the largest sample, originating from Kenya. When studying the seasonal behaviour of the estimates, the regression line was obtained from the full year's data from Burkina Faso. The accuracy of the estimates was assessed by comparing them with the observed rainfall.

3. RESULTS

3.1 GEOGRAPHICAL APPLICABILITY

It is essential to find out whether the EPI can be applied both in the tropical and subtropical region. To find out the performance of the method, a multiple linear correlation was calculated between the observed rainfall and EPI for five African countries (Table 1).

Table 1. Linear correlation coefficient between the observed rainfall and EPI in the five African countries considered in October - December 1985. The sample sizes are in brackets.

Côte d'Ivoire	(48)	0.76
Kenya	(48)	0.76
Morocco	(80)	0.07
Senegal	(32)	0.57
Tunisia	(16)	0.32

The results indicated that a fair multiple linear correlation existed between the precipitation and the EPI in the tropical region, while in the subtropics the correlation remained low. In Morocco the coefficient was particularly poor due to the importance of the orographic relief. As the existence of a good multiple correlation is prerequisite to the successful estimation of the precipitation, the estimation was restricted to the tropical zone. The estimated and observed tropical rainfalls are shown in Table 2.

Table 2. Estimated and observed averaged three-month rainfall (mm) in Côte d'Ivoire, Kenya and Senegal (October - December 1985)

	Estimated	Observed
Côte d'Ivoire	138	167
Kenya	194	209
Senegal	67	23

The estimation of the accumulated precipitation was feasible with a reasonable level of accuracy in the equatorial belt. In Senegal the estimates were not as accurate, probably due to cold non-precipitating cirri of frequent occurrence.

3.2 SEASONAL VARIABILITY

The seasonal rainfall estimates were assessed in Burkina Faso. To gain an insight into the observed behaviour of the rainfall, its yearly cycle is shown in Figure 1. The solid line represents fluctuations of the observed rainfall and the dashed line those of the EPI-all. The EPI-all values were multiplied by an arbitrary scaling factor (9), used for a better visualisation. The solid line shows that three seasons can be distinguished:

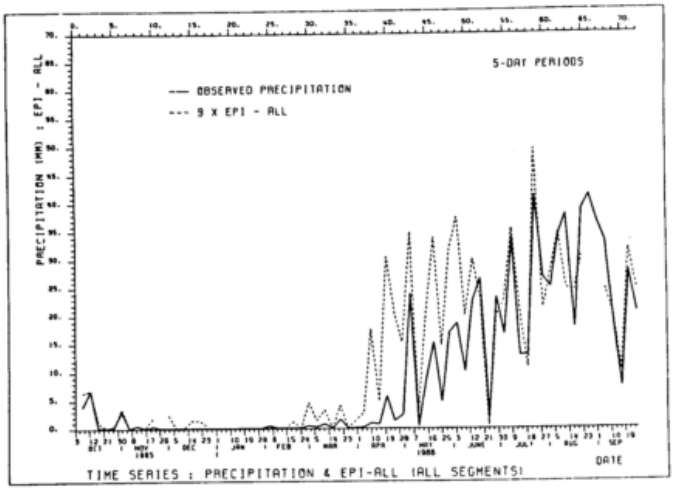


Fig. 1: The variation of the mean 5-day rainfall (mm) (solid line) and EPI-all (dashed line) in Burkina Faso during the one-year period.

(i) predominantly dry from October till the end of February;
(ii) a period of transition from March till early June;
(iii) rainy season from mid June till September.

Comparing the two curves in Fig. 2, they seem to bear a close resemblance and be well in phase. The magnitudes of the two curves, however, differ in a nonconsistent manner: during the transition the EPI-all strongly exceeds the observed rainfall, whereas all through the rainy period the observed and estimated rainfall rather overlap.

The relationship between the EPI and the observed rainfall was investigated more quantitatively by determining the correlation coefficients both for the three seasons and the full year. The results are shown in Table 3. The correlation is generally high except for the rainy reason.

Table 3. Linear correlatin coefficient between the observed rainfall and EPI in Burkina Faso for the three seasons and the whole year (Oct. 1985 - Sept. 1986). The sample sizes are in brackets.

Dry season	(196)	0.77
Transition	(126)	0.73
Rainy season	(154)	0.52
Whole year	(476)	0.77

The regression line used to estimate rainfall was based on the largest possible sample, the full year's data. The results of seasonal and annual rain estimation are shown in Table 4. The yearly rainfall could be estimated to a very high degree of accuracy, while the seasonally calculated rains experienced larger deviations. During the dry season, the estimate was excellent. During the transition period the problem of non-precipitating cold clouds led to a 100 % overestimation of the precipitation.

Table 4. Estimated and observed averaged seasonal and yearly rainfall (mm) in Burkina Faso (October 1985 - September 1986).

	Estimated	Observed
Dry season	24	16
Transition	172	83
Rainy season	412	514
Whole year	608	612

The reasons for the deviation were studied in a greater detail. The strong overestimation could be partly attributed to the abundance of thick non-precipitating cirri at the leading edge of the ITCZ. Another plausible explanation for the underestimation could be the strong evaporation caused by dry conditions in the lower layers of the atmosphere during the transition. During the transition (April), the mean relative humidity based on all the nine synoptic stations of Burkina Faso, was only 40 %, whereas in the rainy season (July) it reached the value of 74 %.

4. CONCLUSIONS

The present study demonstrates the feasibility to use the EPI to approximate seasonal and annual rainfall in the tropical region. The estimates providing a continuous spatial and temporal coverage will be particularly useful in context with climatological programmes, such as the WCRP, in complementing the observations from the sparse conventional rain gauge network.

5. REFERENCES

SCHMETZ, J.; TURPEINEN, O.M.: Estimation of the Upper Tropospheric Relative Humidity Field from Meteosat Water Vapour Image. J. Appl. Met. 20 (1988), (in press).

TURPEINEN, O.M.; ABIDI, A.; BELHAOUANE, W.: Determination of Rainfall with the ESOC Precipitation Index. Mon. Wea. Rev. 115 (1987), 2699-2706.

TURPEINEN, O.M.; DIALLO, A.A.: Estimation of Rainfall in Burkina Faso using the ESOC Precipitation Index. J. Climate. 1 (1988), (submitted).

Comparisons of Satellite Data with Surface-based Remote Sensing Measurements in Utah Winter Orographic Storms

David C. Rogers

Dept. Atmospheric Science
Colorado State Univ.
Fort Collins, CO 80523, USA

Kenneth Sassen
Gregory C. Dodd

Dept. Meteorology
University of Utah
Salt Lake City, UT 84112, USA

1. INTRODUCTION

In recent years, remote sensing techniques have seen increased use in studies of winter orographic storms. Examples include millimeter radar, satellites, radiometers and lidars. Millimeter radars are sensitive to small ice particles and can be used to determine cloud structure (Uttal et al., 1986). Geostationary satellites can provide synoptic and mesoscale storm overviews and measurements of cloud top thermal structure (Reynolds, 1986; Vonder Haar et al., 1986). Surface-based dual wavelength radiometers provide temporal measurements of the liquid and vapor in overlying clouds (Hogg et al., 1983; Rauber et al., 1986), and surface based lidar provides measurements of cloud ice and low level cloud water structure (Sassen et al., 1986). *In situ* measurements by research aircraft and surface-based observing systems provide detailed descriptions of cloud structure within relatively small, well defined regions. These *in situ* measurements are complemented by the remote sensing observations which typically have much larger sample volumes and continuous coverage.

Remote sensing data obtained during a winter storm episode are presented in this paper. Comparisons are made concerning the structure, composition and evolution of cloud features as observed by different techniques.

2. DATA

In support of a federal/state weather modification and research project in Utah, a variety of remote sensing and *in situ* observations were obtained in winter storms during February and March 1987. The surface-based instruments were located in a mountain valley on the western (windward) slope of a 30x50km mountain range. Figure 1 shows the terrain cross section through the instrument site. The remote sensing instruments included:

- Ka band (0.87 cm) reflectivity radar operated in vertical mode (0.5° beam width, 100 m range bins, 5 s sampling interval)
- dual frequency (20.6 and 31.6 GHz) steerable microwave radiometer operated in both vertical and azimuth scanning modes (2.5° beam width). In scanning mode, the radiometer sampled at fixed 25° elevation angle and about 1° increments in azimuth. Each 360° scan took about 15 minutes.
- polarization ruby lidar (0.7μm)

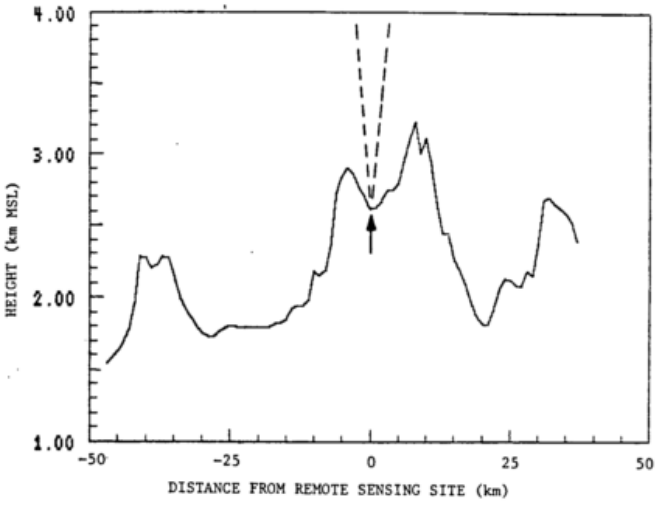


Figure 1. East-West terrain cross section through study area. Arrow shows remote sensing instrument site. Cone scanned by radiometer is indicated by dash lines.

Satellite data at infrared (IR, 10-12 μm) and visible (0.4-0.7 μm) wavelengths were obtained at 30 minute intervals from GOES VISSR. Rawinsondes were launched at 3 h intervals from two locations 10 and 30 km west of the remote sensing instrument site. Precipitation rates were measured by seven recording gages spaced 3 km apart on an east-west line through the instrument site. Surface observations of snow particles were also made.

3. ANALYSIS PROCEDURES

For this study, we defined radar cloud top as the altitude where the top of the radar echo became < -20 dBz. The radar is new and still under development; estimates of its sensitivity may be revised. The altitude error in radar cloud top is probably small since the vertical gradient of reflectivity is usually large near the tops of the clouds studied here. Lidar cloud top was defined as the highest altitude of returned energy; in heavy precipitation or dense water cloud, the lidar is strongly attenuated. Cloud top temperature (CTT) was derived in three independent ways: (1) CTT_R from the radar and rawinsonde data, (2) CTT_L from the lidar and rawinsonde data, and (3) CTT_S from the satellite IR data (assuming emissivity of 1.0). In order to compare these CTT estimates, radar and lidar data were averaged over 30 minute intervals centered on GOES observation times; extremes during each interval were also noted.

Each GOES IR pixel covers an area about 3 km x 7 km. For this comparison study, satellite data were taken from the single pixel corresponding to the surface instrument site and also from the entire Tushar Mountain range (approximately 33 km x 56 km, or 11 pixels x 8 pixels). The average and extremes of satellite CTT were derived from the large sample. In this preliminary study, no compensations were made for cirrus overlying the orographic clouds. Errors in satellite navigation have not been evaluated yet.

4. DESCRIPTION OF STORM AND OBSERVATIONS

The winter storm of 16 February 1987 was associated with an upper level short wave and surface cyclone which formed in the western United States and moved eastward over the project area. Snowfall from this storm was generally widespread, indicating synoptic forcing, but the mountain areas received much greater amounts, indicating significant orographic effects.

As shown in Figure 2, there were three stages to this storm: stage 1 with stable clouds of moderate depth and little to no snowfall; stage 2 with deeper clouds, convective in nature and producing heavier snowfall; and stage 3 characterized by shallow, stable clouds and light snowfall. The history of radiometer data for part of this storm is shown in Figure 3 as a time/azimuth contour plot of liquid water depth, normalized to vertical; data were not available outside the times shown. The figure was constructed from thirty-four 360° scans. In stage 1, there were two areas of high liquid water, one northwest and one southeast of the instrument site. These areas persisted through several successive scans and are probably related to forced ascent of air by the local topography. The minimum southeast is somewhat unexpected since (1) higher terrain exists southeast, (2) there was little precipitation at this time, and (3) cloud-level winds were west to northwest at about 3 ms^{-1}.

During stage 1, the lidar and radar CTT agreed with the maximum satellite CTT (dotted line in Figure 2) but were ~5°C warmer than the average satellite CTT. Rawinsonde data indicated that there may have been cirrus clouds (small dew point depressions at temperatures from -30 to -40°C) which could have reduced the average CTT_s.

During stage 2, there was a single heavy precipitation event which was associated with a mesoscale band of deeper clouds. CTT_r and CTT_s were in general agreement during this stage and showed a 3 h cycle of colder CTT corresponding with the precipitation event. This same trend was found when the single pixel CTT_s over the site was used instead of the mountain-wide 88 pixel average. The wide range between minimum and maximum CTT_s

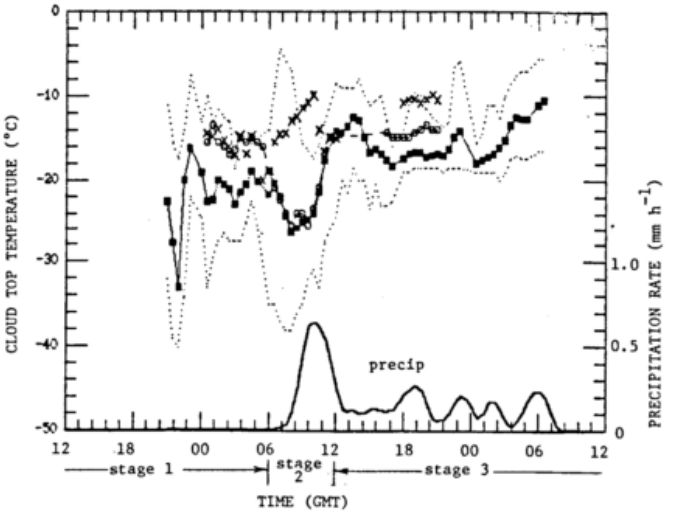


Figure 2. History of average cloud top temperatures (CTT) from remote sensing, and average precipitation rate from gages. From 88 GOES pixels covering mountain range: CTT average (boxes), minimum (dotted), and maximum (dotted). Radar CTT (circles). Lidar CTT (X). February 15, 16, and 17, 1987.

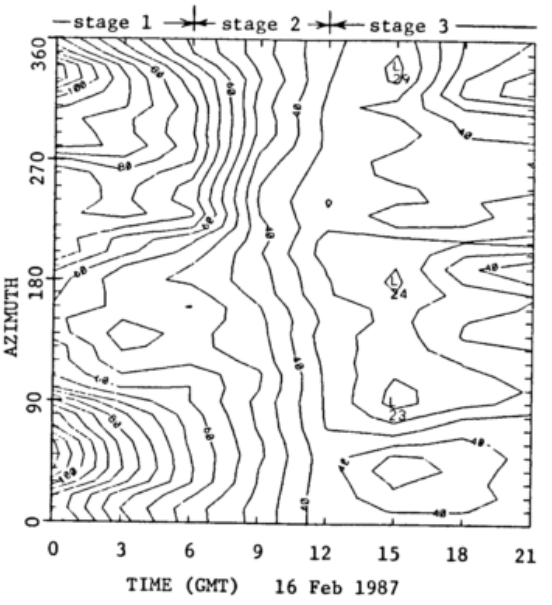


Figure 3. Contours of radiometer liquid water depth (μm).

suggests this was a convective period, which is consistent with the other observations. The large extremes in CTT_s are expected since the satellite samples a much larger area than the radar. In stage 2, the lidar experienced strong attenuation in heavy snowfall and could not measure cloud top. Radiometer liquid water values decreased significantly in stage 2 and showed little dependence on azimuth. The reduction was probably related to heavier snowfall removing the liquid water.

Stage 3 had several periods of light snowfall. The lidar CTT estimate was affected by attenuation in low altitude water cloud. Radar CTT was warmer than satellite CTT; again there was some rawinsonde evidence of cirrus. During this stable period, the cloud top was relatively steady (as indicated by radar and satellite CTT) and uniform (note the small

range between minimum and maximum CTTs). Liquid water (Figure 3) was generally low with a few small regions of greater liquid water.

Two examples of radar time-height reflectivity histories are shown in Figures 4a and 4b. Notice the marked difference between the appearance of radar cloud top as the convective nature of this storm increased (4a) and during the later stable period of shallow cloud (4b). The distinct cloud top elements in 4a are estimated to be about 2 to 6 km in horizontal dimension (from their duration, 10-30 minutes, and the rawinsonde winds, 280°/3 ms^{-1}). These are approximately the same size or slightly smaller than GOES pixels.

Two particular radiometer scans are shown in Figures 5a and 5b. Notice the relatively large values and high variability in 5a (stage 1) compared with 5b (stage 3) which has a uniform background with occasional higher liquid water regions. These higher regions in are estimated to be about 0.6 km in size (from their duration, 70 s, and the rawinsonde winds, northerly at 9 ms^{-1} at cloud top altitude). If this water is near cloud top (1.0 km AGL, cf., Figure 4b), then it is 3 km horizontally distant from the instrument because of the 25° elevation angle. Therefore, it is unlikely that the vertically pointing radar could detect some reflectivity change corresponding to the high liquid water region unless the winds carried the region exactly over the radar. These elements are too small for GOES data to resolve.

5. CONCLUSIONS

In this storm, the different remote sensing techniques provided independent estimates of cloud top temperature. Differences in the estimates were consistent with plausible physical causes, such as cirrus clouds contaminating some of the GOES CTT measurements. The particular advantage of satellite data is the potential to examine orographic cloud top characteristics over large mountainous regions which do not have the benefit of surface-based instrumentation. Additional case study research is needed to clarify the interpretation of these kinds of data and improve their diagnostic capability. The results confirm that, in orographic storms, the radiometric liquid water depends strongly on local terrain and on active ice precipitation processes. Small scale maxima were identified in the liquid water field.

6. ACKNOWLEDGEMENTS

This work was supported by the Utah Division of Water Resources, the National Oceanic and Atmospheric Administration, and National Science Foundation Grant ATM-8704776. We are grateful for the considerable efforts of others involved in this project including the University of Nevada Desert Research Institute, Atmospherics Incorporated, and North American Weather Consultants.

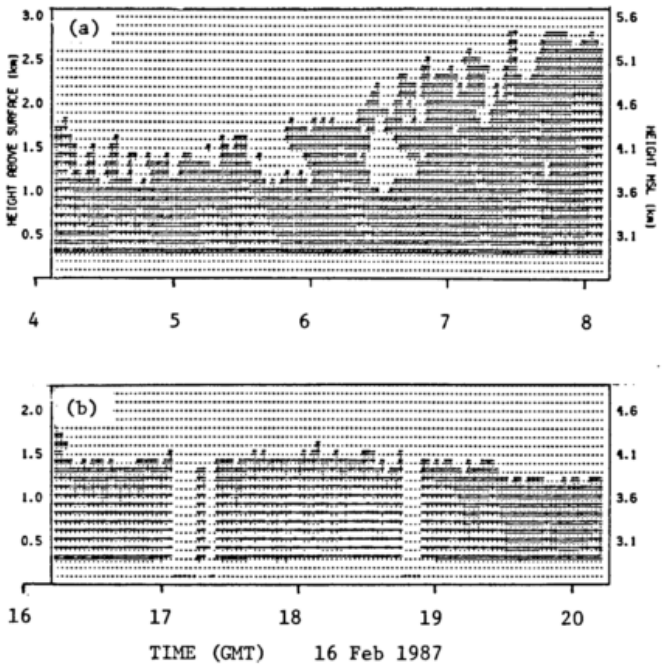


Figure 4. Time-Height radar reflectivity histories for (a) transition period from storm stage 1 to 2, and (b) part of storm stage 3 (gaps are missing data)

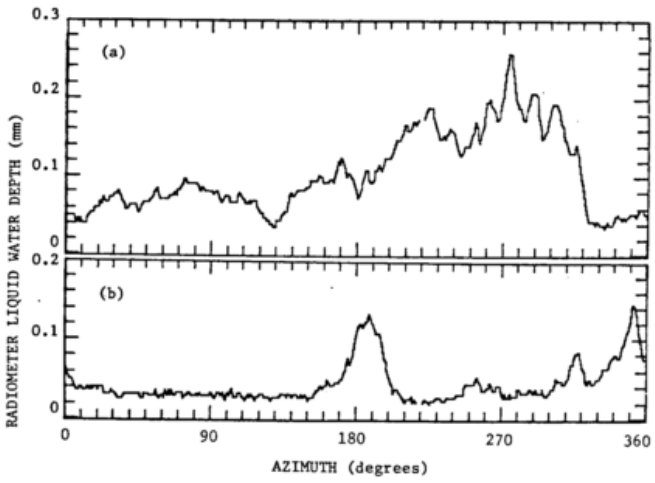


Figure 5. Radiometer liquid water scans for 16 Feb 1987: (a) 04:28-04:45 GMT and (b) 19:40-19:57 GMT. Scans start at 220° and azimuth increases with time.

7. REFERENCES

Hogg, D.C., F.O. Guiraud, J.B. Snider, M.T. Decker and E.R. Westwater, 1983: A steerable dual-channel microwave radiometer for measurement of water vapor and liquid in the troposphere. J. Clim. Appl. Meteor., 22, 789-806.

Reynolds, D.W., 1986: Satellite and surface based remote sensing of Sierra Nevada winter storms: Applications to weather modification Preprints Second Conf. Satellite Meteor. Remote Sensing and Applic., Williamsburg, Amer. Meteor. Soc., Boston, 409-414.

Sassen, K., R.M. Rauber and J.B. Snider, 1986: Multiple remote sensor observations of supercooled liquid water in a winter storm at Beaver, Utah. J. Clim. Appl. Meteor., 25, 825-834.

Uttal, T., R.A. Kropfli and J.B. Snider, 1986: Measurements of vapor flux, liquid water contents, precipitation rates, and riming in a Utah mountain cloud system. Preprints, Conf. Cloud Phys., Snowmass, Colorado, Amer. Meteor. Soc., Boston, j233-236.

Vonder Haar, T.H., J.L. Behunek and D.W. Hillger, 1984: Satellite support to the Sierra Cooperative Pilot Project: 1979 to 1984. Atmos. Sci. Dept., Colorado State Univ., Fort Collins, Colorado, 83pp.

PASSIVE MICROWAVE OBSERVATIONS OF THUNDERSTORMS FROM HIGH-ALTITUDE AIRCRAFT

Gerald M. Heymsfield [1] and Richard Fulton[1,2]

[1]NASA, Goddard Space Flight Center
Greenbelt, MD 20771 USA

[2]General Sciences Corporation
Laurel, MD 20707 USA

1. INTRODUCTION

There has been considerable interest in interpretation of passive microwave measurements in relation to thunderstorm precipitation because of the current and planned spaceborne instruments. The NASA high-altitude (~20 km) ER-2 aircraft made overflights of severe and non-severe Midwest thunderstorms in the central and southeast U. S. during two separate experiments. Down-looking instruments on the aircraft described here are the imaging *M*ulti-Channel *C*loud *R*adiometer (MCR) with channels in the visible, infrared (IR), and near IR, and two passive microwave instruments, the imaging *A*dvanced *M*icrowave *M*oisture *S*ounder (AMMS) at 92 (atmospheric window) and 183 GHz (centered on a water vapor line) and the 45° foward-of-nadir *M*ulti-channel *P*recipitation *R*adiometer at the 18 and 37 GHz window channels.

The passive microwave temperatures from a down-looking radiometer can be interpreted as follows. In the precipitation-free environment, a land background produces relatively warm microwave brightness temperatures (T_B), while an ocean background produces cold temperatures due to water's lower emissivity. In the presence of clouds, the microwave radiances are related to emission and scattering from the hydrometeors. At the higher microwave frequencies (92, 183 GHz), scattering from cloud and precipitation-sized ice particles is the dominant mechanism. At the lower microwave frequencies (<18 GHz), raindrops are the primary contributors to absorption and emission. At low frequencies, ice scattering can be important if there was a large amount of ice at high altitudes. The complex nature of the hydrometeors (size distribution, mixture of phases, ice crystal habit, etc.) often make direct interpretation of the radiances difficult. However, with a multi-frequency approach, considerable insight can be gained concerning the precipitation characteristics. Radiative transfer modeling using assumed and observed vertical profiles of precipitation characteristics, has also provided improved understanding of the relation of microwave radiances to the rain rate near the surface through radiative transfer modeling of simulated clouds with an ice layer overlaying a rain layer (e.g., Wilheit et al., 1983; Wu and Weinman, 1984).

The main objectives of the discussion here are 1) to describe the measurements over thunderstorms from the passive microwave and IR instruments *over land*, and 2) to give insight on the precipitation structure. Two cases are presented, one in 1984 in central Oklahoma and the other in 1986 in Alabama.

2. OBSERVATIONS

This section briefly discusses the remote aircraft and ground-based radar observations of thunderstorms over land from the two field experiments. Figure 1 is a composite of nadir-pointing profiles along the ER-2 flight track of brightness temperature at the 92 and 178 GHz (accidentally displaced from the 183 GHz water vapor line) microwave frequencies and the 10.7 μm IR frequency on 19 May 1984 in Oklahoma. (The MPR instrument at 18 and 37 GHz was unavailable in 1984.) Profiles of radar reflectivity at three altitudes along the flight path are constructed from nearly simultaneous radar volume scan data. The ER-2 passed from south to north over a non-severe multicell-type thunderstorm with an anvil sheared toward the north. The core of the storm on the left side of the figure had a peak reflectivity of about 50 dBZ; the peak cloud tops extended to an altitude of 12 km and the downshear anvil (right side of the figure) settled to an altitude of about 9–10 km.

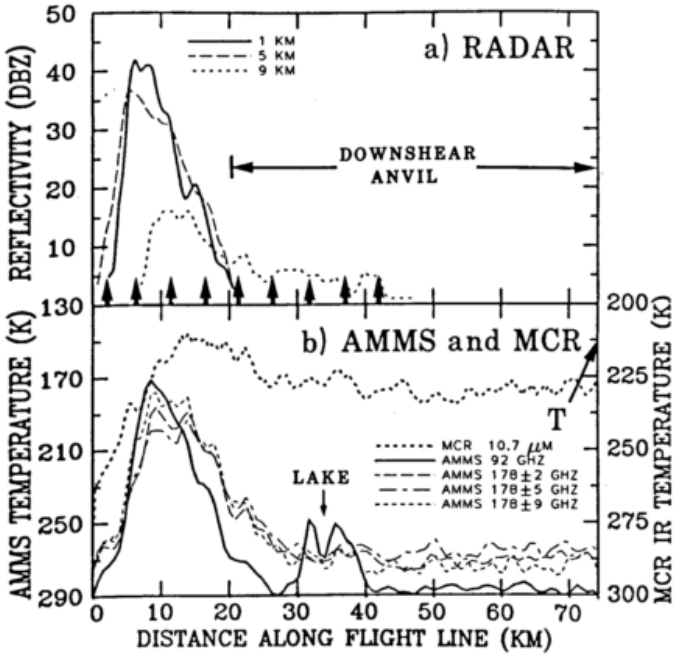


Figure 1. Nadir-pointing profiles for 19 May 1984 Oklahoma case. Given are a) radar reflectivity at 1, 5 and 9 km, and b) AMMS temperatures (4 channels) and MCR-IR temperatures. "T" delineates tropopause temperature.

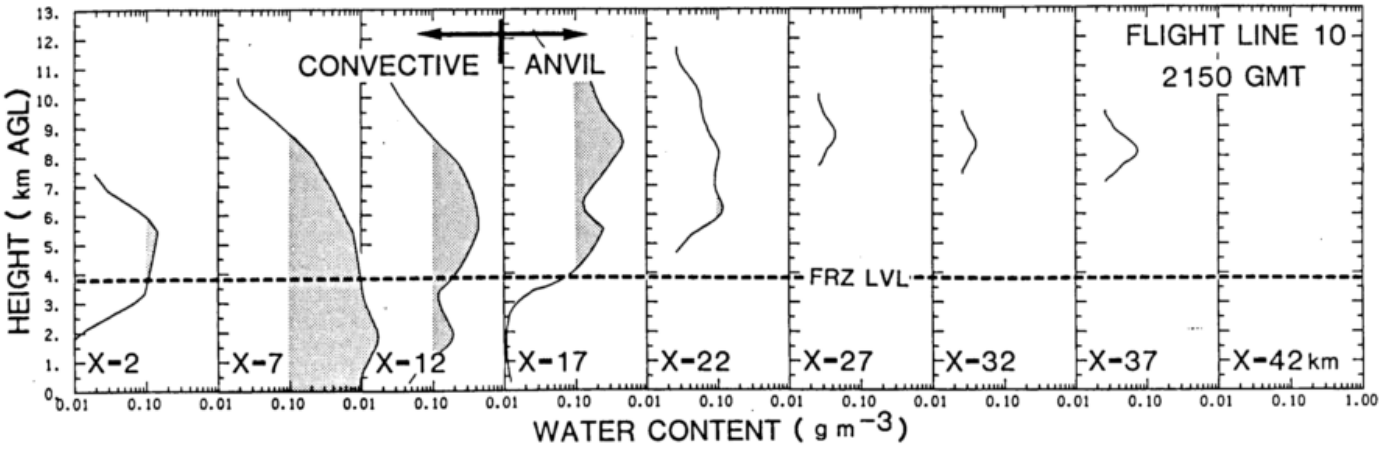
The 92 and 178 GHz microwave frequencies do a very good job of identifying the convective, precipitating region of the storm. The IR frequency, on the other hand, is still able to identify the storm, but the area of cold brightness temperature is signficantly larger than the area of the surface rainfall because of the effect of the extensive downshear anvil. The relative transparency of the anvil at the microwave frequencies compared to the IR frequency is demonstrated in the figure; in fact in the 92 GHz channel, a surface lake feature is detected (relatively cold T_B) between distances 30 and 40 km in the figure despite the overlaying anvil.

The implications of this fact for precipitation estimation from space are obvious; microwave frequencies appear to be more suitable for global precipitation estimation from satellites than infrared frequencies. These higher microwave frequencies (i.e., 92 and 178 GHz), however, *indirectly* identify rain since they respond mainly to the large ice particles and/or higher ice concentrations in the upper half of the storm and not the near-surface raindrops. The extent to which microwave frequencies respond to precipitating clouds with small ice particles or low ice concentrations is a present area of investigation with the ER-2 data.

Figure 2 shows vertical profiles of ice and liquid water content along the same flight line at locations identified by the arrows on the abscissa of Fig. 1a. These profiles were computed from radar reflectivity data using relations for rain below the freezing level and ice above. Note that to the right of x=20 km the microwave T_B's are nearly the background values despite the existence of anvil cirrus, with little or no response when ice contents are less than about 0.1 g m^{-3}.

The addition of the MPR instrument to the ER-2 payload during the 1986 experiment was very valuable and allowed for the first time simultaneous measurements of precipitating clouds at four microwave frequencies. Figure 3 shows profiles of near-surface radar reflectivity, 18, 37, 92, and 183 GHz and

Figure 2. Radar-derived vertical profiles of total water content through various portions of profile in Fig. 1. The x values indicate the locations of individual profiles as shown by the arrows in Fig. 1. Values $\geq$0.1 g m^{-3} are shaded.



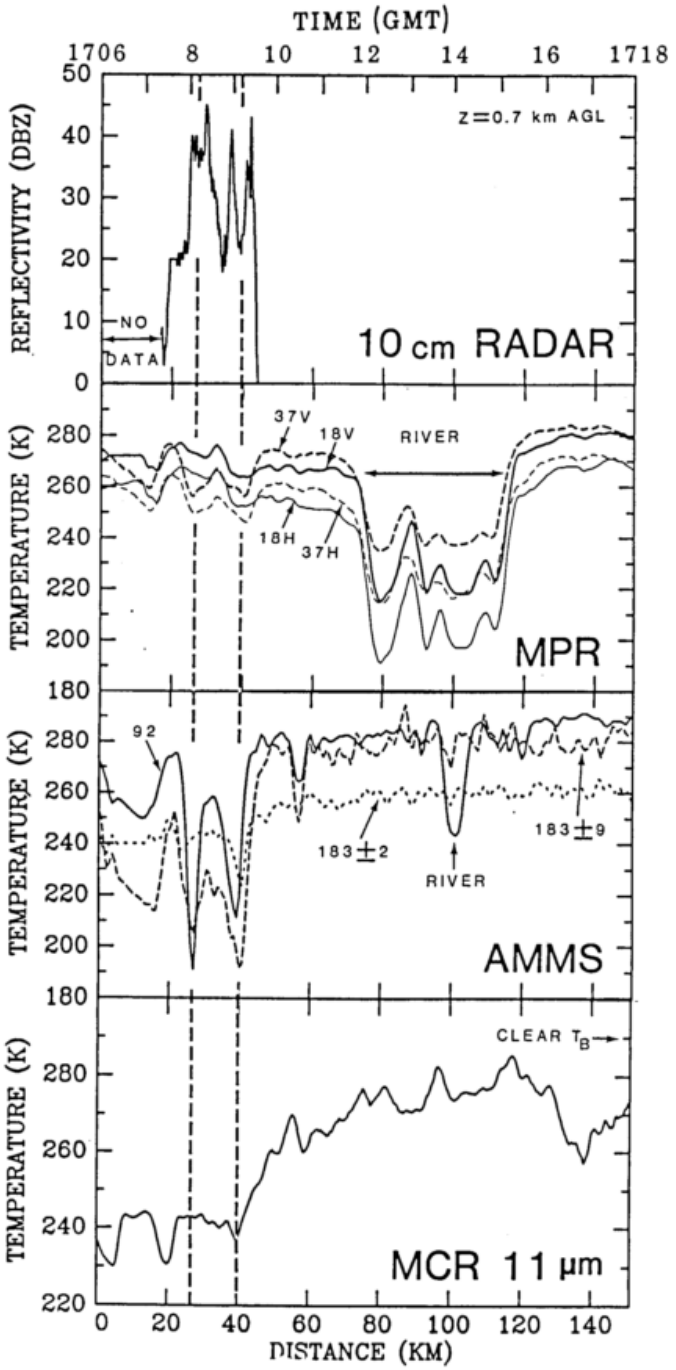


Figure 3. Nadir-pointing profiles for 2 July 1986 in Alabama. The clear atmosphere (background) T_B's correspond to the intersection of the curves with the right axis except as noted for the 11 μm MCR channel.

10.7 μm brightness temperature for one flight line on 2 July 1986 in Alabama. This line is an east to west overflight of convection along a cold front. Convective cloud tops extended to 10 km with a thin overlaying cirrus layer at 13 km. Peak reflectivity is about 45 dBZ. The magnitudes of the T_B depressions at 92 and 183 GHz are less on this day compared to 19 May 1984 (~80 K vs. ~120 K). Note however the corresponding low frequency (i.e., 18 and 37 GHz) T_B depressions over the convection are considerably smaller than at higher frequencies due in part to the lesser importance of ice scattering at these lower frequencies. Smaller ice particle sizes and/or concentrations may also be a cause, since in-situ aircraft particle measurements show that precipitation-sized ice particles are relatively small in these clouds. The large depressions at 18 and 37 GHz at distances of abut 60–120 km in the figure are due to the overflight of a river, with its inherent low emissivity, and not the existence of convection, as evidenced by the radar reflectivity and IR T_B profiles.

3. CONCLUSIONS

The passive microwave radiances in precipitation regions are dependent on the vertical distribution of the precipitation-sized hydrometeors. For this reason, passive microwave measurements from spaceborne instruments identify the precipitating regions better than IR measurements. Over land, the 92 GHz frequency distinguishes quite well the precipitating region from the non-precipitating anvil region. The interpretation of the microwave measurements is complicated by differences in the cloud microphysics between different climatic regions. Cloud and radiative transfer modeling work at NASA Goddard Space Flight Center using simulated and observed vertical profiles of the precipitation will continue to provide considerable insight into the interpretation of the microwave measurements.

REFERENCES

Hakkarinen, I. M., and R. F. Adler, 1988: Observations of precipitation at 92 and 183 GHz: aircraft results. (To appear in *Meteor. and Atmos. Phys.*.)

Heymsfield, G. M., and R. Fulton, 1988: Comparison of high-altitude remote measurements with the radar structure of an Oklahoma thunderstorm: Implications for precipitation estimation from space. (To appear in *Monthly Weather Review*, **10**.)

Wilheit, T. T., 1986: Some comments on passive microwave measurements of rain. *Bull. Amer. Meteor. Soc.*, **67**, 1226–1232.

Wu, R., and J. A. Weinman, 1984: Microwave radiances from precipitating clouds containing aspherical ice, combined phase and liquid hydrometeors. *J. Geophys. Res.*, **89**, 7170–7183.

NUMERICAL FRONTAL ANALYSIS SCHEME FOR OPERATIONAL INTERPRETATIONS OF SATELLITE PICTURES AND PRECIPITATION ESTIMATIONS

Lutz Lesch

Institut für Meteorologie, Freie Universität Berlin

A numerical analysis of fronts near the surface is obtained by using the calculus of front-parallel components and the external baroclinicity parameter following WIPPERMANN. In the presented case study this analysis is applied to case of convective developments at a frontal system and compared with a satellite picture (NOAA 9). Using numerically analyzed upper air charts a method to estimate areal distribution of precipitation is presented.

Upper air analyses, satellite pictures with high resolution and superposition of numerically analyzed fronts near the surface applied to a single case study allow the following classification of precipitation:

The area of maximum precipitation

- is situated within the area of the greatest positive relative vorticity advection at 300 hPa,
- is related to large positive baroclinicity parameter B_x (instability) at 300 hPa with maximum stability ($-B_x$) within the inner area of the frontal zone between 900 and 800 hPa and a non-zero temperature advection B_y between 900 and 800 hPa,
- is located below the quasi divergence-free level (600 hPa) showing minimal absolute vorticity,
- is associated with cloud top temperatures (McCLAIN Ch 4/5, NOAA 9) of $< -52°C$.

Further investigations will follow using the complete ω -equation with smaller grid distances (32 km) and including characteristical features of fronts (like ANA-KATA-front), ageostrophic deviations, computing precipitable water with cloud cluster analysis (maximum likelihood method) and orographic boundary points. Parameterization of position, extent, and intensity of precipitation areas as well as cloud top temperatures, reflexion ability, and dynamical quantities will help to improve the evaluation of precipitation by means of satellite pictures.

A MIDDLE LATITUDE SQUALL LINE IN FRANCE

Geneviève Jaubert, Michel Chong and Jean-Marc Giudicelli

Centre National de Recherche Météorologique (DMN/EERM)
42, Avenue Coriolis 31057 TOULOUSE CEDEX , FRANCE

1. INTRODUCTION

On 20 june 1984, a squall-line system passed over the southwestern part of France and was investigated during the french experiment LANDES-FRONTS 84 (Chalon,1987). This paper focuses on the kinematic structure of the convective region, using data provided by a central meteorological station, a ground station network, two Doppler radars (the RONSARD system) and a conventional meteorological radar. Section 2 describes the environmental characteristics associated with the squall line system. Precipitation structure and surface signature of the system are analysed in section 3 while its kinematic structure is discussed in section 4.

2. METEOROLOGICAL ENVIRONMENT

The 20 june squall-line crossed the experimental zone between 1900 and 2200 (all times UTC). Fig.1 shows a PPI view of the reflectivity pattern as observed at 2015 by the conventional radar located at Bordeaux. Analysis of fig.1 indicates that the squall-line system appeared as an organised line from North to South and extended $250km$ in the North-South direction and $100km$ in the line-transverse direction. This system propagated eastward at $12ms^{-1}$. Maximum echo up to $40dBz$ characterised the convective part of the system.

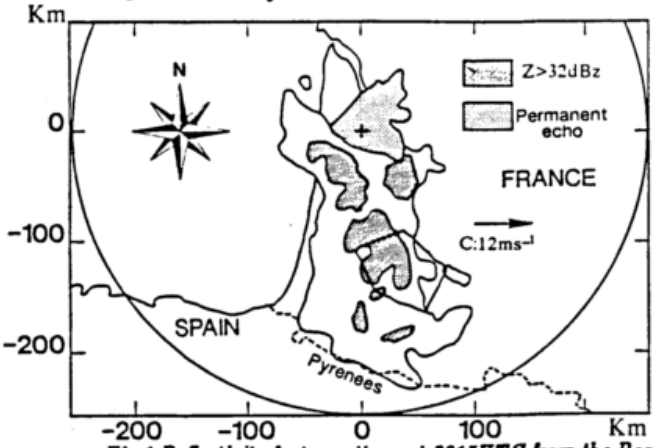


Fig.1.Reflectivity factor pattern at 2015UTC from the Bordeaux radar.The dual-Doppler analysis domain (experimental area) south of Bordeaux,is represented by the polygon.

Pictures taken from METEOSAT satellite showed that the squall-line system formed at the north-western part of Spain at 1500. This system intensified between 1800 and 2130 as it approached and passed over the experimental area as revealed by the Bordeaux radar in surveillance mode. After 2130 its southern part broke up and the eastward propagation slowed down.

Synoptic obeservations at 1200 and above $700hPa$ revealed a south-southwest flow over Spain which was associated with a thalweg zone,West of Portugal. This flow tended to be progressively southwest over the experimental area, due to the presence of the Pyrenees mountains culminating at $3000m$ altitude. At lower levels ($850hPa$ and ground level), the southerly flow was strongly marked by a skirting effect of the Pyrenees by its eastern part and a south-easterly flow could be observed in the southern part of France.

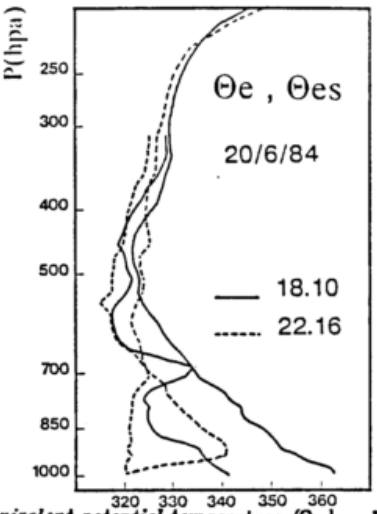


Fig.2.Equivalent potential temperature (Θ_e) and saturated equivalent potential temperature (Θ_{es}) deduced from soundings at 1810 and 2216UTC.

At 1800, the squall-line system reached the french coast and was preceded by a flux convergence line, North-South oriented, at ground level. This convergence line was located about $50km$ ahead of the system and was characterised by the previously-mentioned south-easterly flow and a north-westerly flow.

Fig.2 shows the thermodynamic structure of the environment ahead of and behind the squall-line system, deduced from radiosoundings launched respectively at 1810 and 2216, from the central station located within the dual-Doppler analysis domain, south of Bordeaux (fig.1).

At 1810, the atmosphere was characterised by mid to upper-level moist and potentially unstable air, overhanging a deep layer (1000-$700hPa$) of warm and dry air. The Foehn effect produced by the Pyrenees was mainly responsible for this dry and stable layer which could prevent the convective cells to develop. However, radar data clearly show that the system maintained its activity. This was probably due to a local characteristic commonly observed during the experiment. Indeed,observations of convective cells in presence of Foehn effect were marked by a reduction of this effect coinciding with a rotation of the southerly upper-level flow. In fact, as the system entered the experimental area, the associated surface flow tended to be north-eastward, modifying the skirting and Foehn effects caused by the Pyrenees.

At 2216, the atmosphere became stable and a colder and dry air characterised the low levels.

3. PRECIPITATION STRUCTURE AND SURFACE SIGNATURE

Fig.3 shows a vertical line-transverse section of reflectivity as derived from a composite analysis of dual-Doppler radar data obtained at 1928 and 2111. The squall-line system is assumed to be steady state in the reference frame moving at $12ms^{-1}$. Surface data from a ground station associated with the corresponding radar data are also shown,using the same steady-state hypothesis in a time-space coordinate transformation.

Fig.3 clearly shows a classical structure of the squall-line system, with a forward anvil preceding the convective cells and a trailing anvil cloud marked by a

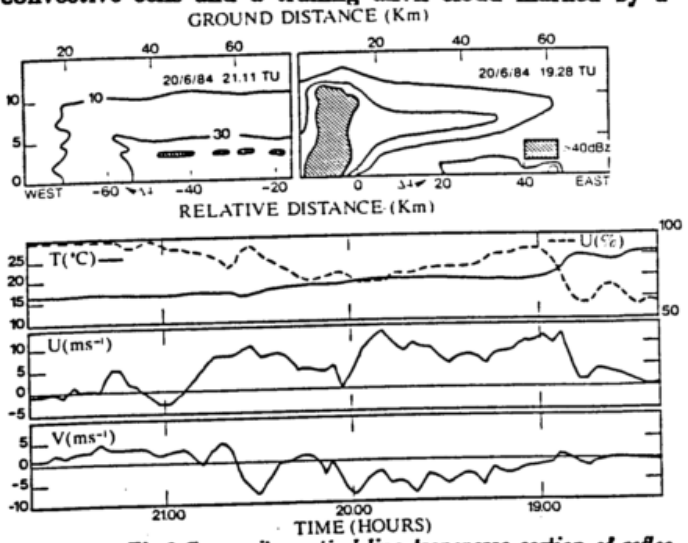


Fig.3. Composite vertical line-transverse section of reflectivity factor derived from Doppler radar observations at 1928 and 2111UTC (upper panel). Surface measurements of temperature, humidity and wind components associated with the radar data are represented in the lower panel.

bright band around 3.5km altitude (the 0^0C isotherm level was located at 3.8km). The forward anvil extended 40km ahead of the leading convective cells and overhung a shallow layer of relatively weak precipitation. The convective cells developed up to 10km.

The surface thermodynamic changes also depict classical features with abrupt changes in temperature, humidity and wind direction as observed at the passage of a leading gust front associated with mid-latitude or tropical squall lines (see,*e.g*, Ogura and Liou,1980; Chong *etal.*,1987). In the present case, the leading gust front was located 50km ahead of the convective cells. It corresponds to the position of the convergence line above-discussed, which propagated eastward at the system ' s speed. The shallow layer of precipitation formed in the forward part of the system could be induced by this convergence. At the arrival of active convective cells, the thermodynamic variables undergo additional but smoother changes.

4. KINEMATICS OF THE CONVECTIVE REGION

As the convective part of the squall-line system entered the dual-Doppler radar analysis domain, a series of coplane scan sequences was performed. Data from 2022 sequence are analysed in this paper, following the processing technique described in Chong(1983)

Fig.4 represents the absolute horizontal flow at 1 and 4km altitude while relative flow are shown in fig.5. Line-transverse component is along x axis. At low levels (below 2.5km), the absolute flow was marked by an eastward component which turned in a south-eastward component at the leading edge of the system (from West to East); no significant vertical motions were observed. At higher levels (above 3km),southerly flow characterised the absolute air circulation and tended to converge in the inner part of the system. fig.4b clearly shows a strong intrusion of this flow which could transport mid-tropospheric moist and potentially unstable ambient air feeding the convective updrafts observed above 2.5km altitude. This high-level convective structure that appeared in the present squall-line is somewhat particular, compared to that of mid-latitude squall-line observed by others (*e.g*,Smull and House, 1987).

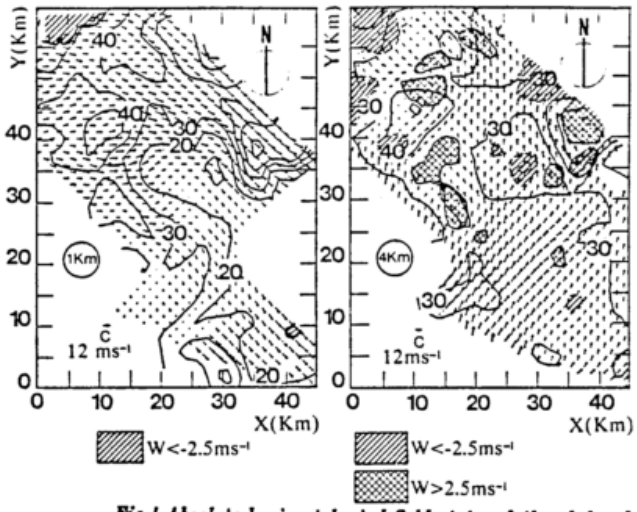


Fig.4. Absolute horizontal wind field at 1 and 4km deduced from dual-Doppler radar data at 2022UTC. Labelled contours represent reflectivity factor (dBz). Vertical motions are also shown (hatched regions).

The relative flow shown in Fig.5 reveals interesting characteristics of the convective air circulation. At low levels air came from the northern part of the system and diverged to south-west in the southern part. It is probable that the flow transported relatively cold air due to evaporation in a subsiding motion. Relative horizontal flow at these levels (below 2.5km) indicates an general front-to-rear flow (inflow) at the leading edge (eastern part) of the

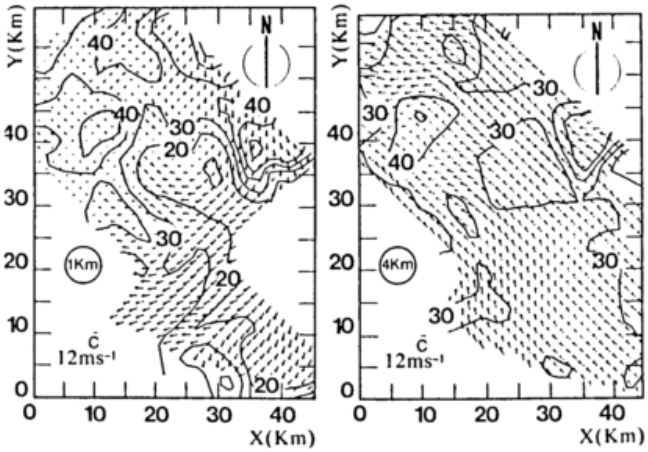


Fig.5. As in Fig.4, but for relative flow. Vertical motions are not show.

system (not visible in Fig.5a). The associated dry an stable air had an effect to reinforce evaporation process leading to the secondary cooling as observed in Fig.3. At higher levels (Fig.5b),inflow from the southern part characterised the relative flow, associated to the previously-mentioned moister ambient air. It tended to flow rearward (*i.e.*,toward the stratiform region of the system), except above 8*km* altitude where a rear-to-front component could be observed. This rear-to-front flow is consistent with the observation of the forward anvil cloud.

The observation of front-to-rear inflow in the present study is similar to other observations of mid-latitude squall-lines. However there exists some fondamental difference, may be due to the proximity of the Pyrenees chain with respect to the experimental area (100*km*). indeed, the relative and absolute flows reveal strong three-dimensional structure in which line-parallel flow was a major component of the wind field.

In order to emphasise the contribution of line-parallel wind component in the airflow structure, mean profiles of vertical and horizontal relative motion and mass transport budget have been evaluated in the convective part of the field (between *km*26 and *km*0 on the *x* axis-Fig.6a and 6b, respectively). The line-transverse (u) component in Fig.6a is mostly rearward with a maximum at mid-level (3*km*). Its variation with height is quite consistent with that observed by Smull and Houze(1987). in contrast, the vertical and line-parallel motions depict a different structure. Upward motion, in our case, is not observed throughout the troposphere, but only above 2.5*km* altitude. Below this, relatively weak motion indicates that convective activity could not be triggered. In fact, stability of the dry ambient air certainly inhibited the convective process. The line-parallel motion (v) in Fig.6a shows a southerly component above 2*km* altitude with a deep layer of high values, while a northerly component characterises the low-level flow.

The mass budgets along line-transverse and line-parallel directions (Fig.6b) also indicate the important role of line-parallel motion in sustaining the horizontal-flux convergence (defined as Fx+Fy>0 or Fz<0) between 1.5 and 7*km* altitude. This convergence mostly contributed to the general upward motion above 3*km* altitude. In fact the line-transverse flow Fx was mainly divergent above this level so that an important contribution of convergent line-parallel flux Fy was necessary to feed the updrafts. Subsequently, the updraft air detrained into the rear part of the convective region and was transported by the rearward flow. Below 3*km* altitude, air is non-divergent due to the equilibrium between the convergent line-transverse flux and the divergent line-parallel one.

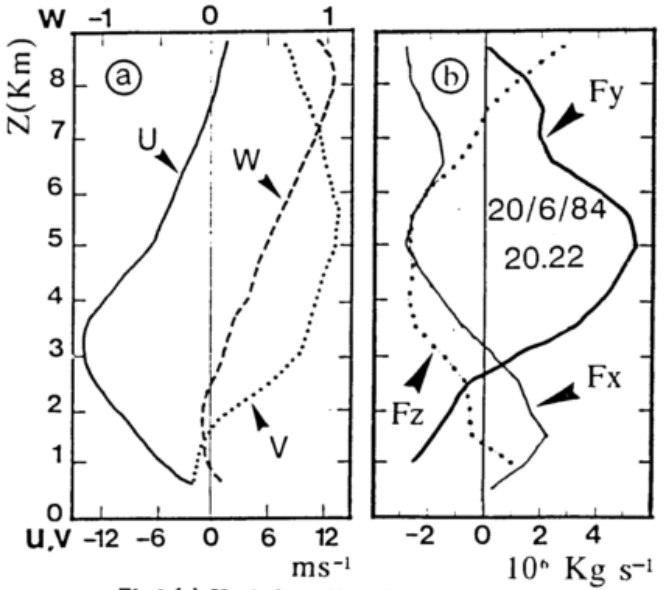


Fig.6.(a)-Vertical profiles of mean relative wind components (u,v,w) and (b)-mass transport budget along the line-transverse(Fx), line-parallel (Fy) and vertical(Fz) directions in the convective part(km26 to km0 on x axis).

5. CONCLUSION

Dual-Doppler radar analysis of a midlle-latitude squall-line has been used to study the kinematic structure of the convective region. Although its general characteristics resemble those of mid-latitude squall-line already observed, its kinematic structure presented some differences. In particular, the three-dimensional structure was mainly enhanced by a considerable line-parallel inflow at mid- to upper level although line-transverse inflow (front to rear flow presented similar features as observed by Smull and Houze (1987). Another point that should be emphasized is the absence of significant vertical motions at low levels and the relatively high level of convective motions. The proximity of the Pyrenees chain and its subsequent effect on the airflow (skirting and Foehn effects) certainly played an important role in the observed kinematic structure. A thorough study of these effects should be made in order to give a more comprehensive analysis of the present squall-line system.

Acknowlogements. LANDES-FRONTS 84 was a cooperative experiment involving several French laboratories.Financial and logistical supports were provided by the Institut National des Sciences de l' Univers, the Direction des Recherches et Etudes Techniques and the participating laboratories.

1. REFERENCES

Chalon,J-P.,1987.Landes-fronts 84, une experience d' etude des bandes convectives associees aux systemes frontaux, *la meteorologie*,VII,7-23

Chong,M.,1983.Les radars meteorologiques Doppler pour l' etude de la convection orageuse.Application à une ligne de grains tropicale *These d' état;Universite PARIS-VI*

Chong,M,P.Amayenc,G.Scialom and J.Testud,1987.A tropical squall line observed during the COPT 81 experiment in west Africa.Part 1:kinematic structure inferred from dual-Doppler radar data, *Mon.Wea.Rev*,115,670-694

Ogura,Y. and M.Liou,1980.The structure of a midlatitude squall line:a case study ,*J.Atmos.Sci.*,37,553-567

Smull,B. and R.Houze,1987.Dual-doppler radar analysis of a midlatitude squall line with a trailing region of stratiform rain ,*J.Atmos.Sci.*,44,2128-2148

A Study of the Dynamics of Squall Lines Using a Non-Hydrostatic Cloud Model

by

David B. Parsons, Richard Rotunno, Joseph B. Klemp, Morris L. Weisman

National Center for Atmospheric Research*
P. O. Box 3000, Boulder, Colorado 80307

1. INTRODUCTION

Active convective cells are often organized into linear features called squall lines. Since squall line can have lifecycles that extend far longer than the typical thunderstorm cell, the question arises as to how the convective circulations interact to form a long-lived system. Early observational studies of squall lines (e.g., Newton, 1950) stressed the importance of lifting of relatively warm, potentially unstable air by shallow pools of cold air in the presence of relatively large vertical shear. Motivated by this early work and other subsequent studies that suggested the importance of vertical wind shear on squall line lifecycle, Rotunno *et al.*, (1988) investigated the interaction between the circulation of the cold pool and ambient vertical shear in the lower layers of the atmosphere. Their studies suggest that the deepest lifting results when the horizontal vorticity in the ambient vertical shear approximately "balances" the horizontal vorticity produced by buoyancy gradients near the leading edge of the cold pool (Fig. 1).

To investigate this balance further, and to study other aspects of squall-line circulations, we have carried out numerical simulations of observed squall lines which occured in four distinctly different environments. The first two squall lines occured at the leading edge of cold fronts. The first case is characterized by large vertical shear, but a lapse rate that was nearly neutrally buoyant to vertical ascent. The environment ahead of the second system is marked by significant potential instability and weak vertical shear. The third case is an example of a prefrontal squall line in a environment of moderate shear and significant potential instability. A study of a fourth tropical system is underway.

The numerical simulations for this study were undertaken using the Klemp-Wilhelmson three-dimensional cloud model (Klemp and Wilhelmson, 1978). The model uses the complete set of non-rotating compressible equations, Kessler type microphysics for the cloud and rain water fields, a radiative upper boundary, and a subgrid turbulent energy equation. A representative rawinsonde ascent ahead of each squall line was used to provide the initial state for each simulation. Further details on the initialization, grid spacing, and domian size are given in Parsons *et al.*, (1988).

2. SIMULATIONS

2.1 Frontal squall line of 5 February 1978

Despite the lack of potential instability in the pre-frontal soundings, this squall line was characterized by heavy precipitation (Fig. 2) and even a weak tornado (Carbone, 1982; Carbone, 1983; Parsons *et al.*, 1987). The simulations replicate the line's overall kinematic and precipitation structures (Fig. 3). In contrast, replacing the ambient vertical shear with a uniform wind (Fig.4) fails to reproduce the observed intensity, as the maximum vertical motions (5.6 m s^{-1} vs. 13 m s^{-1}), the height of the maximum (.6 km vs. 2.0 km), and the rain water content (.4 g/kg to 6.4 g/kg) were all substantially higher in the simulation with ambient vertical shear. The higher water loading area in the shear run also produced a corre-

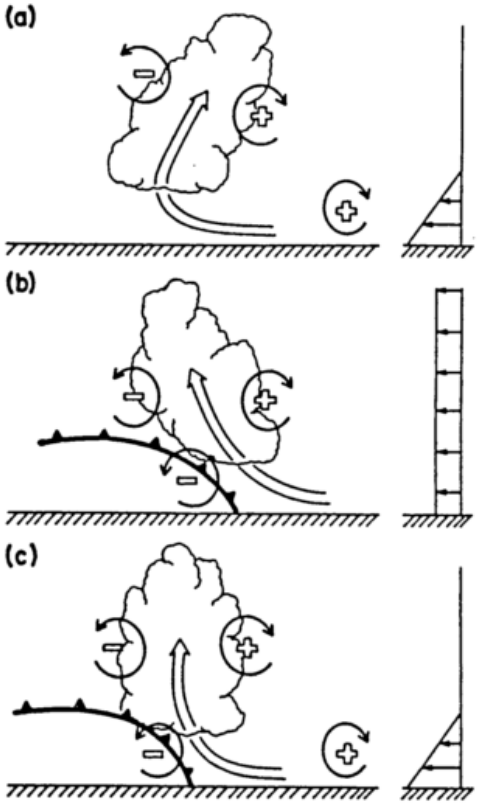


Fig. 1 Schematic diagram showing how a buoyant updraft may be influenced by wind shear and/or a cold pool. a) With shear, the vorticity distribution is biased toward positive vorticity and this causes the updraft to lean downshear. b) With a cold pool, the vorticity distribution is biased by the negative vorticity of the underlying cold pool and causes the updraft to lean upshear. c) With both a cold pool and shear, the two effects may negate each other, and allow a deep updraft.

* The National Center for Atmospheric Research is sponsored by the National Science Foundation.

spondingly larger pressure rise at the leading edge of the cold pool resulting in a flow in the lowest 500 m of the cold pool that is directed toward the rear of the system. This return flow was observed by Carbone, but is not present in either the no shear run or the flow in a simple density current.

From these numerical experiments, we conclude that the narrow and intense band of rainfall (often called the narrow cold frontal rainband) observed at the leading edge of cold fronts of this type (e.g., Browning and Harrold, 1970; Hobbs and Persson, 1982; Parsons and Hobbs, 1983; Bond and Fleagle, 1985) is due in part to an interaction between the large vertical shear (in this case nearly 24 m s $^{-1}$/ lowest 3 km) and the cold air. We feel that the theoretical work of Rotunno *et al.*, 1988 provides an important framework for explaining how the interaction between the cold pool and the vertical shear leads to a deep intense ascent. According to Rotunno *et al.*, 1988), the balance can be expressed mathematically as $c/\Delta u$, where c is the speed of the cold pool and Δu is the horizontal wind change through the vertical

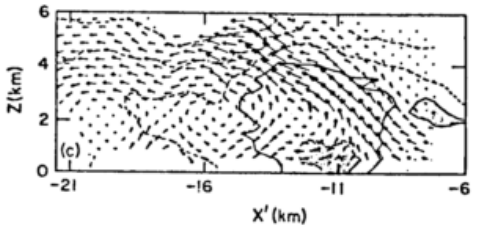


Fig. 2 "Typical" vertical cross-section perpendicular to the frontal squall line of 5 February 1978 showing relative wind and radar reflectivity. The maximum vectors are between 15 and 20 m s^{-1} and the radar reflectivity are shaded at 40 and 50 dBZ. The low-level flow within the cold pool that is directed toward the rear of the system is below the lowest height of radar data at this time. (Adapted from Carbone, 1982.)

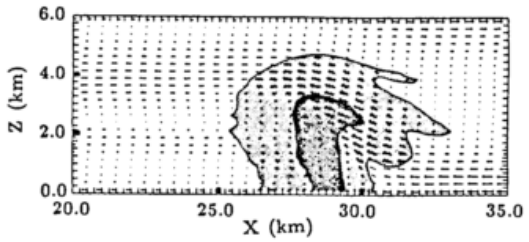


Fig. 3 A vertical cross-section from 4 hrs into a numerical simulation of the 5 February case using the ambient wind and thermodynamic profiles. The maximum vector length is comparable to Fig. 2 and the precipitation mixing ratio in excess of .7 and 4.5 g kg^{-1} are shaded. These mixing ratios are roughly correspond to radar reflectivities of 40 and 55 dbZ.

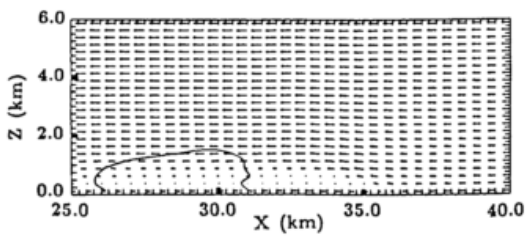


Fig. 4 As in Fig. 3, but with a uniform horizontal wind and precipitation mixing ratio contoured at .35 g kg $^{-1}$.

layer interacting with the cold pool. When this ratio is approximately 1, the balance is optimal, promoting a deeper and more intense updraft. In the simulations, the ratio of $c/\Delta u$ is estimated to be 1.0, while Rotunno *et al.* have argued that the ratio for the observed case is also quite close to 1. In this system, the overall kinematics, cold pool depth and strength and the ambient vertical shear all change little during the simulation period.

2.2 Frontal squall line of 26-27 June 1985

The environment ahead of this squall line (Augustine and Zipser, 1987 and Trier, 1987) was unstable to deep convection with the convective available potential energy (CAPE) in excess of 2570 m^2 s^{-2}. However, the component of vertical shear perpendicular to the front was only 7.5 m s^{-1} in the lowest 2.5 km. These conditions are markedly different than those presented in the previous case, which showed high vertical shear and negligible potential instability. Trier (1987) describes the overall structure of this system as starting with rather active convection, but rapidly weakening and becoming rather disorganized. During the weakening process, the gust front moved rapidly ahead of the existing convection triggering broken lines of relatively weaker cells.

During the first hour of the simulation, the magnitude of the maximum vertical motions decreased to less than 7 m s^{-1}. After the first hour, the maximum updraft took place in a shallow layer at the leading edge of the cold air. This lifting by the cold pool was not sufficient to trigger new areas of deep, intense convection as the cloud tops generally ranged near 7-8 km and maximum rain water contents were on the order of 1 g/kg.

It is interesting to note that after 1 hr the convective activity in this case was much weaker than in the winter system, despite the presence of appreciable potential instability. In this squall line, the overall weak convective activity results from the dominance of the cold pool vorticity over the vertical shear. While the previous frontal squall line had a ratio of c/Δu quite close to 1, the ratio in this squall line approached 2.6. The larger value of the ratio in this case contained contributions from both a colder air mass partly fed by convective downdrafts and a weaker ambient shear.

2.3 Squall line of 10-11 June 1985

The lower level environment ahead of this squall line (Augustine and Zipser, 1987) was characterized by a moist unstable flow (CAPE=3400 m^2 s^{-2}) and moderate vertical shear of the horizontal wind (18 m s^{-1}/lowest 2.5 km). The squall line formed initially as a relatively narrow convective line. Subsequently, the convective cells within the line became quite intense with radar reflectivities in excess of 55 dBZ. In addition, surface observations on 10-

11 June revealed severe weather including tornadoes, significant hail, and high winds. The intense convective activity associated with the line lasted for over 5-7 hours as the system evolved from a narrow convective line to a broad zone of precipitation falling from a middle and upper level anvil.

The simulations of this case seem to replicate the overall structure of the 10-11 June squall line (Fig. 5), including the convective intensity, the slow evolution from a narrow convective band to more stratiform precipitation with embedded convection, and the occurence of a pronounced rear-to-front flow, termed rear inflow jet (Smull and Houze, 1987), below the sloping updraft. An examination of the ratio, $c/\Delta u$ indicates a change from .9 at 1 hr to nearly 1.2 at 4 hrs. Hence, the convective pattern in the squall line should change from a nearly vertical and strong ascent, with a slight tilt (downshear) away from the cold pool, to a slightly weaker lifting that tilts (upshear) back over the cold pool. The basic evolution in the observations and the simulations are consistent with the changes in the balance of horizontal vorticity. While most of the variation in the ratio with time in the model results from an increase in the magnitude and depth of the negatively buoyant air mass, there is also a small decrease (1.5 m s^{-1}) in the magnitude of the vertical shear. Since the observed stability structure puts some limit on the maximum intensity and depth of the cold pool, this squall line becomes quasi-steady with the cold pool vorticity never dominating and the lifting remaining quite deep. Therefore, the ultimate decay of this system must be associated with the squall line encountering an environment less conducive to continued convective activity.

3. CONCLUSIONS

The findings from these case studies indicate that the balance between the horizontal vorticity associated with the cold pool and the horizontal vorticity inherent in the vertical shear provide an important framework for the understanding the lifecycle of the squall line. For example, in the first case, the near optimal balance between the buoyancy gradients associated with the cold air mass and large magnitude of the vertical shear produce intense and relatively deep updrafts in the absence of potential instability. In the second case, the vertical shear is far weaker and the updraft at the leading edge of the cold front becomes, after approximately 1 hr, characterized by a relatively weak, sloping ascent, despite the presence of appreciable potential instability. In the third case, the depth and strength of the cold pool increased with time. A corresponding change in the nature of the convection also took place inasmuch as the line started as a narrow band of deep and intense convection and later evolved into a weaker sloping ascent with trailing stratiform precipitation.

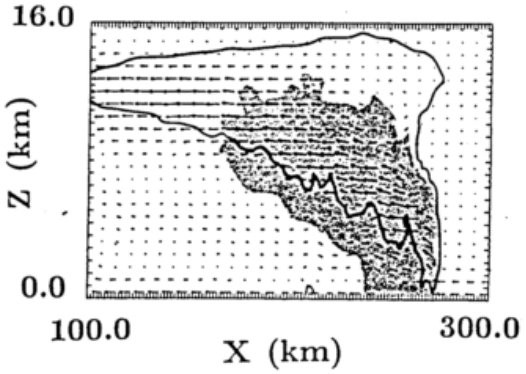


Fig. 5 A vertical cross-section from 3.5 hrs into a numerical simulation of the 10-11 June squall line using the ambient wind and thermodynamic profiles. The maximum vector length is approximately 35 m s^{-1}, the precipitation outline is shaded and the outline of the cloud is denoted by a solid line.

4. REFERENCES

Augustine, J. A. and E. Z. Zipser, 1987: The use of wind profilers in a mesoscale experiment. *Bull. Amer. Meteor. Soc.*, **68**, 4-17.

Bond, N. A. and R. G. Fleagle, 1985: The structure of a cold front. *Quart. J. Roy. Meteor. Soc.*, **111**, 739-759.

Browning, K. A. and T. W. Harrold, 1970: Air motion and precipitation growth at a cold front. *Quart. J. Roy. Meteor. Soc.*, **110**, 369-389.

Carbone, R. E., 1982: A severe frontal rainband. Part I: Stormwide hydrodynamic structure. *J. Atmos. Sci.*, **39**, 258-279.

Carbone, R. E., 1983: A severe frontal rainband. Part II: Tornado parent vortex circulation. *J. Atmos. Sci.*, **40**, 2639-2654.

Hobbs, P.V. and P. O. G. Persson, 1982: The mesoscale and microscale structure and organization of clouds and precipitation in midlatitude cyclones. Part V: The substructure of narrow cold frontal rainbands. *J. Atmos. Sci.*, **39**, 280-295.

Klemp, J. B. and R. B. Wilhelmson, 1978: The simulation of three-dimensional convective storm dynamics. *J. Atmos. Sci.*, **35**, 1070-1096.

Newton, C. W., 1950: The structure and mechanism of the prefrontal squall line. *J. Meteor.*, **7**, 210-222.

Parsons, D. B. and P. V. Hobbs, 1983: The mesoscale and microscale structure and organization of clouds and precipitation in midlatitude cyclones. VII. Formation, development, interaction, and dissipation of rainbands. *J. Atmos. Sci.*, **40**, 559-579.

Parsons, D. B., C. G. Mohr, and T. Gal-Chen, 1987: A severe frontal rainband. Part III: Derived thermodynamic structure. *J. Atmos. Sci.*, **44**, 1615-1631.

Parsons, D.B., R. Rotunno, J.B. Klemp, and M.L. Weisman, 1988: An investigation into the dynamics of squall lines using numerical simualtions of observed systems. *15th Conf. on Severe Local Storms*, Amer. Meteor. Soc., J137-J140.

Rotunno R., J. B. Klemp, and M. L. Weisman, 1988: A theory for strong, long-lived squall lines. *J. Atmos. Sci.*, in press.

Smull, B. F. and R. A. Houze, 1987: Rear inflow in squall lines with trailing stratiform precipitation. *Mon. Wea. Rev.*, **115**, 2869-2889.

Trier, S. B., 1987: The structure and evolution of a cold front and its associated convective system during the 26-27 June 1985 PRE-STORM Experiment. M. S. Thesis, Penn. State University.

PHYSICAL PROCESSES AND OBSERVED FEATURES IN MICROBURST-PRODUCING STORMS

Mark Hjelmfelt and Cathy Kessinger

National Center for Atmospheric Research†

P. O. Box 3000, Boulder, Colorado 80307

1. INTRODUCTION

Microbursts have been the focus of intensive study for the past 12 years, and especially since the Joint Airport Weather Studies (JAWS) project of 1982 (McCarthy *et al.*, 1982). As understanding of the phenomenon grew, an experiment was conducted at Stapleton International Airport, Denver, Colorado to attempt real time detection and warning of microbursts by Doppler weather radar for aviation safety (McCarthy and Wilson, 1985). The success of this experiment led to the establishment of the Terminal Doppler Weather Radar Program (TDWR) by the Federal Aviation Administration, with the purpose of developing an automated, operational detection and warning system for wind shear at major U. S. airports (McCarthy *et al.*, 1986).

Past research has led to the development of hypotheses of physical processes involved in microburst production. The primary processes believed to enhance downdraft strength, potentially resulting in microbursts, include latent heat release due to melting and evaporation, precipitation loading, and dynamically induced pressure forces. In a given cloud, these may all contribute to various degrees and are strongly modulated by the individual cloud environment. Case study analysis of observations and numerical modelling studies suggest that some understanding of the operation of these processes has been obtained.

This presumed understanding and identification of features aloft observed by Doppler radar in some microburst-producing storms has led to the development of microburst nowcasting models (Roberts and Wilson, 1986). An evaluation of these models and of the physical understanding upon which they are based is critical to the development of useful microburst nowcasting algorithms for operational use (Campbell, 1988). In summer 1987, two research programs were held near Denver, Colorado to study microbursts: the Convection Initiation and Downburst Experiment (CINDE) and the first field effort of the TDWR program. These provided extensive new data sets for the study of microbursts.

The present study seeks to examine the understanding of physical processes and features observed by radar and to evaluate microburst nowcasting techniques, based on the 1987 data. Emphasis is placed on increased understanding of low-reflectivity microburst-producing and nonmicroburst-producing clouds and virga lines. In this abstract, findings are illustrated for individual cases. A more statistically based discussion will be presented at the conference.

† NCAR is sponsored by the National Science Foundation.

2. 16 JULY 1987

The microburst-producing virga line of 16 July 1987 is chosen as a "typical" example. Figure 1 shows a photograph of the virga line that produced several microbursts. Note the high cloud base, shallow cloud layer, and the weak rain shaft. Cloud base is over 4 km AGL, with a cloud base temperature of almost -10°C. Cloud tops do not exceed 8 km. Maximum reflectivities observed anywhere in the cloud or precipitation do not exceed 35 dBZ_e. Yet this cloud produced several outflows of more than 10 m s^{-1} differential radial velocity.

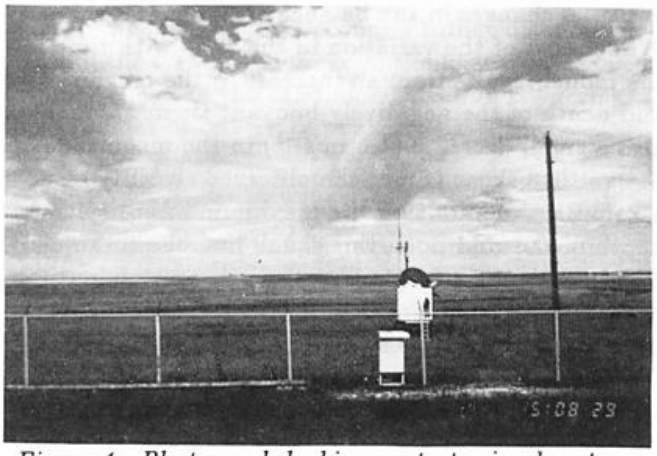


Figure 1. Photograph looking east at microburst-producing cloud on 16 July 1987. Time on photo is PM MDT. The precipitation shaft producing the microburst is about 20 km away.

A sounding taken from a CINDE project mobile van located about 20 km east of the microburst at approximately the same time is shown in Fig. 2 The sounding exhibits a deep near-neutral boundary layer and low humidity conditions (the humidity elements did not report values below 20%; it is believed that a constant mixing ratio near 3.4 g kg^{-1} existed throughout the mixed layer). The sounding entered the glaciated cloud near 500 mb and exited near 400 mb.

Doppler radar observations (not shown) of this cloud reveal a rather stratiform cloud layer with reflectivity cores (precipitation shafts) descending below cloud base. Convergence is observed near cloud base and within the descending reflectivity cores below. Near 2 km AGL, anticyclonic shear is seen in the velocity field associated with a particularly strong microburst of 18 m s^{-1} differential radial velocity.

A time-height profile of reflectivity and radial shear was produced for this microburst. For a 35 minute period, beginning over 15 min before the first observed outflow at the surface, the area of reflectiv-

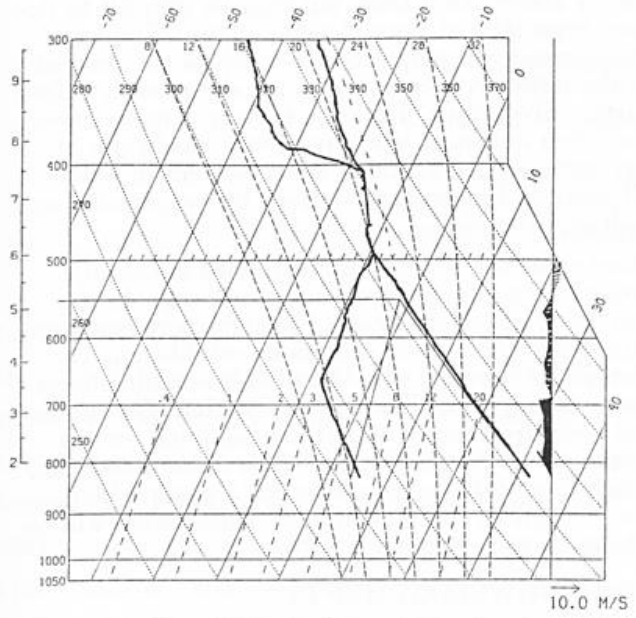


Figure 2. Skew-T log-P thermodynamic chart of sounding taken by mobile van C-1 on 16 July 1987 at 1657 MDT, 20 km east of microburst. O°C level is 556 mb.

ity greater than 20 dBZ_e within the precipitation shaft and in the cloud above was determined. The area of radial divergence/convergence $\geq |4|$ and $|8| \times 10^{-3}$ s^{-1} associated with the shaft was also found. The results are shown in Fig. 3.

Figure 3 shows the cloud layer above 4 km and a descending area of reflectivity. The descent is only traceable below cloud base and clearly begins before microburst occurrence. The core reaches the surface after microburst initiation but before maximum intensity. Convergence aloft is seen at 3 to 4 km, below cloud base but straddling the 0° level (3.4 km). This convergence does not appear until near the passage of the maximum area of reflectivity at that level and continues into the microburst dissipation stage. This may suggest that the convergence is largely a mass continuity response to the descent of the core, rather than contributing directly to the forcing of the downdraft.

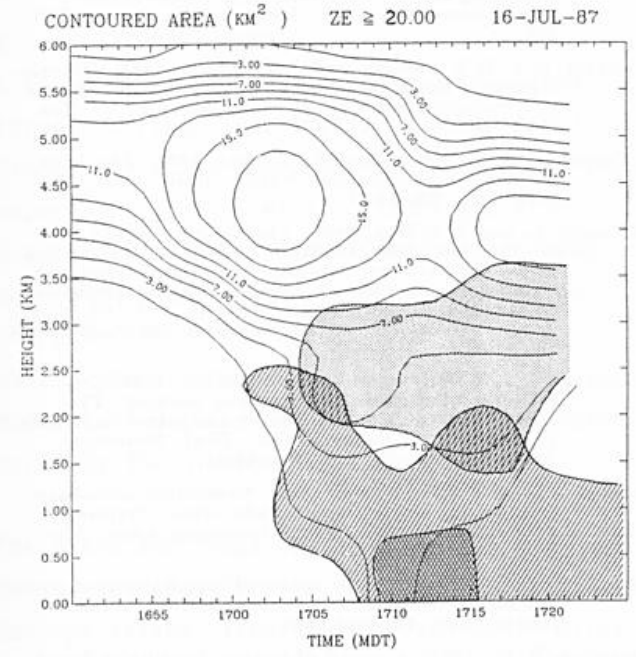


Figure 3. Time–height profile of microburst from cloud line on 16 July 1987. Contours represent area of reflectivity $\geq$ 20 dBZ_e (km^2); areas $\geq$ 1 km^2 of divergence $\geq 4.0\times10^{-3}$ s^{-1} are hatched, while areas of divergence $\geq 4.0\times10^{-3}$ s^{-1} are cross hatched. Convergence $\leq -2.0\times10^{-3}$ s^{-1} is shaded.

A horizontal dual-Doppler wind field taken near the time of maximum surface divergence, 1710 MDT (all times are given in MDT), is shown in Fig. 4. In this figure, two downdrafts are shown, both producing microburst outflows. The one on the lower left is the stronger and is the one for which the time-height profile is shown. In addition to the two areas of strong convergence associated with the downdrafts, note the general convergence along the line. This can make identification of convergence associated with microbursts difficult. First, the general convergence associated with the line may make relevant convergence hard to distinguish. Second, a convergence line may not be visible from a radar looking down the line axis, or it may appear only as azimuthal shear instead of radial shear.

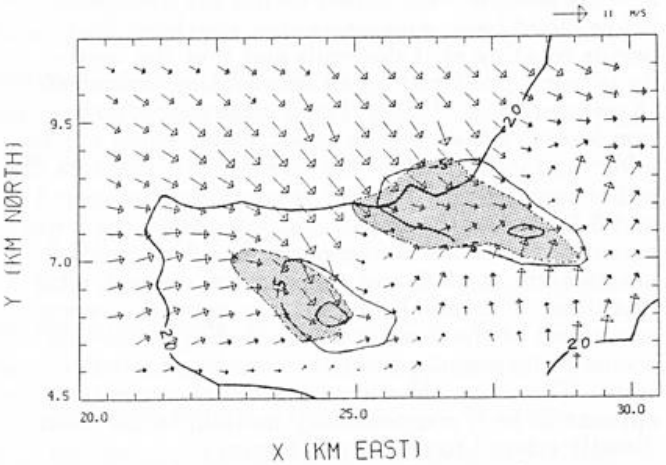


Figure 4. Horizontal winds, reflectivity, divergence and vertical velocity at 3 km AGL, derived from dual-Doppler radar analysis for 1710 MDT on 16 July 1982. Vectors scaled as shown in upper right. 20 dBZ_e reflectivity contour is given by heavy line. The 5 m s^{-1} vertical velocity contour is given by the thin solid line. Shaded regions are convergence $\geq$ 4.0×10^{-3} s^{-1}.

3. THE 4 JULY 1987 MOUNTAIN VIRGA LINE

On 4 July 1987, convective cells began forming over the Rocky Mountains, with radar-detectable echoes present by 1130. Three cells formed over the mountains, propagated to the northeast, and created the virga line of interest as they moved off the mountains and dissipated. Because the radar viewing angle from CP–3 was almost directly down the line axis, the in–cloud, along–axis radial convergence seen in other studies of microburst line storms (Hjelmfelt *et al.*, 1986) cannot be seen. However, looking across the line from CP–2, weak radial convergence is seen from 1248. At its maximum extent, the radial convergence extends from 3.5 to 6.9 km AGL, with maximum horizontal area at the 5.3 km level. A proximity sounding taken at 1356 shows that the freezing level is at 3 km AGL and cloud base is $\approx$ 3.7 km, such that the radial convergence is

occurring within the cloud. The radial convergence is a local maximum over areas where microbursts appear at the surface.

A time-height profile of reflectivity and radial convergence/divergence fields (not shown) was constructed for one microburst contained within the mountain virga line. Surface radial divergence is first seen east of the mountains at 1255. Construction of the profile was completed by enclosing the entire microburst below cloud base where the feature is basically circular and using a circular area $\approx$ 5 km in diameter above cloud base within the stratiform cloud. This microburst has a descending core, and the area of the -5 dBZ_e contour increases near the ground with time, reaching a maximum area of 15 km^2 at 1310. Within the stratiform cloud, the area of reflectivity $\geq$ -5 dBZ_e gradually decreases as the microburst dissipates.

The area ($\geq$ 1 km^2) of radial convergence and divergence $\geq |2| \times 10^{-3}$ s^{-1} was also calculated. Radial divergence begins increasing after the reflectivity core begins its descent and reaches maximum area slightly after the core reaches its maximum at the surface. As the core first reaches the surface, an anticyclonic velocity couplet is observed from CP–3. This feature is contained within the divergence below cloud base, suggesting that the downdraft begins rotating as it descends and that the vorticity is being produced by an accelerating downdraft (Kessinger *et al.*, 1988). Thus, pressure perturbation forces created by the misocyclone would not be a forcing mechanism for the downdraft. The area of radial convergence $\geq$ 1 km^2 is contained between 3 and 6.5 km. As the microburst intensifies, the lower extent of the radial convergence sharply descends nearly 1 km at 1308 and continues to descend after this time. The radial convergence seems to deepen as a result of the downdraft descending, since this occurs some minutes after the core begins its descent. Therefore, the increasing radial convergence appears to be a compensatory motion, rather than directly related to downdraft forcing.

4. LOW-dBZ_e MICROBURST PROXIMITY SOUNDINGS

Analysis of over 30 proximity soundings from 14 project days with low-reflectivity microbursts indicates several features of interest. Surface temperatures average > 30°C. Surface humidities are low, with mixing ratios averaging 5–6g kg^{-1}. In nearly all cases, surface relative humidities are < 30%. The boundary layer is deep, with estimated cloud bases generally > 3 km. Three-fourths of the soundings indicate cloud base above the 0°C level. Boundary layer lapse rates are > 9°C for over 80% of the cases, with a mean lapse rate > 9.3°C. These results are consistent with previous work based on JAWS data (Caracena *et al.*, 1983; Wakimoto, 1985). These soundings are also consistent with downdrafts driven primarily by melting and evaporation in the sub-cloud layer as discussed by Srivastava (1985, 1987).

5. DISCUSSION

Analyses of other cases from 1987 indicate similar results. Descending cores are usually detectable below cloud base, but not in the often stratiform cloud layer above. Convergence may be seen below or above cloud base, but may be difficult to detect, especially at poor viewing angles. Timing of the convergence may precede or follow the descent of the reflectivity core, but is usually present before surface divergence. Rotation is seen in many cases, but often not until after divergence has begun at the surface. Observations are consistent in nearly all cases with downdrafts driven by evaporation and melting processes.

More cases are being examined, both microburst-producing and nonmicroburst-producing. As the picture of microburst cases becomes more firmly established, our concern centers on establishing the distinction between microburst and nonmicroburst cases. Analyses include the application of a numerical downdraft model to aid in examining forcing mechanisms. Single-Doppler observation questions, which have only been mentioned in passing here, are subjects of special concern. These issues will be addressed at the conference.

6. ACKNOWLEDGEMENTS

Special thanks to Ms. D. Davis for editing and typing the manuscript. This work is funded partially by NCAR, the National Science Foundation, and the Federal Aviation Administration through Interagency Agreement DTFA01-82-Y-10513.

7. REFERENCES

Campbell, S. D., 1988: Microburst precursor recognition using an expert system approach. *Preprints: 4th Intl. Conf. on Interactive Information Processing Systems*, Anaheim, Calif., Amer. Meteor. Soc., Boston, 300–307.

Caracena, F., J. McCarthy, and J. A. Flueck, 1983: Forecasting the likelihood of microbursts along the front range of Colorado. *Preprints: 13th Conf. on Severe Local Storms*, Tulsa, Okla., Amer. Meteor. Soc., Boston, 261-264.

Hjelmfelt, M.R., R.D. Roberts, and H.D. Orville, 1986: Observational and numerical study of a microburst line-producing storm. *Preprints, 23rd Radar Meteor. Conf.*, Snowmass, Amer. Meteor. Soc., Boston, J77-J80.

Kessinger, C.J., D.B. Parsons, and J.W. Wilson, 1988: Observations of a storm containing misocyclones, downbursts, and horizontal rotor circulations. Accepted by *Mon. Wea. Rev.*

McCarthy, J., J.W. Wilson, and T.T. Fujita, 1982: The Joint Airport Weather Studies Project. *Bull. Amer. Meteor. Soc.*, **63**, 15-22.

McCarthy, J., and J. Wilson, 1985: The Classify, Locate, and Avoid Wind Shear (CLAWS) Project at Denver's Stapleton International Airport: Operational testing of terminal weather hazard warnings with an emphasis on microburst wind shear. *Preprints, 2nd Intl. Conf. Aviation Weather Systems*, Montreal, Amer. Meteor. Soc., Boston, 247-256.

McCarthy, J., J.W. Wilson, and M.R. Hjelmfelt, 1986: Operational wind shear detection and warning: The "CLAWS" experience at Denver and future objectives. *Preprints, 23rd Radar Meteor. Conf.*, Snowmass, Amer. Meteor. Soc., Boston, 18-21.

Roberts, R.D., and J.W. Wilson, 1986: Nowcasting microburst events using single Doppler radar data. *Preprints, 23rd Radar Meteor. Conf.*, Snowmass, Amer. Meteor. Soc., Boston, 14-17.

Srivastava, R.C., 1985: A simple model of evaporatively driven downdraft: Application to microburst downdraft. *J. Atmos. Sci.*, **42**, 1005-1023.

Srivastava, R. C., 1987: A model of intense downdrafts driven by the melting and evaporation of precipitation. *J. Atmos. Sci.*, **44**, 1752-1773.

Wakimoto, R.M., 1985: Forecasting dry microburst activity over the High Plains. *Mon. Wea. Rev.*, **113**, 1131-1143.

ON THE MICROPHYSICS OF MICROBURSTS

H. D. Orville, F. J. Kopp, R. D. Farley, and Y-C. Chi

Institute of Atmospheric Sciences
South Dakota School of Mines and Technology
Rapid City, South Dakota 57701-3995

1. INTRODUCTION

In some of our recent numerical modeling studies the IAS modeling group has concentrated on the microphysical processes which lead to the formation of microbursts. We have emphasized making quantitative the effects of precipitation loading, and cooling of the downdraft due to graupel/hail melting and rain evaporation. At the last U.S. Cloud Physics Conference held in Snowmass, Colorado, in 1986 we showed that the three effects mentioned above could cause temperature changes of up to 3 to 4^{o}C min^{-1} in a wet microburst (ORVILLE et al., 1986), leading to acceleration changes as large as -0.128 m s^{-2} min^{-1} and to the associated vertical velocity changes of 10 m s^{-1} in one minute. Effects on w from both the dw/dt and da/dt equations are involved.

2. ADDITIONAL CASES

A few more microbursts have been simulated; three described in a thesis by CHEN (1986). Since then a wet microburst in an Alabama field experiment (TUTTLE et al., 1988) and a dry microburst in a Colorado field project have been simulated. Table 1 shows some of the characteristics and results from the five cases, one of them a weak microburst, two moderate and two strong microbursts (as determined by the divergence values.)

The dates and times of the soundings are Denver-Dry (7/14/82-23Z); Denver (7/13/82-20Z); Wallops Island, Virginia (9/12/83-00Z); Miles City, Montana (7/29/75-00Z); and Huntsville, Alabama (7/20/86-12Z).

The Wallops Island and COHMEX cases are similar. They both have moist, tropical soundings that produce copious amounts of rain and graupel/hail in the cloud, but principally rain at the ground. The graupel contents are almost completely melted by the time precipitation reaches the ground. The precipitation shaft is intense and focused over a 2 to 4 km region.

The Denver-Dry and Denver cases are relatively dry microbursts, one very weak. The Miles City case produces intermediate values of precipitation from a rather high cloud base cloud and causes a strong microburst, but was run on a version of our cloud model that did not include snow in the cloud microphysics.

3. A MICROBURST INDEX

In CHEN (1986) the importance of three levels in the atmosphere is discussed -- the cloud base (for the beginning of evaporation), the 0^{o}C isotherm height (the start of melting), and the precipitation center within the cloud (the maximum loading level). In discussions one of us (Chi) has suggested the possibility of developing a "microburst index" (MBI), for describing and possibly forecasting microbursts. The index, based on microphysical considerations, is given by

$$MBI = F_L H_L + F_M H_M + F_E H_E \quad [^{o}C\ min^{-1}\ km] \quad (1)$$

where the F terms are forcing functions (in units of ^{o}C min^{-1}) of the loading, melting and evaporation cooling rates prior to microburst formation and the H values are the height intervals over which loading, melting and evaporation would be occurring.

These H values are easily obtained from the computer results and Table 1 and are given in Table 2. Note that the H_L values are taken at

TABLE 1 - Sounding parameters and maximum values of microburst related characteristics for the simulations of the Denver, Wallops Island, Miles City, and COHMEX cases. The units of each field are given in the brackets. Numbers in the brackets of the velocity change is the horizontal distance over which the change occurred.

Case	Denver-Dry	Denver	Wallops Island	Miles City	COHMEX
Cloud Base (km AGL)	4.0	2.2	1.6	3.4	1.0
0°C Level (km AGL)	3.1	3.3	4.2	4.0	4.6
Graupel/Hail (g/kg)	0.4	2.3	15.9	4.8	15.0
Rain (g/kg)	0.3	3.0	12.2	3.5	16.0
Updraft (m/s)	7.0	15.2	27.3	23.8	29.0
Downdraft (m/s)	3.0 to 4.0	8.2	20.8	18.0	15.0
Velocity Change (m/s)	12.0 [4 km]	22 [3.4 km]	42 [4 km]	44 [6 km]	24.0 [1.6 km]
Divergence (per sec)	$3x10^{-3}$	$11x10^{-3}$	$20x10^{-3}$	$20x10^{-3}$	$15x10^{-3}$
Temperature Deficit (°C)	3	3	6	8.3	--

TABLE 2 - Values of the forcing functions, depth of influence, and microburst index for the five cases, if known.

	Denver-Dry	Denver	Wallops Island	Miles City	COHMEX
F_L	0.25	0.43	1.5		
H_L	x7.0=1.75	x6.6=2.84	x10.0=15.00	9.8	11.0
F_M	0.10	0.25	1.8		
H_M	x3.1=0.31	x3.3=0.83	x4.2=7.56	4.0	4.3
F_E	0.38	0.60-0.80	1.5		
H_E	x4.0=1.56	x2.2=1.54	x1.6=2.40	3.4	0.8
MBI	3.62	5.20	24.96		

the top of the precipitation shafts to the ground level. The distinction between graupel/hail and rain is not important because the mass of precipitating ice is the primary source of the rain, so that the loading is fairly uniform over the entire height interval. The value H_L could be obtained by radar observations of the top of the precipitation column.

The values for H_M and H_E could be obtained from radiosonde soundings, from visual observations (for H_E, i.e. cloud base above ground level), or from model results.

Values of the forcing functions are more difficult to obtain. Examples of such numbers are given in the above references and in Table 2. Generally these values come from model results using a special analysis program in our cloud models that computes various production terms over one time step and produces a field of $\Delta\theta'/\Delta t$ for the various loading, melting and evaporation effects ($\Delta\theta'$ being the temperature change, or "equivalent" temperature for the loading, of the various physical effects).

Results from the cases are presented in Table 2. The analysis program has been run on the 1976 Miles City case (actually integrated back then before the analysis program was written) and on the COHMEX (Alabama) case, a case

actually integrated using a morning sounding **before** the microburst had actually occurred. Consequently, the forcing functions have not been calculated and the MBI is not available for two of the cases. Those columns will be filled in by conference time if we have had a chance to rerun the cases in our current cloud models.

The results for the microburst index indicate a low value for the weak microburst and a higher value for the strong microburst. Also the relative magnitude of the various terms indicate the importance of the microphysical processes. For the dry microburst the evaporation and loading effects are comparable (1.56 and 1.75 respectively) but 5 to 6 time the magnitude of the melting effect. For the Wallops Island wet microburst, the loading and melting terms are most important. The intermediate Denver case shows loading as the largest term, followed by evaporation and melting.

These are only preliminary results, taken from **very** few cases. It remains to be seen if the index can be made more objective, oberva-tional equipment used to provide most of the values, a simpler models devised to yield the microphysical cooling rates. Even without any operational use, though, the understanding that might occur of the primary microphysical forcing mechanism of different types of microbursts is worth pursuing.

Acknowledgments. We thank Ms. Carol Vande Bossche for typing this manuscript and preparing the tables. Support for this research was provided by the National Science Foundation, Division of Atmospheric Sciences, under Grant No. ATM-8603308 and by the National Aeronautics and Space Administration under Grant No. NAG8-632.

REFERENCES

CHEN, J-P.: A numerical simulation of microbursts, M.S. Thesis, Department of Meteorology, S.D. School of Mines and Technology Rapid City, SD, (1986) 126 pp.

ORVILLE, H. D.; FARLEY, R. D.; CHEN, J-P.: Some important cloud microphysical factors in the creation of microbursts, Conf. on Cloud Physics, Snowmass, CO, (1986).

TUTTLE, J. D.; BRINGI, V. N.; ORVILLE, H. D.; KOPP, F. J.: Multiparameter radar study of a microburst: comparison with model results. [Submitted to J. Atmos. Sci., 1988]

Observation of Microbursts from Snow Clouds in Winter Monsoon Season

Hiroshi Uyeda, Ryuichi Shirooka and Katsuhiro Kikuchi

Depart. of Geophysics, Fac. of Sci.,
Hokkaido Univ., Sapporo 060 Japan

1. INTRODUCTION

Under convective snow clouds, strong winds (or gusts) with heavy snowfalls are often experienced along the west coast of northern Japan in the winter monsoon season. Higuchi (1962) suggested the existence of strong downdrafts from snow clouds by photographic observations from an aircraft. However, a synthetic observation of strong downdrafts from snow clouds has not been made. On the other hand, the structures of downbursts from thunderstorms and squall-lines are analyzed by many researchers (eg. Houze, 1977; Wilson et al., 1984). According to up to date knowledges on the downbursts from thunderstorms and down to the scale classifications of them by Fujita (1981), the strong downdrafts from snow clouds are considered as microbursts. However, the features of the microbursts from snow clouds are quite different from bursts from thunderstorms. In order to study the structures of the microbursts from snow clouds, observation were carried out at Sapporo.

2. Observation method

Sapporo, which is the largest city in northern Japan, is located about 15 km southeast from the sea coast of Ishikari bay, Sea of Japan as shown in Fig.1. Snow clouds usually move from the Ishikari bay to Sapporo by north-westerly winter monsoon. The observations were made from the middle of January to the end of February, 1987 in Sapporo, after preparatory observations at Sapporo in 1985 and 1986 and analyses of the data. For comparison, observations were made at Haboro for one month from december 15, 1986. Haboro is located about 100 km north of Sapporo and it faces the Sea of Japan. The observation network around Sapporo is as shown in Fig.1. Conventional weather radar (λ= 3.2 cm) was set on the top of the highest university building, shown by the mark of + in Fig.1, which is about 1 km north of the center of Sapporo. Time series of photographs were taken by 35 mm camera from the radar site. Other than temperature and winds, relative humidity was measured at the

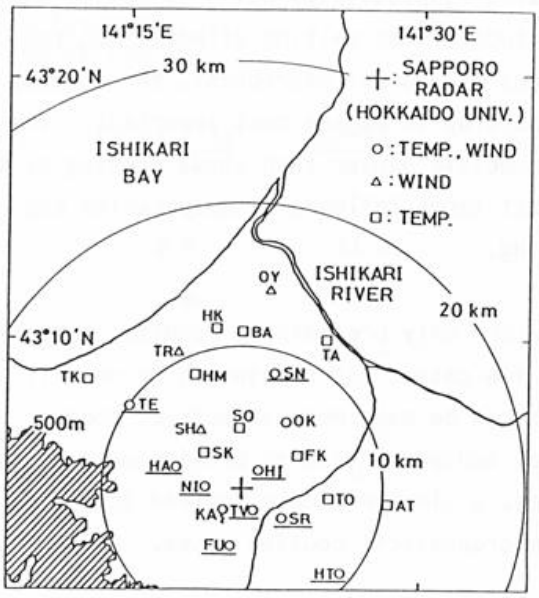


Fig.1: Network of observation points around Sapporo city. Symbols are +: radar site, o: observation sites of temperature and wind, □: temperature, △: wind.



Photo.1: An example of snow trails at 1258 JST, February 1, 1987. The arrows of Bu and Vi show burst-type and virga-type of snow trails.

points of TK, HM, HK, OK, and KA. Micro-barometers were set at the points of SN and the radar site. Surface weather data were read from charts. Sounding data at 09 and 21 JST by JMA (at the point of KA) were used.

3. PHOTOGRAPHIC FEATURES

With time series photographs of snow trails in seven cases, snow trails were classified into two types. An example of snow trails is shown in Photo.1. From the analysis of photographs compared with the location of radar echoes, the heights of cloud top and cloud base were estimated to be 2500 and 800 m respectively. Burst-type trails, which had sharp edges as shown in Photo.1, reached the ground in 1 or 2 minutes from the cloud base. Namely, the fall speed of the trails was about 10 $m \cdot s^{-1}$. Under such trails, the decrease of surface temperature and changes of wind speeds were observed. The horizontal scales of the bursts at the first stage was a few kilometers. With burst-type snow trails, similar shapes as heads of gravity currents were observed and shelf clouds were sometimes observed ahead of the trail. Therefore, burst-type snow trails were considered as microbursts. Virga-type trails had vague edges. And it required about 10 minutes to reach to the ground. Under these trails, significant changes were not observed in surface data.

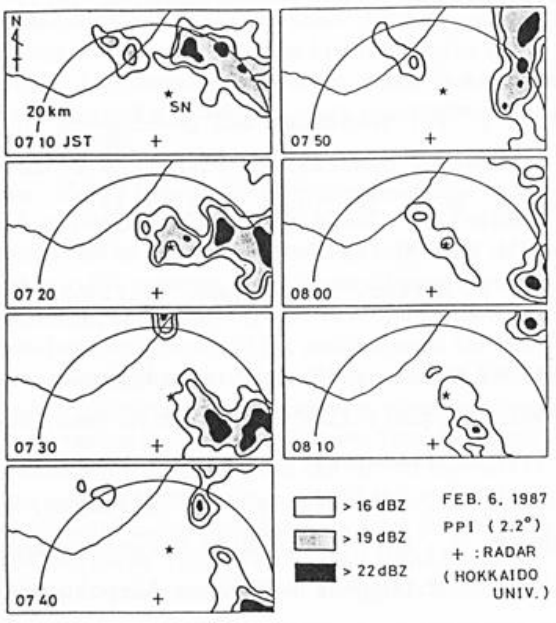


Fig.2: Radar echoes from 710 to 810 JST, February 6, 1987 at 10 minute intervals. A star mark shows the location of the site of SN.

4. RESULTS

4.1 CASE 1 (February 6, 1987)

In the morning of February 6, 1987, the indications of the microbursts were observed at the surface. When the radar echo reached the point of SN at 0720 and 0800 JST as shown in Fig.2, temperature dropped about 2°C as shown by the arrows in Fig.3. Corresponding to these, peaks of wind speed were observed as shown by the circles in Fig.3. The largest peak at 0720 JST was 7 $m \cdot s^{-1}$. However the change of wind direction was not prominent.

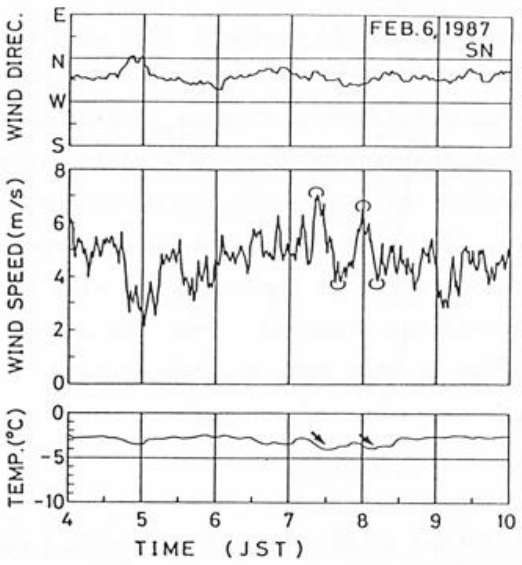


Fig.3: Time series of wind and temperature at the point of SN shown by the star in Fig.2. Wind gust and temperature drop are shown by circles and arrows respectively.

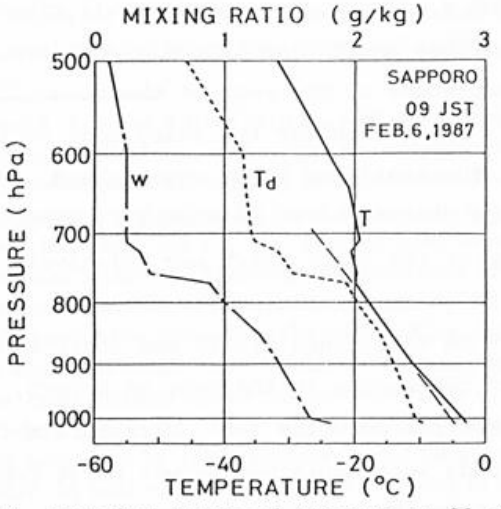


Fig.4: Sounding curve of Sapporo at 21 JST, February 5, 1987. Solid line, dotted line, dot dash line and dashed lines are temperature, dew point, mixing ratio and wet adiabatic respectively.

The sounding curve of Sapporo at 09 JST, February 6, 1987 is shown in Fig.4. Cloud top and cloud base were around 770 hPa(2200 m) and 900 hPa(900 m) respectively. Below the cloud base, the sounding was in conditional instability. If the air mass was descended along wet adiabatic line from cloud base, surface temperature became -4.3°C. This is very close to the temperature of -4.0°C at the point of SN at 0730 JST. The relative humidities were high and over 80 % for water. The temperature drops associated with snow bursts could be explained by wet bursts.

4.2 CASE 2 (February 5, 1987)

The radar echoes and winds at 2020 JST, February 5, 1987 are shown in Fig.5. The band like echo moved from northeast to southeast. Divergent features of surface wind is clear. At the point HA, where the tip of tongue like echo reached, a significant drop of temperature (about 1°C) and the change of wind speed with a peak was observed. From the sounding of Sapporo at 2100 JST, the temperature drop was also explained by wet burst.

5. CONCLUDING REMARKS

The structure of microbursts from snow clouds are summarized as a conceptual model in Fig.6 Wind arrows are shown relative to the ground. Cloud top was below 3 km and cloud base was about 800 m. It usually had an anvil cloud and sometimes shelf cloud ahead. Snow trails had sharp edges at the rear of the cloud motion. The reason for the sharp edge at the rear of the trail and vague edges ahead of the trail are considered to be caused by winds to the rear of the burst which are relatively strong as it is on or close to the sea. In contrast to this, snow trails had sharp edges ahead of the bursts in the case of Haboro, which occurred over the sea. Microbursts from snow clouds were explained by wet burst considered from the sounding data and high humidity before bursts.

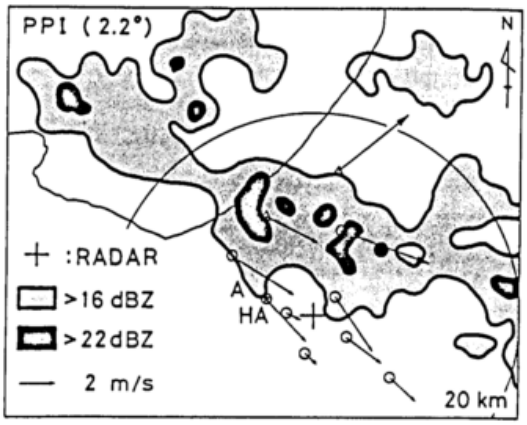


Fig.5: Radar echo at 2020 JST, February 5, 1987. Wind velocities are shown by the arrows.

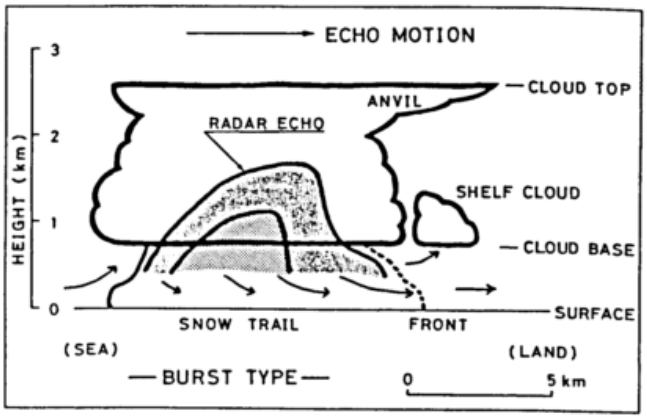


Fig.6: Schematic illustration of microbursts from snow clouds.

Acknowledgments

The authors express their hearty thanks to Sapporo city and other organizations for their kind permision to use meteorological data.

References

FUJITA, T. T.: Tornadoes and Downbursts in the Context of Generalized Planetary Scales. J. Atmos. Sci., 38 (1981), 1511-1532.

HIGUCHI, K.: On the Characteristics of Snow Clouds. J. Meteor. Soc. Japan, 40 (1962), 193-201.

HOUZE, R. A., Jr.,; Structure and Dynamics of a Tropical Squall-line System, Mon. Wea. Rev., 105 (1977), 1540-1567.

WILSON, J. W.; Roberts, R. D.; KESSINGER, C.; McCARTHY, J.: Microburst Wind Structure and Evaluation of Doppler Radar for Airport Wind Shear Detection. J. Climate Appl. Meteor., 23 (1984), 898-915.

EVOLUTION OF CONVECTIVE STORM ALONG BOUNDARY LAYER CONVERGENCE LINES

James Wilson and Cynthia Mueller

National Center for Atmospheric Research*

During the summer of 1987, an intensive study was conducted to examine the initiation of convective storms along boundary layer convergence lines. The study was called "CINDE" (Convection INitiation and Downburst Experiment) and took place near Denver, Colorado. Observations were obtained with 6 Doppler radars, 97 mesonet stations, 3 mobile sounding systems, 5 stationary sounding systems, 3 research aircraft, and time lapse photography from 8 locations. Observations began prior to first cloud development and extended through storm dissipation.

Studies by Wilson and Schreiber (1987) established that at least 80% of the storms in the study area developed along boundary layer convergence lines that can be observed by sensitive Doppler radars. Earlier studies by Byers and Braham (1949) found surface convergence 30 minutes prior to radar echo appearance of convective cells. Zones of enhanced convergence found along outflow boundaries have been recognized as areas of convection initiation by Purdom (1982) and Watson and Holle (1982). Zones of convergence induced by terrain, moisture gradients, and differential heating have also been recognized as favorable areas for thunderstorm development (Szoke et al. 1984; and Schreiber, 1986). The above studies show a casual relationship between convective cloud formation and the position of boundary layer convergence lines. They do not investigate physical principles that determine the timing and precise location of cloud development. This extended abstract combines data from the above sensors to briefly describe the evolution of temperature, moisture, wind, and clouds in the vicinity of a quasi-stationary convergence line on 17 July 1987.

Figure 1 shows a north-south convergence line as observed by Doppler radar and mesonet. The convergence line is the remanent of a weak cold front that moved into the mesonet from the northwest during the morning, and a convergence line of unknown origin moving from the east that collided with the stationary cold front about 1445. At the time of Fig. 1 (1530 MDT), a line of small cumulus stretches along the convergence line. Figure 2 shows this cloud line at 1545 as photographed from the circled mesonet station in Fig. 1. Beginning ~ 1630 this cloud line began to build rapidly producing a solid line of 55 to 65 dBz storms by 1730. Three small tornadoes and numerous downbursts occurred along this line.

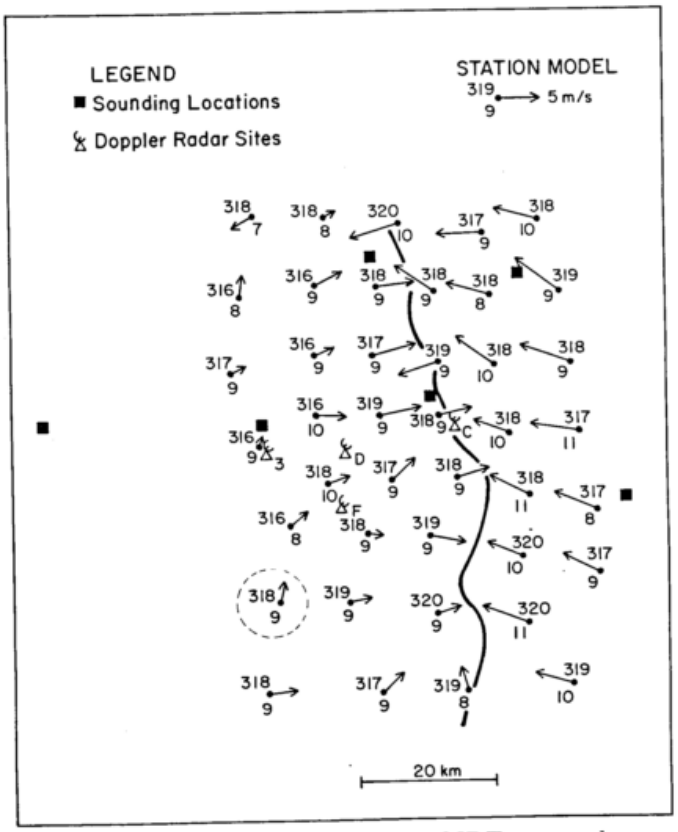


Figure 1. Convergence line at 1530 MDT as seen by mesonet and Doppler radar. The solid line indicates the convergence line as seen from the CP3 and FL2 radars (radars labeled 3 and F). The wind, potential temperature (upper left corner of station model in deg K), and mixing ratio (lower left corner in g/m^3), are shown for each station. The circled station is the location from which the photograph in Fig. 2 is taken.

Figure 3 shows at 4 time periods, east-west cross sections perpendicular and through the convergence line of potential temperatures and mixing ratios. The cross sections are primarily based on soundings taken from 6 locations (see Fig. 1). The sounding data are positioned relative to their east-west distance from the convergence line. The cross sections at 1530 and 1645 also contain data from the NCAR King Air as it flew east-west across the boundary. Examination of these cross sections shows that in the vicinity of the boundary a relatively deep, warm, moist, adiabatic layer developed by 1530. Figures 3c and 3d are quite similar. In both cases, the air in the vicinity of the convergence line is convectively unstable with a lifted index of ~ -5; however, rapid storm development is only occurring at the latter time.

* The National Center for Atmospheric Research is Sponsored by the National Science Foundation



Figure 2. Photograph from circled station in Fig. 1 at 1545 looking NE through SE showing a line of cumulus clouds associated with the convergence line in Fig. 1.

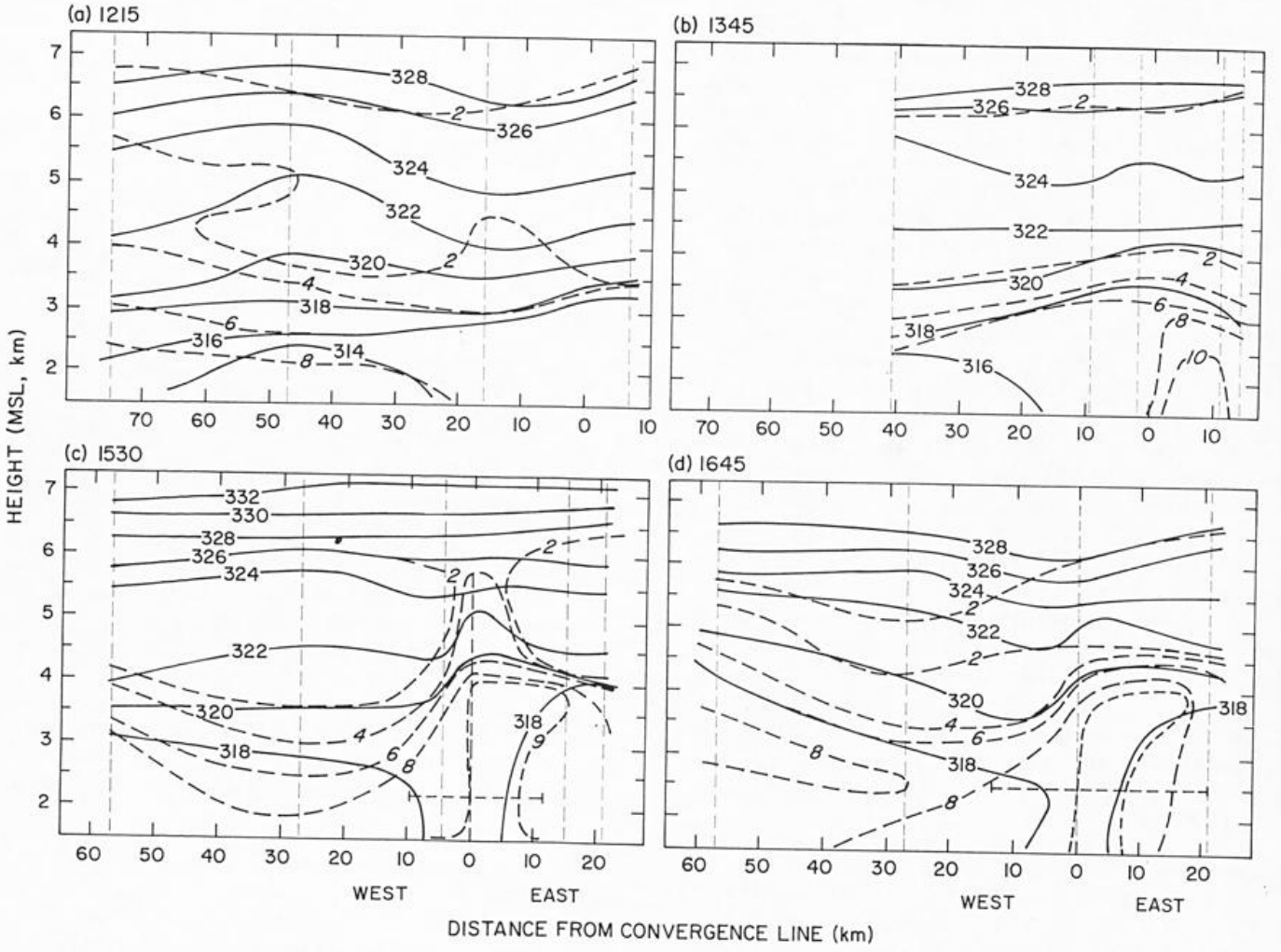


Figure 3. West-east vertical cross sections of potential temperature (solidlines in deg K) and mixing ratio (dashed lines in g/m^3) through the convergence line at four time periods. Analysis based on soundings taken along the light dashed vertical lines. The horizontal dashed lines at 1530 and 1645 represent regions where data were obtained from a research aircraft.

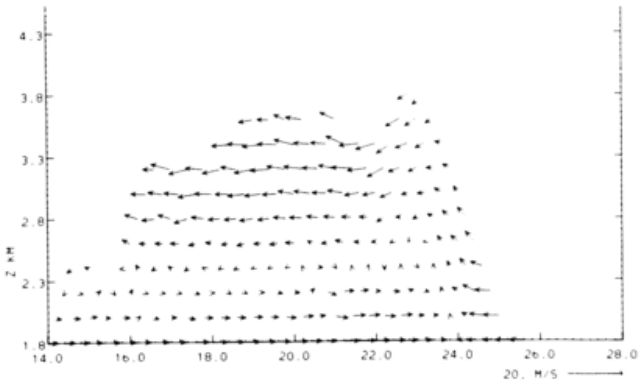


Figure 4. West-east vertical cross section of winds through the convergence line obtained from dual-Doppler analysis. The surface position of the boundary is at X=24.

Doppler radar analyses (not shown) show that the low level convergence steadily increases and deepens during the afternoon. Maximum strengthening occurs between 1430 and 1515 as the two above mentioned convergence lines collide; however, storm development is not a direct result of this collision because it does not begin for another 90 min.

As shown in Fig. 4 from a dual-Doppler analysis at 1530, the low level easterly flow collides with the shallow westerly flow and rides over it. A marked change in this regime occurs after 1600. During the next 60 min., this easterly flow above the boundary gives way to south-westerly flow. At this time, rapid cloud and storm development occurs.

In this case, it appears the low level convergence acts to develop a zone $\sim$ 10-20 km wide of unstable, moist air. It is this zone where significant storm development occurs. The air in the convergence zone was convectively unstable, but it was not until the easterly flow over the convergence line subsided that the rapid storm growth occurred. As proposed by Rotunno et al. (1988), it appears that storm development along boundaries is suppressed when the air flow is forced back over the boundary.

References:

Byers, H. R., and R. R. Braham, Jr., 1949: The Thunderstorm. U.S. Govt. Printing Office, Washington, DC, 287 pp.

Rotunno, R., J. B. Klemp and W. L. Weissman, 1988: A theory for strong long lived squall lines. *J. Atmos. Sci.*

Schreiber, W. E., 1986: Case studies of thunderstorms initiated by radar-observed convergence lines. *Mon. Wea. Rev.*, **114** 2256–2266.

Szoke, E. J., M. L. Weisman, J. M. Brown, F. Caracena and T. W. Schlatter, 1984: A sub-synoptic analysis of the Denver tornado of 3 June 1981. *Mon. Wea. Rev.*, **112**, 790–808.

Watson, A. I., and R. L. Holle, 1982: The relationship between low-level convergence and convective precipitation in Illinois and south Florida NOAA TM ERL OWRM-7, 67 pp.

Wilson, J. W., and W. E. Schreiber, 1986: Initiation of convective storms at radar-observed boundary-layer convergence lines. *Mon. Wea. Rev.*, **114**, 2516–2536.

THE STRUCTURE OF THE CONVECTIVE CELLS AND THE DYNAMICS OF HAILSTORM DEVELOPMENT IN ALAZANI VALLEY

A.I.Kartsivadze, T.G.Salukvadze, R.I.Doreuli, E.I.Khelaya, A.Sh.Balavadze
Geophysics Institute of the Georgian Academy of Sciences
Tbilisi 380093, Z.Rukhadze Str. 1, USSR

The climatic conditions of Alazani Valley situated in East Georgia and from three sides surrounded by the mountain chains are characterized by the great frequency and high intensity of hail phenomena owing to physical-geographical and orographical peculiarities of the region. The Great Caucasus range prevents from the direct cold airmass penetration from the North favour the heat accumulation caused by the warming up of the base surface. For this reason it is growing a contrast between the cold airmass temperature and the temperature of the airmass over Alazani Valley. This being the situation, the atmospheric processes become more active and thunderstorm and hail phenomena become more intensive in this region. The second peculiarity of the orographic effect on atmospheric processes is stipulated by the fact that the mountain chains, extending along the valley edges stretch nearly perpendicularly to do mineering direction of cold airmass motion. This leads to dynamical support formation, enchancing updrafts and intensifying convective phenomena. Orography influences as well on the intramass process development. During daylight hours mountain and valley circulation contributes to formation and development of cumulus over mountain ranges surrounding Alazani Valley and intensifies convective processes. After instability energy realization in plain country conditions the convective processes late in the evening and at night practically calm down. Unlike this in Alazani Valley the cases are not infrequent when the second stage of the intramass convective development is realized. The formation of cumulonimbus clouds occurs directly over the valley late in the evening or even at night hours. Relatively cold air flows down the slopes to the bottom of the valley and force out warmer air vertically upwards. The majority of hail phenomena (70-75%) in Alazani Valley is connected with the frontal processes. Approximately 25-30% of hail cases in Alazani Valley falls on days with intramass processes. The most intensive falls are obtained when the contrast frontal process coincides with the intramass one, characterized by the high value of convective instability. The process becomes more active to an even greater degree when an axis of jet stream is located over Alazani Valley. The investigations of the structure and hailcells dynamics have been carried out using MRL-5 with 3.2 and 10cm wave lengths. There is a special instrument which allows at each scanning to obtain conic or vertical sections from the scopes in radar reflectivity iso-contours every 10D.B. At the same time we have used the data obtained with the help of the special hail and rainfall network. Long-term investigations conducted in Alazani Valley allowed to reveal distinctive features of hailclouds observed in different aerosynoptic conditions. As in North America (BRAUNING 1977, p.1-47), North Caucasus (ABSHAEV 1984, p.6-22) and other count-

ries the hailclouds of Alazani Valley can be divided into three types: single-cell, multicell, supercell. But a number of storms doesn't fit the criteria of this simple three-way classification scheme. Singlecell clouds develop mainly under intramass conditions. When a wind shear is absent or at small values of its vertical gradient singlecell clouds have a vertical axial symmetry (Fig.1)(APKHAIDZE et al, 1978, p.18-28).

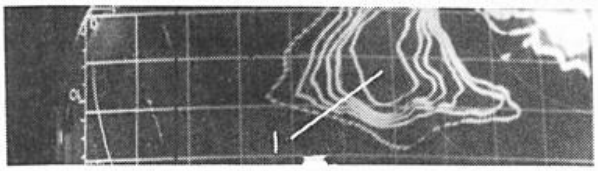


Fig. 1.

The height of the upper cloud boundary fluctuates from 8 to 14km and horizontal dimensions at maximum radar-echo level account for 15km, sometimes for 20-25km. The maximum of radar reflectivity doesn't exceed $3 \cdot 10^{-7} cm^{-1}$ at the height of 5-7km. The lifetime of such a cell after the beginning of its intensive development comes practically to 30-40min. Monocells can produce heavy hailfalls but their duration will not be long. In case of noticeable vertical wind shear a sloping updraft stream appears entailing reorganization of symmetric monocells. Increased radar reflectivity zone is divided by updraft stream into two parts. One part turns out to be in front of stream above weak echo zone, the other - behind it. This part covers hail and rainfall zone (Fig.2, parts I, II, III). Multicell fields have



Fig. 2.

a cluster structure and they cover a great number of convective, mainly singlecell, non-symmetric clouds, the formation and development of which has a migratory character. They are formed in frontal zones and can stretch for dozens kilometers. Upper boundary height of a separate cell can reach 15-16km. Multicell process lifetime avarages 2h. Very seldom one of cells can develop in supercell stage. Fig.3 shows a multicell cloud of three cells (parts I, II, III). Supercell storms are formed in Alazani Valley mainly during the invasion of cold fronts at large energy convection

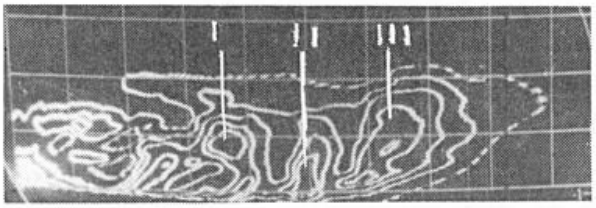


Fig. 3.

reaching the tropospheric upper layers when strong wind shears are observed. Upper boundary of these clouds reaches 12-14km. Once there was a case of 19km. Horisontal dimensions at maximum radar echo level average 30-40km. Radar reflectivity maximum can reach $10^{-6} cm^{-1}$. Figs. 4A and 4B show the vertical radar sections of the same supercell storm at two periods of time with 12 minutes interval.

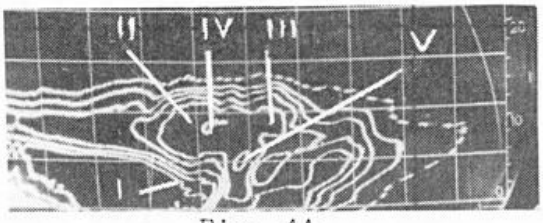


Fig. 4A.

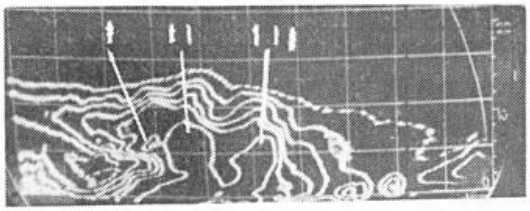


Fig. 4B

It follows from these figures that the hailcells (IV, V) were formed simultaneously in two different parts of increased reflectivity zone, one of which is located in front of and above general

updraft,the other behaid it.In the first case the height of hailformation zone reaches 8-9km,in the second case 5-6km. From Fig.4B we see that after the removal of the general stream in the direction of main draft both hailembryo cells turn out to be behaind the stream, they grow and then two hailfall zones are formed (Fig.4B,parts II,III). At the same time a new hailcell appears (IV).Horizontal extent of hailfall zone at the moment of observation amounts to 10km.In our example the process of formation,growth and hailfall beginning takes no more than 12 minutes. This example clearly shows the regeneration process of hailcells.Statistical analysis of the convective cells dynamics allows to evaluate a possibility of identifying predictors of their development into hailcells (BALAVADZE et al,1986,p.16).The most sensative predictors are: maximum radar reflectivity and its vertical extent,maximum echo height,radar echo upper boundary,increased reflectivity zone. With the help of these predictors using the method of multiple linear regression we succeeded in identifying a complex parameter according to which it is possible at the early stage of convective cell development to evaluate the probability of their overgrowing into hail ones. The investigation of the dynamics of convective clouds development gives hope that in future an ultra-shortterm radar prognosis will be worked out. Comparing measured parameter values with the calculated ones according to theoretical jet model (KACHURIN et al,1985, p.625-628) we see that the height of cloud upper boundary and mean sizes of falling hailstones agree well,but there is a considerable divergence between the values of maximum radar reflectivity,its vertical extent,hailstones kinetic energy and their maximum sizes.

It should be noted that the obtained data can be used when building an empirical model for different hailstorm types as well as for the evaluation of the adequacy degree of the theoretical model of such processes.

References.

ABSHAEV,M.T.: Structure and dynamics of thunderstorm and hail process development in the North Caucasus. Trudy VGI,V.53,1984,p.6-22 (in Russian).

APKHAIDZE,A.A.; BALAVADZE,A.Sh.; DOREULI,R.I.; OSIDZE,I.G.; SALUKVADZE,T.G.; KHARCHILAVA,D.F.: Some results of convective clouds radar investigations in the region of South Georgia upland (in Russian). Proc.of Geophys.Institute of the Georgian Acad.Sci.,vol.XLIV,1978, p.18-28.

BALAVADZE,A.Sh.; ZURASHVILI,Z.I.; KARTSIVADZE,A.I.; SALUKVADZE,T;G;; KHELAYA,E.I.: On the possibility of predicting hail-dangerous cumulonimbus clouds (in Russian). Doklady Vsesojuznogo 7th Sovestchania po radiometeorologii, 1986, Moscow, p.16.

BRAUNING,K.A.: The structure and mechanisms of hailstorms. Meteor.monogr. N 38,1977,p.1-47.

KARTSIVADZE,A.I.; SALUKVADZE,T.G.; KACHURIN,T.G.; An evaluation of hail suppression effectiveness using the method of inadvertent randomization and a numerical analysis. WMP Report N 2, v. II, WMO/TD- N 53, 1985,p.625-628.

EVOLUTION OF MESOCYCLONIC CIRCULATION IN SEVERE STORMS

P.I. Joe and C.L.Crozier
Atmospheric Environment Service,
King Weather Research Station,
4905 Dufferin St., Toronto, Ont., M3H 5T4

1 INTRODUCTION

The association between mesocyclones and tornadoes have been recognized for some time (BROOKS 1949). In general, the tornado has dimensions (1 km) too small to be consistently detected by radar. Therefore, early Doppler radar identification of the mesocyclone and of its developmental phase with respect to tornado initiation is central to the preparation of severe weather warnings by the forecaster. The mesocyclone has been found to be associated with tornadoes 50% of the time and with severe weather 90% of the time (JDOP 1979).

The majority of the research in mesocyclone identification from Doppler radar has been from storms in the mid-West United States which may not be representative of those elsewhere. This paper discusses the evolution of mesocyclones observed from the AES King City operational 5 cm Doppler weather radar in Southern Ontario, Canada; a location with a climate more temperate than that of the mid-West United States and where a different balance of thermodynamic and dynamic influences on the development of severe local storms may lead to significant quantitative differences in kinematic structure.

2 THE RADAR

The radar set used in this study is a fully operational 5 cm Doppler radar (Enterprise Electronic Corporation) and has been in use since late 1985. Table 1 describes the basic parameters of the radar. The system is constantly being improved and upgraded to meet increased demands. The Doppler signal is processed using a SIGMET Fast Fourier Processor. Custom interface hardware allows computer control of the radar and access to the raw radar signals. Multiple CPUs process the data and transmit radar maps to the forecast office of the Ontario Weather Centre among others. These products include CAPPIs, MAX R, Echo Top, Severe Weather, Doppler radial velocity and mesocyclone maps.

The radar operates with two sequential scanning strategies: a 24 elevation conventional volume scan sequence (from 0.3^o to 24.4^o) and a 3 elevation Doppler sequence (usually 0.5^o, 1.4^o and 3.4^o). Each sequence takes approximately 5 minutes; therefore, the radar operates on a 10 minute cycle. In Doppler mode, the pulse repetition frequency (PRF) alternates between 1190 and 892 pulses per second every other 0.5^o of azimuth. Therefore, 720 radials are collected per elevation angle. The alternating PRF data is combined to unfold the radial velocity in real-time to a extended Nyquist velocity of 48 m/s (SIRMANS ET AL 1976).

Table 1: Radar Characteristics

Parameter	Units	Conventional	Doppler
Frequency	MHz	5625	5625
Wavelength	cm	5.33	5.33
Peak Power	kW	260	260
Pulse Duration	μs	2.0	0.5
Pulse Length	m	600	150
Range Resolution	m	300	75
Max. Range	km	256	113
PRF	pps	250	892,1190
Scanning Rate	rpm	6.0	0.75
Gain	dB	48	48
Beamwidth		0.65^o	0.65^o
Samples		8	64

3 MESOCYCLONE ANALYSIS TECHNIQUE

A real-time automatic mesocyclone detection algorithm provides the source of data for this study. The algorithm is modeled after the National Severe Storms Laboratory algorithm as described by ZRNIC ET AL (1985). The technique is based on the Rankine combined vortex mesocyclone model which consists of a circular core in solid body rotation and an external potential flow. The algorithm attempts to identify the linear shear within the central core of the mesocyclone.

Modifications to the NSSL detection algorithm were required because of radar, scanning and wavelength considerations, real-time requirements for operational use and regional weather differences. The dual PRF unfolding scheme can lead to uncertainties which cause artificial shears in the velocity data. Therefore, in this modified approach, only folded radial velocity differences from a single PRF are used and velocity unfolding is not required. The implications of this are that the mesocyclone must be assumed to be symmetric in its velocity field but also that storm motion from a tracking algorithm is not required to remove the mean motion of the storm. This also implies that there is an upper limit to the measurable shear, given by $s_{lim} = V_{Nyquist}/d$ where $V_{Nyquist}$ is the Nyquist fold velocity and d is the azimuthal distance between adjacent radar volumes (gate-to-gate) given by $d = r \times \phi_{diff}$ where r is range and ϕ_{diff} is the azimuthal difference. In addition, mesocyclone signatures detected at multiple elevations are correlated for vertical continuity which facilitates the identification of mesocyclones. Mesocyclones are expected to be detected at mid-levels (3-7 km) of a storm and then lower with time (BURGESS ET AL 1982). Signatures that do not fit this conceptual evolutionary model are not reported. This latter feature eliminates the detec-

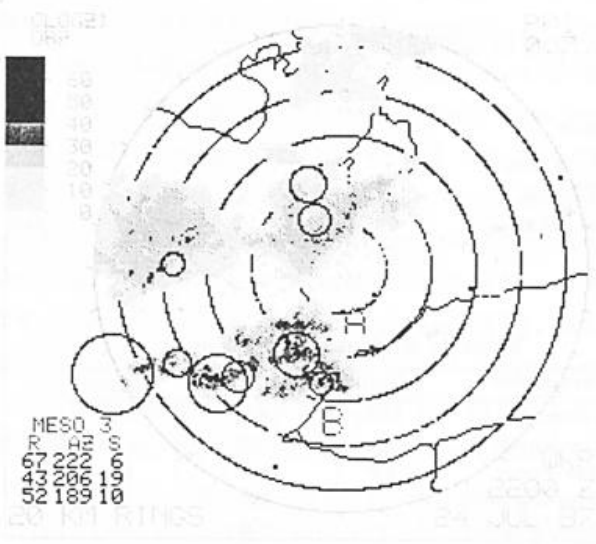


Figure 1: Operational mesocyclone detection display.

tion of the inflow-gust front boundary of the storm, which has a similar radial velocity structure, as a mesocyclone. At the present time, no attempt is made to detect anti-cyclonic mesocyclones (WEILER 1986). The algorithm is also coded to detect the largest contiguous area of shear and therefore smaller circulations within the mesocyclone are not multiply reported (DESROCHERS ET AL 1986).

Fig. 1 presents the operational product from the algorithm. Circles indicate the location of detected mesocyclones. The diameters are drawn at four times the calculated size of the mesocyclone. To aid in the proper identification of spurious shears, the low level reflectivity PPI is underlaid which enables the forecaster visually correlate algorithm identified mesocyclonic shear regions with the reflectivity structure of the storm. In the bottom left hand corner, a table indicates the location and maximum shears (in units of m/s/km) of mature mesocyclones (those detected at more than a single elevation angle).

4 F1 TORNADO CASE STUDY: 24 JULY 1987

On the afternoon of 24 July 1987, the radar coverage area was in warm sector air. Surface air temperatures and dew points at 1700Z were 32^oC and 22^oC, respectively. At about 2000Z, air mass thunderstorms began to develop southwest of the radar.

Two severe thunderstorms as identified by conventional radar are identified on Fig. 1 by the letters A and B at 2200Z. At 2030Z, the first echo of storm B appeared at the edge of the Doppler radar (range 110 km and azimuth of 237^o). The storm moved towards the east at 60 km/hr. At 2100Z, a weak mesocyclone associated with this storm was identified by the detection algorithm and continued to evolve for the next hour till 2200Z. No tornado was reported with this storm.

Storm A developed within radar range; the first echo appeared at 2100Z at a range of 90 km and azimuth of 260^o. It formed about 20 km to the northwest of storm B. The first mesocyclone signature was identified at 2130Z, 30 minutes after first echo detection and

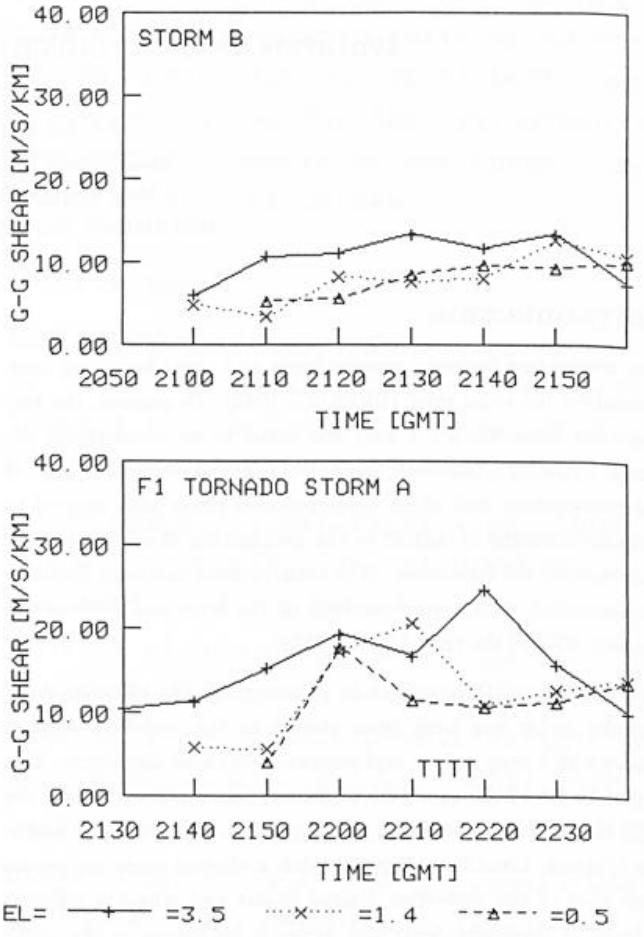


Figure 2: Temporal evolution of the maximum gate-to-gate shear. Tornado touchdown is indicated by TTTT.

continued to develop for 70 minutes until 2240Z. A F1 tornado briefly touched down between 2210Z and 2220Z, damaging the roof of a house.

During its development storm B had slightly higher maximum reflectivities on the lowest (0.5^o) elevation scan; 53 dBZ for B compared to 50 dBZ for A. However, storm A had a constant vertical maximum reflectivity structure (in the lowest 3 km) while B decreased with height (not shown).

The two storms had very different radial velocity structures. Fig. 2 plots the maximum (gate-to-gate) shears found within the boundaries of the mesocyclone for storms A and B as a function of time. In general, greater shears were found with higher elevation and with the tornadic storm. The shear appears to increase dramatically at 2200Z, 20 minutes before tornado touchdown. Based on this one case, a shear value of about 13 m/s/km would discriminate the tornadic from the non-tornadic storm.

Fig. 3 plots the temporal development of the mesocyclone "angular momentum" defined as $\sum r(\phi_e - \phi_b)(v_e - v_b)/N$ where r is the range of the radar gate where significant shear was found, ϕ_e and ϕ_b are the start and end azimuths, v_e and v_b are the start and end radial velocities and N is the number of range gates. Summation is over the shear region where the mesocyclone was identified. Note that this quantity is actually only proportional to angular momentum since mass is not included in its formulation.

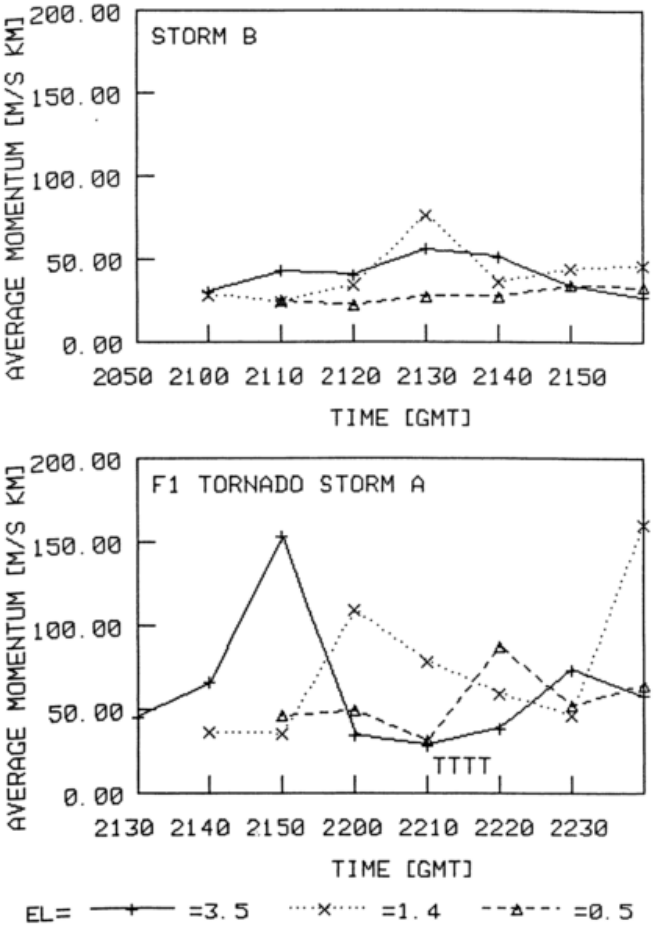


Figure 3: Temporal evolution of the "angular momentum".

Also, this quantity is proportional to the square root of rotational kinetic energy (DESROCHERS ET AL 1986). An angular momentum value of about 50 m/s km appears to discriminate the tornadic from the non-tornadic storm. For the tornadic storm, the angular momentum shows a peak earlier in its evolution than shear and is larger at higher elevations. There is also a distinctive downward progression of the peak with time. Therefore, this quantity shows promise as an indicator of mesocyclone development and may provide longer lead times than with the use of shear alone.

5 DISCUSSION AND SUMMARY

This case study demonstrates the utility of a *5 cm* Doppler radar for severe weather detection. The radar and mesocyclone detection algorithm is sensitive enought to detect weak circulations and mesocyclones associated with weak tornadoes (F1). The use of angular momentum appears to be a better discriminator of tornadic storms than shear and can provide lead times of about 30 minutes for first tornadoes.

This case also illustrates the cability of the Doppler radar to discriminate between the tornadic/non-tornadic storm. Both storms developed in the same environment but only one of the storms was tornadic. This will improve ability of the forecaster to pinpoint the severe storm and provide accurate and timely warnings

The evolutionary structure is similar to mesocyclones found in Oklahoma (BURGESS ET AL 1979) where the mesocyclone begins aloft at mid-levels of the storm and then lowers to the ground. Quantitatively, the mesocylone appeared 30 minutes after first echo detection and lasted for a total of 70 minutes; Oklahoma storms show values of 88 and 91 minutes, respectively. Also, the tornadic mesocyclone was initially detected above an echo free region. The average Oklahoma mesocyclone develops when the vertical radar echo extent is at its maximum.

Shear threshold values which discriminates between tornadic versus non-tornadic storms are similar to those in Oklahoma. However, angular momentum thresholds appear to be quite different (ZRNIC ET AL 1985); the Oklahoma parameterizations for the algorithm would not have detected the tornadic mesocyclone in this case study. This can be attributed to regional differences between storm environments. Differences in radar and detection techniques can not account for this disparity.

Thus, there are considerable regional differences between severe storms. There will be a need to make the mesocyclone detection algorithm (and other severe weather detection algorithms) site specific for various Doppler network sites in Canada and NEXRAD locales in the United States.

6 ACKNOWLEDGEMENTS

The authors are appreciative to J. Scott and H. Herscovitch for their expertise in the development of the operational King Weather Radar Site and to T. Nichols for many helpful discussions and comments.

7 REFERENCES

BROOKS, E.M., 1949: The tornado cyclone, Weatherwise, 2, 32-33.

BURGESS, D.W., V.T. WOOD and R. BROWN, 1982: Mesocyclone evolution statistics, Preprints of the 12^{th} Conf. on Severe Local Storms, San Antonio, Amer. Met. Soc., 422-424.

DESROCHERS, P.R., R.J. DONALDSON and D.W. BURGESS, 1986: Mesocyclone rotational kinetic energy as a discriminator for tornadic and non-tornadic types, Preprints of the 23^{rd} Conf. on Radar Met., Snowmass, Amer. Met. Soc., 1-4.

JOINT DOPPLER OPERATIONAL PROJECT (JDOP) STAFF, 1979: Final report 1976-78, NOAA Tech. Memo. ERL NSSL-86, 88pp.

SIRMANS, D., D. ZRNIC' and B. BUMGARNER, 1976: Extension of maximum unambiguous Doppler velocity by use of two sampling rates, Preprints of the 17^{th} Radar Met. Conf., Seattle, Amer. Met. Soc., 23-28.

WEILER, J.G., 1986: Real-time automated detection of mesocyclones and tornadic vortex signatures, J. Atmos. Oceanic Technol., 3, 98-113.

ZRNIC, D.S., D.W. BURGESS and L. HENNINGTON, 1985: Automatic detection of mesocyclonic shear with Doppler Radar, J. Atmos. Oceanic Technol., 24, 425-438.

A NUMERICAL STUDY OF MULTICELLULAR SEVERE CONVECTIVE STORMS FOLLOWED BY LONG-LASTING HEAVY RAINFALL

Jun-ichi Shiino

Meteorological Research Institute
1-1 Nagamine,Tsukuba-shi
Ibaraki-ken, 305 JAPAN

1. INTRODUCTION

Convective clouds in mesoscale meteorological disturbances are often organized into meso-ß scale multicellular structure and sometimes cause such severe storms as heavy rainfall,heavy snowfall,flush flood, thunderstorm, hazardous hail, downburst, tornado and so on, hence exerting great influence on the social and economical aspects of human activities.

The primary energy source of such convective system is the release of latent heat through the phase change of water substances. However, the importance of drag force of precipitation particles, whose motion is different from that of air parcells, evaporative cooling,horizontal convergence of water vapour due to large scale flow and the vertical shear of ambient wind have been also strongly pointed out by many researchers. Thus meso-ß scale convective system is both physically and dynamically related to a wide range of meteorological phenomena in a complicated manner from microscale to macroscale.

Although a large number of numerical as well as observational studies have been conducted so far on the behavior of convective clouds, the history of researches as well as the understanding on "mesoscale organized convective systems" is still in its early stages.

The purpose of this paper is to investigate in detail this kind of convective system, that is,the organizing and maintenance process as well as the structure of multicellular severe convective storms followed by long-lasting heavy rainfall, by a three-dimensional numerical experiment. Interaction of the convective system with a large-scale flow, splitting, movement and propagation of convective cells, divergence structure in and around the convective system,the formative process of gustfront and meso-high, and their roles to the maintenance of the storm are also investigated through the experiment. Special emphasis is put on the effect of vertical wind shear for the formation of a mesoscale-like multicellular convective storm.

2. OUTLINE OF THE NUMERICAL MODEL

Basic equations of a three-dimensional anelastic model of deep moist convection using the Cartesian coordinate(x,eastward; y,northward;z,upward) ,which are the extension of 2-D model by Soong and Ogura(1973), consist of equation of motion, mass continuity equation, diagnostic pressure equation, thermodynamic equation for potential temperature,continuity equations for water substances. Warm cloud microphysical processes with the Kessler-type parameterization on the precipitation process are incorporated into the model.

Predicted variables are u,v,w(x-,y- and Z-component of velocity,respectively), θ (potential temperature),Qv,Qc,Qr(mixing ratio of water vapour, cloud water and precipitation water,respectively). The detail of the procedure of the whole physical processes is substantially the same as those in Shiino(1983).

The domain size of computation is 32 km, 32 km and 8 km with each grid interval of 1 km, 1 km and 0.5 km, in the direction of x, y, z, respectively. The time step of integration is 20 sec. Boundary conditions are such that they are rigid with free-slip in the upper and lower,however open in the lateral using radiation condition for normal velocity components.

Initial conditions of the atmosphere are assumed to be conditionally unstable,with considerably moist(max.95%) air flow in the lower layer, together with a significant vertical wind shear(veering) in the middle to upper

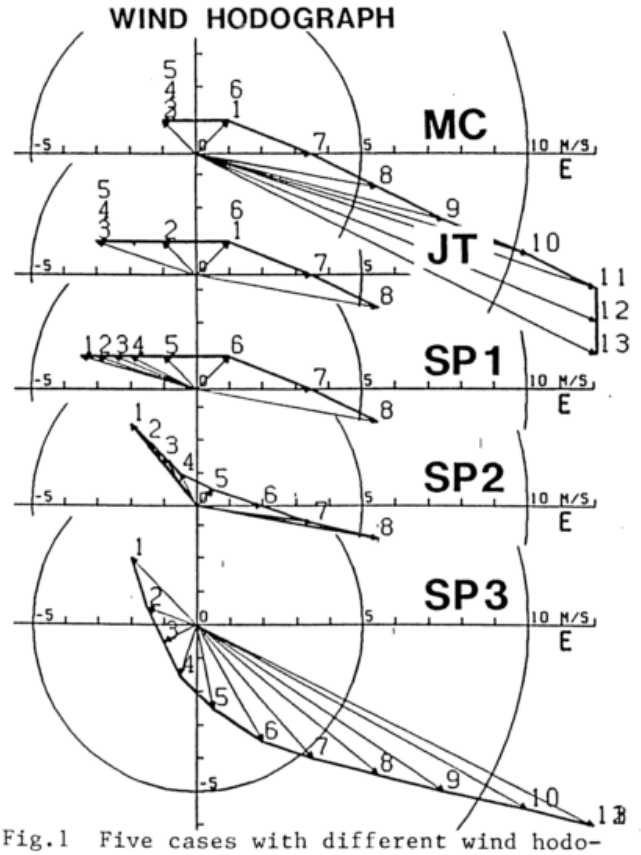


Fig.1 Five cases with different wind hodographs taken in the present study. Figures on the hodographs denote the grid numbers from the lowest level. In cases JT, SP1 and SP2, the profiles above the level of 8 are the same as those in case MC.

layer, these kinds of features being frequently observed in Japan in cases of heavy rainfall. Initial disterbance is given by small θ' with its maximum amplitude of 0.5°C.

3. CASES

Five cases(Fig.1) with different vertical wind profile are taken here to study the effect of vertical wind shear. The essential feature of each case which differentiates each other, lies in the shear in a lower to middle layer up to about the level 6 (abbreviated "LM" layer hereafter) are as follows. The shear in the LM layer in case MC is small in contrast to the significant shear above the LM layer, while in case JT a jet type wind shear in the east-west direction, a kind of linear shear with shear vector from west to east in case SP1, a shear with a little bit different from a linear shear in case SP2 in the LM layer, respectively, are assumed, and in case SP3 the wind profile as well as the shear vector is taken as counterclockwise almost through the layer. In this extended abstract, significant features of severe convective storms obtained in case MC are mainly described together with characteristic differences in the other cases from a viewpoint of organization of convective clouds.

4. RESULTS

Fig.2 shows the process of evolution of a multicellular severe convective storm followed by long-lasting heavy rainfall in case MC. The single cell A is split into two, A and B, with time and moreover some new cells C,D and E are formed between or near the existing cells.Each

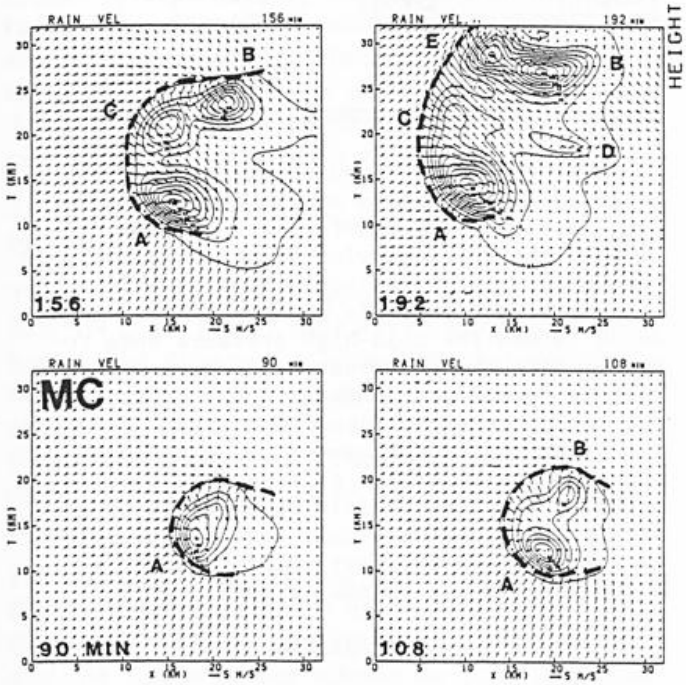


Fig.2 Time and spatial variation of rainfall intensity and air flow near the ground surface in the storm in case MC. Contour lines are every 10 mmhr^{-1}. The broken lines are the gust front.

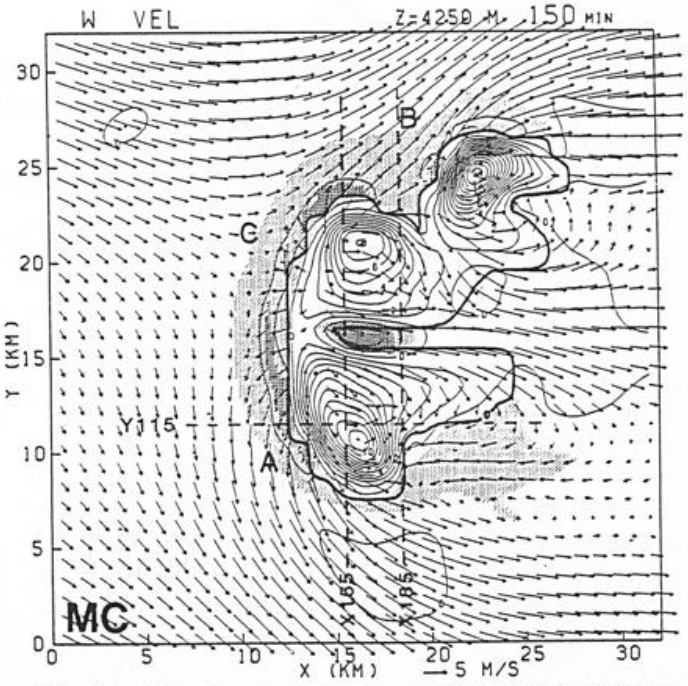


Fig.3 A horizontal cross-section of vertical velocities(contour lines every 1 ms^{-1}) and horizontal velocities(arrows, whose measure being given along the abscissa) in and out of the storm at the level of 4250 m at 150 min. The thick solid line is the boundary of cloud water.The shaded area is that with downdraft.

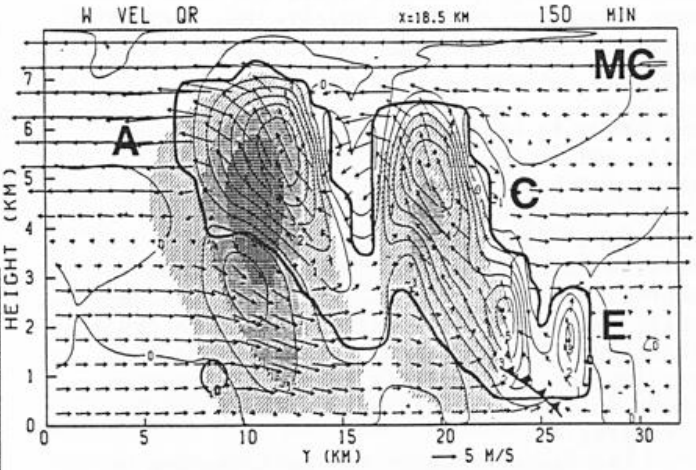


Fig.4 Vertical cross-section of the storm along the broken line X185 in Fig.3. Precipitation water is given by the three kinds of shade, 0.5-3, 3-5 and more than 5 gKg^{-1}, from the outside. Others are as in Fig.3 except for the vertical cross-section.

cell is accompanied by strong diverging outflows. These outflows in combination with the large scale flow build up firmly a series of gustfronts surrounding the cells, especially from the south to west to the north. This is substantially important for the organization as well as the maintenance of the convective cells.

A horizontal cross-section of the storm in its middle level represented in Fig.3 shows that each cell possesses intense updraft velocities, 11 ms^{-1} in A, 14 in B and 8 in C, thus indicating each cell being remarkably developed convective cloud. The airflow toward

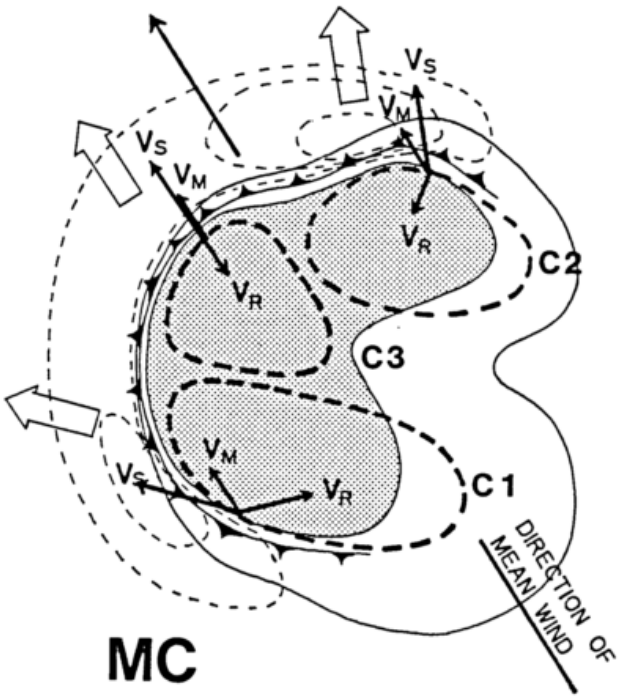


Fig.5 A schematically illustrated model of the storm in case MC.The thick arrows and the vector Vs mean the direction and movement (including propagation) of cells C1, C2 and C3. V_M is the lowlevel mean wind, V_R the storm-relative wind vector,the shaded area the mesoscale cold-high pressure dome, the area with thin broken lines the mesoscale low pressure area and the solid line the outline of the storm.

the storm is blocked significantly by the cells and is forced to make a detour by the storm, with accelerated rapid currents in the north and south flanks of the storm. Another important point which should be noted is the airflow which flows into the cell A from the rear side (right side in this case) of the cell. This noticeable inflow, which is dry in this level, contributes strongly to the development of downdraft in the LM layer as shown in the vertical cross section of the storm(Fig.4).

The features shown in Fig.4, strong updraft in the upper layer and significant downdraft in the LM layer in A, which is in the mature stage, the existence of cell C in its just before the mature stage, together with a newly formed cell E associated with the gustfront and so on,are substantially similar to those schematically illustrated figure of a multicellular severe convectiv storm by Browning et al (1976).

Fig.5 is a schematically depicted horizontal picture of the storm in case MC.The essential features of the figure are the existence of the storm-relative inflow V_R in the LM layer,organized cold-high pressure dome illustrated by the shade, and firmly established gustfront surrounding the convective cells.

The effect of vertical wind shear on the formation of multicell severe storms is shown in Fig.6 by the comparison of the storms, which are depicted by $\int \rho Q_c \, dz$ in each case of Fig.1. The storm in JT is also organized as well as in MC, while in other cases cells in the storm are not organized, splitting into two in SP1, resplitting in SP2 and only the left-moving cell with respect to the lower mean wind V_M keeping alive in SP3.

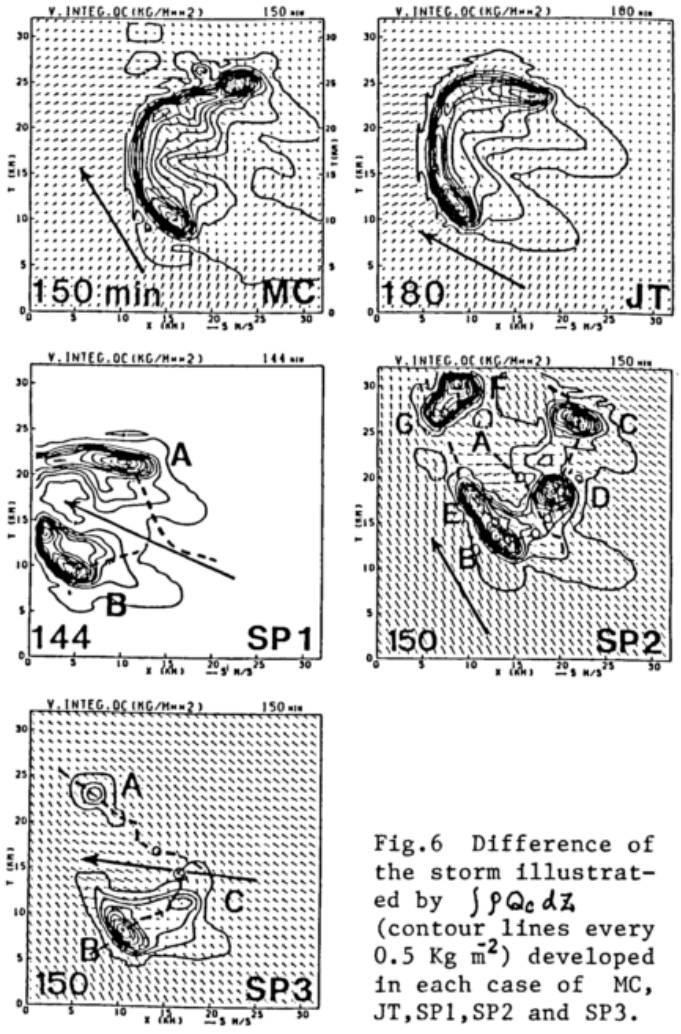


Fig.6 Difference of the storm illustrated by $\int \rho Q_c \, dz$ (contour lines every 0.5 Kg m^{-2}) developed in each case of MC, JT,SP1,SP2 and SP3.

5. CONCLUSION

The development and maintenance of multicell severe convective storms followed by long-lasting heavy rainfall are quite sensitive to the vertical wind shear, especially in the LM layer of large scale flow in which the storm evolves. The main point which should be noted is how the cold-high pressure dome together with the gustfront near the ground surface is formed and behaves in the storm under the influence of vertical wind shear. The result of the present numerical experiment suggests the existence of favorable conditions of the wind profile which cause to grow firmly organized multicell severe convective storms followed by heavy rainfall under a given large scale thermal stratification.

REFERENCES

Browning,K.A., et al.,1976: Mon.Wea.Rev.,104 603-610.

Shiino,J.,1983: J.Met.Soc.Japan. 61, 629-655.

Soong,S.T. and Y.Ogura,1973: J.Atmos.Sci.,30, 879-893.

3-D NUMERICAL MODELLING AND RADAR OBSERVATIONS OF DEEP CONVECTIVE CLOUDS

Hartmut Höller

Institut für Physik der Atmosphäre, DFVLR Oberpfaffenhofen, 8031 Weßling, F.R.G.

1. INTRODUCTION

A number of 3-D cloud models have been developed during the last years. But up to now only very few have considered ice phase processes (e.g. BENNETS and RAWLINS 1981, TRIPOLI and COTTON 1982, COTTON et al. 1982). In this paper a 3-D mesoscale cloud model is described with special emphasize on precipitation growth processes leading to the formation of graupel particles and hailstones. This cloud model application represents one of several model versions of DFVLR's mesoscale model MESOSCOP (Mesoscale Flow and Cloud Model Oberpfaffenhofen). The other versions refer to flow over mountains and turbulent boundary layers (SCHUMANN et al. 1987).

Principally, the complete structure of actual convective storms cannot be detected by radar alone. For example, no data are available on the pressure and the thermodynamic fields or from the echo free regions of the cloud. Therefore a comparison with 3-D numerical cloud model results is especially useful for gaining a better understanding of thunderstorms. A preliminary comparison of the model results with radar measurements of a supercell hailstorm which occured on June 13, 1987 in southern Germany and Austria is shown in the following. The measurements were obtained with the Doppler polarization diversity radar of DFVLR.

2. GENERAL MODEL DESCRIPTION AND NUMERICS

The basic model equations are described in SCHUMANN et al. (1987), only a brief summary is given here. The dynamics is described by conservation laws for density, momentum and a number of scalar entities like entropy or the concentrations of the different cloud particles. The temperature can be obtained by an inversion of the entropy state function.

For numerical integrations on a staggered grid a finite difference method is used which is a combination of the Adams-Bashforth scheme for momentum and the Smolarkiewicz scheme for positive definite scalars. Sound waves are filtered by the implicit treatment of the continuity equation which also requires the solution of an elliptic Helmholtz equation for the pressure change.

3. MODEL MICROPHYSICS

The bulk physical concept is adopted for the treatment of cloud microphysical processes. This implies that the different kinds of cloud particles are represented by their volume concentrations alone and their mass distribution functions are prescribed by certain well defined functions of the concentrations. The present model version uses six particle categories: cloud water and cloud ice (frozen cloud droplets, vapor grown plates and slightly rimed plates) moving with the velocity of the air, rainwater, graupel and hail representing liquid and solid phase precipitation particles, and snowflakes as a further precipitation category. Thus, in addition to the microphysical concept described in SCHUMANN et al., a separate hail category has been added to the model for a better representation of high density hail which has increased fall speeds as compared to the graupel particles. The transition between graupel and hailstones takes place between 0.5 and 1 cm of maximum particle dimension.

The microphysical processes coupling the different kinds of cloud particles or the vapor phase are: condensation of cloud droplets (treated implicitely to achieve water saturation adjustment), evaporation of rain, sublimation of graupel, snow and hail, freezing of cloud droplets and rain, accretion processes for graupel snow and hail, aggregation of snow and melting of ice particles. The latter processes are described by rate equations similar to those of LIN et al. (1983). The depositional growth rate of ice crystals, the autoconversion and accretion processes of droplets, the riming rate of ice crystals and the subsequent growth of these crystals into graupel are treated following HÖLLER (1986), where a more detailed description of the microphysical processes can be found.

4. COMPARISON OF RADAR OBSERVATIONS AND MODEL RESULTS

On June 13, 1987 a supercell hailstorm occured in southern Germany and Austria. A hailswath was observed at the ground in the area of Salzburg. The storm was monitored by the Doppler polarization diversity radar of DFVLR taking reflectivity, differential reflectivity (ZDR) and linear depolarization ratio (LDR) data.

From the ZDR data we can infer the presence of raindrops (see SELIGA and BRINGI, 1976) which are indicated by positive values of ZDR. On the other hand, graupel and hailstones have ZDR values around zero or slightly negative. Following AYDIN et al. (1986) a hail signal can be derived from reflectivity and ZDR values.

As an example Figure 1 shows a horizontal section through the storm at 4 km above MSL. The reflectivity structure clearly shows a hook echo at about x=102 km and y=-34km, a weak echo region at x=106 km and y=-34km and a high reflectivity core at x=102 km and y=-29.5 km. To the east (positive x-axis direction) of the hook positive ZDR values indicate the presence of raindrops. Graupel and hail exclusively can be found in the main reflectivity core and in an eastward extension of moderate reflectivity values at x=112 km and y=-32 km. These regions are represented by the hail signal function in Figure 1b.

For the specification of the initial environmental conditions in the model simulations the sounding of Munich of 12 UTC was used. The wind vector veered from easterly directions in the lowest layers to south-westerly directions in the middle troposphere in combination with a fairly strong absolute amount of shear. The shear vector itself also turned clockwise with height. These conditions in combination with a potential instability are favourable for the development of severe storms propagating to the right of the shear vector at mid-levels (see e.g. WEISMAN and KLEMP 1982). Convection was triggered by an entropy source at the lowest grid level. This source was applied throughout the simulation and was forced to travel with the speed of the observed weak echo region (50 km/h to the east).

The model results for a horizontal cross section at 3.8 km above MSL are shown in Figure 2. In agreement with the observations, the reflectivity contours also show the hook echo, the weak echo region and extensions to the east and to the north. The weak echo region corresponds to the updraft location (maximum updraft speed about 26 m/s). In the outer part of the updraft with relatively weak vertical velocities hail, graupel and rain are present. The temperatures are slightly above the freezing point. The maximum hail and rain concentrations (both below 1 g/kg) can be found at the updraft-downdraft boundary. Most of the precipitation in the high reflectivity region consists of graupel particles (up to 3 g/kg). They are falling in a region of downdraft up to 10 m/s. While the updraft is rotating cyclonically (positive vertical vorticity) the downdraft rotates anticyclonically.

5. CONCLUSIONS

A 3-D cloud model including ice phase processes and a preliminary comparison of the model results with multiparameter radar data has been presented. The principle structures of a supercell hailstorm were simulated by the model, especially the updraft-downdraft structure and the distribution of the different kinds of hydrometeors. These first results indicate that the approach of comparing radar data and 3-D model results is promising for gaining a better understanding of hailstorms and hail producing microphysical processes. Of course, further model improvements are necessary especially for a better quantitative description of hail processes and for a more realistic simulation of convection initiation. Also the model has to be tested for different kind of storms developing under different environmental conditions.

6. REFERENCES

BENNETS, D.A.; RAWLINS, F.: Parameterization of the ice phase in a model of mid-latitude cumulonimbus convection. Quart. J. Roy. Met. Soc. 107 (1981), 477-502.

TRIPOLI, G.J.; COTTON, W.R.: The Colorado State University three-dimensional cloud/mesoscale model - 1982. Part I: General theoretical framework and sensitivity experiments. J. Rech. Atmos. 16 (1982), 185-219.

COTTON, W.R.; STEPHENS, M.A.; NEHRKORN, T.; TRIPOLI, G.J.: The Colorado State University three-dimensional cloud/mesoscale model - 1982. Part II: An ice phase parameterization. J. Rech. Atmos. 16 (1982), 295-320.

SCHUMANN, U.; HAUF, T.; HÖLLER, H.; SCHMIDT, H.; VOLKERT, H.: A mesoscale model for the simulation of turbulence, clouds and flow over mountains: Formulation and validation examples. Beitr. Phys. Atmos. 60 (1987), 413-446.

LIN, Y.L.; FARLEY, R.D.; ORVILLE, H.D.: Bulk parameterization of the snow field in a cloud model. J. Clim. Appl. Meteor. 22 (1983), 1065-1092.

HÖLLER, H.: Parameterization of cloud microphysical processes in a three-dimensional convective mesoscale model. DFVLR-Forschungsbericht, FB 86-02 (1986).

SELIGA, T.A.; BRINGI, V.N.: Potential use of radar reflectivity measurements at orthogonal polarizations for measuring precipitation. J. Appl. Meteor. 15 (1976), 69-76.

AYDIN, K.; SELIGA, T.A.; BALAJI, V.: Remote sensing of hail with a dual linear polarization radar. J. Clim. Appl. Meteor. 25 (1986), 1475-1484.

WEISMAN, M.L.; KLEMP, J.B.: The dependence of numerically simulated convective storms on vertical wind shear and buoyancy. Mon. Wea. Rev. 110 (1982), 504-520.

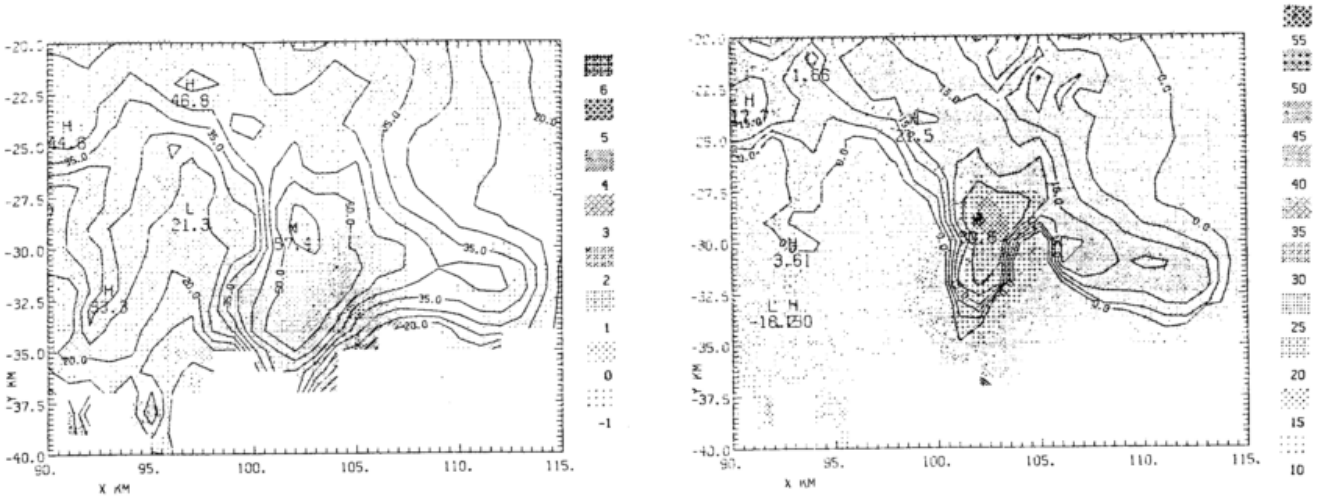


Figure 1 Radar observations at 17.58 UTC of June 13, 1987 interpolated to a horizontal plane at 4 km above MSL. In (a) the reflectivity field T_{HH} (transmitted horizontally, received horizontally) in dBT and a shaded overlay (scale at right margin) of the differential reflectivity ZDR are shown. The x- and y-coordinates refer to the distance from the radar in east and north directions, respectively. In (b) the hail signal is computed according to AYDIN et al., 1986. The overlay field is reflectivity (scale at right margin).

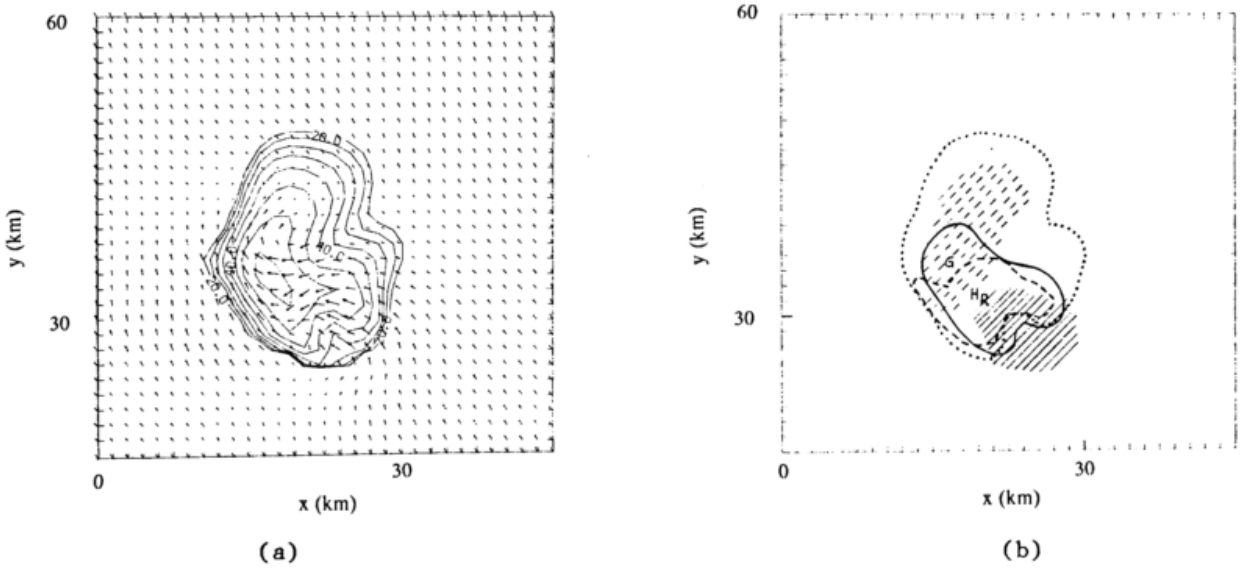


Figure 2 Model results after 40 min of integration time for a horizontal plane at 3.8 km above MSL. In (a) the horizontal velocity field is shown where the maximum velocity is 18 m/s. The reflectivity contours in dBZ are superimposed. In (b) the 0.1 g/kg concentration outlines for hail (solid line), graupel (dotted line) and rain (dashed line) are shown. The hatched regions indicate updrafts (solid hatching) and downdrafts (dashed hatching) larger than 2 m/s in magnitude.

OBSERVED STRUCTURE AND EVOLUTION OF A MESOVORTEX IN THE TRAILING STRATIFORM REGION OF A MCC.

J. Verlinde[1] and W.R. Cotton

Colorado State University, Dept. of Atmospheric Science, Fort Collins, CO 80523

1 Introduction

The role of vorticity centers in precipitating midlatitude weather systems has received a lot of attention in the last decade, and its importance to the evolution of these weather systems has become widely recognized. The focus in research has primarily been on vorticity in convective storm scales, with emphasis on the effects of vorticity on supercell storms and/or tornadoes (see Klemp, 1987, for a summary), which could be observed by Doppler-radar, or on inertially stable vortices on meso-α-scales which could be observed by dense upper-air networks (Bosart and Sanders, 1981; Johnson, 1986; Lin, 1986; Leary and Rappaport, 1987), or even satellites (Johnston, 1982). This paper present an observational study of a mesovortex couplet that developed in a multicellular complex that was one meso-β-scale building block of a MCC during its developing stage.

2 Data and Analysis Procedure

The data used in this study was collected on June 17th, 1985, during the PRE-STORM experiment. The observing systems that have contributed to this study include the two NCAR 5 cm Doppler radars CP-3 and CP-4, and the PRE-STORM upper-air network. The two radars were performing high resolution sector scans, recording both reflectivity and velocity fields. The sector scans were 90° sectors, scanning from base-elevation of 0.2° to 58.0°, completing one scan in about 5 minutes. The data was averaged over four range gates along range to have a datum spacing of about 1 km in the area of interest. The weather system studied moved through this sector in about two hours, from 0100 UT to 0300 UT. Soundings were released from most of the PRE-STORM upper-air network at 0000 UT and 0300 UT. All supplemental rawinsondes were canceled at 0600 UT. The station at Russel, KS, did not do any soundings, which is unfortunate since it was at a strategic location for this study.

3 Synoptic Environment

A surface cold front was oriented roughly west-east over northern Kansas, moving slowly south during the period of interest. The southern and eastern parts of Kansas was characterized by warm advection and high low-level moisture (> 12 g kg^{-1}), and a analysis of the soundings revealed large values of available buoyant energy (Fritsch and Chappel,1980) ahead of the front (1600-2000 m^{2}s^{-1}). A strong SSW'ly low-level jet (15-20 ms^{-1}) was also observed. The 500 mb analysis over Kansas revealed a weak ridge over the area with a weak short-wave trough upstream. These conditions agree to a large extent to the conditions described by Maddox (1983) for the genesis region of a MCC. The shear profile exhibited a clockwise turning shear vector through the lower levels of the atmosphere, similar to that frequently used in modeling studies of tornadic storms (Klemp, 1987).

During the afternoon (~2200 UT 16 June) a north-south oriented line formed over western Kansas, and it slowly moved eastward. At 2300 UT the line split, with the northern section developing into a cell that exhibited a supercell like character, while the southern section propagated as a weak multicellular complex.

[1]Affiliation: South African Weather Bureau, Research Branch.

At later stages the southern section was primarily driven by the outflow of the system to the north, with single cells in the storm going through a life-time of about 1 hour. It is this multicellular system that moved through the radar observational area.

4 Dual-Doppler Analysis Results

Four dual-Doppler volume scans had been analyzed for this study. The first volume scan was at 0107 UT as the storm system just moved into the radar scanning area. The second was at 0140 UT, the third at 0203 UT and the fourth at 0224 UT as the system was moving into extreme range for reliable wind retrieval. There was thus radar coverage for a period of 1 hour and twenty minutes.

Figure 1 shows streamlines of the storm relative horizontal flow fields at levels 2.9, 5.9 and 10.9 km MSL for volume 2. The streamlines are portrayed against the background of reflectivity. Fig 1b shows both the cyclonic and anticyclonic vortices, with the cyclonic vortex larger and more intense than the anticyclone. A feature resembling the low-level cloud flanking line associated with tornadoes can also be seen, in a weak reflectivity line curling around the vortex (X=10, Y=30). This is at the level where the cyclone is of maximum intensity. Looking at Fig 1a,c we can see evidence of the cyclone from 2.9 km up to 10.9 km. The returned signal at lower levels was too low to derive winds, but there are indications that there was cyclonic vorticity at 1.9 km as well as at 11.9 km. Below the anticyclonic vortex a region of anticyclonic vorticity can be seen, although the circulation is not closed. No evidence of dominant anticyclonic vorticity could be found above the anticyclone at 10.9 km. Fig 2 shows streamlines of the storm relative flow at the earliest analyzed time at a height of 5.9 km. At this time the cyclonic vortex was already well established, while the anticyclone only appeared as a region of dominant anticyclonic vorticity with no closed circulation. The proximity of the flow-field relative to the reflectivity field might give some insight into the formation of the circulations. It can be seen that the circulations formed behind one of the leading cells in the multi-cellular storm. This cell was the dominant cell in the storm at this stage, although it was rapidly decaying. The closed 30 dBz contour (X=35, Y=60) in Fig 1a is the remainder of this storm, while a new cell had grown rapidly from nothing at 0107 UT to a ~50 dBz cell at 0140 UT. This cell reached 60 dBz a few minutes later, and then rapidly collapsed. Fig 3 shows the streamlines at 0224 UT. It can be seen that the cyclonic vortex had broken down into two smaller closed circulations at this level. However, at higher levels there still remained one single vortex. The anticyclone is still approximately the same size as before, and very well defined. The multi-cellular storm at this stage was in its death throws, at 0240 UT no radar returns (> 18 dBz) of this storm could be detected by the NWS WSR-57 radar at Wichita.

In order to obtain some general characteristic features of the circulations, it was necessary to objectively define the circulation. Vorticity was calculated at each grid point, and the center of rotation was determined at each level for all volume scans. The average vorticity in circles of various radii around the centers of rotation was then determined. Two definitions for the circulation was used:

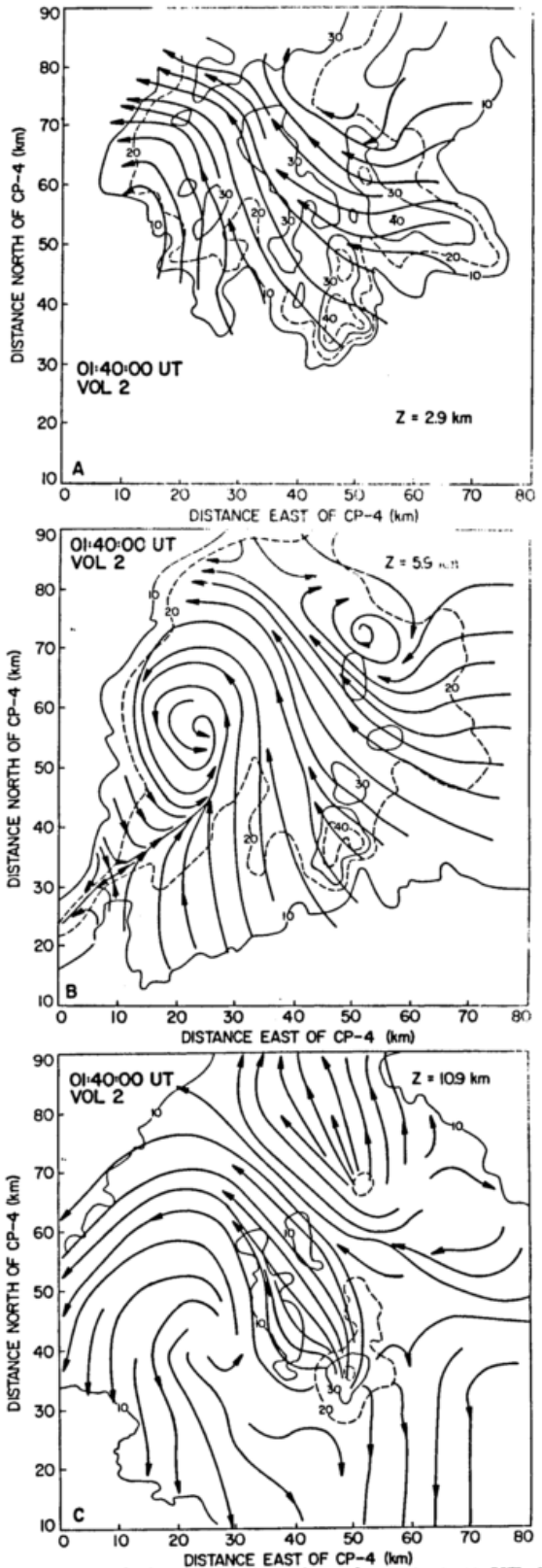


Fig 1. Storm-relative streamlines for volume 2, 0140 UT. Radar reflectivity background in dBz. A) 2.9 km MSL. B) 5.9 km MSL. C) 10.9 km MSL.

1. Radius of circle with mean vorticity $> 2 * 10^{-3} s^{-1}$.
2. Radius of circle with mean vorticity minus one standard deviation greater than zero.

It was hoped that the first definition will identify the areas where strong vorticity is concentrated, while the second definition would indicate the area of more homogeneous vorticity. The calculated radii are given in table 1. The last volume scan presented some problems in that there are two centers of cyclonic vorticity at lower levels, but here we allowed the circulations to

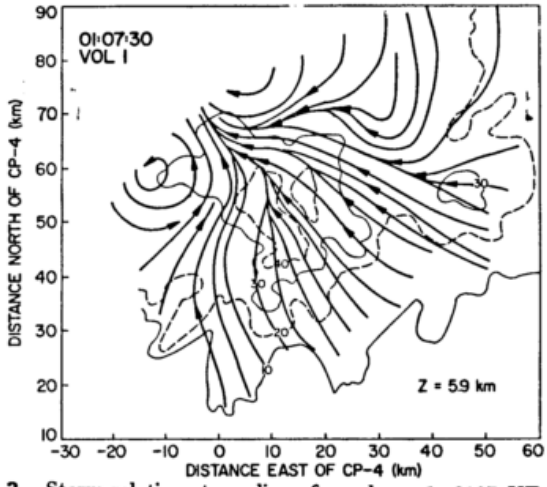


Fig 2. Storm-relative streamlines for volume 1, 0107 UT. Radar reflectivity background in dBZ. 5.9 km MSL.

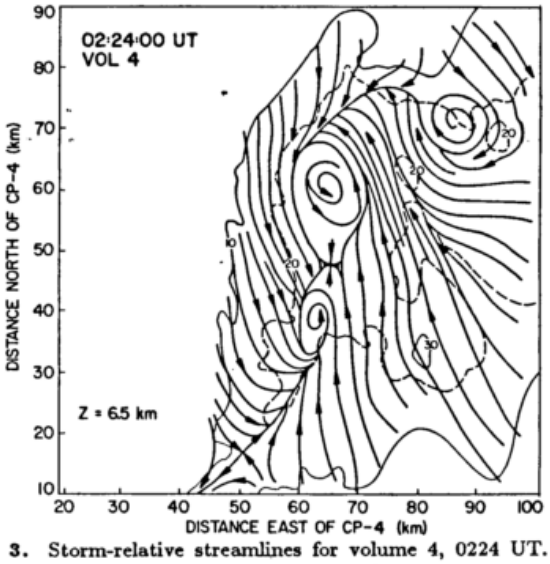


Fig 3. Storm-relative streamlines for volume 4, 0224 UT. Radar reflectivity background in dBZ. 6.5 km MSL.

TABLE 1

Radii of circulation (km) Definition 1.

Height	01:07	01:40	02:03	02:24a	02:24b
2.9	5	-	-	8	15
3.9	7	14	10	8	12
4.9	12	13	12	11	6
5.9	12	11	12	11	6
6.9	11	7	9	11	7
7.9	7	5	-	8	8
8.9	5	4	-	-	-

Radii of circulation (km) Definition 2.

Height	01:07	01:40	02:03	02:24a	02:24b
2.9	6	13	8	8	7
3.9	7	16	10	8	5
4.9	11	16	11	8	5
5.9	12	17	12	9	4
6.9	12	20	20	11	8
7.9	12	21	23	13	14
8.9	14	21	20	22	20
9.9	-	22	20	21	
10.9	-	17	18	14	
11.9	-	13	17	-	

overlap, and at higher levels to have the same center. It can be seen that the strong vorticity tended to be concentrated in the mid layers of the troposphere from 3.9 to 6.9 km, and that the circulation spread higher into the cloud with time.

To determine the dynamic size of the circulation, we calculated the Rossby radius of deformation λ_R (Frank, 1983), using the circulation as defined by the second definition at 0140 UT. Using the moist Brunt-Väisällä frequency we calculated λ_R to be about 35 km. When using the dry Brunt-Väisällä frequency the λ_R is even larger, thus indicating that this is a short lived

dynamically small circulation where the vertical thermal instability is more important that the rotational instability (Cotton and Anthes, 1988).

Next the average vertical velocity in the vortices was calculated. Results are presented in table 2 for the circulation as defined by the first definition. It can be seen that the center of strong vorticity in the cyclonic vortex was dominated by an updraft at the early volume scan, but that the lower levels turned to downdrafts as time progressed. The anticyclonic center however was characterized by downdrafts from the earliest times. Using the second definition (data not shown), a similar pattern was found at lower levels, but since these define the vortex to much greater heights, it was possible to see that both circulations was characterize by anarea of mesoscale ascent ($\sim$ 20 cm$\leq^1$) at the upper levels.

TABLE 2
Average vertical velocity (m s^{-1})

Height	01:07	01:40	02:03	02:24a	02:24b
1.9	-	-	-	-	-
2.9	2.0	-	-	-6.6	-4.4
3.9	1.7	-1.0	-0.5	-1.7	-5.6
4.9	0.9	-0.5	-0.6	-1.2	-3.4
5.9	1.2	0.0	0.1	-0.5	-1.9
6.9	1.2	0.4	0.6	-0.1	-0.7
7.9	1.4	0.5	-	0.3	-0.3
8.9	1.6	0.6	-	-	-
10.9	-	-	-	-	-

A vorticity budget calculation was also performed for the cyclonic vortex in volumes 1 and 3. The vorticity tendency equation was divided into the a) horizontal advection term, b) vertical advection term, c) the tilting term and the stretching term. These terms and their sum, the vorticity tendency, were calculated for each grid point, and then averaged over the circulation as defined by definition 2. Results are presented in fig 4a,b. From fig 4a we can see that except for the lower layer the vorticity tendency was positive throughout the vortex. This agrees with the observation that the vortex intensified to volume 2. We can see that the tilting term contributed positive vorticity throughout the vortex, and that advection terms contributed positively at higher levels. The stretching term at mid levels and the advection terms at lower levels opposed the positive vorticity tendency. The vorticity tendency at a later stage (fig 4b) is negative, except for the 5.9 km level. At this stage only the stretching and vertical advection terms have positive tendencies at mid levels, while the tilting and vertical advection terms are still positive in the upper levels of the cloud. This would indicate that the vortex is in a decay stage, and that vorticity is being concentrated in smaller vortices.

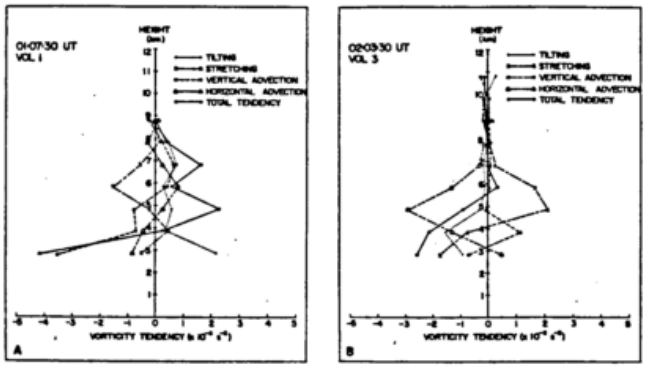


Fig 4. Vorticity tendency due to stretching, tilting, horizontal and vertical advection, and the total tendency as the sum of the other. A) Volume 1, 0107 UT. B) Volume 3, 0203 UT.

5 Summary

A vortex that developed in the trailing anvil of a multi-cellular convective storm has been described. It does not fit the description of any other vortices described in literature. Physically it is bigger than that described in the rotating thunderstorm theory, and it is not associated with the main updraft in the storm. It does however bear resemblance to the vorticity patterns that is predicted in the rotating thunderstorm theories for a similar environmental shear profile, with the cyclonic vortex favored over the anticyclonic vortex. The vortex couple are not observed to be diverging, but rather stay in the same relative position to each other. They are aligned perpendicular to the storm-relative low-level inflow into the storm. Dynamically it is much smaller that the inertially stable vortices observed in MCC's, and it extends through the depth of the cloud, which is contrary to the vertically stacked cyclonic/anticyclonic couplet that is observed at the later stage in the life of MCC's. It appears that the tilting of horizontal vorticity into the vertical is the initial source for vertical vorticity generation, and that at later stages the stretching term dominate. Evaluation of the large scale flow patterns from the sounding network at 0030 UT show no impact of this vortex on the large scale, but rather show an area of anticyclonic vorticity due to the development of the rear inflow into the MCC to the north. It is however thought that this vortex might provide insight in the interaction between convective storm and MCC scale interaction.

6 Acknowledgements

The author JV was supported for his graduate studies by the Weather Bureau of South Africa. The research was supported by the NSF grant ATM-8512480. Some computations were performed at NCAR. NCAR is supported by the NSF. Numerous personnel at NCAR provided helpful assistance.

References

Bosart, L.F. and F.Sanders, 1981: The Johnstown Flood of July 1977: A Long-Lived Convective System. *J. Atmos. Sci.*, **38**, 1616-1642.

Cotton W.R. and R.A. Anthes, 1988: The Dynamics of Clouds and Precipitating Mesoscale systems. To be published. *Academic Press, Inc.*

Frank, W.M., 1983: The Cumulus Parameterization Problem. *Mon. Wea. Rev.*, **111**, 1859-1871.

Fritsch, J.M. and C.F. Chappel, 1980: Numerical Prediction of Convectively Driven Mesoscale Pressure Systems. Part I: Convective Parameterization. *J. Atmos. Sci.*, **37**, 1722-1733.

Johnson, R.H., 1986: The Development of Organized Mesoscale Circulations within Oklahoma-Kansas PRE-STORM Convective Systems. *Preprints Int. Conf. on Monsoon and Mesoscale Meteor.*, Taipei, Taiwan.

Johnston, E.C., 1982: Mesoscale Vorticity Centers Induced by Mesoscale Convective Complexes. *9th Conf. on Wea. Forecasting and analysis.*, Seatle, WA. Amer. Meteor. Soc., 196-200.

Klemp, J.B., 1987: Dynamics of Tornadic Thunderstorms. *Ann. Rev. Fluid Mech.*, **19**,369-402.

Leary, A.L., and E.N. Rappaport, 1987: The Life Cycle and Internal Structure of a Mesoscale Convective Complex. *Mon. Wea. Rev.*, **115**, 1503-1527.

Lin, M.S., 1986: The Evolution and Structure of Composite Meso-α-Scale Convective Complexes. Ph.D. Dissertation, Colorado State University, Dept. Atmos. Science, Ft Collins, C0 80523.

Maddox, R.A. 1983: Large-scale Meteorological Conditions Associated with Midlatitude, Mesoscale Convective Complexes. *Mon. Wea. Rev.*, **111**, 1475-1493.

MELTING LAYER STRUCTURE IN MCC STRATIFORM PRECIPITATION

Paul T. Willis
NOAA/AOML HRD
Miami, FL

and

Andrew J. Heymsfield
NCAR
Boulder, CO

1. INTRODUCTION

This study examines the aircraft observations and theoretical evolution of particles above, through, and below the melting layer in the stratiform region of a mesoscale convective complex which occurred on 10/11 June 1985 during the Oklahoma Kansas Pre-Storm Experiment. The microphysical and thermodynamic measurements not only allowed us to characterize the particle evolution, but also enabled us to compare them with the computed theoretical evolution of the particles in the melting layer, and to quantify the heating and cooling rates through the layer.

2. THE FLIGHT PROFILE AND INSTRUMENTATION

The flight pattern flown was an advecting spiral descent as shown in Fig. 1. The descent rate was adjusted through the profile to approximately correspond to the typical particle fall speeds (1 m s^{-1} above the melting layer and increasing to 5-7 m s^{-1} below).

3. OBSERVATIONS

The temperature and dew-point temperature profiles through the melting layer measured by the aircraft are shown in Fig. 2. There is a nearly "isothermal layer" close to 0°C, but at a mean temperature of about +0.5°C (4122 - 3752m), with fluctuations from near 0°C to just slightly over +1.0°C. There could be a +0.5°C temperature error, but we think that the +0.5°C temperature of the "isothermal layer" is correct because an independent observation of the onset of melting from the particle image data is just below the top of this "isothermal layer". The aircraft 1 s mean vertical winds observed during the descent support the supposition of decoupling of the layers above from those below the melting layer. The high frequency fluctuations are indicative of the level of turbulence.

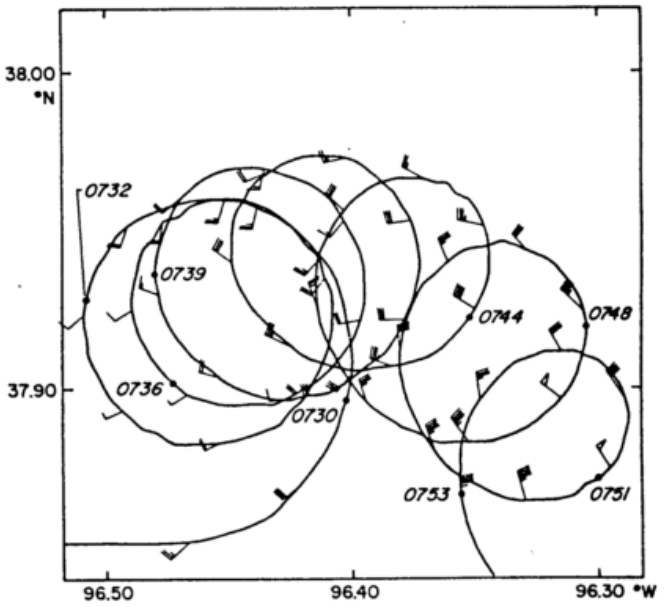


Fig. 1 Advecting spiral descent on 11 June 85.

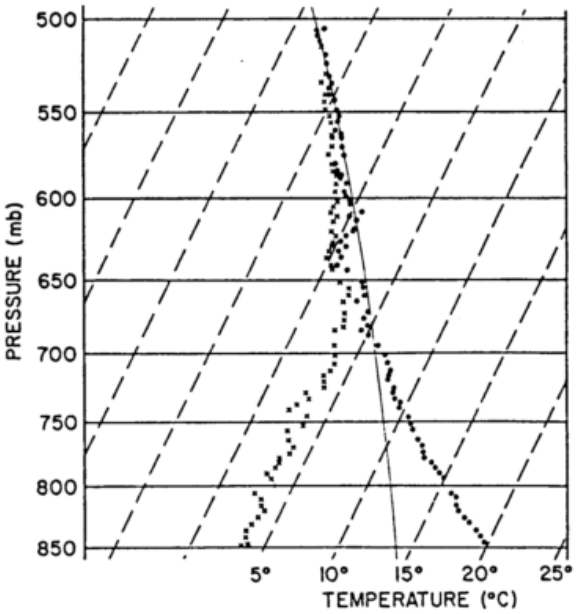


Fig. 2 Aircraft T/T_d skew-T sounding 0740 UTC.

A very high vertical resolution radar profile through the melting layer was constructed (Fig. 3) by averaging the data from the second and third radar range gates from the 3-cm tail radar as it looked horizontally from both sides of the aircraft. The peak in the reflectivity is at 3650 m. There is a

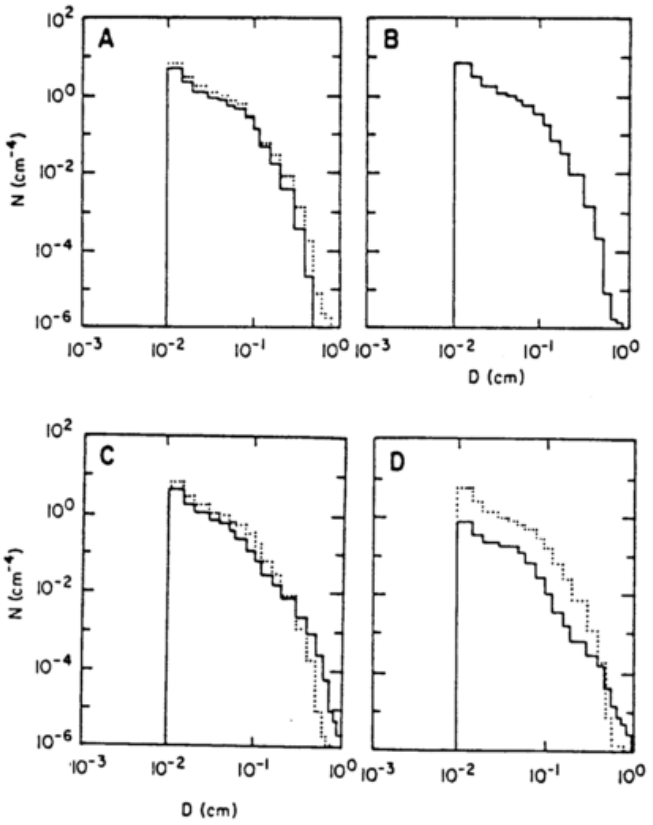


Fig. 4 Particle number density spectra where D is the maximum particle dimension
A.-6.3 to -3.2°C B.-3.1 to -0.9°C
C.-1.1 to 1.1°C D. 0.5 to 5.2°C.

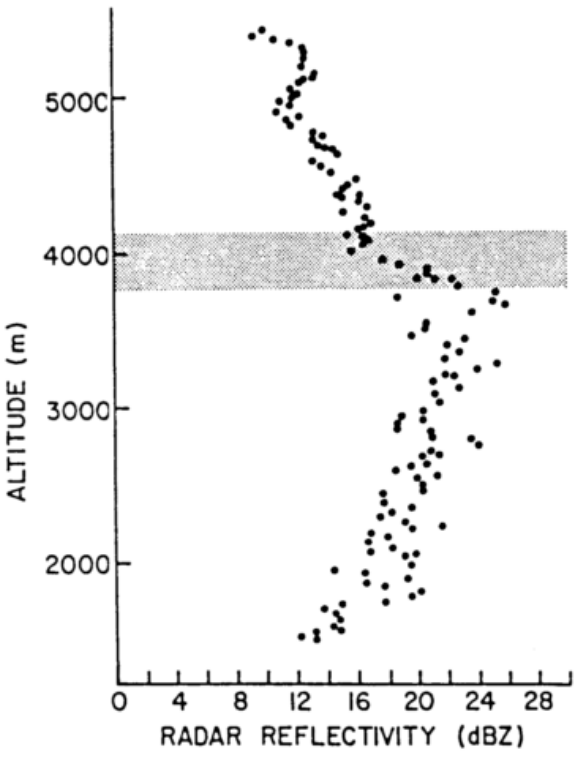


Fig. 3 3 cm tail radar reflectivity profile - shading marks the isothermal layer.

suggestion of a second reflectivity maximum near 3300 m. This secondary maximum is in agreement with the height of the reflectivity peak observed in profiles from tail radar range gate data, and with a profile constructed from the 5-cm lower fuselage radar data. The tail radar reflectivities are accurate to within +/- 2 dBZ based on a comparison with the NCAR CP-4 radar.

Particle-size spectra were assembled in approximately 2°C vertical increments to show the evolution of the distributions through the spiral descent (Fig. 4). From the top of the spiral down to the top of the "isothermal layer" (Fig. 4a-c) the size spectrum broadens due to the formation and growth of aggregates. At the same time, the concentration of small crystals remains nearly constant, or even shows a slight increase (Fig. 5). The concentrations of particles larger than 1.9 mm increase markedly, by about an order of magnitude, in this layer. The particle habits indicate that this growth is due to aggregation of smaller individual crystals, plates and dendrites. Yet, the concentration of these smaller size particles remains nearly constant, or even increases slightly.

In the "isothermal layer" the larger particles continue to grow. The concentrations of large-size particles (Fig. 4c) increase dramatically. The total particle concentration and the concentration of small particles (Fig. 5) decrease dramatically. The size of the largest observed particle D_{max} increases by a factor of two in this layer (Fig. 6).

Directly below the base of the "isothermal layer" the concentration of large-size particles decreases markedly, and yet the very largest aggregates maintain their size, or even continue to grow. D_{max} indicates continued growth through collection, or aggregation, down to 3600 m. This is consistent with the reflectivity profiles that show reflectivity maxima below the "isothermal layer." Below the "isothermal layer" cloud droplets virtually disappear, and the precipitation particle spectra conform to classical rain distributions, but with a few very large partially melted aggregates surviving.

Ice water content profiles were derived from the image data and radar data. The mean

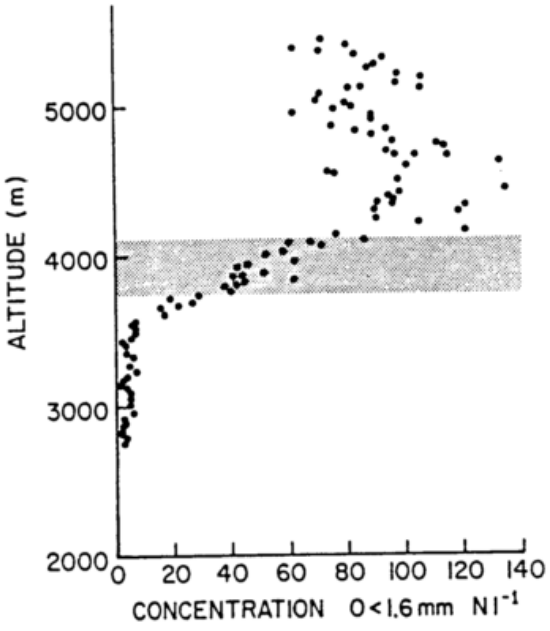


Fig. 5 Particle concentrations D < 1.6 mm ECD.

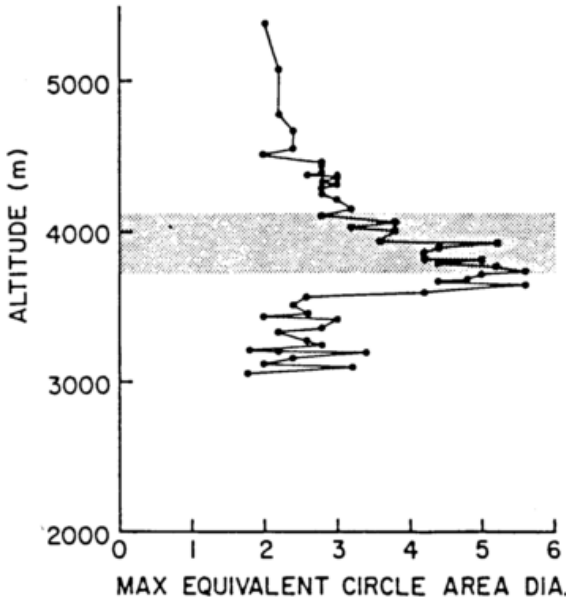


Fig. 6 Maximum ECD in each 10s data summation.

ice water contents above the melting layer are ~ 3 times the liquid water contents just below the melting layer (4.1 km). The ice water content is about 0.4 gm^{-3} near the top of the melting layer. Using a total melting layer depth of 700 m, the computed mean cooling for the layer is 0.224°C.

4. THEORETICAL CALCULATIONS

The evolution of the particle-size spectrum is calculated for levels above, within, and below the melting layer using a theoretical model. Growth/evaporation through diffusion is calculated for the two relative humidities of 100% and 97%. Calculations are made to illustrate the additional survival distance of aggregates below the melting layer. The model is used to illustrate several important microphysical processes in the melting layer. The model calculations show the importance of aggregation to the large particle concentrations in the melting layer. The model calculations of ice water content versus altitude previously described allow us to calculate the heating and cooling rate profiles. These calculations show that above the "isothermal layer" a significant heating occurs due to vapor deposition on the growing ice particles. Within the "isothermal layer" nearly all of a significant amount of cooling takes place in a very thin layer near the onset of melting. This is a consequence of the large fraction of the ice mass contained in the sublimation size particles which melt quickly upon reaching the "isothermal layer".

5. CONCLUSIONS

Measurements and calculations above, in, and below the melting layer have shown that:

- o The layer over which some melting takes place is much deeper than the "isothermal layer". Some large aggregates reach +5°C, and warmer, as ice.
- o The onset of melting is near the top of the "isothermal layer", and most of the mass is melted. Consequently most of the cooling occurs wholly within the "isothermal layer", which is slightly warmer than 0°C.
- o The production of very large aggregates is dramatic after the onset of melting, due both to a melting-induced increase in the terminal velocity difference between similar size hydrometeors, and to enhanced sticking.
- o The radar reflectivity maximum (bright band) is due to these relatively few, very large aggregates that survive to warmer temperatures, and is depressed well below the base of the "isothermal layer".
- o In this case the layers below the melting layer appear to be decoupled from those above.
- o Small crystals are being replenished above the "isothermal layer" apparently due to a fragmentation or breakup process.

DUAL-DOPPLER AND AIRBORNE MICROPHYSICAL OBSERVATIONS IN THE STRATIFORM REGION OF THE 10-11 JUNE MCS OVER KANSAS DURING PRE-STORM

S.A. Rutledge[1], R.A. Houze, Jr.[2], A.J. Heymsfield[3] and M.I. Biggerstaff[4]

[1] Department of Atmospheric Sciences, Oregon State University, Corvallis, OR 97331;
[2,4] Department of Atmospheric Sciences, University of Washington, Seattle, WA 98195;
[3] NCAR P.O. Box 3000, Boulder, CO 80307

1. INTRODUCTION

During May-June 1985 the PRE-STORM (Preliminary Regional Experiment for the Stormscale Operational and Research Meteorology Program-Central Phase) Project was conducted, focusing on Mesoscale Convective Systems (MCS's) as they passed over the Great Plains. The particular case we study herein is the 10-11 June 1985 storm. This storm was characterized by a line of convection trailed by a broad region (~100 km) of stratiform rain. We examine the kinematic and microphysical structure of the trailing stratiform region through dual-Doppler and airborne observations.

2. DUAL-DOPPLER OBSERVATIONS

We discuss the dual-Doppler analysis at 0345 Z on 11 June. At this time the storm was in it's mature phase, shortly after which the convective region weakened. This time corresponds to in-situ airborne observations of particular interest. The dual-Doppler data were obtained from the network located in Kansas, consisting of the NCAR (National Center for Atmospheric Research) CP-3 and CP-4 5 cm radars. Overview details of the techniques used in the dual-Doppler analysis are given in Biggerstaff et al. (this volume). The horizontal flow structure relative to the storm is shown in Figs. 1a-c. The bulk of the convective region had moved out of the domain at this time. The low-level flow (Fig. 1a) was parallel to the convective line, especially in the transition zone and the leading portion of heaviest stratiform precipitation (defined by x=-30 to x=30 km). Strong outflow at the rear of the stratiform precipitation zone was present. This outflow is fed by air entering the rear of the system at upper levels and subsiding in a strong mesoscale downdraft. At 3.9 km (Fig. 1b) the flow was rear-to-front, but again became parallel to the convective line in the transition region. Rear-to-front flow has been previously identified by Smull and Houze (1985). At upper levels (Fig. 1c) the flow had a strong front-to-rear component. This flow transports ice produced in the convective region into the stratiform region which plays an important role in the water budget of the stratiform region (Rutledge and Houze, 1987).

Mean vertical cross-sections for the region bounded by y=-30 to y=30 km are shown in Fig. 2. The reflectivity field (Fig. 2a) is characteristic of stratiform precipitation (note distinct bright band structure). The transition zone is seen as a low-level depression in reflectivity (x=30 to x=55 km). The relative flow perpendicular to the convective line (Fig. 2b) clearly shows the rear inflow layer (shaded). Front-to-rear flow (right to left) above the rear inflow layer is deep and rather uniform with height. The mean vertical velocity (Fig. 2c) shows deep mesoscale lifting throughout the cross-section with speeds to 50 cm/s, and a well-defined mesoscale downdraft of comparable magnitude. The mesoscale downdraft is broad, interrupted only near x=0 by weak upward motion. The mesoscale downdraft gives way to deeper and stronger subsidence in the transition zone resulting from evaporatively driven downdrafts at mid- to low-levels and by the merger of outlows from the upper parts of convective cells with environmental flow near the tropopause (see Biggerstaff et al. this volume). The stronger subsidence in this region may be partly responsible for the observed precipitation minimum in the transition zone. The top of the mesoscale downdraft is roughly associated with the top of the rear inflow jet, at least for x<0 km, suggesting a close link between the penetration of dry air into the rear of the storm and mesoscale subsidence.

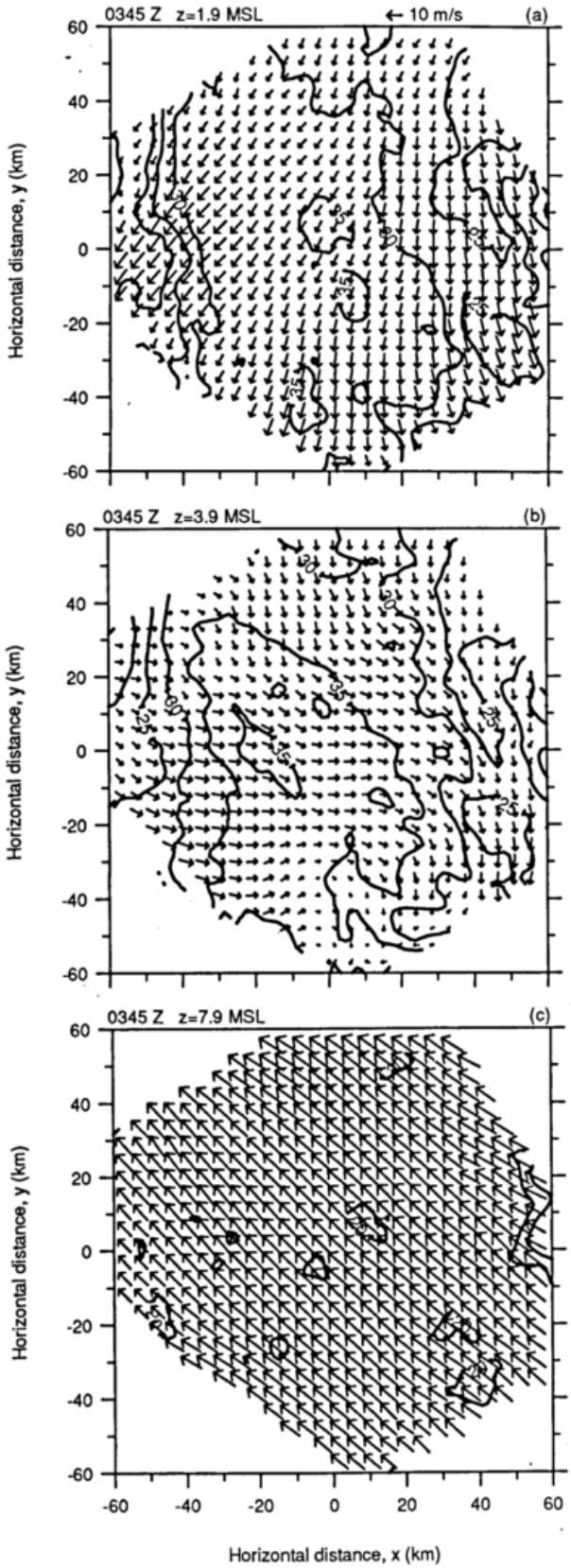


Fig. 1. Relative flow and reflectivity (dBZ) for 0345Z on 11 June 1985. a) z=1.9 km MSL. b) z=3.9 km MSL. c) z=7.9 km MSL.

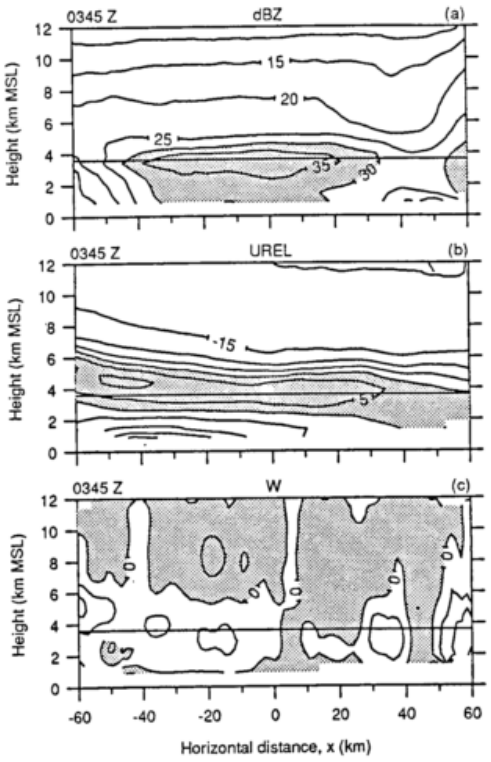


Fig. 2. Mean cross-sections for the region bounded by y=−30 to y=30 km. a) Reflectivity, >30 dBZ shaded. b) Reflective flow perpendicular to convective line. Shading denotes flow from left-to-right. Contour interval is 5 m/s. c) Vertical velocity. Shading denotes upward motion. Contour interval is 50 cm/s. The melting level is denoted by the horizontal line at 3.6 km.

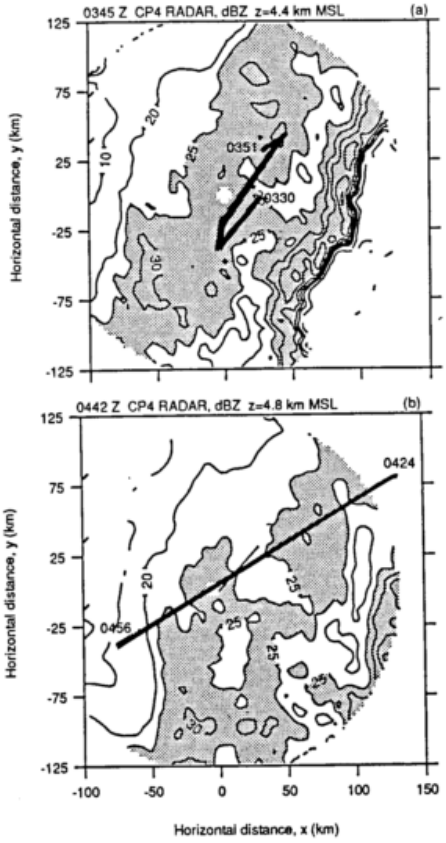


Fig. 3. Reflectivity and aircraft flight tracks. a) dBZ for 0345Z at 4.4 km MSL; NOAA 43 flight track. b) dBZ for 0442Z at 4.8 km MSL; NOAA 42 flight track. Reflectivities > 25 dBZ are shaded.

3. AIRBORNE OBSERVATIONS

Both NOAA (National Oceanic and Atmospheric Administration) WP-3D aircraft obtained in-situ microphysical observations in the trailing stratiform region. From these data mixing ratios for ice were then derived. Particle sizes and habits were determined using the 2-D PMS cloud and precipitation probes. The data collection is summarized by discussing ice water contents and particle habits along the aircraft flight tracks. Two periods of observations are discussed: 0330 to 0351 Z by NOAA 43, consisting of an ascending path from 4.0 to 5.4 km situated along the leading edge of the band of most intense stratiform rain (Fig. 3a); 0424 to 0456 Z by NOAA 42 consisting of a level pass through the stratiform region at 4.8 km MSL (Fig. 3b). The microphysical observations are summarized in Tables 1 and 2.

The observations from NOAA 43 near the transition zone indicate a sharp increase in IWC with height. The marked increase at 0339 Z, with nearly a doubling of the IWC, is associated with the aircraft's ascent through the top of the rear inflow layer, or into the ice-laden front-to-rear flow (Fig. 2b). Particle types were predominantly aggregates of unidentifiable particles, consistent with ice particles produced in convective cells. The increase in IWC with height may also be a result of intense sublimation in the transition zone caused by strong downdrafts (see Fig. 2c).

The microphysical results for NOAA 42 indicate a fairly uniform IWC with the exception of the end of the leg, at which point NOAA 42 passed through the back edge of the intense stratiform precipitation, below the base of the deep stratiform cloud. Particle types were predominantly aggregates of dendrites. Evidently the dendrites were produced above this level (near -14 °C, z=6 km) then drifted downward and aggregated at lower levels. This indicates particle nucleation and growth in the mesoscale updraft. The presence of needles also is an indicator of nucleation in the mesoscale updraft, immediately above flight level. Particle observations also indicated riming growth may have been present. Peak updrafts approached 1 m/s in the stratiform region, which would have generated supercooled water.

Table 1. Ice water contents and particle habits for 0330-0351Z from NOAA 43.

Time (Z)	T (°C)	IWC(g/m^3)	HABITS
0330	-1.0	0.2	Giant* aggregates
0333	-0.3	0.5	"
0336	-0.7	0.6	Large* aggregates
0339	-2.3	1.3	"
0342	-3.6	1.3	Small* aggregates
0345	-3.5	1.9	Small aggregates, needles
0348	-5.1	1.7	"
0351	-6.8	1.4	"

*Giant D > 1 cm; large D > 5 mm, small D < 5 mm.

Table 2. Ice water contents and particle habits for 0424-0456Z from NOAA 42.

Time (Z)	T (°C)	IWC(g/m^3)	HABITS
0424	-4.4	0.89	Aggregates of dendrites, needles
0428	-4.2	1.34	"
0431	-3.6	1.41	Some needles, aggregates
0434	-3.8	1.81	Aggregates, lightly rimed
0437	-3.4	1.25	"
0440	-3.5	1.63	"
0443	-3.2	1.23	Aggregates of dendrites
0446	-2.7	1.37	"
0449	-2.5	1.24	Some dendrites, possible riming
0452	-3.4	0.10	Aggregates, some dendrites
0456	-3.8	0.01	

4. CONCLUSIONS

Dual-Doppler observations revealed three distinct flows in this storm: front-to-rear flow at low levels, strong rear-to-front flow at mid-levels, and deep front-to-rear flow aloft. The rear inflow was responsible for intense sublimation and evaporation at low levels, which resulted in a strong mesoscale downdraft. The front-to-rear flow evidently transported ice particles into the trailing region. Particle observations in the stratiform region indicated in-situ production of ice particles by the mesoscale updraft.

ACKNOWLEDGEMENTS. This research was supported by a series of grants from the National Science Foundation including ATM–8413546, ATM-8521403, ATM–8602411 and ATM–8608467. NCAR is sponsored by the National Science Foundation.

REFERENCES

Biggerstaff, M.I., R.A. Houze, Jr., and S.A. Rutledge, 1988: Vertical drafts in the convective regions of Mesoscale Convective Systems in Kansas. (This preprint volume).

Rutledge, S.A., and R.A. Houze Jr., 1987: A diagnostic modeling study of the trailing stratiform region of a midlatitude squall line. *J. Atmos. Sci.*, **44**, 2640-2656.

Smull, B.F., and R.A. Houze Jr., 1985: A midlatitude squall line with a trailing region of stratiform rain: Radar and satellite observations. *Mon. Wea. Rev.*, **113**, 117-133.

VERTICAL DRAFTS IN THE CONVECTIVE REGIONS OF MESOSCALE CONVECTIVE SYSTEMS IN KANSAS

M.I. Biggerstaff and R.A. Houze, Jr.
University of Washington
Seattle, Washington 98195

S.A. Rutledge
Oregon State University
Corvallis, Oregon 97331

1. Introduction

Several mesoscale convective systems (MCS'S passed through the observational network of the Stormscale Operational and Research Meteorological Program—Central Phase (PRE-STORM). These storms were typically characterized by a line or region of convection, an associated area of stratiform precipitation and distinct mesoscale motions. Two cases, which passed over Kansas on 10-11 June and 28 May 1985, were examples of midlatitude squall lines with trailing regions of stratiform precipitation. The general structural features and single-Doppler radar kinematic analyses emphasizing the mesoscale circulations of these two cases have been presented by Smull and Houze (1987) and Rutledge *et al.* (1988). The third case (3-4 June 1985) contained a more varied pattern of convection which formed into lines for only a brief period and had stratiform rain confined mainly to the northern portion of the system. In this paper, we focus on the convective-scale motions and present results derived by dual-Doppler analysis of the PRE-STORM radar data in these three observed mesoscale systems. We investigate specifically the spatial arrangement and intensity of the updrafts and downdrafts in the convective regions of these storms.

2. Data and method of analysis

All data were obtained with two National Center for Atmospheric Research (NCAR) 5-cm wavelength Doppler radars (CP3 and CP4), which were deployed near Wichita, Kansas, with a 60 km north-northwest/south-southeast baseline. The radars were operated in coordinated sequences of elevation angles, either over 360° in azimuth or over smaller limited area sector scans (Rutledge *et al.*, 1988). We use only the 360° scans in this paper. Several sector scans were also analyzed but led to no significant differences in results. The 360° scans provided regions of dual-Doppler analysis both east and west of the baseline.

For both the 28 May and 10-11 June cases, radar data were collected from 0.2 to 58.0° in elevation. Convective cells were well sampled at the tops, thus allowing an upper boundary condition to be applied in integrating the anelastic continuity equation downward to obtain the vertical velocity. A boundary condition of 0.1 to 0.25 m/s in the convective region and zero elsewhere was used for all of the volumes analyzed for these two days. Values ranging from zero to 2.0 m/s in the convective region and zero to 0.5 m/s elsewhere were tested. The results were not very sensitive to the choice of boundary condition except for the extreme cases. Also, "sponge depths" (in which the initial vertical velocity is determined by multiplying the upper most measured divergence by the depth of the sponge—Knupp, 1987) have been tested for depths of 0.1 to 1.0 km . The mean vertical velocities were relatively unaffected by sponge depths < 0.5 km, but large vertical drafts at upper levels appeared as a result of the boundary condition calculation. This method thus tends to overemphasize the role of the upper-level divergence, which is generally not well sampled and could be affected by sidelobes. By using a near zero but slightly positive vertical velocity as the boundary condition, any significant drafts that are computed are the result of integrating over a fairly deep layer rather than overemphasizing the upper-level divergence.

During 3-4 June, the radars scanned to only 28.0°. For that case, we used between 0.25 and 0.50 m/s in the convective region and zero elsewhere.

As a further check on the vertical velocity calculation, a lower boundary condition was applied to the data after the divergence had been integrated. Since none of the analyses contained data extending to the ground, we took 67% of the residual mass flux in grid columns extending to 500 m above the ground and 33% of the residual mass flux in grid columns extending to only 1 km above the ground. No adjustment was made in columns terminating before 1 km above ground. Thus, only about 70% of the data was adjusted. The divergence was recomputed with the amount of adjustment increasing with height. Then, the adjusted convergence was integrated to

obtain the adjusted vertical velocity. The net result of this adjustment scheme was to reduce the strength of the low-level downdrafts. The upper-level downdrafts were less sensitive to the adjustment. But in some cases they were slightly increased to compensate for low-level updrafts. Since there is evidence that a significant amount of divergence can occur within the lowest 500 m of the atmosphere in convective systems (e.g., Wilson *et al.*, 1984), we consider those results to be less realistic than those shown in here. Moreover, the basic strucutre of vertical drafts were relatively unaffected by this adjustment scheme.

All data were adjusted in position according to the observed mesoscale system motion to a central analysis time to account for the time interval required to collect a full 360° scan. The data were thus shifted a maximum horizontal distance of about 4 km. Horizontal velocities were filtered to remove wavelengths less than 6 km to ensure that this data "advection" did not bias our results. The filtering is also consistent with the upper-level horizontal resolution of the data. The time interval required to complete a full 360° elevation-angle sequence (≈ 10 min) is a major limitation in the data set. However, since results using the smaller sector scans, which took only 6 min to complete did not show any major differences in the structure of vertical drafts, we are confident in the results obtained from the 360° scans.

3. Results

Figures 1 and 2 show typical cross sections normal to the convective line for the two squall-line cases. In both of these systems, a mesoscale area of ascent 20-40 km across and hundreds of kilometers long was observed ahead of and in the zone of highest reflectivity. Fairly continuous enhanced updrafts (>3 m/s) were located within this region and were confined mainly to the area defined by the reflectivity cells. These updrafts generally increased in area and usually tilted upshear with height. Within this fairly continuous sloped convective updraft, separate cores of stronger vertical motion were observed. These cores formed a stair-stepped pattern within the general updraft. The maximum vertical velocities of these cores tended to increase with height. Peak updraft speeds from 10-20 m/s were typically found between 8 to 10 km MSL, although strong updrafts were also found at mid-levels probably associated with the development of new cells at the leading edge of the convective line (e.g. x = 26 km, Figure 2).

Figure 3 shows a vertical cross section through a convective cell in the 3-4 June case. The absence of a broad region of ascent at low to mid levels in Figure 3b may be due to the more varied organization of the convective cells in this storm compared to the 28 May and 10-11 June squall line systems. However, the general structure of the updraft from mid to upper levels was similar to that of the other two cases. The same stair-stepped structure of the enhanced updraft cores was evident.

Each of the systems also exhibited mid to low level convective downdrafts, probably associated with precipitation loading and evaporative cooling, usually within or upshear of the maximum reflectivity core. As illustrated in Figs. 1-3, these low-level downdrafts were several kilometers across and had peak values between 3 and 5 m/s, located within one or two km from the ground. The characteristics of similar low-level downdrafts have been documented by Knupp (1987).

In addition to downdrafts at low levels, convective downdrafts were also observed at upper levels on both sides of the peak reflectivity cores in all three of these systems. These upper-level downdrafts were usually weaker and shallower than the low level downdrafts. Speeds from 1 to 3 m/s and depths from 2 to 4 km were typical. The strongest of these upper-level downdrafts tended to be located ahead of reflectivity cores that tilted downshear with height (Figures 1 and 3). Apparently similar behavior has been seen in recent model simulations of Rotunno *et al.* (1988). Occasionally, upper and lower downdrafts would appear to be vertically aligned (e.g., x = 12 km, Figure 2b), creating columns of downdrafts extending throughout the depth of the troposphere. This result does not imply that the trajectories of air parcels in these columns extended from upper troposphere to the ground. The horizontal velocities (not shown) were about three times as large as the vertical velocities in this region and the widths of these superimposed downdrafts were usually quite narrow.

4. Conclusions

In the three PRE-STORM cases considered here, the structure and types of vertical convective drafts were

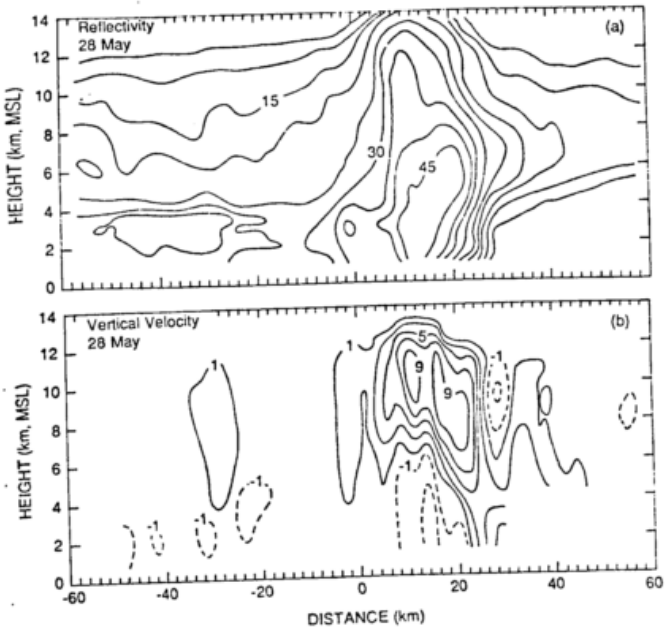


Fig. 1 Vertical cross section through 28 May 85 squall line at 1153 UTC. (a). Reflectivity every 5dBZ starting at 5dBZ. (b). Vertical velocity every 2 m/s from -11 to 11 m/s. Positive values are solid and negative values are dashed.

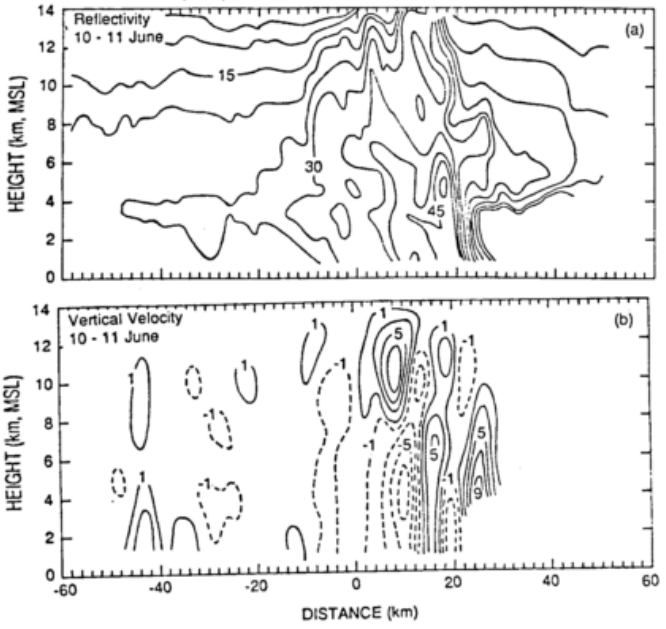


Fig. 2 Same as Fig. 1 except for 10-11 June 85 squall line at 0144 UTC.

very similar. In each case, three basic types of vertical drafts were observed in the convective region: a somewhat continuous tilting updraft, a low-level downdraft and an upper-level downdraft. The strengths and sizes of the vertical drafts varied from case to case and were three-dimensional in character. However, the tendency for the peak updraft to be between 8 and 10 km MSL and the peak low level downdraft to be within 2 km of the ground was common among all three systems.

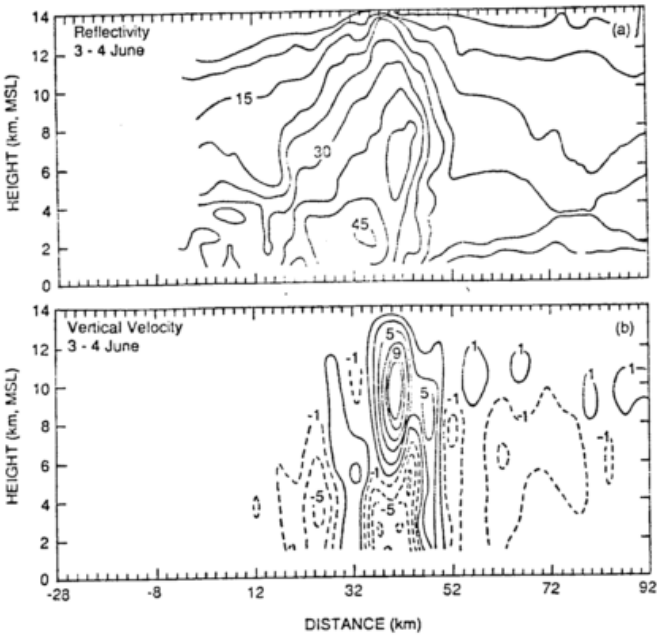


Fig. 3 Same as Fig. 1 except for 3-4 June 85 system at 0109 UTC.

Furthermore, the tendency for upper-level downdrafts to be located adjacent to and immediately ahead of downshear tilting reflectivity cores and for the deepest, strongest low-level downdrafts to be located within upshear tilting reflectivity cores was observed in all three systems.

Acknowledgements This research was supported by NSF grants ATM8413546, ATM8521403 and ATM8602411. NCAR provided partial support for the computing.

REFERENCES

Knupp, K.R., 1987: Downdrafts within High Plains cumulonimbi. Part I: General kinematic structure. J. Atmos. Sci., 44, 987-1008.

Rotunno, R., J.B. Klemp and M.E. Weisman, 1988: A theory for strong long-lived squall lines. Submitted to J. Atmos. Sci..

Rutledge, S.A., M.I. Biggerstaff and R.A. Houze, Jr., 1988: The Oklahoma-Kansas mesoscale convective system of 10-11 June 1985: Precipitation structure and single-Doppler radar analysis. Submitted to Mon. Wea. Rev..

Smull, B.F. and R. A. Houze, Jr., 1987: Rear inflow in squall lines with trailing stratiform precipitation. Mon. Wea. Rev., 115, 2869-2889.

Wilson, J.W., R.D. Roberts, C. Kessinger and J. McCarthy, 1984: Microburst wind structure and evaluation of Doppler radar for airport wind shear detection. J. Climate Appl. Meteor., 23, 898-915.

MESOSCALE PATTERNS OF ICE PARTICLE CHARACTERISTICS IN HURRICANE NORBERT

R.A. Houze, Jr.
University of Washington
Seattle, WA 98195

F.D. Marks, Jr., and R.A. Black
NOAA/AOML
Miami, FL 33149

1. Introduction

The precipitation in the inner-core region of a hurricane (i.e., the region within about 50-100 km of the of the eye) is characterized by a ring of heavy eyewall rain and a surrounding region of lighter stratiform precipitation. Marks (1985) and Marks and Houze (1987) have found that about 60 % of the inner-core precipitation falls in the surrounding annular zone of stratiform rain. Black and Hallet (1986) found that hurricanes are glaciated everywhere above the -5°C level and that convective updrafts in the eyewall region contain graupel along with some supercooled drops while convective downdrafts adjacent to the updrafts tend to be characterized by high concentrations of small ice particles, many of which are columns and needles. The stratiform areas are characterized by aggregated snowflakes. Columnar crystals are also found in the stratiform areas, but only within 10-15 km of convective updrafts. Black and Hallet surmised that much of the ice in the stratiform regions originates through secondary nucleation within the eyewall updrafts and is then redistributed throughout the storm by the upper and midlevel radial outflow component of the secondary circulation associated with the hurricane vortex. Marks and Houze (1987) have shown that the ice particles advected from the upper levels of the eyewall by the radial flow are carried as many as 1 1/2 times around the storm by the strong tangential flow (i.e. the primary circulation) of the vortex before they reach the melting level. Thus, ice particles generated in and detrained from the top of convection at a particular location along the eyewall form a slowly descending plume that spirals gradually outward from the eyewall while winding around the entire storm. In this way, convection at one point in the eyewall seeds the precipitation pattern in the annular region surrounding the eyewall.

Since ice-particle image data are typically collected along an aircraft flight path, and because the routes followed are usually designed to collect a variety of data, of which cloud microphysical measurements are only one part, the horizontal patterns of ice-particle data on which previous results are based have generally been determined only for limited areas of storms. To fill this observational gap, flights in Hurricane Norbert (which occurred off the west coast of Mexico in 1984) were conducted with one NOAA WP-3D aircraft dedicated to mapping the microphysical characteristics of the inner-core region of the storm at the 6 km level (0 to -10°C), which was the highest level at which the aircraft was able to fly on this occasion. (At the same time a second WP3D was operating at a lower level, collecting Doppler radar data to document the kinematic structure of the storm.)

The objectives of the study are to determine the horizontal distribution of ice particle types, concentrations and sizes throughout the inner-core region of the storm at the 6 km flight-level and to infer from these horizontal patterns the influence of the eyewall convection on seeding the annular region around the eyewall.

2. Data and methods of analysis

Two PMS probes were on the aircraft. The "precipitation probe" (2DP) has a diameter range of 0.2-6.4 mm in 0.2 mm steps, while the "cloud probe" (2DC) has a range of 0.05-1.6 mm in 0.05 mm steps. Particles were classified by size according to the equivalent circle diameters of the images on each probe. On the 2DC, the categories were: *2DC-small*— 0.05 to 0.5 mm; *2DC-medium*— 0.55 to 1.05 mm; and *2DC-large:* > 1.05 mm. On the 2DP, they were: *2DP-small*— 0.2 to 2 mm; *2DP-medium*— 2 to 4 mm; and *2DP-large:* > 4 mm. Many particles were observed in each of these size categories, except for 2DP-large, in which category only very few

particles were observed. The 2DC-medium and large particles were further subdivided according to particle shape. Particles for which the eccentricity of an ellipse fitted to the image was > 0.9 (length to width ratio ≈ 3.5:1) were called *columns*, since their images appeared qualitatively to be columnar crystals, while particles for which the eccentricity was < 0.4 were referred to as *nearly round* . Medium and large 2DC images not classified as either columns or nearly round appeared to have been aggregates of ice crystals. The nearly round particles appeared to have been graupel when seen in regions of active convection and aggregates when seen in stratiform regions devoid of significant liquid water.

Only a few images of drops were obtained at the 6 km level, and these were all found in crossings of the eyewall, where the flight-level temperature was maximum. No cloud-liquid water was observed with the Johnson-Williams probe except at these locations. Drops and all bad images as defined by Black and Hallet (1986) were deleted. In addition, "broken" images, which are said to occur if more than one shadow is found between time marks, were deleted.

The number concentrations of particles have been determined for each of the five size categories (2DC-small, medium and large, and 2DP-small and medium) and for the total of all particles seen on both the 2DC and 2DP. In addition, number concentrations of columns and needles (as defined above) were determined. Mass concentrations for the 2DC and 2DP data were computed using the equivalent circle diameters of the images and an ice-particle density of 0.1 g cm^{-3}.

The flight track of the upper-level aircraft consisted of a sequence of overlapping wedge-shaped circuits extending radially outward from the eye and covering all portions of the storm, but emphasizing the most active southwestern quadrant (see Houze *et al.*, 1985, for a map of the flight tracks). The mass and number concentrations were determined for finite increments of the flight path. The mesoscale variations of concentration appeared to be well represented by 5 km resolution data. Hence, a horizontal cartesian coordinate system centered on the storm was divided into a grid of 5-km square bins. Then each 5-km resolution data sample along the flight track was assigned to the cartesian bin in which it was centered. Mesoscale fields were then obtained by averaging all of the samples in each cartesian bin, and drawing contours to represent the gridded and averaged data. These fields are overlaid, for reference, on a pattern of radar reflectivity observed with the lower-fuselage radar of the lower-level aircraft.

3. Results

A measure of the characteristic particle size within

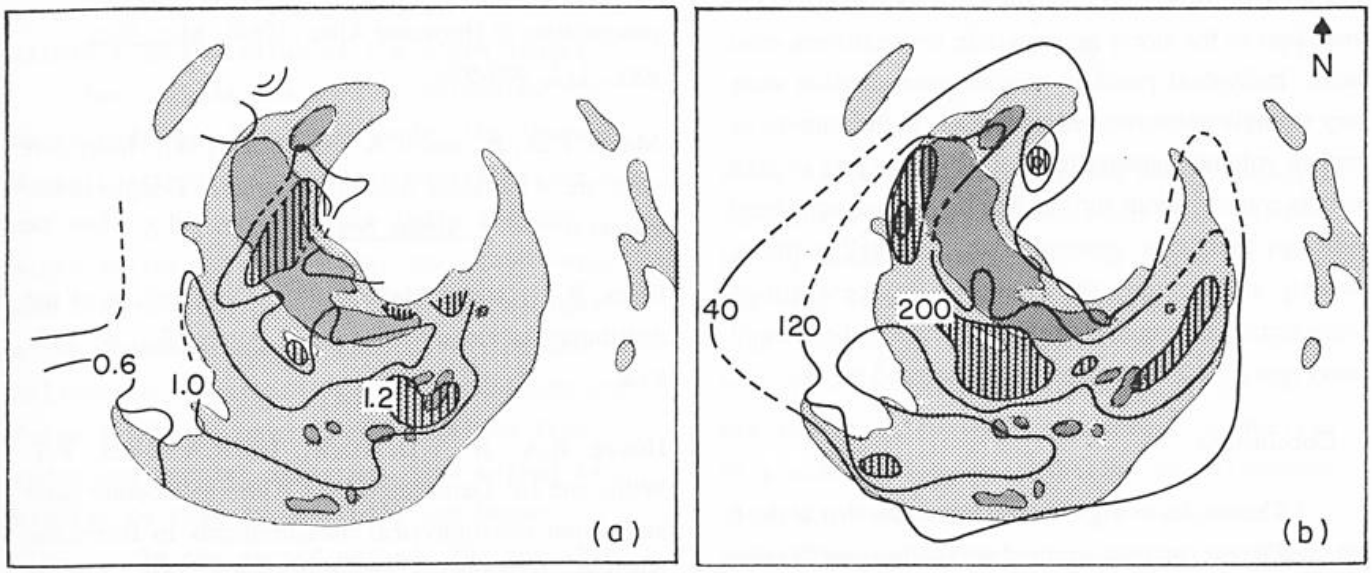


Figure 1. (a) Contours of median diameter of particles observed with the 2DC aboard the NOAA P3 aircraft in Hurricane Norbert shown by solid lines for values of 0.6, 1.0 and 1.2 (interior of 1.0 and 1.2 are hatched) mm. (b) Contours of 2DC particle concentration at the 6 km level shown by solid lines for 40, 120 200 and 280 (interior hatched) per liter. Particle images were obtained at the 6 km level between 0020 and 0420 GMT 25 September 1984. The contours are overlaid on a composite radar reflectivity pattern based on lower-fuselage radar data obtained from 00128-0215 GMT.

an observed population of particles is the *median volume diameter*, defined as the particle diameter that divides the number distribution in half. Isolines of median volume diameters of the size distributions measured by the 2DC probe is shown in Fig. 1a. A similar pattern was seen in the 2DP data, except that the median volume diameters were generally larger for the 2DP. The median volume diameter was highly correlated with radar echo intensity, more so than any of the other fields we derived from the PMS data. Separate elongated maxima of median volume diameter coincided with the eyewall eyewall radar echo surrounding the eye from northwest-southwest-southeast and the stratiform echo band located generally southwest of the eye. Thus, the both the eyewall echo band and the stratiform band were the loci of generally larger ice particles than elsewhere in the storm at the 6 km level.

The total number of particles, per unit volume of air, sampled by the 2DC are indicated in Fig. 1b. Since number concentrations are dominated by the smallest particles present, the 2DC concentrations were always larger than the 2DP, ranging between about 40 and 350 per liter, with typical values of 100 per liter, while the 2DP concentrations (not shown) were 10-70 per liter. The peak values of number concentration (on both the 2DC and 2DP) occurred in a ring surrounding but displaced 10-20 km radially outward from the eyewall radar echo band. A secondary azimuthally elongated maximum of particle concentration was located 60-70 km southwest of the storm center within the stratiform echo band. Individual peaks in number concentration were very strongly anticorrelated with peaks in the patterns of median volume diameter (cf. Fig. 1a). The ring of high particle concentrations surrounding the eyewall echo band indicates that large concentrations of small particles (which dominated the number concentration) characterized the annular strip lying between the eyewall heavy rain zone and the outer stratiform echo region.

4. Conclusions

The results in Figs. 1a and b indicate that at the 6 km level larger particles occurred within the eyewall radar echo region and within the stratiform rainband, while the highest concentrations of particles, nearly all in the small size category, were found in an annular region displaced 10-20 km radially outward from the eyewall rainband. Evidently, small particles in both the convective and stratiform rainbands were swept out by larger particles in the areas of heavier precipitation. This pattern is consistent with the pattern of precipitation fallout suggested by Marks and Houze (1987) for the inner-core region of Hurricane Alicia (see their Fig. 9). According to this pattern, ice particles generated in the eyewall updraft are advected radially outward, with the initially larger particles falling out in the eyewall rainband while the initially smaller particles are carried up and advected outward to fall out eventually in the stratiform rainband region. In the annular region lying between the fallout zones of these two characteristic types of particles, evidently the smaller particles are not as effectively swept out, leaving the zone of higher concentration in between.

Acknowledgments

The authors especially appreciate the help of S. Rosenthal, R. Burpee, P. Willis and J. Gamache. The (NOAA) Office of Aircraft Operations operated the aircraft. Support was provided by NSF grant ATM-8413546 and NOAA grant 40-WCNR-6-02428.

REFERENCES

Marks, F.D., Jr., and R.A. Houze, Jr., 1987: Inner core structure of hurricane Alicia from airborne Doppler radar observations. J. Atmos. Sci., 44, 1296-1317.

Marks, F.D., Jr., 1985: Evolution and structure of precipitation in Hurricane Allen (1980). Mon. Wea. Rev., 113, 909-930.

Marks, F.D., Jr., and R.A. Houze, Jr., 1987: Inner core structure of hurricane Alicia from airborne Doppler radar observations. J. Atmos. Sci., 44, 1296-1317.

Black, R.A., and J. Hallet, 1986: Observations of the distribution of ice in hurricanes. J. Atmos. Sci., 43, 802-822.

Houze, R.A., Jr., F.D. Marks, Jr., R.A. Black, P.T. Willis and J.F. Gamache, 1985: Airborne Doppler radar and cloud microphysical measurements in Hurricane Norbert. Extended Abstracts Volume: 16th Conf. on Hurricanes and Tropical Meteor., Houston. Amer. Meteor. Soc., Boston. pp. 5-6.

THE BULK WATER BUDGET OF HURRICANE NORBERT (1984) AS DETERMINED FROM THERMODYNAMIC AND MICROPHYSICAL ANALYSES RETRIEVED FROM AIRBORNE DOPPLER RADAR

J. F. Gamache, F. D. Marks, Jr., and R. A. Black
NOAA/AOML/Hurricane Research Division, Miami, Florida, USA

R. A. Houze, Jr.
University of Washington, Seattle, Washington, USA

1. Introduction

The main source of energy in a tropical cyclone which maintains the warm core is the release of latent heat of condensation. Shapiro and Willoughby (1982) have shown that the location of this latent heat source relative to the radius of maximum wind is one important factor in storm intensification. It is our goal, therefore, to determine not only the magnitude of the bulk condensation, evaporation, rainfall and water transport, but the intensity distributions of each of these processes as well.

On 24 September 1984, two US NOAA WP-3D research aircraft probed eastern Pacific Hurricane Norbert in a mission to determine the inner core water budget. One aircraft, carrying the airborne Doppler radar flew at 3 km in altitude, while the second flew at 6 km. Reflectivity and wind were determined within a 38 km radius of the storm center.

Two methods are used to determine the water budget. In both methods, the thermodynamic structure and water distributions are assumed to be steady state following the storm motion. In the first the cloud water and ice contents are determined by manipulating formulations for autoconversion and collection, where precipitation contents and formation rates have been determined from radar and Doppler analyses. The method is similar to that of Churchill and Houze (1984). In the second method, the specific humidity and cloud content are determined using the techniques of Hauser and Amayenc (1986). In this method the cloud virtual temperature field has been retrieved from a Doppler thermodynamic retrieval method developed by Roux et al. (1984) and Roux (1985). The total water content (the sum of vapor, water and ice) is computed by solving the water continuity equation with boundary conditions. The cloud water and specific humidity are then computed so they are thermodynamically consistent with the retrieved cloud virtual temperature.

2. The microphysical retrieval

To compute the water budget using the first method, referred to hereafter as the microphysical method, the precipitation formation rates are determined by examining the change in the precipitation content following a parcel of air. In a steady state storm,

$$\frac{dM_p}{dt} = \vec{V}_r \cdot \nabla M_p, \qquad (1)$$

where M_p is the precipitation mass concentration and $\mathbf{V}_r$ is the three-dimensional wind velocity relative to the moving storm center. The wind velocity is the Doppler-analysis wind, and M_p is determined from radar reflectivity. Two mechanisms cause a change in precipitation content: the actual production of precipitation by collection or autoconversion of cloud, and the flux convergence of precipitation falling with respect to the parcel of air. The precipitation formation rate is therefore the difference between the rate of change of precipitation content and the precipitation flux convergence. Thus,

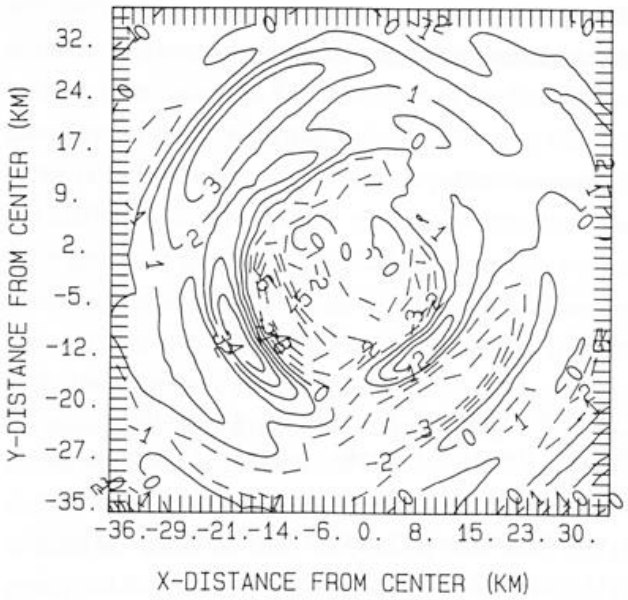


Fig. 1. Vertical wind in m/s. Dashed contours indicate negative (downward) vertical wind.

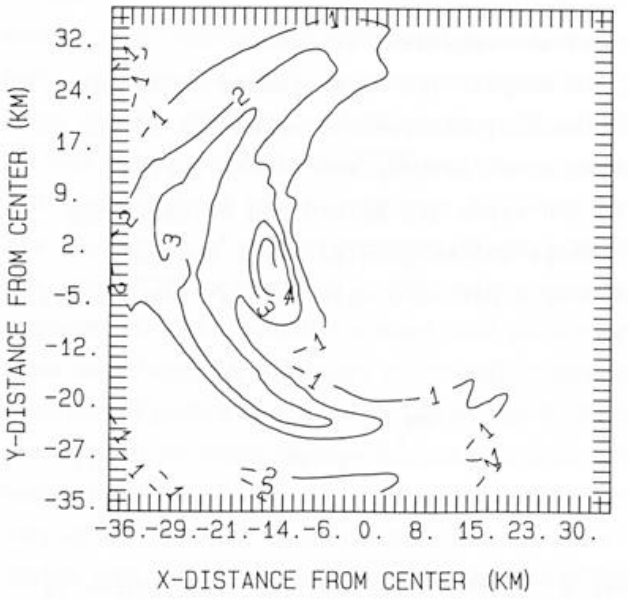


Fig. 2. Precipitation content in .1 g m^{-3}.

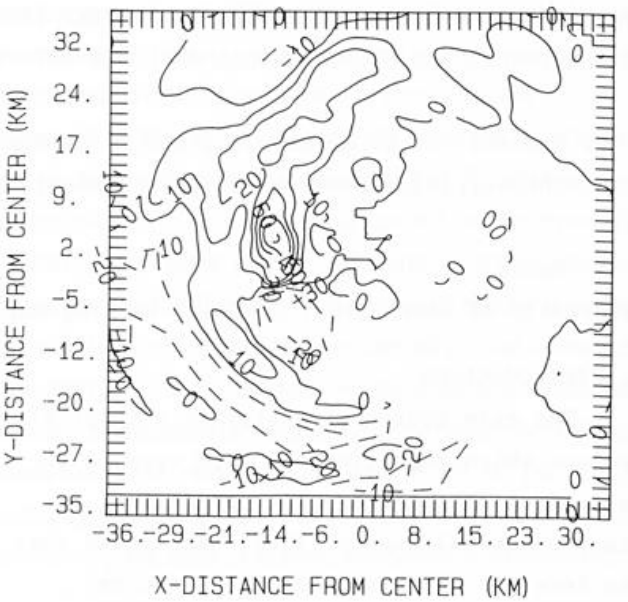


Fig. 3. Precipitation formation rate in .1 g m^{-3} h^{-1}.

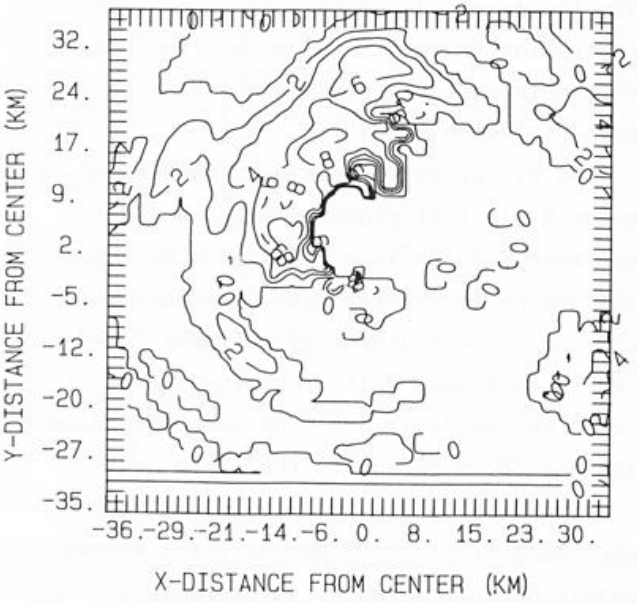


Fig. 4. Cloud water content in .1 g m^{-3}.

$$\left(\frac{dM_p}{dt}\right)_F = \vec{V}_r \cdot \nabla M_p + \frac{\partial}{\partial z}(M_p V_T) - \frac{M_p}{\rho}\frac{d\rho}{dt}, \quad (2)$$

where the left hand side is precipitation formation, the second term on the right side is the precipitation flux divergence, and the third term accounts for changes in air density as the parcel ascends and descends in vigorous drafts. V_T is the terminal fallspeed of the precipitation and ρ is air density. Precipitation formation is also expressed by:

$$\left(\frac{dM_p}{dt}\right)_F = \alpha(M_c - M_{c0}) + M_c f(M_p), \quad (3)$$

where α and β are constants, M_c is the cloud mass concentration, and M_{c0} is an autoconversion threshold value. The first and second terms on the right hand side are

autoconversion and collection, respectively. If $M_c < M_{c0}$, then the first term (autoconversion) on the right hand side is set to zero. Equation (3) may then be solved for M_c. The condensation and evaporation are determined from water continuity using a specific humidity field derived from the cloud virtual temperature. This temperature is retrieved from the Doppler winds. In regions of updraft, saturation is assumed. In regions of downdraft a saturation deficit is determined from the precipitation evaporation rate.

The vertical velocity field at 3 km is shown in Fig. 1, while the precipitation concentration is shown in Fig. 2. The precipitation formation rate determined from the velocity and precipitation fields is shown in Fig. 3. The cloud water concentration determined from (3) is shown in Fig. 4.

3. Thermodynamic retrieval

In the second method, following Hauser and Amayenc (1986), the condensation and evaporation are determined directly from the thermodynamic retrieval of temperature and specific humidity. The specific humidity and cloud water are determined by solving the water continuity equation. The equation is

$$\vec{V}_r \cdot \nabla q_T - \nabla \cdot (K \nabla q_T) = -\frac{1}{\rho} \frac{\partial}{\partial z} (\rho q_p V_T), \quad (4)$$

where the first term on the left hand side is the rate of change of total water mixing ratio q_T following the parcel in the absence of diffusion, the second term on the left hand size is the diffusion of total water, the right hand side is the precipitation flux convergence, and q_p is the precipitation mixing ratio. The flux convergence is again inferred directly from radar reflectivity. Through an iterative process, the temperature, specific humidity, precipitation, cloud and total water fields are made consistent with the retrieved cloud virtual temperature while conforming to the water continuity equation (4). Once q_v is known everywhere, condensation (c) and evaporation (e) may be computed. Following an air parcel,

$$c - e = \vec{V}_r \cdot \nabla q_v. \quad (5)$$

REFERENCES

Churchill, D. D., and R. A. Houze, Jr., 1984: Mesoscale updraft magnitude and cloud-ice content deduced from the ice budget of a tropical cloud cluster. J. Atmos. Sci., 41, 1717-1725.

Hauser, Daniele, and Paul Amayenc, 1986: Retrieval of cloud water and water vapor contents from Doppler radar data in a tropical squall line. J. Atmos. Sci., 43, 823-838.

Roux, F., 1985: The retrieval of thermodynamic fields from multiple-Doppler radar data using the equation of motion and the thermodynamic equation. Mon. Wea. Rev., 113, 2142-2157.

Roux, F., J. Testud, M. Payen and B. Pinty, 1984: West African squall-line thermodynamic structure retrieved from dual-Doppler radar observations. J. Atmos. Sci., 41, 3104-3121.

Shapiro, L. J., and H. E. Willoughby, 1982: The response of balanced hurricanes to local sources of heat and momentum. J. Atmos. Sci., 39, 378-394.

MICROPHYSICS IN A DEEP CONVECTIVE CLOUD SYSTEM ASSOCIATED WITH A MESOSCALE CONVECTIVE COMPLEX–NUMERICAL SIMULATION

Bei-Fen Fan, Jia-Dong Yeh, and William R. Cotton

Dept. of Atmospheric Science, Colorado State University, Fort Collins, CO 80523

G. Tripoli

University of Wisconsin, Dept. of Meteorology, Madison, WI 53715

1 Introduction

In recent years, increasing observational evidence has revealed that the ice particle aggregation process is one of the predominant mechanisms of precipitation formation in a variety of cloud systems. Airborne cloud microphysical data obtained from midlatitude mesoscale convective systems (MCS) also showed that aggregates are an important component of the precipitation in the stratiform region and transition region of midlatitude mesoscale convective complexes (MCC), especially in the stratiform region (Yeh *et al.*, 1986; 1987). In a simulation of orographic cloud snowfall, Cotton *et al.* (1986) demonstrated that aggregation plays an important role in controlling the fields of cloud liquid water content, ice crystal concentrations, and surface precipitation amounts. However, when the aggregation model was applied to the simulation of a MCC, the model underpredicted the amount of aggregates over the stratiform region (Chen, 1986). In this paper a two dimensional version of the Colorado State University (CSU) Regional Atmospheric Modeling System (RAMS) is applied to the simulation of meso-β -scale convective component of a MCC.

2 The study case

The case selected for simulation is a meso-β-scale cloud system associated with a PRE-STORM MCC of 4 June 1985. The MCC developed in association with a short wave trough which passed through the mid-west region of the United States. The synoptic situation and sounding data exhibited some important features: 1) the atmosphere was warm and moist in the low levels, and dry in the middle troposphere; 2) the southerly low level jet of $13 - 15\ ms^{-1}$ at 85 kPa level pumped warm moist Gulf air to the area of PRE-STORM network; 3) there was a deep conditionally unstable layer from 90 kPa to 50 kPa level; 4) the wind hodograph showed that wind shear was strongest beneath the 60 kPa level, above it the southwestly air current prevailed up to the 10 kPa level. The MCC was a rapidly evolving and fast moving, non-linear system, which formed by 0630 GMT and dissipated at about 1400 GMT. Early in its lifecycle, numerous convective cells developed in a random manner. At 0800 GMT the convective echoes started to organize into several meso-β-scale sub-systems (Fortune and McAnelly, 1986). We focus on the simulation of the meso-β-scale convective system. Airborne observations have revealed (Yeh *et al.*, 1987) that the characteristics of ice particles are quite different between the stratiform region and transition region. Most large particles are aggregates and graupel in the transition region, whereas aggregates predominate in the stratiform region. The aggregation process in the stratiform region started at upper and colder levels but become more efficient as the aggregates approached the melting layer.

3 Brief description of model characteristics and design of simulation experiments

A two-dimension version of the CSU RAMS nonhydrostatic cloud model was used to simulate a meso-β-scale convective system. The governing equations and general features of the model system are described in Tripoli and Cotton (1982), Cotton *et al.* (1982; 1986). Several aspects of the aggregation model developed by Cotton et al.(1986) have been improved in the new version of parameterized microphysics, including the division of the ice crystal class into small, non-precipitating crystals and large snow crystals, the introduction of an empirical formula of collection efficiency of ice particles diagnosed from the observed particle size spectrum (Yeh *et al.*, 1988), and changes in the conversion equation from aggregates to graupel. The numerical experiments are summarized in Table 1.

Table 1. The numerical simulation experiments

Simulation experiment	Microphysics model	Collection efficiency of ice particles
Control experiment	New version	$0^0 - -13^0C : E(T_*) = 10^{0.0637T_* + 0.238}$ $T < -13^0C : E(T_*) = Min[10^{0.0357T_* - 0.7}, 0.2]$
Sensitivity Exp.1	Version 5	$-12^0 - -15^0C : E(T_*) = 1.4$ otherwise: $E(T_*) = Min[10^{0.0357T_* - 0.7}, 0.2]$
Sensitivity Exp.2	New version	$-12.5^0 - -15.5^0C$ and saturation for water: $E(T_*) = 1.4$ otherwise: $E(T_*) = 0.3$

The 2-D model domain was 90 km long and 19 km high with a grid scale of $\Delta x = 1$ km and $\Delta z = 0.5$ km. The x-coordinate was selected pointing 60^0 from north, which is basically consistent with the direction of wind shear from the surface to the 60 kPa level and the observed propagating direction of the MCC. The coordinate frame moved with an average speed of 15 ms^{-1} along the x axis. A 10 s timestep was used in the similation for the first hour, and 7.5 s after. The radiative lateral boundary condition and normal mode radiative top boundary condition were used in the simulation as applied in the orograph cloud simulation by Cotton *et al.* (1986). A cold downdraft initialization method is also used to trigger the cloud circulation. The model was initiated with a sounding data taken from Wichita at 0600 GMT 4 June 1985 just before the MCC developed. A mesoscale updraft beneath 6 km level was added in the simulation with a peak value of 0.40 ms^{-1} at the level of 4 km and decreased linearly to 0 ms^{-1} at the levels of 0 and 6 km.

4 Dynamical and thermodynamic properties of the simulated meso-β-scale convective system

The control experiment reveals the general properties of the convective cloud system. The time-height cross section of vertical motion (Fig. 1) shows that the meso-γ-scale convection is basically unsteady. The main convective cells developed in a time interval of about 30 min. The convective core located at the 7.5-8.5 km levels exhibited peak updraft values of 15.0, 20.5, 19.5 and 19.0 ms^{-1} at about 30, 60, 90 and 135 min of similation time. The convection weakened after 135 min and dissipated at 165 min. The meso-β-scale cloud system exhibited characteristics of a multi-celled convective storm for a period of 3 h (Fig. 2). Beneath the updraft, a downdraft developed at about the 8 km level with weaker values of 6-8 ms^{-1}. The fact that the main convective activity concentrated at the mid-upper troposphere suggests that the ice-phase process is important to the evolution of the convective system.

The perturbation pressure field exhibits a meso-low of -1.5 mb at low levels at 30 min of simulation time, and reached to -7.5 mb at 75 min. The meso-low extended to the upshear side and covered the entire domain beneath the 7.5 km level at the end of the simulation with a peak value of -8.0 mb. A weaker high pressure area developed near cloud top. The meso-high with a peak value of 2 mb at 90 min is located on the upshear

side of cloud system at the 8 to 11 km levels (Fig. 3a).

The temperature perturbation field shows a warm core in the cloud at the 6 to 10 km levels. Since the low levels are moist, cooling by evaporation in the downdraft was not evident (Fig. 3b). Cooling by cloud top evaporation can be seen with peak values of -10^0 to -14^0C.

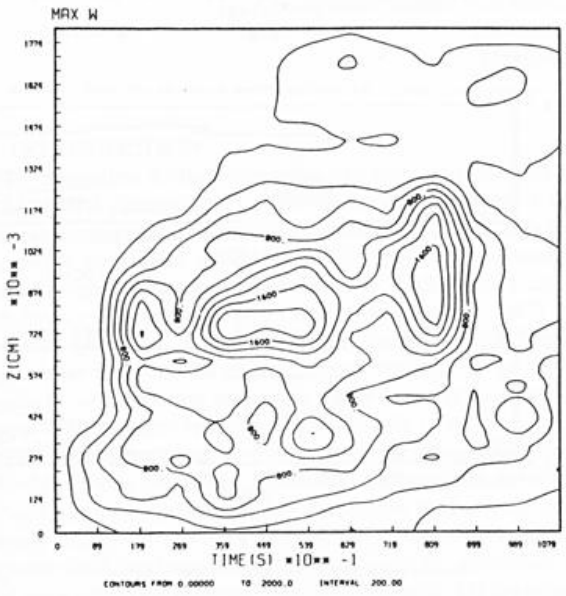


Fig. 1 Time-height cross-section of maximum updraft for control experiment. The contour interval is $2ms^{-1}$.

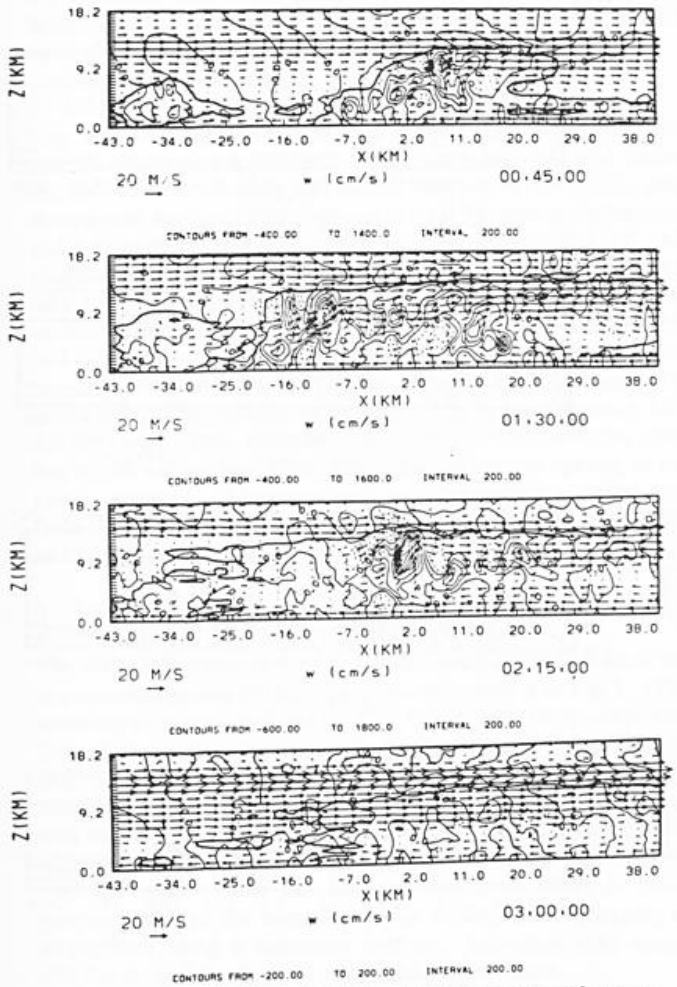


Fig. 2 Vertical velocity and wind vector fields for control experiment at 45, 90, 135 and 180 min simulation time. The contour interval is $2ms^{-1}$.

5 Microphysics of the simulated meso-β-scale convective system

The microphysics show that graupel is primarily concentrated in the strong convective cells which is the main source of convective rainfall after one hour, and aggregates are mainly located in the stratiform region and decaying convective cells which produce the stratiform rainfall. Riming is the predominant precipitation mechanism in convective cells, and aggregation is predominant in the stratiform region. In the transition region, which is near the convective cells and generally composed of decaying convective cells, both riming and aggregation are important. The basic characteristics of precipitation formation is consistent with observation. The results of sensitivity experiments with ice-phase microphysics are summarized as follows:

1. Fig. 4 shows the contours of the mixing ratio of ice-phase particles at 90 min obtained from the sensitivity Exp. 1 listed in the Table 1. It can be seen that the ice crystals occupy the entire cold region above the level of 7 km in the cloud system, and there are no aggregates. Obviously, the aggregation efficiency selected by version 5 of RAMS is too low.

2. Fig. 5 is the same as Fig. 4 except for Exp. 2 in Table 1. Compared to Exp. 1, aggregates dominate the cloud, and pristine crystals and snow crystals are almost totally depleted. The aggregation efficiency is too large.

3. The result of the control experiment is given in Fig. 6. Here the microphysical structure using the diagnosed aggregation efficiency is more reasonable. Pristine crystals and snow crystals are mainly above the 7 km level, while graupel are concentrated in the strong convective cells and somewhat in the decaying cells. The aggregates primarily extend in the stratiform region and decaying convective cells in the layer from 3 to 8 km, which is consistent with the observation that aggregation starts at the upper and colder levels but becomes more efficient near the melting layer.

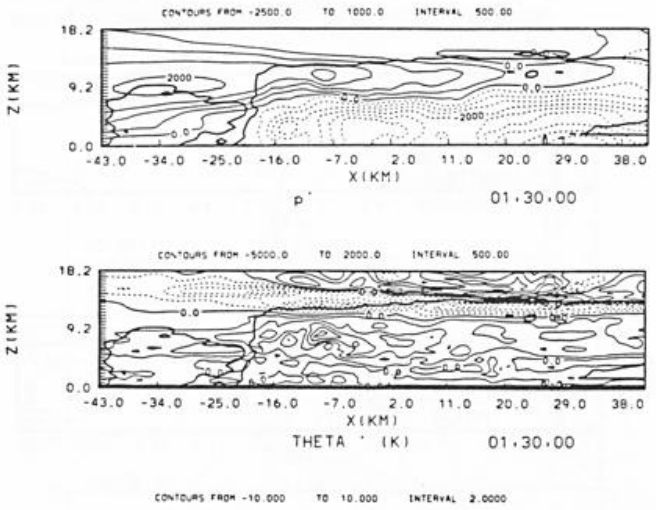


Fig. 3 Perturbation pressure (P') and perturbation potential temperature (θ') fields at intervals of $0.5mb$ for P' and 2^0K for θ' for control experiment at 90 min simulation time.

Acknowledgements

This research was supported by National Science Foundation under Grant #ATM-8512480 and by the Army Research Office under contract #DAAL03-86-K-0175.

REFERENCES

Chen Sue, 1986: Simulation of the stratiform region of a mesoscale convective system. M.S. Thesis, Colorado State University, Fort Collins, CO 80523.

Cotton, W. R., M. A. Stephens, T. Nekrkoln, and G. J. Tripoli, 1982: The Colorado State University three-dimensional cloud /mesoscale model-1982. Part II: An ice phase parameterization. J. de Rech. Atmos., **16** , 295-320.

Cotton, W. R., G. J. Tripoli, R. M. Rauber, and E. A. Mulvihill, 1986: Numerical simulation of the effects of varying ice crystal nucleation rates and aggregation processes on orographic snowfall. J. Clim. Appl. Meteor., **25** , 1658-1680.

Fortune, M. A., and R. L. McAnnelly, 1986: The evolution of two mesoscale convective complexes with different patterns of convective organization. Preprints of Joint Sessions, 23rd Conference on Radar Meteorology and Conference on Cloud Physics, AMS, Snowmass, Colorado, J175-178.

Tripoli, G. J., and W. A. Cotton, 1982: The Colorado State University three-dimensional cloud/mesosvcale model-1982. Part I: General theoretical framework and sensitivity experiments. J. de Rech. Atmos., **16** , 185-220.

Yeh Jia-Dong, M. A. Fortune, and W. R. Cotton, 1986: Micropgysics of the stratified precipitation region of a mesoscale convective system. Same as Fortune and McAnnelly, J151-154.

Yeh Jia-Dong, Bei-Fen Fan, M. A. Fortune, and W. R. Cotton, 1987: Comparison of the microphysics between the transition region and stratiform region in a mesoscale convective complex. Preprints of Third Conference on Mesoscale Processes, AMS, Vancouver, Canada, 188-189.

Yeh Jia-Dong, Bei-Fen Fan, and W. R. Cotton, 1988: Size distribution of precipitation particles in midlatitude mesoscale convective complex. 10*th* International Cloud Physics Conference, 15-20 August 1988, Bad Homburg, FRG.

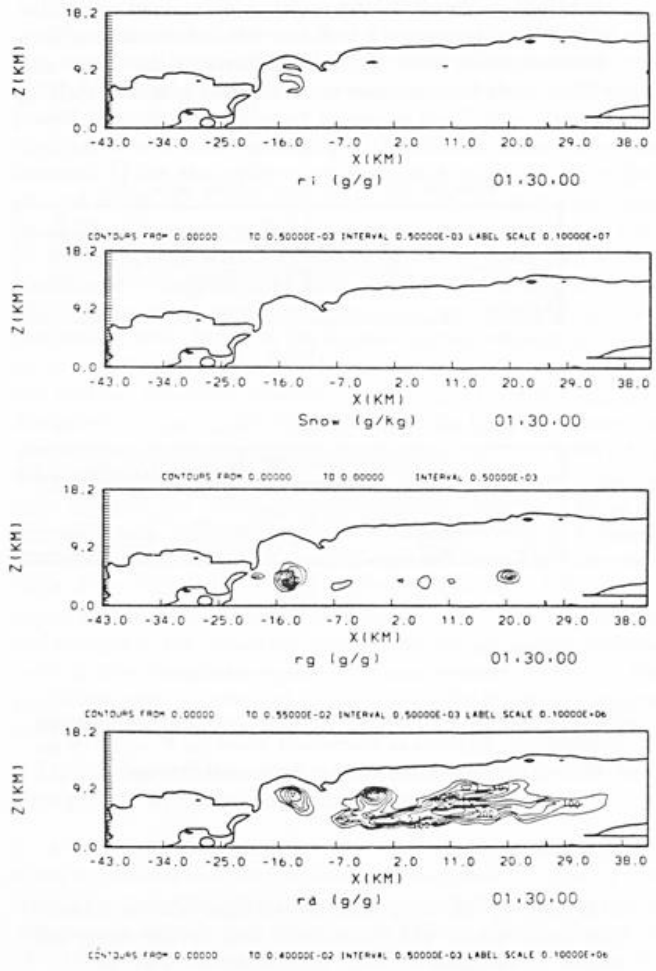


Fig. 5 As in Figure 4 except for Exp. 2.

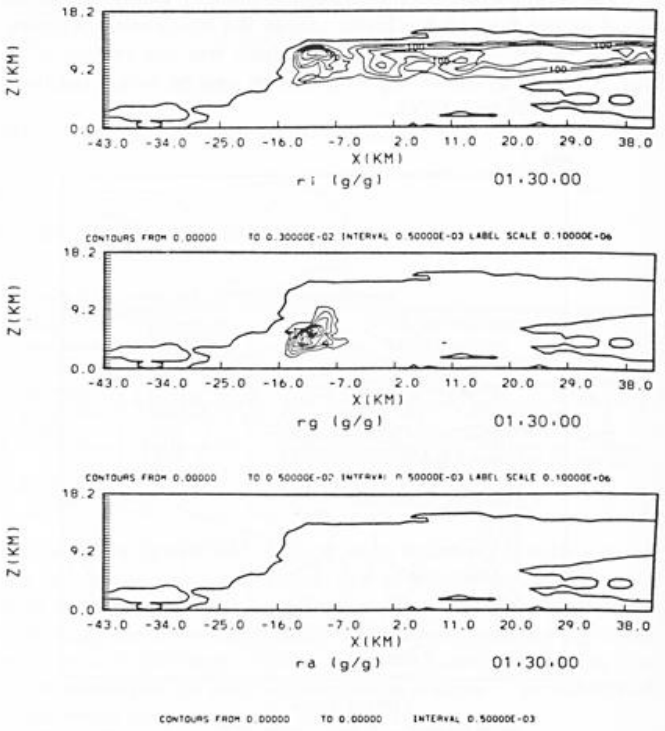


Fig. 4 Micrphysical structure at 90*min* simulation time for Exp. 1. (a) contours of ice crystal mixing ratio, (b) graupel mixing ratio and (c) aggregate mixing ratio, all contours at intervals of $0.5gkg^{-1}$.

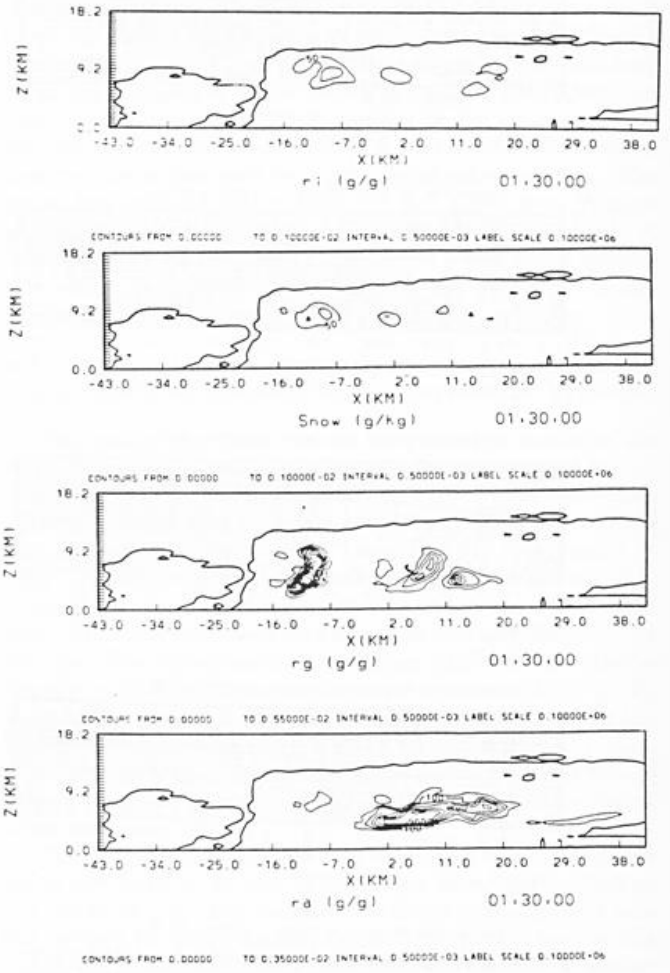


Fig. 6 As in Figure 4 except for control experiment.

OBSERVATIONAL ANALYSIS OF MESOSCALE CONVECTIVE SYSTEM GROWTH AND STRUCTURE

Kevin R. Knupp
Atmospheric Science and Remote Sensing Laboratory, Johnson Research Center
University of Alabama in Huntsville
Huntsville, Alabama 35899 USA

1. INTRODUCTION

Deep convection is often organized into mesoscale clusters ranging in horizontal dimension from less than 20 km to greater than 200 km. In some cases, the mesoscale cluster (referred to herein as a mesoscale convective system or MCS) may be composed of convective cores flanked by stratiform anvil. Such systems can vary in size from ~100 km scale (e.g., Knupp and Cotton, 1987) to ~500 km scale (Maddox, 1980). Although spatial and temporal scales may differ between large and small MCS's, a great deal of similarity in cloud and mesoscale flows appears to exist in some cases. The manner in which the mesoscale flows (e.g., mesoscale ascent within the anvil and mesoscale descent below the anvil) evolves remains abiguous. Moreover, the mechanisms which contribute to the formation of the mesoscale updraft are not completely understood. In this paper, we will consider two hypothesized mechanisms which contribute to mesoscale updraft and associated precipitation formation, namely: (1) detrainment of buoyant air from convective towers, and (2) hydrostatic response to heating associated with deep convection. These two hypotheses are examined with reference to a particular case study in which detailed and comprehensive observations were made over the life cycle of the system.

2. DATA

The upscale development of this system is documented with several observational platforms which were implemented during the Satellite Precipitation and Cloud Experiment (SPACE), conducted over northern Alabama and central Tennessee during June and July, 1986. In this preliminary study, we will consider RADAP data acquired from a WSR-57 radar located at Nashville (BNA), data from two C-band Doppler radars (CP-3 and CP-4), special surface mesonet data (20 stations), and conventional GOES visible and IR imagery acquired at 30 min intervals. Instrument locations are shown in a later figure (Fig. 3a). The RADAP data were collected every 2 deg in azimuth and elevation, at approximately 120-230 km range. Thus, these data depict only major convective cores due to the 4-8 km beam size and azimuthal sample spacing at the ranges involved. Higher spatial and temporal resolution data (reflectivity factor and radial velocity) were available from CP-3 and CP-4.

3. ANALYSIS

3.1 OVERVIEW OF THE MCS DEVELOPMENT

The MCS of interest evolved in a relatively unstable, low-shear environment as shown by the representative sounding in Fig. 1. (The sounding location is indicate by *RSA* in Fig. 3a.) Deep convection formed in a mesoscale cluster by early afternoon in response to large-scale lifting associated with a subtle short-wave trough. At maturity some 4-5 h after first echo, the MCS consisted of an east-west line of broken convective cells (oriented parallel to the shear vector), flanked to the north by a region of stratiform precipitation ~80 km wide. The net MCS motion from north to south (perpendicular to the mean flow) was accomplished primarily by propagation along a mesoscale outflow. Individual cells moved with the mean flow along the major axis of the system.

A time series overview of some MCS characteristics is presented in Fig. 2. First echo (at an 18 dBZ threshold) was observed near 1730 UTC (1130 LST) over the west-central portion of the mesonet, although weak to moderately-intense echoes were observed earlier (1600-2000 UTC) over the southeastern portion of the network. The system exhibited a relatively uniform expansion and intensification from first echo until ~2100 UTC, when maximum echo intensity was recorded in the RADAP data. Surface outflow air was first apparent near 1830 UTC, but low-valued θ_e outflow air was not recorded until ~1930. The surface outflow air continued to expand in area after 1930 and appeared to aid importantly in development of subsequent convection.

Incipient anvil associated with the MCS deep convection first appeared in the visible GEOS satellite imagry at 1900 UTC. As shown in Fig. 3, the anvil exhibited significant expansion from 2000 to 2200 UTC. The visible anvil expanded from ~7,000 km^2 at 2000 to ~36,000 km^2 at 2300. The distribution of precipitation during the MCS developing stages is also shown in the RADAP data (left panels) of Fig. 3. During the early MCS stages (1800-2000), convective echoes appeared as distinct entities, not significantly merged with neighboring cells. By 2000 UTC, cell merger was more prominent as a convective line appeared (labeled A in Fig. 3). Over the next 3 h, this convective line (which was acutally a subset of the MCS) expanded, eventually evolving to the early mature structure shown in Fig. 3b. During the 2 h time interval from 2000 to 2200 UTC, precipitation within the anvil displayed both expansion and an increase in intensity (see Figs. 2 and 3). Development of precipitation within the anvil thus lagged formation of the uniform anvil cloud top by roughly one hour.

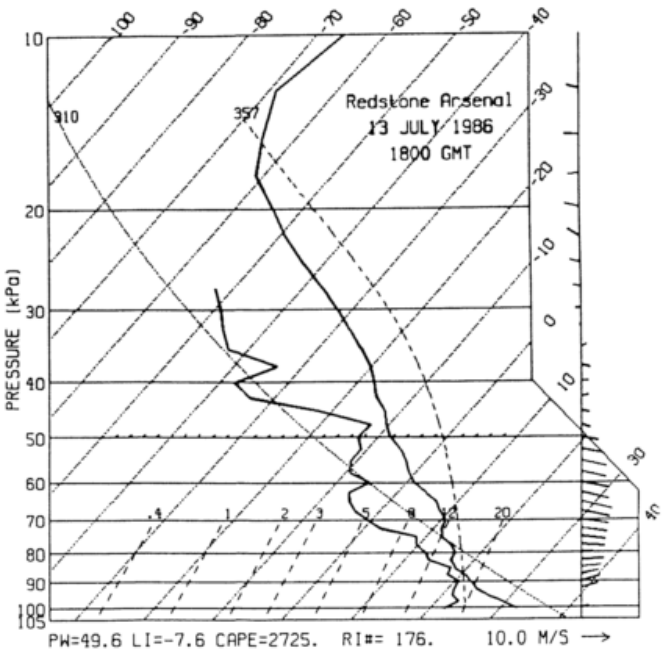


Figure 1. Rawinsonde sounding for 1800 UTC 13 July 1986, plotted on a skew-T, ln diagram. The sounding location is from point RSA shown in Fig. 3a.

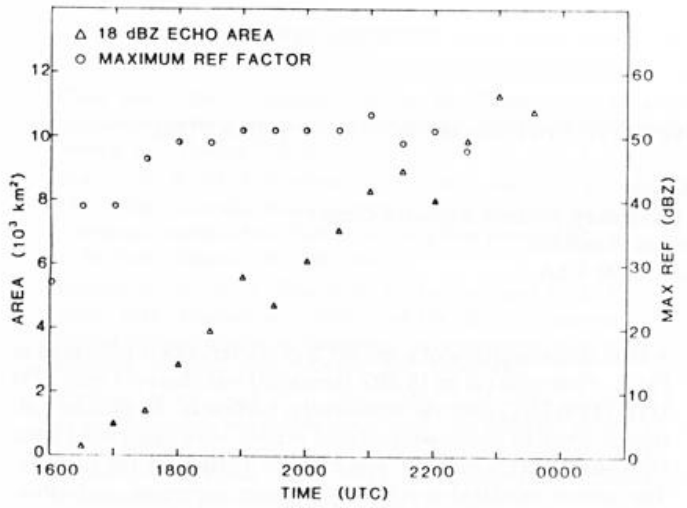


Figure 2. Time series plot of MCS echo area (reflectivity factor > 18 dBZ) and maximum reflectivity factor obtained from the RADAP data. The MCS moved beyond maximum range starting ~2300 UTC, so values beyond this time are underestimated.

3.2 CHARACTERISTICS OF THE ANVIL EXPANSION

The formation of the anvil and its associated mesoscale updraft and precipitation is examined in further detail with the aid of higher-resolution Doppler radar data. Figure 4 presents analyses of reflectivity factor at the 8 km level (which intersect the lower portion of the mature anvil) at two times (2100 and 2200 UTC), between which development of precipitation within the anvil was most rapid. The vertical sections in Fig. 4 display a significant development of precipitation within that anvil during this time period. Such expansion was accomplished by the following mechanisms:

(1) discrete propagation of new cells along the leading (left) edge of the system (see Fig 4a);
(2) development of convection behind the leading edge, as shown in Fig. 4b;
(3) apparent development or intensification of a mesoscale updraft and assoicated divergence within the anvil.

Mechanisms (1) and (2) would supposedly act to provide condensate to the anvil region via (a) detrainment within the upper portion of convective-scale updrafts, and/or (b) incorporation of decaying convective cells into the anvil region through relative motion.

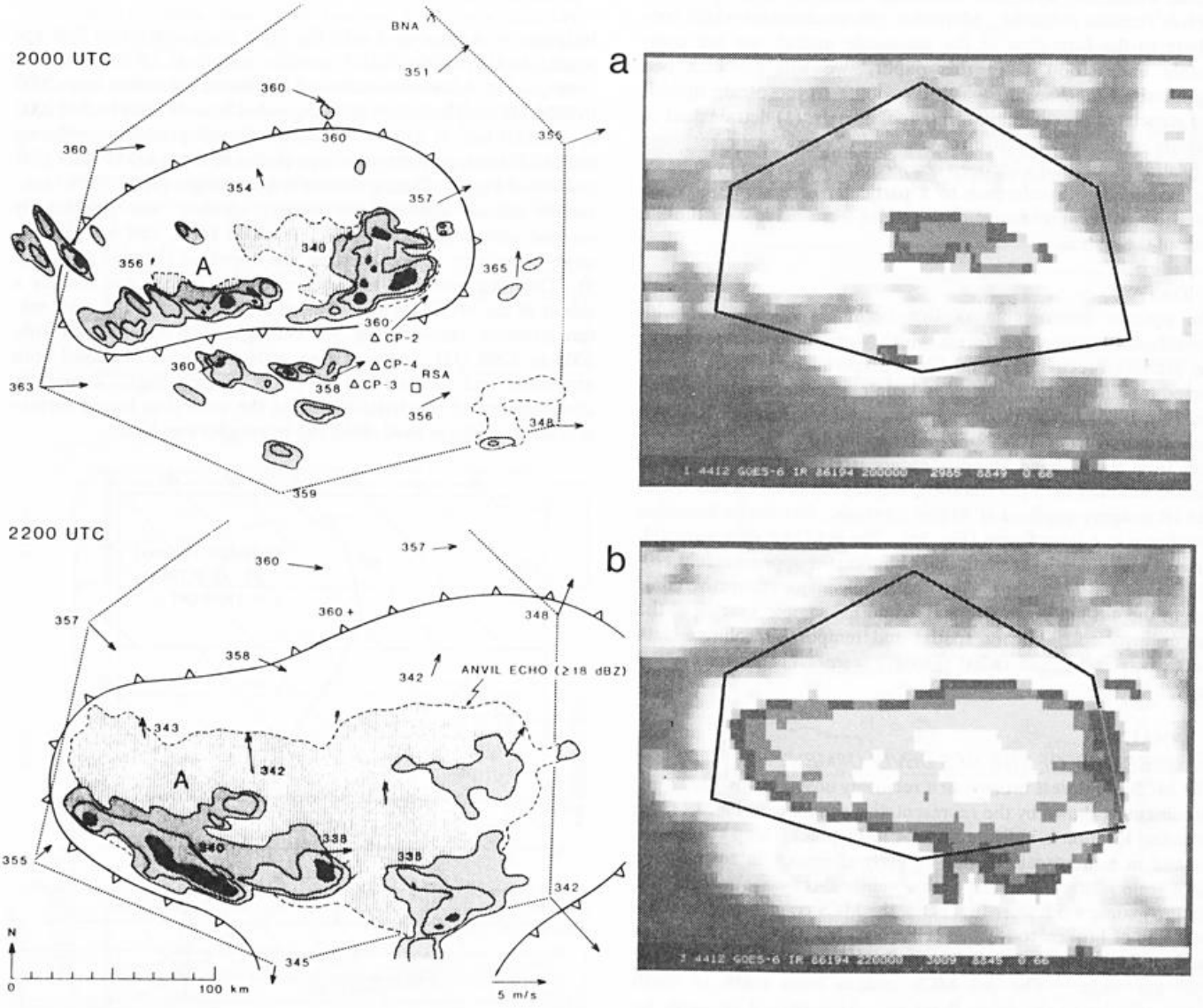


Figure 3. RADAP-derived echo patterns and GOES IR images during the MCS developing stages at 2000 and 2200 UTC. On the left panels, surface mesonet data (wind vectors and θ_e in deg K) are also plotted. Refectivity factor is contoured at 18, 30 and 43 dBZ. Stippling denotes Z > 18 and solid black refers to Z > 43 dBZ. Vertical hatching depicts reflectivity factor > 18 dBZ on the 2 deg elevation scan, which intersects the MCS at about the 10 km level. The right panels are GEOS IR images, with a MB enhancement applied to highlight the anvil region.

Investigation of thunder and hail clouds using remote methods

Vatian M.R., Bakhsoliani M.G., Lomidze N.E., Briliov G.B., Peskov B.E.

I. The task and investigation data

Cumulonimbus clouds accompanied by severe thunderstorm, hail and severe squalls (more than 25m/sec) damage greatly national economy. That's why the important task of forecasting centres is their detection and timely warning.

This work presents: climate characteristics of hail and squalls of different intensity; the evaluation of possibility of their diagnosis, shortrange forecasting using observational data from meteorological radar stations and satellites.

Information used for the investigation was: hail and squall data, obtained by surface meteorological stations and antihail subdivisions in warm period of year (April-October) 1966-1987 over the territory of Georgia, North Caucasus and Krasnodar region; also radar characteristics of cloud and precipitation systems and satellite pictures.

2. Hail and squall climatology

2.1. The day with hail was considered as a case when on the protected territory solid precipitations were registered at least once during a day.

Seasonal distribution of the number of days with hail and its statistic characteristics for the period from april to October 1978-1987 is presented in table 1. Analysing this table one can see that the most dangerouse months when hail occurs are May and June. Mean number of days with hail is 6 when their maximum value is 16. Mean many years number of days with hail reaches 17.4 but their natural frequency is 19% of the general number of days with thunderstorms.

According to radar data the number of detected areas with Cb clouds echo on the protected territory was on an average 3600 for the season. Usually they are accompanied by showers, moderate and seldom catastrophic hail and squalls.

In the warm periods of the year in different regions of the Caucasus catastrophic hail is registered on an average 2 or 3 times. They are accompanied by large grains of hail (diameter up to 8cm) and damage 70-100% of crop production on the area of 100 hectares/I/.

2.2 The day with squall was considered as a case when on the investigated territory wind gusts of 20m/sec and more were registered at least once during a day.

Data analyses for the period from April to October 1966-1985 have showed that according to surface meteorological station data in the East Georgia the frequency of the number of days with squalls of 20 m/sec and more is 35% but with severe squalls (25 m/sec and more) is 15% of all squalls. In 79% of all cases (47 days) severe squalls are observed when cold fronts are passing and in 21% of cases they are observed when wave disturbances are displacing from the South. Seasonal distribution of the number of days with squalls of 20m/sec and more, estimated according to the surface meteorological station data and specialized observations is given in table2. According to this table data they have maximum frequency in May and June (6 days) and minimum frequency is in October (0.2of the day). The most changeable months are August and September (σ =2.2). The mean seasonal many years (1981-1986) number of days with squall of 20m/sec and more reaches 19 but their natural frequency in case of thunderstorms is 24%. These values are several times as much as corresponding values (2.5 days and 1.3%) received only according to the surface meteorological station data.

So special inspections of the territory significantly increase the probability and authenticity of squall detection, this allows to use them effectively both in developing and estimating methods for the diagnose and forecast of squalls.

3. Estimation of possibility of hail and squall in thunder cloud according to meteorological radar station data.

The conditions of squall and hail formation may be characterized indirectly by the following radar

Table 1

Seasonal distribution of statistic characteristics(mean and extream) of the number of days with hail n and their meansquare deviations(σ), variation and natural frequency in thunderstorms(P) in the protected regions of East Georgia for the period from April to October 1978-1987.

Parameters	M O N T H S							Total
	IV	V	VI	VII	VIII	IX	X	IV-X
n max	2	10	16	6	3	6	I	25
n min	0	3	1	0	0	0	0	4
$\bar{n}$	1.0	6.1	5.9	1.9	1.5	0.8	0.2	17.4
σ	0.7	2.3	5.2	1.5	1.3	1.6	0.4	9.0
v	0.70	0.38	0.88	0.79	0.87	2.00	1.00	0.53
P(%)	10	34	25	21	17	15	2	19

Table 2

Seasonal distribution of statistic characteristics(mean and extream) of the number of days with squall of 20m/sec and more n and their meansquare deviation (σ), variation and natural frequency in thunderstorms (P) in the regions of East Georgia for the period from April to October 1978-1987.

Parameters	M O N T H S							Total
	IV	V	VI	VII	VIII	IX	X	IV-X
n max	2	II	9	4	6	5	I	3I
n min	0	0	0	0	0	0	0	0
$\bar{n}$	0.4	5.8	6.2	3.0	2.6	1.2	0.2	19
σ	0.52	1.50	1.80	1.00	2.60	2.20	0.45	9
V	1.30	0.26	0.29	0.33	1.00	1.83	2.25	0.5
P(%)	4	32	30	33	29	10	2	24

parameters of a CB cloud/ I-3/:maximum radar reflectivity in the area of negative temperatures η_m (cm^{-1}) or $\ell g Z$;the height of the echo top of the cloud H (km) and its temperature t_ℓ (°C);the area of the horizontal section of the cloud echo S (sq.km), restricted by the isocounter of reflectivity $\eta = 10^{-12}$ cm^{-1};the thickness $\Delta H_{\Delta\eta}$(km) and the area $S_{\Delta\eta}$(sq.km) of the increased radar reflectivity zone,placed in the field of negative temperatures and restricted by the isocounter $\eta = 10^{-9} cm^{-1}$;the speed of cloud echo displacement V (km/hour).

When the values of these parameters increases,the probability of severe showers,hail and squalls increases too/I-3/.Hail indication was done with the help of observational data of meteorological radar stations with wave length of 10cm, but squalls indication was done with the wave length of 3.2 cm.

3.1 The suggested method of estimation of a hail cloud possibility is based on the utilization of the complex of radar and physical parameters: $\Delta H_{\Delta\eta}$, $t_{\Delta\eta}$, S /I-3/.

Comparison of the indicated parameters with the type of precipitations allowed to isolate in correlated field the areas with showers (I),moderate(II) and catastrophic (III) hail(Figure I) depending on the values of the parameters.

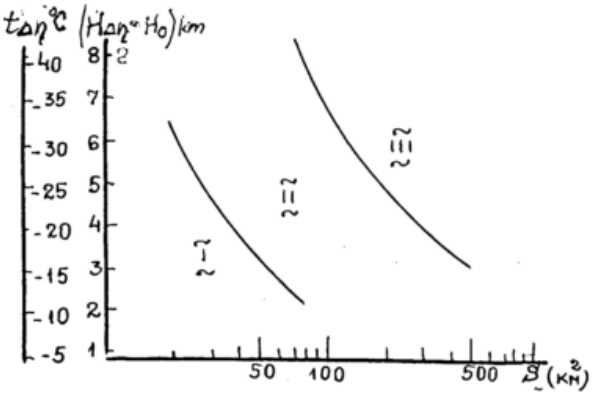


Figure I. Estimation of possibility of showers,moderate and catastrophic hail depending on radar parameter values.

Showers in the region(I) occur with probability more than 90% when S has any value and $t_{\Delta\eta} > -10°C$.In the region(III)catastrophic hail is diagnosed with probability more than 90% when $S > 500$ sq.km and $t_{\Delta\eta} < -15°C$ or when $S > 100$ sq.km and $t_{\Delta\eta} < -40°C$. The additional criteria of catastrophic hail are: $\eta \geq 10^{-8} cm^{-1}$ and $S_{\Delta\eta} > 25$ sq.km.

The examination of the received diagram (Figure I) on the independent data showed that general accuracy is more than 80%.

3.2 Severe squall (25m/sec and more) radar diagnose in space cells 30x30 km of meteorological radar range is done according to values H_ℓ , V_ρ and $\ell g Z$ in persuance of the diagrams on Figure 2.

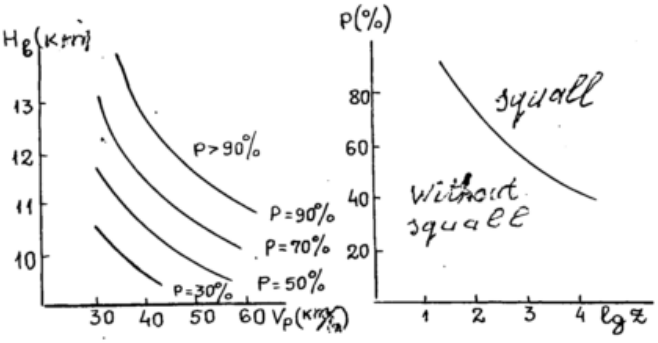


Figure 2. Estimation of possibility of severe squalls (25m/sec and more)depending on radar parameter values.

First P is estimated according to the values $H_\ell$and V_ρ from Figure 2a, then possibility of severe squall is estimated according to the values P and $\ell g Z$ from Figure 2b.

As a rule there are no squalls of 25 m/sec and more when H_ℓ is less than 10km and V_ρ is less than 30km/hour.Squalls are diagnosed with probability $P > 90\%$ when H_ℓ is more than 12km and $V_\rho > 50$km/hour.

As the duration of life of some Cb clouds varies from 0.5 to 2 hours and more, there appears possibility of severe squall forecasting with the same projection.

4. Investigation of severe squalls using satellite data

Though radar methods of diagnoses and very shortrange squall forecasting are effective but their projection is not more than 3-4 hours.

In order to increase severe squall forecast projection cloud and precipitation systems were analysed according to satellite pictures.Cloud parameters which are important for severe squalls such as cloud top(H) and speed of displacement (V) were determined according to /4,5/.

Speed of displacement of cloud systems(V) according to satellite pictures varies from 25km/hour up to 65 km/hour.98% of squalls are

are characterized by V > 30km/hour, it is on the average 35-40km/hour. The difference between mean values of V when severe squalls occur and when they don't occur seem to be statistically significant on the level of significance α =0.05 (non parametric estimation methods wereused).The difference between mean values of H in case of severe squalls (H is more than 11km) and squalls less than 25 m/sec(8) also seem to be significant.

The diagram for squall forecast of 12 hour projection was drawn up according to the value of the above mentioned parameters(Figure 3).

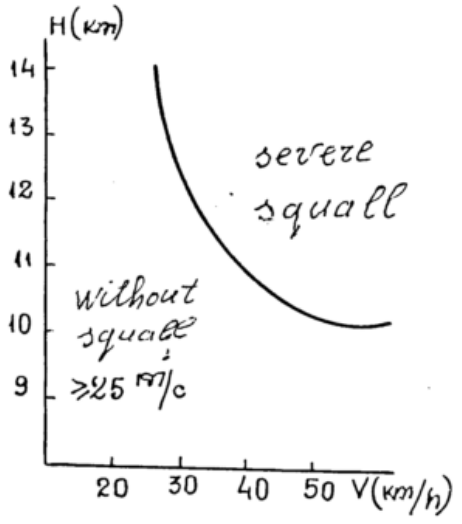


Figure 3.Estimation of possibility of severe squalls depending on the values of cloud system parameters H and V determined with satellite pictures.

On this figure a region of severe squalls and a region of squalls less than 25 m/sec are devided with a line depending on H and V V values.

Some indications about the existance of severe squalls have been determined as a result of analysis of satellite pictures. They are:V-form hollows and high brightness of the front part of Cb cloud system with the sharp front edge moving towards a forecast territory.The frequency of severe squalls reaches 80% when there is cold front Cb cloud system with the V-form hollow.When there is bright cloudness with the sharp front edge it is equal of 20%.

As a result of our researches the method of squall forecast with projection of 12 hours have been suggested.It includes:analysis of satellite pictures and forecast of cloud system evolution according to /.5/;determination of the hight (H),speed(V) and direction of cloud movement and also the time when it reaches a forecast territory; estimation of squall possibility according to Figure 3 taking into account the structure of satellite picture cloud system.Quality of this method is high enough.

Список литературы

I. БерезкинВ.В.,Ватьян М.Р.,Селезнёв Э.Т. Исследование некоторых радиолокационных характеристик параметров кучево-дождевых облаков,сопровождающихся катастрофическими градобитиями в предгорных и горных районах Северного Кавказа.Труды ВГИ, 1972,вып.38,стр.61-69.

2. Бибилашвили Н.Ш.,Бурцев И.И., Серёгин Ю.А. Руководство по организации и проведению противоградовых работ.Л.Гидрометеоиздат,1981,167 с.

3. Ватьян М.Р.,Песков Б.Е. Исследование некоторых радиолокационных характеристик кучево-дождевых облаков,сопровождающихся шквалами различной силы на Северном Кавказе. Труды ВГИ,1977, вып.38,с.50-60.

4. Глушкова Н.И. Прогноз осадков по данным спутниковых и радиолокационных наблюдений. Труды Гидрометцентра СССР,1985,вып. 266,с.21-33

5. Руководство по использованию спутниковых данных в анализе и прогнозе погоды. Л.Гидрометеоиздат,1982,129 с.

STUDY OF CONVECTIVE CLOUDS DEVELOPMENT IN CENTRAL ASIA

A.D.Dzhuraev, H.A.Imamdzhanov, B.Sh.Kadyrov, V.P.Kurbatkin

SANII, Tashkent, USSR

The method of investigation - observations, experiment including cloud processes modification and numerical experiment to compute parameters of convective clouds structure and dynamics - was proposed in the Programme of the Voeikov Main Geophysical Observatory. The 13-year data set of the combined radar, rawinsonde and meteorological observations in several regions of Central Asia served as initial information. The available material allowed revealing of thermodynamics and aerosynoptic conditions for development of thunderstorm with hail processes of different types. The vertical gradient of horisontal component of wind speed (β), velocity of steering flow (V_s) and energy of atmospheric instability (E) are the informative parameters which distinghuish the types of thunderstorm with hail processes. According to the terminology accepted in the USSR, the types of processes are indicated by three letters, the first characterizing movement of cloudy process relative to the steering flow (to the right - R, to the left - L), the second - the location of a cell origin relative to its movement (to the right - R, to the left - L, indefinitely - I) and the third letter indicates shifting of the cell relative to the movement of the processes (the same symbols). The steering flow velocity for these types of clouds have the following relation: V_s (RRL type)> V_s (RLL type)>V_s (RII type)

Knowing β, one can estimate probability of any of those processes (table 1).

Table 1. Frequency in % of various types of clouds for different values

Types of processes	β, c^{-1} $9.9 \cdot 10^{-4}$	$(1\text{-}9)\cdot 10^{-3}$	$1 \cdot 10^{-2}$
N	41	194	122
RRL	48	80	17
RII	20	10	66
RLL	32	10	17

The index of kinetic energy flux distinguishes between shower and hail cloudy processes. The values of are defined by formula proposed by Abshaev M.T.:

$$E = 1.5 \cdot 10^{7} \eta_{3,2}^{0,27} \cdot \eta_{10}^{0,73} [J \cdot m^{-2}]$$

$E_{hail} = 0.21 \pm 0.15$ and $E_{shower} = 0.21 \pm 0.15$ for cloudy processes in Central Asia. The relationship is found between the area where solid precipitation reached the surface and the area of horizontal section of convective cloud radar echo having definite reflectivity value (1). In our conditions $\eta = 5\ 10^{-8}$ at $\lambda = 10$cm. Thus, the methods were to compute benefits of each hail suppression procedure. One-dimensional non-stationary model developed in GGO was used to study the peculiarities of microphysical processes both in their "natural" development and in the case of separate convective process modification. The value of autoconversion coefficient should be present as ini-

tial conditions within the model. In our case this coefficient is 2 g m^{-3}. Analysis of numerical experiments has shown that simulation of modification leads to the case that cloud water content doesn't reach its maximum value which it could get in the case of "natural" development; besides, the time of maximum shifts 5-7 min earlier. Time of precipitation has shifted as well (Fig. 1).

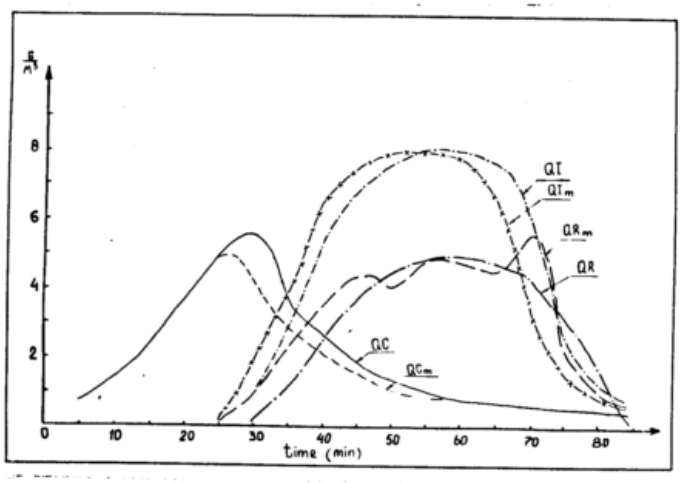


Fig.1: History of microphysical cloud parameters (m - modification)

It is interesting to note that the development of cloudy process can be divided into stages by the time of maximum value of liquid drops water content, crystal particles and precipitation particles. The first stage ranges from the time maximum water content of cloud drops (Q_C), the second - between the maximum water content (Q_C) and water content of crystal particles (Q_I), and the third one is from maximum till maximum of water content of rainfall (Q_R). Such division of cloud development into stages allows the assessment of cloud resources using available radar data and to use more reliably the existing techniques of cloud modification. The results obtained during simulation of modification indicate that the second part of the first stage of cloud development is the optimal moment for modification initiation.

REFERENCES

1. IMAMDZHANOV, H.: Parametricheskaya model grozo-gradovyh oblakov. (Parametric model of thunderstorm with hail clouds). Trudy SANII Goskomgydrometa. 1984, Nr.100(181), p. 14-21.